

Novel neutral iridium catalysts for effective
hyperpolarisation and hydrogenation:
a synthetic and mechanistic study

Amy Jane Ruddlesden

Doctor of Philosophy

University of York

Chemistry

August 2017

Abstract

Since 2009, when the Signal Amplification By Reversible Exchange (SABRE) process, which transfers polarisation from *parahydrogen* to substrates in a non-hydrogenative manner, was first published, substantial efforts have been made in method optimisation and catalyst development. This work presents multi-step syntheses and studies on a series of novel neutral bidentate iridium carbene complexes, $[\text{Ir}(\text{COD})(\text{R-NHC-O})]$. The carbene ligands have a pendent phenolate group, incorporating the electron-withdrawing substituents, NO_2 , COOMe , Cl and H . The reactivity of each complex with substrate and hydrogen has enabled the identification of several intermediates, including dihydride COD complexes, $[\text{Ir}(\text{H})_2(\text{COD})(\text{R-NHC-O})]$. COD hydrogenation facilitates the formation of SABRE-active pyridyl dihydride species with structures dependent on the R substituent and solvent used. In DCM, the Ir-O bond is stable and complexes of $[\text{Ir}(\text{H})_2(\text{R-NHC-O})(\text{py})_2]$ form. However, in methanol, when the electron density is increased as R is changed to an H substituent, complete Ir-O bond cleavage occurs to form $[\text{Ir}(\text{H})_2(\text{H-NHC-O})^-(\text{py})_3]^+$.

When studied with *parahydrogen*, these complexes act as efficient SABRE catalysts for a variety of substrates in a range of polarity solvents. They undergo the necessary substrate and hydrogen exchange processes, leading to the observation of enhanced NMR signals for pyridine, nicotinamide, nicotine and nicotinaldehyde. The SABRE activity of these neutral catalysts has been optimised and expanded, as polarisation transfer to several amine molecules, including phenethylamine and tryptamine has been demonstrated in DCM. However, selectivity is reduced, as SABRE-active species, C-H activated products and iridium dimer complexes form, particularly at low substrate concentrations. Addition of phosphine ligands to the mixtures inhibits dimer formation and leads to greater ^1H NMR signal enhancements due to stabilisation of the metal complexes.

A study into the *parahydrogenation* of phenylacetylene using the NO_2 -containing catalyst has also been completed. Although it was less reactive than Crabtree's catalyst it proved more stable due to minimal degradation over time.

Table of Contents

Abstract	3
Table of Contents	4
List of Figures	13
List of Tables	37
Acknowledgements	42
Declaration	43
1. Introduction	44
1.1. NMR and the use of hyperpolarisation	45
1.1.1. Optical pumping	47
1.1.2. Dynamic Nuclear Polarisation (DNP)	48
1.1.3. Hydrogen and its spin isomers	49
1.2. Metal carbene and phosphine complexes	53
1.3. Other coordinating ligands	57
1.4. Hydrogenation reactions	58
1.4.1. Heterogeneous catalysts	60
1.4.2. Homogeneous catalysts	61
1.4.3. PASADENA and ALTADENA	63
1.4.3.1. PASADENA	63
1.4.3.2. ALTADENA	63
1.5. NMR and catalysis with parahydrogen	65
1.6. Signal Amplification By Reversible Exchange	67
1.7. Polarisation transfer catalysts	69
1.8. Molecules suitable for polarisation transfer	71
1.9. Potential for MRI	74
1.10. Project aims	77
2. Development of neutral bidentate iridium carbene complexes	78

2.1. Introduction.....	78
2.2. Synthesis of pre-catalyst derivatives.....	83
2.3. Characterisation of pre-catalyst derivatives.....	88
2.4. Reactivity of pre-catalyst derivatives.....	99
2.4.1. Reactivity of 1 in CD ₂ Cl ₂ and C ₆ D ₆	99
2.4.2. Reactivity of 2 in CD ₂ Cl ₂ and C ₆ D ₆	104
2.4.3. Reactivity of 3 in CD ₂ Cl ₂ and C ₆ D ₆	107
2.4.4. Reactivity of 4 in CD ₂ Cl ₂ and C ₆ D ₆	110
2.4.5. Reactivity of 1 in CD ₃ OD.....	111
2.4.6. Reactivity of 2 in CD ₃ OD.....	111
2.4.7. Reactivity of 3 in CD ₃ OD.....	116
2.4.8. Reactivity of 4 in CD ₃ OD.....	117
2.5. Further investigations of complex 2	118
2.6. Rationalising the differences between the catalysts.....	122
2.6.1. UV-visible spectroscopy analysis.....	122
2.6.2. Formation of carbonyl complexes	127
2.7. Conclusion	129
3. Reactivity of neutral bidentate iridium carbene complexes	132
3.1. Introduction.....	132
3.2. Elucidation of the reaction pathway and reactivity of complex 6	139
3.2.1. Hydride signals for complex 6 in CD ₂ Cl ₂	140
3.2.2. Ligand exchange rate analysis for 6	146
3.2.3. Mechanistic studies to determine the effect of pyridine concentration on ligand exchange in 6	151
3.2.4. Analysis of the effect of solvent on exchange	160
3.3. Ligand exchange rates.....	161

3.3.1.	Ligand exchange rate analysis for 8 and 15.....	161
3.3.2.	Ligand exchange rate analysis for 10 _A and 10 _B	165
3.3.3.	Ligand exchange rate analysis for 12 _A , 12 _B and 16.....	166
3.4.	Analysis of pyridine T ₁ relaxation times	168
3.5.	Conclusion	174
4.	Exploiting neutral iridium carbene complexes in SABRE catalysis	177
4.1.	Introduction.....	177
4.2.	Polarisation tests with pyridine.....	181
4.2.1.	Studies using complex 1	181
4.2.1.1.	Initial tests.....	181
4.2.1.2.	Effect of polarisation transfer field.....	183
4.2.1.3.	OPSY NMR experiments	185
4.2.1.4.	Proton signal enhancements as a function of temperature.....	188
4.2.1.5.	SABRE activity in different solvents	192
4.2.2.	Studies using complex 2	197
4.2.3.	Studies using complexes 3 and 4	202
4.3.	Polarisation tests with other substrates	203
4.3.1.	Studies using complex 1 with nicotinamide	203
4.3.1.1.	Initial tests.....	203
4.3.1.2.	Effect of polarisation transfer field.....	207
4.3.1.3.	OPSY NMR experiments	208
4.3.1.4.	Proton signal enhancements as a function of temperature.....	210
4.3.2.	Studies using complex 2 with nicotinaldehyde	212
4.3.3.	Studies using complex 2 with nicotine	216
4.4.	Conclusion	220
5.	Optimisation of SABRE catalysis for a new ligand class	222

5.1. Introduction.....	222
5.2. Analysing polarisation transfer to amines.....	227
5.2.1. Ammonia	228
5.2.2. Benzylamine	229
5.2.3. Phenethylamine.....	233
5.2.4. Tryptamine.....	236
5.2.5. Summary	238
5.3. Exploiting PPh ₃ to aid complex stabilisation.....	239
5.3.1. Addition of PPh ₃ to samples containing pyridine.....	239
5.3.2. Benzylamine	244
5.3.3. Phenethylamine.....	246
5.3.4. Tryptamine.....	248
5.4. Use of other phosphines.....	250
5.4.1. PCy ₃	251
5.4.2. P ⁱ Pr ₃	256
5.4.3. PBz ₃	257
5.4.4. PPh ₂ Cy.....	259
5.4.5. Summary	260
5.5. Conclusion	261
6. Kinetic studies on the hydrogenation activity of a series of neutral iridium carbene catalysts.....	262
6.1. Introduction.....	262
6.2. Monitoring the parahydrogenation of phenylacetylene	269
6.2.1. The use of ¹ H OPSY NMR spectroscopy to study reaction kinetics	270
6.2.2. Hydrogenation of phenylacetylene using Crabtree's catalyst.....	272
6.2.3. Hydrogenation of phenylacetylene using the neutral bidentate carbene complexes	276

6.3.	Monitoring the parahydrogenation of styrene	281
6.4.	Elucidating the hydrogenation mechanisms	283
6.5.	Conclusion	288
7.	Conclusions and future studies	289
7.1.	Development of neutral bidentate iridium carbene complexes	289
7.2.	SABRE reactivity of neutral bidentate iridium carbene complexes	299
7.3.	Hydrogenation activity of neutral bidentate iridium carbene complexes	305
7.4.	Summary	308
8.	Experimental	309
8.1.	Calculations	309
8.1.1.	Method for calculating standard errors	309
8.1.2.	Arrhenius and Eyring-Polanyi equations used to calculate activation parameters	310
8.2.	Modelling ligand exchange	311
8.2.1.	Modelling pyridine ligand exchange in complexes of $[\text{Ir}(\text{H})_2(\text{R-NHC-O})(\text{py})_2]$	311
8.2.2.	Modelling pyridine ligand exchange in complexes of $[\text{Ir}(\text{H})_2(\text{R-NHC-O}^-)(\text{py})_3]^+$	312
8.2.3.	Modelling H_2 ligand exchange in complexes of $[\text{Ir}(\text{H})_2(\text{R-NHC-O})(\text{py})_2]$	313
8.2.4.	Modelling H_2 ligand exchange in complexes of $[\text{Ir}(\text{H})_2(\text{R-NHC-O}^-)(\text{py})_3]^+$	314
8.3.	Polarisation methods for NMR experiments	315
8.3.1.	Method A ²	315
8.3.2.	Method B ⁸⁸	315
8.3.3.	Calculation of ¹ H NMR enhancement factors	316
8.4.	General information	317

8.4.1. NMR	317
8.4.2. X-ray Crystallography	317
8.4.3. UV-vis and IR	318
8.4.4. Mass Spectrometry	318
8.4.5. Elemental Analysis	318
8.5. Precursor synthesis.....	319
8.5.1. 1-(2,4,6-trimethylphenyl)-1H-imidazole ¹²⁵	319
8.5.2. [Ir(COD)Cl] ₂ ¹⁴⁶	320
8.6. NO ₂ carbene synthesis	321
8.6.1. 3-(2-hydroxy-5-nitrobenzyl)-1-(2,4,6-trimethylphenyl) imidazolium bromide ¹²⁵	321
8.6.2. Silver(I) 3-(2-methylene-4-nitrophenolate)-1-(2,4,6-trimethylphenyl) imidazolylidene ¹²⁵	323
8.6.3. Iridium(I) (3-(2-methylene-4-nitrophenolate)-1-(2,4,6-trimethylphenyl) imidazolylidene)(cyclooctadiene), 1 ¹⁴⁶	324
8.6.4. Iridium(III) (3-(2-methylene-4-nitrophenolate)-1-(2,4,6-trimethylphenyl) imidazolylidene)(dihydride)(pyridine) ₂ , 6A	328
8.6.5. Iridium(I) (3-(2-methylene-4-nitrophenolate)-1-(2,4,6-trimethylphenyl) imidazolylidene)(dicarbonyl), 17.....	329
8.6.6. Iridium carbene phenethylamine dimer, 21 _{phenethylamine}	330
8.6.7. Iridium(III) (3-(2-methylene-4-nitrophenolate)-1-(2,4,6-trimethylphenyl) imidazolylidene)(hydride)(benzylamine)(C-H activated benzylamine), 22 _{benzylamine}	332
8.6.8. Iridium(III) (3-(2-methylene-4-nitrophenolate)-1-(2,4,6-trimethylphenyl) imidazolylidene)(hydride)(tryptamine)(C-H activated tryptamine), 22 _{tryptamine}	333
8.6.9. Iridium(III) (3-(2-methylene-4-nitrophenolate)-1-(2,4,6-trimethylphenyl) imidazolylidene)(dihydride)(pyridine)(triphenylphosphine), 23 _{pyridine}	336

8.6.10. Iridium(III) (3-(2-methylene-4-nitrophenolate)-1-(2,4,6-trimethylphenyl) imidazolylidene)(dihydride)(pyridine)(triphenylphosphine), 24 _{pyridine}	339
8.6.11. Iridium(III) (3-(2-methylene-4-nitrophenolate)-1-(2,4,6-trimethylphenyl) imidazolylidene)(dihydride)(PPh ₃) ₂ , 25	340
8.6.12. Iridium(III) (3-(2-methylene-4-nitrophenolate)-1-(2,4,6-trimethylphenyl) imidazolylidene)(PCy ₃)(phenethylamine)(dihydride), 26 _{PCy₃}	343
8.6.13. Iridium(III) (3-(2-methylene-4-nitrophenolate)-1-(2,4,6-trimethylphenyl) imidazolylidene)(PR ₃)(phenethylamine)(dihydride), 27	344
8.6.14. [Ir(H) ₅ (PCy ₃) ₂], 28 _{PCy₃}	346
8.6.15. [Ir(H) ₂ (MeCN) ₂ (PCy ₃) ₂][BF ₄]	347
8.6.16. Iridium(III) (3-(2-methylene-4-nitrophenolate)-1-(2,4,6-trimethylphenyl) imidazolylidene)(P ⁱ Pr ₃) ₂ (dihydride), 29	348
8.6.17. Iridium(III) (3-(2-methylene-4-nitrophenolate)-1-(2,4,6-trimethylphenyl) imidazolylidene)(PR ₃) ₂ (dihydride), 30	349
8.7. H carbene synthesis	351
8.7.1. 2-benzyloxybenzaldehyde	351
8.7.2. 2-benzyloxybenzyl alcohol ¹⁴⁸	352
8.7.3. 2-benzyloxybenzyl bromide	353
8.7.4. 3-(2-benzyloxy benzyl)-1-(2,4,6-trimethylphenyl) imidazolium bromide	354
8.7.5. 3-(2-hydroxy benzyl)-1-(2,4,6-trimethylphenyl) imidazolium bromide	355
8.7.6. Silver(I) 3-(2-methylenephenolate)-1-(2,4,6-trimethylphenyl) imidazolylidene.....	356
8.7.7. Iridium(I) (3-(2-methylenephenolate)-1-(2,4,6-trimethylphenyl) imidazolylidene)(cyclooctadiene), 2.....	357
8.7.8. Iridium(III) (3-(2-methylenephenolate)-1-(2,4,6-trimethylphenyl) imidazolylidene)(dihydride)(pyridine) ₂ , 8.....	360

8.7.9. Iridium(I) (3-(2-methylenephenoxide)-1-(2,4,6-trimethylphenyl)imidazolylidene)(cyclooctadiene)(pyridine), 13.....	362
8.7.10. Iridium(III) (3-(2-methylenephenoxide)-1-(2,4,6-trimethylphenyl)imidazolylidene)(cyclooctadiene)(dihydride)(pyridine), 14.....	363
8.7.11. Iridium(III) (3-(2-methylenephenoxide)-1-(2,4,6-trimethylphenyl)imidazolylidene)(dihydride)(pyridine) ₃ , 15.....	364
8.7.12. Iridium(I) (3-(2-methylenephenolate)-1-(2,4,6-trimethylphenyl)imidazolylidene)(dicarbonyl), 18.....	365
8.8. COOMe carbene synthesis.....	366
8.8.1. Methyl 4-benzyloxy-3-formyl benzoate.....	366
8.8.2. Methyl 4-benzyloxy-3-hydroxymethyl benzoate.....	367
8.8.3. Methyl 4-benzyloxy-3-bromomethyl benzoate.....	368
8.8.4. 3-(methyl 4-benzyloxy-3-benzyl benzoate)-1-(2,4,6-trimethylphenyl)imidazolium bromide.....	369
8.8.5. 3-(methyl 3-benzyl-4-hydroxy benzoate)-1-(2,4,6-trimethylphenyl)imidazolium bromide.....	370
8.8.6. Iridium(I) (3-(methyl 3-benzyl-4-hydroxy benzoate)-1-(2,4,6-trimethylphenyl)imidazolylidene)(cyclooctadiene), 3.....	371
8.8.7. Iridium(III) (3-(methyl 3-benzyl-4-hydroxy benzoate)-1-(2,4,6-trimethylphenyl)imidazolylidene)(dihydride)(pyridine) ₂ , 10 _A and 10 _B ...	375
8.8.8. Iridium(I) (3-(methyl 3-benzyl-4-hydroxy benzoate)-1-(2,4,6-trimethylphenyl)imidazolylidene)(dicarbonyl), 20.....	377
8.9. Cl carbene synthesis.....	378
8.9.1. 4-hydroxy-4-(2-benzyloxy-5-chlorophenyl)-2-butanone.....	378
8.9.2. 2-benzyloxy-5-chloro benzaldehyde.....	379
8.9.3. 2-benzyloxy-5-chloro benzyl alcohol.....	380
8.9.4. 2-benzyloxy-5-chloro benzaldehyde dimethyl acetal.....	381
8.9.5. 2-benzyloxy-5-chloro benzaldehyde.....	382

8.9.6. 2-benzyloxy-5-chloro benzyl alcohol	383
8.9.7. 2-benzyloxy-5-chloro benzyl bromide.....	384
8.9.8. 3-(2-benzyloxy-5-chloro benzyl)-1-(2,4,6-trimethylphenyl) imidazolium bromide	385
8.9.9. 2-(tert-butyldimethylsilyloxy)-5-chloro benzaldehyde	386
8.9.10. 2-(tert-butyldimethylsilyloxy)-5-chloro benzyl alcohol	387
8.9.11. 2-(tert-butyldimethylsilyloxy)-5-chloro benzyl bromide	388
8.9.12. 3-(5-chloro-2-hydroxybenzyl)-1-(2,4,6-trimethylphenyl) imidazolium bromide	389
8.9.13. Iridium(I) (3-(5-chloro-2-methylene phenolate)-1-(2,4,6-trimethylphenyl) imidazolylidene)(cyclooctadiene), 4.....	390
8.9.14. Iridium(III) (3-(5-chloro-2-methylene phenolate)-1-(2,4,6- trimethylphenyl)imidazolylidene)(dihydride)(pyridine) ₂ , 12 _A and 12 _B ...	393
8.9.15. Iridium(III) (3-(5-chloro-2-methylene phenoxide)-1-(2,4,6- trimethylphenyl)imidazolylidene)(dihydride)(pyridine) ₃ , 16.....	395
8.9.16. Iridium(I) (3-(5-chloro-2-methylene phenolate)-1-(2,4,6-trimethylphenyl) imidazolylidene)(dicarbonyl), 19	396
Abbreviations	397
References.....	399

List of Figures

Figure 1: Energy levels present when a sample containing spin- $\frac{1}{2}$ nuclei is in a magnetic field and the Zeeman effect that occurs when the magnetic field is increased	45
Figure 2: Optical pumping of rubidium due to its absorption of circularly polarised light ⁸	47
Figure 3: Structures of organic radicals used for DNP ¹⁰	48
Figure 4: Apparatus used to form parahydrogen from normal hydrogen (Reprinted from Duckett, S. B.; Wood, N. J. <i>Coord. Chem. Rev.</i> 2008, 252, 2278, Copyright © 2008 with permission from Elsevier) ¹⁶	50
Figure 5: The proportion of parahydrogen increases as the temperature decreases (Reprinted from Green, R. A.; Adams, R. W.; Duckett, S. B.; Mewis, R. E.; Williamson, D. C.; Green, G. G. R. <i>Prog. Nucl. Magn. Reson. Spectrosc.</i> 2012, 67, 1, Copyright © 2012 with permission from Elsevier) ¹	51
Figure 6: The possible transitions in a two-spin system	51
Figure 7: The populated spin states of normal H ₂ and p-H ₂ and their corresponding NMR spectra resulting from the spin transitions shown	52
Figure 8: Formation of [W(CO) ₅ (COCH ₃ (Ph))] ²³	53
Figure 9: Resonance structures for Fischer-type carbenes	53
Figure 10: Formation of the stable Arduengo carbene, 1,3-di-1-adamantylimidazol-2-ylidene ²⁸	54
Figure 11: Tolman Cone Angle for phosphine ligands ³⁰	55
Figure 12: Formation of [Ta(CHC(CH ₃) ₃)(CH ₂ C(CH ₃) ₃) ₃] ^{23, 32}	55
Figure 13: Bonding in Fischer, Schrock and N-heterocyclic carbenes	56
Figure 14: First generation (A) and second generation (B) Grubbs catalysts containing Schrock carbenes ³³⁻³⁴	56

Figure 15: Bonding interactions for ligands commonly used in metal catalysts	57
Figure 16: Transitions and spectrum resulting from hydrogenation of e.g. an alkene using normal hydrogen.....	58
Figure 17: Reduction of CO ₂ with H ₂ using an aminoborane complex ⁴⁷	59
Figure 18: H ₂ addition to an aromatic triphosphenylbenzene leads to P=C bond hydrogenation followed by a hydride shift leading to a bicyclo product (Reprinted with permission from Longobardi, L. E.; Russell, C. A.; Green, M.; Townsend, N. S.; Wang, K.; Holmes, A. J.; Duckett, S. B.; McGrady, J. E.; Stephan, D. W., J. Am. Chem. Soc. 2014, 136 (38), 13453 Copyright © 2014 American Chemical Society)	59
Figure 19: Steps involved in heterogeneous hydrogenation of a double bond on a metal surface ⁵⁹	60
Figure 20: Mechanism for hydrogenation using [RhCl(PPh ₃) ₃] ⁶⁸	61
Figure 21: Mechanism for hydrogenation using [Ir(COD)(L) ₂] ⁺⁶⁹	62
Figure 22: Chiral ligands R-BINAP (A) and PHOX (B) used for enantioselective synthesis	62
Figure 23: The populated spin states, transitions and resulting spectra from hydrogenation using parahydrogen under PASADENA conditions (A) and ALTADENA conditions (B).....	64
Figure 24: Hydrogenation of acrylonitrile to propionitrile to demonstrate signal enhancements using p-H ₂ . ¹ H NMR spectra before reaction was conducted (a), during hydrogenation (b), after the enhancement had decayed (c) and a simulation of the enhanced spectra from the theory (d) (Reprinted with permission from Bowers, C. R.; Weitekamp, D. P. J. Am. Chem. Soc. 1987, 109, 5541. Copyright © 1987 American Chemical Society) ⁷⁷	65
Figure 25: Vinyl hydride and alkyl hydride intermediates on the pathway to hydrogenation of diphenylacetylene using [Pd(PEt ₃) ₂ (OTf) ₂] with p-H ₂ ⁸²	66
Figure 26: The route to polarisation transfer via SABRE.....	67

Figure 27: Schematic for how chemical shift differences between nuclei increase as the magnetic field is increased	68
Figure 28: $[\text{Ir}(\text{H})_2(\text{IMes})_3]\text{Cl}$ formed upon activation of $[\text{Ir}(\text{COD})(\text{IMes})\text{Cl}]$ with substrate and H_2 , via intermediate $[\text{Ir}(\text{COD})(\text{IMes})(\text{sub})]\text{Cl}$	69
Figure 29: Formation of the mixed substrate species $[\text{Ir}(\text{H})_2(\text{IMes})(\text{PCy}_3)(\text{pyridine})(\text{CH}_3\text{CN})][\text{BF}_4]$ and equilibration with the $[\text{Ir}(\text{H})_2(\text{IMes})(\text{PCy}_3)(\text{substrate})_2][\text{BF}_4]$ complexes (where Mes = 2,4,6-trimethylphenyl) ⁸⁶	70
Figure 30: $[\text{Ir}(\text{H})_2(\text{PNP})(\text{py})][\text{BF}_4]$ and the formation of the dihydride-dihydrogen intermediate $[\text{Ir}(\text{H})_2(\text{H}_2)(\text{PNP})][\text{BF}_4]$ ⁹⁸	70
Figure 31: The formation of dimethyl maleate from the parahydrogenation of dimethyl acetylenedicarboxylate with the p- H_2 derived protons labelled with an asterisk. Cat. = $[\text{Rh}(\text{COD})(\text{dppb})(\text{PPh}_3)_2][\text{BF}_4]$ where dppb is 1,4-bis(diphenylphosphino)butane ^{102, 106}	72
Figure 32: 50 MHz ^{13}C NMR spectrum of dimethyl maleate produced from the parahydrogenation of dimethyl acetylenedicarboxylate (Reprinted with permission from Barkemeyer, J.; Haake, M.; Bargon, J. J. Am. Chem. Soc. 1995, 117, 2927. Copyright © 1995 American Chemical Society) ¹⁰⁶	72
Figure 33: A plot showing how the ^1H NMR signal enhancement for acetonitrile varies when using $[\text{Ir}(\text{H})_2(\text{IMes})(\text{PPh}_3)(\text{pyridine})(\text{acetonitrile})][\text{BF}_4]$ at different polarisation transfer fields and how using deuterated ligands affects the observed enhancement levels (Reprinted with permission from Fekete, M.; Bayfield, O.; Duckett, S. B.; Hart, S.; Mewis, R. E.; Pridmore, N.; Rayner, P. J.; Whitwood, A., Inorg. Chem. 2013, 52 (23), 13453-13461. Copyright © 2013 American Chemical Society AuthorChoice via Creative Commons CC-BY agreement http://pubs.acs.org/page/policy/authorchoice_ccby_termsfuse.html) ⁸⁶	73
Figure 34: Water-soluble phosphine and NHC ligands incorporated into catalysts ¹¹⁴⁻¹¹⁵	75
Figure 35: Heterogeneous SABRE catalysts ¹¹⁸⁻¹¹⁹	76

Figure 36: A potential framework for a bidentate NHC-containing iridium complex ...	77
Figure 37: General synthetic route to form symmetric iridium carbene complexes.....	78
Figure 38: The mechanism for formation of the imidazole ring of mesityl imidazole...	79
Figure 39: Synthetic route to form asymmetric imidazolium salts used by He et al. ¹²⁹ .	79
Figure 40: Synthetic route to form asymmetric iridium carbene complexes used by Fürstner et al. ¹³⁰	80
Figure 41: Chiral bidentate phosphorus-derived ligands for asymmetric hydroformylation ¹³³	80
Figure 42: Reaction of trans-[Ir(CO)(PPh ₃) ₂ (OR)] with CO and TCNE ¹³⁴⁻¹³⁵	81
Figure 43: Iridium(I) NHC phenoxide complex and its conversion to an iridium(III) bis-phenolate COD species and an iridium(III) bis-phenolate acetonitrile complex, as described by Weinberg et al. ¹⁴⁴	82
Figure 44: Synthetic route to the NO ₂ -containing complex, 1.....	83
Figure 45: Synthetic procedure to form complexes 2 and 3	84
Figure 46: Reaction scheme to form the aldol condensation product along with its ¹ H NMR spectrum showing its ¹ H NMR resonances and splitting patterns (labelled structure inset).....	85
Figure 47: Modified synthetic procedure to form complex 4 using TBDMSCl to create the TBDMS phenol protecting group.....	87
Figure 48: Labels for complex 1, as referred to in the text.....	88
Figure 49: Comparison of the ¹ H NMR spectra, at 253 K and 298 K, for complex 1 in CD ₂ Cl ₂ . Regions of interest, where the fluxional behaviour slows to allow the detection of separate peaks, are indicated with the dashed lines. The labels indicate the proton resonances as shown in Figure 48 with the specific changes referred to in the text.....	89

Figure 50: Lineshape analysis equations ¹⁵¹ and corresponding ¹ H NMR spectra used to calculate the mesityl group rotation rates.....	90
Figure 51: Eyring-Polanyi plot of rate data calculated from experimental ¹ H NMR spectra for mesityl rotation in complex 1 as a function of temperature.....	91
Figure 52: ¹³ C{ ¹ H} NMR spectra of 1 at 243 K and 298 K specifically depicting the resolved ¹³ C signals for the C-Ir atom at ~ δ 175 and two COD C-H atoms at ~ δ 85 ...	92
Figure 53: ORTEP plot of 1 with H atoms removed for clarity and the thermal ellipsoids set at a 50 % probability level	92
Figure 54: Line drawing of complex 2 showing the labelling scheme employed	96
Figure 55: ¹ H NMR spectrum of 2 in CD ₂ Cl ₂ at 298 K, showing the inequivalent CH ₂ linker protons, labelled as 7 and the COD alkene protons (* indicates the residual solvent peak)	97
Figure 56: ORTEP plot of 3 with H atoms removed for clarity and the thermal ellipsoids set at a 50 % probability level	97
Figure 57: Oxidative addition of H ₂ to 1 in CD ₂ Cl ₂ leads to the formation of two isomers of 5, 5 _A and 5 _B . These species yield the diagnostic temperature-sensitive hydride resonances shown in the ¹ H NMR spectra on the right	99
Figure 58: [Ir(H) ₂ (COD)(NCCH ₃)(PMe ₃)] [BF ₄] formed when H ₂ adds to [Ir(COD)(NCCH ₃)(PMe ₃)] [BF ₄] ¹⁵⁸	100
Figure 59: An example of an iridium-pyridylpyrrolide complex which exhibits reversible binding of H ₂ ¹⁵⁹	101
Figure 60: The reaction of 1 with pyridine and hydrogen forms 6 in CD ₂ Cl ₂	101
Figure 61: ¹ H EXSY ¹⁶³ NMR spectra showing nOe signals of 6 _A when selectively exciting the signal for H _A (A) and the signal for H _B (B). The hydride resonances for 6 _B are also seen	103
Figure 62: Potential structure formed when 6 is reacted with Et ₃ SiH and the corresponding ¹ H NMR spectra of the hydride region after addition of increasing	

equivalents of Et ₃ SiH, from 0 eq. to 5 eq. (A to F) showing no change in the hydride signals (* denotes singlet hydride species discussed in Section 3.2).....	104
Figure 63: Reaction of 2, in CD ₂ Cl ₂ / C ₆ D ₆ , with H ₂ leads to the formation of the major dihydride complex 7 _A which then forms the bis-pyridyl iridium species, 8, after COD hydrogenation in the presence of pyridine. 8 is a product in which the Ir-O bond is retained.....	105
Figure 64: ¹ H NMR spectra of the aromatic and hydride regions of a solution containing 8 after the reaction of 2 with pyridine and hydrogen in CD ₂ Cl ₂ (A) and in C ₆ D ₆ (B) at 294 K (* denotes free pyridine in solution)	107
Figure 65: 10 _A and 10 _B formed from the reaction of 3 with pyridine and hydrogen in CD ₂ Cl ₂	108
Figure 66: ¹ H COSY NMR spectrum of a CD ₂ Cl ₂ sample of 10 _A and 10 _B , showing coupling between the hydride signals at δ -21.95 and -28.48 and those at δ -22.56 and -25.47	108
Figure 67: 2D ¹ H NOESY NMR experiment of a CD ₂ Cl ₂ sample of 10 _A and 10 _B at 303 K showing exchange between all four hydride ligands of 10 _A and 10 _B	109
Figure 68: Two conformational isomers, 12 _A and 12 _B present in CD ₂ Cl ₂ and C ₆ D ₆	110
Figure 69: ¹ H NMR spectra showing the aromatic and hydride regions for samples of 12 _A and 12 _B in CD ₂ Cl ₂ (A) and C ₆ D ₆ (B). The inset image shows the four bound pyridine environments in CD ₂ Cl ₂ (*)......	111
Figure 70: Complex 2 and the intermediate, 13, formed on the addition of pyridine...	112
Figure 71: Formation of 14 upon addition of hydrogen to 13 and subsequent formation of 15 on warming the sample.....	113
Figure 72: ¹ H NMR spectrum of the aromatic and hydride regions after the reaction of 2 with pyridine and hydrogen, in CD ₃ OH, to form 15 showing the singlet hydride signal	113

Figure 73: Aromatic region of the ^1H NMR spectra of complex 13 (left-hand side), with signals for free pyridine indicated by * and the signal for the ortho proton of the bound pyridine ligand of complex 13 indicated by * (A). On addition of H_2 the formation of 14 is indicated by a significant change in the chemical shift of the ortho proton of the bound pyridine ligand in 14 shown by * (B). The meta and para protons of the bound pyridine ligands in 13 and 14 overlap due to incomplete conversion to 14. A similar shift is observed for the COD CH protons, shown on the right-hand side.....	115
Figure 74: 10_{A} that forms in methanol.....	116
Figure 75: 12_{A} and 16 present in a CD_3OH sample of 4 with pyridine and H_2	117
Figure 76: Equilibrium constant between 8 and 15 and the initial concentrations of 2 and pyridine.....	118
Figure 77: Linear Van't Hoff equation and reaction coordinate diagram for an exothermic reaction.....	119
Figure 78: Linear Van't Hoff plot for calculating standard enthalpy and entropy changes for the equilibrium between complex 8 binding pyridine, to form complex 15.....	120
Figure 79: Reaction of 8 with formic acid leads to Ir-O bond cleavage and the formation of 15 now containing a protonated phenol side arm, along with production of protonated pyridine which inhibits SABRE.....	121
Figure 80: Chemical shift changes observed on addition of increasing equivalents of formic acid (0 to 15 equivalents, indicated by *) to a CD_2Cl_2 solution of 8 to form protonated 15 and protonated free pyridine (labelled ortho, para and meta ^1H NMR signals) (A) 0 eq., (B) 3 eq., (C) 6 eq., (D) 9 eq., (E) 12 eq. and (F) 15 eq.	121
Figure 81: Ruthenium bis-phosphine complexes with substituents containing varying electron-withdrawing and donating capabilities	123
Figure 82: UV-vis spectra in methanol of $[\text{Ir}(\text{COD})(\text{IMes})\text{Cl}]$ (A) and 2 (C) showing the three absorption bands in the visible region and the disappearance of these bands upon activation with pyridine and hydrogen to form $[\text{Ir}(\text{H})_2(\text{IMes})(\text{py})_3]\text{Cl}$ (B) and 15 (D) respectively	124

Figure 83: UV-vis spectra for the photolysis of colourless $[\text{IrCl}(\text{CO})(\text{PPh}_3)_2(\text{O}_2)]$ at 366 nm to reform the coloured square planar $[\text{IrCl}(\text{CO})(\text{PPh}_3)_2]$ complex with its three absorption bands (Reprinted with permission from Geoffroy, G. L.; Hammond, G. S.; Gray, H. B. J. Am. Chem. Soc. 1975, 97, 3933. Copyright © 1975 American Chemical Society) ¹⁶⁸	125
Figure 84: The three absorption bands present for 2 in DCM, methanol and benzene with no indication for solvatochromism, commensurate with no change in absorption maxima in the different solvents	125
Figure 85: Comparison of the absorption spectra for the Ir(I) complexes (A) 1, (B) 3, (C) 4, (D) 2 and (E) $[\text{Ir}(\text{COD})(\text{IMes})\text{Cl}]$	126
Figure 86: The structure of the $[\text{Ir}(\text{R-NHC-O})(\text{CO})_2]$ complexes developed here (left) and their corresponding IR spectra of the CO region (right)	128
Figure 87: Examples of Fe-PNNP catalysts, for transfer hydrogenation of acetophenone, and half-sandwich Ir-NHC complexes used for transfer hydrogenation of ketones and imines, with different derivatives providing different activities in each reaction ¹⁷³	132
Figure 88: Palladium complexes used for cross-coupling boronic acids with an aromatic moiety containing a suitable leaving group, and the range of substituted Buchwald phosphine ligands that can be used ¹⁷⁴	133
Figure 89: Pd-NHC complexes used in cross-coupling reactions as described by Fang et al. ¹⁷⁶	134
Figure 90: Asymmetric hydrogenation of β -aryl ketoesters using $[\text{RuCl}_2(4,4'-(\text{R})\text{-BINAP})]$ catalysts containing a number of different R groups ¹⁸⁰	134
Figure 91: Iridium alkoxo complexes and the β -hydrogen elimination reaction (Adapted with permission from Zhao, J.; Hesslink, H.; Hartwig, J. F. J. Am. Chem. Soc. 2001, 123, 7220. Copyright © 2001 American Chemical Society) ¹⁸¹	135
Figure 92: Ester hydrolysis reaction studied by Hammett and the subsequent equation used to calculate corresponding σ_p values for substituents, R ¹⁸²⁻¹⁸³	136

Figure 93: The ionisation of substituted phenols used to calculate the corresponding Hammett values, σ_p^- , for substituents, R, where the same equation as shown in Figure 92 is used ¹⁴⁵	137
Figure 94: Hammett plot for β -hydrogen elimination from complexes A to D detailed in Table 13 (Reprinted with permission from Zhao, J.; Hesslink, H.; Hartwig, J. F. J. Am. Chem. Soc. 2001, 123, 7220. Copyright © 2001 American Chemical Society) ¹⁸¹	138
Figure 95: The hydride region of the ¹ H NMR spectrum of a solution containing 1, pyridine and hydrogen in CD ₂ Cl ₂ at 298 K after activation for 48 hours	139
Figure 96: Products formed by the reaction of 1 with pyridine and H ₂	140
Figure 97: ¹ H NMR spectra of the two main hydride signals for 6 showing how the peaks resolve as the temperature is decreased from 303 to 223 K. The rate of interconversion between the two conformers, 6 _A and 6 _B (drawn above) is slowed which leads to the peak resolution	141
Figure 98: 2D ¹ H NOESY NMR spectrum at 233 K showing both nOe interactions (red) and exchange (blue) between the hydride resonances of the two conformational isomers of 6	142
Figure 99: Kinetic model for the conversion between the major isomer 6 _A and the minor isomer 6 _B assuming a simple intramolecular interconversion	142
Figure 100: Plot showing the conversion of 6 _A into 6 _B upon the selective excitation of H _A	144
Figure 101: Plot showing the conversion of 6 _B into 6 _A upon the selective excitation of H _A '	144
Figure 102: Summary of possible isomer forms present for the bidentate iridium carbene dihydride complexes in solution and the intermediate that occurs on pyridine dissociation.....	145
Figure 103: 2D ¹ H NOESY NMR spectrum at 298 K showing hydride ligand exchange in 6.....	146

Figure 104: The proportions of 6_{HH} and 6_{HD} determined by integration, on analysing the deuterium incorporation into the hydride signal of 6_{HH} at $\delta -29.22$ at 270 K in CD_3OD	147
Figure 105: An Eyring-Polanyi plot for pyridine and H_2 dissociation and hydride interconversion as a function of temperature, for a CD_3OH sample of 6 mol% 1 and 0.08 M pyridine under H_2	150
Figure 106: The rates of pyridine and hydride loss from 6 in CD_2Cl_2 in relation to the number of equivalents of pyridine added, calculated by integration. The data for pyridine loss and hydride interconversion are on the left scale and the data for H_2 loss are on the right scale	152
Figure 107: The rates of pyridine and hydride loss from 6 in CD_3OH in relation to the number of equivalents of pyridine added, calculated by integration. The data for pyridine and H_2 loss are on the left scale and the data for hydride interconversion are on the right scale	152
Figure 108: Four examples of stable 16-electron iridium dihydride species containing pincer ligands ¹⁸⁴⁻¹⁸⁷	153
Figure 109: Iridium dihydride-dihydrogen complexes which undergo facile hydride-hydrogen interconversion ^{189, 193-195}	154
Figure 110: Demonstrating the Berry pseudorotation mechanism occurring in trigonal bipyramidal PF_5 , which exchanges the axial F ligands with two of the equatorial F ligands via a square-based pyramidal intermediate ¹⁹⁸	155
Figure 111: Bailar and Ray-Dutt twist mechanisms for interconversion of tris-chelated aluminium complexes containing α -isopropenyltropolonate or α -isopropyltropolonate ligands	155
Figure 112: Iridium complexes containing dihydrogen bonded functionalities ²⁰⁵⁻²⁰⁷ and the reactivities of two specific examples showing H_2 loss ²⁰⁸ and hydride-hydrogen interconversion ²⁰⁹⁻²¹⁰	156

Figure 113: Equilibrium between the iridium dihydride complex and the iridium dihydrogen complex described by Gottker-Schnetmann et al. ²¹¹	157
Figure 114: Formation of 6 from 1 with the vacant site represented through the shaded orbital and the blue and magenta hydride ligand labels detailing the hydride interchange processes. Contributing to the rate of hydride interconversion, <i>k_{hydride interconversion}</i> , is both route A (including the rate of pyridine loss, <i>k_{py loss}</i> , and the rate of formation of the dihydrogen complex, <i>k_{η2 – H2 formation}</i>) and route B (intramolecular switching)	159
Figure 115: Reaction of 2 with pyridine and hydrogen in CD ₂ Cl ₂ or C ₆ D ₆ to form 8 and in CD ₃ OD to form 15	161
Figure 116: An Eyring-Polanyi plot for pyridine exchange and hydride-hydrogen exchange at differing temperatures in CD ₃ OH for a sample containing 8 mol% 2 and 0.07 M pyridine	163
Figure 117: Possible interactions between pyridine and benzene, DCM, methanol and ethanol	169
Figure 118: The dependence of the T ₁ relaxation time on the rotational correlation time, τ _c of a molecule. For pyridine, its τ _c value lies to the left of the minimum point, with an increase in viscosity of the solution causing a decrease in the both the correlation time and the T ₁ value.....	169
Figure 119: Summary of isomer forms and the interconversion processes that occur for the bidentate iridium carbene dihydride complexes in solution.....	175
Figure 120: Iridium dihydride bis-pyridine fragment showing magnetic inequivalence of the hydride ligands due to their different coupling values to the protons of the pyridine ligands	177
Figure 121: Observation by Eisenschmid et al. ²²² showing the magnetic inequivalence of the p-H ₂ derived protons due to their different couplings to the deuterium atoms of the 1,1,2,2-tetradeuteroethane product.....	178

Figure 122: Isomer interconversion between cis-cis-cis-[Ru(H) ₂ L ₂ (CO) ₂] and trans-cis-cis-[Ru(H) ₂ L ₂ (CO) ₂] ²²³ and the formation of the ¹³ C-containing derivative with different couplings	179
Figure 123: Structures of [Ru(H) ₂ (PPh ₃) ₃ (CO)], showing its chemically inequivalent hydride ligands, and cis-[Ru(H) ₂ (dppe) ₂], showing its magnetically inequivalent hydride ligands due to their different coupling values to the ³¹ P nuclei highlighted in red.....	180
Figure 124: Pyridine showing labelling of protons and their positions within the heterocycle with respect to the nitrogen binding atom	181
Figure 125: ¹ H NMR spectra of a sample containing 0.1 M pyridine and 5 mol% 1 in CD ₃ OD under 3 bars of H ₂ after; (A) thermal equilibrium at high field; and (B) polarisation transfer from p-H ₂ at 6.5 x 10 ⁻³ T and 60 °C	182
Figure 126: ¹³ C NMR spectra of a sample containing 0.1 M pyridine and 5 mol% 1 in CD ₃ OD after polarisation transfer at; (A) 60 °C and 6.5 x 10 ⁻³ T; (B) 60 °C and 2 x 10 ⁻³ T	183
Figure 127: ¹ H NMR spectra field plots of a sample containing 0.1 M pyridine and 5 mol% 1 in CD ₃ OD after polarisation transfer from p-H ₂ at r.t. and varying PTF; (A) H _{A/E} ; (B) H _C ; (C) H _{B/D}	184
Figure 128: The ¹ H OPSY NMR pulse sequence	186
Figure 129: ¹ H OPSY-dq NMR spectra of a sample containing 0.1 M pyridine and 5 mol% 1 in CD ₃ OD after polarisation transfer at; (A) 0 °C and 6.5 x 10 ⁻³ T; (B) 60 °C and 6.5 x 10 ⁻³ T.....	186
Figure 130: ¹ H OPSY-dq NMR spectra of a sample containing 0.1 M pyridine and 5 mol% 1 in CD ₃ OD after polarisation transfer at r.t. and; (A) 2.5 x 10 ⁻³ T; (B) 0 x 10 ⁻⁴ T; (C) -2.5 x 10 ⁻³ T; (D) -5 x 10 ⁻³ T; (E) -6.5 x 10 ⁻³ T; (F) -7.5 x 10 ⁻³ T; (G) -1 x 10 ⁻² T; (H) -1.25 x 10 ⁻² T; (I) -1.5 x 10 ⁻² T	187
Figure 131: Pyridine proton enhancements as a function of temperature after polarisation transfer from p-H ₂ using 5 mol% 1 and 0.1 M pyridine at 2 x 10 ⁻⁴ T	188

Figure 132: Pyridine proton enhancements as a function of temperature after polarisation transfer from p-H ₂ using 5 mol% 1 and 0.1 M pyridine at 6.5 x 10 ⁻³ T ...	189
Figure 133: Pyridine proton enhancements as a function of temperature after polarisation transfer from p-H ₂ using 5 mol% [Ir(COD)(IMes)Cl] and 0.1 M pyridine at 2 x 10 ⁻⁴ T	190
Figure 134: Pyridine proton enhancements as a function of temperature after polarisation transfer from p-H ₂ using 5 mol% [Ir(COD)(IMes)Cl] and 0.1 M pyridine at 6.5 x 10 ⁻³ T	190
Figure 135: Temperature effects on normalised enhancements of the H _{A/E} ¹ H NMR resonance of pyridine after polarisation transfer using p-H ₂ at 2 x 10 ⁻⁴ T in CD ₃ OD (0.6 ml); each sample contains 5 mol% pre-catalyst ([Ir(COD)(IMes)Cl] or 1) and pyridine (0.1 M)	191
Figure 136: Temperature effects on normalised enhancements of the H _{A/E} ¹ H NMR resonance of pyridine after polarisation transfer using p-H ₂ at 6.5 x 10 ⁻³ T in CD ₃ OD (0.6 ml); each sample contains 5 mol% pre-catalyst ([Ir(COD)(IMes)Cl] or 1) and pyridine (0.1 M)	191
Figure 137: The hydride region of each ¹ H NMR spectra when polarising pyridine using 1 in the specified solvents along with their dielectric constants, ε, and viscosities, η (cP), at 25 °C.....	193
Figure 138: Enhanced ¹ H NMR spectrum for a CD ₂ Cl ₂ sample containing 0.05 M pyridine and 15 mol% 1 at 298 K and 6.5 x 10 ⁻³ T with 3 bars of p-H ₂ demonstrating that polarisation is also transferred in a cis fashion to proton resonances of the bound pyridine ligands and the carbene backbone of 6	196
Figure 139: Three samples containing 2 in CD ₂ Cl ₂ with increasing equivalents of pyridine showing the formation of 15 from 8 ; (A) 14 eq., (B) 42 eq. and (C) 72 eq....	199
Figure 140: ¹ H NMR spectra field plots of a sample containing 0.1 M pyridine and 5 mol% 2 in CD ₃ OD after polarisation transfer from parahydrogen at r.t. and varying PTFs from -140 x 10 ⁻⁴ T to 20 x 10 ⁻⁴ T with the largest signals at a field of -70 x 10 ⁻⁴ T; (A) H _{A/E} ; (B) H _C ; (C) H _{B/D}	201

Figure 141: Nicotinamide showing labelling of protons	203
Figure 142: ^1H NMR spectra of a sample containing 0.1 M nicotinamide and 5 mol% 1 in CD_3OD after; (A) thermal equilibrium at high field; and (B) polarisation transfer from p- H_2 at 6.5×10^{-3} T and 60°C	204
Figure 143: ^1H NMR spectra of a sample containing 0.1 M nicotinamide and 5 mol% 1 in CD_3OD at thermal equilibrium (A) and after polarisation transfer from p- H_2 at 60°C and 6.5×10^{-3} T. Between each run (B-E) the sample was cooled to r.t. before the process was repeated.....	205
Figure 144: ^{13}C NMR spectra of a sample containing 0.1 M nicotinamide and 5 mol% 1 in CD_3OD after polarisation transfer from p- H_2 at 60°C and 2×10^{-4} T (A) and 6.5×10^{-3} T (B).....	206
Figure 145: $^{13}\text{C}\{^1\text{H}\}$ NMR spectra of a sample containing 0.1 M nicotinamide and 5 mol% 1 in CD_3OD after polarisation transfer from p- H_2 at 60°C and 2×10^{-4} T (A) and 6.5×10^{-3} T (B).....	206
Figure 146: ^1H NMR spectra field plots of a sample containing 0.1 M nicotinamide and 5 mol% 1 in CD_3OD after polarisation transfer from p- H_2 at r.t. and varying PTF; (A) H_A ; (B) H_D ; (C) H_B ; (D) H_C	207
Figure 147: ^1H OPSY-dq NMR spectra of a sample containing 0.1 M nicotinamide and 5 mol% 1 in CD_3OD after polarisation transfer from p- H_2 at 60°C and 2×10^{-4} T (A) and 6.5×10^{-3} T (B)	208
Figure 148: ^1H OPSY-dq NMR spectra of a sample containing 0.1 M nicotinamide and 5 mol% 1 in CD_3OD after polarisation transfer from p- H_2 at r.t. and; (A) 2.5×10^{-3} T; (B) 0×10^{-4} T; (C) -2.5×10^{-3} T; (D) -5×10^{-3} T; (E) -6.5×10^{-3} T; (F) -7.5×10^{-3} T; (G) -1×10^{-2} T; (H) -1.25×10^{-2} T; (I) -1.5×10^{-2} T.....	209
Figure 149: Nicotinamide proton enhancements as a function of temperature after polarisation transfer from p- H_2 using 5 mol% 1 and 0.1 M pyridine at 6.5×10^{-3} T...	210

Figure 150: Nicotinamide proton enhancements as a function of temperature after polarisation transfer from p-H ₂ using 5 mol% Ir(COD)(IMes)Cl and 0.1 M pyridine at 6.5 x 10 ⁻³ T	211
Figure 151: Temperature effects on normalised enhancements of the H _A ¹ H NMR resonance of nicotinamide after polarisation transfer using p-H ₂ at 6.5 x 10 ⁻³ T; one containing nicotinamide (0.1 M) and Ir(COD)(IMes)Cl (5 mol%) in CD ₃ OD (0.6 ml) and one containing nicotinamide (0.1 M) and 1 (5 mol%) in CD ₃ OD (0.6 ml).	211
Figure 152: Nicotinaldehyde showing labelling of protons	212
Figure 153: ¹ H NMR spectra after shaking a 0.05 M nicotinaldehyde sample containing 14 mol% 2 in CD ₂ Cl ₂ (A) and C ₆ D ₆ (B) with p-H ₂ at 6.5 x 10 ⁻³ T	213
Figure 154: The structure and proton labels of the hemiacetal form of nicotinaldehyde	214
Figure 155: ¹ H NMR spectrum after shaking a 0.05 M nicotinaldehyde sample containing 14 mol% 2 in CD ₃ OD with p-H ₂ at 6.5 x 10 ⁻³ T at 298 K.....	214
Figure 156: Aromatic region of the ¹ H NMR spectra after shaking a 0.05 M nicotinaldehyde sample containing 14 mol% 2 in CD ₃ OD with p-H ₂ at 6.5 x 10 ⁻³ T at 298 K, with the labelled structures and their corresponding ¹ H NMR signals	214
Figure 157: Different SABRE-active complexes formed in CD ₃ OD	216
Figure 158: Nicotine showing labelling of protons.....	216
Figure 159: ¹ H NMR spectra after shaking a 0.05 M nicotine sample containing 14 mol% 2 in CD ₂ Cl ₂ (A), C ₆ D ₆ (B) and CD ₃ OD (C) with p-H ₂ at 6.5 x 10 ⁻³ T	217
Figure 160: ¹ H NMR spectra of the major hydride signals present in a solution of δ _{nicotine} in CD ₂ Cl ₂ at 298 K (A) and 240 K (B)	218
Figure 161: The isomers of δ _{nicotine} formed in CD ₂ Cl ₂ , C ₆ D ₆ and CD ₃ OD, depending on the orientation of the chiral nicotine ligands.....	219
Figure 162: Nitrogen-containing heterocycles (from left to right); isoxazole, ⁸¹ 3-amino-1,2,4-triazine, ¹¹³ quinolone, ²³⁸ pyrazole, ⁸⁴ pyridazine, ⁹⁴ and pyrazinamide ⁹⁷	222

Figure 163: Two proposed binding modes between amino acids and activated Crabtree's catalyst that enable polarisation transfer when reacted with p-H ₂ ²³⁹	223
Figure 164: Route to observing enhanced signals for the solvent OH peak occurring via proton exchange in acidic medium ²⁴⁰	223
Figure 165: Biosynthesis of serotonin from tryptophan in the body ²⁴² and structures of some other amine-containing neurotransmitters; norepinephrine, dopamine and histamine	224
Figure 166: Examples of monoamine oxidase inhibitors containing amine groups; the amine is present as a hydrazine group in phenelzine and hydracarbazine, an amide group in moclobemide and a primary amine in (1S,2R)-(-)-tranylcypromine	225
Figure 167: The structures of two local anaesthetics, tetracaine and prilocaine, both containing amine functionalities	225
Figure 168: The structure of aniline yellow with the azo group highlighted in red	226
Figure 169: Summary of the different complexes formed when 1 is reacted with an amine substrate in the presence of H ₂ where A is the expected SABRE-active product as observed when pyridine is the substrate, B is a singlet hydride species which does not undergo PHIP and C is a dimer species seen at low concentrations of substrate	227
Figure 170: The SABRE-active monomer species, δ_{ammonia} , and a postulated dimeric structure, $2\delta_{\text{ammonia}}$	228
Figure 171: Single scan ¹ H NMR spectra at thermal equilibrium (A) and on the addition of p-H ₂ at 6.5 x 10 ⁻³ T (B) showing the polarised hydride ligands and the SABRE-enhanced benzylamine signals	229
Figure 172: SABRE-active species $\delta_{\text{benzylamine}}$ and complex $2\delta_{\text{benzylamine}}$ containing only one hydride ligand, formed on reaction of benzylamine with 1 in CD ₂ Cl ₂ under 3 bars of H ₂	230
Figure 173: Full structure of complex $2\delta_{\text{benzylamine}}$ (N ₁ signifies benzylamine)	230

Figure 174: Iridium dimer $21_{\text{benzylamine}}$ and the alkene-dihydride species 5 , formed on reaction of benzylamine with 1 in CD_2Cl_2 under 3 bars of H_2	231
Figure 175: ^1H COSY NMR spectrum showing coupling between the four hydride signals of $21_{\text{benzylamine}}$	231
Figure 176: Three tetrahydride iridium dimer species described by Gruber et al. ²⁵⁰ (A and B) and Bianchini et al. ²⁵¹ (C).....	234
Figure 177: The hydride region of the ^1H NMR spectrum for complex A as detailed in Figure 176 (Reprinted with permission from Gruber, S.; Neuburger, M.; Pfaltz, A. <i>Organometallics</i> 2013, 32, 4702. Copyright © 2013 American Chemical Society) ²⁵⁰ .	234
Figure 178: Line drawing of complex $21_{\text{phenethylamine}}$ (N signifies phenethylamine).....	235
Figure 179: The structure of tryptamine, the SABRE-active monomer species, $6_{\text{tryptamine}}$, and the dimeric structure, $21_{\text{tryptamine}}$ formed on reaction of tryptamine with 1 in CD_2Cl_2 under H_2	236
Figure 180: ORTEP plot of $22_{\text{tryptamine}}$, showing the C-H activated metallocycle, with H atoms (apart from NH, NH_2 and hydride ligand) omitted for clarity and the thermal ellipsoids set at a 50 % probability level.....	237
Figure 181: ORTEP plot of 23_{pyridine} with solvent and H atoms omitted for clarity and the thermal ellipsoids set at a 50 % probability level.....	240
Figure 182: Formation of complex 24_{pyridine} and 25 , with excess PPh_3 in solution	242
Figure 183: ORTEP plot of 25 with solvent and H atoms omitted for clarity and the thermal ellipsoids set at a 50 % probability level	242
Figure 184: Potential intermediates formed when using weakly coordinating substrate ligands	243
Figure 185: The three major species identified in the hydride region present at 298 K for a sample containing 1 , PPh_3 and benzylamine under 3 bars of H_2 with hydride characterisation data detailed at the specified temperatures	244

Figure 186: Thermal ^1H NMR spectrum for benzylamine (A) and hyperpolarised spectrum (B) at 6.5×10^{-3} T showing enhanced signals for the hydride ligands as well as for the amine, CH_2 and aromatic protons of benzylamine.....	245
Figure 187: Major species present in an activated CD_2Cl_2 sample containing 1, phenethylamine and PPh_3 under 3 bars of H_2 with hydride characterisation data detailed at the specified temperatures.....	247
Figure 188: Major species present in an activated CD_2Cl_2 sample containing 1, tryptamine and PPh_3 under 3 bars of H_2	248
Figure 189: Enhanced ^1H NMR spectrum for tryptamine using 1 with PPh_3 and p- H_2 at 6.5×10^{-3} T showing significantly enhanced signals for the hydride ligands. A large H_2 signal is also observed, consistent with rapid consumption of p- H_2 , and only minimal polarisation of the tryptamine substrate	249
Figure 190: Labelled structures of complexes 26_{PCy_3} and 27_{PCy_3} where N is phenethylamine	251
Figure 191: Broad hydride signals of 27_{PCy_3} at 298 K in CD_2Cl_2	252
Figure 192: The structure of 28_{PCy_3} and its corresponding ^1H and ^{31}P NMR spectra at 263 K, showing the hydride signal (A) and phosphorus signal (B) with the sextet splitting due to the five hydride ligands (cyclohexyl decoupled)	253
Figure 193: Reaction between $[\text{Ir}(\text{H})_5(\text{PCy}_3)_2]$, 28_{PCy_3} , and HBF_4 in the presence of acetonitrile to form $[\text{Ir}(\text{H})_2(\text{MeCN})_2(\text{PCy}_3)_2][\text{BF}_4]$	253
Figure 194: The structure of $[\text{Ir}(\text{H})_2(\text{MeCN})_2(\text{PCy}_3)_2][\text{BF}_4]$ and its corresponding ^1H and ^{31}P NMR spectra at 263 K, showing the hydride signal (A) and phosphorus signal (B) with the triplet splitting due to the two hydride ligands (cyclohexyl decoupled) ..	254
Figure 195: ORTEP plot of the imidazolium tetrafluoroborate salt with the BF_4 and H atoms omitted for clarity and the thermal ellipsoids set at a 50 % probability level	255
Figure 196: Hydride signals of 27_{PiPr_3} , 28_{PiPr_3} and 29_{PiPr_3} at 298 K in CD_2Cl_2	256
Figure 197: Labelled structures of 27_{PiPr_3} and 29_{PiPr_3} formed when P^iPr_3 is used.....	256

Figure 198: Labelled structures of 26 _{PBz3} , 27 _{PBz3} and 30 _{PBz3} formed when 1 is reacted with phenethylamine in the presence of PBz ₃ and H ₂	258
Figure 199: Hydride signals of 26 _{PBz3} , 27 _{PBz3} and 30 _{PBz3} at 298 K in CD ₂ Cl ₂	258
Figure 200: Labelled structures of 26 _{PPh2Cy} , 27 _{PPh2Cy} and 30 _{PPh2Cy}	259
Figure 201: Hydride signals of 26 _{PPh2Cy} , 27 _{PPh2Cy} and 30 _{PPh2Cy} at 298 K in CD ₂ Cl ₂	259
Figure 202: The NMR spectra acquired at different time intervals during the enzyme-catalysed hydrolysis of sucrose (S, δ 5.41) to form the product α -glucose (P $_{\alpha}$, δ 5.22) and the slow conversion of α -glucose to β -glucose (P $_{\beta}$, δ 4.64) (Reprinted with permission from Her, C.; Alonzo, A. P.; Vang, J. Y.; Torres, E.; Krishnan, V. V. J. Chem. Educ. 2015, 92, 1943. Copyright © 2015 American Chemical Society) ²⁶⁷	263
Figure 203: Reaction of benzonitrile oxide with ethyl trans-cinnamate completed in the ionic liquid 1-butyl-3-methylimidazol-3-ium bis(trifluoromethanesulfonyl)imide, with the starred protons indicating those used to monitor the progress of the reaction ²⁶⁹	263
Figure 204: Selectivity observed on hydrogenation of citral in hexane using Pt/SiO ₂ with 20 atm of H ₂ , at 298 K to form the partially saturated aldehyde, citronellal, or the partially saturated alcohol, citronellol. At high temperature very little carbon-carbon double bond hydrogenation is observed which leads to the unsaturated alcohols geraniol and nerol ²⁷⁰	264
Figure 205: Reaction of citral in hexane with 20 atm of H ₂ over a heterogeneous Pt/SiO ₂ catalyst at 423 K showing the selectivity for the production of the alcohol (UALC) over the partially saturated species (PSALD and PSALC) as shown in Figure 204 (Reprinted from Singh, U. K.; Albert Vannice, M. Journal of Catalysis 2000, 191, 165, Copyright © 2000, with permission from Elsevier) ²⁷⁰	265
Figure 206: Intensities of enhanced signals for bound ethylbenzene (squares) and free ethylbenzene (triangles) formed from the hydrogenation of styrene using [Rh(dppb)(COD)][BF ₄] and the DYPAS NMR method (Reprinted with permission from Hubler, P.; Giernoth, R.; Kummerle, G.; Bargon, J. J. Am. Chem. Soc. 1999, 121, 5311. Copyright © 1999 American Chemical Society) ²⁷⁴	267

Figure 207: The decrease in ^1H OPSY NMR signal intensity observed during the hydrogenation of ethyl propiolate to ethyl acrylate using $[\text{Rh}(\text{COD})(\text{DIOP})][\text{BF}_4]$ as the catalyst. The hydrogenation was conducted in D_2O in the presence of SDS (sodium dodecyl sulfate) and consecutive ^1H OPSY NMR spectra were recorded until the enhanced signal intensity decreased to zero (Reproduced from Tang, J. A.; Gruppi, F.; Fleysler, R.; Sodickson, D. K.; Canary, J. W.; Jerschow, A. Chem. Commun. 2011, 47, 958 with permission of The Royal Society of Chemistry http://dx.doi.org/10.1039/C0CC03421E) ²⁷⁶	268
Figure 208: The hydrogenation of phenylacetylene to form styrene and then ethylbenzene.....	269
Figure 209: The decay of parahydrogen derived signals upon hydrogenation of phenylacetylene to styrene using Crabtree's catalyst, $[\text{Ir}(\text{COD})(\text{PCy}_3)(\text{py})][\text{PF}_6]$	273
Figure 210: Relative concentration of styrene produced from summing the integrals of styrene after each OPSY spectrum using Crabtree's catalyst.....	274
Figure 211: Letort's logarithmic graphs to determine reaction order with respect to time for shake one (A) and shake two (B) showing the decrease in order using Crabtree's catalyst	275
Figure 212: The decay of parahydrogen derived signals upon hydrogenation of phenylacetylene to styrene using 1	276
Figure 213: Relative concentration of styrene produced from summing the integrals of styrene after each OPSY spectrum using 1	277
Figure 214: Letort's logarithmic graphs to determine reaction order with respect to time for shake one (A) and shake two (B) showing the constant order using 1	278
Figure 215: ^1H OPSY-dq spectra of the hydrogenation of phenylacetylene using Crabtree's catalyst (A), complex 1 (B) and complex 2 (C) showing the large signal for H_2 at $\sim \delta$ 4.6 in (C).....	280

Figure 216: Reversible equilibration between the η^2 -alkene and alkyl form showing coupling that could lead to polarisation transfer described by Andriollo et al. for an osmium phosphine complex ²⁸¹	282
Figure 217: Hydrogenated signals for ethyl benzene using Crabtree's catalyst (A) and using 1 (B) also showing a large H ₂ signal and enhanced styrene signals.....	282
Figure 218: Initial ¹ H OPSY-dq spectra for phenylacetylene hydrogenation using Crabtree's catalyst (A), showing signals for COE and hydride species (inset) and using complex 1 (B) with no signals corresponding to hydrogenation of COD or hydride species (inset).....	283
Figure 219: Possible mechanistic routes for hydrogenation to form ethyl benzene from phenylacetylene using Crabtree's catalyst	285
Figure 220: The proposed mechanistic pathway for the hydrogenation of phenylacetylene to form styrene using [Ir(COD)(ⁱ Pr ₂ PCH ₂ CH ₂ OMe)][BF ₄] as described by Esteruelas et al. ²⁷⁹	286
Figure 221: Structure of the neutral bidentate iridium carbene complexes with the described R group in the para position to the phenolate group.....	289
Figure 222: Main synthetic steps required to form the bidentate iridium carbene derivatives	290
Figure 223: Formation of the dialkene-dihydride complexes, upon addition of H ₂ and subsequent formation of the bis-pyridyl dihydride complexes in the presence of pyridine and H ₂ , via singlet hydride intermediates. The isomer structures are also shown due to ring-flip of the seven-membered metallocycle	291
Figure 224: Summary of the isomer forms present for the bidentate iridium carbene dihydride complexes in solution and the intermediate that occurs on pyridine dissociation showing the electron-donating ability of the phenolate	292
Figure 225: Reaction of 2 with pyridine, in CD ₃ OD, to form 13 and subsequent H ₂ addition to form dihydride complex 14 before COD hydrogenation leads to complex 15, with Ir-O bond dissociation.....	292

Figure 226: Hydride interconversion due to pyridine addition to differing faces of the bidentate ligand and the route to hydride interconversion via the formation of a dihydrogen intermediate	295
Figure 227: Structures and corresponding Tolman Electronic Parameters of three NHC derivatives	297
Figure 228: Bis(dichloroimidazolylidene) iridium complex developed by Viciano et al. for hydrosilylation of terminal acetylenes ²⁸⁷	298
Figure 229: Formation of an anilide hydride iridium complex ²⁹⁰	298
Figure 230: Structures of nicotinaldehyde, its hemiacetal form, and nicotine	300
Figure 231: Structures of ammonia, benzylamine, phenethylamine and tryptamine....	301
Figure 232: Inactive complexes formed using 1 under H ₂ with amine substrates in CD ₂ Cl ₂	301
Figure 233: Isomers 23 and 24 and the bis-phosphine complex 25.....	302
Figure 234: Trans-phosphine isomer, 29, and [Ir(H) ₅ (PCy ₃) ₂], 28	302
Figure 235: Potential synthetic route to form a tridentate iridium carbene complex containing a bound phenolate and phosphine ligand	303
Figure 236: Formation of [Ir(H) ₂ (P-NHC-O)(py)] from [Ir(COE)(P-NHC-O)].....	303
Figure 237: Demonstration of phase-extraction used to remove the polarisation transfer catalyst from hyperpolarised substrate, suitable for MRI studies ²⁹³	304
Figure 238: The hydrogenation of phenylacetylene to form styrene and ethyl benzene	305
Figure 239: ¹ H OPSY NMR spectrum after p-H ₂ addition to a sample containing 2.0 mol% Crabtree's catalyst and 120 mM phenylacetylene in CD ₂ Cl ₂ , showing the enhanced signals for styrene, ethyl benzene, COE and hydride species.....	305

Figure 240: A decay curve corresponding to the observed rate of p-H ₂ consumption for the hydrogenation of phenylacetylene using 1, the growth curve corresponding to the production of styrene over time and the double logarithmic plot enabling the determination of the reaction order with respect to time	306
Figure 241: ORTEP plot of the imidazolium tetrafluoroborate salt with the BF ₄ and H atoms omitted for clarity and the thermal ellipsoids set at a 50 % probability level	321
Figure 242: ORTEP plot of 1 with H atoms omitted for clarity and the thermal ellipsoids set at a 50 % probability level	325
Figure 243: Visible region of the absorption spectra for 1 in DCM at different concentrations as listed in Table 52	327
Figure 244: Calibration graph used to calculate the molar absorption coefficient for the absorption band of 1 at 406 nm using the data in Table 52	327
Figure 245: ORTEP plot of 22 _{tryptamine} , with H atoms (apart from the NH, NH ₂ and hydride ligand) omitted for clarity and the thermal ellipsoids set at a 50 % probability level	334
Figure 246: ORTEP plot of 23 _{pyridine} , with solvent and H atoms omitted for clarity and the thermal ellipsoids set at a 50 % probability level.....	337
Figure 247: ORTEP plot of 25, with solvent and H atoms omitted for clarity and the thermal ellipsoids set at a 50 % probability level	341
Figure 248: Visible region of the absorption spectra for 2 in DCM at different concentrations as listed in Table 56	359
Figure 249: Calibration graph used to calculate the molar absorption coefficients for the three absorption bands of 2 in DCM at 373, 425 and 490 nm using the data in Table 56	359
Figure 250: ORTEP plot of 3 with H atoms omitted for clarity and the thermal ellipsoids set at a 50 % probability level	372

Figure 251: Visible region of the absorption spectra for 3 in DCM at different concentrations as listed in Table 58 374

Figure 252: Calibration graph used to calculate the molar absorption coefficients for the three absorption bands of 3 at 380, 432 and 491 nm using the data in Table 58 374

Figure 253: Visible region of the absorption spectra for 4 in DCM at different concentrations as listed in Table 59 391

Figure 254: Calibration graph used to calculate the molar absorption coefficients for the three absorption bands of 4 at 381, 430 and 491 nm using the data in Table 59 392

List of Tables

Table 1: The spin isomers of molecular hydrogen.....	49
Table 2: Hammett parameters, σ_p and σ_p^- , for the four substituents NO ₂ , COOMe, Cl and H showing the increase in their electron-donating capabilities from NO ₂ to H, with H being the most electron-donating group ¹⁴⁵	82
Table 3: Experimentally calculated rate data for methyl group rotation in complex 1 as a function of temperature	91
Table 4: Selected bond lengths and angles for complex 1	93
Table 5: Selected bond lengths for complex 1, [Ir(COD)(IMes)(OSiMe ₃)] and [Ir(COD)(IMes)(py)] ⁺ where X denotes O or N as detailed for each of the three complexes.....	94
Table 6: Selected bond angles for complex 1, [Ir(COD)(IMes)(OSiMe ₃)] and [Ir(COD)(IMes)(py)] ⁺ where X denotes O or N as detailed for each of the three complexes.....	95
Table 7: Selected bond lengths and angles for complex 3	98
Table 8: Ratios showing how the relative proportions of 1 and 6 change during the reaction of a CD ₂ Cl ₂ solution containing 12 mol% 1 and 0.22 M pyridine under 3 bars of H ₂ seen at 253 K	102
Table 9: Concentrations of iridium complexes to determine equilibrium constants at different temperatures in a CD ₂ Cl ₂ : CD ₃ OH sample (9: 1) containing 2 and pyridine under 3 bars of H ₂	119
Table 10: Summary of the molar absorption coefficients for the detailed Ir(I) complexes	123
Table 11: Comparisons of the CO stretching frequencies for the four complexes shown in Figure 86 along with the literature data for [Ir(IMes)(CO) ₂ Cl]	128
Table 12: Summary of the major complexes formed when the four pre-catalysts 1, 2, 3 and 4 are reacted with pyridine and hydrogen in methanol and dichloromethane.....	130
Table 13: Iridium alkoxo complexes with different R groups, their Hammett parameters, σ_p , and rates of β -hydrogen elimination (Adapted with permission from Zhao, J.;	

Hesslink, H.; Hartwig, J. F. J. Am. Chem. Soc. 2001, 123, 7220. Copyright © 2001 American Chemical Society) ¹⁸¹	137
Table 14: ¹ H EXSY NMR data for the percentage signals present for either 6 _A or 6 _B after selectively exciting the indicated hydride signal at 233 K	143
Table 15: Exchange rate and lifetime data for pyridine and H ₂ dissociation and hydride interconversion at the specified temperatures in a CD ₃ OH sample containing 6 mol% 1 and 0.08 M pyridine (H _B δ -29.2 and H _A δ -21.6).....	149
Table 16: Activation parameters calculated from the Arrhenius and Eyring-Polanyi plots for pyridine and H ₂ dissociation and hydride interconversion for a CD ₃ OH sample containing 6 mol% 1 and 0.08 M pyridine under H ₂	150
Table 17: Rates of pyridine and hydride ligand dissociation from 6 in CD ₂ Cl ₂ at 298 K and in CD ₃ OH at 294 K as a function of increasing equivalents of pyridine	151
Table 18: Pyridine and hydrogen dissociation rates and the rates of hydride interconversion for samples of 15 mol% 1 and 0.05 M pyridine in the specified solvents at 298 K under 3 bars of H ₂	160
Table 19: Pyridine and hydrogen dissociation rates and the rates of hydride interconversion for samples of 15 mol% 2 and 0.05 M pyridine in the specified solvents at 294 K under 3 bars of H ₂	162
Table 20: Exchange rate and lifetime data for pyridine dissociation and hydride dissociation at different temperatures in CD ₃ OH for a sample containing 8 mol% 2 and 0.07 M pyridine under 3 bars of H ₂	162
Table 21: Activation parameters calculated from the Arrhenius and Eyring-Polanyi plots for pyridine dissociation and hydride dissociation in CD ₃ OH for a sample containing 8 mol% 2 and 0.07 M pyridine. The Gibbs Free energy of activation, ΔG [‡] , is calculated at 300 K using the Gibbs Free Energy equation (ΔG [‡] = ΔH [‡] - TΔS [‡]) with the calculated ΔH [‡] and ΔS [‡] values given in the table	164
Table 22: Pyridine dissociation rates, complex lifetimes and hydride exchange rates of 10 _A and 10 _B , for CD ₂ Cl ₂ , CD ₃ OD, CD ₃ OH and C ₆ D ₆ samples containing 10 mol% 3 and 0.06 M pyridine at 298 K under 3 bars of H ₂	165
Table 23: Exchange rate information for pyridine and hydrogen loss and hydride interconversion for 12 _A and 12 _B present in a CD ₂ Cl ₂ sample containing 9 mol% 4 and	

0.08 M pyridine and a C ₆ D ₆ sample containing 7 mol% 4 and 0.1 M pyridine, both under 3 bars of H ₂ at 298 K.....	166
Table 24: Exchange rate information for pyridine and hydrogen loss and hydride interconversion for 12 _A and 16 present in a CD ₃ OH sample containing 5 mol% 4 and 0.16 M pyridine under 3 bars of H ₂ at 298 K.....	167
Table 25: T ₁ values calculated for the protons of pyridine (0.05 M) in the specified solvent samples under air, degassed and once activated with 1 (15 mol%) under 3 bars of H ₂ at 298 K	170
Table 26: T ₁ values for the three proton sites of each of the three pyridine environments (free pyridine, pyridine trans to hydride and pyridine trans to carbene) within a CD ₂ Cl ₂ solution of pyridine (0.05 M) once activated with 1 (15 mol%) under 3 bars of H ₂ at 298 K and at 263 K. At 263 K the T ₁ value for the para proton signal of the pyridine ligand bound trans to a hydride ligand could not be determined due to signal overlap.....	172
Table 27: Pyridine dissociation rates and T ₁ values for three samples of 16 mol% 2 and 0.05 M pyridine under 3 bars of H ₂ in C ₆ D ₆ , CD ₂ Cl ₂ and CD ₃ OD at 298 K.....	173
Table 28: Summary of the active catalyst species formed in CD ₂ Cl ₂ and CD ₃ OD, along with the ¹ H NMR chemical shifts of their hydride and CH ₂ linker signals	174
Table 29: Comparison of the ligand exchange rates and lifetimes of the dihydride complexes 6, 10 _A , 12 _A and 8 in CD ₂ Cl ₂ at 298 K	176
Table 30: Pyridine ¹ H NMR signal enhancements for a series of 0.05 M pyridine and 15 mol% 1 solutions at 298 K and 6.5 x 10 ⁻³ T with 3 bars of p-H ₂ after 48 hours and 24 days	194
Table 31: Pyridine proton enhancement values using 0.07 M pyridine with 10 mol% 2 in C ₆ D ₆ , CD ₂ Cl ₂ and CD ₃ OD under 3 bars of p-H ₂ after activation for 48 hours and 6 days at a polarisation transfer field of 6.5 x 10 ⁻³ T.....	197
Table 32: Pyridine proton enhancement values using 0.33 M pyridine with 2.3 mol% 2 in CD ₂ Cl ₂ and CD ₃ OD under 3 bars of p-H ₂ at 6.5 x 10 ⁻³ T and 298 K.....	198
Table 33: SABRE enhancements for the protons of pyridine for samples containing 0.06 M pyridine and 10 mol% 3 under 3 bars of p-H ₂ at 6.5 x 10 ⁻³ T.....	202

Table 34: SABRE enhancements for three activated samples of 4 under 3 bars of H ₂ at 6.5 x 10 ⁻³ T; a CD ₂ Cl ₂ sample containing 9 mol% 4 and 0.08 M pyridine, a C ₆ D ₆ sample containing 7 mol% 4 and 0.1 M pyridine and a CD ₃ OH sample containing 5 mol% 4 and 0.16 M pyridine	202
Table 35: Nicotinaldehyde proton enhancement values using 0.05 M nicotinaldehyde with 14 mol% 2 in C ₆ D ₆ and CD ₂ Cl ₂ after activation for 48 hours and 5 days under 3 bars of H ₂ at 6.5 x 10 ⁻³ T	212
Table 36: The proton enhancement values of nicotinaldehyde and its hemiacetal form, using a CD ₃ OD solution of 0.05 M nicotinaldehyde with 14 mol% 2 after 48 hours and 5 days at 6.5 x 10 ⁻³ T and 298 K	215
Table 37: ¹ H NMR signal enhancements of the aromatic protons of nicotine using 0.05 M nicotine with 14 mol% 2 in the specified solvents under 3 bars of p-H ₂ at 298 K and 6.5 x 10 ⁻³ T	216
Table 38: Summary of the ¹ H NMR signal enhancements for the protons of pyridine for samples of each pre-catalyst in CD ₂ Cl ₂ at 298 K and 6.5 x 10 ⁻³ T.....	220
Table 39: SABRE ¹ H NMR signal enhancements at 298 K and 6.5 x 10 ⁻³ T for the two samples containing 6.5 mol% 1 and 0.08 M benzylamine (~ 18 eq.) and 33 mol% 1 and 0.03 M benzylamine (~ 2 eq.)	232
Table 40: Selected bond lengths and angles for the crystal structure of 22 _{tryptamine} as shown in Figure 180.....	238
Table 41: Selected bond lengths and angles for the crystal structure of 23 _{pyridine} as shown in Figure 181	240
Table 42: Selected bond lengths and angles for the crystal structure of 25 as shown in Figure 183	243
Table 43: Tolman Cone Angles and Electronic Parameters for five different phosphines	250
Table 44: NMR characterisation data at 263 K for [Ir(H) ₂ (MeCN) ₂ (PCy ₃) ₂][BF ₄].....	254
Table 45: Hydrogenation rates in moles of substrate reduced per mole of catalyst per hour for four different alkenes using Crabtree's iridium catalyst and Wilkinson's rhodium catalyst ⁴⁴	266

Table 46: Rate and order values for two identically produced samples of Crabtree's catalyst used for the hydrogenation of phenylacetylene	275
Table 47: Average values for the hydrogenation rates of phenylacetylene to styrene using the enhanced signal decay data and the cumulatively summed data, along with the orders of reaction determined from the rate data based on the enhanced signal decay. The four catalysts detailed are Crabtree's catalyst and complexes 1, 3 and 4	280
Table 48: Summary of the major SABRE-active products formed when the four pre-catalysts 1, 2, 3 and 4 are reacted with pyridine and hydrogen in methanol and dichloromethane	293
Table 49: T ₁ values for the three proton sites of each of the three pyridine environments (free pyridine, pyridine trans to hydride and pyridine trans to carbene) within a CD ₂ Cl ₂ solution of pyridine (0.05 M) once activated with 1 (15 mol%) under 3 bars of H ₂ at 298 K and 263 K. The T ₁ value for the para proton signal of the pyridine ligand bound trans to a hydride ligand could not be determined due to signal overlap.....	296
Table 50: Crystal data for the structural refinement of 3-(2-hydroxy-5-nitrobenzyl)-1-(2,4,6-trimethylphenyl) imidazolium tetrafluoroborate	322
Table 51: Crystal data for the structural refinement of 1	325
Table 52: Concentration and absorbance values for six samples of 1 in DCM at different concentrations	326
Table 53: Crystal data for the structural refinement of 2 _{tryptamine}	334
Table 54: Crystal data for the structural refinement of 2 _{pyridine}	337
Table 55: Crystal data for the structural refinement of 25	341
Table 56: Concentration and absorbance values for six samples of 2 in DCM at different concentrations	358
Table 57: Crystal data for the structural refinement of 3	372
Table 58: Concentration and absorbance values for eight samples of 3 in DCM at different concentrations.....	373
Table 59: Concentration and absorbance values for seven samples of 4 in DCM at different concentrations.....	391

Acknowledgements

Firstly, I would like to offer my thanks to my supervisor, Simon Duckett, for his support and advice during my PhD and for allowing and encouraging me to present my work at external conferences.

Secondly, I would like to thank all the members of the Duckett group in the Centre for Hyperpolarisation in Magnetic Resonance (CHyM) at York, particularly Ryan, who I worked with as an undergraduate when he supervised my Nuffield research bursary. Without his encouragement, I may never have become interested in the research field at all! I'd also like to thank Pete and Mike for their help with organic synthesis ideas and all my friends in the office over the years for all the good chats and fun times together; thank you Vicky, Barby, Kate, Tom, Pete, Olga, Emma, Rhianna, Chris and Will. I know I can always rely on you all for a good laugh and respite from research. Finally, thank you to Denise and Lyndsay, particularly over the last year, for sending me all of Simon's handwritten comments and to Vicky and Richard for making sure I had all the compounds I needed and could use all four of the NMR spectrometers over weekends when necessary!

There are several people in the department without whom my thesis would not be complete. Thanks to the XRD team, Adrian Whitwood, Sam Hart and Rachel Bean, who solved my lovely crystal structures, especially the challenging twinned ones. Also thank you to Karl Heaton for the mass spectrometry data and Graeme McAllister for the CHN elemental analysis data.

Since I joined Johnson Matthey with a process development position after 3 years of PhD research, I also extend my thanks to my colleagues and bosses who allowed me time to travel back to York to finish off some experiments. Without the support from work, writing up and completing would have been much more of a challenge!

Finally, I'd like to thank my family and friends; particularly my Mum and Dad and best friend Alan, for all their encouragement and support and for enabling me to escape the stresses of research sometimes!

Declaration

I declare that this thesis is a presentation of original work and I am the sole author. This work has not previously been presented for an award at this, or any other, University. All sources are acknowledged as References.

The publications listed below contain work detailed in this thesis.

Ruddlesden, A. J.; Duckett, S. B., Solvent responsive catalyst improves NMR sensitivity via efficient magnetisation transfer. *Chem. Commun.* **2016**, 52 (54), 8467-8470.

Ruddlesden, A. J.; Mewis, R. E.; Green, G. G. R.; Whitwood, A. C.; Duckett, S. B., Catalytic Transfer of Magnetism Using a Neutral Iridium Phenoxide Complex. *Organometallics* **2015**, 34 (12), 2997-3006.

Lloyd, L. S.; Asghar, A.; Burns, M. J.; Charlton, A.; Coombes, S.; Cowley, M. J.; Dear, G. J.; Duckett, S. B.; Genov, G. R.; Green, G. G. R.; Highton, L. A. R.; Hooper, A. J. J.; Khan, M.; Khazal, I. G.; Lewis, R. J.; Mewis, R. E.; Roberts, A. D.; Ruddlesden, A. J., Hyperpolarisation through reversible interactions with parahydrogen. *Catal. Sci. Technol.* **2014**, 4, 3544-3554.

1. Introduction

This work focuses on improving the sensitivity of NMR spectroscopy via hyperpolarisation. The introduction starts with a discussion of the principles of NMR and gives an overview of the hyperpolarisation techniques that can be used to increase NMR signal intensities. These methods are known as optical pumping, Dynamic Nuclear Polarisation (DNP) and *Parahydrogen* Induced Polarisation (PHIP). The emphasis of this work is on PHIP, which can be hydrogenative or non-hydrogenative, and which requires the use of a metal catalyst. Initial PHIP studies used a rhodium-based phosphine complex but developments since then have focused on iridium-based phosphine and subsequently iridium-based carbene complexes, due to their greater activity. These developments are detailed, along with a review of current research in the area of the non-hydrogenative Signal Amplification By Reversible Exchange (SABRE) process. This technique leads to signal enhancements of NMR-active nuclei within suitable substrate molecules such as pyridine, when reacted with *parahydrogen* in solution. A description of the reaction route to form the SABRE-active charged iridium carbene catalysts is given. In these complexes the carbene ligands are symmetric and monodentate. Neutral complexes containing multidentate asymmetric carbene ligands have thus far not been explored. Furthermore, the potential application of SABRE to improve Magnetic Resonance Imaging (MRI) is reviewed with details of heterogeneous iridium catalysts. The aim of this thesis, using *parahydrogen* and neutral iridium carbene complexes to improve NMR sensitivity, is then presented.

1.1. NMR and the use of hyperpolarisation

Nuclear Magnetic Resonance (NMR) is a hugely important technique for chemists as it enables molecular characterisation based on the environments of different spins within a system. Every nucleus with a non-zero spin quantum number has a magnetic dipole which possesses spin angular momentum.¹ The magnetic moment, μ , of a nucleus is directly proportional to the spin angular momentum and the gyromagnetic ratio, γ . For example, a ^1H nucleus has a magnetic spin quantum number, I , of $1/2$. When a ^1H nucleus is placed inside a magnetic field the nucleus can be aligned in two different orientations; either with the direction of the external magnetic field, B_0 , or against it. These orientations equate to the magnetic quantum number, m , which has $2I + 1$ values and therefore for a spin- $1/2$ nuclei, m has two values, equal to $+1/2$ (α), 'spin up' and $-1/2$ (β), 'spin down' as shown in Figure 1. When there is no applied magnetic field, these two orientations have the same energy, however, when a magnetic field is applied they separate out so that each orientation has a slightly different energy, with the energy difference, ΔE . This is due to the Zeeman effect, where, as the strength of the magnetic field increases, the energy difference between the levels is also increased. The $+1/2$ (α) state is aligned with the field therefore is the most stable so has the lowest energy and the $-1/2$ (β) state is aligned against the field. The chemical shift (frequency, ω) of different nuclei within a magnetic field depends on both the field strength, B , and the gyromagnetic ratio, γ , of the nucleus that is probed, as shown by $\omega = \gamma B$.

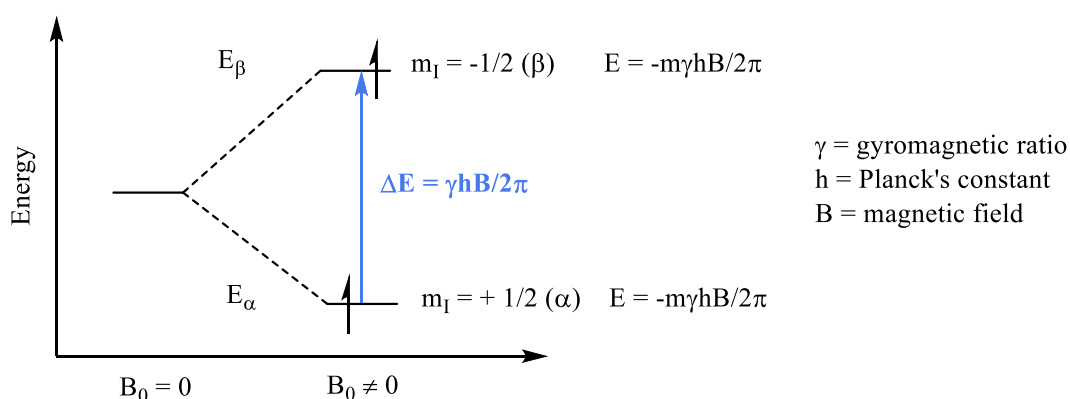


Figure 1: Energy levels present when a sample containing spin- $1/2$ nuclei is in a magnetic field and the Zeeman effect that occurs when the magnetic field is increased

For NMR, the spin transitions can only occur from a more populated state to a less populated state, so for example, when only one spin changes from the $+1/2$ level to

the $-1/2$ level, to produce an observable single quantum coherence signal. Because the energy difference between the two levels is small when in an applied field (lower energy than kT where k is the Boltzmann constant and T is the temperature), the transition requires a small amount of energy. The levels are populated according to the Boltzmann distribution, meaning that there is only a slight excess of spins in the lower energy level.

$$\frac{N_{\beta}}{N_{\alpha}} = e^{-\Delta E/kT}$$

This means that the energy difference for protons with a gyromagnetic ratio of $2.675 \times 10^8 \text{ rad s}^{-1} \text{ T}^{-1}$ in a 9.4 T magnetic field strength is equal to $2.65 \times 10^{-25} \text{ J}$ and therefore the population difference is approximately one spin in every 31000 at 298 K.

$$\begin{aligned} \Delta E &= \frac{\gamma h B}{2\pi} = \frac{2.675 \times 10^8 \text{ rad s}^{-1} \text{ T}^{-1} \times 6.626 \times 10^{-34} \text{ m}^2 \text{ kg s}^{-1} \times 9.4 \text{ T}}{2\pi} \\ &= 2.65 \times 10^{-25} \text{ J} \end{aligned}$$

$$\frac{N_{\beta}}{N_{\alpha}} = e^{-2.65 \times 10^{-25} \text{ J} / 1.38 \times 10^{-23} \text{ J K}^{-1} \times 298 \text{ K}} = 0.9999356 = \frac{15520}{15519}$$

Therefore, the number of transitions that are observed is small, which means that NMR is inherently insensitive.² There are a few ways to combat this although there are associated problems;

1. use a large number of scans which takes a longer amount of time
2. use a large amount of sample which is not necessarily available
3. use a stronger magnet which is expensive
4. use chemical means to polarise samples

This last method, termed hyperpolarisation, is when a population difference is altered so that it is much larger than normal. Therefore, the number of transitions that can now be observed is considerably larger. There are several methods that exist to artificially enhance the population difference within a sample; optical pumping, Dynamic Nuclear Polarisation (DNP) or the use of spin isomers.

1.1.1. Optical pumping

Optical pumping is a method used to increase the nuclear spin polarisation of a sample above its thermal equilibrium, using light. For NMR experiments, the nuclei that can be polarised are limited to spin- $1/2$ noble gas isotopes such as ^3He and ^{129}Xe . For the optical pumping procedure, a glass cell is used, which contains the noble gas of interest, an alkali metal vapour which acts as an important polarisation intermediate,³ and nitrogen gas. During the optical pumping process, circularly polarised laser light is used to excite electrons that are present in the alkali metal, such as rubidium, which then enables polarisation of the ^3He or ^{129}Xe nuclei via collisions.⁴ The wavelength of the laser light must be tuned to the correct wavelength for it to be absorbed by the alkali metal, which is about 795 nm for rubidium. Both the electron spin and the nuclear spin of the alkali metal are polarised. The process works because of the exchange of angular momentum from the polarised photons to the nuclei of rubidium.⁵ The inert nitrogen must be present to quench excited atoms that would otherwise undergo radiative decay and depolarise the noble gas.⁶ Hyperpolarised ^{129}Xe has shown promise in MRI studies as an agent for lung imaging.⁷⁻⁸ Figure 2 shows how rubidium absorbs the circularly polarised light which leads to polarisation build-up of one rubidium electronic ground state.⁸

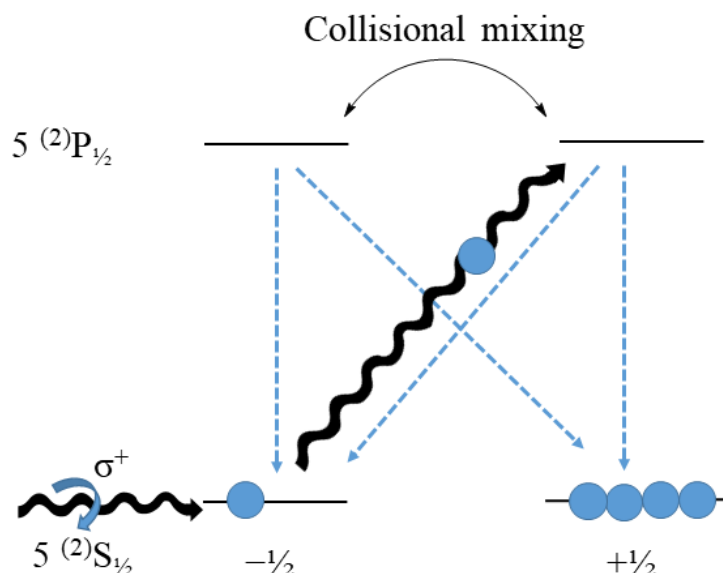


Figure 2: Optical pumping of rubidium due to its absorption of circularly polarised light⁸

1.1.2. Dynamic Nuclear Polarisation (DNP)

Like optical pumping, DNP involves the transfer of polarisation from unpaired electron spins to nuclear spins, in either solids or liquids. The gyromagnetic ratio of an electron is about 660 times larger than that of a proton spin, meaning the maximum theoretical enhancement of a proton signal using DNP is about 660 times the thermal signal.⁹ The DNP process uses an NMR sample which is doped with a species containing an unpaired electron, which acts as the polarisation source. Typically, a stable organic radical such as those shown in Figure 3 is used,¹⁰ which must be homogeneously distributed throughout the sample. The sample is then frozen at very low temperature (< 100 K) and polarisation transfer is achieved via microwave irradiation of the sample, as the energy differences between electron spin states are considerably larger than for proton spins and the irradiation must be near or at the electron paramagnetic resonance (EPR) transition. Commonly, hours of polarising time are needed to build-up polarisation in the sample. Before acquisition of a hyperpolarised NMR spectrum, dissolution of the sample and transfer to an NMR spectrometer must occur.¹¹

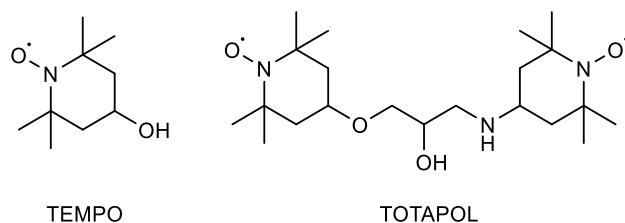


Figure 3: Structures of organic radicals used for DNP¹⁰

Several polarising mechanisms are possible in DNP experiments where electron and nuclear spins are strongly coupled. For liquids, the Overhauser effect operates⁹ whilst for solids, the solid effect (a two-spin process between an electron and a nucleus),¹²⁻¹⁴ the cross effect¹³⁻¹⁴ and thermal mixing (three-spin processes between two coupled electrons and a nucleus)¹⁰ are possible. For high magnetic fields, the cross effect dominates if the linewidth and breadth of the electron EPR spectrum are larger than the Larmor frequency of the nuclei to be polarised. Spin diffusion can then disperse the polarisation throughout the sample.¹⁰ However, the equipment needed to polarise samples is particularly expensive as well as the polarisation time being long.

1.1.3. Hydrogen and its spin isomers

Hydrogen is a homonuclear diatomic molecule. Each hydrogen atom has a nucleus with one spin and spin order of $\pm\frac{1}{2}$ and therefore for molecular hydrogen, H_2 , with two spins, H_1 and H_2 , there are four spin isomers (Table 1), depending on the orientation of the two spins. In order to distinguish between $\alpha\beta$ and $\beta\alpha$, the linear combinations are taken and normalised.¹⁵

Table 1: The spin isomers of molecular hydrogen

	$H_1 H_2$	$H_1 H_2$	$H_1 H_2$	$H_1 H_2$
Spins	$\uparrow\uparrow$	$\uparrow\downarrow$	$\downarrow\uparrow$	$\downarrow\downarrow$
	$\alpha_1 \alpha_2$	$\alpha_1 \beta_2$	$\beta_1 \alpha_2$	$\beta_1 \beta_2$
	$\alpha \alpha$	$\alpha \beta$	$\beta \alpha$	$\beta \beta$
M	+1	0	0	-1
Linear combinations for 4 spin isomers	$\alpha\alpha$	$\frac{1}{\sqrt{2}}(\alpha\beta + \beta\alpha)$	$\frac{1}{\sqrt{2}}(\alpha\beta - \beta\alpha)$	$\beta\beta$
Spin isomer	<i>ortho</i>	<i>ortho</i>	<i>para</i>	<i>ortho</i>

These four isomers correspond to two different states, known as *orthohydrogen* and *parahydrogen*. There are three isomers of *orthohydrogen*, $\alpha\alpha$, $\beta\beta$ and $1/\sqrt{2}(\alpha\beta + \beta\alpha)$ and these are triply degenerate. They are symmetric with respect to exchange of the nuclei and the spins are aligned so they have an overall magnetic moment and are NMR active.¹ The fourth isomer, *parahydrogen*, $1/\sqrt{2}(\alpha\beta - \beta\alpha)$, is antisymmetric with respect to exchange of the nuclei and the spins are opposed so there is no overall magnetic moment and therefore *parahydrogen* is NMR silent.¹

These isomers derive from the Pauli Exclusion Principle which states that two identical fermions cannot occupy the same quantum state simultaneously. The total wavefunction for the two identical fermions must be antisymmetric with respect to exchange of the nuclei. The total wavefunction of hydrogen contains electronic, translational, vibrational, rotational and nuclear parts.¹⁶ The electronic, translational,

and vibrational parts are all symmetric and therefore the product of the rotational and nuclear parts has to be antisymmetric.

$$\Psi_{total} = \Psi_{elec}\Psi_{trans}\Psi_{vib}\Psi_{rot}\Psi_{nuc}$$

This means that for an antisymmetric nuclear configuration i.e. *parahydrogen*, the rotational levels are symmetric i.e. $J = 0, 2, 4...$ and for the symmetric nuclear configuration i.e. *orthohydrogen*, the rotational levels are antisymmetric i.e. $J = 1, 3, 5...$ ¹⁶ Because *parahydrogen* occupies the lower rotational states, it is more stable and this fact is exploited in the production of *parahydrogen* from normal hydrogen. At room temperature with normal hydrogen, each of the four spin isomer energy levels are equally populated, so 75 % of H₂ is *orthohydrogen* and 25 % is *parahydrogen*.¹⁷ However, as the temperature is lowered and the spin-flip from *orthohydrogen* to *parahydrogen* is made possible by the use of a paramagnetic silica/FeCl₃ catalyst, the percentage of *parahydrogen* in the mixture increases up until about 99 % at 20 K.¹⁶ The paramagnetic catalyst aids the required spin conversion of hydrogen, by interactions between its own inhomogeneous magnetic field, formed due to its spin magnetic moments, and the magnetic moments of the hydrogen molecule.¹⁸⁻¹⁹ The set-up required to form *parahydrogen* is shown in Figure 4 and the percentage of *parahydrogen* in relation to the temperature is shown in Figure 5.

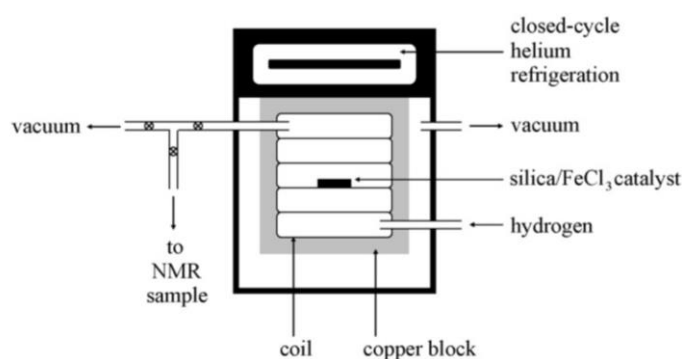


Figure 4: Apparatus used to form parahydrogen from normal hydrogen (Reprinted from Duckett, S. B.; Wood, N. J. *Coord. Chem. Rev.* **2008**, 252, 2278, Copyright © 2008 with permission from Elsevier)¹⁶

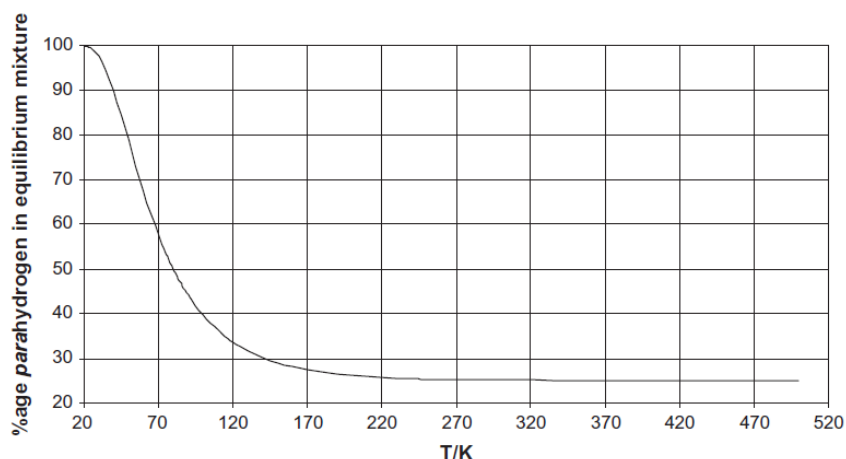


Figure 5: The proportion of parahydrogen increases as the temperature decreases (Reprinted from Green, R. A.; Adams, R. W.; Duckett, S. B.; Mewis, R. E.; Williamson, D. C.; Green, G. G. *R. Prog. Nucl. Magn. Reson. Spectrosc.* **2012**, 67, 1, Copyright © 2012 with permission from Elsevier)¹

For a two-spin system, such as an alkene that contains two protons, there are four energy levels and the transitions that are observable in NMR are single quantum coherence transitions where only one spin flips. Other transitions, where more than one spin changes, are not allowed by the normal selection rule; however, higher quantum coherence transitions do occur. For example, in an alkene where double quantum coherence and zero quantum coherence transitions exist, these must be converted into single quantum coherence transitions using a specific pulse sequence to be observed. These different spin transitions for a two-spin system are shown in Figure 6.

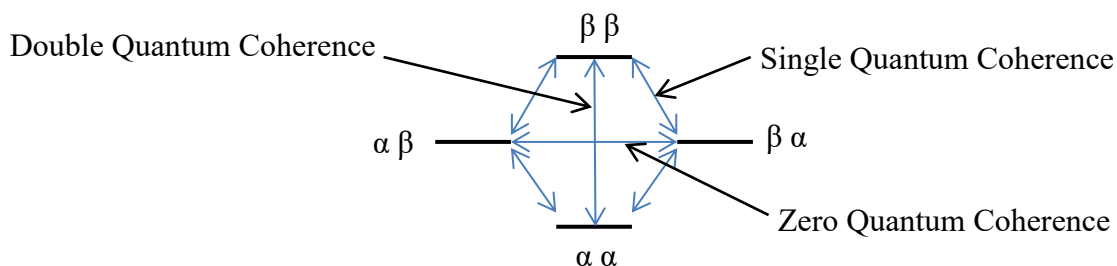


Figure 6: The possible transitions in a two-spin system

When a sample that just contains normal hydrogen is in a magnetic field, all four states are approximately equally populated with only a slight excess in the lower energy states. Only transitions from the lowest energy *ortho* states to the higher energy *ortho* states give rise to the observed signal (see Figure 7). With *parahydrogen* only the

singlet state is occupied, which is symmetric and NMR silent so no signal is seen for pure *parahydrogen* (see Figure 7).²⁰ Only when the symmetry of the *parahydrogen* is broken and the H-H bond is split i.e. into two hydrides or incorporated into a hydrogenated product, does it become NMR active and able to cause large ¹H NMR signal enhancements within a sample.

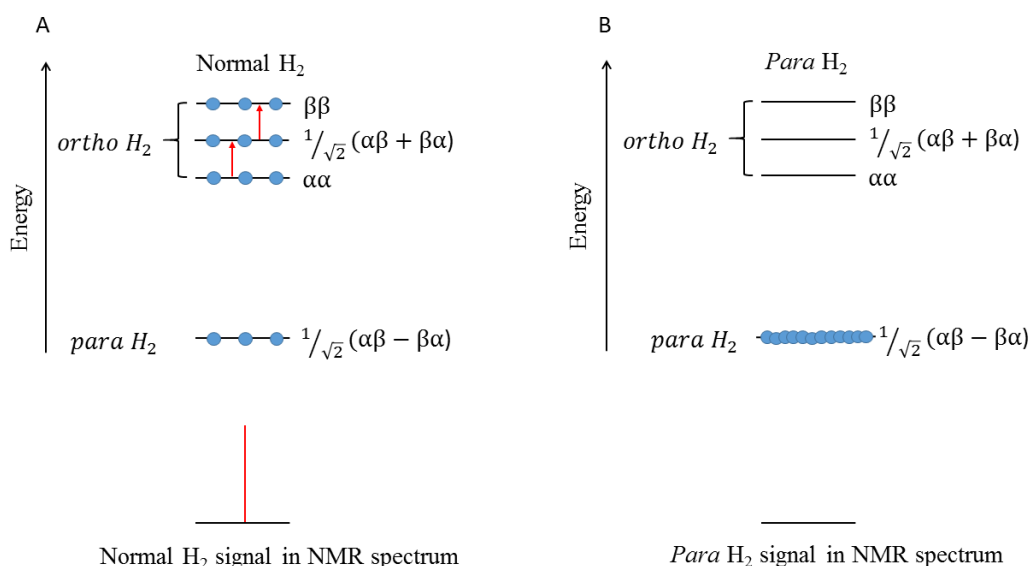


Figure 7: The populated spin states of normal H₂ and *p*-H₂ and their corresponding NMR spectra resulting from the spin transitions shown

For *parahydrogen* to be split, a metal catalyst is commonly used. For example, a metal could accept hydrogen in a concerted *cis* fashion to form two hydrides²¹⁻²² and then act as a hydrogenation catalyst to hydrogenate an alkene to an alkane. However, a metal could also accept hydrogen as two hydrides and not transfer these hydrides into an organic product, but instead transfer the polarisation present in the *parahydrogen*-derived hydrides to an organic product, without changing the chemical identity of the product.

Many metal catalysts used contain carbene ligands, where a metal-carbon double bond may exist. A carbene is a compound that contains a carbon atom that is neutral and divalent with six electrons in its valence shell.²³ Since the early 1960s, significant research has led to the discovery of a variety of stable carbene complexes.

1.2. Metal carbene and phosphine complexes

Metal carbene complexes typically contain metal-carbon double bonds. The first example of this type of complex was discovered by E. O. Fischer in 1964.²⁴ Addition of a methyl group to $[\text{W}(\text{CO})_6]$ using LiCH_3 , followed by protonation then methylation using CH_2N_2 , was found to form the diamagnetic complex $[\text{W}(\text{CO})_5(\text{COCH}_3(\text{CH}_3))]$. Upon subsequent analysis, it was shown that the structure contained a tungsten-carbon double bond.²⁴ The same process occurred using LiPh (see Figure 8), to gain the tungsten-carbon double-bonded $[\text{W}(\text{CO})_5(\text{COCH}_3(\text{Ph}))]$ complex. It was shown that the incoming anion adds to one of the initial CO ligands to form the carbene from the CO ligand, without ligand substitution.²³

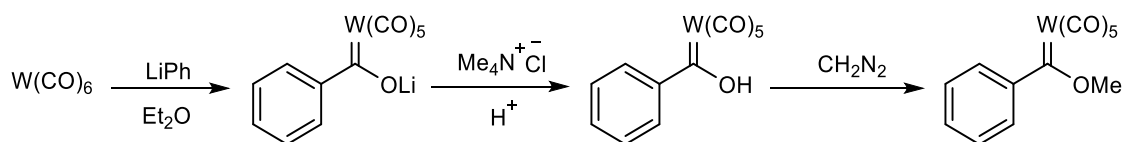


Figure 8: Formation of $[\text{W}(\text{CO})_5(\text{COCH}_3(\text{Ph}))]$ ²³

Since then, other carbenes with this similar structure have been known as Fischer-type carbenes.²⁵⁻²⁶ The metal centre is in a low oxidation state and is therefore electron rich. This means that the carbene ligand contains an electrophilic carbon that is prone to nucleophilic attack.²⁷ The bonding in a Fischer carbene has σ -donor and π -acceptor characteristics and the carbene can either be stabilised by π -back donation from the metal d-orbitals into the empty carbene p-orbital or by π -donation from heteroatom substituents on the carbene itself. This stabilisation means that the singlet form is favoured so the carbene itself has two spin-paired electrons. Resonance structures, such as in Figure 9, can be drawn to show the importance of the electron-donating heteroatom substituents.²⁷ This leads to a metal-carbon bond order of between one and two, which depends on the π -donor capabilities of the carbene substituents.

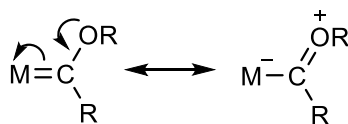


Figure 9: Resonance structures for Fischer-type carbenes

More recently, a specific type of Fischer carbene has been described, called an N-heterocyclic carbene (NHC), which contains very strongly electron-donating substituents, so that only a formal single bond is formed between the carbon and the metal centre.²³ One of these highly stable NHCs was first produced in 1991 by A. J. Arduengo, hence these are sometimes referred to as Arduengo carbenes.²⁸ The 1,3-di-1-adamantylimidazol-2-ylidene was formed via deprotonation of 1,3-di-1-adamantylimidazolium chloride, as shown in Figure 10, and was obtained as a crystalline solid.

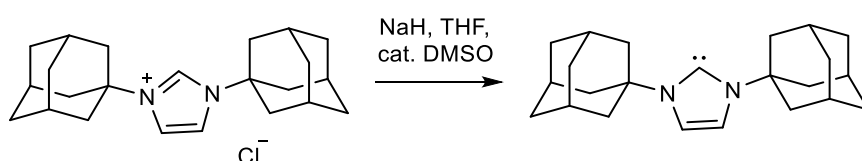


Figure 10: Formation of the stable Arduengo carbene, 1,3-di-1-adamantylimidazol-2-ylidene²⁸

These types of carbenes are singlet carbenes and are often considered to only act as σ -donor ligands due to poor π -back donation from the metal to the carbon. This is because the carbene is strongly stabilised by π -donating nitrogen groups that donate electron density into the empty p-orbital of the carbene. The imidazole ring retains its aromaticity as there is a delocalised π -system across the N-C-N bonds and so these are highly stable carbenes with a metal-carbon bond order considered to be one.

Because NHCs are strong σ -donor ligands and very unreactive, they are commonly compared to phosphine ligands, which also have good σ -donor characteristics and often act as spectator ligands within a reaction. However, studies by Huang et al.²⁹ have shown that NHCs often have stronger M-C bonds than the comparable M-P bonds and therefore form more stable metal complexes. The electronic and steric effects of phosphine donor ligands are strongly affected by the groups attached to the phosphorus donor, because they interact directly. In 1977, Tolman published data describing how the steric and electronic properties of the phosphine ligand, PR_3 , in a metal complex were affected when the R groups were altered.³⁰ He analysed the effect of different R groups on the stretching frequencies of the CO bond in $[\text{Ni}(\text{CO})_3(\text{PR}_3)]$ complexes, in relation to the reference phosphine, P^tBu_3 . This showed that the greater σ -donor properties of the R groups, the lower the stretching frequencies of the CO bonds. The Tolman Electronic Parameter describes this. Phosphines also have

varying steric bulk depending on the R groups in $[\text{Ni}(\text{CO})_3(\text{PR}_3)]$ complexes and the Tolman Steric Parameter describes this, where the Ni-P bond length is fixed. The PR_3 ligand forms a cone shape, as depicted in Figure 11, and the steric effect is measured based on the cone angle, θ , thus the bulkier the R groups, the larger the angle.

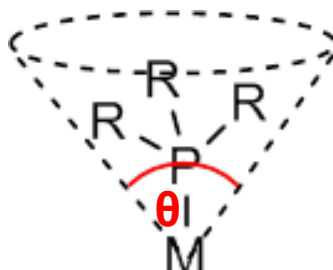


Figure 11: Tolman Cone Angle for phosphine ligands³⁰

These two factors, electronic and steric, are related and thus it is difficult to fine tune one property without altering the other. For NHCs however, the R groups attached to each nitrogen atom of the heterocycle are much further away from the bonding carbene. Therefore, electronic effects are subtler and it is steric effects that mainly dominate the bonding in NHCs. The bulkier the R groups of an NHC, the longer and weaker the M-C bond.³¹

Another type of carbene complex was described in 1974 by R. R. Schrock,³² but this complex did not contain a stabilised carbene. The reaction of $\text{LiCH}_2\text{C}(\text{CH}_3)_3$ with $[\text{Ta}(\text{CH}_2\text{C}(\text{CH}_3)_3)_3\text{Cl}_2]$ was shown to form a carbene complex containing a tantalum-carbon bond via α -H abstraction (Figure 12).^{23, 32}

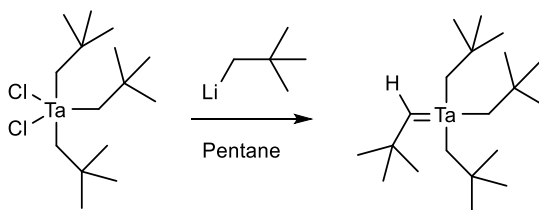


Figure 12: Formation of $[\text{Ta}(\text{CHC}(\text{CH}_3)_3)(\text{CH}_2\text{C}(\text{CH}_3)_3)_3]$ ^{23, 32}

In comparison to Fischer carbenes, Schrock carbenes, as they have come to be known, contain a high oxidation state metal centre and therefore the carbene carbon is nucleophilic and able to react with electrophiles. Schrock carbenes contain no stabilising substituents and thus the triplet state, containing two unpaired electrons, is

favoured. Therefore, in Schrock carbenes, the double bond between the metal and the carbene arises due to mutual π -donation. Bonding in all three carbene types is shown in Figure 13.

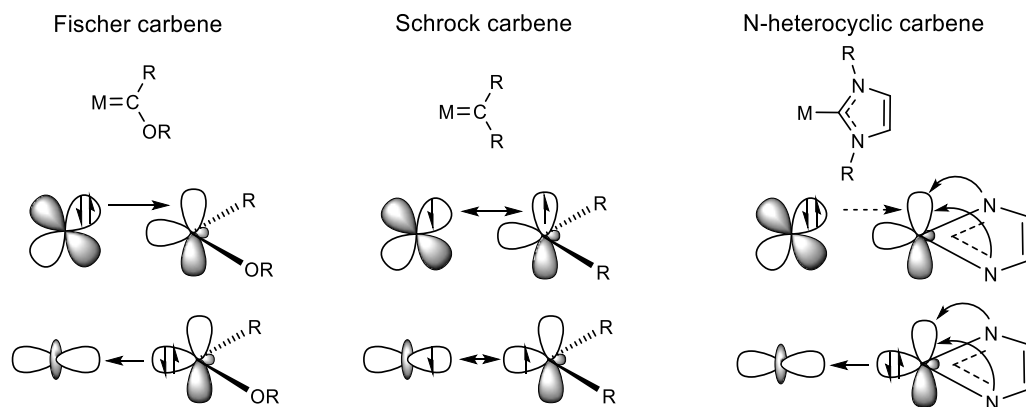


Figure 13: Bonding in Fischer, Schrock and N-heterocyclic carbenes

Schrock carbenes have emerged as being important in alkene metathesis. For example, the series of alkene metathesis catalysts first developed by R. H. Grubbs³³ all contain a ruthenium-carbon double bond, with the carbon bonded to an H and a phenyl derivative. The first generation catalysts also contain a phosphine ligand which is replaced by an NHC in the second generation catalysts (see Figure 14).³⁴ This makes the catalysts more stable to air and water so that they can be more easily handled.³⁵ This is particularly important for catalysts which are routinely used both for academic research and industrial applications.

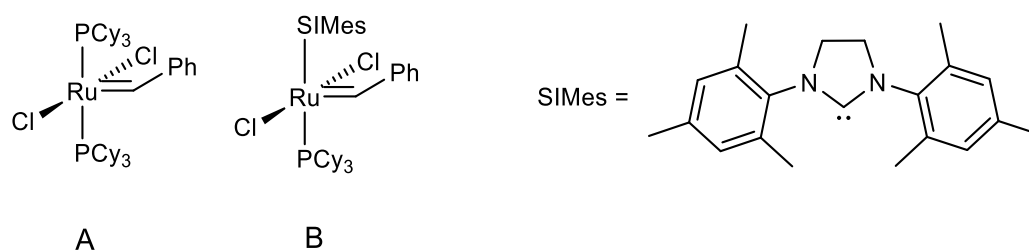


Figure 14: First generation (A) and second generation (B) Grubbs catalysts containing Schrock carbenes³³⁻³⁴

1.3. Other coordinating ligands

Many metal phosphine-containing and NHC-containing catalysts exist, particularly those of late transition metals, which have a wide variety of uses varying from homonuclear and heteronuclear bond formation reactions to carrying out catalytic reductions of substrates.³⁶⁻⁴³ As well as phosphines and NHCs, some other ligands that are commonly used in metal complexes include amines, carbonyls, alkenes, halides and alkoxides. These are often desirable due to their labile nature or required reactivity. For example, Crabtree's catalyst contains a cyclooctadiene ligand which can easily be hydrogenated during a reaction to enable the binding of other substrate ligands.⁴⁴ A number of binding modes are possible depending on the type of ligand, as shown in Figure 15. For example, amines act as σ -donor ligands due to the nitrogen lone pair donating into a metal orbital. No back donation can occur as the other p-orbitals are already involved in bonding. Alkenes bind to metal centres because a σ -donor interaction exists from the centre of the double bonds to the metal and a π -acceptor interaction exists as the metal can back donate electron density into the π^* antibonding orbital of the alkenes. This type of bonding also exists for CO ligands. Alkoxides act as both σ -donor and π -donor ligands because their lone pair can donate into the empty metal d-orbital. These bonding interactions should be considered when choosing and optimising ligands for desired catalytic activity.

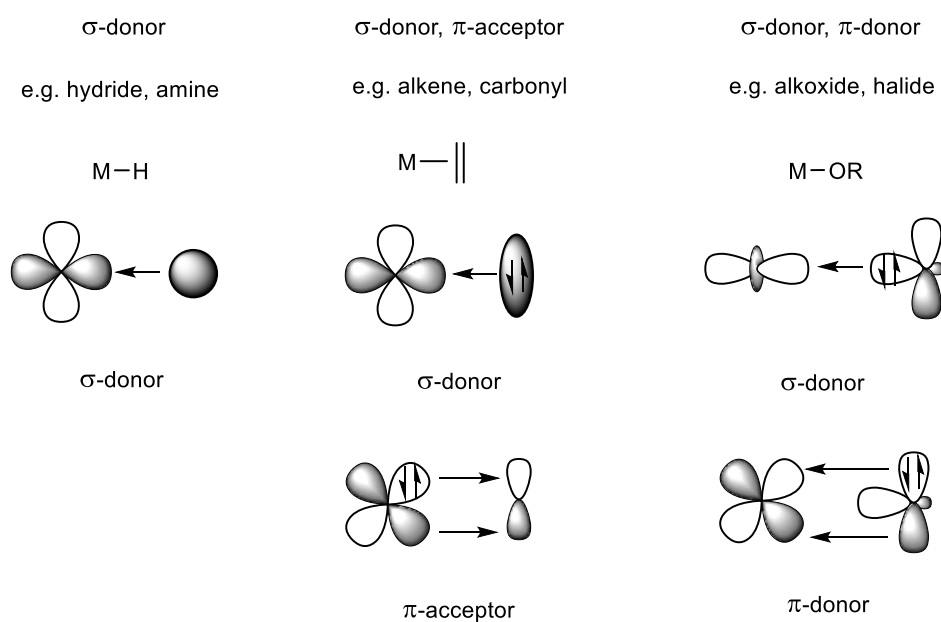


Figure 15: Bonding interactions for ligands commonly used in metal catalysts

1.4. Hydrogenation reactions

Many studies involving the hydrogenation of unsaturated substrates have been conducted using hydrogen as the direct source of H atoms. Typically, double or triple bonds are hydrogenated using H₂ gas and a catalyst where both the substrate and H₂ can bind to a metal centre. This acts as a site for hydrogenation which enables the addition of hydrogen across a multiple bond. When normal hydrogen is used to hydrogenate a multiple bond, all the states are approximately equally populated so transitions can occur from each lower energy state and the resulting signal intensities are small as shown in Figure 16.

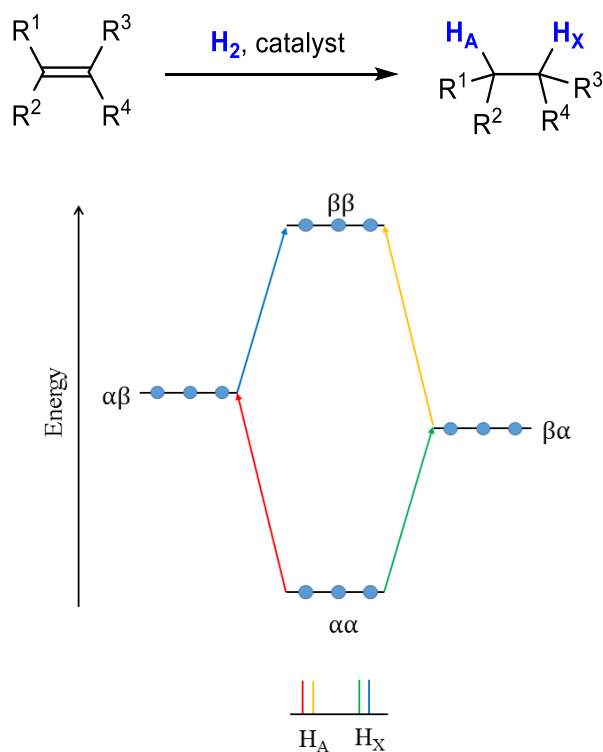


Figure 16: Transitions and spectrum resulting from hydrogenation of e.g. an alkene using normal hydrogen

The catalysts used for hydrogenation reactions are typically inorganic metal complexes, however, several non-metal main group systems have also been described. Frustrated Lewis Pairs⁴⁵⁻⁴⁸ are a major area of research with one specific example being the hydrogenation of carbon dioxide using an aminoborane complex as shown in Figure 17.⁴⁷ This leads to the formation of several reduced CO₂ borate species as depicted in Figure 17.

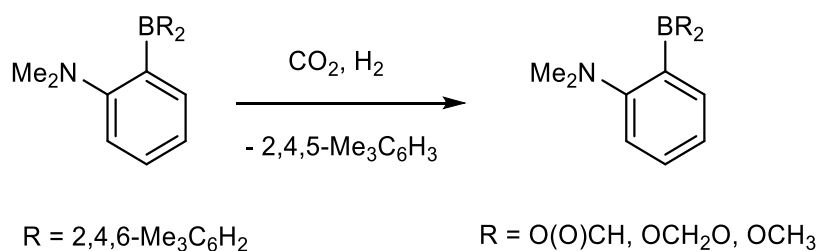


Figure 17: Reduction of CO_2 with H_2 using an aminoborane complex⁴⁷

A catalyst-free hydrogenation of an aromatic triphosphabenzene has also been described by Longobardi et al.⁴⁸ in 2014, where H_2 adds to a phosphorus-carbon double bond. Subsequent rearrangement leads to the formation of a bicyclo product, due to a hydride shift which causes the formation of a P-P bond and ring contraction. This contraction is irreversible, although H_2 addition before the hydride shift is reversible. This is shown in Figure 18.

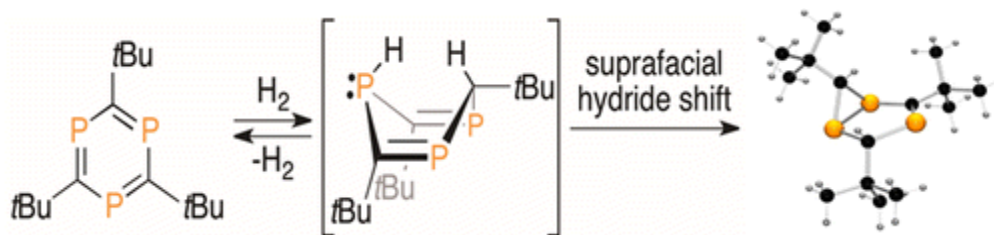


Figure 18: H_2 addition to an aromatic triphosphabenzene leads to $\text{P}=\text{C}$ bond hydrogenation followed by a hydride shift leading to a bicyclo product (Reprinted with permission from Longobardi, L. E.; Russell, C. A.; Green, M.; Townsend, N. S.; Wang, K.; Holmes, A. J.; Duckett, S. B.; McGrady, J. E.; Stephan, D. W., *J. Am. Chem. Soc.* **2014**, 136 (38), 13453 Copyright © 2014 American Chemical Society)

However, the work described herein focuses on inorganic metal complexes and these can be either heterogeneous or homogeneous complexes.

1.4.1. Heterogeneous catalysts

Heterogeneous catalysts are typically solid phase, being dispersed within a reaction solution. The first major breakthrough in heterogeneous catalysis was made by Paul Sabatier in the early 1900s when he was investigating the addition of hydrogen to organic molecules and found that the reaction could be improved by the addition of a small amount of nickel to a reaction flask.⁴⁹⁻⁵² This led to the development of the Sabatier process for which he was awarded the Nobel Prize in Chemistry in 1912. The Sabatier process involves the reduction of CO₂ to methane and water using H₂ gas and a nickel catalyst.⁵³ Since then, the range of solid-supported catalysts used has grown, with typical heterogeneous catalysts now using precious metals such as palladium, platinum, rhodium and ruthenium; however, less expensive alternatives like nickel can still be used. Common examples are Lindlar's catalyst, which contains palladium on calcium carbonate as the main structure and acts as a selective alkyne to alkene hydrogenation catalyst,⁵⁴ and Raney nickel, which has a wider scope.⁵⁵⁻⁵⁷ Important industrial uses of heterogeneous catalysts are the Fischer-Tropsch process for creating hydrocarbons from carbon monoxide and hydrogen (typically using Co, Fe or Ru based catalysts) and the Haber-Bosch process for creating ammonia from nitrogen and hydrogen (typically using Fe or Ru based catalysts). Many of these catalyst applications require high pressures and/or temperatures. It can be difficult to determine exact mechanisms for hydrogenation reactions using heterogeneous catalysts although it is widely accepted that both hydrogen and the substrate adsorb to the surface of a solid and then the H atoms are transferred stepwise to each atom of a multiple bond (see Figure 19).⁵⁸⁻⁵⁹ Due to the reversibility of step B, atom scrambling can occur if D₂ is used instead of H₂, as an H atom can transfer back to the support and lead to the formation of isomer mixtures. Only very weak interactions exist between the metal surface and the saturated substrate so that it leaves the surface site, ready for a new reaction to occur.

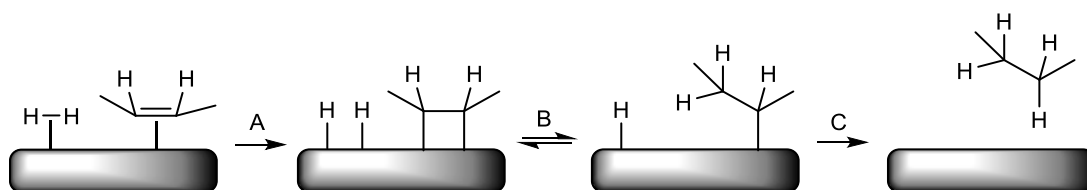


Figure 19: Steps involved in heterogeneous hydrogenation of a double bond on a metal surface⁵⁹

1.4.2. Homogeneous catalysts

In 1965, in the field of homogeneous catalysis, Wilkinson and Coffey independently discovered $[\text{RhCl}(\text{PPh}_3)_3]$ which was shown to act as a very efficient hydrogenation catalyst at low temperatures and pressures.⁶⁰⁻⁶² This was to become known as Wilkinson's catalyst and was followed by a number of other multiple phosphine-containing rhodium and ruthenium complexes, developed by Wilkinson, Schrock and Osborn.⁶³⁻⁶⁷ The mechanism of hydrogenation using these catalysts is well studied and understood, involving ligand loss and solvent stabilisation, and then oxidative addition of hydrogen to form a dihydride species, followed by substrate binding. Migratory insertion of one hydride to one end of the multiple bond occurs, which is then followed by reductive elimination to reform the active catalytic complex (see Figure 20).⁶⁸

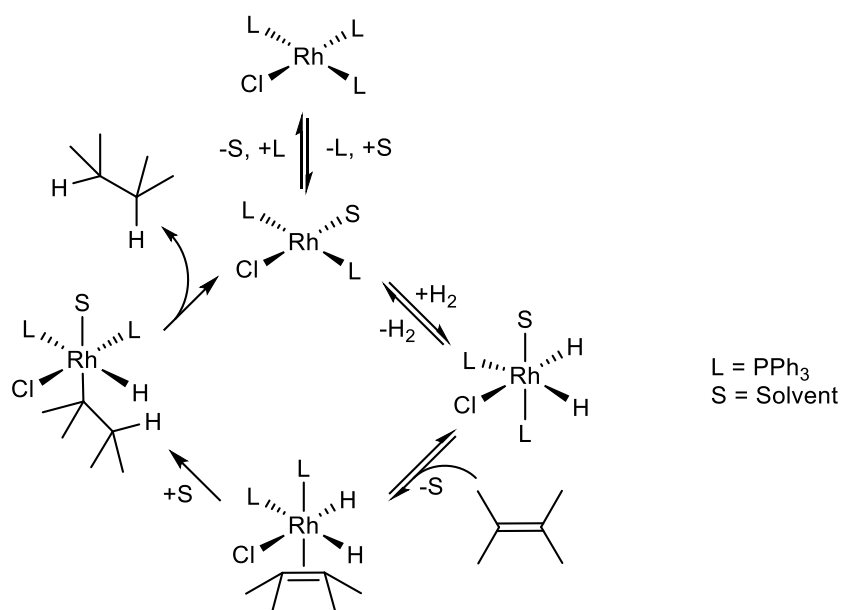


Figure 20: Mechanism for hydrogenation using $[\text{RhCl}(\text{PPh}_3)_3]$ ⁶⁸

These complexes are typically solvent-stabilised and can be limited and inhibited by the ligand dissociation that is required.⁴⁴ In the 1970s Crabtree developed an iridium analogue of Wilkinson's catalyst containing only one phosphine ligand and the easily hydrogenated bidentate ligand cyclooctadiene (COD). He deduced that since heterogeneous catalytic systems do not require a ligand loss step in order for substrate coordination to occur, homogeneous catalysis could potentially be improved by using non-coordinating solvents and enabling easy access to the metal centre by reducing the

number of other binding ligands.⁴⁴ This proved successful with the production of Crabtree's complex, $[\text{Ir}(\text{COD})(\text{PCy}_3)(\text{py})][\text{PF}_6]$, with the mechanism now able to continually cycle once the initial activation via COD hydrogenation has occurred (see Figure 21).⁶⁹ This time the mechanism proceeds via initial binding of the alkene substrate followed by oxidative addition of hydrogen. This is common for these complexes where the starting pre-catalyst cannot be regenerated because of the ligand hydrogenation.

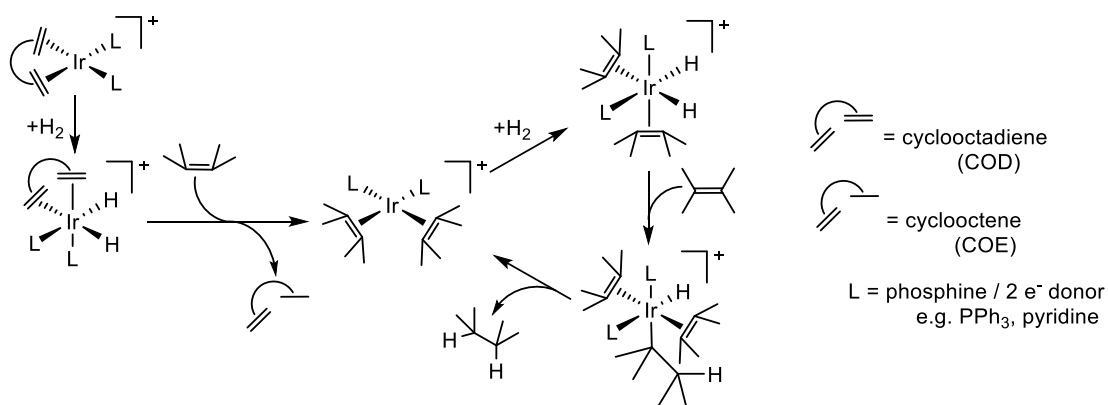


Figure 21: Mechanism for hydrogenation using $[\text{Ir}(\text{COD})(\text{L})_2]^+$ ⁶⁹

Since then, numerous homogeneous catalysts have been developed containing more specialised chiral ligands to enable enantioselective catalysis of functional groups such as alkenes and ketones.⁷⁰⁻⁷³ Many of the ligands are chelating chiral phosphines or C-N bidentate ligands that are chiral to induce chirality within the product. Examples include BINAP, which is used in the Noyori asymmetric hydrogenation of ketones for which Noyori, Knowles and Sharpless were awarded the Nobel Prize in 2001, as well as PHOX derived ligands (see Figure 22). However, these specially modified ligands can get complicated and thus expensive, particularly for major industrial uses.

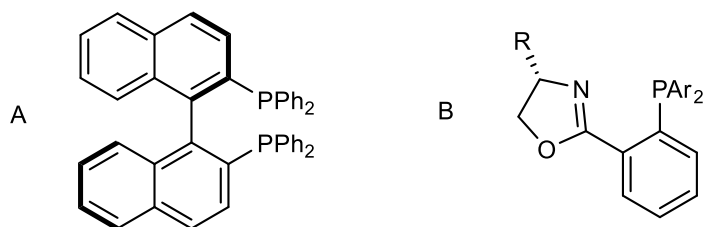


Figure 22: Chiral ligands R-BINAP (A) and PHOX (B) used for enantioselective synthesis

1.4.3. PASADENA and ALTADENA

One method used to monitor homogeneous hydrogenation reactions is ^1H NMR spectroscopy. Changing the nature of hydrogen used for hydrogenation, from normal H_2 to *p*- H_2 , can have several benefits when analysing reactions by NMR. When *p*- H_2 is reacted with a substrate, different magnetic states evolve from its initial $1/\sqrt{2}$ ($\alpha\beta - \beta\alpha$) singlet state. This means the initial singlet state can occupy the $\alpha\beta$ and/or the $\beta\alpha$ state so that a large population difference is created. This can lead to signal enhancements within a sample and therefore previously undetectable reactive intermediates as well as enhanced products can be observed by NMR.⁷⁴⁻⁷⁶ This can prove particularly useful for mechanistic studies and identifying low concentration analytes. Two NMR methods of visualising hyperpolarisation exist, known as PASADENA and ALTADENA, depending on whether the experiment is conducted in a high or low magnetic field.

1.4.3.1. PASADENA

When a reaction with a substrate, a metal catalyst and *parahydrogen* occurs within the high field of a spectrometer, the initial *parahydrogen* singlet state, $\alpha\beta - \beta\alpha$, mixes with one triplet state, $\alpha\beta + \beta\alpha$, and evolves to occupy both the $\alpha\beta$ and $\beta\alpha$ states approximately equally because, within the high magnetic field, these two states are similar in energy. Therefore, transitions from these states form a pair of antiphase doublets due to emission from both states to the $\alpha\alpha$ state and absorption from both states to the $\beta\beta$ state, as shown in Figure 23. This is known as *Parahydrogen And Synthesis Allow Dramatically Enhanced Nuclear Alignment* (PASADENA).⁷⁷

1.4.3.2. ALTADENA

When a reaction with a substrate, a metal catalyst and *parahydrogen* occurs in the low magnetic field outside of a spectrometer the initial *parahydrogen* singlet state, $\alpha\beta - \beta\alpha$, remains intact. It cannot mix with the initial triplet state because the energy difference is too great. Therefore, only the $\beta\alpha$ state remains populated. This means that an absorption peak at one chemical shift is observed due to the transition to the $\beta\beta$ state and an emission peak at a different chemical shift is observed due to the transition to the

$\alpha\alpha$ state (see Figure 23). This is called Adiabatic Longitudinal Transport After Dissociation Engenders Net Alignment (ALTADENA).⁷⁸

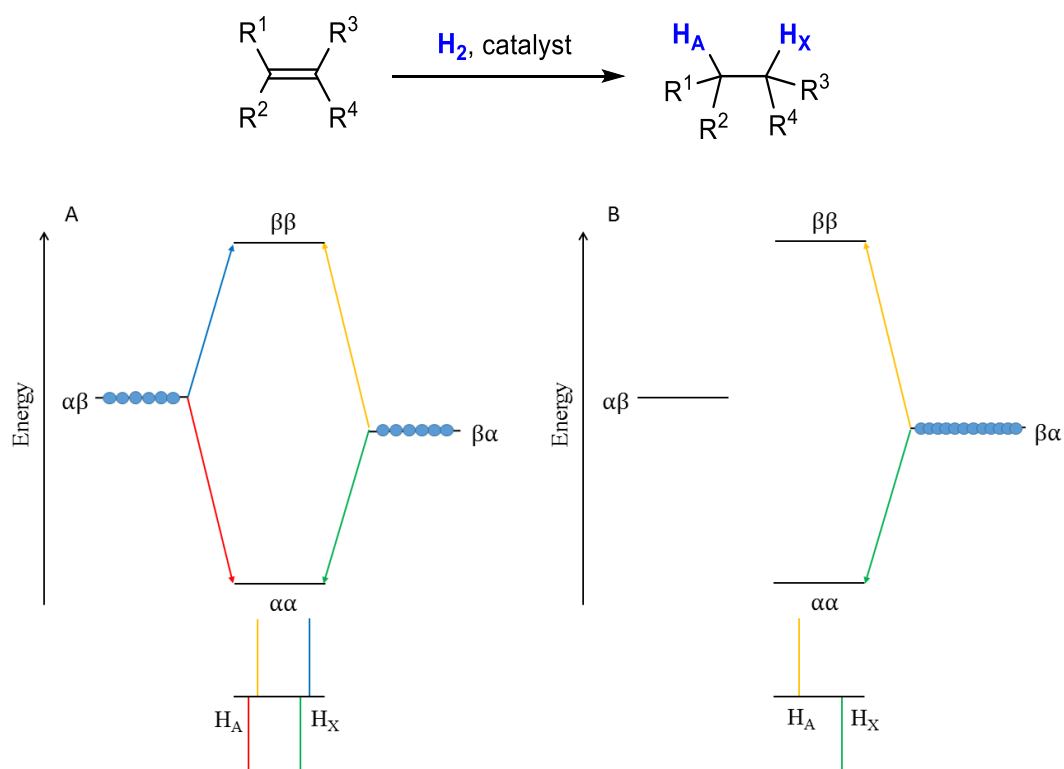


Figure 23: The populated spin states, transitions and resulting spectra from hydrogenation using parahydrogen under PASADENA conditions (A) and ALTADENA conditions (B)

Both PASADENA and ALTADENA are hydrogenative processes where the enhancement is observed due to incorporation of the H atoms from *parahydrogen* into the product molecule. However, another process that does not involve any chemical transformation of substrates is called Signal Amplification By Reversible Exchange (SABRE).² This can be thought of as equivalent to ALTADENA, as it occurs at low magnetic field, but it is non-hydrogenative.

Orthohydrogen can also be used for polarisation but it is not as powerful as *parahydrogen* because there is a smaller population difference as both the $\alpha\alpha$ and the $\beta\beta$ states are populated and the $1/\sqrt{2}(\alpha\beta + \beta\alpha)$ state splits to half occupy the $\alpha\beta$ state and half occupy the $\beta\alpha$ state.¹⁵

1.5. NMR and catalysis with *parahydrogen*

As discussed in Sections 1.4.1 and 1.4.2, many carbene and phosphine complexes have been shown to act as catalysts for a variety of different applications. Catalysts have been used in reactions involving *parahydrogen*, to give enhanced signals and monitor reaction intermediates and products, as lower concentration intermediates can be more easily observed when signals derived from them are enhanced.⁷⁹⁻⁸¹ *Parahydrogen-Induced Polarisation* (PHIP) was first predicted by Bowers and Weitekamp in 1986²⁰ and a year later they published work on the hydrogenation of acrylonitrile to propionitrile using Wilkinson's catalyst and *parahydrogen* (see Figure 24).⁷⁷ This reaction was conducted in the high field of the magnet and is an example of the PASADENA process.⁷⁷

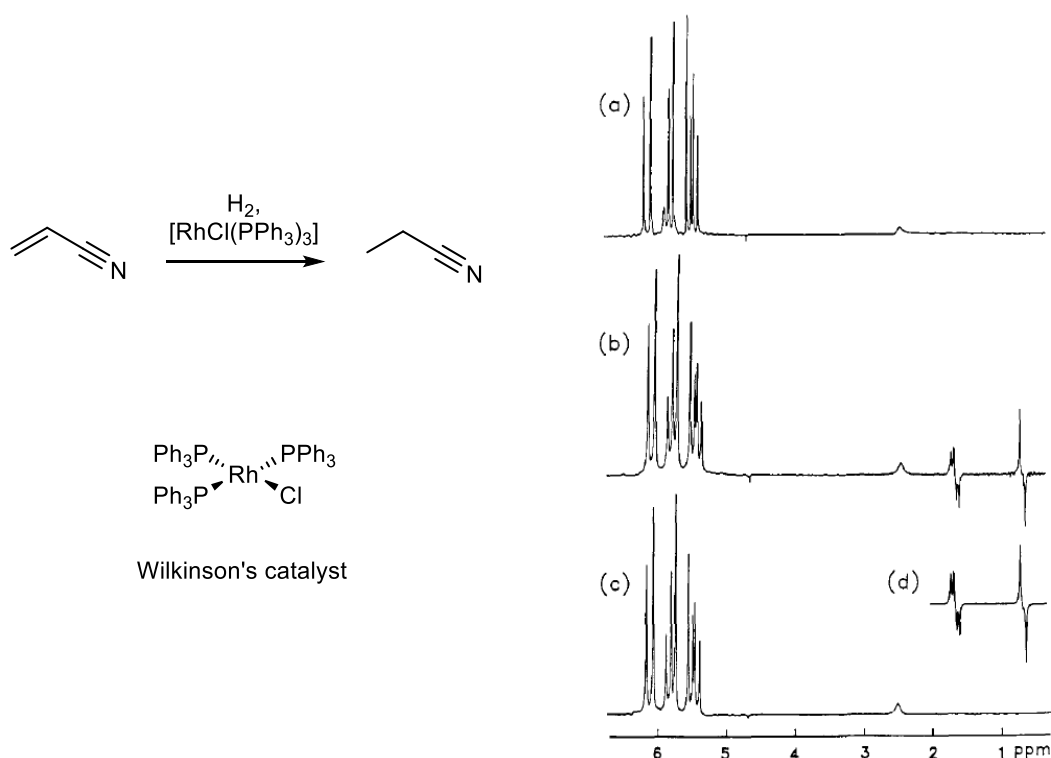


Figure 24: Hydrogenation of acrylonitrile to propionitrile to demonstrate signal enhancements using *p*-H₂. ¹H NMR spectra before reaction was conducted (a), during hydrogenation (b), after the enhancement had decayed (c) and a simulation of the enhanced spectra from the theory (d) (Reprinted with permission from Bowers, C. R.; Weitekamp, D. P. *J. Am. Chem. Soc.* **1987**, 109, 5541. Copyright © 1987 American Chemical Society)⁷⁷

Other more recent examples of PHIP include the formation of intermediates on hydrogenation pathways, such as the palladium bis-phosphine vinyl hydride intermediates shown in Figure 25.⁸² Without the use of $p\text{-H}_2$, signals for these low concentration complexes would not be observable and mechanistic studies of hydrogenation would be more difficult to follow and identify.

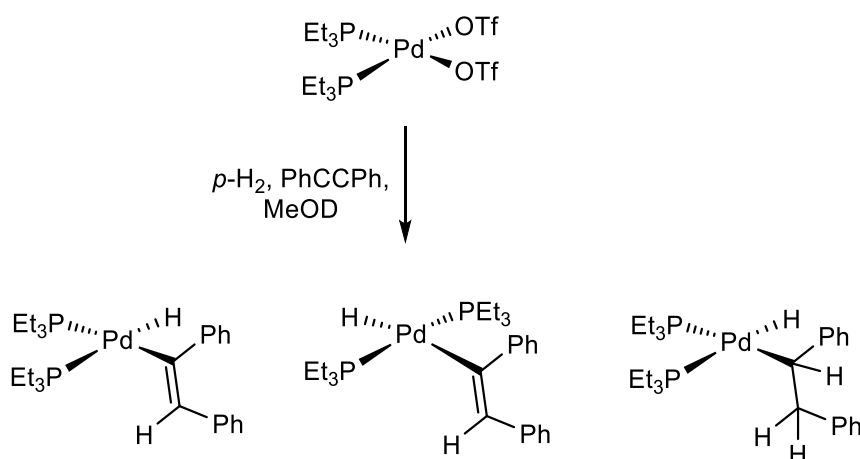


Figure 25: Vinyl hydride and alkyl hydride intermediates on the pathway to hydrogenation of diphenylacetylene using $[\text{Pd}(\text{PEt}_3)_2(\text{OTf})_2]$ with $p\text{-H}_2$ ⁸²

The most recent development in this field of PHIP is the non-hydrogenative use of $p\text{-H}_2$ as a polarisation source in the SABRE technique.

1.6. Signal Amplification By Reversible Exchange

In SABRE, the substrate, metal complex and *parahydrogen* are mixed in the low magnetic field outside of the spectrometer, as for ALTADENA, but without hydrogenation taking place.⁸³ The substrate and *parahydrogen* bind to an iridium complex, as shown in Figure 26, and polarisation is transferred from the hydrides, originating from *parahydrogen*, to the substrate protons, via *J*-coupling. The substrate used remains chemically unchanged during the catalysis.⁸³ The catalysts employed for SABRE have been shown to take the form of cationic iridium complexes, which possess either phosphine⁸³⁻⁸⁶ or NHC ligands.⁸⁷⁻⁸⁸

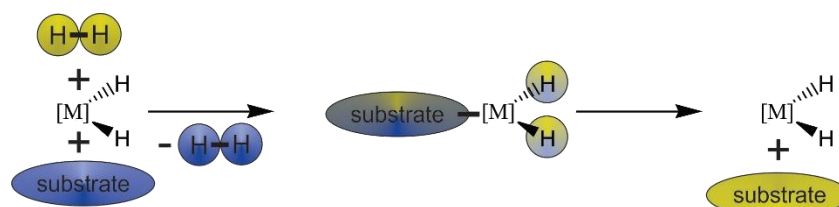
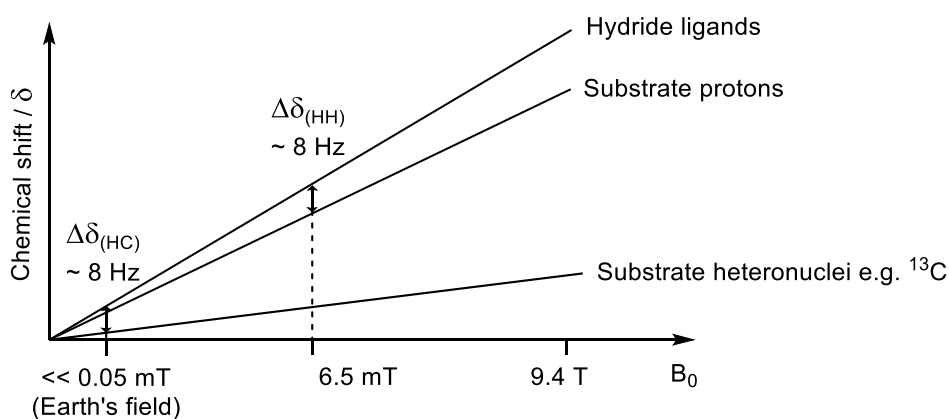


Figure 26: The route to polarisation transfer via SABRE

For efficient polarisation transfer, the chemical shift difference, between the hydride ligands and the nuclei on the substrate which are to be polarised, has to be approximately equal to the *J*-coupling between the hydride ligands.⁸⁹ For example, a typical value for the *J*-coupling between hydride ligands is about 5-10 Hz and the chemical shift difference between these hydrides and protons on a substrate is commonly about 30-40 ppm. This equates to a minimum of 12000 Hz chemical shift difference between hydride ligands and substrate protons on a 400 MHz spectrometer. Thus, for optimum transfer, low fields are required; for proton nuclei at 6.5 mT (0.277 MHz), the chemical shift difference of 30 ppm is now equivalent to about 8.3 Hz which closely matches the $^2J_{\text{HH}}$ coupling between the hydride ligands. This is detailed in Figure 27. This can also be explained using the Level Anti-Crossing approach, where at low field, the energies of the spin states become close, which enables mixing of these states so that polarisation transfer can occur efficiently.⁹⁰⁻⁹¹ The Polarisation Transfer Field (PTF) also affects the energies of magnetic spin states that are populated during magnetisation transfer and thus affects the appearance of enhanced proton spectra.



High field e.g. 9.4 T = 400 MHz where 30 ppm = 12000 Hz
 Lower field e.g. 6.5 mT = 0.277 MHz where 30 ppm = 8.3 Hz

Figure 27: Schematic for how chemical shift differences between nuclei increase as the magnetic field is increased

The first example of a pre-catalyst that reversibly binds hydrogen and can thus be used for SABRE⁸⁷ was Crabtree's complex, developed by R. Crabtree in 1979⁴⁴ whilst looking into iridium derivatives of Wilkinson's catalyst, $[\text{RhCl}(\text{PPh}_3)_3]$.^{60, 75} Wilkinson's catalyst is an efficient hydrogenation catalyst, that also undergoes PHIP,⁷⁵ and Crabtree was further investigating these species. Whilst in the development stages, George Morris, a graduate student who was working for Crabtree, observed that $[\text{Ir}(\text{COD})(\text{PCy}_3)(\text{py})][\text{PF}_6]$ could reversibly bind hydrogen. Crabtree's catalyst, as it became known, was shown to carry out hydrogenation reactions of sterically bulky alkenes, be stable to oxidation and be more active than Wilkinson's catalyst.^{44, 92} In 2009, it was also shown to act as a pre-catalyst for SABRE, being able to transfer polarisation from $p\text{-H}_2$ to protons of a substrate, without chemically transforming the substrate.²

Since 2009, several different SABRE catalysts have been discovered and developed in order to find the most efficient polarisation transfer catalyst for different applications and in different solvent systems.⁸⁶⁻⁸⁸

1.7. Polarisation transfer catalysts

One of the most successful hyperpolarisation transfer pre-catalysts used to date is $[\text{Ir}(\text{COD})(\text{IMes})\text{Cl}]$ (where COD is cyclooctadiene and IMes is 1,3-bis(2,4,6-trimethylphenyl)imidazole-2-ylidene) which contains an N-heterocyclic carbene motif.⁸⁷⁻⁸⁸ Upon the addition of a substrate, the labile chloride can be displaced and a substrate binds in its place to form species of the kind $[\text{Ir}(\text{COD})(\text{IMes})(\text{substrate})]\text{Cl}$.⁹³⁻⁹⁴ When shaken with *para*hydrogen and a substrate the COD is hydrogenated and the catalyst forms the active species $[\text{Ir}(\text{H})_2(\text{IMes})(\text{substrate})_3]\text{Cl}$ as shown in Figure 28.⁸⁸ *Para*hydrogen adds as two hydride ligands which are magnetically inequivalent but chemically equivalent and three substrate ligands also bind to the iridium centre to create a charged octahedral complex. Polarisation is then transferred to the substrates that are in the *trans* positions to the hydride ligands. This complex has proved active for a wide range of substrates which include pyridine,⁸⁸ nicotinamide,⁹⁵⁻⁹⁶ isoniazid,⁹⁷ pyrazinamide,⁹⁷ pyrazole⁸⁴ and acetonitrile.⁸⁶ Exchange between the substrates being free in solution and bound to the complex means that polarisation is transferred to the substrates. This results in visible hyperpolarisation in the substrate molecules in solution. Multiple visits of the substrate and reintroduction of fresh *p*-H₂ to the catalyst centre results in build-up of polarisation of the substrate so can lead to even greater signal enhancements being observed for free substrate molecules in solution.¹ The use of the NHC ligand in the catalyst dramatically increased the enhancement levels relative to those with PCy₃ as shown for Crabtree's catalyst.^{2, 87-88, 97} Many other pre-catalysts of the same class as $[\text{Ir}(\text{COD})(\text{IMes})\text{Cl}]$ have been developed with modified symmetric NHC ligands to alter the steric and electronic properties and affect the overall catalyst reactivity.⁸⁷

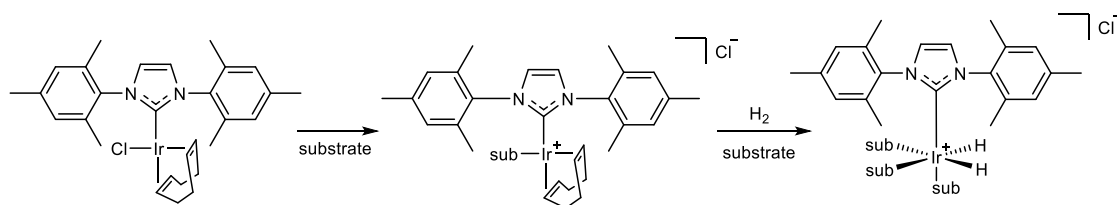


Figure 28: $[\text{Ir}(\text{H})_2(\text{IMes})(\text{sub})_3]\text{Cl}$ formed upon activation of $[\text{Ir}(\text{COD})(\text{IMes})\text{Cl}]$ with substrate and H₂, via intermediate $[\text{Ir}(\text{COD})(\text{IMes})(\text{sub})]\text{Cl}$

An alternative catalyst system has also been reported that is based on $[\text{Ir}(\text{H})_2(\text{IMes})(\text{PCy}_3)(\text{substrate})_2][\text{BF}_4]$.⁸⁶ The substrates are now pyridine and acetonitrile. The mixed substrate-containing catalyst, $[\text{Ir}(\text{H})_2(\text{IMes})(\text{PCy}_3)(\text{pyridine})(\text{CH}_3\text{CN})][\text{BF}_4]$, which is also charged, proved most effective for SABRE even though it contains a pair of chemically and magnetically inequivalent hydride ligands (see Figure 29). These results confirmed that it is possible to block two coordination sites in the SABRE catalyst with non-labile ligands, without suppressing activity and whilst retaining a charged system. Species such as $[\text{Ir}(\text{H})_2(\text{IMes})(\text{PCy}_3)(\text{pyridine})_2][\text{BF}_4]$ with magnetically inequivalent but chemically equivalent hydride ligands, whilst being directly related to $[\text{Ir}(\text{H})_2(\text{IMes})(\text{substrate})_3]\text{Cl}$, proved less effective due to poor ligand exchange.

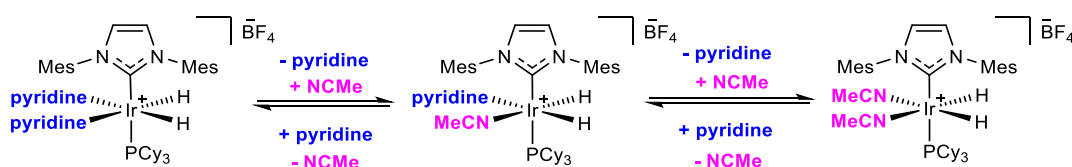


Figure 29: Formation of the mixed substrate species

$[\text{Ir}(\text{H})_2(\text{IMes})(\text{PCy}_3)(\text{pyridine})(\text{CH}_3\text{CN})][\text{BF}_4]$ and equilibration with the $[\text{Ir}(\text{H})_2(\text{IMes})(\text{PCy}_3)(\text{substrate})_2][\text{BF}_4]$ complexes (where Mes = 2,4,6-trimethylphenyl)⁸⁶

More recently a different charged iridium system has been developed, containing a further blocking site in its coordination sphere. Here, a pincer ligand binds through two phosphine sites which are bridged via a pyridyl linker to create a PNP chelate.⁹⁸ The activated *cis*-dihydride complex reacts with *p*-H₂ and enables polarisation transfer to pyridine via SABRE. However, limited signal enhancement is seen due to slow ligand exchange and rapid *p*-H₂ consumption due to the $[\text{Ir}(\text{H})_2(\text{H}_2)(\text{PNP})][\text{BF}_4]$ intermediate in solution (see Figure 30). This again proves how catalyst development can be very important for designing optimised systems.

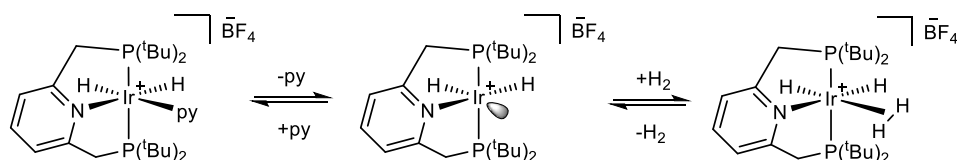


Figure 30: $[\text{Ir}(\text{H})_2(\text{PNP})(\text{py})][\text{BF}_4]$ and the formation of the dihydride-dihydrogen intermediate $[\text{Ir}(\text{H})_2(\text{H}_2)(\text{PNP})][\text{BF}_4]$ ⁹⁸

1.8. Molecules suitable for polarisation transfer

The vast majority of the substrates that have been polarised via SABRE contain N-heterocycles with the most common motif being that of a pyridyl ring.^{84, 94, 96-97} Other species that have been used more recently, still bind to the metal centre via a nitrogen atom but contain a cyano group, such as acetonitrile and benzonitrile.⁹⁹ This is due to the binding and lability characteristics that are suitable to enable exchange with free substrate in solution rather than the binding being too strong which would inhibit exchange.

Most studies involve direct proton polarisation, either by *p*-H₂ incorporation or SABRE polarisation transfer and this is becoming particularly well optimised,⁹⁷ but development towards achieving stronger polarisation of heteronuclei such as ¹³C, ¹⁵N and ³¹P is currently limited. Analysis of these nuclei has advantages in that their spin relaxation times are longer, hence the hyperpolarised signal lasts longer, and in contrast to ¹H NMR, the background signal is comparably smaller.¹⁰⁰

Polarisation transfer to heteronuclei was first observed by Morris and Freeman in 1979 for a ¹³C NMR spectrum of pyridine.¹⁰¹ They described a new NMR method called Insensitive Nuclei Enhanced by Polarisation Transfer (INEPT) which enabled transfer of polarisation from thermally equilibrated proton nuclei to carbon nuclei. However, this requires a specially modified pulse sequence at high field under PASADENA conditions. Since then, this technique has been used with *p*-H₂ to further enhance heteronuclei signals such as ¹⁵N, ¹³C and ²⁹Si.^{85, 102-104}

In 1989, direct observation of polarised ³¹P was observed by Eisenschmid et al. using PHIP.¹⁰⁵ The oxidative addition of *p*-H₂ to a square planar iridium(I) complex containing a chelating phosphine ligand demonstrated ³¹P polarisation through nOe interactions between phosphine ligands and the hydrides that were *p*-H₂ derived. Direct ³¹P NMR analysis showed antiphase phosphorus signals for the phosphine ligands. This concept has since been expanded to include other heteronuclei such as ¹³C. For example, hydrogenation of a suitable substrate, such as dimethyl acetylenedicarboxylate to produce dimethyl maleate, shown in Figure 31, enables observation of enhanced carbon signals under PASADENA conditions (see Figure 32).^{102, 106}

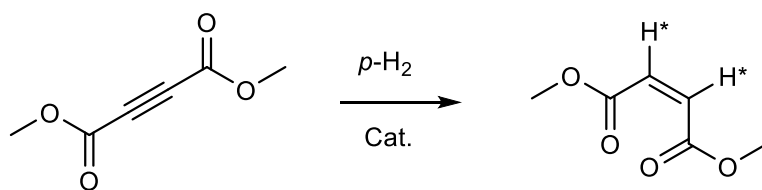


Figure 31: The formation of dimethyl maleate from the parahydrogenation of dimethyl acetylenedicarboxylate with the $p\text{-H}_2$ derived protons labelled with an asterisk. Cat. = $[\text{Rh}(\text{COD})(\text{dppb})(\text{PPh}_3)_2][\text{BF}_4]$ where *dppb* is 1,4-bis(diphenylphosphino)butane^{102, 106}

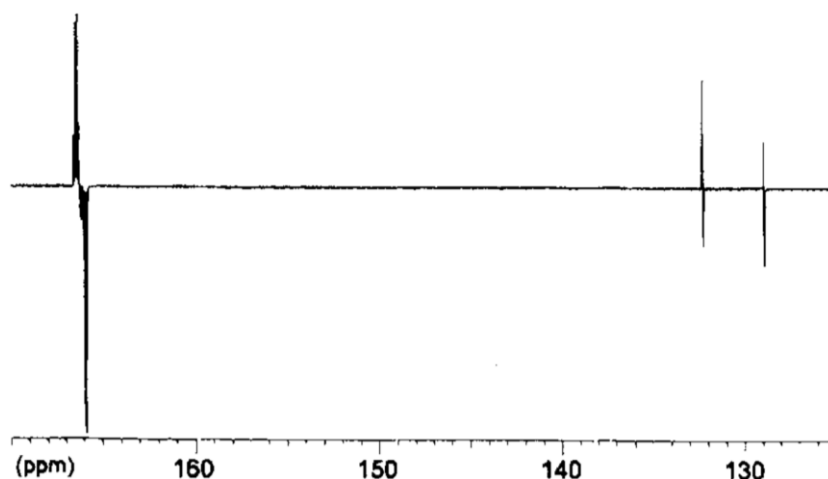


Figure 32: 50 MHz ^{13}C NMR spectrum of dimethyl maleate produced from the parahydrogenation of dimethyl acetylenedicarboxylate (Reprinted with permission from Barkemeyer, J.; Haake, M.; Bargon, J. *J. Am. Chem. Soc.* **1995**, 117, 2927. Copyright © 1995 American Chemical Society)¹⁰⁶

More recently, polarisation transfer via SABRE to ^{13}C , ^{15}N , ^{19}F and ^{31}P has been reported to occur at very low magnetic fields outside of the spectrometer and be readily observed directly.^{2, 89, 100, 107-108} Polarisation using the common SABRE pre-catalyst, $[\text{Ir}(\text{COD})(\text{IMes})\text{Cl}]$ has been used to facilitate ^{15}N NMR polarisation,¹⁰⁷⁻¹⁰⁸ as well as ^{31}P NMR polarisation, with phosphorus-substituted pyridine substrates, such as diethyl 3-pyridylphosphonate, demonstrating up to 3500-times greater ^{31}P NMR signal when compared to a thermal spectrum.¹⁰⁹ Direct phosphine polarisation has also been observed when using $[\text{Ir}(\text{H})_2(\text{PPh}_3)_3\text{Cl}]$ with $p\text{-H}_2$ at elevated temperatures to initiate phosphine exchange.¹¹⁰

Another factor that is being explored is the effect of deuteration of both substrate and catalyst protons within systems.^{86, 88, 95, 109, 111} It has been shown that a reduction in the number of protons on a substrate, that can accept polarisation, results in increased

enhancement observed for the remaining proton sites. This is because there are fewer protons to share the polarisation.⁸⁴ In addition, deuterated substrates can also exhibit longer lifetimes due to less proton coupling, resulting in longer T_1 relaxation times. Furthermore, deuteration of the other catalyst ligands, such as NHCs and phosphines, also leads to significantly increased signal being transferred to the desired substrate proton sites.⁸⁶ For example, Figure 33 shows how the enhanced proton signal for acetonitrile, using the catalyst system $[\text{Ir}(\text{H})_2(\text{IMes})(\text{PPh}_3)(\text{pyridine})(\text{acetonitrile})][\text{BF}_4]$, is increased upon deuteration of the other catalyst ligands.⁸⁶

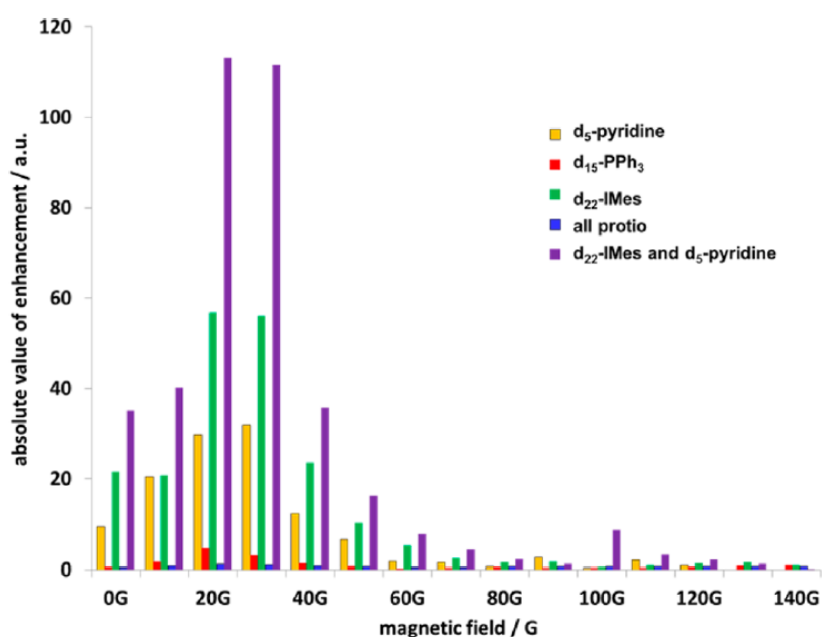


Figure 33: A plot showing how the ^1H NMR signal enhancement for acetonitrile varies when using $[\text{Ir}(\text{H})_2(\text{IMes})(\text{PPh}_3)(\text{pyridine})(\text{acetonitrile})][\text{BF}_4]$ at different polarisation transfer fields and how using deuterated ligands affects the observed enhancement levels (Reprinted with permission from Fekete, M.; Bayfield, O.; Duckett, S. B.; Hart, S.; Mewis, R. E.; Pridmore, N.; Rayner, P. J.; Whitwood, A., *Inorg. Chem.* **2013**, 52 (23), 13453-13461. Copyright © 2013 American Chemical Society AuthorChoice via Creative Commons CC-BY agreement http://pubs.acs.org/page/policy/authorchoice_ccby_termsfuse.html)⁸⁶

Deuteration has also been shown to affect polarisation transfer to heteronuclei via SABRE. Burns et al.¹⁰⁹ have demonstrated that deuteration of ethyl groups in a phosphonate ethyl ester species prevents leaching of polarisation from the ^{31}P to the ^1H atoms, due to the larger frequency difference that is present between phosphorus and deuterium. These are significant advances as they could ensure that the most optimised systems can be developed and used.

1.9. Potential for MRI

In comparison to the obvious experimental benefits of using $p\text{-H}_2$ to analyse reaction intermediates, kinetics and mechanisms, the potential use of PHIP in MRI has been realised more recently. Advantages of the enhanced signal in MRI are higher sensitivity images with improved signal-to-noise and better resolution which could greatly aid clinicians by potentially enabling earlier diagnosis of disease.¹¹²

Much of the testing completed for many catalysts and different substrates has been carried out in methanol as the solvent of choice. However, in order to expand SABRE for use in clinical diagnosis, more biocompatible solvent systems have to be used, such as ethanol⁹⁷ and ethanol/water mixtures.^{95, 113} This raises the issue of catalyst solubility in water. In order to overcome this, a number of water-soluble systems have been developed incorporating solubilising groups such as sulfonates, amines, alcohols and polyethylene glycol (PEG) chains as shown in Figure 34.¹¹⁴⁻¹¹⁶ Some of these systems have been charged which further aids water solubility. However, they also suffer due to the lower solubility of hydrogen in water.

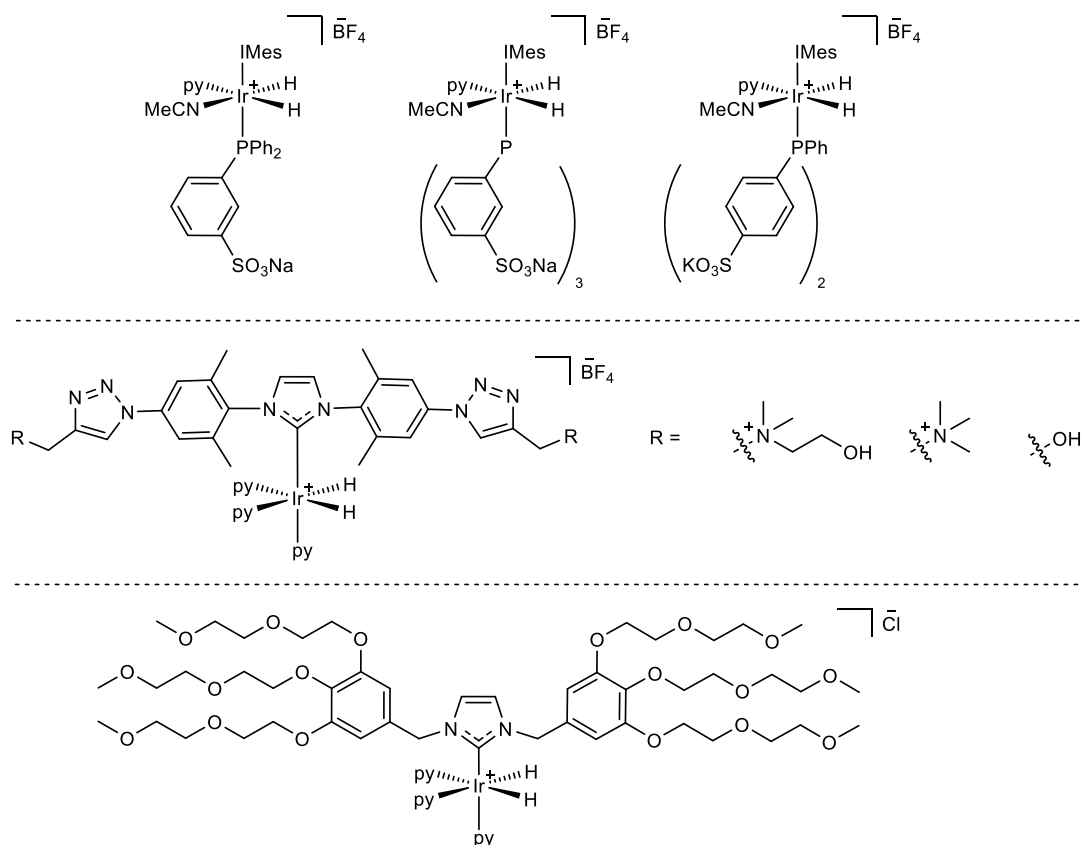


Figure 34: Water-soluble phosphine and NHC ligands incorporated into catalysts¹¹⁴⁻¹¹⁵

Another factor to consider prior to injection for a clinical use is the toxicity of the catalyst. The effect of the catalyst on the patient must be minimised, whether that means total removal of the catalyst before injection or only being able to administer very low concentrations. One recent study has shown that deactivation of the catalyst is possible without quenching the polarisation level of the substrate. Binding of a bidentate ligand such as bipyridine or 1,10-phenanthroline disables the ligand exchange and thus blocks the catalyst.¹¹⁷ However, this can be wasteful as the catalyst is rendered inactive and therefore cannot be reused for further polarisation tests.

Studies to aid catalyst removal have therefore explored the option of using heterogeneous catalysts instead of the more developed, more commonly used homogeneous catalysts. This would enable easier removal of the catalyst by filtration followed by injection of the polarised substrate in solution. The catalyst could then be reused upon addition of more substrate and solution.

One example of a heterogeneous system involves the use of polymer microbeads with bound 4-dimethylaminopyridine groups to bind the [Ir(COD)(IMes)][PF₆] pre-

catalyst.¹¹⁸ Other nanoscale heterogeneous catalysts, one with a nanoparticulate structure containing a TiO₂ core functionalised with PMAA (poly(methacrylic acid))¹¹⁹ and one with a polymer ‘comb’ type structure made of PVP (polyvinylpyridine),¹¹⁹ have also been tested. However, for all catalysts, the levels of enhancement were markedly reduced in comparison to using free [Ir(COD)(IMes)Cl], although the use of the TiO₂/PMAA-derived pre-catalyst proved to be the most efficient with up to 40-fold enhancements observed for pyridine. One promising observation was that no catalyst leaching occurred during the SABRE reactions and therefore all enhancements could be attributed to the heterogeneous catalyst. Furthermore, the possibility of reusing the catalyst was investigated and proved to be feasible.¹¹⁹ More development of this could prove promising for taking SABRE towards clinical use. The structures of these heterogeneous catalysts are depicted in Figure 35.

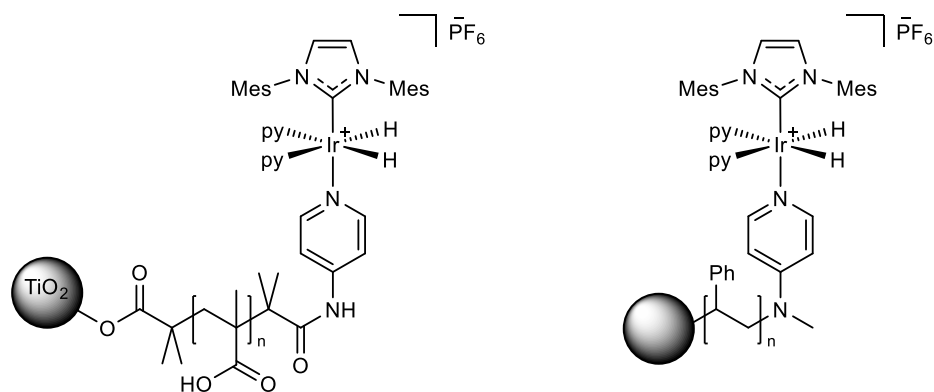


Figure 35: Heterogeneous SABRE catalysts¹¹⁸⁻¹¹⁹

Another problem to overcome for MRI use is the short lifetime of the hyperpolarised state which means high quality images must be collected rapidly before the signal decays back to thermal equilibrium. Several studies have been carried out investigating T_1 relaxation and lengthening the lifetime of the hyperpolarised state. This can be achieved in a number of ways, such as specific substrate design and synthesis¹⁰⁹ and the use of heteronuclei which take longer to relax.¹⁰⁷⁻¹⁰⁸ Another area which enables longer detection times and which could prove particularly important, is the use of hyperpolarised long-lived states which can be harnessed to provide enhanced signals.¹²⁰⁻¹²⁴ Overall, this is a major challenge that needs to be addressed in order for SABRE to be efficiently exploited in the field of MRI.

1.10. Project aims

The aim of this project is to investigate the effect of blocking a binding site within the catalyst coordination sphere, using a non-labile ligand to see whether a reduction in the number of substrates, as depicted in Figure 36, would enable polarisation to be distributed among fewer substrates so greater enhancements could be observed. Also, the analysis of ligand exchange rates within the bidentate species could enable the determination of the optimal exchange for most effective polarisation transfer. This is the principle behind using bidentate NHCs.

Several bidentate species could be synthesised to address a number of different issues such as exchange rates, magnetic and chemical inequivalence, solubility and activation. The chelating pendent arm could be varied to contain different functional groups to determine the electronic and steric effects on polarisation transfer.

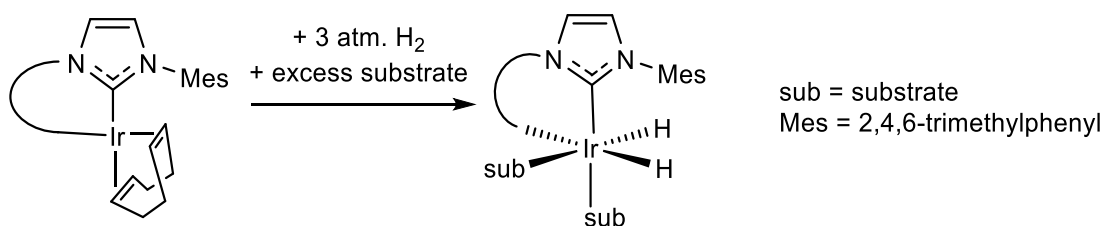


Figure 36: A potential framework for a bidentate NHC-containing iridium complex

The blocking of this substrate binding site could also enable stabilisation of the complexes and therefore more weakly binding ligands could be used as substrates. This may enable the polarisation of more labile substrate species. It is known that the efficiency of polarisation transfer is affected by a number of variables, such as concentrations of each reactant, ligand exchange rates and subsequent substrate relaxation rates.⁹¹ Specific catalyst design could enable better manipulation of some of these catalyst and system dependent parameters.

2. Development of neutral bidentate iridium carbene complexes

2.1. Introduction

The incorporation of N-heterocyclic carbenes into polarisation transfer catalysts for use in SABRE has so far involved monodentate, symmetric carbenes.^{87, 93} The most efficient pre-catalyst which incorporates one of these symmetric NHC ligands, is $[\text{Ir}(\text{COD})(\text{IMes})\text{Cl}]$ (where COD is cyclooctadiene and IMes is 1,3-bis(2,4,6-trimethylphenyl)imidazole-2-ylidene), although many others are known, containing both aromatic and aliphatic groups as indicated in Figure 37.⁹³

The general synthetic route to create iridium-based pre-catalysts containing carbene ligands involves the formation of an imidazolium salt, followed by complexation with the metal to create the pre-catalyst. The carbene itself is formed from an imidazole ring, where the carbon atom sandwiched between the two nitrogen atoms forms the carbene centre that bonds to the metal. Typically, a strong base is used to deprotonate the carbon atom to form the free carbene, before reaction with an iridium metal source, commonly either $[\text{Ir}(\text{COD})\text{Cl}]_2$ or $[\text{Ir}(\text{COD})\text{OMe}]_2$. A general synthetic route to produce such iridium carbene complexes is shown in Figure 37.

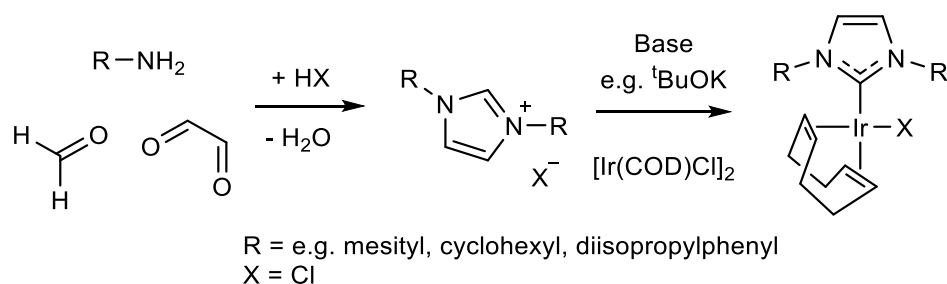


Figure 37: General synthetic route to form symmetric iridium carbene complexes

The formation of the imidazole ring occurs via a Debus-Radziszewski type multi-component reaction with glyoxal, formaldehyde, and two equivalent amine precursors. Figure 38 shows the mechanism of imidazole formation when two different amine sources are used.¹²⁵⁻¹²⁶ This reaction proceeds with initial formation of a di-imine via condensation of the mesityl amine and ammonia with glyoxal and subsequent

elimination of water. This di-imine then undergoes condensation with formaldehyde and further loss of water to form the imidazole ring.

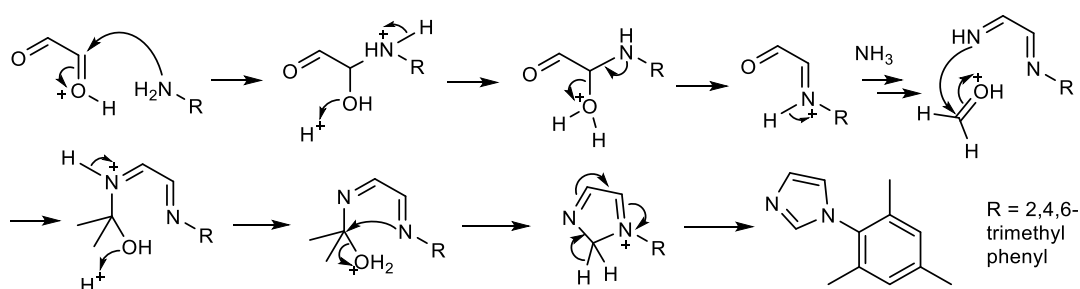


Figure 38: The mechanism for formation of the imidazole ring of mesityl imidazole

The large range of symmetric iridium carbene complexes that have been produced have been synthesised using two equivalents of the same amine precursor.¹²⁷ However, this synthetic route (see Figure 37) does not easily allow for modification of the carbene backbone to produce asymmetric carbene variants.

Several different routes exist for forming asymmetric imidazolium salt precursors which can then be used to produce asymmetric NHC ligands for specialist catalytic applications. One involves the initial formation of one side of the backbone, such as the mesityl imidazole shown in Figure 38, followed by a nucleophilic substitution reaction with a compound containing a good leaving group, such as a halide. This procedure allows for a larger scope when deciding what other substituents or groups to include in the coordination sphere of iridium.¹²⁸

A second possible method, with a recent example described by He et al.,¹²⁹ involves the stepwise coupling of two distinct amine compounds with a central molecule that forms part of the imidazole ring, using Buchwald-Hartwig coupling, as shown in Figure 39. This enables the incorporation of multiple amine molecules to introduce differing functionalities on the imidazole ring.¹²⁹

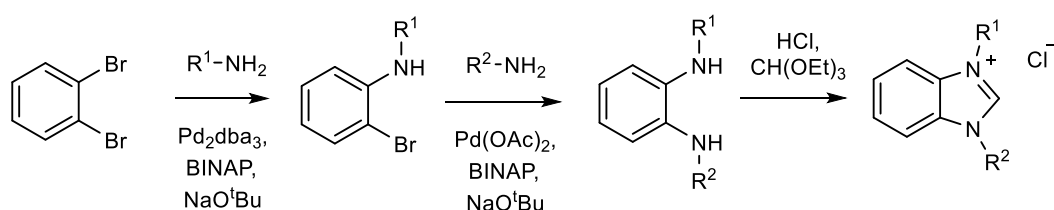


Figure 39: Synthetic route to form asymmetric imidazolium salts used by He et al.¹²⁹

A third method, developed by Fürstner et al.,¹³⁰ is a modular approach where different substituents can be incorporated into the resulting imidazolium salt. The initial formation of an oxazolium salt is followed by a heterocycle-interconversion step. This is achieved by reacting the oxazolium salt with a desired primary amine to form the required substituted imidazolium salt, as shown in Figure 40.

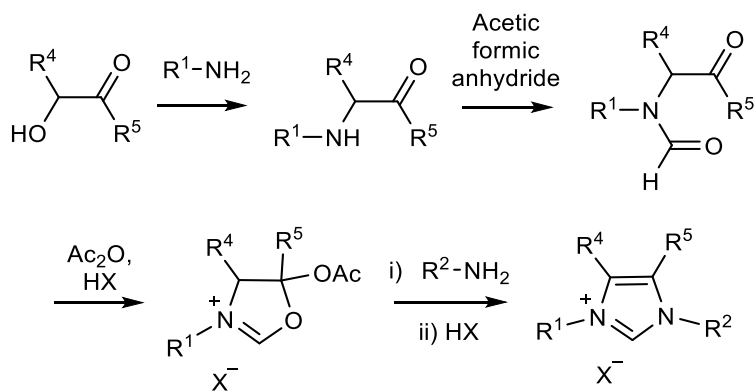


Figure 40: Synthetic route to form asymmetric iridium carbene complexes used by Fürstner et al.¹³⁰

To achieve more selective reactivity, the incorporation of multi-dentate ligands in the synthesis of metal complexes has become particularly important in the area of asymmetric catalysis, where chelating complexes can be used.¹³¹⁻¹³² Carbonylation is one such synthetic step, which is important in reactions such as hydroformylation, where typically carbon monoxide is reacted with hydrogen and a carbon-carbon double bond to introduce functionality. The development of specialised chelating chiral phosphine ligands and their use as directing ligands, such as those shown in Figure 41 for the asymmetric hydroformylation of styrene,¹³³ can impart chirality into the organic products.

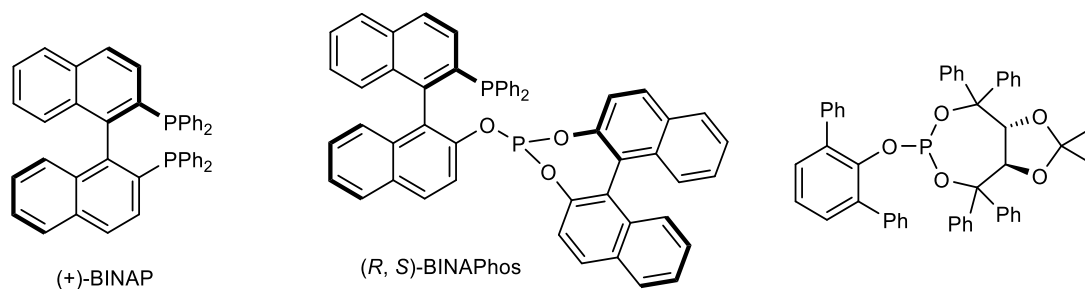


Figure 41: Chiral bidentate phosphorus-derived ligands for asymmetric hydroformylation¹³³

More specifically, carbonylation reactions have been studied using iridium alkoxide complexes as the catalysts of choice, with the formation of carbon-oxygen bonds being achieved via the reaction of CO with the bound alkoxide ligand. In the 1980s, Rees et al.¹³⁴⁻¹³⁵ demonstrated the formation of carboalkoxy compounds of the form *trans*-[Ir(CO)(PPh₃)₂(ROCO)] (where R = Me, ⁿPr, ^tBu or Ph), via the direct addition of CO to the corresponding alkoxide as shown in Figure 42.¹³⁶ The formation proceeds via nucleophilic attack of the alkoxide anion on the intermediate [Ir(CO)₃(PPh₃)₂]⁺, with phenoxide being the least reactive of the series due to its weakest nucleophilicity. Further reactivity of *trans*-[Ir(CO)(PPh₃)₂(MeO)] was probed via the addition of tetracyanoethylene (TCNE), to isolate the penta-coordinate distorted trigonal bipyramidal alkoxy-alkene complex [Ir(CO)(PPh₃)₂(MeO)(TCNE)] as shown in Figure 42.¹³⁷ This demonstrates the stability of these complexes with electron deficient alkene ligands, due to π -back donation into the alkene double bond.

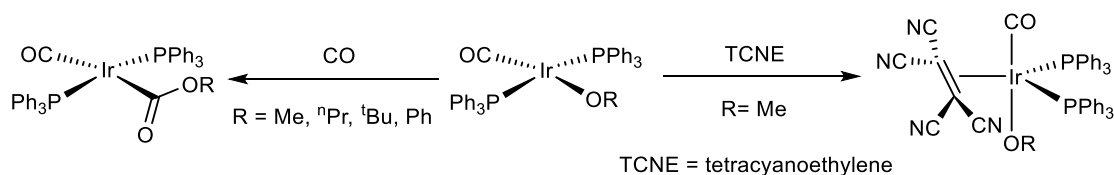


Figure 42: Reaction of *trans*-[Ir(CO)(PPh₃)₂(OR)] with CO and TCNE¹³⁴⁻¹³⁵

Further development of NHC and alkoxide ligands for catalysis has led to combining the two, to form chelating alkoxide-carbene complexes, with a number of transition metal, lanthanide and group 13 metal examples described in the literature.^{125, 138-144} These can be used to catalyse synthetic steps such as polymerisation¹³⁸⁻¹³⁹ and amination¹⁴⁰ reactions. One particular example described by Weinberg et al.¹⁴⁴ contains an NHC alkoxide which can bind to iridium in either a bidentate or a tridentate pincer fashion, forming both Ir(I) and Ir(III) complexes as shown in Figure 43. The Ir(I) complex adopts a square planar conformation and the related Ir(III) COD complex acts as a hydrogenation catalyst for the reduction of cyclohexene to cyclohexane.¹⁴⁴

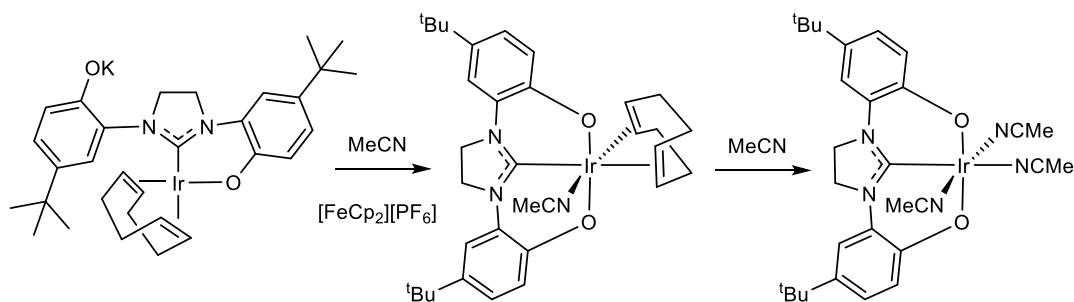


Figure 43: Iridium(I) NHC phenoxide complex and its conversion to an iridium(III) bis-phenolate COD species and an iridium(III) bis-phenolate acetonitrile complex, as described by Weinberg et al.¹⁴⁴

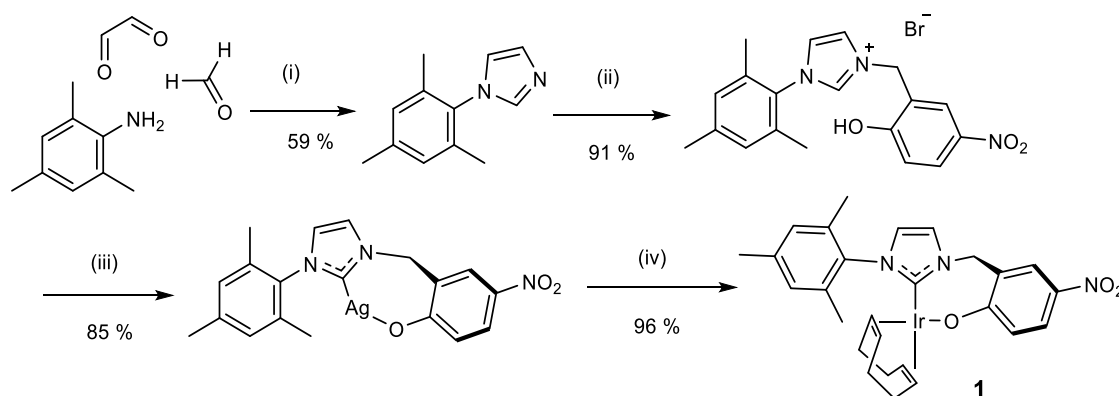
This chapter describes the synthesis of several asymmetric imidazolium salts, exploiting the first asymmetric synthetic route described above. Multi-step synthetic procedures are then used to form a series of neutral bidentate iridium carbene complexes, with a pendent phenolate arm and NO₂, H, COOMe and Cl substituents in the *para* position with respect to the phenolate. These substituents were chosen in accordance with the need to produce a range of complexes with electron-withdrawing effects as shown by the Hammett parameters in Table 2 (see Section 3.1 for an explanation of the different Hammett parameters). The imidazolium salts formed are then used to produce novel NHC alkoxide iridium complexes by a transmetallation reaction with [Ir(COD)Cl]₂. These complexes are fully characterised and their reactivity with pyridine and hydrogen discussed. Full characterisation data for the compounds synthesised on the routes to these NHC alkoxide iridium complexes can be found in the Experimental Sections 8.5, 8.6, 8.7, 8.8 and 8.9.

Table 2: Hammett parameters, σ_p and σ_p^- , for the four substituents NO₂, COOMe, Cl and H showing the increase in their electron-donating capabilities from NO₂ to H, with H being the most electron-donating group¹⁴⁵

Substituent	Hammett parameter, σ_p	Hammett parameter, σ_p^-
NO ₂	0.78	1.27
COOMe	0.45	0.75
Cl	0.23	0.19
H	0.00	0.00

2.2. Synthesis of pre-catalyst derivatives

The synthesis of complex, **1**, containing an NO₂ substituent in the *para* position to the phenolate, used 2-hydroxy-5-nitrobenzyl bromide as the starting material. This creates an asymmetric imidazolium salt following a known procedure as shown in Figure 44.¹²⁵ NO₂ is an electron-withdrawing group that could stabilise the phenolate anion that subsequently binds to the iridium centre to create the proposed chelate complex. To create the imidazolium salt, the reaction of mesityl imidazole with 2-hydroxy-5-nitrobenzyl bromide was undertaken which formed the imidazolium bromide in high yield. Upon heating with silver(I) oxide in THF/toluene, formation of the silver carbene was observed along with the production of a variety of silver salts, which were removed via filtration through Celite and washing with DCM.¹²⁵ A transmetallation reaction with [Ir(COD)Cl]₂ led to the desired air-stable iridium product, **1** (see Section 2.3 for a discussion of the characterisation data), along with precipitation of the silver chloride by-product.¹⁴⁶



Reagents and conditions:

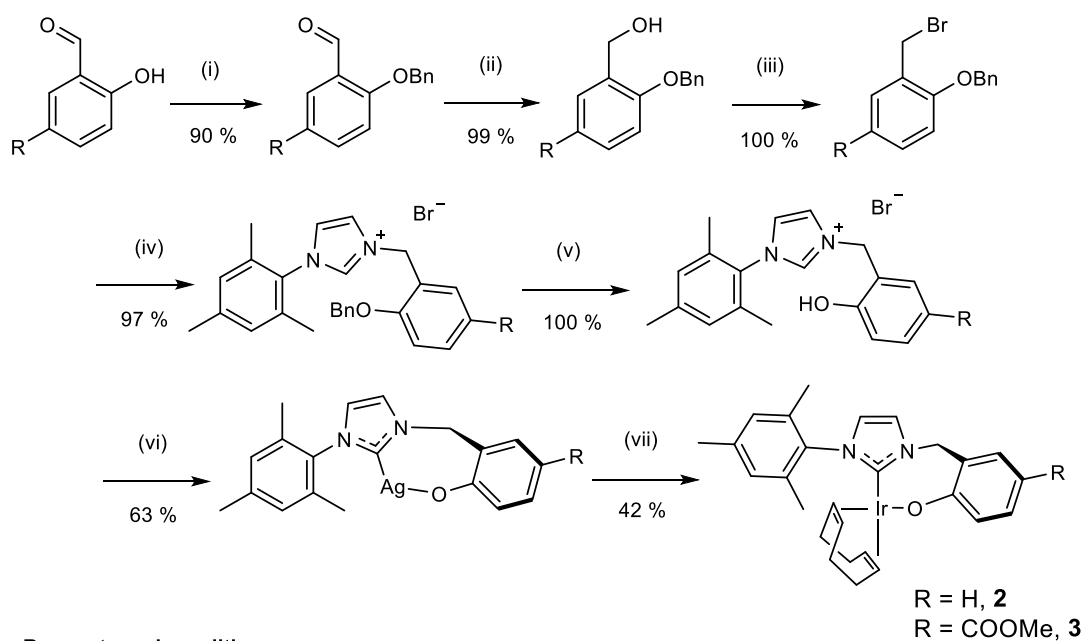
(i) Acetic acid, NH₄OAc, 70 °C, 18 h; (ii) 2-hydroxy-5-nitrobenzylbromide, toluene, reflux, 18 h; (iii) Ag₂O, THF, toluene, reflux, 3 h; (iv) [Ir(COD)Cl]₂, THF, r.t., 18 h

Figure 44: Synthetic route to the NO₂-containing complex, **1**

The [Ir(COD)Cl]₂ used in the transmetalation step to synthesise all the iridium complexes, was formed by heating a mixture of IrCl₃·3H₂O and COD in a solution of propan-2-ol and water at 90 °C for 3 hours, under an atmosphere of nitrogen.¹⁴⁶ The initially dark grey solution turned red on production of the desired iridium dimer, [Ir(COD)Cl]₂, which precipitated from the solution on cooling, in a yield of 62 %.

A more complicated route was used to synthesise the phenyl-based pre-catalyst **2**, as shown in Figure 45, as the benzyl bromide starting material was not commercially

available. Initial protection of the phenol was achieved using benzyl bromide.¹⁴⁷ This was followed by reduction of the aldehyde to the primary alcohol with NaBH₄ in methanol¹⁴⁸ and subsequent substitution to create the protected benzyl bromide.¹⁴⁹ Reaction of this with preformed mesityl imidazole led to the imidazolium bromide salt¹²⁵ which underwent benzyl cleavage with Pearlman's catalyst. Hydrogenation at room temperature, under 5 bars of H₂, proved very slow, so heating at 60 °C for 6 hours was carried out to drive the reaction to completion. Reaction with silver(I) oxide at room temperature, followed by transmetallation, afforded the air-sensitive iridium carbene complex, **2**, in 42 % yield as a dark orange solid.



Reagents and conditions:

(i) Acetone, K₂CO₃, BnBr, reflux, 2 h; (ii) NaBH₄, MeOH, 0 °C then r.t., 30 min; (iii) PBr₃, DCM, r.t., 2 h; (iv) 1-(2,4,6-trimethylphenyl)-1H-imidazole, toluene, reflux, 18 h; (v) MeOH, Pd(OH)₂/C, H₂, r.t., 20 h then 60 °C, 6 h; (vi) Ag₂O, DCM, r.t., 16 h; (vii) [Ir(COD)Cl]₂, THF, DCM, r.t., 4 h

Figure 45: Synthetic procedure to form complexes 2 and 3

The same synthetic route used for **2** was followed to make the COOMe-containing pre-catalyst, **3**, as the ester was stable to hydrogenolysis. A methyl ester was introduced to try and improve catalyst stability but maintain reactivity, as its electron-withdrawing Hammett parameter lies between that of NO₂ and H as detailed in Table 2. For the last step of this synthesis, isolation of the silver carbene complex was not conducted. Instead, the silver carbene was reacted in situ, following confirmation of its production via mass spectrometry. This approach was followed as the silver carbene is unstable and showed very broad signals by ¹H NMR spectroscopy. When [Ir(COD)Cl]₂

was added to the COOMe silver carbene solution, rapid transmetallation occurred to produce the desired iridium carbene complex, **3**, in 79 % yield. The air/moisture stability of **3** lies between that of **1** and **2**, consistent with its Hammett parameter; decomposition in solution under air takes days rather than minutes, as occurs for **2**. The pre-catalyst is, however, stable as a solid and in solution when stored under a nitrogen atmosphere.

For the synthesis of the Cl-containing derivative, **4**, on a small scale, the same route to make **2** and **3** was initially followed as this had proven successful before. However, upon scale-up, the use of acetone as a solvent for the benzyl protection step, combined with heating at 40 °C for 3 days led to an aldol condensation reaction occurring, as shown in Figure 46, with a yield of 82 %. This was evident from the corresponding ¹H NMR spectrum as also shown in Figure 46.

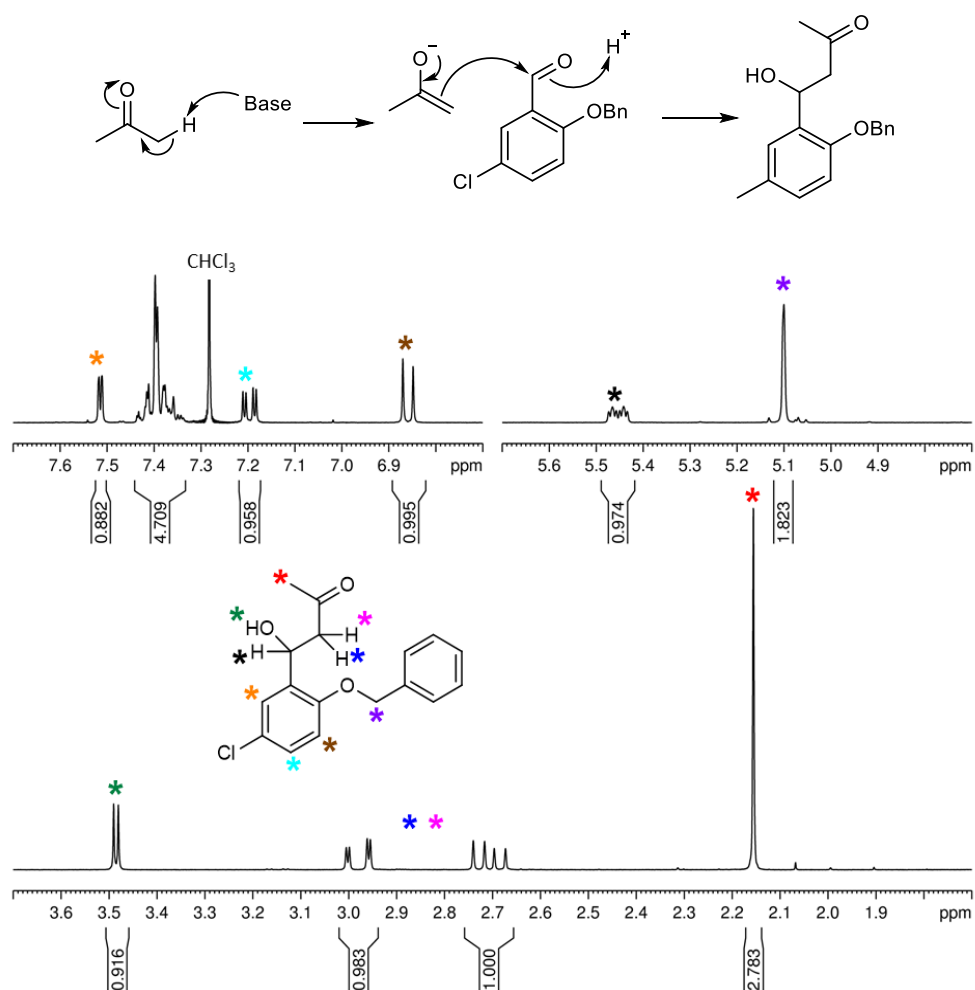
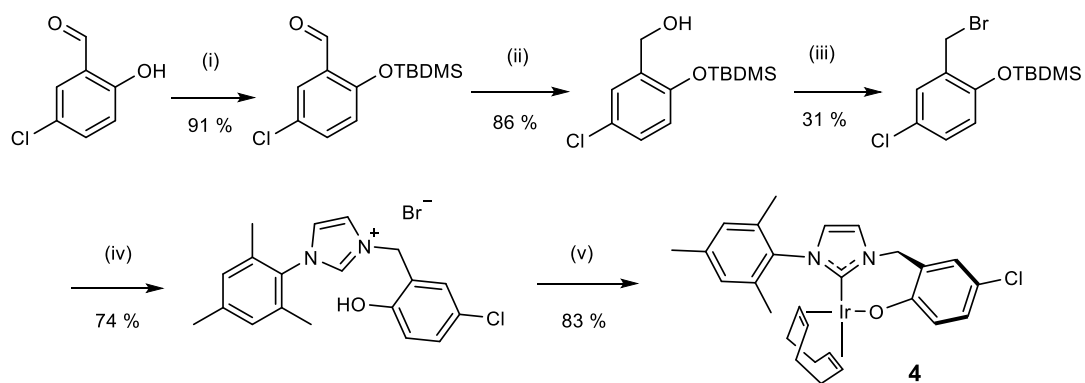


Figure 46: Reaction scheme to form the aldol condensation product along with its ¹H NMR spectrum showing its ¹H NMR resonances and splitting patterns (labelled structure inset)

In the ^1H NMR spectrum in Figure 46, a singlet exists for the methyl protons of the aldol product at δ 2.16. Signals for three inequivalent coupled protons are at δ 2.71, 2.98 and 5.45; the signals at δ 2.71 and 2.98 share a large 2J -coupling constant of 17.6 Hz, indicative of their close bonding proximity. Each one is also coupled to the single proton signal at δ 5.45. Due to this undesired reaction, the solvent was changed to DMF.

For the aldehyde reduction step, methanol is commonly used, however, on scale-up this formed the dimethyl acetal benzaldehyde product, which was converted back to the aldehyde using catalytic *paratoluenesulfonic acid* in toluene. THF was the solvent used for the subsequent reduction step to form the benzyl alcohol. The bromination and imidazolium salt formation proved successful, however, no selective deprotection step for the benzyl ether cleavage was found. Instead, LCMS analysis confirmed a mixture of debenzylated product at m/z 327.2 (M-Br-Bn+H)⁺, dechlorinated product at m/z 383.3 (M-Br-Cl+H)⁺ and a product no longer containing either the chlorine or benzyl group at m/z 293.2 (M-Br-Cl-Bn+2H)⁺. To overcome this, it was decided to complete the synthesis from the 5-chlorosalicylaldehyde product using *tert*-butyldimethylsilylchloride (TBDMSCl) to form the TBDMS protecting group as shown in Figure 47. This could then be cleaved further down the line, using solid supported *tert*-butylammonium fluoride (TBAF).

Whilst testing the reaction which forms the imidazolium bromide salt, it was found that after heating at 70 °C for 24 hours, just over half of the product had also had the TBDMS group cleaved. Therefore, rather than using TBAF to cleave this group, the reaction on a larger scale was heated at 110 °C for 48 hours to ensure full deprotection of the phenol substituent, as well as imidazolium salt formation. The silver carbene was not isolated but reacted in situ to produce the desired iridium pre-catalyst, **4**, as shown in Figure 47, with an overall yield of 15 % for the five-step route.



Reagents and conditions:

(i) TBDMSCl, Et₃N, DCM, r.t., 20 h; (ii) NaBH₄, THF, r.t., 30 min; (iii) PBr₃, DCM, r.t., 1 h; (iv) 1-(2,4,6-trimethylphenyl)-1H-imidazole, toluene, 110 °C, 48 h; (v) Ag₂O, DCM, r.t., 3 h then [Ir(COD)Cl]₂, r.t., 1 h

*Figure 47: Modified synthetic procedure to form complex **4** using TBDMSCl to create the TBDMS phenol protecting group*

2.3. Characterisation of pre-catalyst derivatives

Comparison of the ^1H NMR spectroscopic data for **1** (Figure 48) at 298 K in CD_2Cl_2 revealed that its proton chemical shifts are strongly temperature dependent.

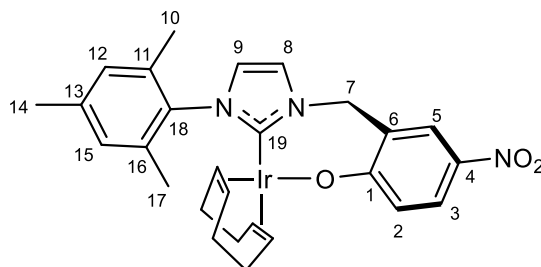


Figure 48: Labels for complex **1**, as referred to in the text

At 298 K, protons in the aliphatic range and the COD alkene protons yield very broad signals so that it is not easy to make specific proton assignments. Signals for the CH_2 linker protons in position 7 (see Figure 48) are also broadened into the baseline. As the temperature is lowered from 298 K to 253 K all the signals sharpen, as depicted in Figure 49. The CH_2 linker protons are now clearly inequivalent and appear as two doublets at δ 6.60 and 4.79 with a coupling constant of 14.0 Hz. This behaviour is a consequence of the fact that these protons are diastereotopic, with hindered rotation about the $\text{Ir-C}_{\text{carbene}}$ bond. They become equivalent by inversion of the conformation of the seven-membered ring through ring-flip and alkoxide lone pair inversion.¹⁴⁴ The large chemical shift difference arises due to their exo and endo orientations with respect to the seven-membered metallocycle.¹⁵⁰ Full characterisation data are presented in the Experimental Section 8.6.3.

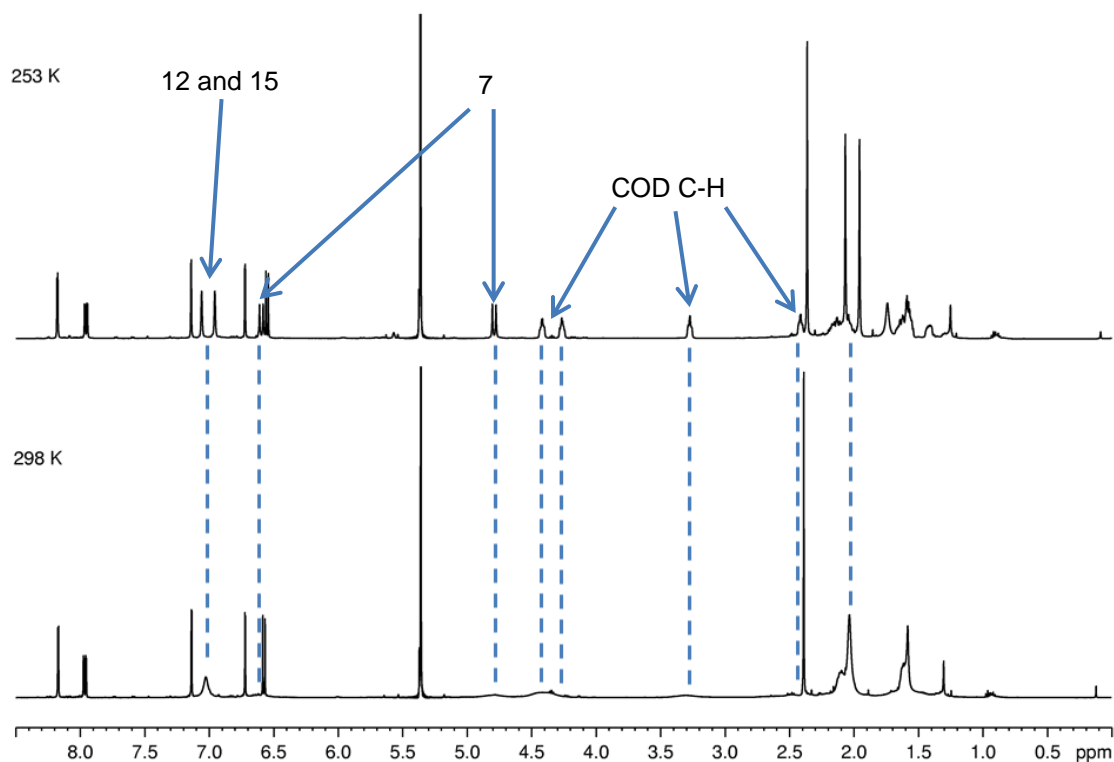
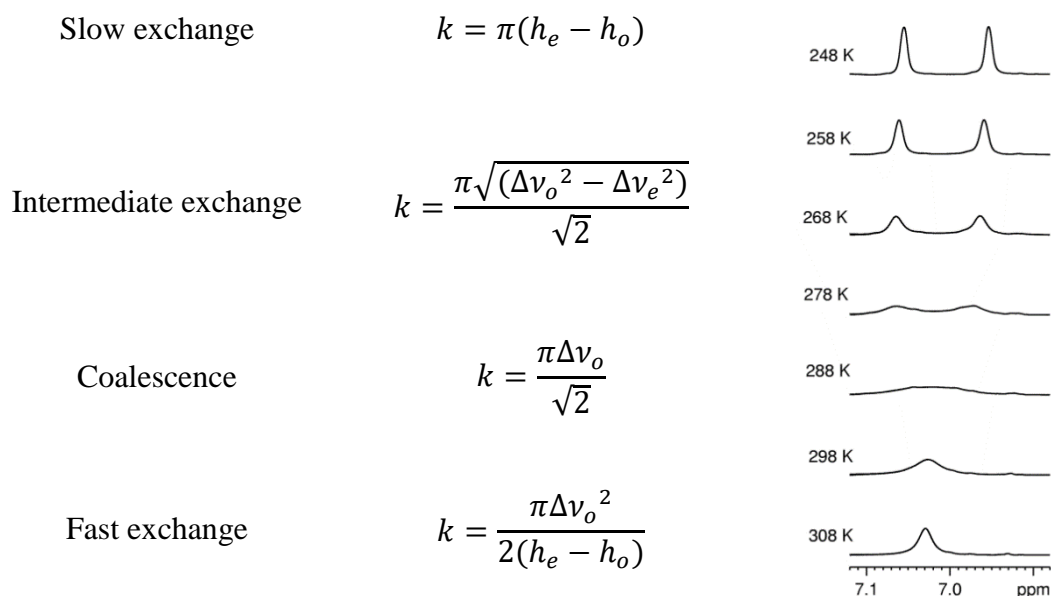


Figure 49: Comparison of the ^1H NMR spectra, at 253 K and 298 K, for complex **1** in CD_2Cl_2 . Regions of interest, where the fluxional behaviour slows to allow the detection of separate peaks, are indicated with the dashed lines. The labels indicate the proton resonances as shown in Figure 48 with the specific changes referred to in the text

A separate dynamic process involves intramolecular ring rotation of the mesityl group. At 298 K, the two protons that correspond to positions 12 and 15 appear as a broad singlet at $\sim \delta$ 7.03 but on cooling to 253 K, two singlets resolve at δ 7.06 and 6.96. This corresponds to hindered rotation of the mesityl ring around the single C-N bond that connects it to the imidazole ring. Full analysis of this dynamic behaviour is possible by examining the temperature dependence of exchange and the NMR linewidths.¹⁵¹ This has been achieved using the experimentally determined NMR spectra exemplified in Figure 50 and involves measuring both the linewidth at half the maximum peak height when exchange does not occur, h_o , and the chemical shift difference between the signals of interest, $\Delta\nu_o$. Calculation of rate constants at each temperature, which are detailed in Table 3, is possible using the equations shown in Figure 50. Estimation of the activation parameters for this process was achieved using both Arrhenius and Eyring-Polanyi equations which are fully described in the Experimental Section 8.1.2.



where: k = rate constant / s^{-1}

h_e = peak width at half height with exchange

h_o = peak width at half height with no exchange / $5.03 s^{-1}$

$\Delta\nu_e$ = peak frequency difference with exchange

$\Delta\nu_o$ = peak frequency difference with no exchange / $50.46 s^{-1}$

Figure 50: Lineshape analysis equations¹⁵¹ and corresponding ¹H NMR spectra used to calculate the mesityl group rotation rates

For this mesityl rotation, the Arrhenius equation gave an activation energy (ΔH^\ddagger) of $67.8 \pm 3.1 \text{ kJ mol}^{-1}$ with an R^2 value of 0.9958, which compares to $65.5 \pm 3.1 \text{ kJ mol}^{-1}$ from the Eyring-Polanyi equation with R^2 being 0.9954. The small but positive ΔH^\ddagger values are commensurate with a rotation process.¹⁵²⁻¹⁵³ The Eyring-Polanyi equation also enables calculation of the activation entropy for the process, which was calculated to be $28.0 \pm 10.9 \text{ J K}^{-1} \text{ mol}^{-1}$ with an R^2 value of 0.9954 (Figure 51). This small positive entropy value is also consistent with an intramolecular rotation process,¹⁵²⁻¹⁵³ suggesting no large change in order as would be expected for a reaction. The corresponding Gibbs Free Energy for the process at 300 K was calculated to be $57.1 \pm 1.0 \text{ kJ mol}^{-1}$. All the activation parameters are calculated from data that uses twice the value for the experimental rate constant because at the transition state the

reaction has an equal probability of continuing forward to the products or back to the reactants.

Table 3: Experimentally calculated rate data for mesityl group rotation in complex **1** as a function of temperature

T / K	1/T / K ⁻¹	k / s ⁻¹	ln(2k / s ⁻¹)	ln(2k/T / s ⁻¹ K ⁻¹)
248	0.00403	0	-	-
258	0.00388	3.77	2.02	-3.53
268	0.00373	15.7	3.45	-2.14
278	0.00360	48.8	4.58	-1.05
288	0.00347	112	5.41	-0.25
298	0.00336	260	6.26	0.56
308	0.00325	766	7.33	1.60

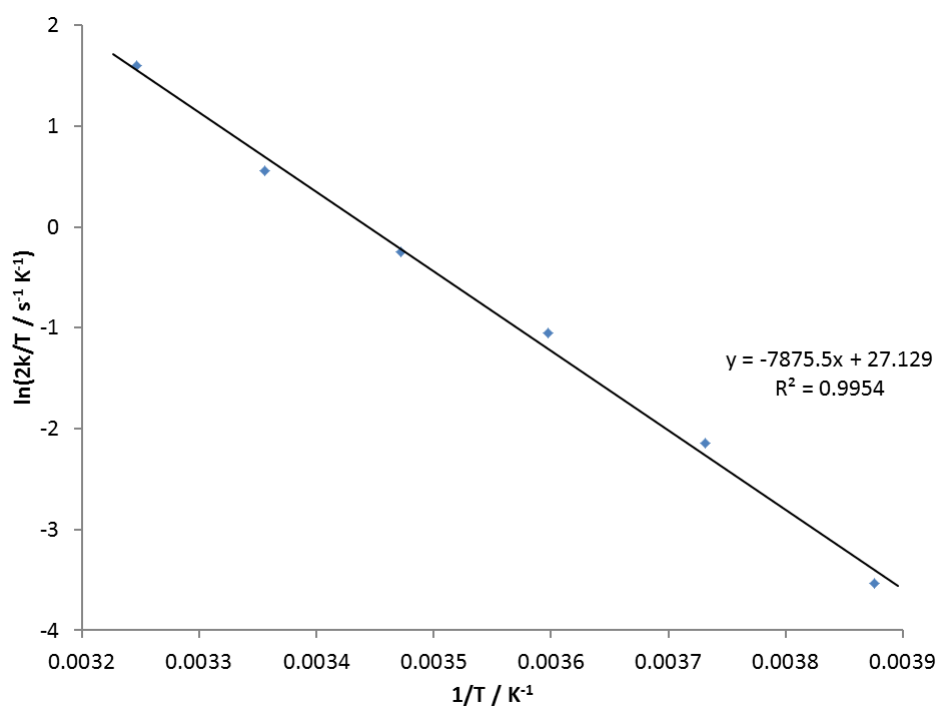


Figure 51: Eyring-Polanyi plot of rate data calculated from experimental ¹H NMR spectra for mesityl rotation in complex **1** as a function of temperature

Analysis of the $^{13}\text{C}\{^1\text{H}\}$ spectrum of complex **1** shows that the carbon resonances are also temperature dependent due to its fluxional behaviour in solution (see Figure 52). At 298 K, the $^{13}\text{C}\{^1\text{H}\}$ spectrum contains broad peaks and not all the expected carbon nuclei are observable, but on cooling to 243 K, the signals resolve. Two specific regions of interest are depicted in Figure 52. Firstly, at 298 K the peak for the carbene carbon is not visible, but at 243 K it appears in the same region as the peak for the quaternary carbon of C-OIr at $\sim \delta$ 175. Secondly, ^{13}C NMR signals for two of the COD alkene carbon atoms also sharpen upon cooling to 243 K, as shown in Figure 52.

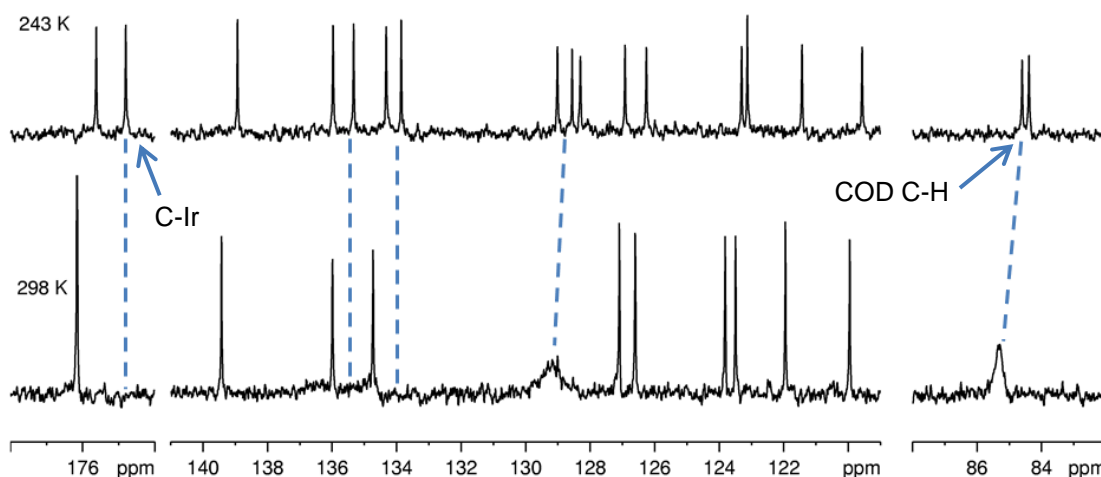


Figure 52: $^{13}\text{C}\{^1\text{H}\}$ NMR spectra of **1** at 243 K and 298 K specifically depicting the resolved ^{13}C signals for the C-Ir atom at $\sim \delta$ 175 and two COD C-H atoms at $\sim \delta$ 85

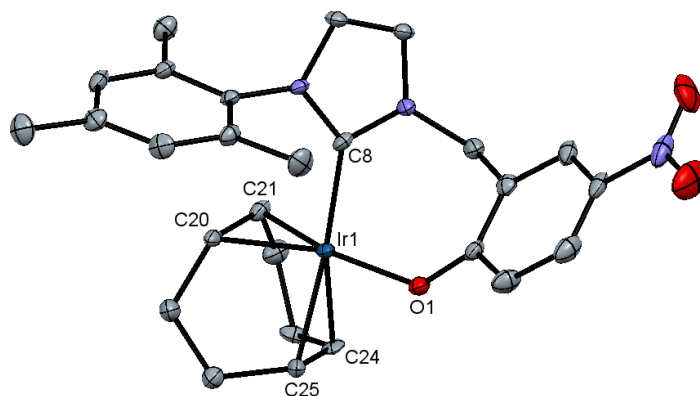


Figure 53: ORTEP plot of **1** with H atoms removed for clarity and the thermal ellipsoids set at a 50 % probability level

The structure of **1** was further confirmed by X-ray diffraction, in collaboration with Adrian Whitwood, Sam Hart and Rachel Bean in the XRD department at York. A

suitable single crystal was grown via the slow diffusion of hexane into a concentrated DCM solution of **1**. It crystallised in the $P2_1/n$ space group, yielding unit cell parameters for a, b and c of 8.7533(3), 19.4098(11) and 13.9131(4) Å respectively and for α , β and γ of 90, 90.472(3) and 90 ° respectively. The crystal exhibited both pseudomerohedral and multicrystal twinning, indicated by the high residual electron density of $8 \text{ e } \text{Å}^{-3}$. This was significantly reduced to $1.81 \text{ e } \text{Å}^{-3}$ when a partially occupied iridium site was included in the model. Figure 53 shows the corresponding ORTEP plot of complex **1**, determined at 110 K. Key data for bond lengths and angles are shown in Table 4. The geometry around the iridium centre is distorted square planar with the corresponding bond angles all being close to 90 °.

Table 4: Selected bond lengths and angles for complex **1**

Atoms	Length / Å	Atoms	Angle / °
Ir-O	2.067(3)	C(carbene)-Ir-O	92.88(14)
Ir-C(carbene)	2.049(4)	O-Ir-C(COD <i>t</i> O)	159.87(16)
Ir-C(COD <i>t</i> O)	2.111(5)	O-Ir-C(COD <i>t</i> O)	158.95(17)
Ir-C(COD <i>t</i> O)	2.101(5)	O-Ir-C(COD <i>t</i> carbene)	89.92(16)
Ir-C(COD <i>t</i> carbene)	2.185(4)	O-Ir-C(COD <i>t</i> carbene)	86.12(15)
Ir-C(COD <i>t</i> carbene)	2.183(4)	C(carbene)-Ir-C(COD <i>t</i> O)	96.10(17)
C-C(COD <i>t</i> O)	1.444(7)	C(carbene)-Ir-C(COD <i>t</i> O)	87.03(17)
C-C(COD <i>t</i> carbene)	1.393(7)	C(carbene)-Ir-C(COD <i>t</i> carbene)	154.46(18)
		C(carbene)-Ir-C(COD <i>t</i> carbene)	168.35(17)
		C(COD <i>t</i> O)-Ir-C(COD <i>t</i> carbene)	89.69(18)
		C(COD <i>t</i> O)-Ir-C(COD <i>t</i> carbene)	81.46(17)
		C(COD <i>t</i> O)-Ir-C(COD <i>t</i> carbene)	81.48(18)
		C(COD <i>t</i> O)-Ir-C(COD <i>t</i> carbene)	98.06(18)
		C(phenyl ring)-O-Ir	132.6(3)

Complex **1** (detailed in Table 4) can be compared to two related distorted square planar complexes, $[\text{Ir}(\text{COD})(\text{IMes})(\text{OSiMe}_3)]$ containing a siloxide ligand and $[\text{Ir}(\text{COD})(\text{IMes})(\text{py})]^+$ containing a pyridine ligand (see Table 5).¹⁵⁴⁻¹⁵⁵

Table 5: Selected bond lengths for complex **1**, $[\text{Ir}(\text{COD})(\text{IMes})(\text{OSiMe}_3)]$ and $[\text{Ir}(\text{COD})(\text{IMes})(\text{py})]^+$ where X denotes O or N as detailed for each of the three complexes

	1 X = O	$[\text{Ir}(\text{COD})(\text{IMes})(\text{OSiMe}_3)]$ X = O ¹⁵⁴	$[\text{Ir}(\text{COD})(\text{IMes})(\text{py})]^+$ X = N ¹⁵⁵
Atoms	Length / Å	Length / Å	Length / Å
Ir-X	2.067(3)	2.020(4)	2.0954(17)
Ir-C(carbene)	2.049(4)	2.050(5)	2.0762(19)
Ir-C(COD <i>t</i> X)	2.111(5)	2.107(5)	2.1259(19)
Ir-C(COD <i>t</i> X)	2.101(5)	2.125(6)	2.137(2)
Ir-C(COD <i>t</i> carbene)	2.185(4)	2.181(5)	2.136(2)
Ir-C(COD <i>t</i> carbene)	2.183(4)	2.150(6)	2.193(2)
C=C(COD <i>t</i> X)	1.444(7)	1.407(5)	1.399(3)
C=C(COD <i>t</i> carbene)	1.393(7)	1.375(6)	1.402(3)

Complex **1** has an Ir-O bond length of 2.067(3) Å which compares well to that of 2.020(4) Å reported for the siloxide complex. Furthermore, in both oxygen-containing complexes, the Ir-COD bond distances, *trans* to O, are short and the C=C bonds of the COD ligand are lengthened. The same effect occurs in the pyridine-containing complex. For **1** the Ir-C(COD *t* O) bond lengths are 2.111(5) Å and 2.101(5) Å which are the same, within error, as those of the siloxide complex (2.125(6) Å and 2.107(5) Å). The C=C(COD *t* O) bond of the alkoxide complex (1.444(7) Å) is lengthened slightly more than the siloxide complex (1.407(5) Å) due to more electron donation from the metal centre into the π^* antibonding orbitals of the C=C bond. This

means the Ir-O alkoxide donates the most electron density to iridium which then donates more into the bound alkene. The Ir-O siloxide bond is more ionic in character so donates less electron density. For both the alkoxide and siloxide complexes, the C=C(COD *t* carbene) bonds are shortened (1.393(7) Å and 1.375(6) Å respectively) showing that the carbene also donates electron density to the metal centre. In the pyridine complex, the C=C bond lengths of the COD group are 1.399(3) Å and 1.402(3) Å which are very similar and show there is no significant difference in back donation into these from either the carbene or the nitrogen atom of the pyridine ligand. Consequently, the phenoxide ligand in **1** is the most electron-donating ligand of this series and its iridium metal centre is therefore the most electron rich.

Table 6: Selected bond angles for complex **1**, [Ir(COD)(IMes)(OSiMe₃)] and [Ir(COD)(IMes)(py)]⁺ where X denotes O or N as detailed for each of the three complexes

	1 X = O	[Ir(COD)(IMes)(OSiMe ₃)] X = O¹⁵⁴	[Ir(COD)(IMes)(py)] ⁺ X = N¹⁵⁵
Atoms	Angle / °	Angle / °	Angle / °
C(carbene)-Ir-X	92.88(14)	88.2(2)	94.45(7)
X-Ir-C(COD <i>t</i> X)	159.87(16)	167.3(2)	165.08(7)
X-Ir-C(COD <i>t</i> X)	158.95(17)	153.8(2)	154.83(8)
X-Ir-C(COD <i>t</i> carbene)	89.92(16)	92.6(2)	88.73(7)
X-Ir-C(COD <i>t</i> carbene)	86.12(15)	91.3(2)	87.68(7)
C(carbene)-Ir-C(COD <i>t</i> X)	96.10(17)	95.9(2)	93.25(8)
C(carbene)-Ir-C(COD <i>t</i> X)	87.03(17)	91.5(2)	90.13(8)
C(carbene)-Ir-C(COD <i>t</i> carbene)	154.46(18)	150.7(2)	151.59(8)
C(carbene)-Ir-C(COD <i>t</i> carbene)	168.35(17)	172.3(2)	170.12(8)

The bond angles for these three complexes can also be compared (see Table 6). Complex **1** has a smaller bond angle between the C(carbene)-Ir-O compared to the C(carbene)-Ir-N as the chelate locks the complex in place and forces a smaller bite angle. However, this angle is not as small as for the siloxide complex, due to steric bulk of the bidentate ligand forcing the angle to be slightly wider. With the smaller bond angle of [Ir(COD)(IMes)(OSiMe₃)], the orbital overlap will be increased which may also be a slight contributing factor to explain why it has the shorter, stronger Ir-O bond in comparison to **1**, where the angle is forced larger and thus leads to a slightly lower orbital overlap and reduced bond length.

On changing the substituent from NO₂ to H, the ¹H NMR spectrum in CD₂Cl₂ at 298 K alters considerably. For complex **2**, as labelled in Figure 54, the ¹H NMR spectrum is shown in Figure 55 and full characterisation data are included in the Experimental Section 8.7.7. In the presence of air/moisture, complex **2** was not stable and rapid decomposition occurs, unlike stable complex **1**. This is accompanied by a colour change, from bright orange to brown. However, complex **2** can be stored indefinitely in a glovebox as a solid and is stable in solution under a nitrogen atmosphere. Signals for the CH₂ linker protons of complex **2** appear in the ¹H NMR spectrum at δ 6.55 and 5.15 at 294 K, with a mutual coupling constant of 14.9 Hz, demonstrating their diastereotopic nature, as seen for **1**. At 294 K, all the expected proton resonances of **2** are resolved. Four inequivalent COD alkene protons are visible as multiplet signals at δ 4.39 (2H), 3.22 and 2.78.

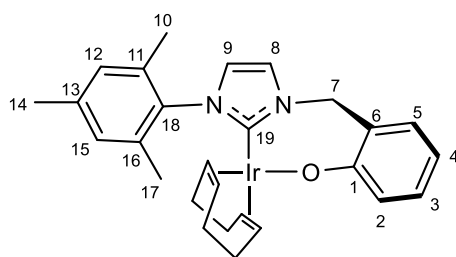


Figure 54: Line drawing of complex **2** showing the labelling scheme employed

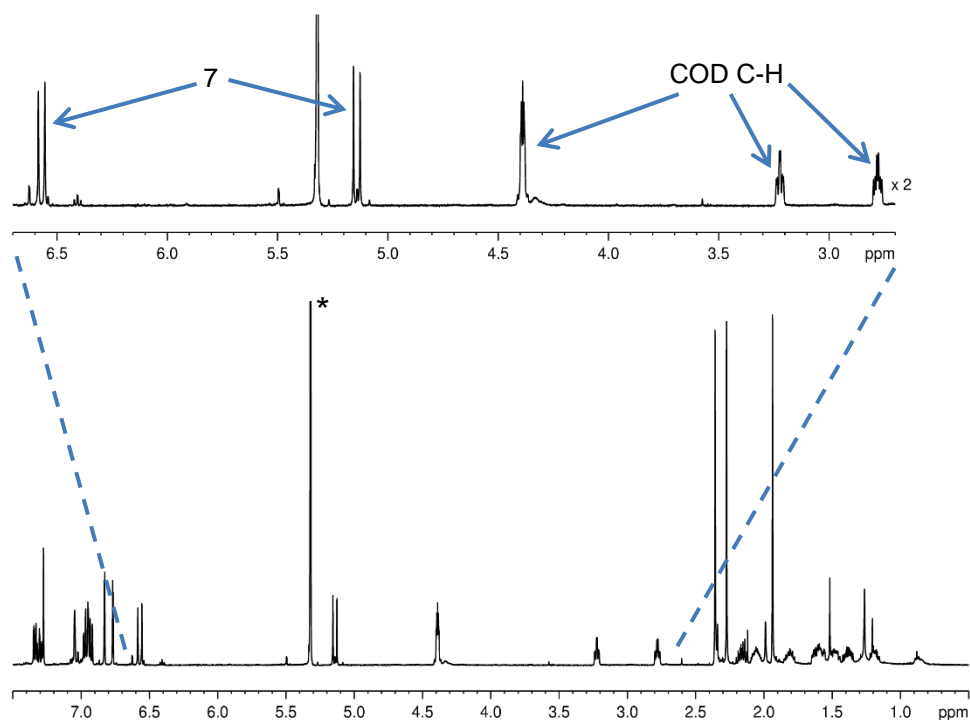


Figure 55: ^1H NMR spectrum of **2** in CD_2Cl_2 at 298 K, showing the inequivalent CH_2 linker protons, labelled as 7 and the COD alkene protons (* indicates the residual solvent peak)

In contrast, the proton spectrum of **3** resembles that of **1**, as at room temperature the CH_2 linker protons are not visible and the two $\text{CH}_{\text{mesityl}}$ protons appear as a very broad singlet, but on cooling they resolve. A single crystal of **3**, suitable for X-ray diffraction grew via the slow diffusion of hexane into a concentrated DCM solution of **3**. It crystallised into the P-1 space group, yielding unit cell parameters for a, b and c of 13.7657(5), 14.4796(6) and 14.5701(6) Å respectively and for α , β and γ of 61.959(4), 87.209(3) and 80.925(3) ° respectively. The residual electron density was $1 \text{ e } \text{Å}^{-3}$.

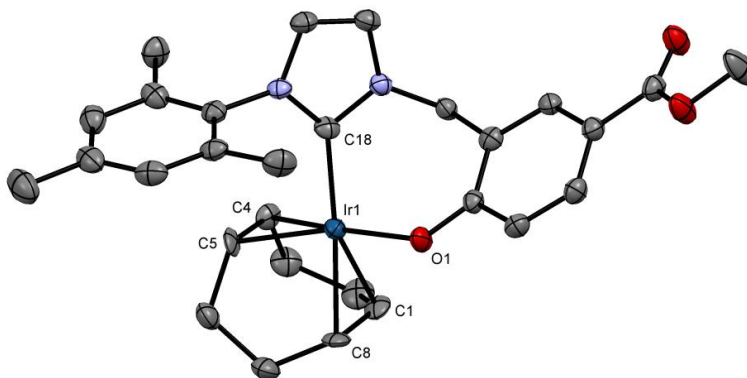


Figure 56: ORTEP plot of **3** with H atoms removed for clarity and the thermal ellipsoids set at a 50 % probability level

Figure 56 shows the corresponding ORTEP plot of complex **3**, determined in collaboration with Adrian Whitwood, Sam Hart and Rachel Bean in the XRD department at York, and measured at 110 K, with key data shown in Table 7. The geometry around the iridium centre is distorted square planar with the corresponding bond angles all close to 90°. The COOMe substituent in **3** is slightly less electron-withdrawing than the NO₂ group in **1** but there are no significant differences between the complexes' bond lengths or angles. The ¹H NMR spectrum of **4** is also like **1** and **3**, with broad signals at 298 K for the COD CH protons and the CH₂ linker protons. At 243 K, the four COD CH protons are visible at δ 4.32, 4.27, 3.09 and 2.26 with the two CH₂ linker protons at δ 6.44 and 4.60 sharing a common ²J-coupling of 13.7 Hz.

Table 7: Selected bond lengths and angles for complex **3**

Atoms	Length / Å	Atoms	Angle / °
Ir-O	2.060(3)	C(carbene)-Ir-O	90.25(14)
Ir-C(carbene)	2.047(4)	O-Ir-C(COD t O)	163.50(15)
Ir-C(COD t O)	2.119(4)	O-Ir-C(COD t O)	155.50(15)
Ir-C(COD t O)	2.097(4)	O-Ir-C(COD t carbene)	86.94(15)
Ir-C(COD t carbene)	2.143(4)	O-Ir-C(COD t carbene)	88.07(14)
Ir-C(COD t carbene)	2.184(4)	C(carbene)-Ir-C(COD t O)	93.45(16)
C-C(COD t O)	1.430(6)	C(carbene)-Ir-C(COD t O)	96.44(16)
C-C(COD t carbene)	1.394(6)	C(carbene)-Ir-C(COD t carbene)	151.05(17)
		C(carbene)-Ir-C(COD t carbene)	171.06(16)
		C(COD t O)-Ir-C(COD t carbene)	82.05(17)
		C(COD t O)-Ir-C(COD t carbene)	90.62(16)
		C(COD t O)-Ir-C(COD t carbene)	81.67(17)
		C(COD t O)-Ir-C(COD t carbene)	97.97(17)
		C(phenyl ring)-O-Ir	136.4(3)

2.4. Reactivity of pre-catalyst derivatives

2.4.1. Reactivity of **1** in CD₂Cl₂ and C₆D₆

Addition of normal hydrogen to **1** in CD₂Cl₂ at 298 K showed no observable change in the ¹H NMR spectrum. However, on cooling to 253 K two broad hydride signals are visible. This, along with a very broad signal for free hydrogen in solution, suggests very rapid hydride exchange at 298 K and that the dihydride complex forms immediately. The hydride peaks have very low intensity but two pairs are visible at 253 K, one sharp set at δ -9.81 and -21.48 and another broad set at δ -10.86 and -21.53 (Figure 57), which are consistent with sites *trans* to alkene (~ δ -10) and *trans* to oxygen (~ δ -21). These products, two isomers of **5** which form due to differing conformations of the seven-membered metallocycle, are due to oxidative addition of H₂ to the iridium centre, as shown in Figure 57, and they exist in equilibrium with **1** where a steady-state of just 5 % conversion is achieved under these conditions, precluding their full characterisation.

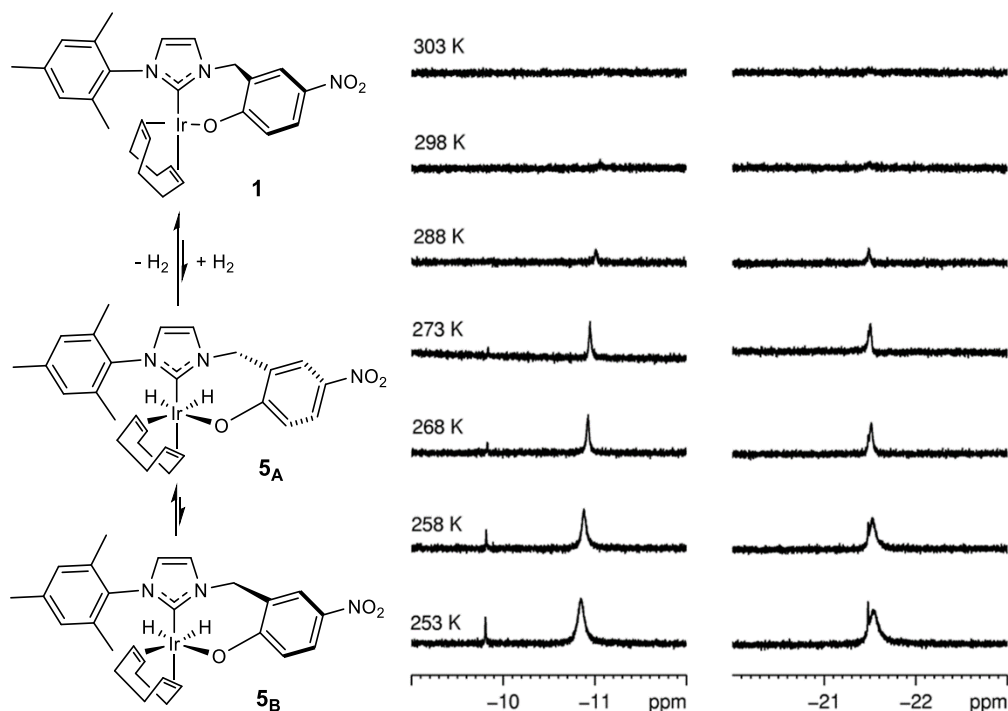


Figure 57: Oxidative addition of H₂ to **1** in CD₂Cl₂ leads to the formation of two isomers of **5**, **5A** and **5B**. These species yield the diagnostic temperature-sensitive hydride resonances shown in the ¹H NMR spectra on the right

At 253 K four signals are still present for the bound COD alkene protons of **1** so COD is not labile under a hydrogen atmosphere. A ^1H COSY NMR spectrum showed no coupling between the hydride resonances although this may be due to their low signal intensities. It is proposed that the two pairs differ due to their arrangement with respect to the conformation of the seven-membered metallocycle as depicted in Figure 57. The rapid reaction with H_2 demonstrates the potential for the complex to have hydrogenation activity.

Details of similar iridium COD dihydride species have been published previously.^{69, 156-159} Such a complex is formed when $[\text{Ir}(\text{COD})(\text{NCCH}_3)(\text{PMe}_3)][\text{BF}_4]$ binds H_2 as two hydride ligands as shown in Figure 58, and comparable spectral changes to those described for H_2 addition to **1** have been reported.¹⁵⁸ For the dihydride complex $[\text{Ir}(\text{H})_2(\text{COD})(\text{NCCH}_3)(\text{PMe}_3)][\text{BF}_4]$ the hydride resonances appear at δ -12.70 and -17.01 in the ^1H NMR spectrum in CD_2Cl_2 at 243 K.¹⁵⁸ In this species, the dihydrogen adds across the alkene-Ir-NCCH₃ axis to form the dihydride product. This occurs as the H_2 adds across the ligand axis which contains the weakest π -acid and is therefore the most electron rich.¹⁶⁰ Hence the iridium centre contains enough electron density to back donate into the σ^* antibonding orbital of dihydrogen to break its sigma bond and create two hydride ligands. Hydrogen addition to complex **1** occurs in a similar manner by adding across the alkene-Ir-O bond. Furthermore, work by Crabtree et al.¹⁵⁶⁻¹⁵⁷ in the late 1970s has also shown these dihydride-dialkene complexes to be important intermediates in homogeneous hydrogenation reactions which is discussed further in Section 6.1.

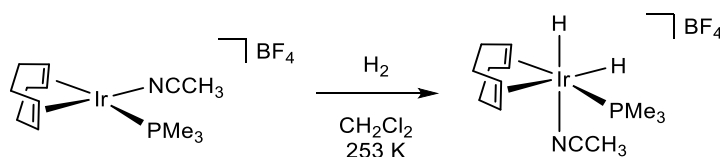


Figure 58: $[\text{Ir}(\text{H})_2(\text{COD})(\text{NCCH}_3)(\text{PMe}_3)][\text{BF}_4]$ formed when H_2 adds to $[\text{Ir}(\text{COD})(\text{NCCH}_3)(\text{PMe}_3)][\text{BF}_4]$ ¹⁵⁸

Another species that demonstrates reversible binding of hydrogen contains the strong anionic pyrrolide ligand¹⁵⁹ as shown in Figure 59, which is similar to the hard anionic phenolate ligand in **1**. This complex is neutral overall, containing an electron rich metal centre that facilitates oxidative addition and reductive elimination of H_2 .

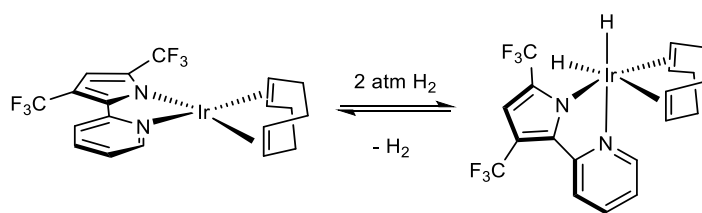


Figure 59: An example of an iridium-pyridylpyrrolide complex which exhibits reversible binding of H_2 ¹⁵⁹

The reactivity of **1** with pyridine was also investigated, however, in CD_2Cl_2 at 298 K only very minor changes in the 1H NMR spectra were seen, as well as an increase in the signals for free COD in solution. After 6 days, the signals for **1** dominate and the clean conversion to a single identifiable product was not observed. These data show that the COD ligand of **1** is labile¹⁶¹ so that other ligands can bind,¹⁶² or decomposition occurs, but in this case the Ir-O bond is not cleaved. On cooling to 243 K, the signals in the 1H NMR spectrum for the bound COD CH protons of **1** are still present. If the phenolate ligand was displaced by a pyridine ligand, to form a zwitterionic-type species, then two of the signals for these COD CH protons would be expected to shift upfield, due to no longer being in a *trans* position to the electronegative oxygen atom. Upon subsequent addition of H_2 to this solution, the formation of a new dihydride species, **6**, in approximately 60 % yield was observed after a further three days of reaction. This reveals that although reactivity with substrate alone is limited, once hydrogen is present to hydrogenate the COD ligand to COE and then COA, which no longer binds to the iridium centre, pyridine binding becomes possible.

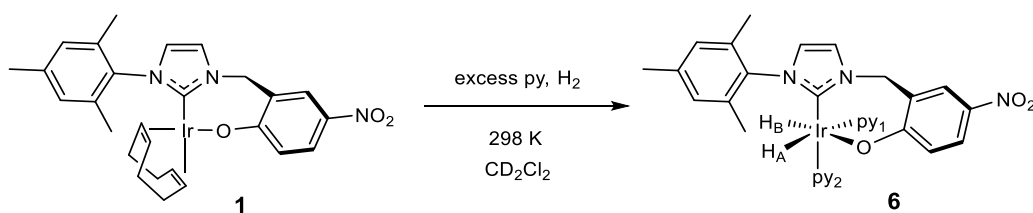


Figure 60: The reaction of **1** with pyridine and hydrogen forms **6** in CD_2Cl_2

When **1** was reacted with pyridine and hydrogen in a freshly prepared CD_2Cl_2 solution, the slow but complete conversion to **6** was observed. After 6 hours at 298 K, the 1H NMR spectrum at 253 K showed only a slight reduction in the intensity of the bound COD alkene peaks of **1** along with a signal for free COD and COE in solution. After 24 hours, the 1H NMR spectrum at 253 K again showed reduced intensity signals

for **1** and larger peaks for free COD and COE in solution. The $^{13}\text{C}\{^1\text{H}\}$ NMR spectrum at 253 K, followed the same trend. The ^1H COSY NMR spectrum showed peaks for bound pyridine and carbene ligands at different chemical shifts to those of **1**, indicating partial conversion to **6**. After 17 days, the ^1H NMR spectrum at 253 K showed 100 % conversion to form **6**, containing two bound pyridine ligands (see Figure 60) and two very broad hydride signals, along with COE and COA in solution. Cooling further to 223 K enabled the hydride signals to resolve which revealed two isomers of **6**, the major form **6_A** (83 %) and the minor form **6_B** (17 %), due to different conformations of the seven-membered metallocycle. These are discussed in detail in Section 3.2.1. At temperatures greater than 253 K, where an averaged signal is observed, the complex is referred to as **6**. It is likely that the time taken for full activation is lengthened, when compared to $[\text{Ir}(\text{COD})(\text{IMes})\text{Cl}]$, due to no initial counter ion displacement. Table 8 shows how the ratios of **1** and **6** vary as a function of reaction time.

Table 8: Ratios showing how the relative proportions of **1** and **6** change during the reaction of a CD_2Cl_2 solution containing 12 mol% **1** and 0.22 M pyridine under 3 bars of H_2 seen at 253 K

Reaction time	Complex 1 (δ 7.95 signal) / %	Complex 6 (δ 8.04 signal) / %
0 hours	100	0
6 hours	78	22
24 hours	60	40
6 days	25	75
17 days	0	100

On cooling to 233 K the signals for the pyridine ligands of the major isomer, **6_A**, are well resolved, however, at 298 K, there is a considerable difference in the appearance of the signals for the bound pyridine ligands. Those of the ligand in the *cis* position to the hydrides (py_2) remain sharp, but those of the ligand in the *trans* position to a hydride (py_1) become much broader and difficult to distinguish. This suggests that the latter pyridine undergoes rapid exchange at 298 K and thus averaged ^1H NMR signals are observed. The chemical shifts of py_1 appear at δ 8.31, 6.97 and \sim 7.04 whilst

those for py_2 appear at δ 8.96, 7.11 and 7.66. The *ortho* proton peak of py_1 shifts slightly with temperature, due to inhibition of exchange, whilst the py_2 signals do not. The hydride signals are present at δ -21.36 and -28.88 with a common coupling of 8.9 Hz. Full characterisation data for $\mathbf{6}_A$ at 233 K are given in the Experimental Section 8.6.4.

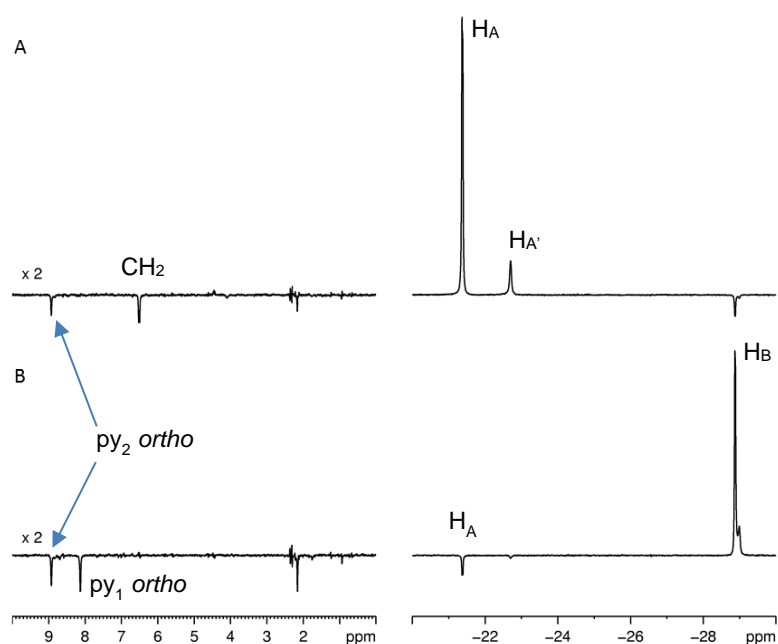


Figure 61: 1H EXSY 163 NMR spectra showing *nOe* signals of $\mathbf{6}_A$ when selectively exciting the signal for H_A (A) and the signal for H_B (B). The hydride resonances for $\mathbf{6}_B$ are also seen

When probing the hydride ligands using 1H EXSY NMR at 243 K as shown in Figure 61, H_A shows an *nOe* interaction with the py_2 *ortho* 1H signal at δ 8.92 and with one of the CH_2 linker protons at δ 6.48. This is consistent with H_A lying in the perpendicular plane to the metallocycle containing the CH_2 linker. On the other hand, H_B lies much further away from the CH_2 linker and thus shows an *nOe* interaction with both pyridine ligands which lie *cis* to it; the py_2 *ortho* 1H signal at δ 8.92 and the py_1 *ortho* 1H signal at δ 8.13.

To determine if the bound phenolate ligand in $\mathbf{6}$ can be displaced, increasing equivalents of triethylsilane were added to a CD_2Cl_2 solution of $\mathbf{6}$. Any reaction to trap the phenolate would be apparent on analysing the hydride region of the 1H NMR spectra for any change in hydride signals as shown in Figure 62. However, at 298 K no change was observed, suggesting that the oxygen ligand of $\mathbf{6}$, under these conditions, is strongly

bound to iridium. This shows that the whole system must be evaluated, as based on bond dissociation energies alone, a stronger Si-O bond ($800 \pm 13 \text{ kJ mol}^{-1}$) would be anticipated to form in preference to a weaker Ir-O bond ($414 \pm 42 \text{ kJ mol}^{-1}$).¹⁶⁴

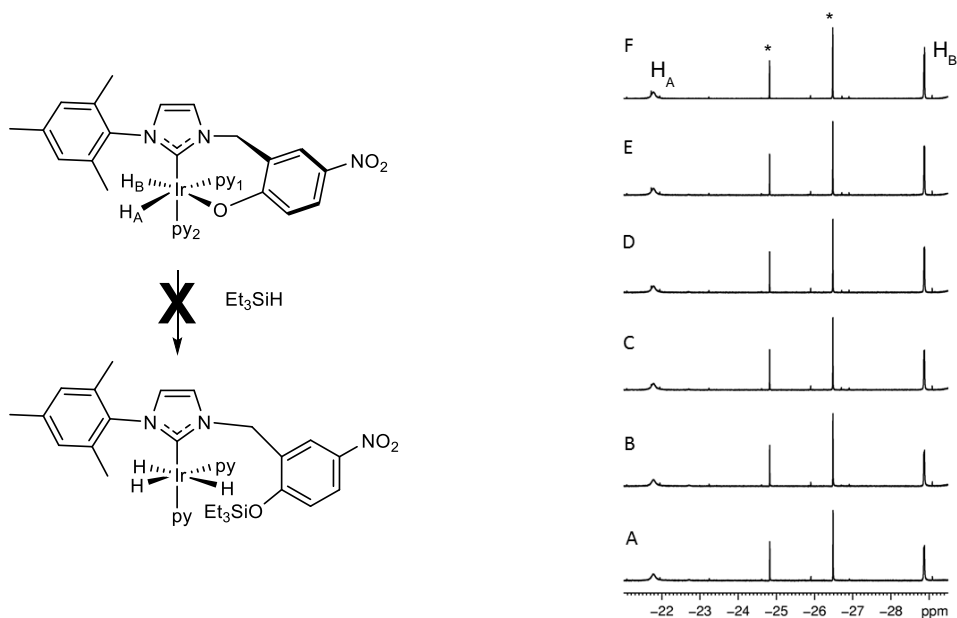


Figure 62: Potential structure formed when **6** is reacted with Et_3SiH and the corresponding ^1H NMR spectra of the hydride region after addition of increasing equivalents of Et_3SiH , from 0 eq. to 5 eq. (A to F) showing no change in the hydride signals (* denotes singlet hydride species discussed in Section 3.2)

2.4.2. Reactivity of **2** in CD_2Cl_2 and C_6D_6

To understand the effect on reactivity when the substituent on the carbene ligand is changed from NO_2 in complex **1** to H in complex **2**, a CD_2Cl_2 sample of **2** was analysed in a similar way to that described for **1** in Section 2.4.1. Now, at 298 K, the four COD alkene protons of **2** could be identified at δ 4.37 (2H), 3.22 and 2.77, however, upon cooling to 243 K the NMR signals become very broad and unresolved. This means that at 298 K the complex is undergoing rapid motion that is faster than the NMR timescale so broadening effects are not observed. However, upon cooling, this motion is slowed so that the signals are no longer well defined. In C_6D_6 , at 298 K, again the four COD alkene protons could be identified at δ 4.85 (2H), 3.21 and 2.90.

However, no low temperature studies could be conducted in benzene due to its melting point of 5.5 °C.

When H₂ is added to a CD₂Cl₂ sample of **2** at 255 K, a limited reaction occurs. Four hydride signals are observed, corresponding to two species which are two isomers of **7**. The major signals for **7_A** appear at δ -12.35 and -18.25 and the minor ones for **7_B** appear at δ -12.39 and -17.64. These two isomers reflect ring-flip conformers of the metallocycle. The structure of the major isomer is shown in Figure 63 with its low concentration precluding full characterisation. When the reaction is followed with *p*-H₂ these hydride signals do not show any PHIP enhancement. However, upon warming to 298 K, these minor hydride signals are broadened into the baseline of the NMR spectrum and again the only detectable species is complex **2**. Furthermore, when pyridine is added to a CD₂Cl₂ or C₆D₆ solution of **2** at 298 K, no reaction was observed. Instead, the proton peaks for **2** remain resolved. This behaviour is the same as that observed for complex **1**, demonstrating that the pathway to full activation of these complexes is different to what has previously been observed, but consistent between these new complexes. Here, the pathway does not proceed via ligand substitution, as for the chloride-containing iridium carbene complexes, where the most studied and understood species is [Ir(COD)(IMes)Cl].⁹⁴

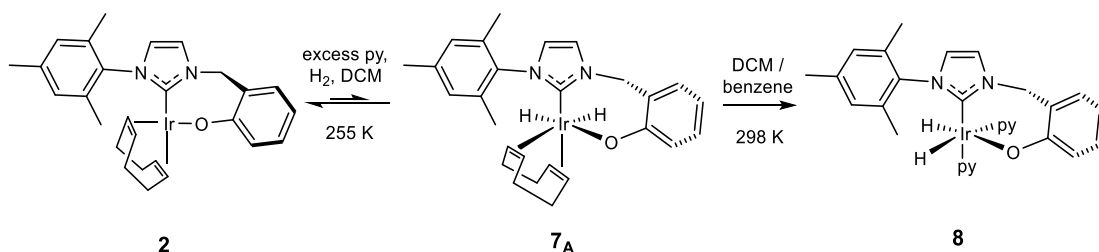


Figure 63: Reaction of **2**, in CD₂Cl₂ / C₆D₆, with H₂ leads to the formation of the major dihydride complex **7_A** which then forms the bis-pyridyl iridium species, **8**, after COD hydrogenation in the presence of pyridine. **8** is a product in which the Ir-O bond is retained

On full activation with pyridine and H₂, which takes several days at 298 K, the detectable signals alter to those of the new iridium species, **8** (see Figure 63). In these aprotic solvents, two inequivalent hydride signals are visible, as shown in their corresponding ¹H NMR spectra in Figure 64. Their signals appear in CD₂Cl₂ at δ -22.55 and -25.49 with a coupling constant of 8.1 Hz and in C₆D₆ at δ -21.94 and -24.52 with a coupling constant of 7.7 Hz. This suggests that the Ir-O bond is retained in both

samples. This is further supported by the fact that the CH₂ linker protons remain diastereotopic, as two distinct doublets are seen in both CD₂Cl₂ and C₆D₆. In CD₂Cl₂ they are present at δ 5.76 and 5.29, with a coupling constant of 14.8 Hz, whilst in C₆D₆ they appear at δ 6.30 and 5.67, with a coupling constant of 14.6 Hz. It is interesting to note that despite the two bound pyridine ligands existing in distinct environments in both CD₂Cl₂ and C₆D₆, separate signals for the *ortho* protons are only observed in CD₂Cl₂, whilst in C₆D₆ the corresponding signals appear at the same chemical shift. Furthermore, the ¹H NMR signals in the C₆D₆ sample are broader than those in CD₂Cl₂, suggesting the ligands undergo exchange and that this occurs more rapidly in the less polar solvent (see Section 2.4.2). In both samples singlet-based hydride species are visible (see Figure 64), although their low concentration (< 6 %) precludes their full characterisation (see Section 3.2 for further discussion). In CD₂Cl₂ the hydride signals appear at δ -23.85 and -26.54, whilst in C₆D₆ a signal is visible at δ -23.29. Characterisation data for complex **8** in CD₂Cl₂ are given in the Experimental Section 8.7.8. Despite extensive NMR analysis, the chemical shift of the carbene carbon could not be identified at 298 K. Furthermore, at 298 K the *ortho* and *para* proton signals for the py₁ bound ligand are very broad, consistent with it undergoing rapid exchange, and thus this precluded determination of the chemical shifts of the corresponding ¹³C NMR signals. On cooling to 263 K, these *ortho* and *para* ¹³C signals are present at δ 154.4 and 135.4. Characterisation data for **8** in C₆D₆ are also given in the Experimental Section 8.7.8.

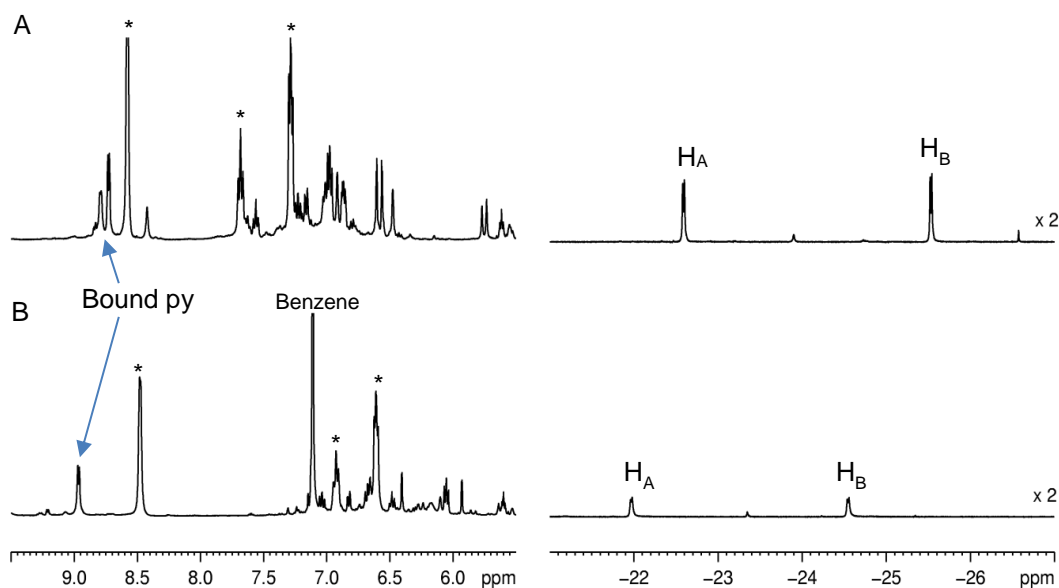


Figure 64: ^1H NMR spectra of the aromatic and hydride regions of a solution containing **8** after the reaction of **2** with pyridine and hydrogen in CD_2Cl_2 (A) and in C_6D_6 (B) at 294 K (* denotes free pyridine in solution)

2.4.3. Reactivity of **3** in CD_2Cl_2 and C_6D_6

For complex **3** in CD_2Cl_2 , the addition of pyridine leads to no reaction, as observed previously in Section 2.4.1 for **1**. The reactivity of **3** with H_2 is also like **1** and **2**, as two pairs of minor hydride species are observed, only under PHIP conditions or thermally after a considerable number of scans. These pairs are present at δ -10.79 and -20.79 , for the most prominent COD dihydride species, **9_A**, and at δ -9.85 and -22.88 for **9_B**. Their low concentrations ($< 2\%$) precluded further characterisation.

When both pyridine and H_2 are added to a CD_2Cl_2 solution of **3**, the activation time is again days, however, unlike for **2**, two inequivalent dihydride isomers are present. These are isomers of complex **10**, **10_A** and **10_B**, as shown in Figure 65.

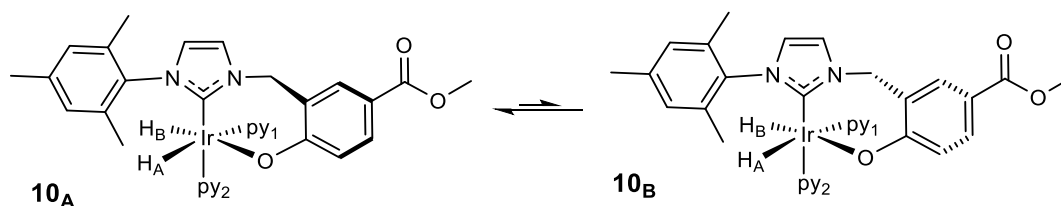


Figure 65: **10_A** and **10_B** formed from the reaction of **3** with pyridine and hydrogen in CD_2Cl_2

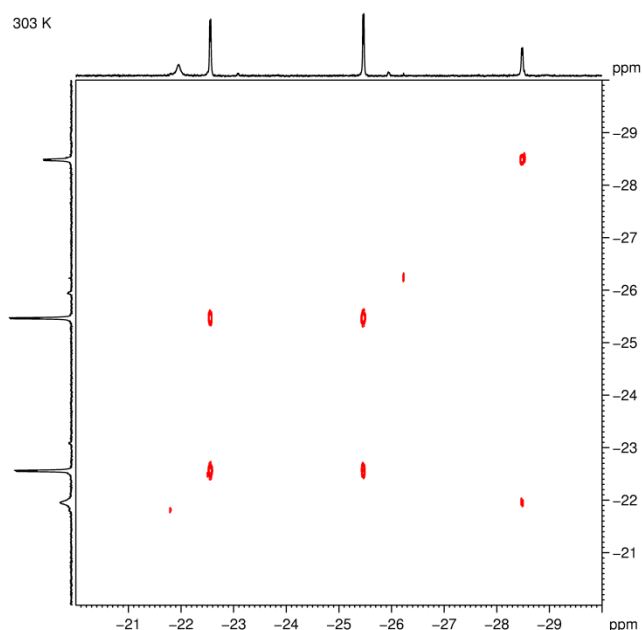


Figure 66: 1H COSY NMR spectrum of a CD_2Cl_2 sample of **10_A** and **10_B**, showing coupling between the hydride signals at δ -21.95 and -28.48 and those at δ -22.56 and -25.47

The two isomers again form due to ring-flip of the seven-membered metallocycle, and are distinguished by their hydride resonances; one broader pair of hydride signals exists at δ -21.95 and -28.48 with a mutual coupling of 8.3 Hz for complex **10_A**, and a sharper pair of hydride signals exists at δ -22.56 and -25.47 now with a common coupling of 8.0 Hz for complex **10_B**. The ratio of the two species was found to be 37: 63 respectively for a sample containing 0.07 M pyridine and 10 mol% **3**. Figure 66 shows the corresponding 1H COSY NMR spectrum which details the hydride ligand connectivity. When the concentration of pyridine was reduced, such that the sample contained 0.04 M pyridine and 17 mol% **3**, the ratio reversed to be equal to 86: 14. At 303 K, all four hydride signals were shown to undergo exchange with each other, according to 2D 1H NOESY NMR experiments, as shown in Figure 67.

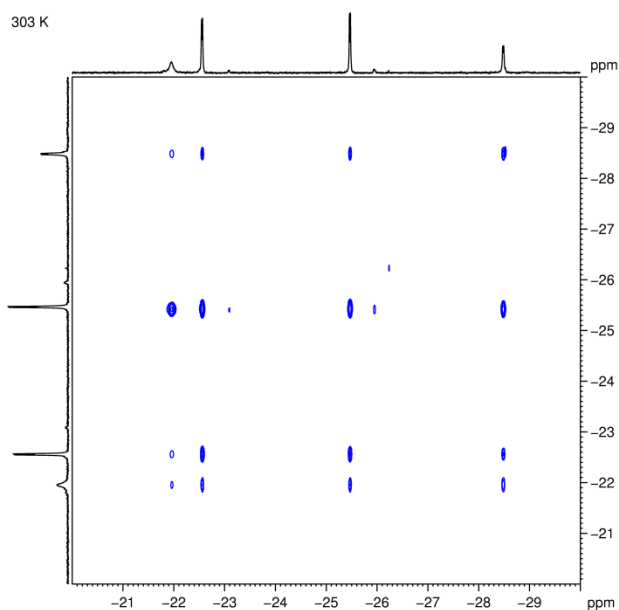


Figure 67: 2D ^1H NOESY NMR experiment of a CD_2Cl_2 sample of $\mathbf{10}_\text{A}$ and $\mathbf{10}_\text{B}$ at 303 K showing exchange between all four hydride ligands of $\mathbf{10}_\text{A}$ and $\mathbf{10}_\text{B}$

As described for complexes $\mathbf{6}_\text{A}$ and $\mathbf{6}_\text{B}$ in Section 2.4.1, the exchange between the ring-flip isomers of $\mathbf{10}$ is expected to continue at low temperatures, however, on cooling to 273 K, the signals for $\mathbf{10}_\text{A}$ are broadened, precluding these studies. It is anticipated that at low temperature, exchange between hydride ligands on the same complexes is inhibited, because there is no pyridine ligand exchange, consistent with that observed for complexes $\mathbf{6}_\text{A}$ and $\mathbf{6}_\text{B}$. Both species contain two bound pyridine ligands, with their respective *ortho* proton signals at δ 9.01 (*trans* to carbene) and 8.40 (*trans* to hydride) for complex $\mathbf{10}_\text{A}$ and at δ 8.82 (*trans* to hydride) and 8.76 (*trans* to carbene) for complex $\mathbf{10}_\text{B}$. Because only two pyridine environments exist for both complexes, and due to two of their hydride ligands exhibiting a large upfield shift, the Ir-O bond is retained in both species. They also both contain diastereotopic CH_2 linker protons at δ 4.56 and 6.15 ($^2J(\text{HH}) = 14.0$ Hz) for complex $\mathbf{10}_\text{A}$ and at δ 5.32 and 5.87 ($^2J(\text{HH}) = 14.6$ Hz) for complex $\mathbf{10}_\text{B}$. After a longer time (< 2 weeks), all of complex $\mathbf{10}_\text{A}$ had converted into complex $\mathbf{10}_\text{B}$. Complex $\mathbf{10}_\text{A}$ is the kinetic isomer and complex $\mathbf{10}_\text{B}$ is the more thermodynamically stable isomer. NMR characterisation data in CD_2Cl_2 for species $\mathbf{10}_\text{A}$ and $\mathbf{10}_\text{B}$ are detailed in the Experimental Section 8.8.7.

When $\mathbf{3}$ reacts with pyridine and H_2 in C_6D_6 , after 72 hours the major dihydride species at 298 K is $\mathbf{10}_\text{A}$ (~ 70 %), with two bound pyridine ligands and two hydride ligands; these are visible as a broad singlet at δ -21.24 and a broad doublet at δ -28.00

($^2J(\text{HH}) = 7.7 \text{ Hz}$). Another broad pair of hydride signals appears at $\delta -21.67$ and -28.42 ($\sim 10 \%$) which convert into signals for **10A** over time. Two other monohydride signals are present at $\delta -24.03$ (*trans* to pyridine) and -25.54 (*trans* to oxygen) ($\sim 10 \%$), which are thought to be due to COD-containing intermediate species (see Section 3.2). In C_6D_6 , there is also a minor pair of hydride signals ($\sim 10 \%$) at $\delta -22.01$ and -24.58 , which couple via a ^1H COSY NMR spectrum and correspond to **10B**.

2.4.4. Reactivity of **4** in CD_2Cl_2 and C_6D_6

The reactivity of **4** with pyridine and hydrogen in CD_2Cl_2 and C_6D_6 is like that of **3** described in Section 2.4.3, as with pyridine alone it demonstrates no reactivity and, with hydrogen, two very minor ($< 2 \%$) dihydride species are formed. Their signals, which are at $\delta -10.74$ and -20.19 and $\delta -12.56$ and -21.49 , are only easily observed under PHIP conditions and correspond to COD dihydride species **11A** and **11B**. On activation with both pyridine and hydrogen, two distinct conformational isomers of **12** form, with signals for one species being much broader than the other at 298 K (see Figure 68 and Figure 69). They exchange with each other as well as with hydrogen on the NMR timescale, thus demonstrating the same activation behaviour as for complex **3**. NMR characterisation data, which are very similar to those for the two isomers of **10** in Section 2.4.3, are included in the Experimental Section 8.9.14. The exchange of py_1 in complex **12A** was too rapid to elucidate the chemical shifts of all its proton and carbon atoms and due to considerable peak overlap several other resonances could not be determined.

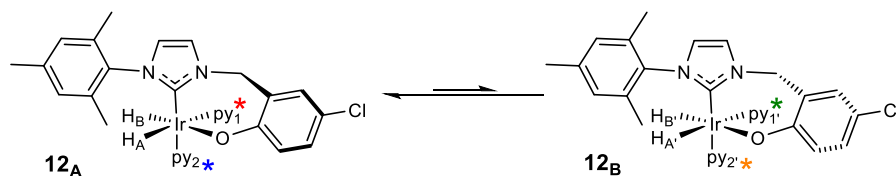


Figure 68: Two conformational isomers, **12A** and **12B** present in CD_2Cl_2 and C_6D_6

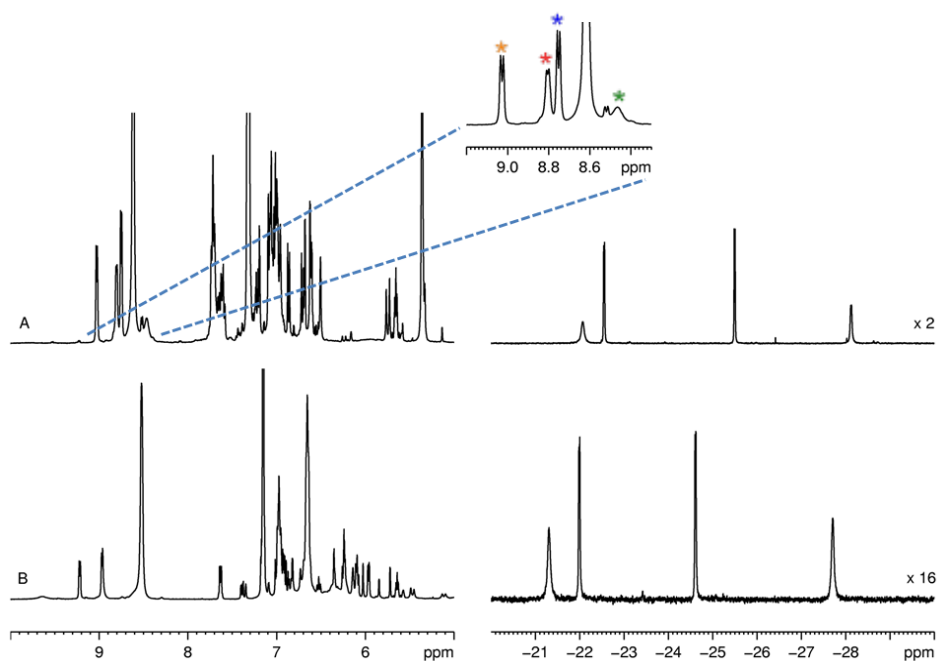


Figure 69: ^1H NMR spectra showing the aromatic and hydride regions for samples of **12_A** and **12_B** in CD_2Cl_2 (A) and C_6D_6 (B). The inset image shows the four bound pyridine environments in CD_2Cl_2 (*)

2.4.5. Reactivity of **1** in CD_3OD

For stable complex **1**, when the solvent is changed to CD_3OD , its reactivity is the same as that described in Section 2.4.1 in the solvent CD_2Cl_2 . Activation of **1** with pyridine and H_2 also leads to the formation of complex **6** and the same two hydride signals are apparent in the ^1H NMR spectrum at δ -21.62 and -29.22 with a coupling constant of 8.7 Hz. The CH_2 linker protons remain inequivalent and appear as broad doublets at δ 4.68 and 6.25 with a coupling constant of 13.5 Hz.

2.4.6. Reactivity of **2** in CD_3OD

In the protic solvent CD_3OD , **2** acts very differently when compared to similar solutions in CD_2Cl_2 and C_6D_6 . Upon dissolving **2** in CD_3OD , the corresponding ^1H NMR spectrum changes and the peaks all become very broad so assignment at 298 K is not possible. However, on cooling to 243 K the signals resolve which enables full

characterisation of the complex, as detailed in the Experimental Section 8.7.7. The CH₂ linker protons are visible as two doublet signals at δ 6.26 and 5.30 with a common coupling of 15.0 Hz, whilst the four COD alkene protons are all visible as multiplet signals at δ 4.39, 4.28, 3.20 and 2.86.

Upon the subsequent addition of pyridine at 243 K, the peaks remain resolved and a four-coordinate square planar intermediate, **13** is formed cleanly as shown in Figure 70. Complex **13** contains the carbene ligand, one bound pyridine ligand and the bidentate COD ligand, with four inequivalent alkene protons at δ 4.02, 3.86, 3.78 and 3.27. The upfield chemical shift of the CH protons of the bound COD ligand, compared to those of **2**, are consistent with COD no longer binding *trans* to the oxygen ligand and thus the phenolate has dissociated. In methanol, the proposed zwitterionic structure can be stabilised by interactions with the solvent. Furthermore, when ¹⁵N-labelled pyridine is used, all four COD CH protons show long-range coupling to the pyridine nitrogen atom, observed via an HMQC spectrum. The CH₂ linker protons remain diastereotopic, appearing at δ 6.40 and 5.64 with a coupling constant of 14.6 Hz, as no plane of symmetry exists within the molecule. Full characterisation data for **13** are given in the Experimental Section 8.7.9.

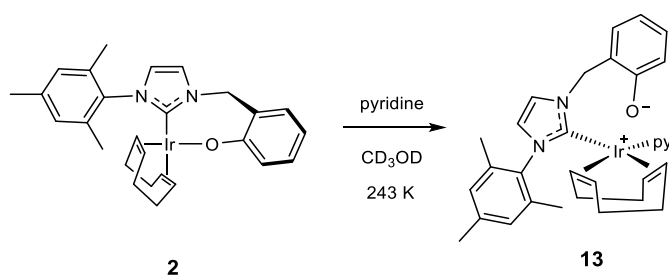


Figure 70: Complex **2** and the intermediate, **13**, formed on the addition of pyridine

Upon addition of *p*-H₂ to **13** at 243 K two PHIP enhanced hydride signals are observed at δ -12.34 and -17.50 which are shown to couple via ¹H COSY NMR spectra and correspond to the alkene dihydride complex, **14** (see Figure 71). This reaction does not go to completion and instead a mixture of **13** and **14** is formed in an approximate ratio of 1.2: 1. The downfield chemical shifts of the hydride ligands are consistent with them binding *trans* to carbon and nitrogen respectively, commensurate with Ir-O bond cleavage. The hydride ligand signal at δ -17.50 also demonstrates a *trans* ²J-coupling to the pyridine nitrogen, equal to 16.8 Hz. In **14**, the CH₂ linker protons again remain

diastereotopic, appearing at δ 5.00 and 4.70 with a coupling constant of 15.2 Hz, as the complex contains no plane of symmetry. Full characterisation data for **14** are given in the Experimental Section 8.7.10.

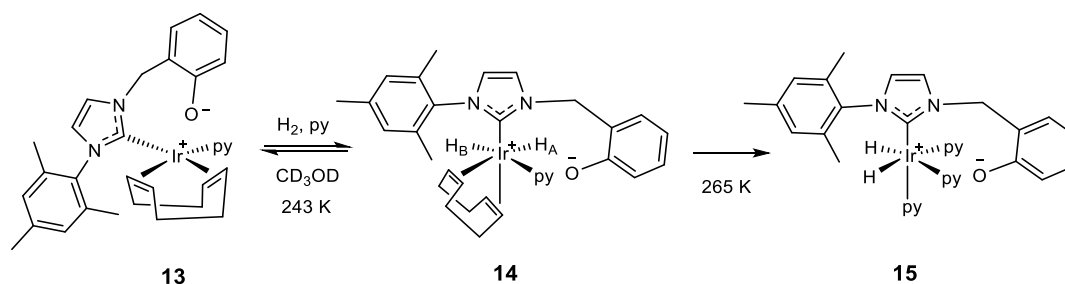


Figure 71: Formation of **14** upon addition of hydrogen to **13** and subsequent formation of **15** on warming the sample

Upon warming to 265 K, a hydride signal at δ -22.18 for complex **15** (Figure 71) is visible. By 298 K, this is the major species present in solution and the signals remain sharp and resolved, as shown in Figure 72. Characterisation is now possible.

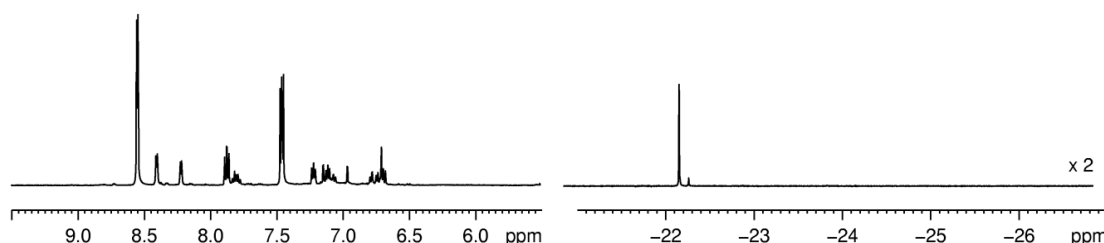


Figure 72: ^1H NMR spectrum of the aromatic and hydride regions after the reaction of **2** with pyridine and hydrogen, in CD_3OH , to form **15** showing the singlet hydride signal

Overall the hydride region showed the presence of two species, with the major singlet at δ -22.34 reflecting 96 % of the species and the minor singlet at δ -22.43 making up the other 4 %. The major species is the tris-pyridyl dihydride complex **15**, where the chelating ligand is dissociated at the oxygen side arm. The two species undergo very rapid exchange with deuterium in solution from the CD_3OD solvent and the signals corresponding to the major and minor hydride-deuteride complexes appear at δ -22.29 and -22.39 respectively. This is accompanied by the formation of HD in solution and 30 minutes after the addition of fresh hydrogen, both signals in the hydride region of the spectrum correspond to the hydride-deuteride species. Due to this rapid deuteration no exchange rates for hydride dissociation could be calculated in CD_3OD .

The rest of the proton spectrum confirms the identity of **15**, due to the presence of signals for two bound pyridine environments in a 2: 1 ratio, indicative of the two pyridine ligands *trans* to hydride ligands and the one *trans* to the carbene respectively. The CH₂ linker protons now appear as one signal at δ 4.83 which integrates to two equivalent protons and means that these are no longer diastereotopic; the oxygen is no longer bound and the phenolate can freely rotate. Full characterisation data for **15** are given in the Experimental Section 8.7.11. Overall, the reaction from **2** to form **15** in CD₃OH, is much faster than the equivalent reaction seen in CD₂Cl₂ or C₆D₆.

Upon cooling this sample to 250 K, along with the subsequent reaction with *p*-H₂, two very minor, very broad, weakly PHIP enhanced hydride signals are visible at δ -22.6 and -26.2 which must correspond to species **8**, where the Ir-O bond is retained. However, its very low concentration and the fact that it undergoes rapid exchange, even at low temperature, precluded any further characterisation.

Intermediates, **13** and **14**, lie on the pathway to the formation of **15**. This reactivity follows the same pathway as described for [Ir(COD)(IMes)Cl], which starts with displacement of the chloride ligand by a substrate ligand, so that the chloride becomes a counter ion.⁹⁴ This charged 16-electron complex is stabilised by the polar protic solvent, methanol, which is not possible when CD₂Cl₂ or C₆D₆ are used.

Figure 73 depicts the key ¹H NMR spectroscopic changes observed on addition of H₂ to a CD₃OD solution of **13**. Focusing on the aromatic region, a large chemical shift difference is observed between the *ortho* protons of the pyridine ligand bound *trans* to the COD ligand in **13** and the pyridine ligand bound *trans* to a hydride ligand in **14**. This large downfield shift is due to the pyridine ligand experiencing a decrease in electron density which occurs on oxidising the metal centre from Ir(I) to Ir(III) and thus leads to reduced shielding from the applied magnetic field. Similar downfield shift effects are observed for the CH protons of the COD ligand in **13** compared to **14**, also shown in Figure 73. The fourth CH_{COD} proton of **14** overlaps with the CH_{COD} proton of **13** that is visible at $\sim \delta$ 4 in Figure 73 B and the doublet signal that is present at $\sim \delta$ 4.7 Figure 73 B corresponds to one of the protons of the CH₂ linker of **14**.

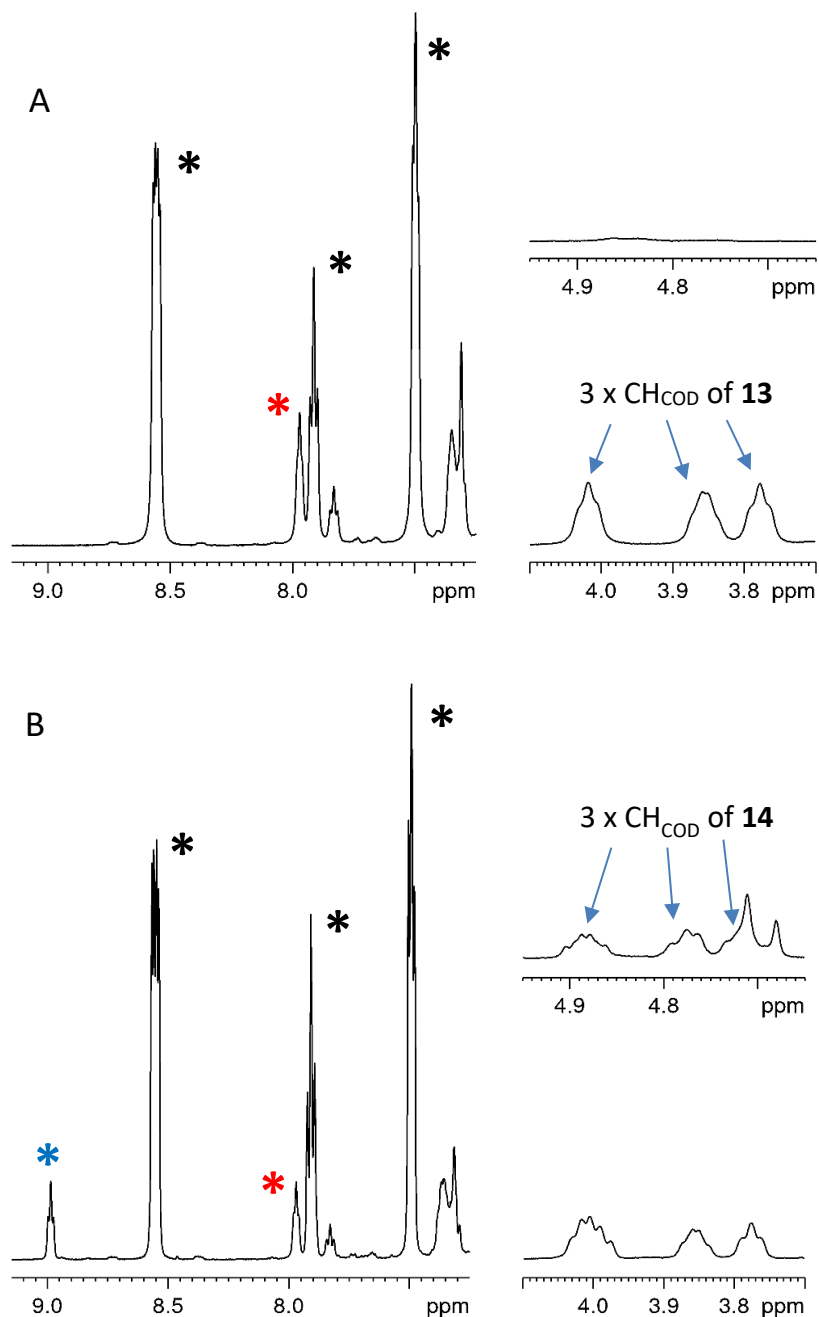


Figure 73: Aromatic region of the ^1H NMR spectra of complex **13** (left-hand side), with signals for free pyridine indicated by * and the signal for the ortho proton of the bound pyridine ligand of complex **13** indicated by * (A). On addition of H_2 the formation of **14** is indicated by a significant change in the chemical shift of the ortho proton of the bound pyridine ligand in **14** shown by * (B). The meta and para protons of the bound pyridine ligands in **13** and **14** overlap due to incomplete conversion to **14**. A similar shift is observed for the COD CH protons, shown on the right-hand side

2.4.7. Reactivity of **3** in CD₃OD

In CD₃OD, complex **3** demonstrates very similar reactivity to that of **1** (see Section 2.4.5). For a sample containing 10 mol% **3** and 0.06 M pyridine, in CD₃OD, full activation to the bis-pyridine species, **10_A**, occurs within a couple of hours and after 70 hours significant deuteration of the *ortho* proton sites of pyridine has occurred. Approximately 40 % of the signal remained for the *ortho* ¹H NMR signal. This deuteration affect was not visible in the aprotic solvents. The two signals for the hydride ligands of **10_A** appear as broad singlets at δ -21.66 and -29.04 in the ¹H NMR spectrum. The corresponding *ortho* proton signals for the bound pyridine ligands appear at δ 8.90 (*trans* to carbene) and 8.23 (*trans* to hydride). Full NMR characterisation data for **10_A**, as shown in Figure 74, are given in the Experimental Section 8.8.7.

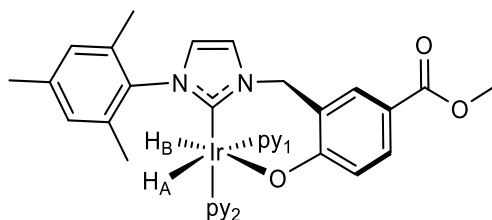


Figure 74: **10_A** that forms in methanol

When the concentration of pyridine in solution is increased, so that a sample contained 4 mol% **3** and 0.32 M pyridine, formation of **10_A** and a tris-pyridyl, Ir-O bond-cleaved species was observed, in an approximate ratio of 87: 13. The low concentration of the tris-pyridyl species and the multiple overlapping signals precluded its full characterisation although the signals for the hydride ligands at δ -22.40 and two bound pyridine environments at δ 8.41 (2 x py) and δ 8.18 (1 x py) could be identified.

2.4.8. Reactivity of **4** in CD₃OD

For complex **4**, in CD₃OD, a sample containing 5 mol% **4** and 0.16 M pyridine reacted to form two species; one with inequivalent hydride ligands and the other exhibiting equivalent hydride ligands. Two very broad signals for the inequivalent hydride ligands of **12A** were present at δ -21.72 and -28.72 but the Ir-O bond cleaved product, **16**, was also formed as shown in Figure 75. For complex **16** the hydride signal was present in the ¹H NMR spectrum at δ -22.29. Due to the formation of the tris-pyridyl dihydride species, this exhibits similar behaviour to that observed for complex **2**, as described in Section 2.4.6, and therefore, with more electron-donating substituents on the phenolate, the Ir-O bond becomes weaker and less stable. Full NMR characterisation data for **12A** and **16** are included in the Experimental Sections 8.9.14 and 8.9.15 respectively.

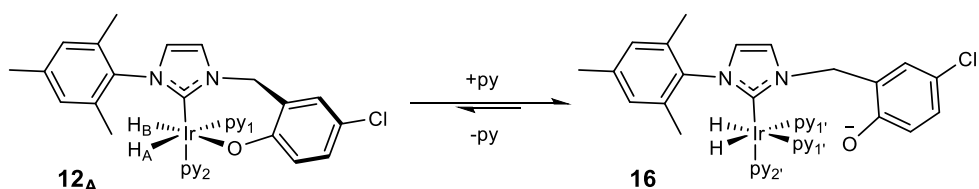


Figure 75: **12A** and **16** present in a CD₃OH sample of **4** with pyridine and H₂

The four complexes described in this section all contain electron-withdrawing substituents in the *para* position to the phenolate within the carbene backbone. Investigations were carried out to create an imidazolium salt derivative with the electron-donating dimethylamino group in the *para* position to the phenolate. However, despite multiple synthesis attempts, isolation of the desired imidazolium salt was not possible due to decomposition of the reaction mixture during the synthesis. This rapid degradation, combined with the knowledge that the H-containing complex demonstrates reduced stability in comparison to the electron-withdrawing complex derivatives, meant that this route was not pursued.

2.5. Further investigations of complex **2**

It has been shown that the reaction of complex **2** with pyridine and H₂ cleanly forms two different structures **8** and **15**, depending on the solvent used. Therefore, to determine whether complexes **8** and **15** exist in equilibrium, a sample containing **2** and pyridine was prepared in CD₂Cl₂, and once activated with H₂, CD₃OH was added such that the solution contained 10 % CD₃OH by volume. Both **8** and **15** were observed, showing that they do exist in equilibrium and that Ir-O bond cleavage and reformation occurs easily. To analyse this equilibrium and determine the free enthalpy and entropy changes between the two species, the sample was cooled from 303 K in 10 °C steps and the ratio of the two isomers was measured. The total sum of the integrals for the free pyridine *ortho* proton signal and the two isomers at 273 K was used to gauge the total amount of pyridine in the sample: this was used as the maximum for all calculations. The concentrations and equilibrium constants for the sample were calculated at the different temperatures using the equation shown in Figure 76 and the data are presented in Table 9.

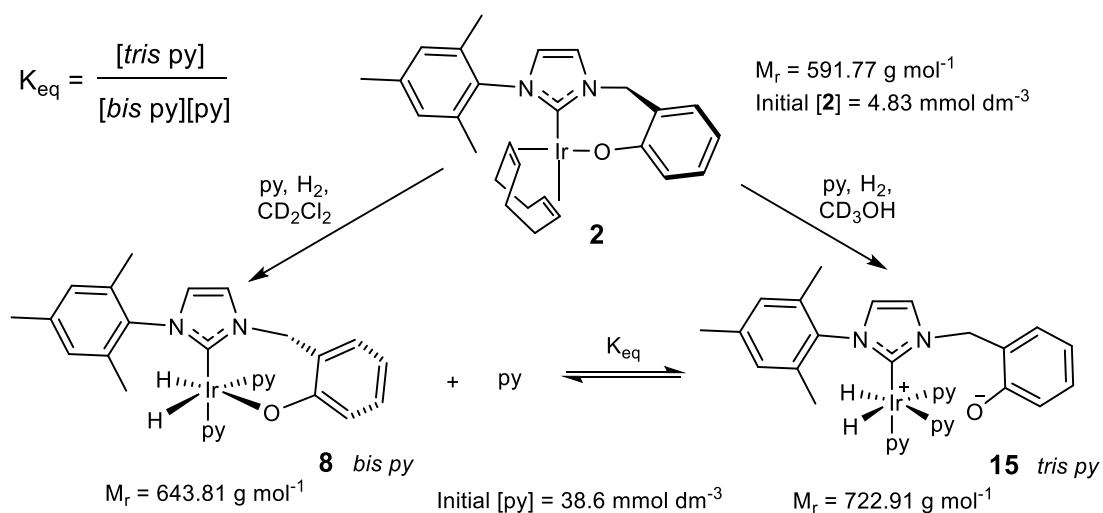


Figure 76: Equilibrium constant between **8** and **15** and the initial concentrations of **2** and pyridine

Table 9: Concentrations of iridium complexes to determine equilibrium constants at different temperatures in a CD_2Cl_2 : CD_3OH sample (9: 1) containing **2** and pyridine under 3 bars of H_2

T / K	Amounts of free py and complexes 8 and 15 / %			Iridium complex amounts / %		Concentrations of free py, 8 and 15 / $mmol\ dm^{-3}$			Equilibrium constants / $mol^{-1}\ dm^3$	
	Free py	8	15	8	15	[8]	[15]	[py]	K_{eq}	$\ln K_{eq}$
303	86.0	12.1	1.86	86.7	13.3	4.19	0.64	33.2	4.62	1.53
293	84.3	12.5	3.14	79.9	20.1	3.86	0.97	32.6	7.70	2.04
283	82.8	11.9	5.30	69.2	30.8	3.34	1.49	32.0	13.9	2.64
273	81.2	10.2	8.58	54.3	45.7	2.62	2.21	31.4	26.9	3.29
263	80.2	7.47	12.3	37.8	62.2	1.82	3.00	31.0	53.2	3.97
253	78.4	5.84	15.7	27.1	72.9	1.31	3.52	30.3	88.9	4.49
243	77.2	4.43	18.4	19.4	80.6	0.94	3.89	29.8	139	4.94

To calculate the standard enthalpy (ΔH^θ) and entropy (ΔS^θ) changes for the reaction of **8** with free pyridine to form **15**, the linear form of the Van't Hoff equation is used as shown in Figure 77. Plots of $1/T$ vs $\ln K_{eq}$ are used to determine the enthalpy and entropy changes from the gradient and intercept respectively (see Figure 78).

$$\ln K_{eq} = -\frac{\Delta H^\theta}{RT} + \frac{\Delta S^\theta}{R}$$

where: K_{eq} = equilibrium constant / $mol^{-1}\ dm^3$

ΔH^θ = standard enthalpy change / $kJ\ mol^{-1}$

ΔS^θ = standard entropy change / $J\ K^{-1}\ mol^{-1}$

R = Gas constant / $8.314\ J\ K^{-1}\ mol^{-1}$

T = temperature / K

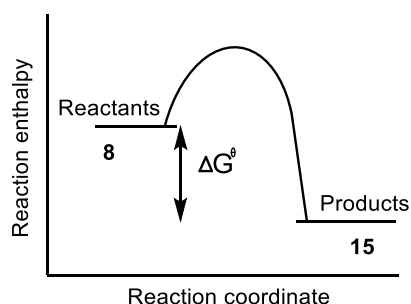


Figure 77: Linear Van't Hoff equation and reaction coordinate diagram for an exothermic reaction

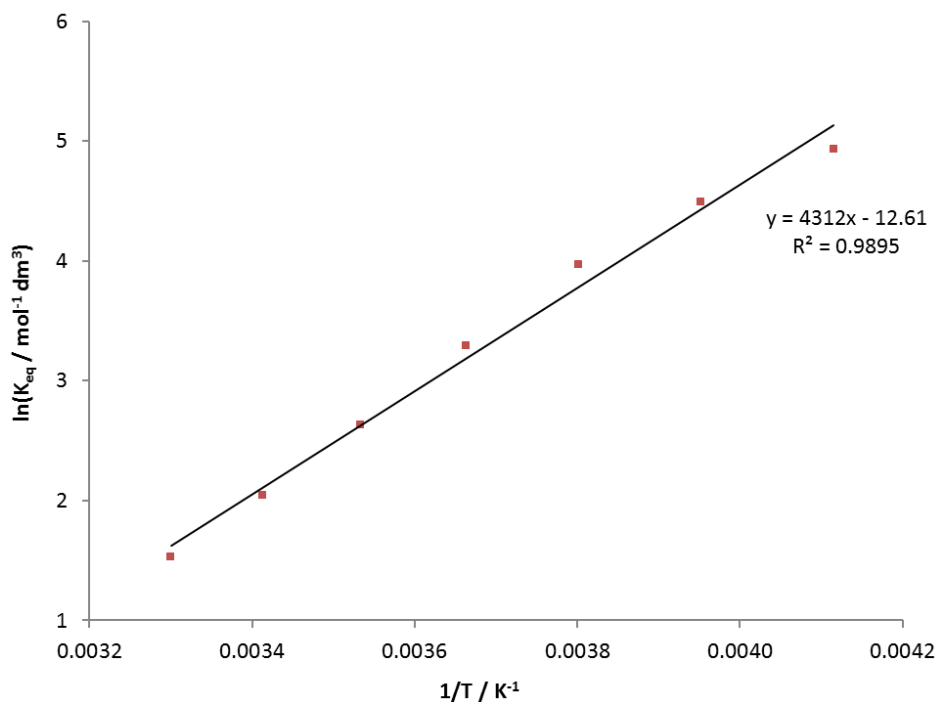


Figure 78: Linear Van't Hoff plot for calculating standard enthalpy and entropy changes for the equilibrium between complex **8** binding pyridine, to form complex **15**

The reaction to form **15** from **8**, via Ir-O bond cleavage and pyridine binding, is exothermic. This is obvious from the positive gradient and negative enthalpy change of $-36.0 \pm 2.8 \text{ kJ mol}^{-1}$. The standard entropy change of $-105.2 \pm 10.0 \text{ J K}^{-1} \text{ mol}^{-1}$ is also negative as expected because there is an increase in order in the system as two species form one. The change in Gibbs Free Energy of the system at 300 K was calculated to be $-4.4 \pm 4.1 \text{ kJ mol}^{-1}$ which is very low, indicating minimal energy difference exists between the two species.

As the addition of methanol to a CD_2Cl_2 solution of **8** promotes Ir-O bond cleavage, it was hypothesised that the addition of acid to another CD_2Cl_2 sample would cause the same effect. On reaction of a CD_2Cl_2 solution of **8** with formic acid, the two hydride ligands of **8**, at $\delta -22.56$ and -25.50 , were slowly replaced by a hydride ligand at $\delta -22.25$ due to a new species, the protonated form of **15**, as shown in Figure 79. As the acid concentration increases, the amount of **15** increases and the hydride signals for **8** become much broader, until **15** is the dominant species in solution. This must be accompanied by phenolate protonation. The chemical shifts for the protons of free pyridine are also pH dependent as shown in Figure 80, which is consistent with protonation of the pyridine in solution. Once the pyridine is protonated, SABRE is

hindered and testing with *p*-H₂ leads to no signal enhancements. This is because the nitrogen no longer has a free lone pair of electrons available for binding to the iridium.

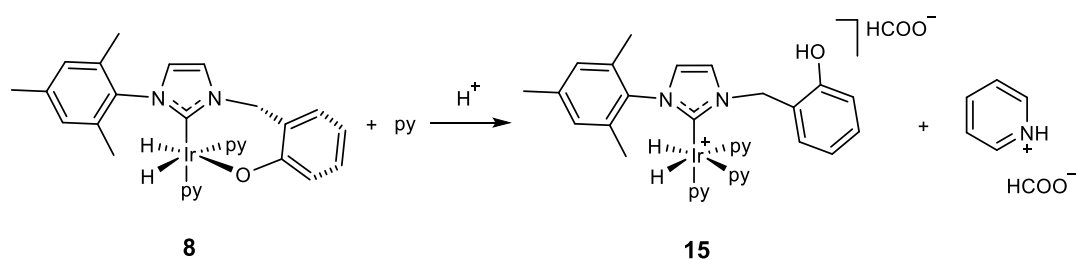


Figure 79: Reaction of **8** with formic acid leads to Ir-O bond cleavage and the formation of **15** now containing a protonated phenol side arm, along with production of protonated pyridine which inhibits SABRE

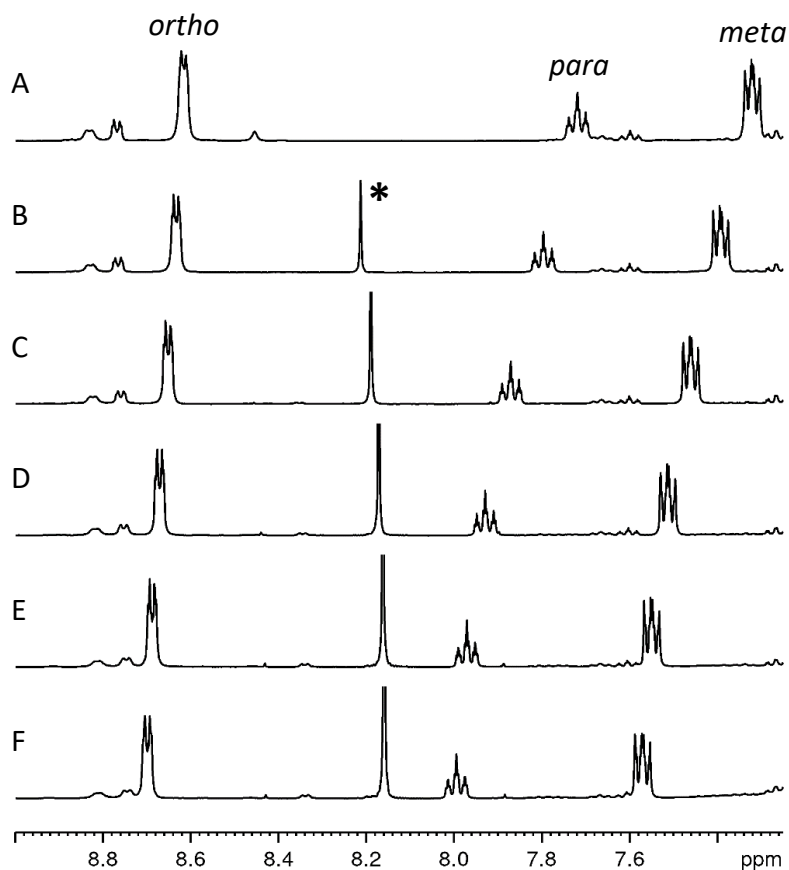


Figure 80: Chemical shift changes observed on addition of increasing equivalents of formic acid (0 to 15 equivalents, indicated by *) to a CD₂Cl₂ solution of **8** to form protonated **15** and protonated free pyridine (labelled ortho, para and meta ¹H NMR signals) (A) 0 eq., (B) 3 eq., (C) 6 eq., (D) 9 eq., (E) 12 eq. and (F) 15 eq.

2.6. Rationalising the differences between the catalysts

2.6.1. UV-visible spectroscopy analysis

All the bidentate carbene complexes form yellow/orange coloured solutions. The most common pre-catalyst for SABRE, [Ir(COD)(IMes)Cl], forms a yellow methanol solution with three absorption bands at 374, 427 and 491 nm, with very similar behaviour being observed in DCM. The complexes **2**, **3** and **4** also show these three absorption bands appearing at approximately 380, 430 and 490 nm, with molar absorption coefficients of between approximately 300 and 3000 dm³ mol⁻¹ cm⁻¹. These large values are consistent with charge-transfer bands. A summary of the actual absorption wavelengths for each complex with their corresponding absorption coefficients is given in Table 10. These values were calculated by applying the Beer-Lambert law, $A = \epsilon cl$ (where A = absorbance, ϵ = molar absorption coefficient and l = cell path length) to multiple samples of each pre-catalyst at differing concentrations (see Experimental Sections 8.6.3, 8.7.7, 8.8.6 and 8.9.13).

On analysing the series of bidentate carbene complexes, based on their corresponding Hammett parameters, the values for the absorption bands of **2** all appear at shorter wavelengths, and thus higher energies, in comparison to the absorption bands of **3** and **4**. Complex **2** contains the most electron-donating substituent (H) on the phenolate ring. Complexes **3** and **4**, which exhibit very similar wavelength bands, have more electron-withdrawing substituents on the phenolate ring (COOMe and Cl respectively) and thus it is predicted that for complex **1**, which contains the most electron-withdrawing NO₂ substituent, the shortest wavelength absorption band would appear at a longer wavelength again, indicating a lower energy transition. Therefore, relating to the maximum absorption, the shortest wavelength band follows the trend of **4** \approx **3** > **2** corresponding to Cl \approx COOMe > H. However, for the longer wavelength bands, the differences in the absorption wavelengths are very small. This contrasts with that observed for the similar absorption spectra of a number of ruthenium complexes as shown in Figure 81, containing phosphine ligands with varying electron-donating and withdrawing substituents.¹⁶⁵ For these complexes, the most electron-withdrawing substituent, C₂F₅, gives the lowest wavelength absorption bands, with the electron-

donating substituents Et, Me and Ph exhibiting very similar wavelength bands at slightly longer wavelengths.¹⁶⁵ Like the neutral iridium carbene complexes developed here, these ruthenium complexes each demonstrate very different reactivities with H₂ and CO due to the differing substituents.

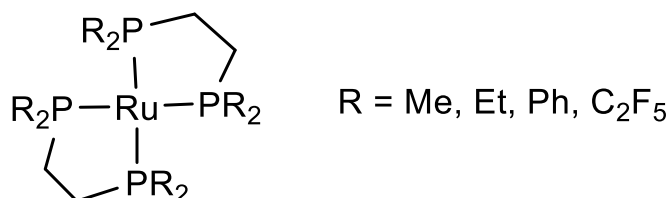


Figure 81: Ruthenium bis-phosphine complexes with substituents containing varying electron-withdrawing and donating capabilities

Table 10: Summary of the molar absorption coefficients for the detailed Ir(I) complexes

Sample	1 in DCM	2 in DCM			[Ir(COD)(IMes)Cl] in methanol		
Wavelength / nm	406	373	425	490	374	427	491
$\epsilon / \text{dm}^3 \text{mol}^{-1} \text{cm}^{-1}$	21060	1017	1326	249	1349	2065	457
		3 in DCM			4 in DCM		
Wavelength / nm		380	432	491	381	430	491
$\epsilon / \text{dm}^3 \text{mol}^{-1} \text{cm}^{-1}$		3280	1481	427	2407	1519	429

On analysing the activated solutions of [Ir(COD)(IMes)Cl] and **2** with pyridine and H₂ in CH₃OH, to form [Ir(H)₂(IMes)(py)₃]Cl and **15** respectively, these three absorption bands disappear with the maximum absorption now shifted into the UV region of the spectra as shown in Figure 82. This is consistent with the solutions all turning almost colourless once in their active dihydride forms. The same loss of colour is observed for **8**, **10**, **12** and **16**.

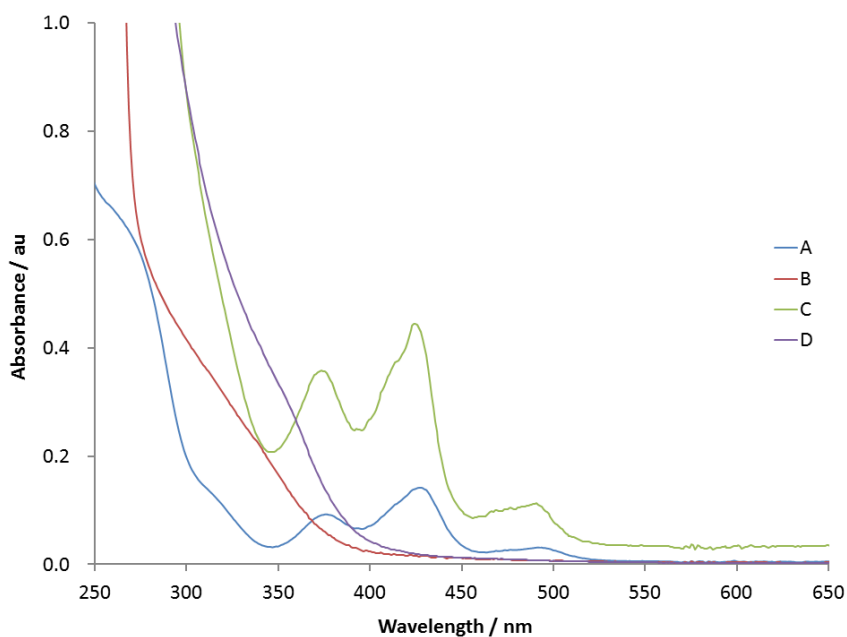


Figure 82: UV-vis spectra in methanol of $[\text{Ir}(\text{COD})(\text{IMes})\text{Cl}]$ (A) and **2** (C) showing the three absorption bands in the visible region and the disappearance of these bands upon activation with pyridine and hydrogen to form $[\text{Ir}(\text{H})_2(\text{IMes})(\text{py})_3]\text{Cl}$ (B) and **15** (D) respectively

Some similar iridium(I) square planar complexes, also containing an anionic ligand, have been described by Geoffroy et al.¹⁶⁶⁻¹⁶⁸ Their discussions in the 1970s led them to believe that these species demonstrated metal-to-ligand charge-transfer transitions from occupied metal d-orbitals to molecular orbitals derived from a mix of π -orbitals on the ligands and empty metal p-orbitals.¹⁶⁶ An example species included $[\text{IrCl}(\text{CO})(\text{PPh}_3)_2]$ which shows very similar spectra to those observed for $[\text{Ir}(\text{COD})(\text{IMes})\text{Cl}]$, **2**, **3** and **4** with three distinct bands.¹⁶⁷ It is also shown that this complex reversibly adds both hydrogen and oxygen and the latter species $[\text{IrCl}(\text{CO})(\text{PPh}_3)_2(\text{O}_2)]$, is described as colourless due to loss of the characteristic visible absorption signals (see Figure 83).¹⁶⁸ The bands may shift to higher energy and no longer lie in the visible range. However, more recent studies by Perutz et al. in the 1990s suggest that the ligand orbitals actually play a very minor role and they assigned these transitions to metal d-to-p-orbital transitions.^{165, 169-171} Discussions show that complexes that demonstrate true charge-transfer transitions often show solvatochromism due to stabilisation of an excited or ground state due to a shift in charge or creation of an ion pair. However, when varying the solvent used to dissolve **2**, the same absorption spectra in DCM, methanol and benzene were observed with the

three absorption bands between 350 and 500 nm visible at the same wavelengths as shown in Figure 84.

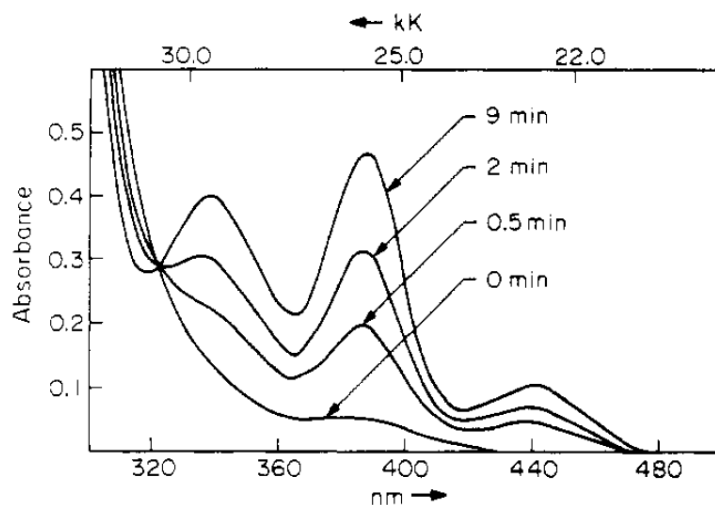


Figure 83: UV-vis spectra for the photolysis of colourless $[\text{IrCl}(\text{CO})(\text{PPh}_3)_2(\text{O}_2)]$ at 366 nm to reform the coloured square planar $[\text{IrCl}(\text{CO})(\text{PPh}_3)_2]$ complex with its three absorption bands (Reprinted with permission from Geoffroy, G. L.; Hammond, G. S.; Gray, H. B. *J. Am. Chem. Soc.* **1975**, 97, 3933. Copyright © 1975 American Chemical Society)¹⁶⁸

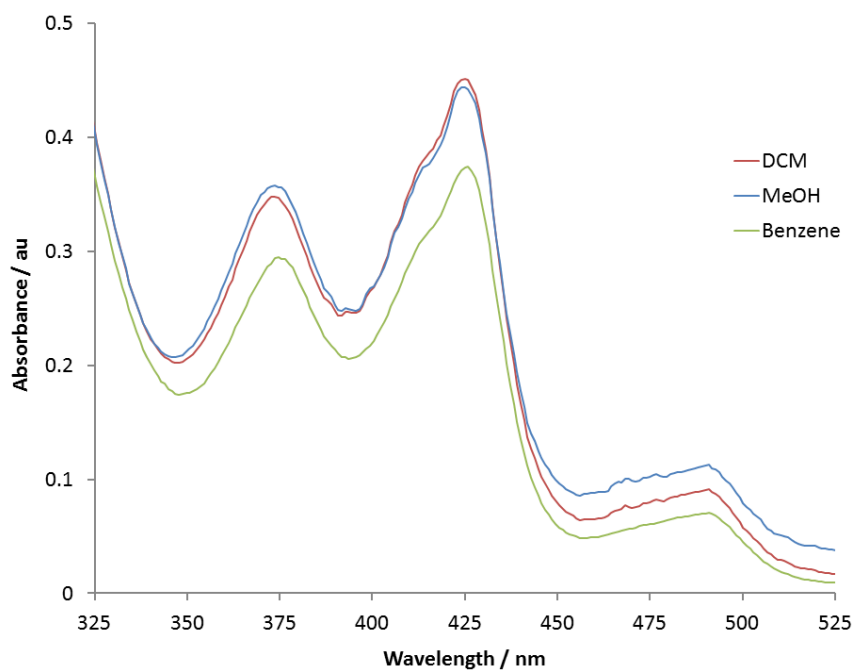


Figure 84: The three absorption bands present for **2** in DCM, methanol and benzene with no indication for solvatochromism, commensurate with no change in absorption maxima in the different solvents

Figure 84 indicates that this species does not demonstrate solvatochromism and neither the ground state nor the excited state is stabilised by a change of solvent. This is inconsistent with the assignment of metal-to-ligand charge-transfer bands and instead demonstrates that metal d-to-p-orbital transitions are more likely. Pyridine does not absorb in the region between 350 and 550 nm and therefore the absorption band in the activated complex is due to the complex itself and not excess pyridine in solution.

In contrast, complex **1** only exhibits one absorption band in the region between 350 and 550 nm, at 406 nm with a considerably larger molar absorption coefficient of $21060 \text{ dm}^3 \text{ mol}^{-1} \text{ cm}^{-1}$, compared to those of $[\text{Ir}(\text{COD})(\text{IMes})\text{Cl}]$, **2**, **3** and **4**, as shown in Table 10. This is despite **1** containing the same iridium, COD and Ir-O core. It is thought that complex **1** should also exhibit the three absorption bands with similar wavelengths and absorption coefficients, however, they are masked by the very large intraligand charge-transfer band from the NO_2 group in the carbene backbone. Solutions of **1** are a very strong orange colour, consistent with the large molar absorption coefficient. Analysis of the activated complex, **6**, still gives a strong absorption band at 398.6 nm with an absorption coefficient of $10975 \text{ dm}^3 \text{ mol}^{-1} \text{ cm}^{-1}$. Figure 85 shows the absorption spectra for all five complexes. Each set of data has been normalised such that the highest absorption value of each spectrum is equal to one.

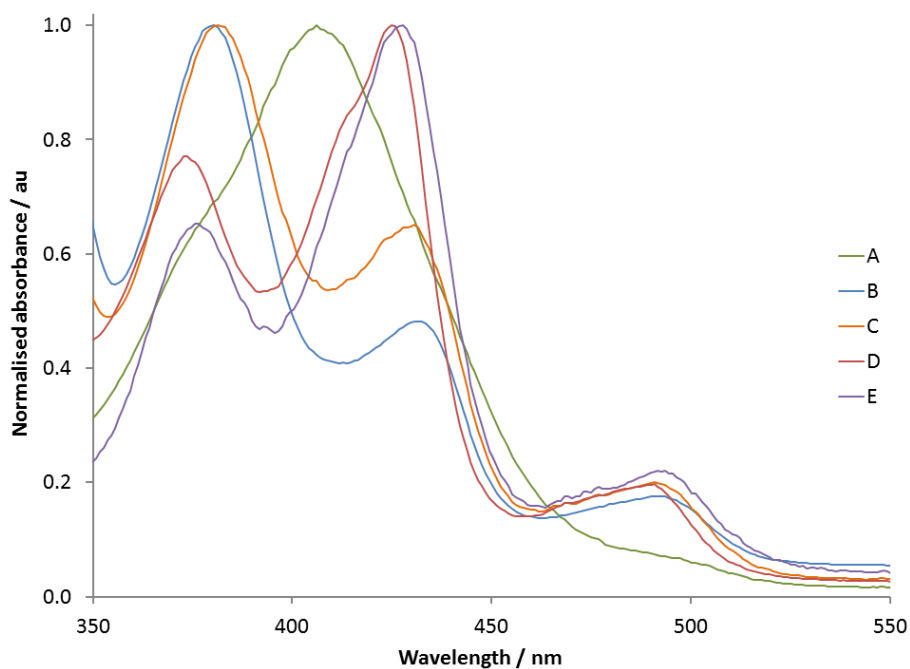


Figure 85: Comparison of the absorption spectra for the Ir(I) complexes (A) **1**, (B) **3**, (C) **4**, (D) **2** and (E) $[\text{Ir}(\text{COD})(\text{IMes})\text{Cl}]$

2.6.2. Formation of carbonyl complexes

To analyse the electronic parameters of the different carbene complexes, the carbonyl derivatives were synthesised by dissolving the COD-containing carbene complexes in DCM and bubbling CO through each solution for 10 minutes (see Experimental Sections 8.6.5, 8.7.12, 8.8.8 and 8.9.16). The use of IR spectroscopy to measure the stretching frequencies of the two resulting carbonyl ligands can be linked to the strength of the electron back-donation from the iridium centre. Therefore, the electronic properties of the system can be probed.

For **17**, which contains an electron-withdrawing nitro group *para* to the phenoxide bond, the two CO frequencies were at 2065.5 and 1971.9 cm⁻¹. For **18**, where the NO₂ has been replaced by a more electron-donating H atom, the two CO stretches were at 2058.3 and 1974.3 cm⁻¹. These correspond to symmetric and asymmetric stretching frequencies of the CO ligands. Due to the electron-donating characteristics of the carbene and phenolate ligands, electron back-donation occurs which strengthens the *trans* Ir-CO bonds, thereby weakening the C≡O bonds, meaning less energy is required to vibrate them. The more electron-donating carbene phenolate ligand in **18** results in a slightly lower C≡O frequency of 2058.3 cm⁻¹ compared to the strongly electron-withdrawing nitro derivative **17** where ν_{CO} is equal to 2065.5 cm⁻¹ as less electron density is available on the iridium centre to back donate to the carbonyl ligand. The chlorine-containing derivative, **19**, shows very similar ν_{CO} values to complex **18**, however, the COOMe derivative, **20**, shows the largest deviation in both CO stretching frequencies. Figure 86 shows the structure of the complexes on the left, with their corresponding IR spectra on the right. From analysing these values, no distinct trend is apparent between the electron-donating properties of the phenoxide ligand and the corresponding CO stretching frequencies. The CO stretching frequencies of each carbonyl ligand are summarised in Table 11, with a more detailed explanation of the Hammett parameters and corresponding electronic effects given in Section 3.1. The literature values for the CO stretching frequencies of [Ir(IMes)(CO)₂Cl] are also included in Table 11, showing that the values for the iridium carbonyl complexes developed here are very similar to those of an established complex.¹⁷²

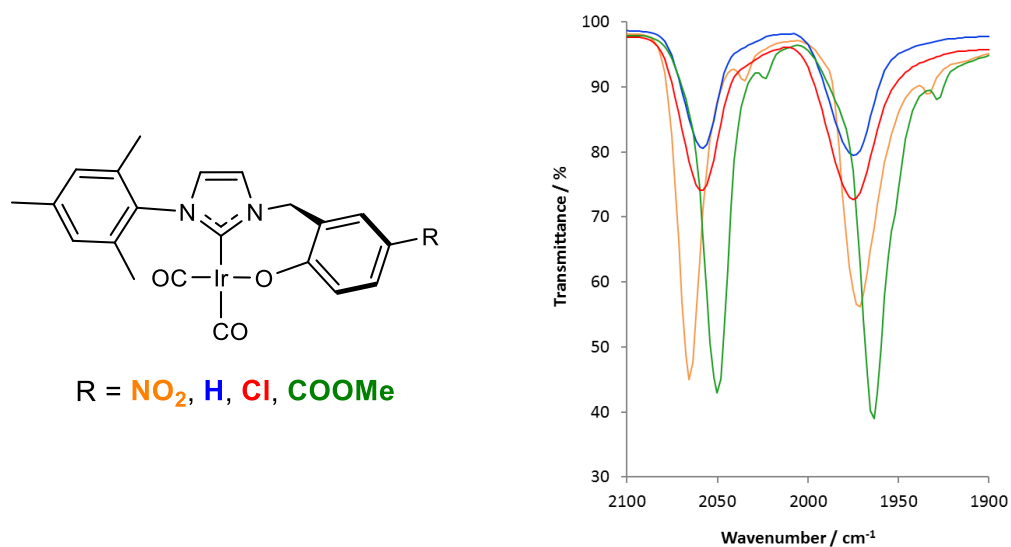


Figure 86: The structure of the $[\text{Ir}(\text{R-NHC-O})(\text{CO})_2]$ complexes developed here (left) and their corresponding IR spectra of the CO region (right)

Table 11: Comparisons of the CO stretching frequencies for the four complexes shown in Figure 86 along with the literature data for $[\text{Ir}(\text{IMes})(\text{CO})_2\text{Cl}]$

Complex	R	Hammett parameters		CO stretching frequencies / cm^{-1}	
		σ_p	σ_p^-		
17	NO ₂	0.78	1.27	1971.9	2065.5
18	H	0.00	0.00	1974.3	2058.3
19	Cl	0.23	0.19	1974.8	2058.9
20	COOMe	0.45	0.75	1964.0	2050.2
$[\text{Ir}(\text{IMes})(\text{CO})_2\text{Cl}]^{172}$	-	-	-	1979.8	2066.4

2.7. Conclusion

In this chapter, several new neutral iridium complexes, each containing a bidentate carbene with a substituted phenolate side arm, have been described. The derivatives contain NO₂, COOMe, Cl and H in the *trans* position to the phenolate. Multi-step synthetic routes have been designed to produce the desired complexes, with all of them involving the synthesis of an imidazolium bromide salt via a direct nucleophilic substitution reaction between mesityl imidazole and the corresponding benzyl bromide, to form the carbene precursor. The use of silver(I) oxide produced the silver carbene complex which could be easily transmetallated with [Ir(COD)Cl]₂ to form the desired iridium complexes **1**, **2**, **3** and **4**. In solution, NMR spectroscopy reveals the dynamic behaviour of these complexes, commensurate with rapid seven-membered ring-flipping, detailed for complex **1**.

The reactivity of each complex has been investigated in both dichloromethane and methanol, with both the solvent and the substituent lying in the *para* position to the phenolate, having a large effect on the speciation. The stability of the Ir-O bond is also greatly affected.

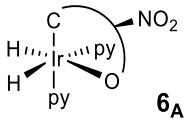
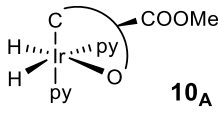
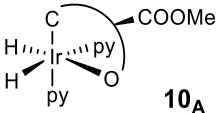
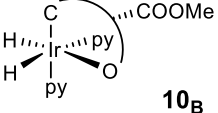
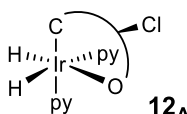
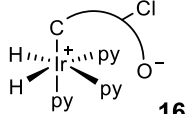
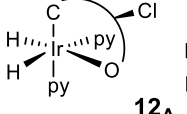
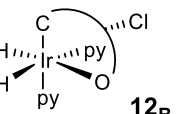
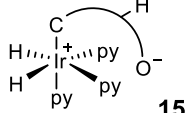
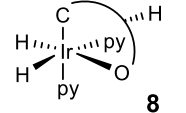
In CD₂Cl₂, all four complexes demonstrated limited reactivity with H₂ with two minor iridium COD dihydride intermediate species being observed for each complex. These species form due to the orientation of the seven-membered metallocycle and are only visible under PHIP conditions or thermally after a considerable number of scans. After longer time periods (several days) and in the presence of pyridine, the COD ligand is hydrogenated in all cases and the Ir-O bond is retained, leading to the formation of bis-pyridyl dihydride isomers. As the electron-donating ability of the phenolate substituent increases and the substituent becomes smaller, the favoured orientation of the seven-membered metallocycle changes from the orientation of **6A**, where the phenolate ring points away from the pyridine ligand, to the orientation of **8**, where the phenolate ring points towards the pyridine ligand, with **10B** and **12B** being favoured and more thermodynamically stable than **10A** and **12A**.

However, in methanol, as the substituent becomes more electron-donating, the stability of the Ir-O bond decreases so that for **1**, the Ir-O bond is retained, whilst for **2** the Ir-O bond is completely cleaved. For **4**, higher concentrations of pyridine favour Ir-

O bond cleavage, leading to formation of the tris-pyridyl dihydride species. The reaction with pyridine and H₂, leading to hydrogenation of COD and formation of the activated dihydride complexes is much faster in methanol than CD₂Cl₂ (hours rather than days), as methanol can act to stabilise any intermediates.

Overall, derivative **2** (H) proved to have much lower stability in comparison to **1** (NO₂) whilst the stability of the two complexes, **3** and **4** with σ_p^- values lying between H and NO₂ demonstrated intermediate stability. The reactivity of the COOMe derivative, **3**, was found to be like that of complex **1** due to their Hammett parameters being adjacent in the series and consequently, the Cl derivative, **4**, was found to share a similar behaviour to that of complex **2**. The different structures formed in both methanol and dichloromethane for each of the four complexes, in order from the most electron-withdrawing *para* substituent to the least electron-withdrawing *para* substituent, are summarised in Table 12.

Table 12: Summary of the major complexes formed when the four pre-catalysts **1**, **2**, **3** and **4** are reacted with pyridine and hydrogen in methanol and dichloromethane

Pre-catalyst	Major product(s) formed with pyridine and H ₂ in CD ₃ OD	Major product(s) formed with pyridine and H ₂ in CD ₂ Cl ₂		
1	 6_A			
3	 10_A	 10_A	 10_B	
4	 12_A	 16	 12_A	 12_B
2	 15	 8		

To compare the electronic effects of the four carbene derivatives, their UV-vis spectra were analysed to gain information about the electronic transitions within the complexes, giving rise to their individual colours. It was found that all the complexes, **1**, **2**, **3** and **4** exhibit charge-transfer bands in the visible region of the spectra. The three complexes **2**, **3** and **4** all show three bands each, at approximately 380, 430 and 490 nm, with molar absorption coefficients of between approximately 300 and 3000 dm³ mol⁻¹ cm⁻¹. In contrast, **1** only has one band attributable to an intraligand charge-transfer band at 406 nm with a much higher molar absorption coefficient of ~ 21000 dm³ mol⁻¹ cm⁻¹. A study of the absorption characteristics of **2**, shows that these absorption bands exhibit no solvatochromism and they are thus assigned as metal d-to-p-orbital transitions. Furthermore, reactions of the COD complexes with CO to form carbonyl complexes were also investigated which shows that the carbene is more electron-donating than the phenolate with the *trans* CO stretching frequencies lying at ~ 1970 and ~ 2060 cm⁻¹ respectively.

3. Reactivity of neutral bidentate iridium carbene complexes

3.1. Introduction

Understanding how reactions are affected by the electronic effects of ligand-based substituents is important when elucidating reaction mechanisms and pathways, particularly when the aim is to improve a catalytic system so that it can perform optimally. This has been achieved for many different reactions with hydrogenation,¹⁷³ palladium-catalysed cross-coupling¹⁷⁴ and carbonylation¹⁷⁵⁻¹⁷⁶ being three such examples. Focusing on hydrogenation, a review by Wang et al.¹⁷³ discusses the large variety of homogeneous transition metal catalysts used to promote transfer hydrogenation reactions. Several tetradentate PNNP iron-based complexes are active, as shown in Figure 87, where modification of the backbone, by increasing the size of substituents bound to the N-centred ligands, increases catalytic activity.¹⁷⁷ Further tunability can be achieved by changing the phosphorus atom substituents. There are also examples of transition metal complexes, using ruthenium, rhodium and iridium, with an iridium-containing example shown in Figure 87, which contain NHC ligands, where the nature of the groups on the imidazole moiety strongly affects the subsequent reactivity of the catalyst.

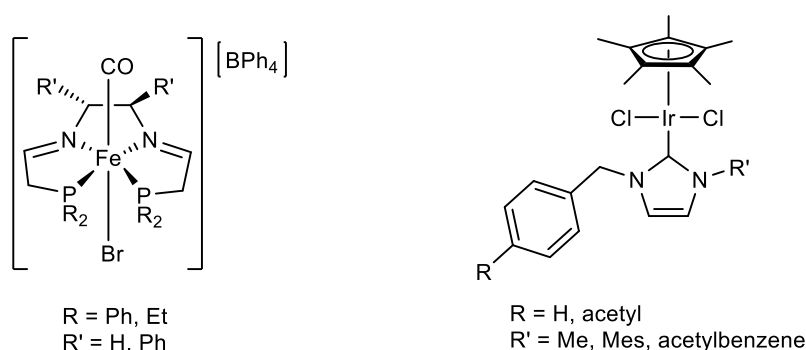


Figure 87: Examples of Fe-PNNP catalysts, for transfer hydrogenation of acetophenone, and half-sandwich Ir-NHC complexes used for transfer hydrogenation of ketones and imines, with different derivatives providing different activities in each reaction¹⁷³

One transition metal which is very widely used to achieve organic transformations is palladium, particularly for carbonylation and cross-coupling

reactions. The field of cross-coupling has grown significantly over the last couple of decades, with the Nobel Prize in 2010 being awarded to Heck, Negishi and Suzuki for their contributions.¹⁷⁸⁻¹⁷⁹

Commonly combined with phosphine ligands, the palladium catalysts produced are often stable, versatile and their reactivities are often tuneable, due to the wide range of phosphine ligands that are available. A review by Gildner et al.¹⁷⁴ describes the importance of mono and bidentate phosphine ligands in palladium catalysis and how both the steric and electronic properties of the ligands can affect catalytic activity. Phosphine ligands discussed include commonly used PPh₃, PCy₃, P^tBu₃ and the pincer ligands diphenylphosphinoethane and diphenylphosphinoferrocene along with the *tert*-butyl and *iso*-propyl derivatives. One typical phosphine ligand structure used for cross-coupling¹⁷⁴ and carbonylation¹⁷⁵⁻¹⁷⁶ reactions is based on a biphenyl core, derivatised with a phosphine which can then bind to the metal centre. Further substituents on the biphenyl core are used to tune the catalyst so that it has the desired reactivity. These ligand types were developed by Buchwald and several examples are shown in Figure 88.^{174, 176} A review by Gildner et al.¹⁷⁴ shows how changing the substituents on the phosphine ligand affects the catalyst's ability to couple unstable fluorine-containing boronic acids with activated aromatic rings.

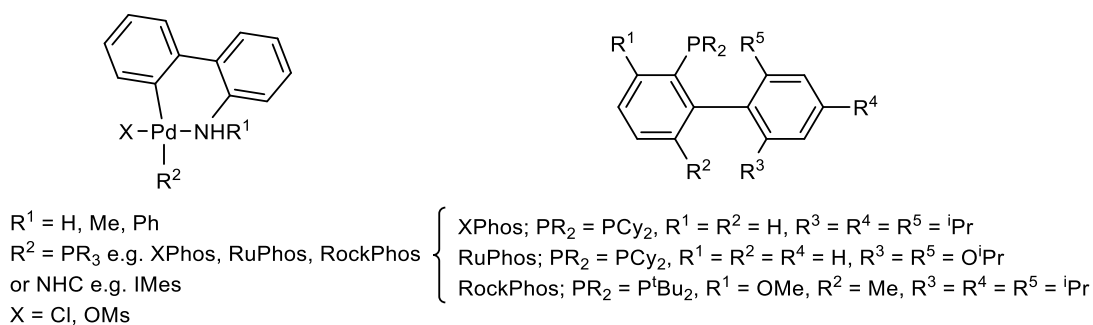


Figure 88: Palladium complexes used for cross-coupling boronic acids with an aromatic moiety containing a suitable leaving group, and the range of substituted Buchwald phosphine ligands that can be used¹⁷⁴

More recently, NHC ligands have been used in place of phosphine ligands, due to them being more robust and having stronger σ -donor capabilities. In 2014, Fang et al.¹⁷⁶ published a review of palladium NHC complexes for cross-coupling reactions, with four examples shown in Figure 89. NHCs can exert a larger effect on the

coordination sphere of an active metal catalyst, when compared to phosphine ligands, due to their structure encasing the metal centre rather than forming a cone directed away from the metal centre, such as occurs with phosphine ligands.¹⁷⁶

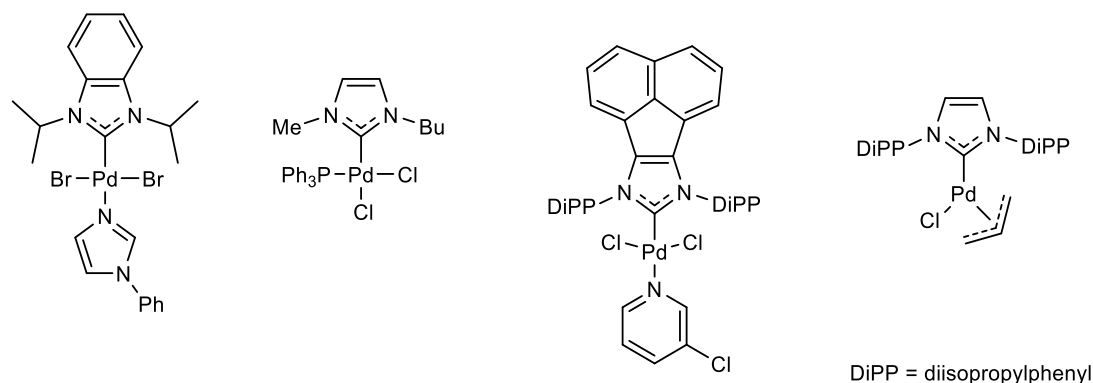


Figure 89: Pd-NHC complexes used in cross-coupling reactions as described by Fang *et al.*¹⁷⁶

Several studies which are of direct relevance to this project, are now described. One study, in 2004, by Hu *et al.*,¹⁸⁰ reports on a ruthenium-based catalyst that showed high enantioselectivities for the asymmetric hydrogenation of β -aryl ketoesters as shown in Figure 90.

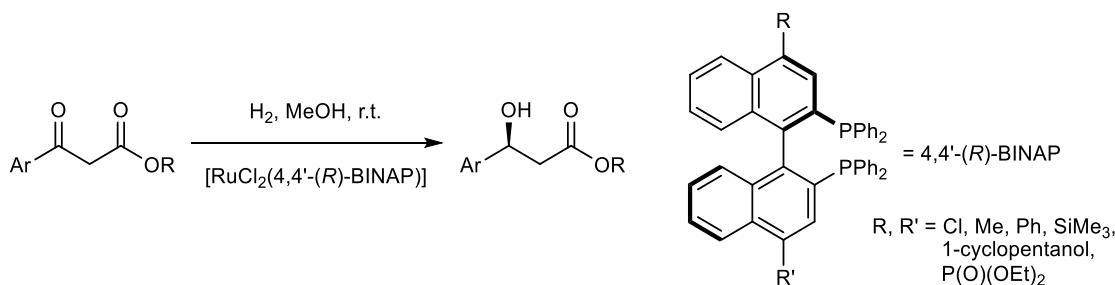


Figure 90: Asymmetric hydrogenation of β -aryl ketoesters using $[RuCl_2(4,4'-(R)-BINAP)]$ catalysts containing a number of different *R* groups¹⁸⁰

Here, the electronic and steric properties of several 4,4'-substituted BINAP derivatives were investigated. The highest enantioselectivities were achieved using the most sterically demanding ligands with electron-donating substituents in the four position whereas the introduction of phenyl substituents was found to decrease the selectivity. This behaviour was rationalised in terms of the stabilisation of a transition state; bulky groups repel the phenyl of the β -aryl ketoester substrates and thus destabilise the transition state, whereas π - π stacking interactions between phenyl rings on the catalyst and substrate stabilise the transition state. This work shows how

dramatic selectivity effects can easily be achieved by slight modification of a catalyst backbone, and how harnessing the power of catalyst optimisation can allow the development of highly useful and effective systems.

The effect of electron-donating and withdrawing substituents on reaction rates is demonstrated in the following example. It features a study, by Zhao et al., of substituent effects on the rate of β -hydrogen elimination from some square planar alkoxo-containing iridium complexes, $[\text{Ir}(\text{OR})(\text{CO})(\text{PPh}_3)_2]$ (Figure 91).¹⁸¹ The R group of the alkoxide contains a benzene ring with *para* substituents varying from an electron-donating methoxy group to an electron-withdrawing trifluoromethyl group.

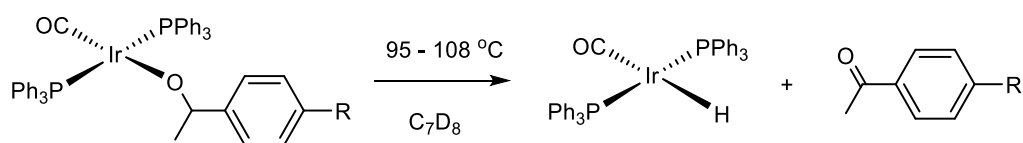
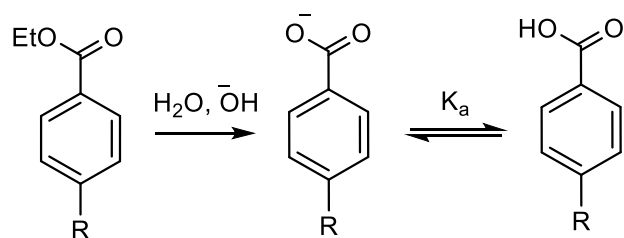


Figure 91: Iridium alkoxo complexes and the β -hydrogen elimination reaction (Adapted with permission from Zhao, J.; Hesslink, H.; Hartwig, J. F. *J. Am. Chem. Soc.* **2001**, 123, 7220.

Copyright © 2001 American Chemical Society)¹⁸¹

One classic way of viewing said effects is through the use of Hammett parameters. In the 1930s, Louis Hammett was interested in the relationship between reaction rates and equilibrium constants for a number of organic reactions.¹⁸²⁻¹⁸³ The specific reaction he focused on was the hydrolysis of benzoic ester derivatives containing a variety of substituents in the *para* position to the ester group on the ring, as shown in Figure 92. Using these compounds excluded competing steric effects that arise when using *ortho* substituted compounds. He analysed the hydrolysis rate of each benzoic acid derivative and compared them to the pK_{a} s of the corresponding acids. He noticed that a distinct correlation was present between the pK_{a} s of the derivatives and the electronic properties of the *para* substituent on the ring. He thus denoted a new parameter, σ_{p} , as detailed in Figure 92. This relates the electron-donating or withdrawing capabilities of a substituent, relative to H, to the ratio of the $\log K_{\text{a}}$ s of the substituted species and benzoic acid. Negative σ_{p} values correspond to electron-donating substituents and positive σ_{p} values correspond to electron-withdrawing substituents.



$$\sigma_p = \log \frac{K_a(RC_6H_4COOH)}{K_a(C_6H_5COOH)} = pK_a(C_6H_5COOH) - pK_a(RC_6H_4COOH)$$

Figure 92: Ester hydrolysis reaction studied by Hammett and the subsequent equation used to calculate corresponding σ_p values for substituents, R ¹⁸²⁻¹⁸³

The Hammett parameter, σ_p , can be used in the determination of reaction mechanisms. When a reaction is studied using a series of compounds with different substituents, a plot of the corresponding σ_p values against $\log(k_R/k_H)$ gives a straight line, with the gradient, ρ , giving an indication of the sensitivity of the reaction to a change in the electronics of a substituent. When ρ is positive, the mechanism involves a build-up of electron density in the transition state compared to the starting material. Conversely, when ρ is negative there is a decrease in electron density in the transition state.

Since Hammett first described the parameter σ_p , two modified versions have been developed. This is because when *para* substituents are conjugated with the reaction centre, enhanced resonance effects can be observed. The two modified values which are used to describe this effect are σ_p^+ (for substituents that stabilise positive charges via resonance) and σ_p^- (for substituents that stabilise negative charges via resonance). The σ_p^- values are based on the ionisation of substituted phenols as shown in Figure 93 and they are applicable to the electron-withdrawing substituents used in this work, as detailed in Section 2.1. This is because as the electron-withdrawing capability of the *para* substituent decreases, more electron density is available to add into the metal centre via the increased electron density on the phenolate oxygen. This should lead to an increase in the rates of ligand loss from the complex and subsequent ligand exchange as mentioned in Section 2.4. However, the resonance effect may also lead to a change in the Ir-O bond length and influence the conformation of the seven-membered metallocycle. This may contribute to a change in entropy and thus lead to other changes within the system, such as in the carbene interaction.

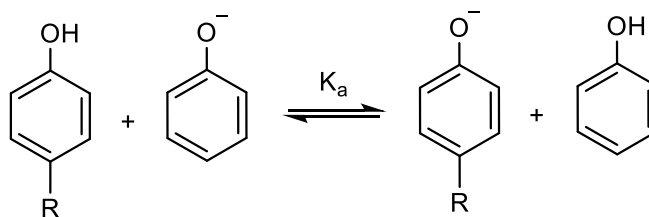


Figure 93: The ionisation of substituted phenols used to calculate the corresponding Hammett values, σ_p^- , for substituents, R, where the same equation as shown in Figure 92 is used¹⁴⁵

The study shown in Figure 91 investigated four different substituents, H, OMe, Cl and CF₃ with their corresponding Hammett parameters detailed in Table 13. The study demonstrates that as the substituent becomes more electron-donating, the rates of β -hydrogen elimination increase. The Hammett plot in Figure 94 gives a ρ value of -0.94 which signifies a decrease in electron density in the transition state of the reaction which is consistent with the mechanism proceeding via PPh₃ dissociation to form the 14-electron Ir(I) transition state. This is followed by β -hydrogen elimination via activation of the C-H bond which is favoured when electron-donating substituents can increase the electron density on the proton that becomes the hydride.¹⁸¹ Subsequent associative substitution using PPh₃, releases the ketone product. This shows that the *para* substituent can have a large effect on the electron density of atoms that are multiple bonds away.

Table 13: Iridium alkoxo complexes with different R groups, their Hammett parameters, σ_p , and rates of β -hydrogen elimination (Adapted with permission from Zhao, J.; Hesslink, H.; Hartwig, J. F. *J. Am. Chem. Soc.* **2001**, 123, 7220. Copyright © 2001 American Chemical Society)¹⁸¹

Complex	R substituent	Hammett parameter, σ_p	Elimination rate / $k_{\text{obs}} / \times 10^4$
A	H	0.00	3.5
B	OMe	-0.27	7.3
C	Cl	$+0.23$	2.0
D	CF ₃	$+0.54$	1.2

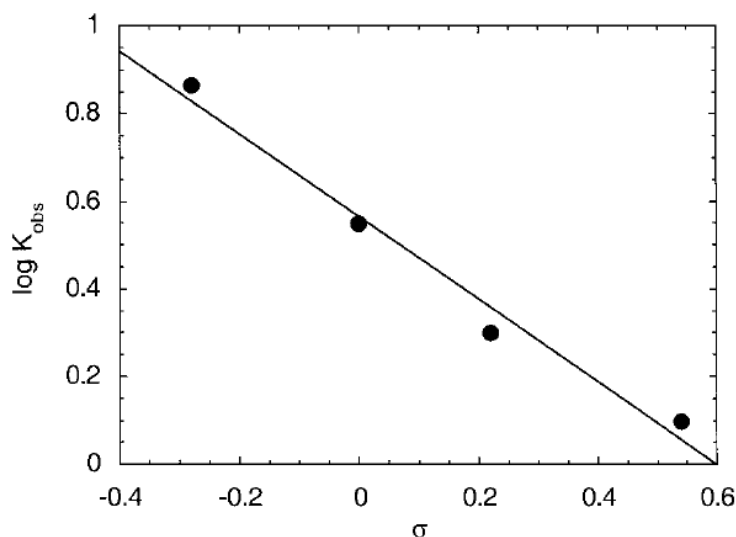


Figure 94: Hammett plot for β -hydrogen elimination from complexes A to D detailed in Table 13 (Reprinted with permission from Zhao, J.; Hesslink, H.; Hartwig, J. F. *J. Am. Chem. Soc.* **2001**, *123*, 7220. Copyright © 2001 American Chemical Society)¹⁸¹

Overall, these studies demonstrate the importance of selecting the right ligand substituents. This can be related to the complexes developed here, where the change from a *para* NO₂ group to a *para* H group on the phenolate ring of the bidentate NHC has a large effect on the iridium centre, leading to the varied speciation observed. In this chapter, the full activation pathway is analysed, along with an understanding of the complicated mechanisms of ligand exchange that the different active species undergo.

3.2. Elucidation of the reaction pathway and reactivity of complex **6**

In Section 2.4.1, the reactivity of **1** with pyridine and hydrogen to form complex **6**, containing two hydride ligands, two pyridine ligands and the bidentate carbene ligand, has been described. Here, a more detailed study into the route to form **6** from **1** via **5** was completed to identify any other reaction intermediates on the pathway to COD hydrogenation, as the ^1H NMR spectrum shown in Figure 95, shows other hydride species at δ -24.83 and -26.50 , in addition to those of **6** (at $\sim \delta$ -22 and -29).

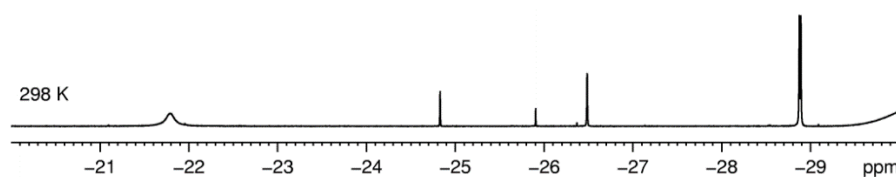


Figure 95: The hydride region of the ^1H NMR spectrum of a solution containing **1**, pyridine and hydrogen in CD_2Cl_2 at 298 K after activation for 48 hours

The signals at δ -24.83 and -26.50 both show nOe interactions with the carbene backbone and possible bound COD or COE. They do not show any nOe interaction with pyridine but are also not formed in the absence of pyridine, therefore, pyridine must play an important role in stabilising these potentially unstable intermediates and aiding the formation of stable 18-electron species. Their very low concentrations precluded any further characterisation. Furthermore, these singlet hydride signals disappear over time and their chemical shifts are temperature independent. Very similar singlet hydride signals have been observed upon activation of the other complexes, **2**, **3** and **4** with pyridine and hydrogen, as detailed in Sections 2.4.2 and 2.4.3. Overall, these observations suggest that these hydride ligands are due to two monohydride isomers of the complex undergoing COD hydrogenation, formed after hydride migration, with the hydride at δ -24.83 being *trans* to the nitrogen atom of the bound pyridine ligand and the hydride at δ -26.50 being *trans* to the oxygen ligand of the carbene as depicted in Figure 96. These structures could be confirmed by identifying ^{15}N -H couplings if ^{15}N -pyridine were to be used, with such an example being described by Martin et al. in 2003.¹⁵⁸ A full summary of the route to activation of **1** with pyridine and hydrogen is given in Figure 96.

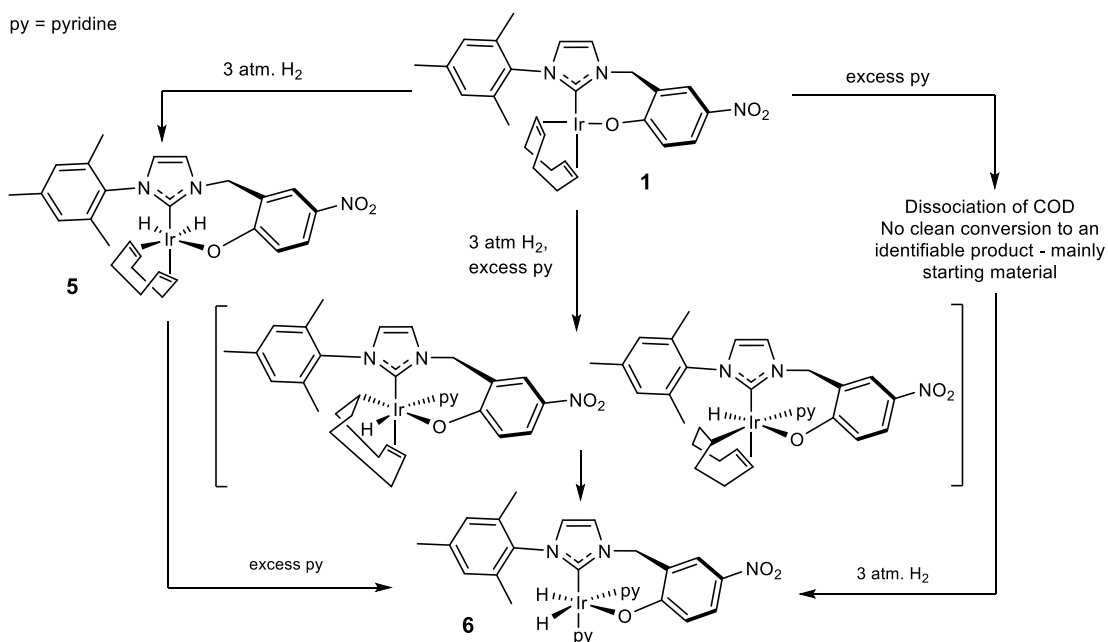


Figure 96: Products formed by the reaction of **1** with pyridine and H₂

Overall, the activation pathway is very different to that described for [Ir(COD)(IMes)Cl] as no ligand displacement occurs so no complex equivalent to [Ir(COD)(IMes)(py)]Cl forms. Instead the bidentate complex remains neutral. Furthermore, H₂ addition occurs directly to **1** whereas the H₂ addition route which forms the active catalyst [Ir(H)₂(IMes)(py)₃]Cl is via [Ir(COD)(IMes)(py)]Cl, as that route is faster than the direct addition of H₂ to [Ir(COD)(IMes)Cl].⁸⁸

3.2.1. Hydride signals for complex **6** in CD₂Cl₂

On cooling a solution of **6** in CD₂Cl₂, its two hydride signals exhibit temperature dependence as detailed in Section 2.4.1. At 233 K, both signals separate to form two pairs of doublet hydride signals with the major isomer, **6_A**, at δ -21.35 and -28.88 (²*J*(HH) = 8.7 Hz) and the minor isomer, **6_B**, at δ -22.68 and -29.02 (²*J*(HH) = 7.0 Hz) with relative intensity 83: 17. This is exemplified in Figure 97 and is due to the existence of two conformational isomers of **6**, where the carbene backbone orientation, either at the oxygen link or the CH₂ linker, differ.¹⁵⁰

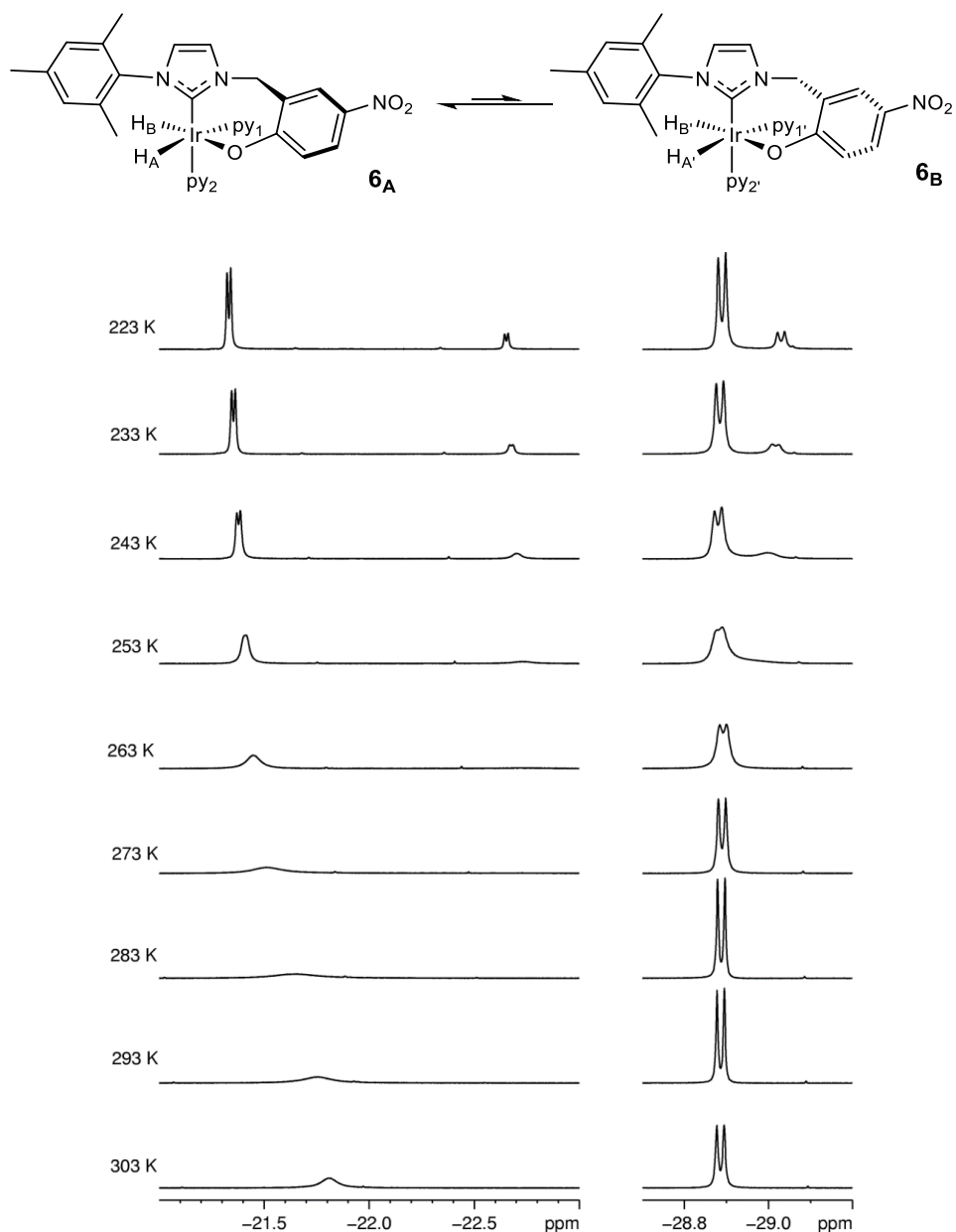


Figure 97: ^1H NMR spectra of the two main hydride signals for **6** showing how the peaks resolve as the temperature is decreased from 303 to 223 K. The rate of interconversion between the two conformers, **6_A** and **6_B** (drawn above) is slowed which leads to the peak resolution

At 233 K, the 2D ^1H NOESY NMR spectrum shown in Figure 98 shows that site-specific exchange occurs between the two conformers (blue) and that the hydride signals are linked via nOe interactions (red). This nOe effect is only visible between the two hydrides of the same complex at 233 K. This site-specific exchange is also observed for the two pairs of bound pyridine ligands as labelled in Figure 97; py_1 exchanges with py_1' and py_2 exchanges with py_2' but at 233 K no exchange is observed between the two different bound pyridine sites. The formation of two conformational

isomers is consistent with Ir-O bond retention and differing orientations of the metallocycle so the exchange processes detailed here are due to intramolecular ring-flip.

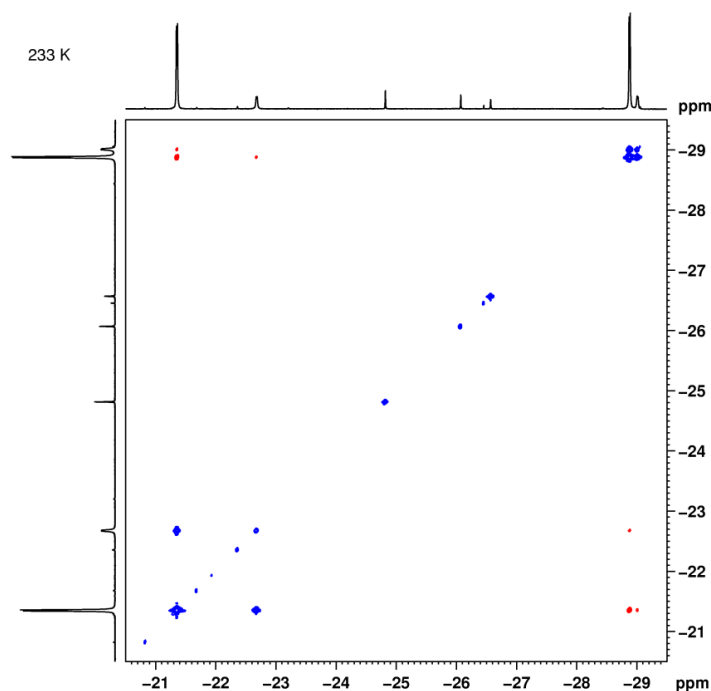
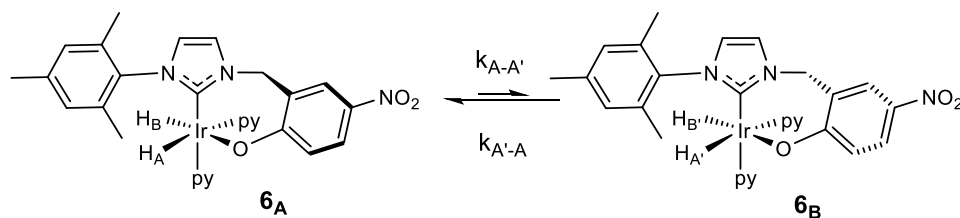


Figure 98: $2D^1H$ NOESY NMR spectrum at 233 K showing both nOe interactions (red) and exchange (blue) between the hydride resonances of the two conformational isomers of **6**

Analysis of data collected in a series of 1H EXSY NMR experiments at 233 K enabled calculation of the interconversion rates between H_A (major isomer, **6A**) and $H_{A'}$ (minor isomer, **6B**), using the kinetic model detailed in Figure 99. The exchange rates between H_B and $H_{B'}$ could not be calculated due to their small difference in chemical shift.



$$[6A]_t = [6A]_0 - k_{A-A'}[6A]t + k_{A'-A}[6B]t$$

$$[6B]_t = [6B]_0 + k_{A-A'}[6A]t - k_{A'-A}[6B]t$$

Figure 99: Kinetic model for the conversion between the major isomer **6A** and the minor isomer **6B** assuming a simple intramolecular interconversion

These ^1H EXSY NMR experiments involve selectively irradiating H_A and then H_A' . The percentage proportion of each isomer is then calculated after ten different mixing times, from 0.005 s to 0.350 s (see Table 14). When selectively irradiating the hydride signal at $\delta -21.35$, the exchange rate for conversion of H_A into H_A' was calculated to be $4.00 \pm 0.08 \text{ s}^{-1}$ and an estimate of the back reaction was given as $\sim 20 \text{ s}^{-1}$. When selectively irradiating the hydride signal at $\delta -22.68$ the exchange rate for conversion of H_A' into H_A was calculated to be $19.8 \pm 0.3 \text{ s}^{-1}$ and an estimate of the back reaction was given as $\sim 5 \text{ s}^{-1}$. These exchange rate values are very similar and show that the major isomer converts slowly to the minor isomer and therefore this process is unfavourable, but once it has converted, it rapidly converts back. This can be rationalised in terms of unfavourable steric clashes between the NO_2 -substituted aromatic ring of the carbene and the pyridine ligand that is bound *trans* to a hydride ligand in complex **6B**. In complex **6A** this is minimised as the NO_2 -containing ring now points towards the much smaller hydride ligand on the complex.

Table 14: ^1H EXSY NMR data for the percentage signals present for either **6A** or **6B** after selectively exciting the indicated hydride signal at 233 K

Selective irradiation	$\delta -21.35$		$\delta -22.68$	
	$[\text{H}_\text{A}] / \%$	$[\text{H}_\text{A}'] / \%$	$[\text{H}_\text{A}] / \%$	$[\text{H}_\text{A}'] / \%$
0.005	97.91	2.09	90.37	9.63
0.010	96.19	3.81	82.90	17.10
0.050	88.42	11.58	43.77	56.23
0.070	86.38	13.62	33.73	66.27
0.100	85.01	14.99	26.70	73.30
0.150	83.97	16.03	22.60	77.40
0.200	83.76	16.24	21.21	78.79
0.250	83.54	16.46	20.76	79.23
0.300	83.57	16.43	20.42	79.58
0.350	83.59	16.41	20.75	79.25

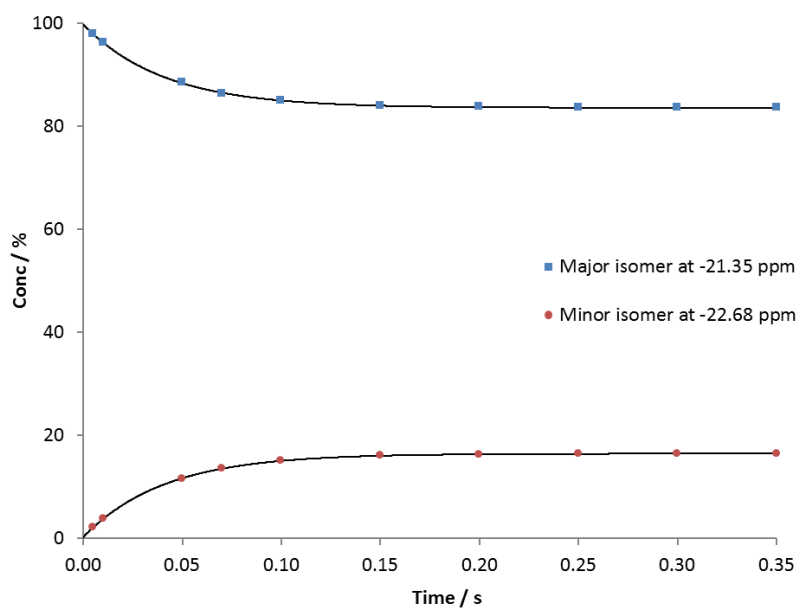


Figure 100: Plot showing the conversion of $\mathbf{6}_A$ into $\mathbf{6}_B$ upon the selective excitation of H_A

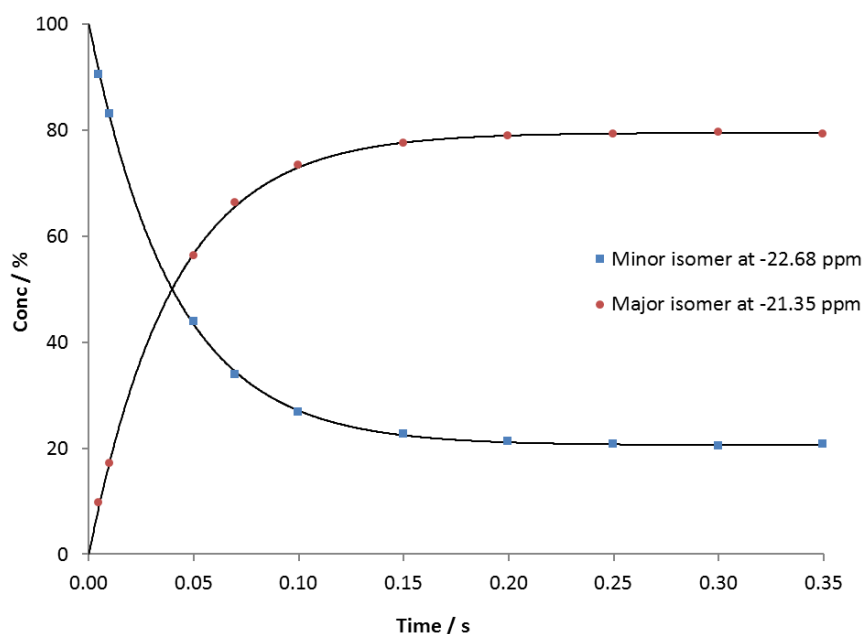


Figure 101: Plot showing the conversion of $\mathbf{6}_B$ into $\mathbf{6}_A$ upon the selective excitation of $H_{A'}$

The two complexes $\mathbf{6}_A$ and $\mathbf{6}_B$ interconvert by a ring-flip process and the difference between them is only observed at low temperature when the rate of ring-flip is decreased. However, isomer exchange can also occur without the ring-flip occurring, after the exchange of a pyridine ligand and is observed at higher temperatures, as hypothesised in Section 3.2.3. A summary of the possible complexes present in solutions of these dihydride complexes is given in Figure 102. The relative orientations

of the CH₂ linker protons are indicated and they point either towards or away from the oxygen depending on the orientation of the seven-membered metallocycle.

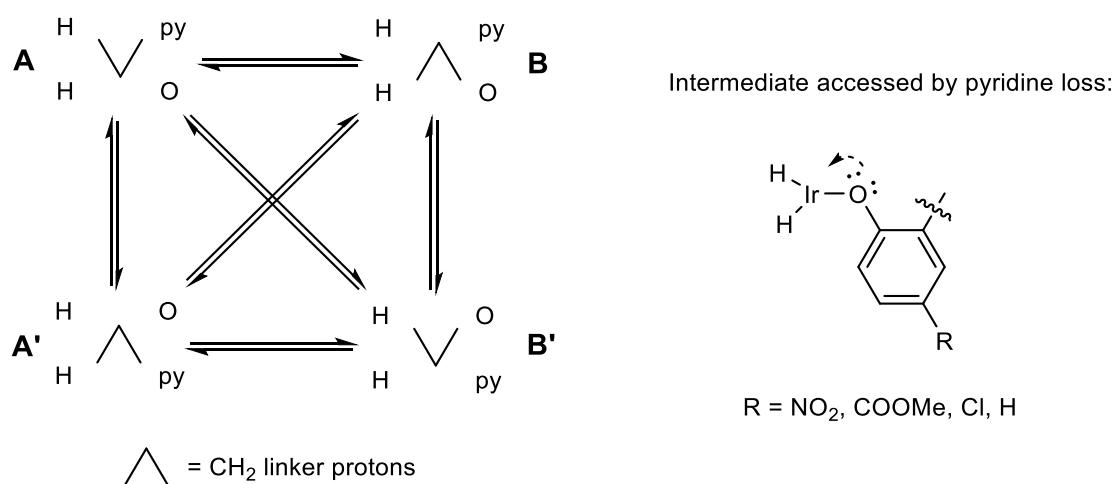


Figure 102: Summary of possible isomer forms present for the bidentate iridium carbene dihydride complexes in solution and the intermediate that occurs on pyridine dissociation

For these complexes when the substrate is pyridine, **A** and **A'** are equivalent and **B** and **B'** are equivalent, as pyridine is not chiral. For conversion between **A** and **A'** or **B** and **B'**, pyridine loss is followed by ring-flip and subsequent rebinding of pyridine on the opposite side of the phenolate arm. This process leads to hydride interconversion between H_A and H_B on the same complex, with the ¹H NMR chemical shifts for these hydride ligands being at approximately δ -22 and -28 respectively. The equilibrium between **A** and **B** or **A'** and **B'** is due to ring-flip being the only process in operation and this leads to interconversion between the pyridine and hydride ligands on different complexes as described for **6A** and **6B** at low temperature. The final mechanism for conversion between **A** and **B'** or **A'** and **B** results from pyridine loss and subsequent rebinding of pyridine on the opposite side of the phenolate arm, but without the ring-flip process occurring. It is predicted that **A** and **A'** are the most stable isomers as in this orientation, the metallocycle forces the aromatic ring containing the substituent to point away from the pyridine ligand. In both **B** and **B'**, the orientation means that the aromatic ring is always pointing towards the pyridine ligand. These mechanistic steps and exchange processes will be further considered when the other complexes, **2**, **3**, and **4** are analysed.

3.2.2. Ligand exchange rate analysis for **6**

At 298 K, the 2D ^1H NOESY NMR spectrum shown in Figure 103 shows that the two hydride signals for complex **6** undergo reversible exchange as well as exchange with H_2 in solution. The pyridine ligand in the *trans* position to a hydride ligand also undergoes exchange at 298 K, with free pyridine in solution. Now the minor isomer exchange is very rapid so the signals for **6A** and **6B** are averaged to those of **6**.

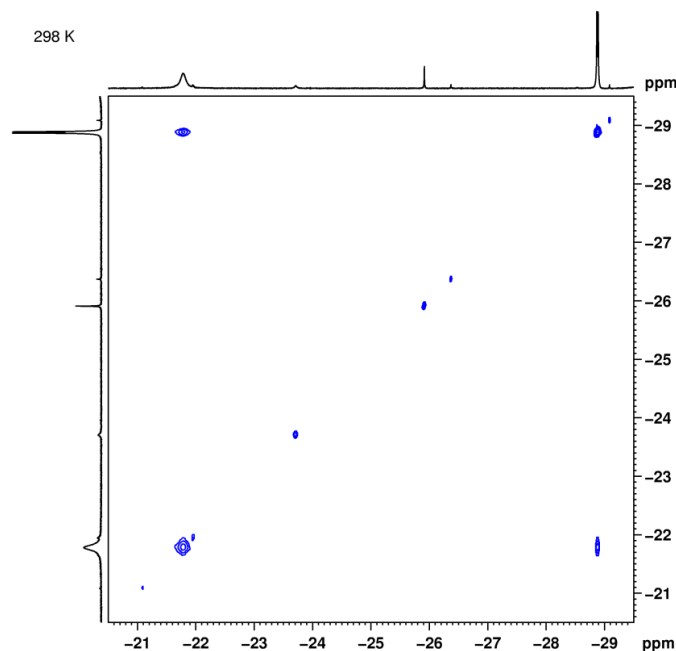


Figure 103: 2D ^1H NOESY NMR spectrum at 298 K showing hydride ligand exchange in **6**

These exchange processes are essential for efficient SABRE and hydrogenation catalysis as fresh hydrogen and substrate ligands must bind to the metal centre. Pyridine substrates must undergo exchange with free pyridine in order for polarisation to transfer and be observed in the free substrates, and to refresh the polarisation source the hydride ligands have to exchange with free *para*hydrogen in solution. The exchange rates for these processes were calculated at 298 K in CD_2Cl_2 using ^1H EXSY NMR experiments as previously described in Section 3.2.1. It is important to optimise the ligand exchange rates so the catalysis can be optimised as is typically the case for catalytic reactions. For this system, using **6**, the exchange between free pyridine and both pyridine sites were first calculated. For a sample containing 4 mol% **1** and 0.65 M pyridine, only the pyridine *trans* to the hydride exchanged with free pyridine on the NMR timescale with an experimental rate constant of $0.28 \pm 0.03 \text{ s}^{-1}$ and the pyridine *cis* to the hydrides did

not exchange. This was consistent with the fact that in the ^1H NMR spectrum, the signals for py_2 are better resolved than the signals for py_1 as also mentioned in Section 2.4.1. In the same sample at 298 K, the hydride signal at $\delta -28.88$ was selectively excited as the signal at $\delta -21.8$ was too broad to accurately monitor. The hydride dissociation rate to form H_2 was $0.067 \pm 0.002 \text{ s}^{-1}$, with the rate of hydride interconversion shown to be $0.79 \pm 0.02 \text{ s}^{-1}$.

Previous studies examine these exchange processes in methanol, as it is the most effective solvent to use with charged complexes such as $[\text{Ir}(\text{H})_2(\text{IMes})(\text{py})_3]\text{Cl}$. However, when CD_3OD was used, hydrogen-deuterium exchange between complex $\mathbf{6}_{\text{HH}}$ and deuterium from the deuterated solvent occurred. This affects the hydrogenation potential of the system as deuterium atoms are introduced into a species rather than hydrogen atoms. Thus, the product identity is modified. At 243 K, in CD_3OD the two hydride ligands of $\mathbf{6}_{\text{HH}}$ are visible as no H-D exchange on the NMR timescale occurs at this temperature. On warming to 270 K, the hydride signal at $\delta -29.22$ exchanges with deuterium to form complex $\mathbf{6}_{\text{HD}}$, containing one deuteride and one hydride ligand. The proportions of H-H complex vs H-D complex were obtained by integration and the concentrations as a function of time are shown in Figure 104. The rate of incorporation of deuterium into $\mathbf{6}_{\text{HH}}$, was calculated to be $(4.24 \pm 0.06) \times 10^{-5} \text{ s}^{-1}$ and is thus very slow. On warming to 298 K the rate of deuterium incorporation increases to $(8.19 \pm 0.08) \times 10^{-4} \text{ s}^{-1}$ which is approximately 20 times faster than the same process at 270 K.

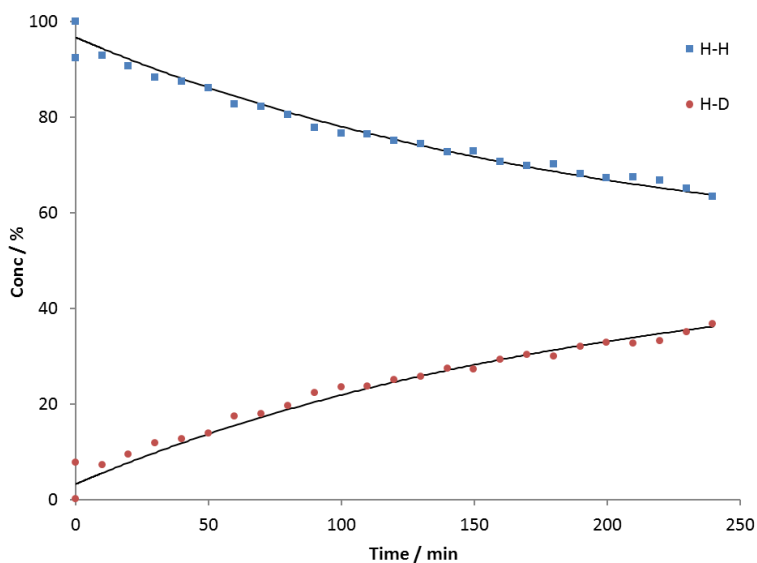


Figure 104: The proportions of $\mathbf{6}_{\text{HH}}$ and $\mathbf{6}_{\text{HD}}$ determined by integration, on analysing the deuterium incorporation into the hydride signal of $\mathbf{6}_{\text{HH}}$ at $\delta -29.22$ at 270 K in CD_3OD

It should be noted that an amount of complex **6** will also be present as the D-D complex, **6DD**, which is not apparent in the hydride region of the ^1H NMR spectra. However, as deuterium incorporation into **6** to form the H-D species is slow it is anticipated that the second incorporation of a deuterium atom to form the D-D species would also be very slow and not visible on the timescale studied here. It would be possible to analyse the relative amounts of the complexes, **6HH**, **6HD** and **6DD** by studying the pyridine region of the ^1H NMR spectra of these reactions. However, due to the small amounts of the different species, their continual exchange and overlapping signals, this was beyond the scope of this study.

When CD_3OD was replaced with CD_3OH , a more accurate analysis of the hydride-hydrogen exchange process was possible, due to inhibition of the hydride deuteration. For a CD_3OH sample containing 9 mol% **1** and 0.05 M pyridine under H_2 , the rate of pyridine dissociation *trans* to the hydride ligand was $0.79 \pm 0.04 \text{ s}^{-1}$, again consistent with the signals for py_2 in the ^1H NMR spectrum being more resolved than the signals for py_1 . In comparison to the pyridine dissociation rate constant of 11.7 s^{-1} per mole of pyridine when using $[\text{Ir}(\text{COD})(\text{IMes})\text{Cl}]$,⁸⁸ the rate here is considerably slower which explains why $[\text{Ir}(\text{COD})(\text{IMes})\text{Cl}]$ is a better catalyst for SABRE. The rate of hydride interconversion was $2.05 \pm 0.06 \text{ s}^{-1}$ with an H_2 loss rate of $0.33 \pm 0.02 \text{ s}^{-1}$.

Another important factor that affects catalytic activity is the reaction temperature. CD_3OH was a suitable solvent to use for these studies, due to its higher boiling point compared to CD_2Cl_2 . Thus, activation parameters for the pyridine and hydrogen dissociation steps and the hydride interconversion process detailed in Section 3.2.3 were calculated by analysing the ligand exchange rates at increasing temperatures from 278 K to 303 K (see Table 15). Table 15 also details the calculated lifetimes for **6** in CD_3OH at each temperature. The lifetime of the complex is directly related to the rate of pyridine dissociation in solution. Therefore, for the same sample of **6** in CD_3OH , where the pyridine dissociation rate was $0.79 \pm 0.04 \text{ s}^{-1}$, the lifetime of **6** was $1.28 \pm 0.05 \text{ s}$.

$$\text{Lifetime} = \frac{1}{n \times \text{pyridine dissociation rate}} \quad \text{where } n = \text{number of pyridine ligands that can dissociate}$$

Table 15: Exchange rate and lifetime data for pyridine and H₂ dissociation and hydride interconversion at the specified temperatures in a CD₃OH sample containing 6 mol% **1** and 0.08 M pyridine ($H_B \delta -29.2$ and $H_A \delta -21.6$)

T / K	Rate of pyridine dissociation / s⁻¹	Rate of H₂ dissociation from H_B / s⁻¹	Rate of hydride interconversion from H_B to H_A / s⁻¹	Lifetime of active complex / s
278	0.17 ± 0.02	0.09 ± 0.02	0.19 ± 0.02	5.88 ± 0.69
283	0.29 ± 0.11	0.11 ± 0.01	0.52 ± 0.04	3.45 ± 1.31
288	0.53 ± 0.04	0.19 ± 0.03	1.09 ± 0.11	1.89 ± 0.14
293	0.83 ± 0.02	0.36 ± 0.03	1.84 ± 0.16	1.20 ± 0.02
298	1.33 ± 0.23	0.54 ± 0.03	2.86 ± 0.18	0.76 ± 0.13
303	2.52 ± 0.30	0.96 ± 0.06	3.59 ± 4.25	0.40 ± 0.04

Here, the higher temperatures cause faster pyridine exchange and decrease the lifetime of **6**. Activation parameters from Arrhenius and Eyring-Polanyi analyses are summarised in Table 16 with the Eyring-Polanyi plot in Figure 105. The rate for hydride interconversion at 303 K was excluded from the analysis due to its large error. The Eyring-Polanyi plot shows that the pyridine and hydrogen dissociation processes occur with a common gradient for their activation parameters. Therefore, these two processes are linked, with pyridine loss preceding H₂ loss which must occur to create the 16-electron intermediate with a vacant site for fresh *p*-H₂ binding (see Section 3.2.3). However, the gradient for the activation parameters for the hydride interconversion process is slightly different, consistent with this process being affected by not only the pyridine dissociation, but also by another pathway, as indicated by the hydride interconversion rates being faster than the pyridine dissociation rates. Other possible exchange pathways to explain this are described in Section 3.2.3. The values for the activation enthalpy for pyridine and H₂ dissociation are very similar within error, with the hydride interconversion process exhibiting a larger activation barrier. The values for the activation entropy demonstrate large errors and so it is impossible to state whether the process is dissociative or otherwise. For hydride interconversion, the

slightly lower Gibbs Free Energy value is commensurate with this process having faster exchange rates and being the most favourable process.

Table 16: Activation parameters calculated from the Arrhenius and Eyring-Polanyi plots for pyridine and H₂ dissociation and hydride interconversion for a CD₃OH sample containing 6 mol% **1** and 0.08 M pyridine under H₂

		$E_a / \Delta H^\ddagger /$ kJ mol^{-1}	$\Delta S^\ddagger / \text{J K}^{-1}$ mol^{-1}	R^2	$\Delta G^\ddagger (300 \text{ K})$ $/ \text{kJ mol}^{-1}$
Pyridine dissociation	Arrhenius	73.5 ± 3.3	-	0.9966	-
	Eyring-Polanyi	71.1 ± 3.3	2.4 ± 11.5	0.9964	70.4 ± 0.2
Hydrogen dissociation	Arrhenius	69.9 ± 7.3	-	0.9862	-
	Eyring-Polanyi	67.5 ± 7.3	-17.3 ± 24.7	0.9853	72.7 ± 0.2
Hydride inter-conversion	Arrhenius	91.7 ± 14.4	-	0.9787	-
	Eyring-Polanyi	89.3 ± 14.4	70.5 ± 50	0.9775	68.2 ± 0.6

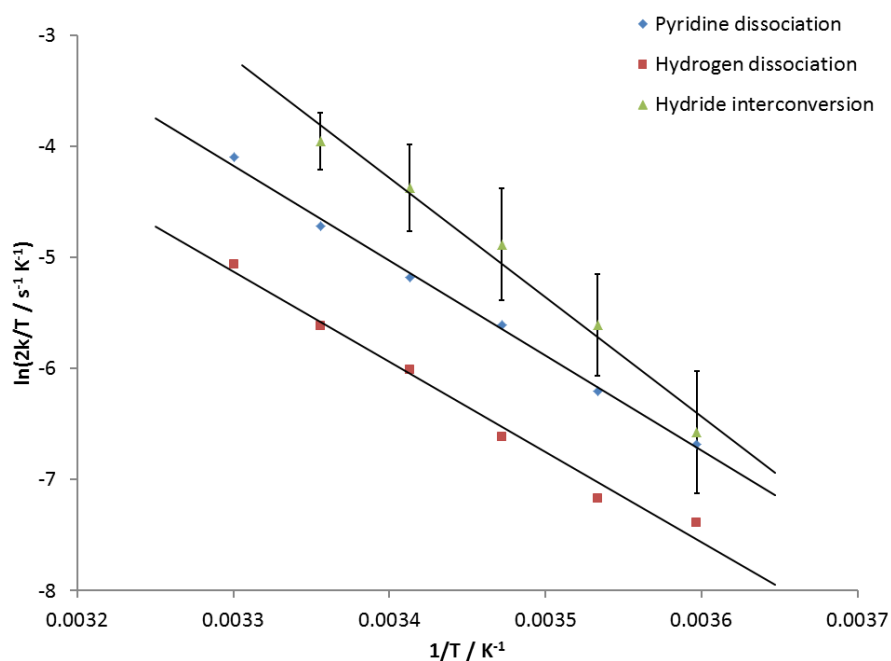


Figure 105: An Eyring-Polanyi plot for pyridine and H₂ dissociation and hydride interconversion as a function of temperature, for a CD₃OH sample of 6 mol% **1** and 0.08 M pyridine under H₂

3.2.3. Mechanistic studies to determine the effect of pyridine concentration on ligand exchange in **6**

To understand the full reaction mechanism that leads to the SABRE effect, studies on the pyridine and hydride exchange processes occurring in **6** were conducted in both CD₂Cl₂ and CD₃OH. These ligand exchange rates, calculated at different pyridine concentrations in CD₂Cl₂ and CD₃OH are shown in Table 17 and depicted graphically in Figure 106 and Figure 107.

Table 17: Rates of pyridine and hydride ligand dissociation from **6** in CD₂Cl₂ at 298 K and in CD₃OH at 294 K as a function of increasing equivalents of pyridine

CD ₂ Cl ₂ : py equivalents by integration	Rate of py loss / s ⁻¹	Rate of H ₂ loss / s ⁻¹	Rate of hydride interconversion from δ -28.88 (H _B) to -21.76 (H _A) / s ⁻¹
15	0.28 ± 0.03	0.079 ± 0.001	0.72 ± 0.01
25	0.28 ± 0.03	0.067 ± 0.002	0.79 ± 0.02
30	0.31 ± 0.01	0.053 ± 0.002	0.78 ± 0.02
50	0.28 ± 0.03	0.042 ± 0.002	0.74 ± 0.02
CD ₃ OH: py equivalents by integration	Rate of py loss / s ⁻¹	Rate of H ₂ loss / s ⁻¹	Rate of hydride interconversion from δ -29.22 (H _B) to -21.62 (H _A) / s ⁻¹
6	0.83 ± 0.06	0.850 ± 0.110	2.02 ± 0.11
10	0.79 ± 0.04	0.330 ± 0.016	2.05 ± 0.06
15	0.78 ± 0.02	0.230 ± 0.015	2.07 ± 0.05
20	0.80 ± 0.02	0.162 ± 0.004	2.09 ± 0.08
25	0.76 ± 0.04	0.092 ± 0.002	2.06 ± 0.08
30	0.72 ± 0.01	0.072 ± 0.004	2.07 ± 0.08

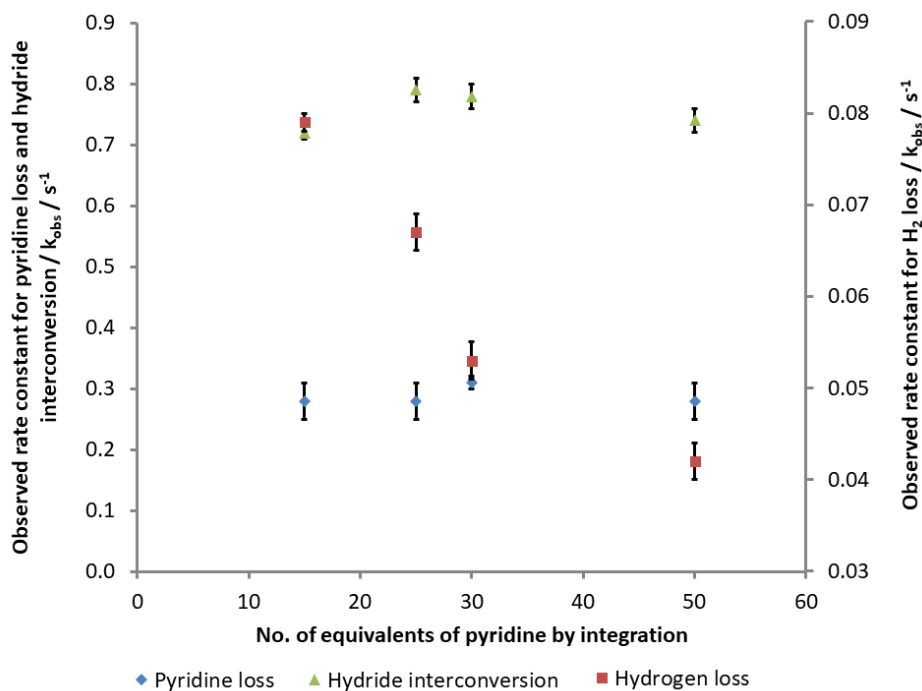


Figure 106: The rates of pyridine and hydride loss from **6** in CD_2Cl_2 in relation to the number of equivalents of pyridine added, calculated by integration. The data for pyridine loss and hydride interconversion are on the left scale and the data for H_2 loss are on the right scale

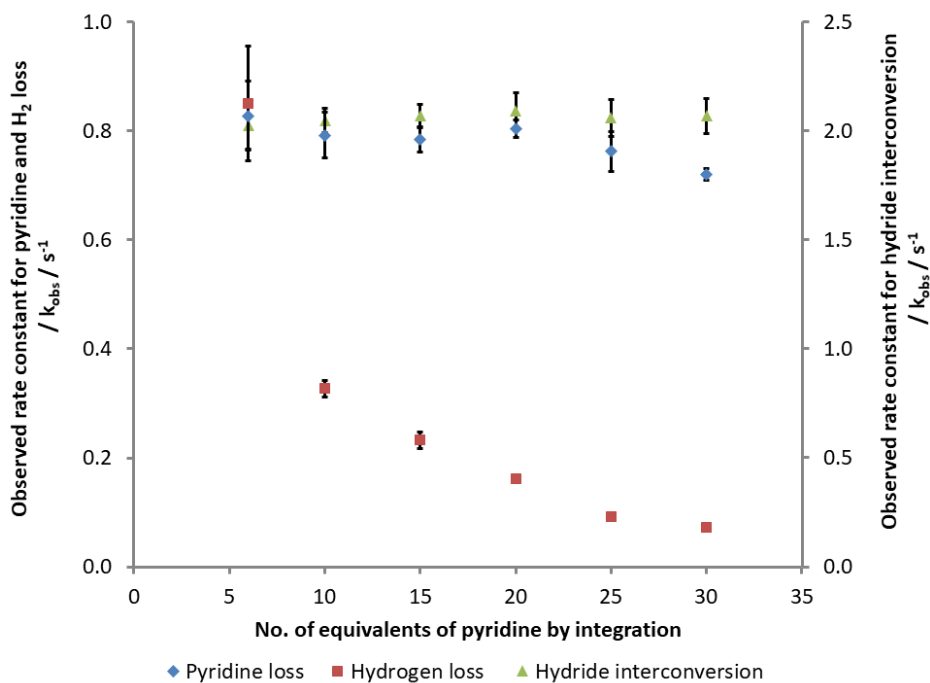


Figure 107: The rates of pyridine and hydride loss from **6** in CD_3OH in relation to the number of equivalents of pyridine added, calculated by integration. The data for pyridine and H_2 loss are on the left scale and the data for hydride interconversion are on the right scale

For a successful catalytic system, it is imperative to know how changing concentrations affects the cycle as this can change its efficiency. In both CD_2Cl_2 and CD_3OH the rate of pyridine dissociation was found to be independent of pyridine concentration. However, the addition of pyridine inhibits hydrogen loss, as the rates of hydrogen loss decreased upon addition of pyridine. The decrease in hydride dissociation rate relates to complex **6** being more likely to rebind a pyridine ligand than lose hydrogen when there is a larger excess of pyridine in solution. Therefore, for most efficient hydrogen reactivity, low concentrations of substrate should be used.

The negative effect of pyridine concentration on H_2 loss rate means that the process of pyridine dissociation precedes H_2 loss and is therefore consistent with previous studies where the loss of a substrate produces a 16-electron intermediate where the hydride ligands are equivalent.^{88, 94} Several stable 16-electron iridium(III) dihydride species have been described in the literature, which are stabilised by phosphine-derived pincer ligands, such as PCP and PNP. Four examples are depicted in Figure 108, described by Rimoldi et al.,¹⁸⁴ Gottker-Schnetmann et al.¹⁸⁵⁻¹⁸⁶ and Choualeb et al.¹⁸⁷

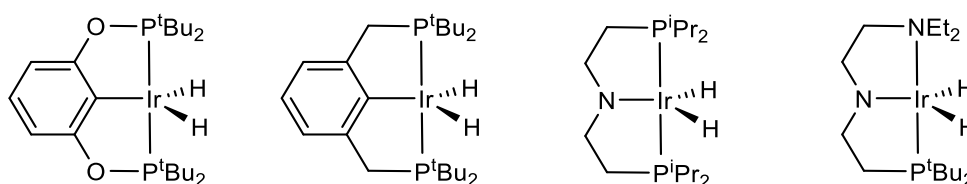


Figure 108: Four examples of stable 16-electron iridium dihydride species containing pincer ligands¹⁸⁴⁻¹⁸⁷

The binding of hydrogen to the 16-electron species formed on loss of substrate, leads to the formation of an important dihydride-dihydrogen intermediate as predicted by DFT for the complex $[\text{Ir}(\text{H})_2(\text{H}_2)(\text{IMes})(\text{py})_2]\text{Cl}$.⁸⁸ Other similar “ $\text{Ir}(\text{H})_2(\text{H}_2)$ ” species have been described by Mediati et al. containing phosphine ligands, as shown in Figure 109, which undergo facile exchange due to the low energy barrier of interconversion.¹⁸⁸⁻¹⁹² There are also a number of analogous pincer complexes where hydrogen addition to the dihydride complex leads to formation of the “ $\text{Ir}(\text{H})_2(\text{H}_2)$ ” complexes. Some examples are shown in Figure 109. Studies of the $[(\text{PCP})\text{IrH}_4]$ and $[(\text{POCOP})\text{IrH}_4]$ complexes, by Hebden et al.,¹⁹³ indicate that in solution phase NMR spectra, they are present as dihydride-dihydrogen complexes whereas solid state methods show tetrahydride species. This is consistent with low energy barriers to interconversion.

Computational studies of the cyclohexyl-based pincer complex in Figure 109 also show a low energy difference of only 0.59 kJ mol^{-1} between the lower-lying tetrahydride species and the dihydride-dihydrogen complex.¹⁹⁴ Hauger et al.¹⁹⁵ have also described the rapid exchange process that occurs on addition of H_2 to $[\text{Ir}(\text{H})_2\text{Br}(\text{P}^t\text{Bu}_2\text{Ph})_2]$ such that the fluxionality of the addition product, $[\text{Ir}(\text{H})_2\text{Br}(\text{H}_2)(\text{P}^t\text{Bu}_2\text{R})_2]$, means it is unobservable.

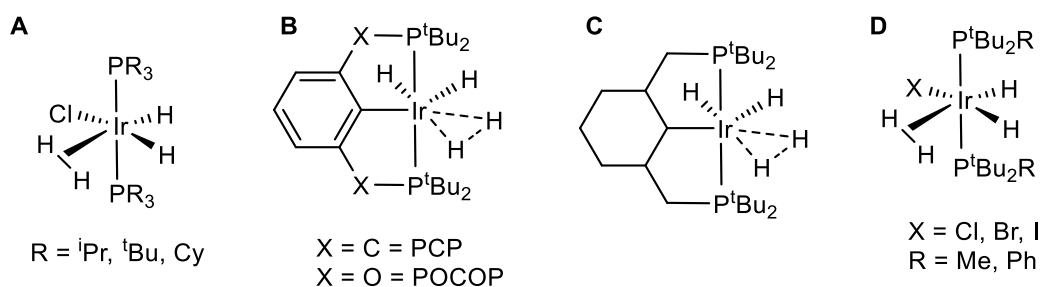


Figure 109: Iridium dihydride-dihydrogen complexes which undergo facile hydride-hydrogen interconversion^{189, 193-195}

When the 18-electron dihydride-dihydrogen intermediate loses H_2 , pyridine can rebind; if pyridine does bind, then there is an equal chance of the hydride ligands either swapping or retaining their positions, depending on which side of the bidentate carbene the pyridine ligand enters from. This hydride interconversion process is labelled ‘Hydride interconversion route A’ in Figure 114. The rate of hydride site interconversion is dependent on the rate of pyridine loss and rebinding to the complex. If the rate of pyridine loss is subtracted from the hydride site interconversion rate, then the rate that remains corresponds to a different process that also enables hydride site interconversion to occur, without pyridine loss. Several competing pathways could be envisaged;

1. Pseudorotation mechanisms such as Berry pseudorotation and turnstile rotation¹⁹⁶⁻¹⁹⁷ are common for penta-coordinated metal centres but due to the greater stereochemical rigidity of octahedral complexes these typically do not occur. When one of these rotation mechanisms does occur, it results in changing the two ‘axial’ ligands with two of the ‘equatorial’ ligands so that the ligands which were originally in a *trans* position to each other end up in a *cis* configuration as shown in Figure 110 for PF_5 .¹⁹⁸ This is prevented from occurring in complex **6** due to the rigid binding of the chelating ligand.

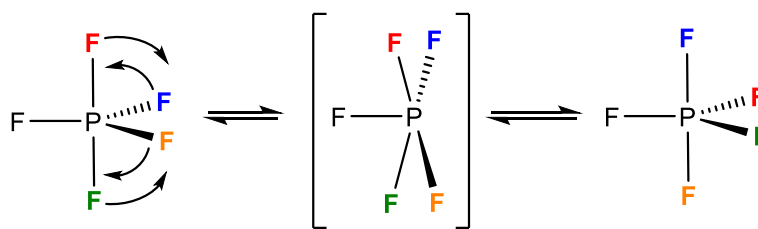


Figure 110: Demonstrating the Berry pseudorotation mechanism occurring in trigonal bipyramidal PF_5 , which exchanges the axial F ligands with two of the equatorial F ligands via a square-based pyramidal intermediate¹⁹⁸

2. Trigonal twist mechanisms such as the Bailar twist¹⁹⁹ or Ray-Dutt twist²⁰⁰⁻²⁰² are possible although these typically occur for complexes containing three bidentate ligands. The binding atoms of the sets of bidentate ligands exchange places, thus interconverting two chiral isomers. This is shown in Figure 111 for tris-chelated aluminium complexes containing α -isopropenyltropolonate or α -isopropyltropolonate ligands described by Amati et al.,²⁰³ where their computational study has shown that both the Bailar and Ray-Dutt twist mechanisms are possible. In complex **6**, these trigonal twist mechanisms would also lead to conversion of the other sites within **6** and since it has been shown in Section 3.2.2 that the pyridine ligand *trans* to the carbene ligand does not undergo any exchange, these processes are not feasible.

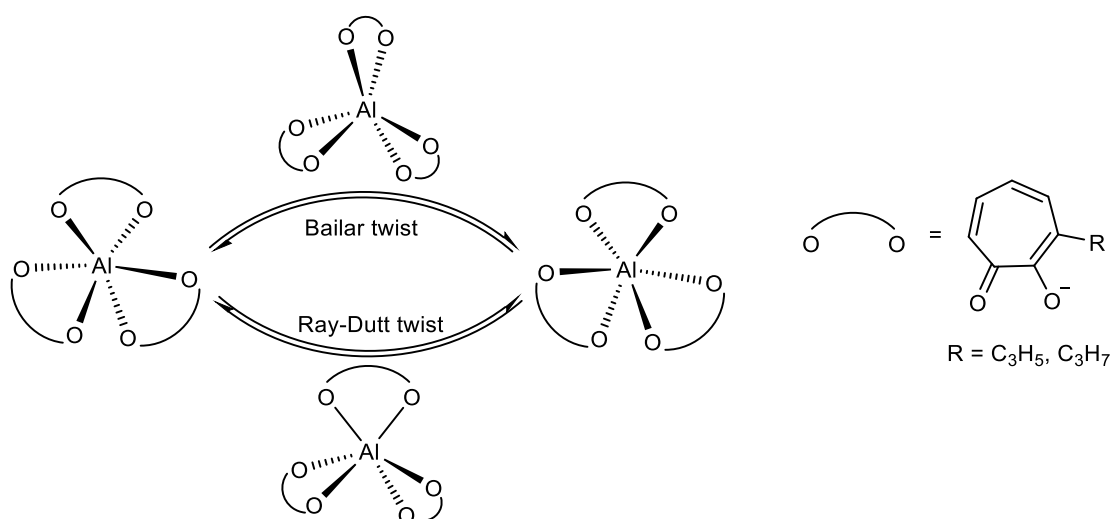


Figure 111: Bailar and Ray-Dutt twist mechanisms for interconversion of tris-chelated aluminium complexes containing α -isopropenyltropolonate or α -isopropyltropolonate ligands

3. Elimination and rebinding of one hydride ligand via the dihydrogen bonded system, IrH---HO, could occur due to the presence of the Ir-O group. However, in protio solvents such as methanol, very rapid H/D exchange happens and thus if this elimination mechanism occurred it is predicted to be unobservable. A number of transition metal complexes exist where a hydride ligand acts as a proton acceptor and hydrogen bonds to a proton donor. Commonly these are NH or OH bonds, where short distances of approximately 2 Å between the hydride ligand and NH/OH functionality²⁰⁴⁻²⁰⁵ indicate hydrogen bonding and they can be either inter or intramolecular. Some complexes exhibiting intramolecular hydrogen bonding are shown in Figure 112. These complexes typically demonstrate reversible exchange between the dihydrogen form of the complex and can undergo elimination of H₂ as also shown in Figure 112.

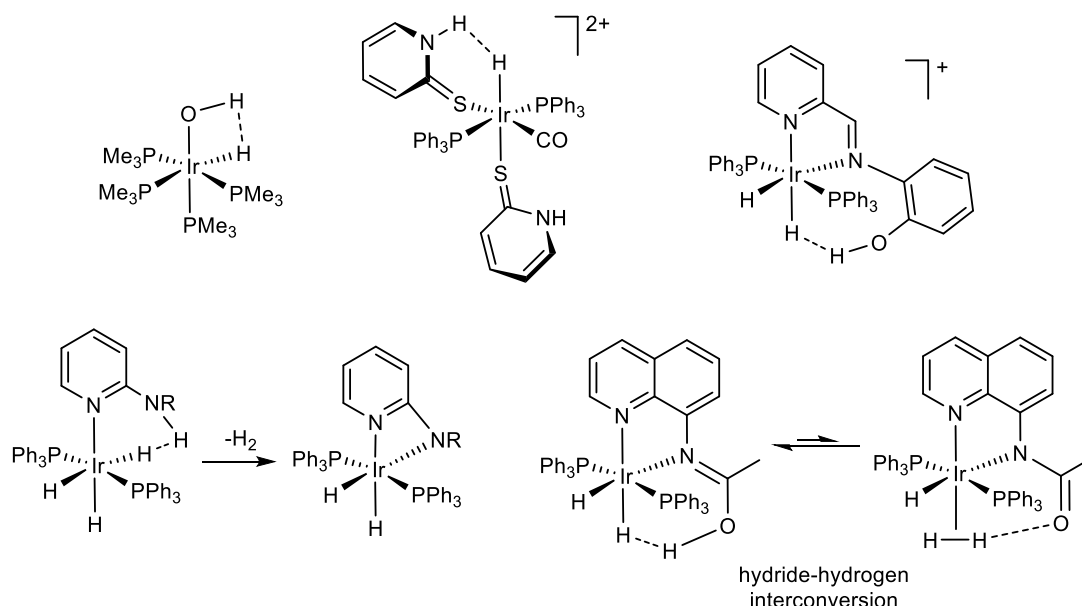


Figure 112: Iridium complexes containing dihydrogen bonded functionalities²⁰⁵⁻²⁰⁷ and the reactivities of two specific examples showing H₂ loss²⁰⁸ and hydride-hydrogen interconversion²⁰⁹⁻²¹⁰

As these processes have been ruled out because of the reasons described, the extra hydride site interconversion process can be considered as intramolecular, proceeding via the formation of a dihydrogen complex and subsequent rotation of the dihydrogen ligand. It is known that complex **6** can activate dihydrogen to form a dihydride complex, due to the electron rich nature of the dihydrogen molecule in comparison to the electron poor iridium metal centre. Therefore, it is feasible that a

similar dihydride-dihydrogen exchange process could occur to form a dihydrogen complex from **6** as shown for ‘Hydride interconversion route B’ in Figure 114. Furthermore, as **6** is an efficient SABRE catalyst, which will be discussed in the next chapter, the lifetime of the dihydrogen species must be very short so as not to destroy the *p*-H₂. This interconversion route must be rapid to allow the hydride interconversion rates to be faster than the pyridine dissociation rates.

Some examples of dihydride-dihydrogen interconversion have been described for iridium complexes containing pincer ligands. Gottker-Schnetmann et al.²¹¹ have described the equilibrium between an iridium dihydride complex and an iridium dihydrogen complex, as shown in Figure 113, where the equilibrium depends on the polarity of the solvent. The dihydride species is favoured in CD₂Cl₂ whereas the dihydrogen complex is favoured in toluene.²¹¹

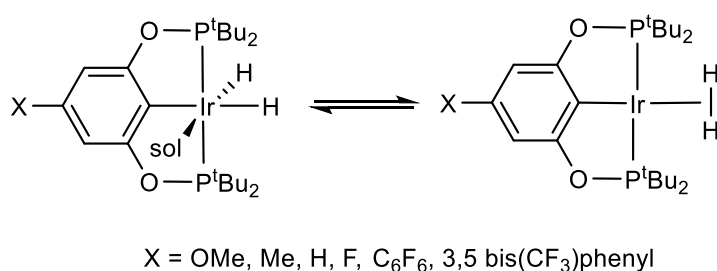


Figure 113: Equilibrium between the iridium dihydride complex and the iridium dihydrogen complex described by Gottker-Schnetmann et al.²¹¹

In the exchange pathway of **6**, the dihydrogen-containing transition state is likely to be low-lying in energy, due to it being unstable because the iridium is bonded to very electronegative groups, and thus its simple rotation is easily achieved. In 2004, DFT studies by Gelabert et al.²¹² of [Cp*Ir(dmpm)(H₂)]₂[B(C₆F₅)₄]₂, where dmpm is bis-dimethyldiphosphinomethane, predicted that the dihydrogen complex was only 5.9 kJ mol⁻¹ higher in energy than the dihydride species, with the transition state between the dihydride species and the dihydrogen species lying only 1.3 kJ mol⁻¹ higher in energy than the dihydrogen species. Another computational study by Hebden et al.¹⁹³ analysed the energy differences between dihydride and dihydrogen forms of the iridium pincer complexes, **B** in Figure 109. Again, the energy differences between the species are less than 13 kJ mol⁻¹, with *cis*-[(POCOP)Ir(H₂)(H)₂] being 2.0 kJ mol⁻¹ lower in energy than

[(POCOP)Ir(H)₄] in cyclohexane solution. For the PCP complex, the opposite is true, with [(PCP)Ir(H)₄] being favoured over the dihydride-dihydrogen complex.

Other studies also show that the energy difference between a metal-H₂ complex and a metal-dihydride complex is small.²¹³ Li et al.²¹³ have shown that for a number of Fe and Ru complexes, the dihydrogen complexes are most stable, whereas for Os, the dihydride species is the most stable. In relation to the bond distances between two H atoms, in either a dihydride species or a dihydrogen species, Morris²¹⁴ has described many complexes where the H-H bond lengths increase as the ligands change from dihydrogen to dihydride species. Furthermore, when electronegative atoms such as Cl or O, which are σ -donor and π -donor ligands, are in a *trans* position to the dihydrogen ligand, the H-H bond is elongated in comparison to when the *trans* ligand is H, C, P or N which are only σ -donor ligands.²¹⁴ Thus, complexes containing electronegative ligands that can be involved in σ - and π -donation are more likely to exist as dihydride species.

Overall, the exchange mechanism for **6** is more complicated than the mechanism that has previously been described for [Ir(COD)(IMes)Cl]. The full pathway for **6** is depicted in Figure 114, showing pyridine loss, hydride interchange and the important dihydride-dihydrogen intermediate. Based on this mechanism, analysis of the experimental pyridine dissociation rates involves direct observation of this rate determining step because it is the first step in the process and is the direct loss of pyridine from the active complex. When looking at the hydride dissociation rate, however, the experimental rate is no longer the first step in the cycle as depicted in the mechanism shown in Figure 114. Instead, the experimentally determined rate constants, k_{obs} , contain information about both the pyridine loss rate, the dihydrogen binding rate and then the dihydride dissociation rate.

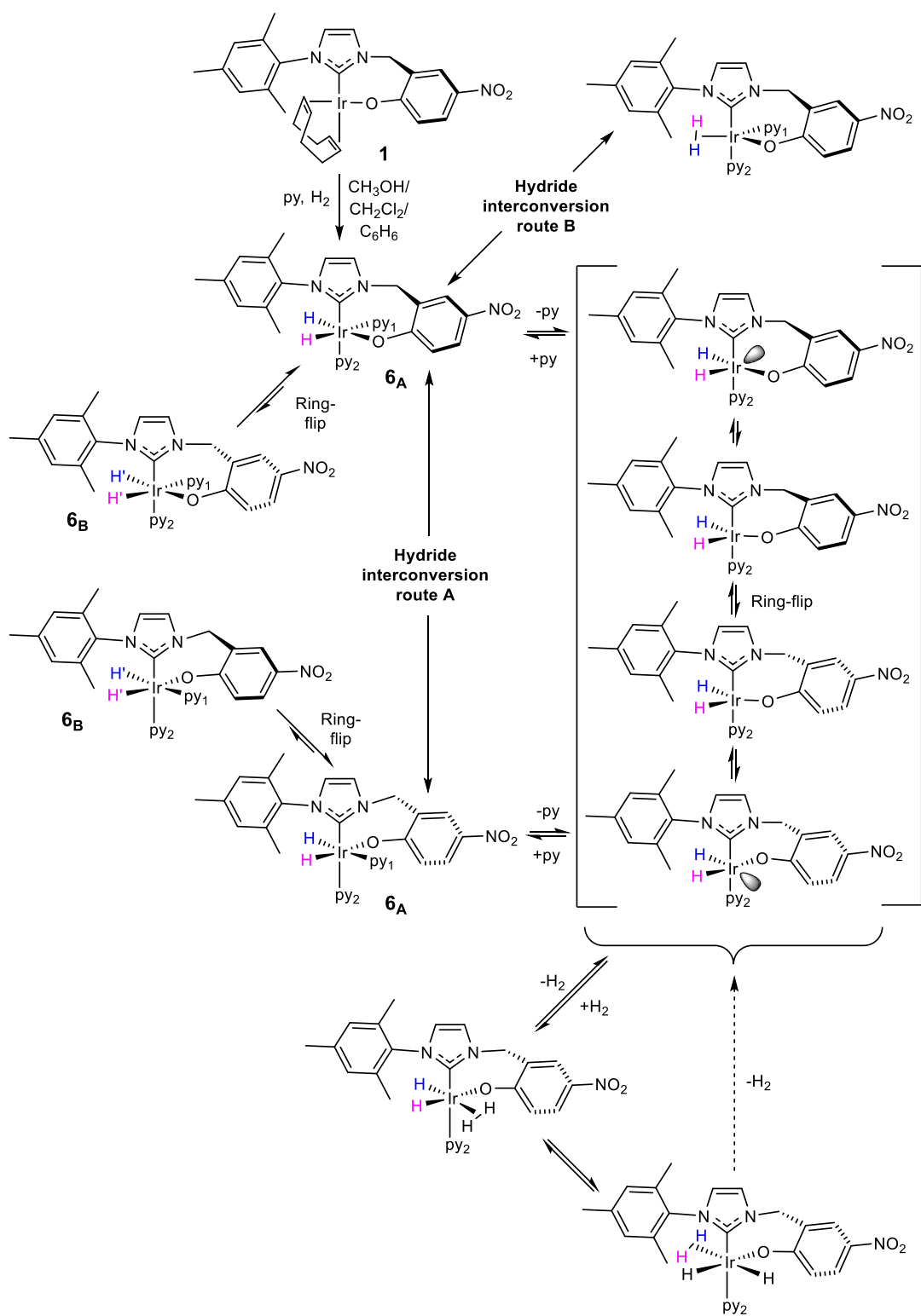


Figure 114: Formation of **6** from **1** with the vacant site represented through the shaded orbital and the blue and magenta hydride ligand labels detailing the hydride interchange processes. Contributing to the rate of hydride interconversion, $k_{\text{hydride interconversion}}$, is both route A (including the rate of pyridine loss, $k_{\text{py loss}}$, and the rate of formation of the dihydrogen complex, $k_{\eta^2-\text{H}_2 \text{ formation}}$) and route B (intramolecular switching)

3.2.4. Analysis of the effect of solvent on exchange

In Section 3.2.2, ligand exchange rates for **6** in CD₂Cl₂ and CD₃OD were shown to be considerably different and an investigation into the range of solvents that enable ligand exchange was therefore conducted. Pyridine and hydride dissociation rates may differ between solvents because of their varying polarities and therefore solvation capabilities. Selective ¹H EXSY NMR experiments were used, as previously described in Section 3.2.1, and the different rates for pyridine dissociation, hydrogen dissociation and hydride interconversion are shown in Table 18, along with the calculated lifetimes of the corresponding complexes. The rates of hydride interconversion in the ethanol and methanol solvents are shown to be faster than pyridine dissociation, consistent with the previous discussion in Section 3.2.3. Here, the ligand exchange rates will also be affected by the H₂ solubility differences between the five solvents which will affect the overall concentration of H₂ in solution. The experimental values in ethanol and methanol are also more inaccurate than the previous studies due to analysis of the simultaneous H-D exchange which also occurs within the polar protic solvents, between the deuterium of the alcohol and the H₂ in solution. In all solvents tested, **6** is the major complex in solution. Here, the least polar solvents promote faster exchange presumably due to their inability to bind to and solvate the 16-electron intermediate shown in brackets in Figure 114.

Table 18: Pyridine and hydrogen dissociation rates and the rates of hydride interconversion for samples of 15 mol% **1** and 0.05 M pyridine in the specified solvents at 298 K under 3 bars of H₂

Solvent	Rate of pyridine dissociation / s ⁻¹	Rate of hydrogen dissociation from H _B / s ⁻¹	Rate of hydride interconversion from H _B to H _A / s ⁻¹	Lifetime of active complex / s
C ₆ D ₆	7.39 ± 0.05	1.03 ± 0.01	4.23 ± 0.05	0.135 ± 0.001
THF- <i>d</i> ₈	5.97 ± 0.17	0.89 ± 0.01	2.06 ± 0.06	0.167 ± 0.005
CD ₂ Cl ₂	3.46 ± 0.07	0.51 ± 0.02	0.75 ± 0.02	0.289 ± 0.006
Ethanol- <i>d</i> ₆	0.95 ± 0.01	0.77 ± 0.05	1.48 ± 0.03	1.053 ± 0.011
CD ₃ OH	1.51 ± 0.03	0.92 ± 0.02	3.88 ± 0.11	0.662 ± 0.013

3.3. Ligand exchange rates

3.3.1. Ligand exchange rate analysis for **8** and **15**

In CD_2Cl_2 and C_6D_6 , **2** forms **8** as described in Section 2.4.2, which is equivalent to the reactivity of **1**. This is shown in Figure 115.

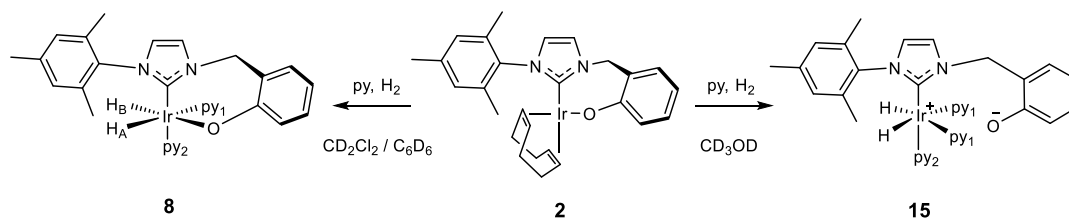


Figure 115: Reaction of **2** with pyridine and hydrogen in CD_2Cl_2 or C_6D_6 to form **8** and in CD_3OD to form **15**

Here, however, in CD_2Cl_2 , the hydride ligands of **8** appear at δ -22.55 and -25.49 in the ^1H NMR spectrum and it is predicted that due to no bulky substituent being present on the phenolate ring, the complex conformation is likely to be the **B** form as indicated in Figure 102. If the minor isomer does form, it will not be observed if very rapid exchange occurs. The ligand exchange rates for **8** are summarised in Table 19, and in both CD_2Cl_2 and C_6D_6 they are faster than those of complex **6** as given in Section 3.2.2. This matches the prediction based on the work of Zhao et al.¹⁸¹ where the higher electron density at the metal centre promotes H_2 loss. In CD_3OD , complex **15** forms as described in Section 2.4.6. Here, the pyridine dissociation rate for **15** was measured, but as rapid deuteration of the hydride ligands occurs, this precluded determination of the hydride dissociation rates. The pyridine dissociation rate is slower in CD_3OD than in both CD_2Cl_2 and C_6D_6 (see Table 19).

Table 19: Pyridine and hydrogen dissociation rates and the rates of hydride interconversion for samples of 15 mol% **2** and 0.05 M pyridine in the specified solvents at 294 K under 3 bars of H_2

Solvent	Rate of pyridine dissociation / s^{-1}		Lifetime of active complex / s	
C_6D_6	13.5 ± 0.6		0.074 ± 0.003	
CD_2Cl_2	3.74 ± 0.06		0.267 ± 0.004	
CD_3OD	1.35 ± 0.03		0.370 ± 0.008	
	Rate of hydrogen dissociation / s^{-1}		Rate of hydride interconversion / s^{-1}	
	From H_A	From H_B	From H_A to H_B	From H_B to H_A
C_6D_6	3.01 ± 0.11	2.98 ± 0.06	5.52 ± 0.12	5.61 ± 0.20
CD_2Cl_2	0.78 ± 0.01	0.79 ± 0.01	1.59 ± 0.03	1.57 ± 0.03

Table 20: Exchange rate and lifetime data for pyridine dissociation and hydride dissociation at different temperatures in CD_3OH for a sample containing 8 mol% **2** and 0.07 M pyridine under 3 bars of H_2

T / K	Rate of pyridine dissociation / s^{-1}	Observed rate of hydrogen dissociation / s^{-1}	Lifetime of active complex / s
278	0.13 ± 0.01	0.08 ± 0.01	3.71 ± 0.13
283	0.29 ± 0.01	0.10 ± 0.01	1.70 ± 0.06
288	0.56 ± 0.02	0.26 ± 0.03	0.89 ± 0.04
293	1.13 ± 0.07	0.48 ± 0.02	0.44 ± 0.03
298	2.02 ± 0.08	0.88 ± 0.02	0.25 ± 0.01
303	3.86 ± 0.12	1.71 ± 0.03	0.13 ± 0.01

The activation parameters for the different processes in **15** were calculated using the exchange rates at six different temperatures as shown in Table 20. CD_3OH was used

to eliminate exchange with deuterium which causes formation of the hydride-deuteride complex and HD in solution, as described in Section 3.2.2.

The values for the rates of pyridine dissociation and hydride dissociation of **15** are like those of complex **6** (see Section 3.2.2) so the activation parameters are predicted to be similar. As for the lifetimes of the active complexes, the same effect as described in Section 3.2.2 is seen.⁹³ Furthermore, in **15**, there are two substrate ligands to exchange compared to only one in **6**. However, the errors associated with the exchange rates of **15** are much lower than those of complex **6** as detailed in Section 3.2.2. This may be due to concentration or solubility differences between the samples. Figure 116 shows the Eyring-Polanyi plots used to determine the activation parameters, which are summarised in Table 21. The activation enthalpy and entropy values calculated for both pyridine dissociation and hydride loss are very similar (see Table 21). The entropy values of $71.3 \pm 5.3 \text{ J K}^{-1} \text{ mol}^{-1}$ and $56.1 \pm 30.6 \text{ J K}^{-1} \text{ mol}^{-1}$ for pyridine dissociation and hydride loss respectively are both positive and indicative of a dissociative mechanism.

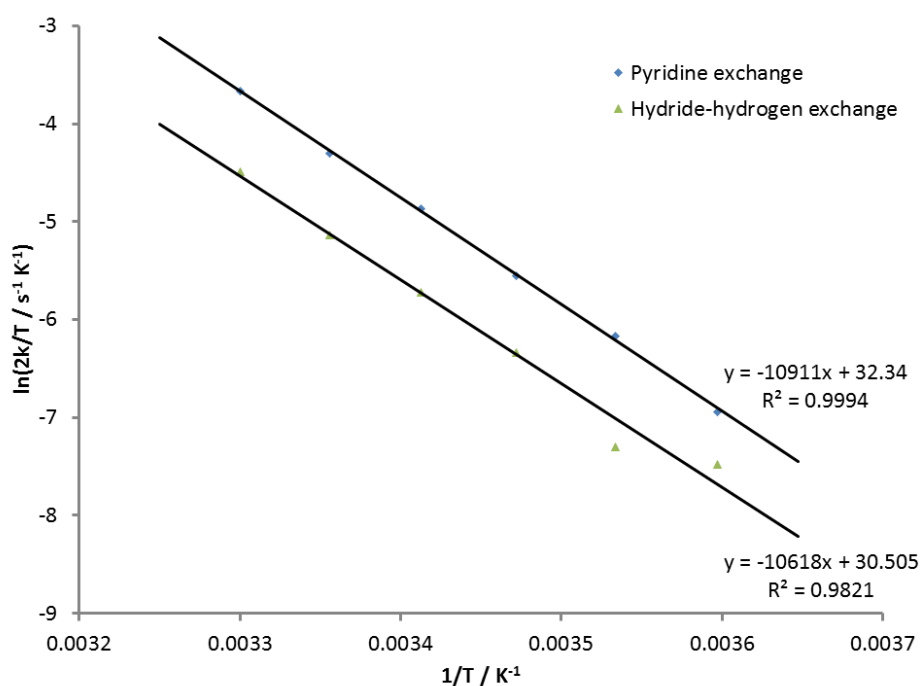


Figure 116: An Eyring-Polanyi plot for pyridine exchange and hydride-hydrogen exchange at differing temperatures in CD_3OH for a sample containing 8 mol% **2** and 0.07 M pyridine

Table 21: Activation parameters calculated from the Arrhenius and Eyring-Polanyi plots for pyridine dissociation and hydride dissociation in CD₃OH for a sample containing 8 mol% **2** and 0.07 M pyridine. The Gibbs Free energy of activation, ΔG^\ddagger , is calculated at 300 K using the Gibbs Free Energy equation ($\Delta G^\ddagger = \Delta H^\ddagger - T\Delta S^\ddagger$) with the calculated ΔH^\ddagger and ΔS^\ddagger values given in the table

	Pyridine dissociation		Hydrogen dissociation	
	Arrhenius	Eyring-Polanyi	Arrhenius	Eyring-Polanyi
E_a / ΔH^\ddagger / kJ mol⁻¹	93.1 ± 1.5	90.7 ± 1.6	90.7 ± 9.1	88.3 ± 9.1
ΔS^\ddagger / J K⁻¹ mol⁻¹	-	71.3 ± 5.3	-	56.1 ± 30.6
R² value	0.9994	0.9994	0.9829	0.9821
ΔG^\ddagger / kJ mol⁻¹	-	69.3 ± 0.1	-	71.5 ± 0.1

3.3.2. Ligand exchange rate analysis for **10_A** and **10_B**

For complex **3**, in CD₂Cl₂, both **10_A** and **10_B** are formed with differing orientations of the metallocycle (see Figure 102). Complex **10_A** is equivalent to complex **6_A**, whilst **10_B** matches complex **8**. In CD₂Cl₂, the exchange rates for pyridine dissociation and hydrogen loss were calculated once all the complex had formed **10_B**, where the hydride signals at δ -22.56 and -25.47 were both sharp, and selective excitation of each hydride in turn was possible. However, in C₆D₆, very broad and overlapping signals for the bound pyridine ligands precluded calculation of reliable exchange rates, although the broad character of the signals is consistent with rapid exchange (faster than in CD₂Cl₂). In CD₃OH complex **10_A** is formed and deuteration effects are eliminated. However, efficient analysis of the hydride signal H_A, at $\sim \delta$ -22 in both CD₃OH and C₆D₆ was not possible as the signals were too broad or overlapped with other minor hydride signals, like that observed in **6**. All the ligand exchange rates are detailed in Table 22.

Table 22: Pyridine dissociation rates, complex lifetimes and hydride exchange rates of **10_A** and **10_B**, for CD₂Cl₂, CD₃OD, CD₃OH and C₆D₆ samples containing 10 mol% **3** and 0.06 M pyridine at 298 K under 3 bars of H₂

Solvent	Pyridine dissociation rate / s ⁻¹		Active complex lifetime / s	
	CD ₂ Cl ₂	2.63 ± 0.21		0.38 ± 0.03
CD ₃ OD	3.00 ± 0.09		0.33 ± 0.01	
	Rate of hydride interconversion / s ⁻¹		Rate of hydrogen dissociation / s ⁻¹	
	H _A to H _B	H _B to H _A	H _A to H ₂	H _B to H ₂
CD ₂ Cl ₂	1.33 ± 0.06	1.39 ± 0.07	1.17 ± 0.03	1.21 ± 0.03
	H _B to H _A		H _B to H ₂	
CD ₃ OH	13.7 ± 0.4		1.20 ± 0.12	
C ₆ D ₆	8.09 ± 0.31		1.45 ± 0.07	

3.3.3. Ligand exchange rate analysis for **12_A**, **12_B** and **16**

For complex **4**, in both CD₂Cl₂ and C₆D₆, the two isomers **12_A** and **12_B** (as shown in Figure 102) are again seen and their corresponding ligand exchange rates are detailed in Table 23.

*Table 23: Exchange rate information for pyridine and hydrogen loss and hydride interconversion for **12_A** and **12_B** present in a CD₂Cl₂ sample containing 9 mol% **4** and 0.08 M pyridine and a C₆D₆ sample containing 7 mol% **4** and 0.1 M pyridine, both under 3 bars of H₂ at 298 K*

Solvent	Rate of py loss from 12_A / s ⁻¹	Rate of py loss from 12_B / s ⁻¹	Rate of py ₂ interconversion from 12_A to 12_B / s ⁻¹	Rate of py ₂ interconversion from 12_B to 12_A / s ⁻¹
C₆D₆	Too broad and overlapped to measure			
CD₂Cl₂	4.15 ± 0.26	Too broad to measure	0.54 ± 0.03	0.80 ± 0.08
	Rate of H₂ loss from 12_A / s⁻¹		Rate of H₂ loss from 12_B / s⁻¹	
	From H _A	From H _B	From H _A '	From H _B '
C₆D₆	5.50 ± 0.39	6.03 ± 0.20	Too broad to measure	
CD₂Cl₂	2.04 ± 0.04	2.04 ± 0.07	Too broad to measure	
	Rate of hydride interconversion for 12_A / s⁻¹		Rate of hydride interconversion for 12_B / s⁻¹	
	From H _A to H _B	From H _B to H _A	From H _A ' to H _B '	From H _B ' to H _A '
C₆D₆	6.63 ± 0.26	6.68 ± 0.18	Too broad to measure	
CD₂Cl₂	1.57 ± 0.05	1.81 ± 0.10	Too broad to measure	

As for complexes **6_A** and **6_B** at low temperature, site-specific exchange was also observed for isomers **12_A** and **12_B** although now at room temperature. In CD₂Cl₂, the

ratio of **12A**: **12B** was 1.4: 1 which equates with the rates of conversion between **12A** and **12B** as calculated from the site-specific exchange between the pyridine ligands in the *trans* position to the carbene which do not undergo dissociative exchange. However, in C_6D_6 the isomers were present in a 1: 1 ratio. Despite attempts to gain information about the kinetics of the complexes formed in C_6D_6 , the 2D NMR spectra were unclear. This is due to multiple overlapping signals for the pyridine environments and all the signals being very broad at 298 K.

In CD_3OD , both **12A** and **16** formed, containing inequivalent and equivalent hydride ligands respectively, as detailed in Section 2.4.8. The rates of conversion from **12A** to **16**, as detailed in the exchange rate data given in Table 24, suggest **16** is the more stable isomer with the ratio being like that of 1: 1.6, obtained from integration.

*Table 24: Exchange rate information for pyridine and hydrogen loss and hydride interconversion for **12A** and **16** present in a CD_3OH sample containing 5 mol% **4** and 0.16 M pyridine under 3 bars of H_2 at 298 K*

	Rate of py loss from 12A / s^{-1}	Rate of py loss from 16 / s^{-1}	Rate of py ₂ interconversion from 12A to 16 / s^{-1}		Rate of py ₂ interconversion from 16 to 12A / s^{-1}
CD₃OH	7.27 ± 0.50	1.78 ± 0.07	1.74 ± 0.04		0.98 ± 0.03
	Rate of H ₂ loss from 12A / s^{-1}		Rate of hydride interconversion in 12A / s^{-1}		Rate of H ₂ loss from 16 / s^{-1}
	H _A	H _B	H _A to H _B	H _B to H _A	H
CD₃OH	Too broad to measure		Too broad to measure		1.33 ± 0.05

In all three solvents, the rates of hydride site exchange between the isomers, for example from H_A in **12A** to H_A in **12B** in CD_2Cl_2 , could not be measured, due to the signals for **12B** being very broad at 298 K. The same rapid exchange was observed for complex **12A** in CD_3OH , which precluded determination of the hydride site interchange between complexes **12A** and **16** in this solvent system.

3.4. Analysis of pyridine T_1 relaxation times

For a species to return to thermal equilibrium, after it is probed during an NMR experiment, it must undergo relaxation processes. It is known that there are several conditions that affect the relaxation of a system, particularly the T_1 (longitudinal/spin-lattice) relaxation. This is the release of energy from an analyte to its surroundings and is therefore strongly dependent on the presence of other species within the system. For pyridine, the effective relaxation times of its *ortho*, *meta* and *para* protons are 28.8 s, 26.4 s and 30.1 s respectively.⁹³ However, upon the addition of [Ir(COD)(IMes)Cl] and hydrogen to pyridine in methanol, the active catalyst that is formed dramatically decreases the T_1 values for these protons to 12.6 s, 14.7 s and 18.9 s respectively, for a sample containing 0.1 M pyridine and catalyst loading of 5 mol%. This is because the active catalyst undergoes exchange processes which aid the relaxation of the pyridine signals.⁹³ A similar effect is expected when the catalyst used is complex **1**.

However, the effect of solvent on relaxation was unknown. Therefore, T_1 values of the protons of pyridine were calculated in the samples of different solvents, from non-polar benzene to polar methanol. Tests were conducted on samples containing pyridine (0.05 M) in air, degassed and then in the presence of **1** (15 mol%) and 3 bars of H_2 . The samples under normal air (Table 25) all contain paramagnetic oxygen which aids the relaxation process of analytes and as the solubility of oxygen varies with solvent,²¹⁵ these values cannot be directly compared without taking into account the solubility differences. However, upon degassing the samples there are still a large range of T_1 values (Table 25) which can therefore be attributed to the effect of the solvent within the system. Pyridine can participate in several different interactions, either between the pyridine molecules themselves or with the solvent molecules, depending on the characteristics of the solvent in which it is dissolved. Since pyridine is a planar aromatic molecule, it can form stacked systems stabilised by π - π interactions between rings. Furthermore, because pyridine has a very similar aromatic ring structure to benzene, these π - π stacking interactions are also likely to form as mixed structures and a number of computational studies have investigated these systems.²¹⁶⁻²¹⁸ Due to its nitrogen lone pair, pyridine is also known to participate in hydrogen bonding as an H-bond acceptor.²¹⁹⁻²²¹ Therefore, hydrogen bonding interactions are likely to exist

between pyridine and the H-bond donor solvents dichloromethane, methanol and ethanol. Some of these potential interactions are shown in Figure 117.

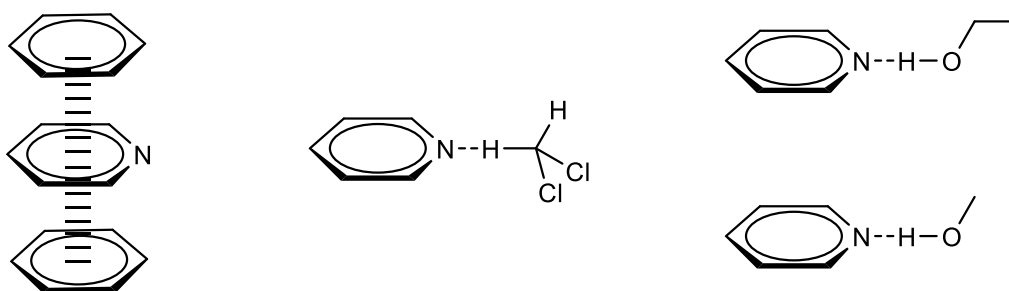


Figure 117: Possible interactions between pyridine and benzene, DCM, methanol and ethanol

In addition, the differing viscosities of the solvents will affect the molecular motion (rotational correlation times, τ_c) of the pyridine molecules leading to effective changes in T_1 values. It is known that correlation time, τ_c is related to the relative molecular mass, M_r , of a molecule, such that $\tau_c \approx M_r \times 10^{-12}$ and therefore for pyridine, $\tau_c \approx 79$ ps. This lies to the left of the minimum point depicted in Figure 118, which shows how the T_1 depends on the correlation time of a molecule. However, these effects will be minimal.

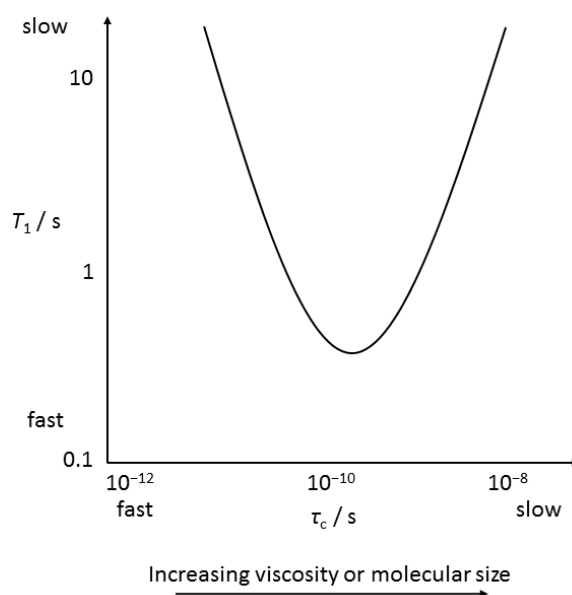


Figure 118: The dependence of the T_1 relaxation time on the rotational correlation time, τ_c of a molecule. For pyridine, its τ_c value lies to the left of the minimum point, with an increase in viscosity of the solution causing a decrease in the both the correlation time and the T_1 value

In relation to Figure 118, solvents with a higher viscosity are predicted to shorten the T_1 value of the pyridine molecule. This is consistent with what is observed when ethanol is used as its viscosity is approximately double that of the other solvents, as shown in Table 25. Pyridine therefore demonstrates the lowest T_1 values in ethanol, when tested under air, under vacuum and in the presence of active catalyst and H_2 .

Table 25: T_1 values calculated for the protons of pyridine (0.05 M) in the specified solvent samples under air, degassed and once activated with **1** (15 mol%) under 3 bars of H_2 at 298 K

Solvent		C_6D_6	THF- d_8	CD_2Cl_2	Ethanol- d_6	CD_3OD
Viscosity / cP	At 25 °C	0.60	0.46	0.41	1.07	0.54
T_1 of Pyridine in air / s	<i>ortho</i>	7.7	18.2	10.3	5.1	6.7
	<i>meta</i>	7.7	23.8	9.3	5.0	6.9
	<i>para</i>	7.6	24.4	9.4	5.6	7.4
T_1 of Pyridine in degassed solution / s	<i>ortho</i>	74.5	25.4	47.0	22.9	13.3
	<i>meta</i>	58.7	62.1	42.0	18.1	26.2
	<i>para</i>	57.5	65.1	41.8	30.0	38.6
T_1 of Pyridine in solution with 1 under 3 bars of H_2 / s	<i>ortho</i>	8.8	9.1	10.4	7.2	12.2 *
	<i>meta</i>	10.3	12.5	12.9	6.3	11.0 *
	<i>para</i>	11.5	12.6	13.8	8.3	13.5 *

* Actually for 9 eq. of pyridine (0.07 M pyridine and 10 mol% **1**) due to the lower solubility of **1** in methanol. For 11 eq. of pyridine, the T_1 values for the *o*, *m* and *p* protons of pyridine were 13.1 s, 11.7 s and 14.7 s respectively. It is anticipated that the T_1 values for pyridine in a sample containing 0.05 M pyridine and 15 mol% **1** would be lower again by ~ 1 s.

Upon addition of **1** and H_2 to the pyridine samples to form the active complex, **6**, the T_1 values for every sample dramatically decrease with respect to the degassed samples. This is due to the rate of pyridine exchange that occurs between the complex and free pyridine in solution, which relates to the lifetime of the active catalyst, and therefore this rate needs to be optimised to promote the most efficient polarisation transfer and thus produce the largest signal enhancements.

The fastest ligand exchange rates (see Section 3.2.4) in C_6D_6 and THF correlated to lower T_1 values. In CD_2Cl_2 , the ligand exchange rate, and thus T_1 value, seems to be at an optimum. The T_1 values for the methanol sample are longer than expected, however, this could be because the catalyst is the least soluble in methanol and deuteration of the pyridine *ortho* protons occurs over time, which hinders relaxation, thus lengthening T_1 .

It is known that the effective T_1 values decrease as the number of interactions with the catalyst increase and therefore at a higher concentration of pyridine, each pyridine molecule will have fewer interactions with the catalyst so the T_1 values are anticipated to be higher. To test this, a sample containing 2.5 mol% **1** and 0.2 M pyridine in methanol was examined to compare the effect of the catalyst on T_1 relaxation. The corresponding T_1 values of pyridine were found to be 23.0 s, 20.1 s and 27.9 s for the *ortho*, *meta* and *para* protons respectively, which is an approximate doubling compared to the T_1 values of the samples containing four times less pyridine.

To gauge a further understanding of how the rate of pyridine ligand exchange affects the effective corresponding proton T_1 values in CD_2Cl_2 , T_1 values for the free pyridine and two bound pyridine ligands were calculated at 263 K and 298 K, with the data given in Table 26. The values at 298 K, when pyridine exchange occurs at an observed rate of $3.46 \pm 0.07 \text{ s}^{-1}$, show that the free pyridine and the exchanging pyridine ligand have effective T_1 values for their *ortho* protons of 10.4 s and 8.5 s respectively. On cooling to 263 K and thus completely inhibiting pyridine ligand exchange on the NMR timescale, the effective T_1 values for the *ortho* protons of free pyridine are 16.3 s, whilst those for the pyridine ligand in the *trans* position to the hydride ligand reduce to 2.3 s, commensurate with those for the pyridine bound *trans* to carbene at 298 K, which does not undergo exchange. This shows that when there is no interaction between pyridine and the catalyst, the T_1 values are increased and when pyridine is permanently bound, the values decrease, hence longer time periods associated with the metal centre lead to assisted relaxation. Ligand exchange at 298 K leads to averaged T_1 values thus the values depend on the ligand exchange rates and are affected by temperature.

These T_1 values have also been normalised by dividing through by the largest T_1 value of 16.3 s. At 263 K, the T_1 values of free pyridine are approximately seven times larger than the T_1 values for the non-exchanging pyridine sites. However, at 298 K, the

T_1 values for free pyridine and the exchanging pyridine are similar, with the values for the non-exchanging pyridine being three times lower.

Table 26: T_1 values for the three proton sites of each of the three pyridine environments (free pyridine, pyridine *trans* to hydride and pyridine *trans* to carbene) within a CD_2Cl_2 solution of pyridine (0.05 M) once activated with **1** (15 mol%) under 3 bars of H_2 at 298 K and at 263 K. At 263 K the T_1 value for the *para* proton signal of the pyridine ligand bound *trans* to a hydride ligand could not be determined due to signal overlap

	T_1 of free pyridine in solution / s			T_1 of pyridine bound <i>trans</i> to hydride / s			T_1 of pyridine bound <i>trans</i> to carbene / s		
	<i>o</i>	<i>m</i>	<i>p</i>	<i>o</i>	<i>m</i>	<i>p</i>	<i>o</i>	<i>m</i>	<i>p</i>
CD₂Cl₂									
At 298 K	10.4	12.9	13.8	8.5	11.4	12.8	2.8	3.4	4.9
At 263 K	16.3	15.5	15.5	2.3	1.8	-	1.8	2.1	2.7
Normalised at 298 K	0.64	0.79	0.85	0.52	0.70	0.79	0.17	0.21	0.30
Normalised at 263 K	1	0.95	0.95	0.14	0.11	-	0.11	0.13	0.17

A similar study was conducted using complex **2** with pyridine and H_2 in C_6D_6 , CD_2Cl_2 and CD_3OD . The pyridine dissociation rates for the samples were measured at 298 K along with the T_1 values for the protons of the free and bound pyridine ligands.

Here, again due to ligand exchange, the T_1 values for the protons of free pyridine and the pyridine ligand bound *trans* to the hydride ligand are weighted average values that depend on the specific rate of exchange, as detailed in Table 27. This can be modelled but is beyond the scope of this work. Due to signal overlap of the *ortho* protons of both bound pyridine ligands in C_6D_6 , the value of 2.98 s is also an average of the T_1 values of both the exchanging and the non-exchanging pyridine ligand. The T_1 value for the non-exchanging pyridine ligand is predicted to be even shorter than the exchanging ligand. This is because it remains bound to the metal centre which speeds up its relaxation.

Table 27: Pyridine dissociation rates and T_1 values for three samples of 16 mol% **2** and 0.05 M pyridine under 3 bars of H_2 in C_6D_6 , CD_2Cl_2 and CD_3OD at 298 K

Solvent	Rate of py dissociation / s^{-1}	Lifetime / s	T_1 of free py / s			T_1 of bound <i>ortho</i> py / s	
			<i>ortho</i>	<i>meta</i>	<i>para</i>	<i>trans</i> to H	<i>trans</i> to carbene
C₆D₆	24.8 ± 0.5	0.040 ± 0.001	8.38	8.93	9.72	2.98	
CD₂Cl₂	7.30 ± 0.03	0.137 ± 0.001	9.20	10.32	10.99	8.98	2.70
CD₃OD	1.35 ± 0.03	0.370 ± 0.007	5.57	6.88	7.93	4.00	1.96

In 2016, Barskiy et al.⁹¹ described an analytical model for the SABRE process which considers the relaxation processes involved in SABRE. They report the average T_1 value for the protons of free pyridine in solution as ~ 27.5 s which reduces to ~ 3.6 s on average for the protons of the pyridine ligands when they are bound to the iridium metal centre. This proton lifetime of the bound ligands was determined using the inversion recovery method, focusing on the pyridine ligand in the *trans* position to the carbene ligand, which does not undergo exchange.⁹¹ This is similar to the values given in Table 27 for complexes **8** and **15**. Furthermore, strong coupling with the hydride protons, which occurs in the active SABRE complex, decreases the T_1 value of the protons of pyridine,⁹¹ in-line with that seen here.

Overall, interactions with the metal centre aid the relaxation of the pyridine substrates, as predicted based on previous descriptions using $[Ir(COD)(IMes)Cl]$. The effects, however, are also solvent dependent, with considerably different relaxation effects observed in the different solvents. It is important to note that all the T_1 values measured here are larger than the time it takes to conduct the SABRE experiments described in Chapter 4 and therefore none of the substrates in the samples have undergone any substantial T_1 relaxation before an enhanced spectrum is acquired. Therefore, these differences should not have any significant impact on the enhancement values obtained.

3.5. Conclusion

This study has shown that the electronic effect of the substituent on the phenolate ring has a large influence on the conformation of the active catalyst formed in solution. Multiple isomers of each complex are present as first detailed in Figure 102 in Section 3.2.1, with the hydride and CH₂ linker chemical shifts typically being indicative of the isomers present. The ¹H NMR chemical shifts for the hydride ligands of **A** and **A'** commonly appear at approximately δ -21 and -28 whilst for the hydride ligands of **B** and **B'**, they appear at about δ -22 and -25. As the substituent on the phenolate becomes more electron-donating, the favoured isomer changes from one form to another as shown in the summary in Table 28. The isomer labels, **A** and **B** refer to those given in Figure 119.

Table 28: Summary of the active catalyst species formed in CD₂Cl₂ and CD₃OD, along with the ¹H NMR chemical shifts of their hydride and CH₂ linker signals

Pre-catalyst	Isomer A or B	Solvent	Active catalyst	H _A chemical shift / δ	H _B chemical shift / δ	CH ₂ linker chemical shifts / δ
1	A	CD ₂ Cl ₂	6	-21.36	-28.88	4.46 and 6.48
3	A	CD ₂ Cl ₂	10 _A	-21.95	-28.48	4.56 and 6.15
3	B	CD ₂ Cl ₂	10 _B	-22.56	-25.47	5.32 and 5.87
4	A	CD ₂ Cl ₂	12 _A	-22.08	-28.12	4.48 and 5.95
4	B	CD ₂ Cl ₂	12 _B	-22.55	-25.50	5.34 and 5.76
2	B	CD ₂ Cl ₂	8	-22.55	-25.49	5.29 and 5.76
1	A	CD ₃ OD	6	-21.62	-29.22	4.68 and 6.25
3	A	CD ₃ OD	10 _A	-21.66	-29.04	4.63 and 6.17
4	A	CD ₃ OD	12 _A	-21.72	-28.72	4.60 and 6.11
4	C	CD ₃ OD	16	-22.29	-22.29	4.88
2	C	CD ₃ OD	15	-22.33	-22.33	4.83

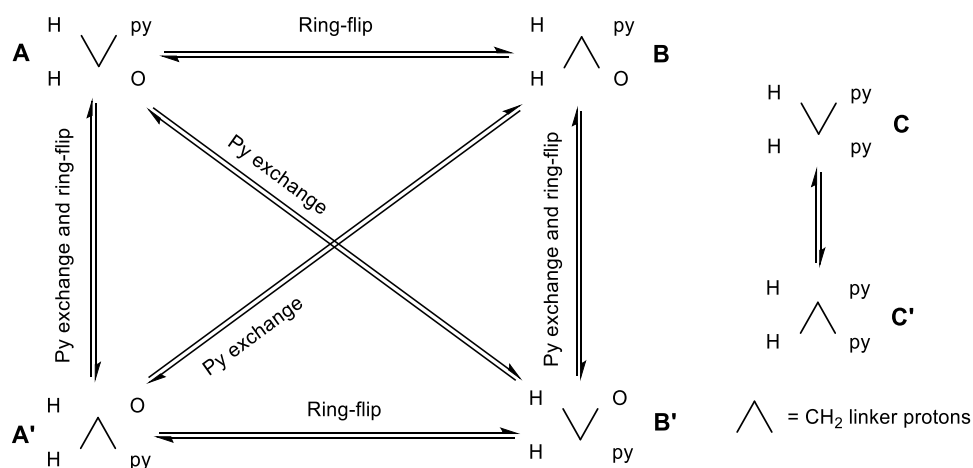


Figure 119: Summary of isomer forms and the interconversion processes that occur for the bidentate iridium carbene dihydride complexes in solution

In CD₂Cl₂, two isomers of the active catalyst form due to ring-flip of the seven-membered metallocycle. The Ir-O bond remains stable, despite the increase in electron density through the series, NO₂ < COOMe < Cl < H, indicated by the decreasing Hammett parameters, σ_p^- , 1.27 > 0.75 > 0.19 > 0.00. However, the electron density associated with the iridium metal centre, caused by varying the phenolate substituent, does affect the equilibrium position of the isomers. When the electron density on the metal centre is low, due to the presence of the strongly electron-withdrawing NO₂ group, isomer **A** dominates. However, as the substituent on the phenolate becomes more electron-donating, isomer **B** forms and then becomes the main species when the substituent is H, the most electron-donating. This is commensurate with the change in the chemical shift difference between the hydride signals, which is about δ 7 for isomer **A** but drops to about δ 3 for isomer **B**. Furthermore, the chemical shift difference between the inequivalent protons of the CH₂ linker also decreases on flipping from **A** to **B**. For **A**, the difference is about δ 1.7 whereas for **B** this reduces to about δ 0.4.

In methanol, where the Ir-O bond is retained, isomer **A** is the dominant form and **B** is not observed. This is the case for the most electron-withdrawing substituents, NO₂ and COOMe which have σ_p^- values of 1.27 and 0.75 respectively. This reactivity is like that seen in CD₂Cl₂. Isomer **B** may not be observed due to too rapid exchange between the two isomers, even at 258 K, precluding signal resolution. However, in CD₃OD, due to its ability to solvate the build-up of charge on the complexes as the electron density on the metal is increased, the Ir-O bond can cleave. Therefore, when the substituent on

the metal centre is Cl, with a σ_p^- value of 0.19, some of species **C** forms with equivalent hydride ligands, and once the electron-donating H substituent is present, with a σ_p^- value of 0.00, all the species formed is the Ir-O bond cleaved product **C**.

When the substrate is changed to being chiral, it is predicted that **A** and **A'** and **B** and **B'** are no longer equivalent as the stereogenic centre will affect these isomers. This hypothesis is analysed further in Section 4.3.3, when the substrate, pyridine, is replaced with the chiral molecule, nicotine. A summary of these different complexes and their corresponding exchange processes is detailed in Figure 119.

All the isomers detailed in Table 28 undergo substrate and H₂ exchange with the corresponding ligand exchange rates for the samples in CD₂Cl₂, given in Table 29. The fastest overall ligand exchange processes are observed for complex **12_A** containing the Cl substituent, with a σ_p^- value of 0.19, which lies between that of H and COOMe. Therefore, this slightly electron-withdrawing substituent imparts the optimum electronic properties for ligand exchange when the substrate is pyridine. This indicates that when the substituent in the *para* position to the phenolate is too electron-withdrawing, there is not enough electron density on the metal centre to enable rapid oxidative addition of hydrogen to the iridium centre. Furthermore, as the substituent becomes too electron-donating, the metal centre cannot accommodate the extra electron density and thus this is also not favoured. Other potential effects on the system are detailed in Section 3.1. The following chapters will analyse the SABRE activity of these complexes to determine the effect of electron density on polarisation transfer efficiency.

Table 29: Comparison of the ligand exchange rates and lifetimes of the dihydride complexes **6**, **10_A**, **12_A** and **8** in CD₂Cl₂ at 298 K

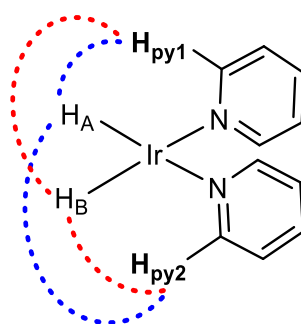
Pre-catalyst	R group	Hammett parameter / σ_p^-	Active catalyst	Rate of py loss / s ⁻¹	Rate of H ₂ loss from H _B / s ⁻¹	Rate of hydride interconversion (H _B to H _A) / s ⁻¹
1	NO ₂	1.27	6	3.46 ± 0.07	0.51 ± 0.02	0.75 ± 0.02
3	COOMe	0.75	10_B	2.63 ± 0.21	1.21 ± 0.03	1.39 ± 0.07
4	Cl	0.19	12_A	4.15 ± 0.26	2.04 ± 0.07	1.81 ± 0.10
2	H	0.00	8	3.74 ± 0.06	0.79 ± 0.01	1.57 ± 0.03

4. Exploiting neutral iridium carbene complexes in SABRE catalysis

4.1. Introduction

The field of SABRE catalysis has so far been limited to the use of symmetric monodentate carbene complexes which, when in their SABRE-active form, are present as charged species as discussed in Section 1.7. It has previously been stated in Section 1.1.3, that polarisation transfer via the SABRE approach is only possible by breaking the symmetry of the $p\text{-H}_2$, to unlock its polarising capabilities. This can be achieved by the formation of complexes with either chemically equivalent but magnetically inequivalent hydride ligands, or through complexes where the hydride ligands are both chemically and magnetically inequivalent.

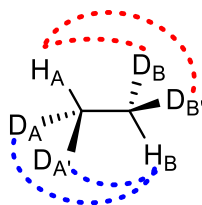
When *parahydrogen* oxidatively adds to a metal complex, it does so in a pairwise manner so that the hydride ligands remain spin-spin coupled. When the two created hydride ligands lie *trans* to two identical ligands, they remain chemically equivalent and both appear in the ^1H NMR spectra at the same chemical shift. However, differing coupling networks are established within the complex, as depicted in Figure 120, for an iridium dihydride bis-pyridine fragment, where the 4J -coupling value between the labelled pyridine proton, H_{py} , and H_A differs from that formed with H_B . This is the basis of magnetic inequivalence.



$$J_{\text{H}_\text{A}\text{H}_{\text{py}1}} \neq J_{\text{H}_\text{A}\text{H}_{\text{py}2}} \quad J_{\text{H}_\text{B}\text{H}_{\text{py}1}} \neq J_{\text{H}_\text{B}\text{H}_{\text{py}2}}$$

Figure 120: Iridium dihydride bis-pyridine fragment showing magnetic inequivalence of the hydride ligands due to their different coupling values to the protons of the pyridine ligands

In 1987, Eisenschmid et al.²²² studied the hydrogenation of some deuterated alkenes using *p*-H₂ and a rhodium catalyst, [Rh₃Cl₃H₂(CO)₂((Ph₂PCH₂)₂PPh)₂]⁺ under thermal conditions. For the starting alkene, CD₂CD₂, they showed that despite the two protons of the alkane product, CHD₂CHD₂, being chemically equivalent, they demonstrated signal enhancements due to their magnetic inequivalence caused by their differing couplings to the deuterium atoms present. This is shown in Figure 121.



$$J_{H_A D_B} \neq J_{H_A D_{B'}} \quad J_{H_B D_A} \neq J_{H_B D_{A'}}$$

Figure 121: Observation by Eisenschmid et al.²²² showing the magnetic inequivalence of the *p*-H₂ derived protons due to their different couplings to the deuterium atoms of the 1,1,2,2-tetradeuteroethane product

Another study further demonstrated the need for inequivalence and the effect of coupling differences on the enhancements observed when using thermal PHIP experiments. In 1996, Duckett et al.²²³ analysed the reactivity of [Ru(H)₂L₂(CO)₂] (where L = AsMe₂Ph, PMe₂Ph, PMe₃) with *p*-H₂ and showed that the two isomers of the complexes, the *cis-cis-cis* form and the *trans-cis-cis* form as shown in Figure 122, both exhibit enhanced hydride signals. Despite the *trans-cis-cis* isomer having both chemically and magnetically equivalent hydride ligands, it still demonstrated PHIP due to isomer exchange with the *cis-cis-cis* isomer, without loss of H₂, as depicted in Figure 122. When one CO ligand in the *trans-cis-cis* isomer of [Ru(H)₂(PMe₃)₂(CO)₂] was replaced with an equivalent ¹³C-labelled CO ligand, the symmetry of the complex was broken and significant enhancements of the *p*-H₂ derived hydride ligands were observed. This was due to the hydride ligands becoming magnetically inequivalent due to the different coupling networks existing with the ¹³CO ligand. This thus proved an effective route to enable PHIP enhancements of the hydride ligands, just via isotopic perturbation of the coupling network.

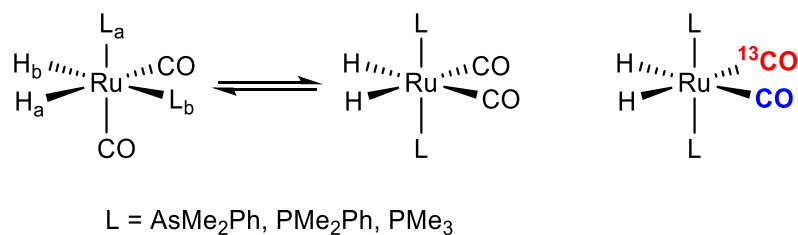


Figure 122: Isomer interconversion between *cis-cis-cis*-[Ru(H)₂L₂(CO)₂] and *trans-cis-cis*-[Ru(H)₂L₂(CO)₂]²²³ and the formation of the ¹³C-containing derivative with different couplings

A more recent example of exploiting hydride inequivalence to enable observation of PHIP, compares two dihydride phosphine complexes where the *p*-H₂ symmetry is broken in two different ways.²²⁴ In [Ru(H)₂(PPh₃)₃(CO)] the hydride ligands are chemically inequivalent, whereas in *cis*-[Ru(H)₂(dppe)₂] (where dppe = bis-diphenylphosphinoethane) the hydride ligands are magnetically inequivalent. A time-resolved NMR study of the photochemically initiated loss of H₂ showed that this step occurs on the picosecond timescale with binding of *p*-H₂ occurring on the microsecond timescale. Traditionally, *p*-H₂ is represented by $-\frac{1}{2}(2I_xS_x + 2I_yS_y + 2I_zS_z)$, where $\frac{1}{2}(2I_xS_x + 2I_yS_y)$ is the zero quantum coherence term (ZQ_x) and $\frac{1}{2}(2I_zS_z)$ is the longitudinal two-spin-order term. Under thermal reactivity, *p*-H₂ adds asynchronously, which causes the amplitude of the ZQ_x coherence to average to zero, leaving the observable transitions arising from the longitudinal two-spin-order term $\frac{1}{2}(2I_zS_z)$.²²⁴ This is explained in Section 1.4.3, in terms of the bulk magnetisation model, only populating the αβ/βα energy levels. Here, however, because the *p*-H₂ reactivity in these experiments is initiated photochemically, by a laser which is synchronised with the NMR spectrometer, the ZQ_x coherence is created synchronously and is thus well-defined. Because the laser is synchronised with the spectrometer, the delay time between the laser shot to initiate the reaction and the acquisition of the NMR spectra can be altered. This is termed a pump-probe experiment, where during the time delay, for chemically inequivalent hydride ligands, the ZQ_x state evolves coherently into ZQ_y and hence, using a 90 ° radio frequency probe NMR pulse, a signal can be observed, even though I_zS_z + ZQ_x itself is invisible. This is possible because the 90 ° pulse rotates the 2I_zS_z and ZQ_x into unobservable zero and double quantum terms respectively, and the ZQ_y term into an observable single quantum term.²²⁴ This is in contrast to a 45 ° pulse which has to be used to analyse thermal reactivity due to the presence of the 2I_zS_z spin-order term. Photochemically, the evolution of ZQ_x into ZQ_y results in the enhanced

hydride NMR spectra of the complexes exhibiting oscillating amplitudes with different frequencies. For $[\text{Ru}(\text{H})_2(\text{PPh}_3)_3(\text{CO})]$, this oscillation frequency of 1101 ± 3 Hz, is equal to the frequency difference between the two chemically inequivalent hydride resonances. However, for *cis*- $[\text{Ru}(\text{H})_2(\text{dppe})_2]$ this frequency of 83 ± 5 Hz is equal to the difference in spin-spin coupling between the hydride ligands and their coupling with the ^{31}P nuclei highlighted in Figure 123, which is the origin of their magnetic inequivalence.

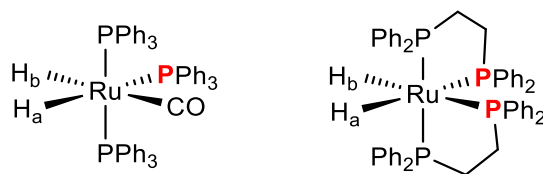


Figure 123: Structures of $[\text{Ru}(\text{H})_2(\text{PPh}_3)_3(\text{CO})]$, showing its chemically inequivalent hydride ligands, and *cis*- $[\text{Ru}(\text{H})_2(\text{dppe})_2]$, showing its magnetically inequivalent hydride ligands due to their different coupling values to the ^{31}P nuclei highlighted in red

Before the work described here was started all the examples in the literature of active catalysts for SABRE achieved the breakage in *p*- H_2 symmetry by the creation of complexes in which the hydride ligands derived from *p*- H_2 are made magnetically inequivalent. Very little knowledge of the effect of chemical and magnetic inequivalence was known with regard to SABRE-active catalysts. Since 2013, a few examples of polarisation transfer using catalysts with inequivalent hydride ligands have been published. In one specific case, where polarisation of ^{31}P using $[\text{Ir}(\text{H})_2(\text{PPh}_3)_3\text{Cl}]$ is achieved, the essential ligand exchange processes of the H_2 and the PPh_3 ligand lying *trans* to a hydride ligand, are facilitated at high temperatures in toluene. The chemical inequivalence arises from one hydride ligand being *trans* to a phosphorus and the other being *trans* to the chloride ligand.¹¹⁰

In this work, the use of bidentate NHC complexes has enabled the production of dihydride species which undergo the necessary ligand exchange processes for SABRE as described in Section 3.3. In this chapter, the chemical and magnetic inequivalence of these hydride ligands is exploited to use the complexes as SABRE catalysts. Due to their neutral nature, their activity in a range of solvents using a range of substrates has also been examined.

4.2. Polarisation tests with pyridine

In this work, full characterisation and ligand exchange studies have been completed using pyridine as the substrate. Pyridine is a six-membered heterocycle containing one nitrogen site. It is a suitable SABRE substrate because it can reversibly bind to iridium through its basic nitrogen and this facilitates exchange, whilst couplings to proton nuclei enable polarisation transfer. Its ability to be polarised via the SABRE approach has been well studied and it is commonly the first substrate tested, due to it being the initial model substrate for SABRE.^{2, 83, 87, 225}

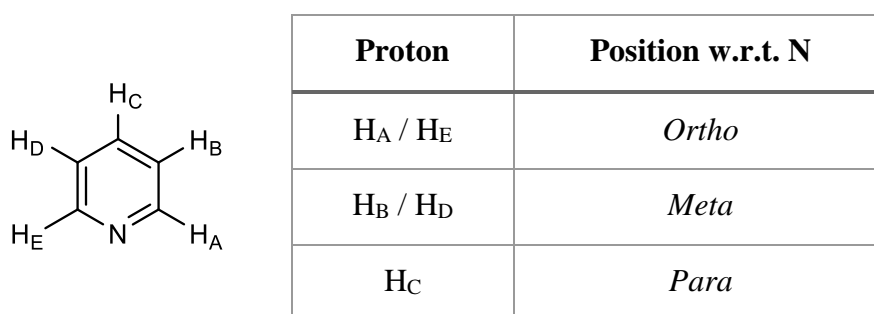


Figure 124: Pyridine showing labelling of protons and their positions within the heterocycle with respect to the nitrogen binding atom

4.2.1. Studies using complex 1

4.2.1.1. Initial tests

Initial SABRE tests using complex 1 with pyridine and *p*-H₂, gave a maximum enhancement of approximately 250-fold, for the *ortho* proton signal of free pyridine in solution. The enhanced ¹H NMR spectra in Figure 125 was acquired after the addition of *p*-H₂ to a Young's NMR tube containing pre-activated catalyst and substrate. This tube was shaken in the low magnetic field outside of the NMR spectrometer before being inserted into the magnet for interrogation (see Experimental Section 8.3.1). Due to the study in Section 3.2.2 that showed faster ligand exchange rates occur in methanol at higher temperatures, a temperature of 60 °C was chosen. Previous studies using [Ir(COD)(IMes)Cl] show that the most efficient Polarisation Transfer Field (PTF) is approximately 6.5 x 10⁻³ T and thus this was used in the initial studies described here.

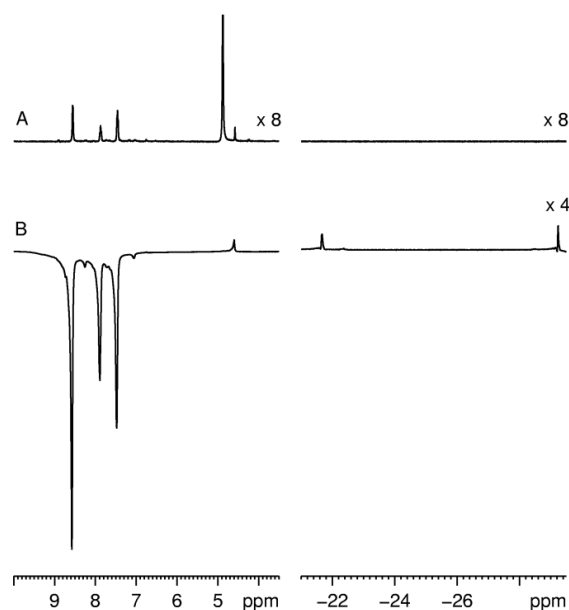


Figure 125: ^1H NMR spectra of a sample containing 0.1 M pyridine and 5 mol% **I** in CD_3OD under 3 bars of H_2 after; (A) thermal equilibrium at high field; and (B) polarisation transfer from $p\text{-H}_2$ at 6.5×10^{-3} T and 60°C

As well as observing signal enhancements of the protons of pyridine, analysis of the ^{13}C NMR spectra under the polarisation conditions using $p\text{-H}_2$ were completed, to determine where polarisation was transferred within the pyridine molecules. These tests led to polarised ^{13}C NMR spectra being obtained after a single scan, as shown in Figure 126, where enhanced signals for the three carbon environments of free pyridine are observed at δ 124, 137 and 149 for the *meta*, *para* and *ortho* carbon sites respectively. Here, as ^{13}C is excited without decoupling, each ^{13}CH environment is present as a doublet signal due to the J -coupling that exists between themselves and the polarised proton nuclei that they are coupled to. The signals arise from the creation of both I_z and I_zS_z states which have in phase and antiphase signals respectively. The antiphase character of the signals in Figure 126 is thus indicative of the I_zS_z state being the major term that is populated during SABRE. Therefore, when the ^{13}C signal is decoupled from the attached proton the I_zS_z state is removed and hence the enhancement is decreased.

The polarisation of heteronuclei can occur in two ways; either through indirect transfer (as here) when polarisation is transferred to coupled protons and then through to heteronuclei that couple to the polarised protons,^{2, 83, 99, 109} or via direct transfer to the heteronuclei which can occur when the coupling system is established directly between the hydride ligands and the heteronuclei of a substrate at extremely low field.^{107-108, 116,}

226-228 These tests show that the coupling network that exists within the pyridine molecules is sufficient for polarisation transfer to occur, once proton nuclei of the substrate molecules are polarised. This could prove important for studies where the polarisation can be captured and held on heteronuclei, before unlocking the polarisation using specially devised NMR pulse programs.

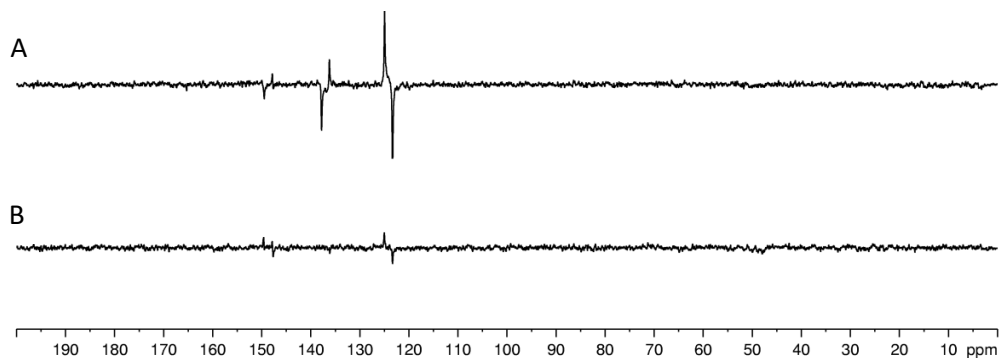


Figure 126: ¹³C NMR spectra of a sample containing 0.1 M pyridine and 5 mol% **1** in CD₃OD after polarisation transfer at; (A) 60 °C and 6.5 x 10⁻³ T; (B) 60 °C and 2 x 10⁻³ T

4.2.1.2. Effect of polarisation transfer field

As has been shown for pyridine, the magnitude of polarisation transfer is affected considerably by the field at which the polarisation step occurs. This is due to having to establish the desired coupling network so that the chemical shift difference, between the hydride ligands and the nuclei on the substrate which are to be polarised, is approximately equal to the *J*-coupling between the hydride ligands, as discussed in Section 1.6.² To determine the most effective PTF using **1** with pyridine and *p*-H₂, the enhanced Zeeman amplitudes of each of the *ortho*, *meta* and *para* proton signals for pyridine were analysed using an automated flow system that is compatible with methanol. This involves a polariser cell where the solution is placed and then *p*-H₂ is bubbled through the solution for a set time period before automatic transfer into the magnet.⁸⁸ The magnetic field that the solution experiences can be varied linearly by changing the current in the polariser coil, which is then used to investigate the effect of the PTF and determine the optimum magnetic field (see Experimental Section 8.3.2). These tests show that using **1** with pyridine and *p*-H₂, the maximum signal enhancement is gained at a PTF of 6.5 x 10⁻³ T (see Figure 127). Overall, the *ortho* protons are more

readily populated than the *meta* protons which are again more populated than the *para* protons of pyridine. This population trend may be due to the optimum coupling being established between the different proton environments and the hydride ligands.¹⁰⁸ Similar effects have also been seen for other catalyst systems and the magnetic field at which the phase change occurs can vary depending on the system studied.⁸⁶ This study shows that in order to achieve the best polarisation levels, a field of 6.5×10^{-3} T needs to be employed. Furthermore, both the *ortho* and *para* signals appear in emission throughout the magnetic field range studied, but the *meta* proton signal exhibits a phase change from emission to absorption at approximately -2.5×10^{-3} T. The appearance of the *meta* signal has been seen for pyridine many times before and is likely due to the complex behaviour of the H-H coupling over the time of the experiment and is also dependent on whether the polarisation transfer occurs directly or indirectly.¹ The imbalance in line intensities again suggests that I_z and $I_z S_z$ type terms result, as described in Section 4.2.1.1 for the ^{13}C signals. These different populated states can be probed using OPSY.

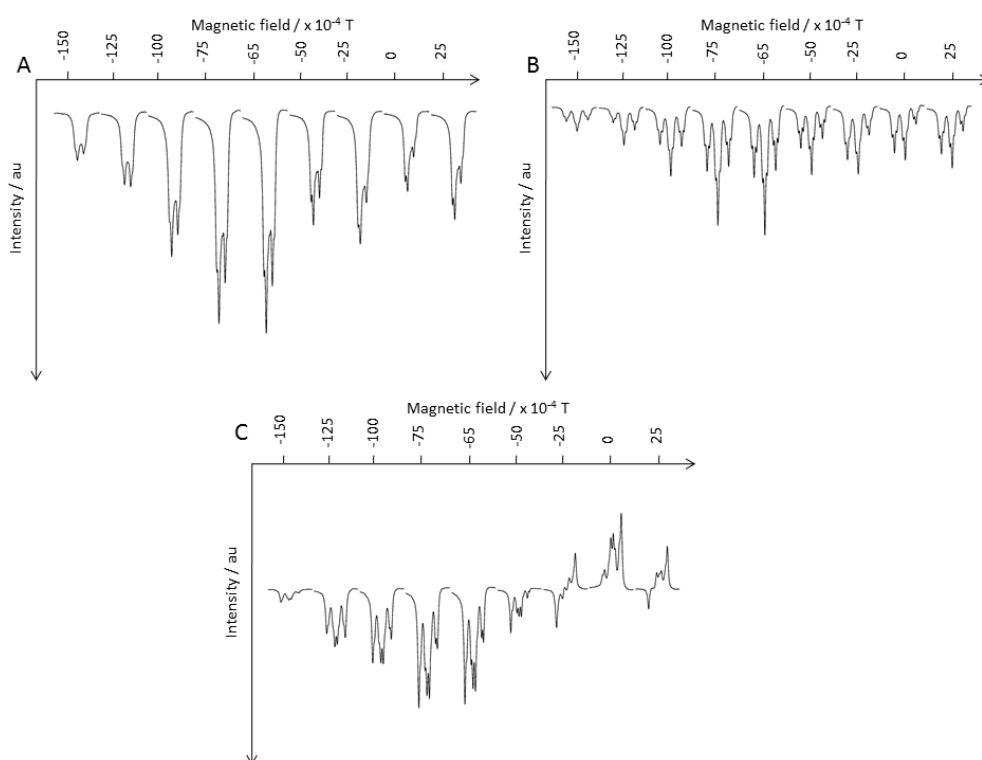


Figure 127: ^1H NMR spectra field plots of a sample containing 0.1 M pyridine and 5 mol% **I** in CD_3OD after polarisation transfer from $p\text{-H}_2$ at r.t. and varying PTF; (A) $H_{A/E}$; (B) H_C ; (C) $H_{B/D}$

4.2.1.3. OPSY NMR experiments

The ^1H NMR spectra shown in Sections 4.2.1.1 and 4.2.1.2 are acquired using a normal ^1H NMR pulse sequence and therefore, as well as the polarised signals, weaker thermal signals are also observed. One ^1H NMR spectroscopic method to eliminate the signals observed from thermal magnetisation is known as Only *Parahydrogen* Spectroscopy (OPSY). This approach involves specifically designed pulse sequences to study only those signals that are hyperpolarised and therefore created from the *p*- H_2 derived nuclei.²²⁹ Thermal signal is therefore not observed. OPSY works by using gradient pulses to enable coherence selection.²²⁹⁻²³⁰ Both double quantum OPSY sequences and zero quantum OPSY sequences can be exploited, to probe magnetisation shared between two spins. Because *p*- H_2 is described by a spherically symmetric magnetic state, any NMR pulse applied to it results in the same magnetic state and therefore it is NMR silent. This is why its symmetry has to be broken, by converting it into two hydrides on a metal centre.

$$p\text{H}_2 = 2I_xS_x + 2I_yS_y + 2I_zS_z$$

Under PHIP, the $2I_xS_x + 2I_yS_y$ term (ZQ_x) averages to zero over the reaction as described in Section 4.1 and the $2I_zS_z$ term survives. The Z magnetisation has a coherence order of 0 whereas x and y magnetisations have coherence orders of 1. For an OPSY-dq NMR experiment, for example, upon the application of a 90_x° pulse to the $2I_zS_z$ state, the magnetisation vectors are put into the transverse plane and become $2I_yS_y$. This double quantum coherence evolves further under the chemical shift operator and the effect can be dephased or rephased using a gradient pulse. In the case of the double quantum coherence, application of a second 90_y° pulse and a second gradient pulse with double the area of the first gradient is needed to produce a signal. Any single quantum coherences remain dephased and hence signals derived from the initial *p*- H_2 state are seen selectively. If the second gradient pulse is equal to zero, zero quantum coherence is selected and an OPSY-zq NMR experiment is completed. This pulse sequence is depicted graphically in Figure 128. The SABRE effect also creates longitudinal terms such as I_zS_z between coupled spins in the hyperpolarised targets.

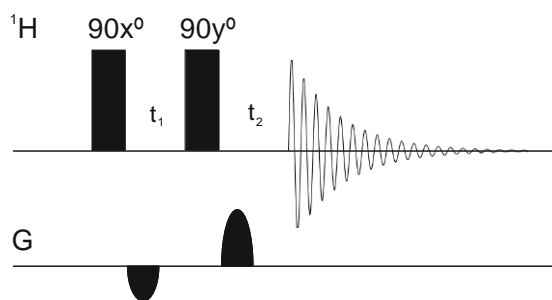


Figure 128: The ^1H OPSY NMR pulse sequence

To remove the additional thermal signal, studies of a sample containing 0.1 M pyridine and 5 mol% **1** in CD_3OD using an OPSY-dq NMR sequence with $p\text{-H}_2$ were used to analyse the SABRE effect. OPSY-dq NMR spectra of **6** in CD_3OD (see Figure 129) show that the two hydride signals of **6** are derived from $p\text{-H}_2$. This shows that **6** is the active SABRE catalyst as these hydride ligands transfer their polarisation to the pyridine substrates. Therefore, the pyridine ligands are also observed as they are coupled to the $p\text{-H}_2$ derived hydride nuclei which creates similar I_zS_z type magnetisation between them. The ^1H NMR spectra in Figure 129 were again acquired by adding $p\text{-H}_2$ to a Young's NMR tube containing the sample of interest and shaking the sample in the low magnetic field outside the NMR spectrometer before interrogation. The spectra clearly show that at a higher temperature, the signal enhancement is greater, due to faster ligand exchange, as discussed in Section 3.2.2, hence greater polarisation build-up in free pyridine occurs.

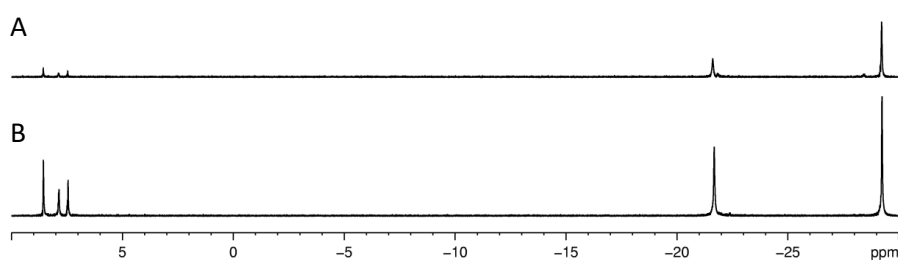


Figure 129: ^1H OPSY-dq NMR spectra of a sample containing 0.1 M pyridine and 5 mol% **1** in CD_3OD after polarisation transfer at; (A) $0\text{ }^\circ\text{C}$ and $6.5 \times 10^{-3}\text{ T}$; (B) $60\text{ }^\circ\text{C}$ and $6.5 \times 10^{-3}\text{ T}$

To improve the repeatability of the experiments, the automated flow system was used.⁸⁸ Figure 130 shows ^1H OPSY-dq NMR spectra obtained at different PTFs with the maximum enhancement at a PTF of $2.5 \times 10^{-3}\text{ T}$. The PTF also affects the signal enhancement of ^1H OPSY-zq NMR spectra, where the maximum enhancement is now

at a magnetic field of between 6.5 and 7.5×10^{-3} T. This means that at different PTFs, different magnetic states, including the higher order double quantum coherence, are optimally enhanced. Thus, analysing specific states provides an insight into the range of magnetic states that are created during the SABRE process.^{94, 96} These studies are beyond the scope of this work.

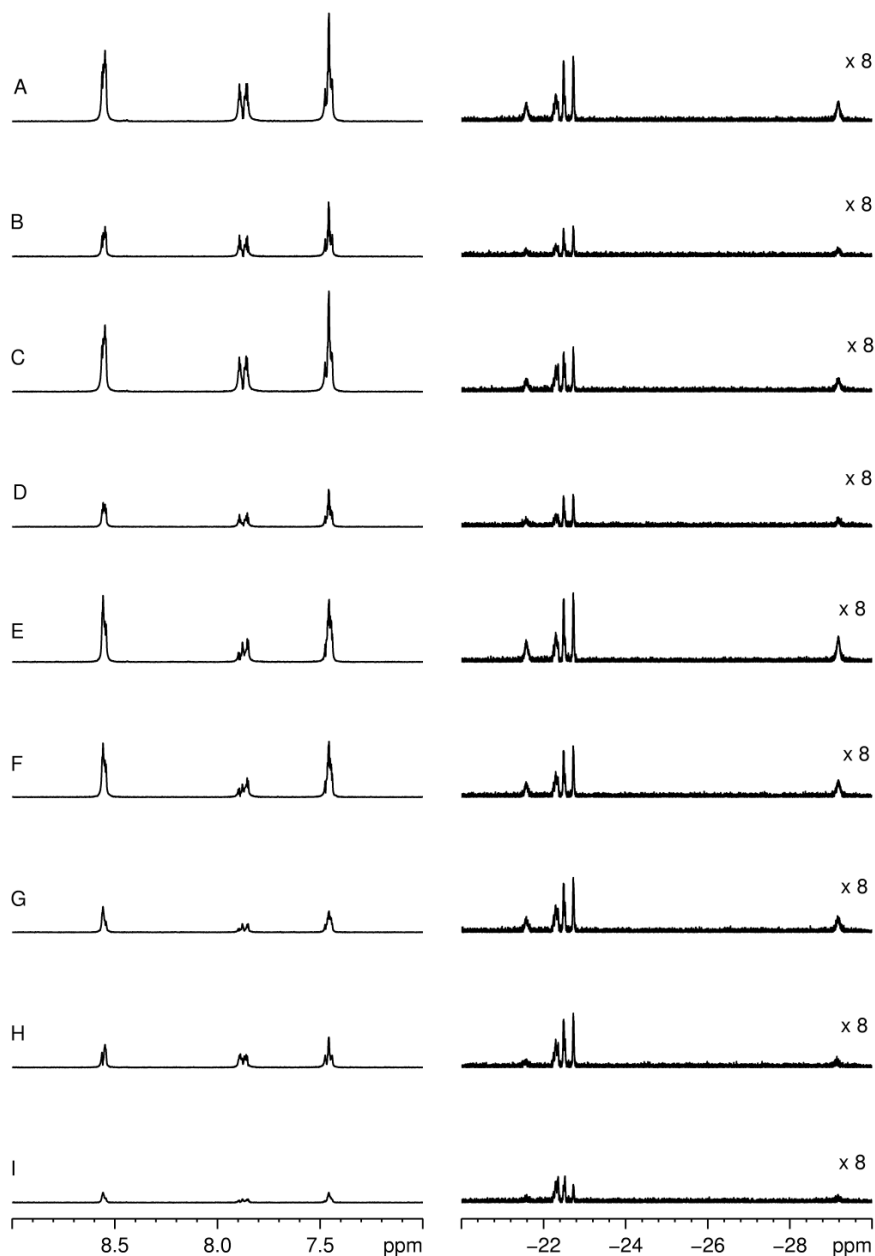


Figure 130: ^1H OPSY-dq NMR spectra of a sample containing 0.1 M pyridine and 5 mol% **1** in CD_3OD after polarisation transfer at r.t. and; (A) 2.5×10^{-3} T; (B) 0×10^{-4} T; (C) -2.5×10^{-3} T; (D) -5×10^{-3} T; (E) -6.5×10^{-3} T; (F) -7.5×10^{-3} T; (G) -1×10^{-2} T; (H) -1.25×10^{-2} T; (I) -1.5×10^{-2} T

4.2.1.4. Proton signal enhancements as a function of temperature

As for traditional catalysis, temperature can have a large effect on the enhancement levels due to ligand exchange rate variation, as detailed in Section 3.2.2. It was anticipated that at the higher temperatures studied, where ligand exchange is the most rapid, the signal enhancement values would also be higher. Thus shake-and-drop polarisation transfer experiments were conducted at temperatures ranging from ~ 273 K to ~ 333 K, which was the safest maximum temperature to test with the solvent methanol. The sample, containing **6**, was heated in a water bath at each desired temperature for 1 minute, then *p*-H₂ was introduced into the headspace of the sample and the sample was again brought back up to temperature for a further 10 seconds before being shaken at the desired field and acquiring a ¹H NMR spectrum. The effect of temperature was tested at both the low magnetic field of 2×10^{-4} T (Figure 131) as well as at the optimum PTF of 6.5×10^{-3} T (Figure 132), to see whether the same effect was observed with the change in field.

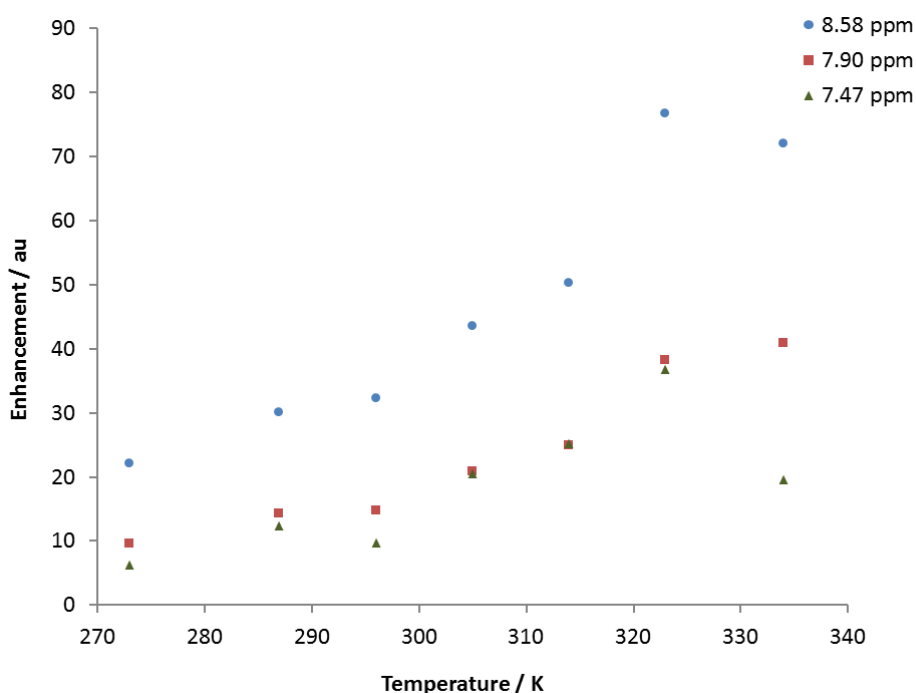


Figure 131: Pyridine proton enhancements as a function of temperature after polarisation transfer from *p*-H₂ using 5 mol% **1** and 0.1 M pyridine at 2×10^{-4} T

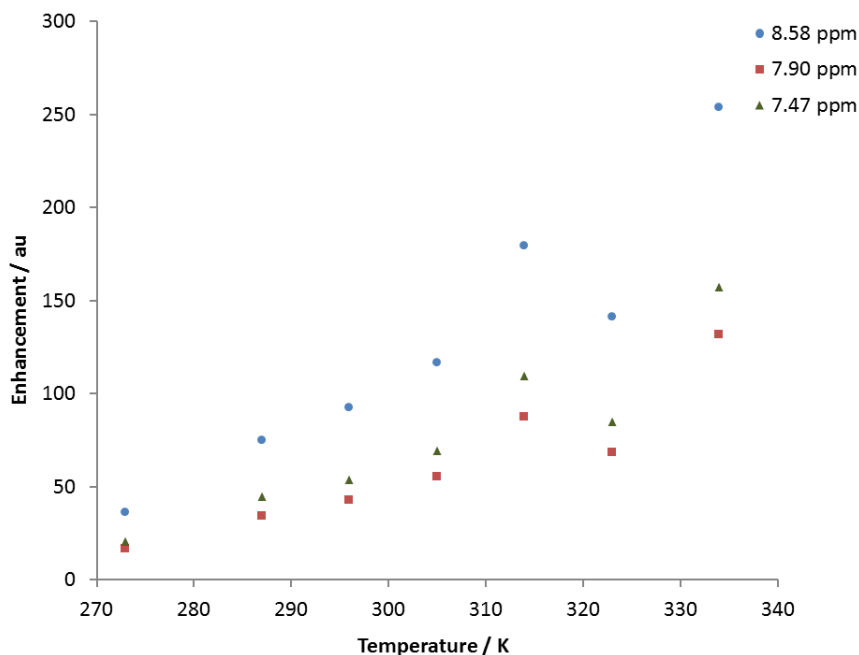


Figure 132: Pyridine proton enhancements as a function of temperature after polarisation transfer from $p\text{-H}_2$ using 5 mol% **1** and 0.1 M pyridine at 6.5×10^{-3} T

Analysis of each proton environment for pyridine shows that upon increasing the temperature, the enhancement level also increases, at both magnetic fields, as anticipated. It was predicted that the exchange rates and thus enhancement levels would increase up to a maximum when the polarisation transfer would be at an optimum, which may not be achievable here, due to the boiling point of methanol being $64.7\text{ }^\circ\text{C}$. The exchange rates determine the lifetime of the active polarisation transfer catalyst species as discussed in Section 3.2.2. At higher temperatures, the rates would become too fast for efficient polarisation transfer as the active catalyst's lifetime is significantly reduced and the coupling system's lifetime is insufficient.^{87, 89, 93}

When the most efficient catalyst for SABRE to-date is used, in order to compare the trends with that observed for **6**, the enhancement levels for pyridine when polarised using $[\text{Ir}(\text{H})_2(\text{IMes})(\text{py})_3]\text{Cl}$, which forms from the pre-catalyst $[\text{Ir}(\text{COD})(\text{IMes})\text{Cl}]$, are initially at a plateau and then decrease over the temperature range studied, at both 2×10^{-4} T (Figure 133) and 6.5×10^{-3} T (Figure 134). This suggests that at below ambient temperature the exchange rates for efficient polarisation transfer are at an optimum and at higher temperatures they become too fast for efficient polarisation transfer to occur.⁹³

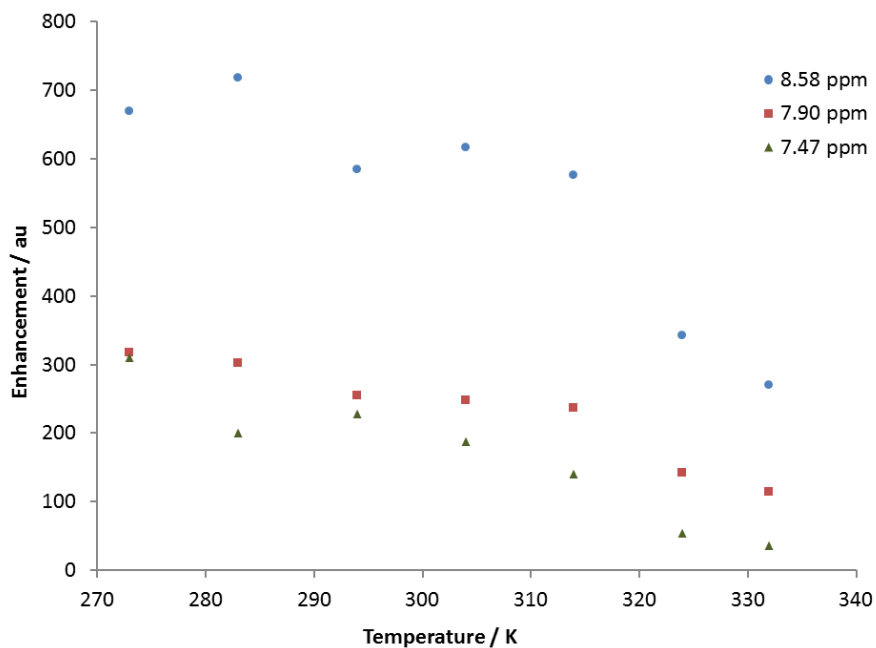


Figure 133: Pyridine proton enhancements as a function of temperature after polarisation transfer from $p\text{-H}_2$ using 5 mol% $[\text{Ir}(\text{COD})(\text{IMes})\text{Cl}]$ and 0.1 M pyridine at $2 \times 10^{-4} T$

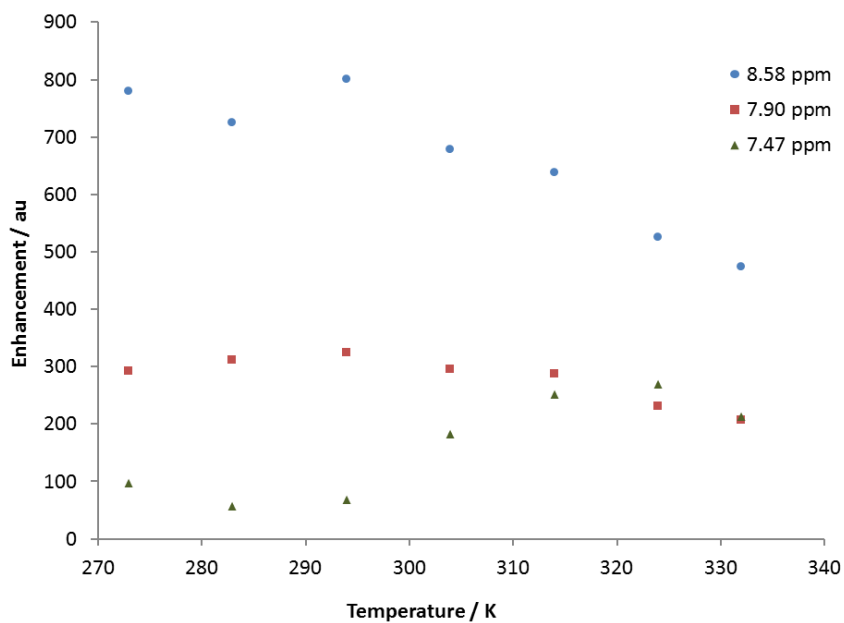


Figure 134: Pyridine proton enhancements as a function of temperature after polarisation transfer from $p\text{-H}_2$ using 5 mol% $[\text{Ir}(\text{COD})(\text{IMes})\text{Cl}]$ and 0.1 M pyridine at $6.5 \times 10^{-3} T$

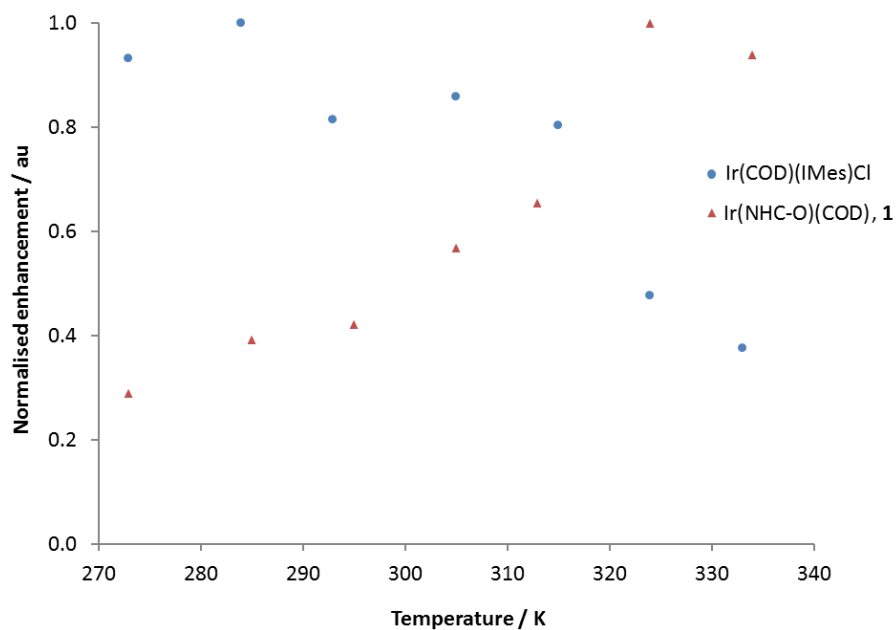


Figure 135: Temperature effects on normalised enhancements of the H_{AE} 1H NMR resonance of pyridine after polarisation transfer using $p-H_2$ at 2×10^{-4} T in CD_3OD (0.6 ml); each sample contains 5 mol% pre-catalyst ([Ir(COD)(IMes)Cl] or **1**) and pyridine (0.1 M)

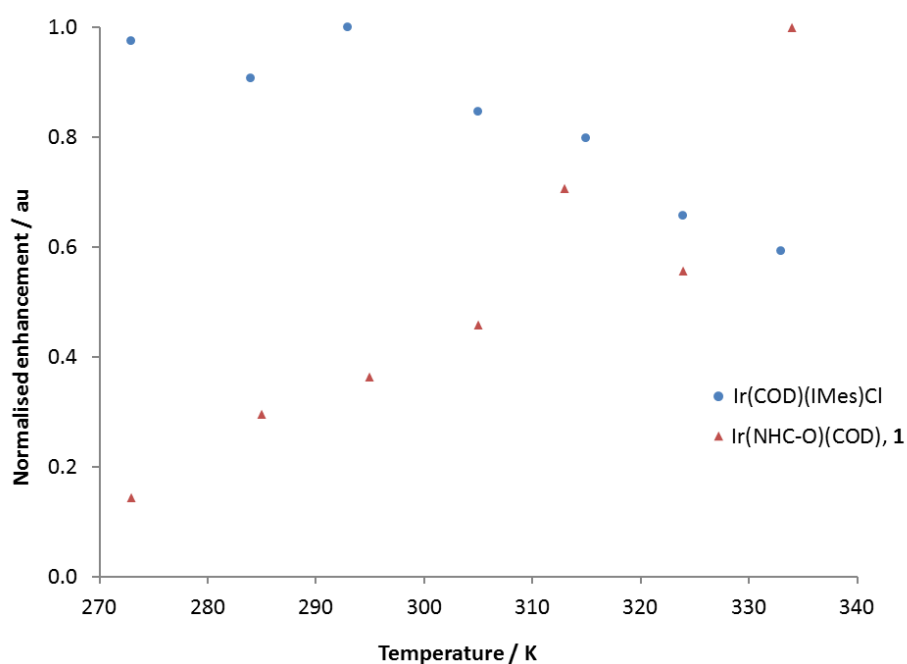


Figure 136: Temperature effects on normalised enhancements of the H_{AE} 1H NMR resonance of pyridine after polarisation transfer using $p-H_2$ at 6.5×10^{-3} T in CD_3OD (0.6 ml); each sample contains 5 mol% pre-catalyst ([Ir(COD)(IMes)Cl] or **1**) and pyridine (0.1 M)

To directly compare the general trend in pyridine enhancements when using [Ir(COD)(IMes)Cl] and **1** each data set must be normalised by dividing through by the largest enhancement factor gained when using each catalyst separately. This is shown in Figure 135 and Figure 136 and agrees with previous studies.⁹³ These data show that although [Ir(COD)(IMes)Cl] is the best pre-catalyst so far, for newly developed pre-catalysts, such as **1**, optimisation of each variable is very important to gain the best performance.

4.2.1.5. SABRE activity in different solvents

As **6** remains neutral, it should demonstrate a wider solvent tolerance than current charged SABRE catalysts such as [Ir(H)₂(IMes)(py)₃]Cl, which is important when considering suitable substrates for SABRE, as not all can be used in the polar protic solvent methanol, for example those containing exchangeable protons. Thus, a large area of unexplored substrate possibilities exists, for example amines and alcohols. Testing of neutral **1**, in a variety of solvents, with varying dielectric constants and viscosities was carried out to determine whether SABRE catalysis was restricted to the traditionally used solvent, methanol. SABRE studies using pyridine as the substrate were carried out in five different deuterated NMR solvents; C₆D₆, THF, CD₂Cl₂, C₂D₅OD and CD₃OD. Complex **1** demonstrated improved solubility in polar aprotic and non-polar solvents such as DCM and benzene since it is not a charged species. Polarisation transfer to pyridine was also shown to be efficient. It was found that SABRE occurs in all the solvents that were studied and signal enhancements of the hydrides (see Figure 137) as well as the protons of pyridine were observed (see Table 30).

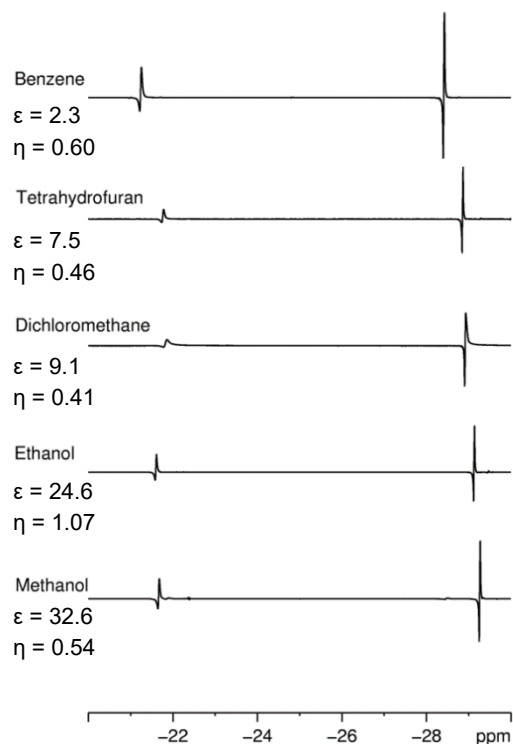


Figure 137: The hydride region of each ^1H NMR spectra when polarising pyridine using **1** in the specified solvents along with their dielectric constants, ϵ , and viscosities, η (cP), at 25 °C

It was found that upon increasing dielectric constant of solvent, from benzene to methanol, the hydride *trans* to oxygen shifts slightly downfield and remains as a sharp signal. However, the hydride *trans* to pyridine appears much broader in all cases as it sits opposite to the exchanging pyridine ligand. The enhancements observed for the protons of pyridine are the mean average values from a set of four, along with the calculated standard error.²³¹ In all the solvent systems studied, the active catalyst is formed but because of its slow production the level of SABRE enhancement observed in DCM, benzene and THF is initially lower than in methanol, which is typically used for SABRE. The solvent viscosity may also affect polarisation transfer due to relaxation effects (see Section 3.4) and in the lower viscosity solvents, more efficient mixing of the sample ensures better accessibility to fresh *p*- H_2 . This is particularly evident when comparing the alcohol samples which are both fully activated after 48 hours; the total signal enhancement of pyridine in methanol is more than double that of ethanol, which equates with a doubling in viscosity on changing from methanol to ethanol.

Table 30: Pyridine ^1H NMR signal enhancements for a series of 0.05 M pyridine and 15 mol% **I** solutions at 298 K and 6.5×10^{-3} T with 3 bars of $p\text{-H}_2$ after 48 hours and 24 days

Solvent		C_6D_6	THF- d_8	CD_2Cl_2	Ethanol- d_6	CD_3OD
PHIP for hydride site after 48 hours	<i>trans</i> to O	317 ± 13	337 ± 88	231 ± 25	519 ± 84 *	350 ± 28 *
Py ^1H NMR enhancement after 48 hours / fold	<i>ortho</i>	116 ± 6	90 ± 8	138 ± 14	71 ± 5	182 ± 9
	<i>meta</i>	90 ± 4	54 ± 5	98 ± 17	26 ± 3	126 ± 9
	<i>para</i>	54 ± 3	49 ± 5	63 ± 7	30 ± 2	81 ± 4
PHIP for hydride site after 24 days	<i>trans</i> to O	273 ± 14	243 ± 26	133 ± 24	1132 ± 257 *	15 ± 4 *
Py ^1H NMR enhancement after 24 days / fold	<i>ortho</i>	488 ± 54	579 ± 24	316 ± 68	281 ± 29	27 ± 4
	<i>meta</i>	391 ± 53	402 ± 50	237 ± 80	135 ± 24	21 ± 4
	<i>para</i>	219 ± 28	262 ± 12	141 ± 33	141 ± 7	17 ± 2

* The enhancement levels for the hydride ligand in ethanol and methanol are shown as signal-to-noise ratios due to the signal for the hydride ligand not being visible in the thermal spectra. For the other samples, the enhancement values are given based on the small thermal signal that was observed.

After 24 days, the samples were retested (see Table 30) to see the effect of time on enhancement levels and determine the relative stability of the complex in different solvents. Although initially (after 48 hours) it appears the catalyst is a more efficient polarisation transfer catalyst in the polar solvent, methanol, over time its efficiency in non-polar solvents improves and no complex degradation is observed in DCM, benzene or THF. However, after 24 days the signal enhancements seen in methanol had severely dropped off. This relates to the 2H-labelling of the pyridine due to H-D exchange with the solvent and incorporation of deuterium into the *ortho* proton site of the pyridine; 50 % deuteration of the *ortho* proton signal for pyridine was observed after 24 days. It could also be due to instability of the samples in methanol after longer time periods as the sample degrades. In comparison, when using ethanol, the ^1H signal enhancements for pyridine had increased after 24 days, despite 40 % deuteration of the *ortho* proton

signal for pyridine in ethanol. This could be due to slower activation in ethanol than methanol and improved stability in ethanol. The enhancements for the non-polar solvents are now much larger than for the polar solvents. This relates to the slower activation of the catalyst in non-polar solvents and the fact that deuteration does not occur in benzene, DCM or THF. It could also be due to the solubility of the catalyst as the fact that it is neutral means it is more soluble in the less polar solvents. Slower activation is thought to occur because non-polar solvents such as benzene are either unable or only weakly able to be involved in the coordination sphere of the catalyst to aid activation. Other factors to consider are; the balance needed between time for activation and enhancement factor and the solubility of hydrogen in each different solvent.

On closer inspection, polarisation is seen to be transferred to other proton nuclei within the active complex. Analysis of the enhanced ^1H NMR spectra of a CD_2Cl_2 sample containing 0.05 M pyridine and 15 mol% **1** at 298 K with 3 bars of *p*- H_2 shows enhanced signals for the bound pyridine ligands, and resonances of the carbene backbone of **6**. This is shown in Figure 138, with the minor enhanced signals labelled corresponding to the structure. This polarisation transfer to other proton resonances in the complex, and not just those of the bound pyridine lying in the *trans* position to the hydrides, is due to the magnetically inequivalent nature of the hydride ligands. These enhancements are very small due to the much less efficient coupling that is present between the hydrides and these protons, due to the larger distance between them. Similar enhanced signals for the complex are seen in both CD_3OD and C_6D_6 , although they exhibit very low intensities, in comparison to those for pyridine, particularly in the thermal ^1H NMR spectra. This therefore precludes their quantification and the determination of the most effective solvent system for polarisation transfer to the protons of the carbene backbone.

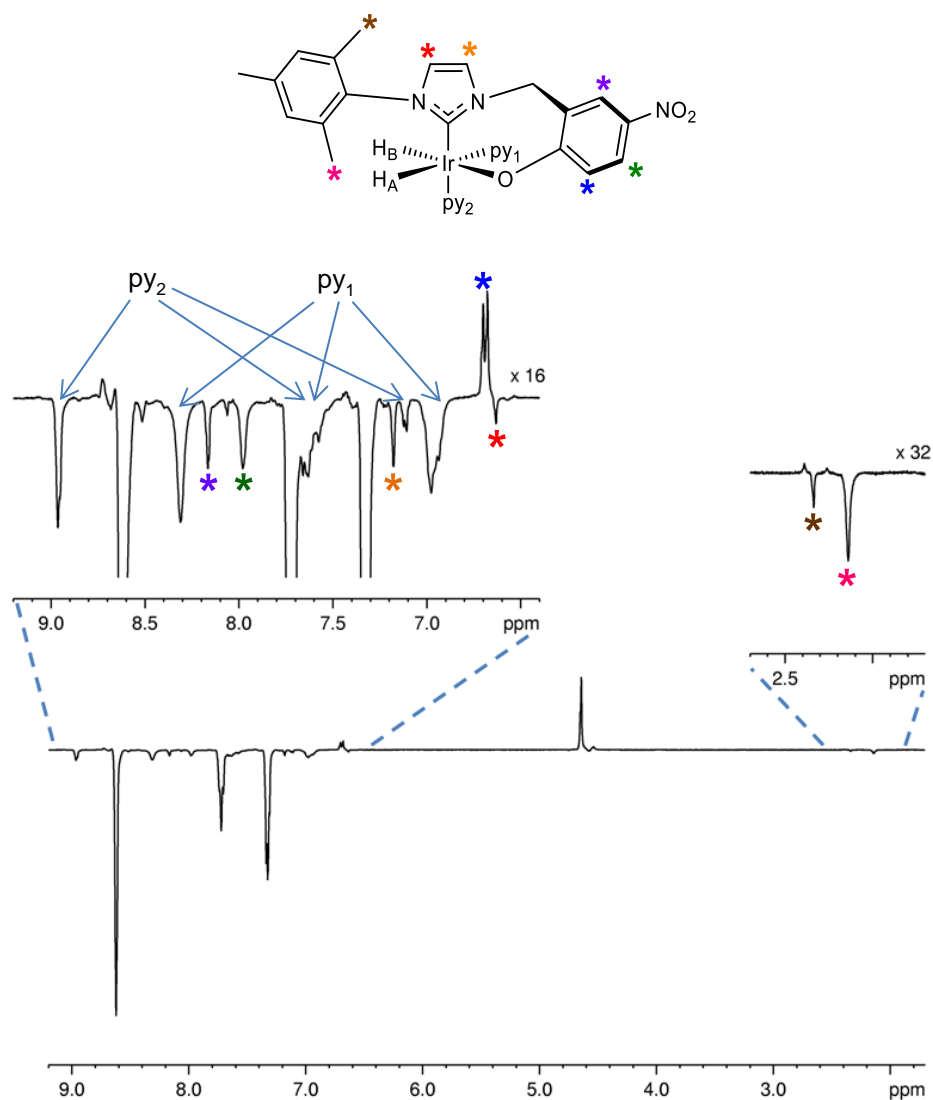


Figure 138: Enhanced ^1H NMR spectrum for a CD_2Cl_2 sample containing 0.05 M pyridine and 15 mol% **1** at 298 K and 6.5×10^{-3} T with 3 bars of $p\text{-H}_2$ demonstrating that polarisation is also transferred in a *cis* fashion to proton resonances of the bound pyridine ligands and the carbene backbone of **6**

The fact that polarisation is observed to transfer weakly across the Ir-O-C bond is important when considering potential substrate molecules. Molecules containing oxygen donor atoms which can bind to the iridium metal centre may be suitable substrates for the polarisation transfer process. They must be able to interact with the metal centre to enable the coupling network to establish as well as undergo reversible binding. The presence of the oxygen linker does not totally inhibit polarisation transfer.

4.2.2. Studies using complex 2

Using **2**, polarisation transfer to pyridine occurred in all three solvent samples tested, as detailed in Table 31. Therefore, both complex **8**, containing only one magnetisation-accepting pyridine ligand, and complex **15** containing two, act as efficient SABRE catalysts. However, these studies show that polarisation transfer is more effective in the less polar aprotic solvents where one of the ligand binding sites is blocked by the phenolate ligand, as overall these give the largest signal enhancements.

Table 31: Pyridine proton enhancement values using 0.07 M pyridine with 10 mol% **2** in C₆D₆, CD₂Cl₂ and CD₃OD under 3 bars of p-H₂ after activation for 48 hours and 6 days at a polarisation transfer field of 6.5 x 10⁻³ T

Solvent	Starting material: active product ratio (activation time)	Pyridine ¹ H NMR enhancement (fold)		
		<i>ortho</i>	<i>meta</i>	<i>para</i>
C ₆ D ₆	42: 58 (48 hours)	796 ± 20	544 ± 35	371 ± 14
	0: 100 (6 days)	843 ± 27	600 ± 30	404 ± 13
CD ₂ Cl ₂	26: 74 (48 hours)	754 ± 3	254 ± 14	472 ± 5
	0: 100 (6 days)	877 ± 32	337 ± 57	450 ± 22
CD ₃ OD	0: 100 (48 hours)	426 ± 5	47 ± 28	243 ± 3

Retesting of the CD₂Cl₂ and C₆D₆ samples after 6 days, once no starting material remained, showed a slight increase in the average enhancement factors. These values are nearly double the values obtained when using complex **1**, which links to the exchange rates being much faster (see Section 3.2.4). The enhancements in CD₂Cl₂ and C₆D₆ are much larger than those in CD₃OD, despite the catalyst not being fully activated. In CD₂Cl₂ the enhancement factor for the *para* proton is nearly double that of the *meta* protons which is opposite to the effect in C₆D₆ where the *meta* protons are more strongly enhanced than the *para* proton. The enhancement seen for the *meta* protons in CD₃OD is also much less than the same signals in CD₂Cl₂ and C₆D₆ due to it potentially having some antiphase character cancelling out the overall enhancement that

is observed. Overall, the enhancement factors of all samples are largest for the *ortho* protons of pyridine. These *ortho* protons are most strongly coupled to the *p*-H₂ derived hydrides, although the *meta* and *para* protons also couple to the hydride ligands to receive polarisation. Furthermore, the different protons of pyridine couple together and can transfer polarisation between each other. However, the effect of *T*₁ relaxation acts to reduce the level of polarisation, and this reduction is enhanced by interactions between the substrates and catalyst, as previously described in Section 3.4.⁹¹

For the CD₂Cl₂ and C₆D₆ samples, the signals for all three of the proton environments of pyridine appear with a negative phase with respect to the thermal spectra. However, in CD₃OD only the *ortho* and *para* signals appear with a negative phase and the *meta* proton signal appears positive. The appearance of the enhanced signals depends on the spin states that are populated, which is strongly affected by the magnetic field used for polarisation transfer and dependent on coupling within the system.⁹¹ Comparing these different samples indicates that the solvent in which polarisation transfer is conducted, can also affect the spin-order terms that are populated at the time of magnetisation transfer from *p*-H₂ to substrate ligands. Thus, this is another factor that needs to be considered when optimising polarisation transfer to specific longitudinal spin states.

To demonstrate catalyst activity at lower catalyst loadings, samples containing larger excesses of pyridine were tested with the enhancement results shown in Table 32. The observed enhancement values dramatically decrease due to the inhibition of *p*-H₂ exchange, relating to the fact that H₂ dissociation occurs after pyridine dissociation as discussed in detail in Section 3.2.3. However, limited SABRE catalysis does still occur.

Table 32: Pyridine proton enhancement values using 0.33 M pyridine with 2.3 mol% **2** in CD₂Cl₂ and CD₃OD under 3 bars of *p*-H₂ at 6.5 x 10⁻³ T and 298 K

	Pyridine ¹H NMR SABRE enhancement (fold)		
Solvent	<i>ortho</i>	<i>meta</i>	<i>para</i>
CD₂Cl₂	32 ± 2	12 ± 3	15 ± 1
CD₃OH	8 ± 1	4 ± 1	5 ± 1

It is interesting to note that for the CD₂Cl₂ sample, as the amount of pyridine is increased, the Ir-O bond becomes unstable, and is cleaved, and the binding of an extra pyridine ligand is facilitated. This therefore leads to the formation of varying amounts of **15** as shown in the ¹H NMR spectra in Figure 139. At greater excesses of pyridine, more of this product forms. As hydride ligands are strong σ-donors they exert a large *trans* effect and weaken the Ir-O bond. To reduce the amount of electron density on the iridium metal centre when the pyridine concentration is higher, it is therefore more favourable to bind a σ-donor pyridine ligand when compared to a σ-donor and π-donor alkoxide ligand, making trapping of the Ir-O bond cleaved form feasible. The higher concentration of pyridine also increases the potential to stabilise the charge build-up. This matches the behaviour when acid is added to **8**, in that the Ir-O bond is broken, which may also indicate more generally, the reversible binding ability of the phenolate in solution.

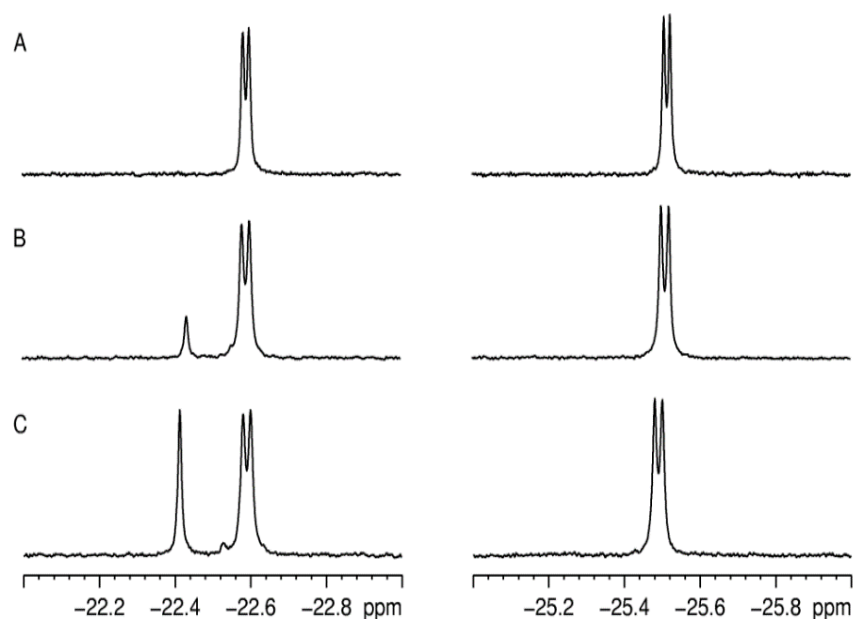


Figure 139: Three samples containing **2** in CD₂Cl₂ with increasing equivalents of pyridine showing the formation of **15** from **8**; (A) 14 eq., (B) 42 eq. and (C) 72 eq.

Because the catalyst forms the zwitterionic species in CD₃OD, it was decided to test its activity in ethanol and in an ethanol: water mixture (30: 70) to see if it showed improved solubility and thus activity for biological applications. Despite having activity in pure deuterated ethanol, with ¹H NMR signal enhancements for pyridine of 240 ± 23, 40 ± 18 and 130 ± 12 for the *ortho*, *meta* and *para* protons respectively, catalyst

solubility was dramatically decreased when 70 % of the solvent from an activated ethanol sample was removed and replaced with D₂O. The sample turned cloudy and although a broad enhanced hydride signal was visible at $\delta -22.46$ for **15**, polarisation transfer to pyridine was very poor.

The effect of the PTF used for magnetisation transfer was also examined using a CD₃OD sample. The appearance of the proton enhancement plots as a function of PTF depend on the J_{HH} coupling between the hydride ligands and protons on the substrate ligands and the spin states which are then populated, as described in Section 1.6. The PTF affects the spin states that are populated as each spin state lies at a different energy, dependent on the applied field.⁹¹ Therefore, when the PTF is changed, spin state energies are changed and thus the levels of polarised enhanced signals are affected. This leads to the varied signal intensities seen in the plots in Figure 140.

In this study, the *ortho* and *para* proton signals of pyridine are all in the same phase and show the same behaviour with the maximum signal enhancement occurring at a PTF of -7.0×10^{-3} T. This is similar to what has previously been reported for pyridine using [Ir(COD)(IMes)Cl].^{88, 93} The two profiles also show a slight increase in signal enhancement at zero magnetic field although this is significantly less than at -7.0×10^{-3} T. In comparison, the signal for the *meta* protons of pyridine is considerably different and shows four phase changes. Again, the maximum enhancement is at -7.0×10^{-3} T in the same phase as for the *ortho* and *para* protons. A second maximum is observed again at zero field, this time with similar intensity to the previous maximum but with the opposite phase. These field effects are shown in Figure 140.

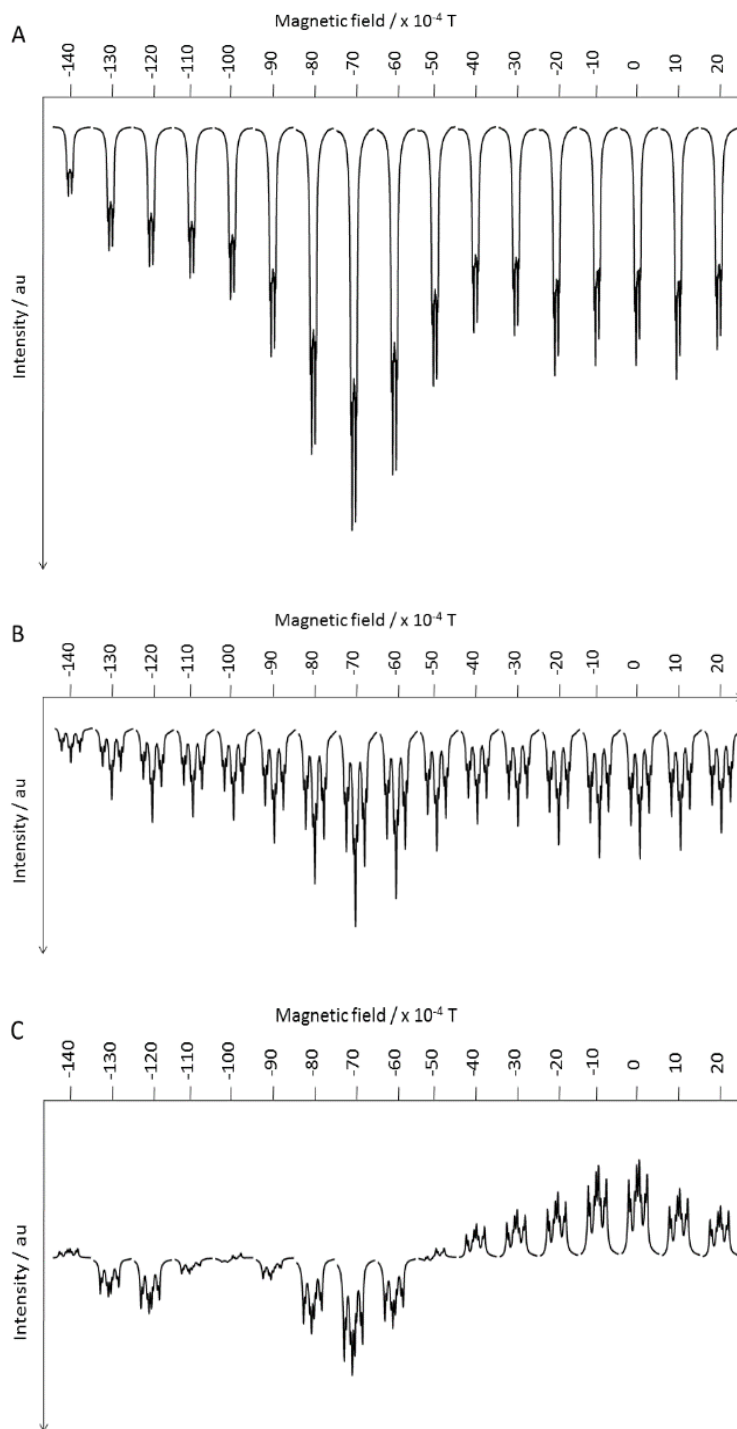


Figure 140: ¹H NMR spectra field plots of a sample containing 0.1 M pyridine and 5 mol% **2** in CD₃OD after polarisation transfer from parahydrogen at r.t. and varying PTFs from -140×10^{-4} T to 20×10^{-4} T with the largest signals at a field of -70×10^{-4} T; (A) H_{A/E}; (B) H_C; (C)

H_{B/D}

4.2.3. Studies using complexes 3 and 4

Using **3**, CD₂Cl₂ is the most effective solvent for promoting magnetisation transfer from *p*-H₂ to the protons of pyridine. The enhancements for the CD₂Cl₂ sample were measured when the solution contained **10_A** and **10_B** in a 37: 63 ratio.

Table 33: SABRE enhancements for the protons of pyridine for samples containing 0.06 M pyridine and 10 mol% **3** under 3 bars of *p*-H₂ at 6.5 x 10⁻³ T

Solvent	Pyridine ¹ H NMR enhancement (fold)		
	<i>ortho</i>	<i>meta</i>	<i>para</i>
C₆D₆	438 ± 53	264 ± 44	170 ± 25
CD₂Cl₂	778 ± 65	370 ± 78	416 ± 37
CD₃OD	261 ± 24	152 ± 28	121 ± 12

Using **4**, CD₂Cl₂ is again the most effective solvent for promoting magnetisation transfer from *p*-H₂ to the protons of pyridine. All three samples have multiple activated species present in solution that can all act as polarisation transfer catalysts.

Table 34: SABRE enhancements for three activated samples of **4** under 3 bars of H₂ at 6.5 x 10⁻³ T; a CD₂Cl₂ sample containing 9 mol% **4** and 0.08 M pyridine, a C₆D₆ sample containing 7 mol% **4** and 0.1 M pyridine and a CD₃OH sample containing 5 mol% **4** and 0.16 M pyridine

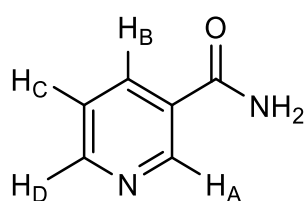
Solvent	Starting material: active product ratio (activation time)	Pyridine ¹ H NMR enhancement (fold)		
		<i>ortho</i>	<i>meta</i>	<i>para</i>
C₆D₆	68: 32 (24 hours)	574 ± 83	367 ± 96	227 ± 49
	29: 71(72 hours)	679 ± 54	407 ± 59	276 ± 27
CD₂Cl₂	42: 58 (24 hours)	680 ± 42	357 ± 49	359 ± 25
	8: 92 (72 hours)	1113 ± 137	586 ± 119	651 ± 78
CD₃OD	0: 100 (4 hours)	216 ± 28	28 ± 18	130 ± 18

4.3. Polarisation tests with other substrates

4.3.1. Studies using complex 1 with nicotinamide

4.3.1.1. Initial tests

Nicotinamide (Figure 141) is a biologically relevant derivative of pyridine that also binds to the iridium centre of the polarisation transfer catalyst via its basic aromatic nitrogen site. The lone pair on the amide nitrogen atom is less available for binding to the iridium centre due to delocalisation into the carbonyl bond. Nicotinamide is a member of the vitamin B group of molecules and nicotinic acid is metabolised to form nicotinamide within the body.²³²⁻²³³ It is used by the body to form nicotinamide adenine dinucleotide (NAD) and nicotinamide adenine dinucleotide phosphate (NADP) which are important coenzymes involved in many enzymatic oxidation and reduction reactions, such as glycolysis and the Krebs Cycle.²³²⁻²³³ Being able to demonstrate signal enhancement of biologically relevant substrates via SABRE is important for MRI applications. Being able to selectively polarise important drug molecules or precursors would be advantageous for imaging as patients would have to spend less time in the claustrophobic conditions of an MRI scanner and better resolution images could be obtained thereby enabling earlier diagnosis.¹¹²



Proton label	Chemical shift / δ
H _A	9.04
H _B	8.31
H _C	7.56
H _D	8.71

Figure 141: Nicotinamide showing labelling of protons

It has previously been shown that polarisation transfer to nicotinamide using the SABRE approach and the [Ir(COD)(IMes)Cl] pre-catalyst is effective and enables large signal enhancements to be observed. This substrate has been extensively studied using *p*-H₂ with the automated flow system.⁹⁶ Since nicotinamide has proven itself as a

successful SABRE substrate it was thought that the neutral pre-catalyst, **1** should be tested for effectiveness at polarisation transfer. It was shown that at 6.5×10^{-3} T and 60 °C substantial SABRE enhancement was observed (see Figure 142).

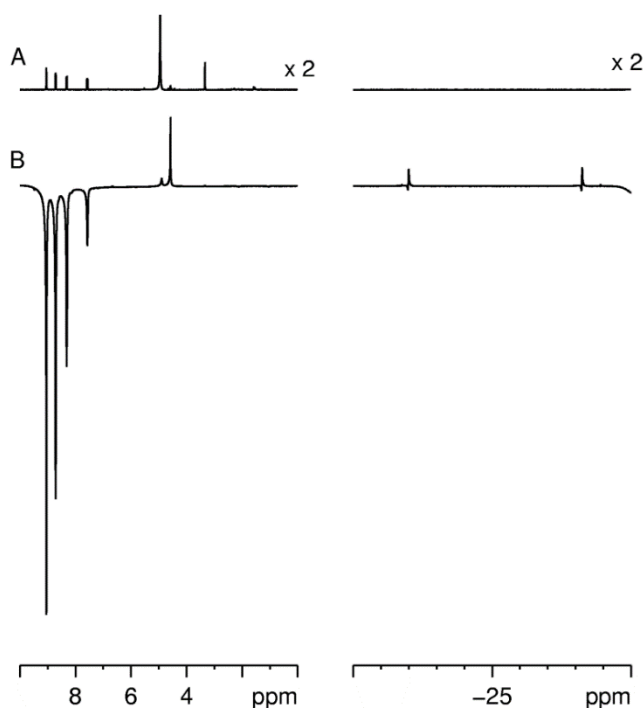


Figure 142: ¹H NMR spectra of a sample containing 0.1 M nicotinamide and 5 mol% **1** in CD₃OD after; (A) thermal equilibrium at high field; and (B) polarisation transfer from *p*-H₂ at 6.5×10^{-3} T and 60 °C

Analysis of pyridine had shown that at higher temperatures enhancements increased and this preliminary test shown in Figure 142 also seemed to demonstrate this therefore it was decided to repeatedly test the enhancements of nicotinamide at the higher temperature of 60 °C. Upon activation for 1 minute at 60 °C the enhancement levels for the four protons of nicotinamide were initially low (see Figure 143). However, when repeated, the levels increased so that the longer the overall time that was spent at elevated temperature, the larger the signal enhancement of the protons. This is also due to continued activation of the sample.

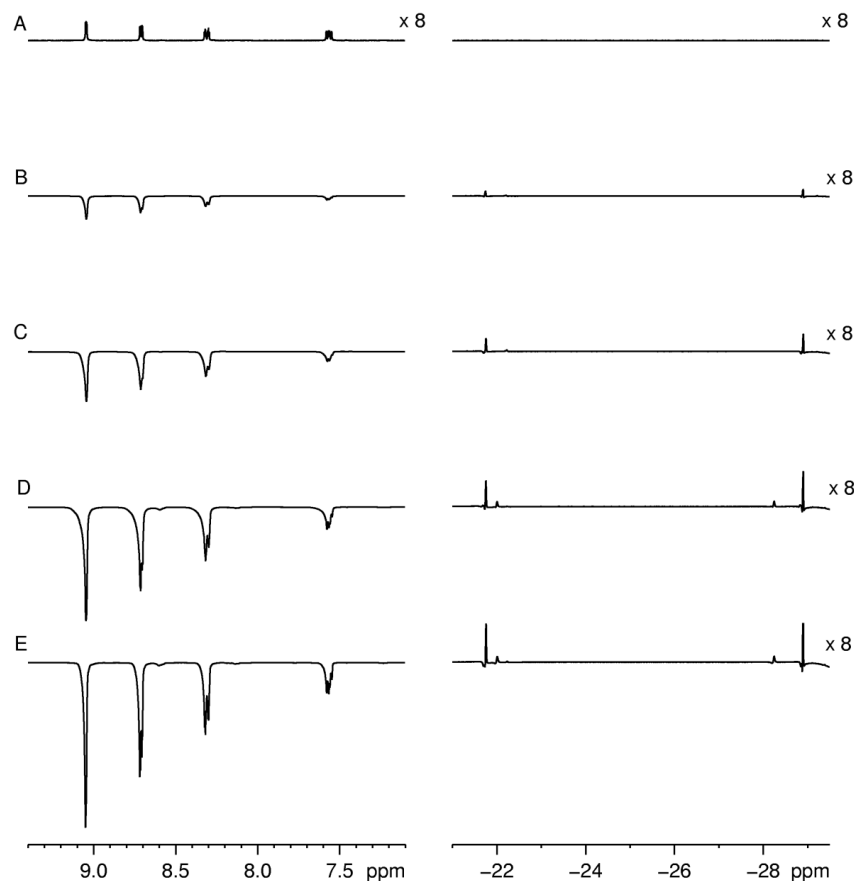


Figure 143: ^1H NMR spectra of a sample containing 0.1 M nicotinamide and 5 mol% **1** in CD_3OD at thermal equilibrium (A) and after polarisation transfer from $p\text{-H}_2$ at 60 °C and 6.5×10^{-3} T. Between each run (B-E) the sample was cooled to r.t. before the process was repeated

Like with pyridine, enhanced ^{13}C spectra were obtained with one scan after polarisation transfer at different fields and temperatures (see Figure 144). Again, the combination of a PTF of 6.5×10^{-3} T and a temperature of 60 °C gave the best signal enhancements of the carbon nuclei within nicotinamide and the ^{13}C spectra show improved signal enhancement when compared to the $^{13}\text{C}\{^1\text{H}\}$ spectra, for reasons discussed in Section 4.2.1.1 (see Figure 145). The enhanced ^{13}C NMR signals correspond to free nicotinamide in solution, with the largest signal apparent in both the ^{13}C and $^{13}\text{C}\{^1\text{H}\}$ spectra at approximately δ 125, corresponding to the *meta* carbon position (bonded to H_C) within free nicotinamide. Therefore, the established coupling network at a magnetic field of 6.5×10^{-3} T, ensures that the most efficient polarisation transfer is to this carbon atom.

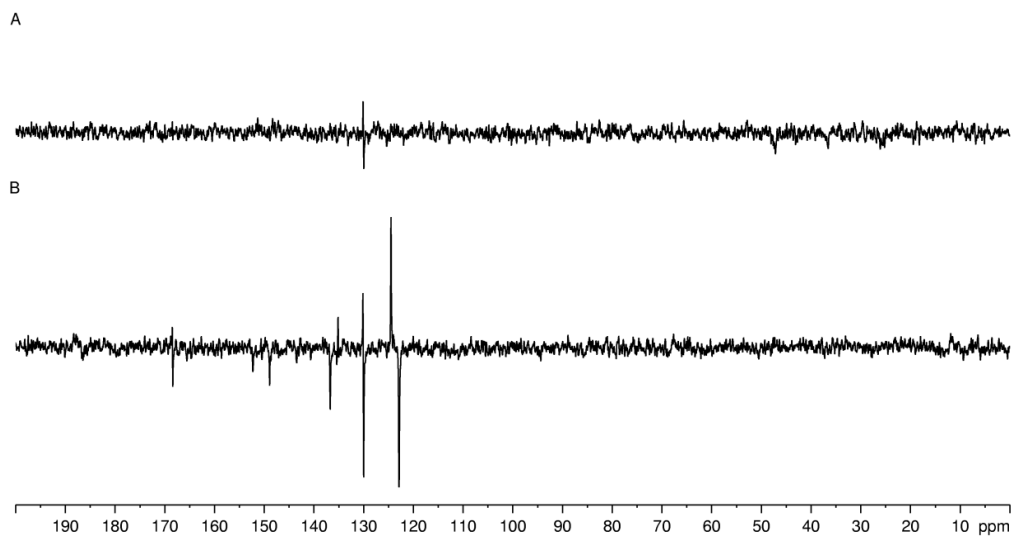


Figure 144: ^{13}C NMR spectra of a sample containing 0.1 M nicotinamide and 5 mol% **1** in CD_3OD after polarisation transfer from $p\text{-H}_2$ at 60 °C and 2×10^{-4} T (A) and 6.5×10^{-3} T (B)

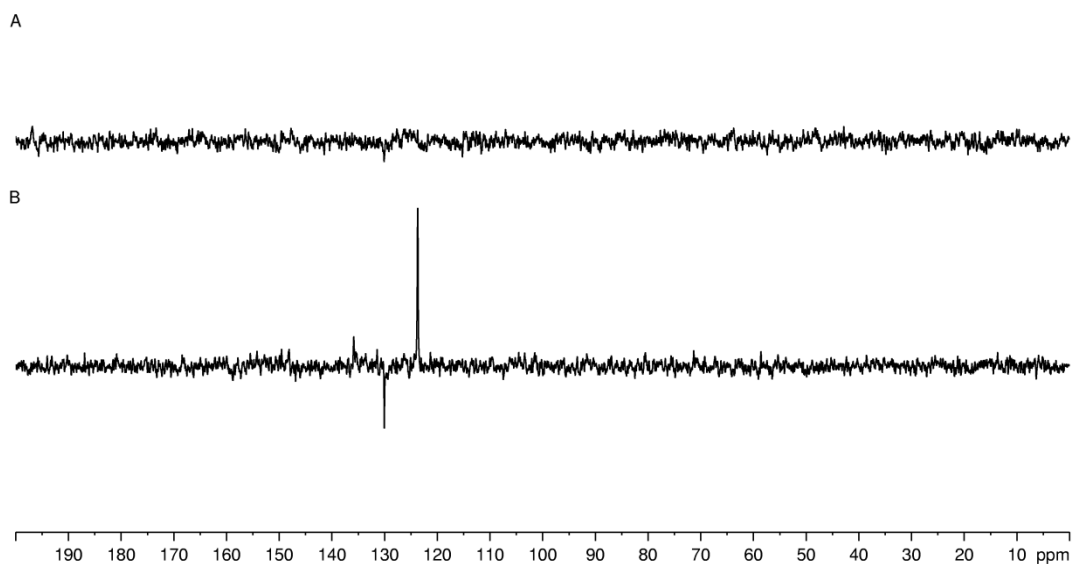


Figure 145: $^{13}\text{C}\{^1\text{H}\}$ NMR spectra of a sample containing 0.1 M nicotinamide and 5 mol% **1** in CD_3OD after polarisation transfer from $p\text{-H}_2$ at 60 °C and 2×10^{-4} T (A) and 6.5×10^{-3} T (B)

4.3.1.2. Effect of polarisation transfer field

It is known that changing the PTF affects the proton polarisation of each of the four sites of nicotinamide.⁹⁶ Therefore using ^1H NMR spectra the enhancement levels as the field is varied can be determined. For nicotinamide, all four proton sites are polarised, with the isolated H_A site showing the greatest signal enhancement. H_D shows the next largest enhancement, followed by H_B . These three proton sites are in the *ortho* and *para* positions of the heterocycle with respect to the nitrogen site and all demonstrate signals in emission. The proton site H_C , is *meta* with respect to the nitrogen in the ring and undergoes two phase changes from absorption to emission and back again between approximately -1.5×10^{-2} T and -1.25×10^{-2} T and at approximately -5×10^{-3} T. Similar trends have previously been observed for nicotinamide when polarised using $[\text{Ir}(\text{COD})(\text{IMes})\text{Cl}]$.⁹⁶

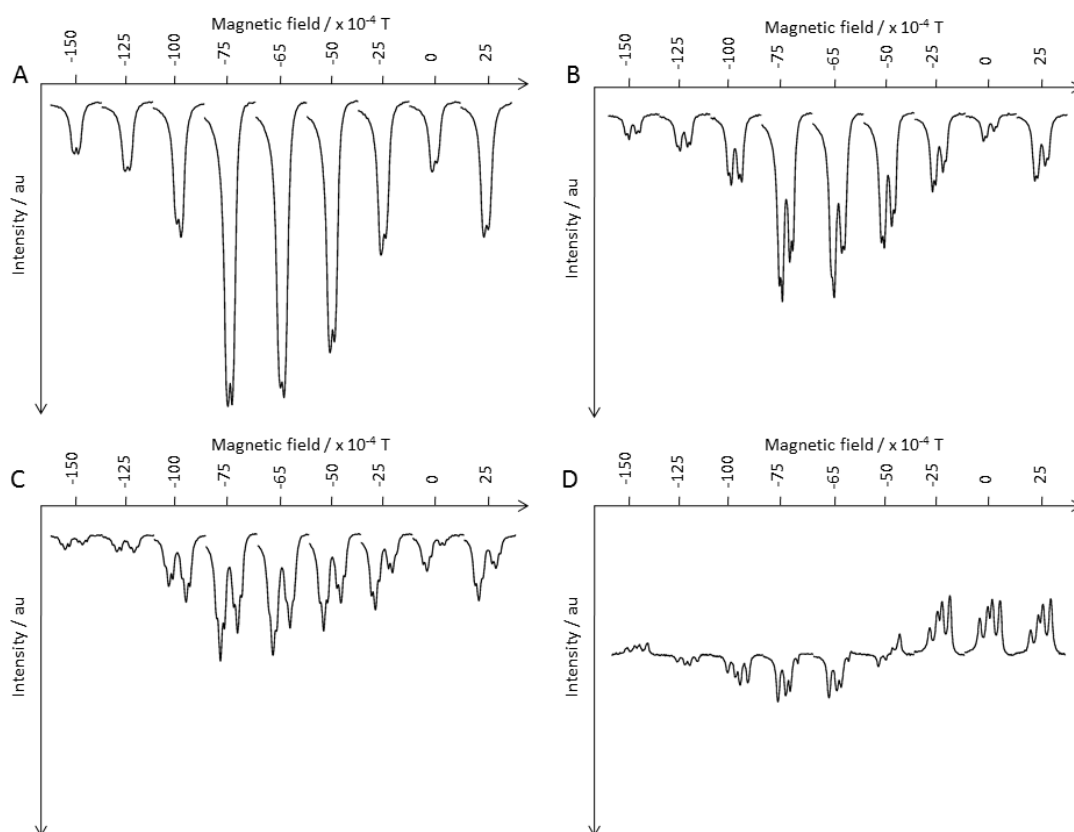


Figure 146: ^1H NMR spectra field plots of a sample containing 0.1 M nicotinamide and 5 mol% **1** in CD_3OD after polarisation transfer from $p\text{-H}_2$ at r.t. and varying PTF; (A) H_A ; (B) H_D ; (C) H_B ; (D) H_C

4.3.1.3. OPSY NMR experiments

Again, the use of the OPSY sequence enabled the most efficient PTF to be calculated for the zero quantum and double quantum magnetisation states. Initially, OPSY-dq tests were conducted on a sample after it had been warmed at 60 °C for 1 minute, as this had proven most effective for pyridine (see Figure 147). This again showed that 6.5×10^{-3} T was a better PTF compared to 2×10^{-4} T.

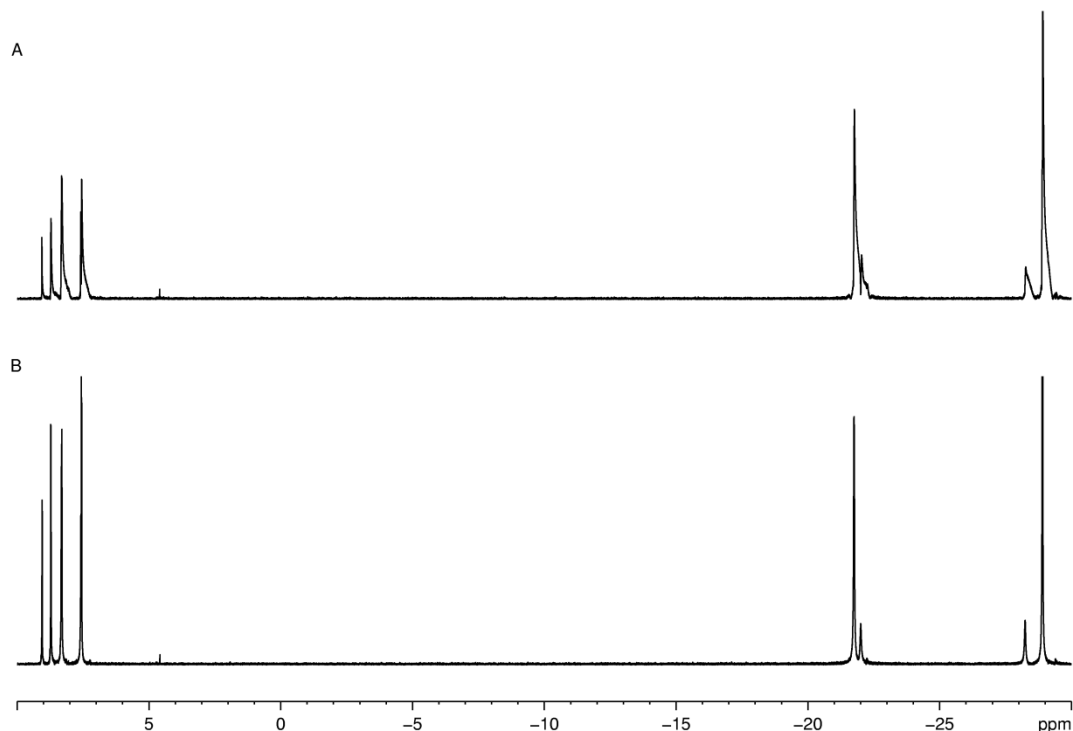


Figure 147: ^1H OPSY-dq NMR spectra of a sample containing 0.1 M nicotinamide and 5 mol% **1** in CD_3OD after polarisation transfer from $p\text{-H}_2$ at 60 °C and 2×10^{-4} T (A) and 6.5×10^{-3} T (B)

Using the flow probe a field plot could be produced to determine the effect that changing the field has on the signal enhancements. The largest signals, particularly for the two protons in the *ortho* position to the nitrogen atom, were observed at a PTF of between 6.5×10^{-3} T and 7.5×10^{-3} T for both OPSY-dq (Figure 148) and OPSY-zq which is consistent with what was observed for pyridine. A minor pair of enhanced hydride signals are also seen in these experiments which are proposed to correspond to a conformational isomer of the active catalyst species, due to ring-flip of the seven-membered metallocycle as discussed previously in Sections 2.3 and 2.4.

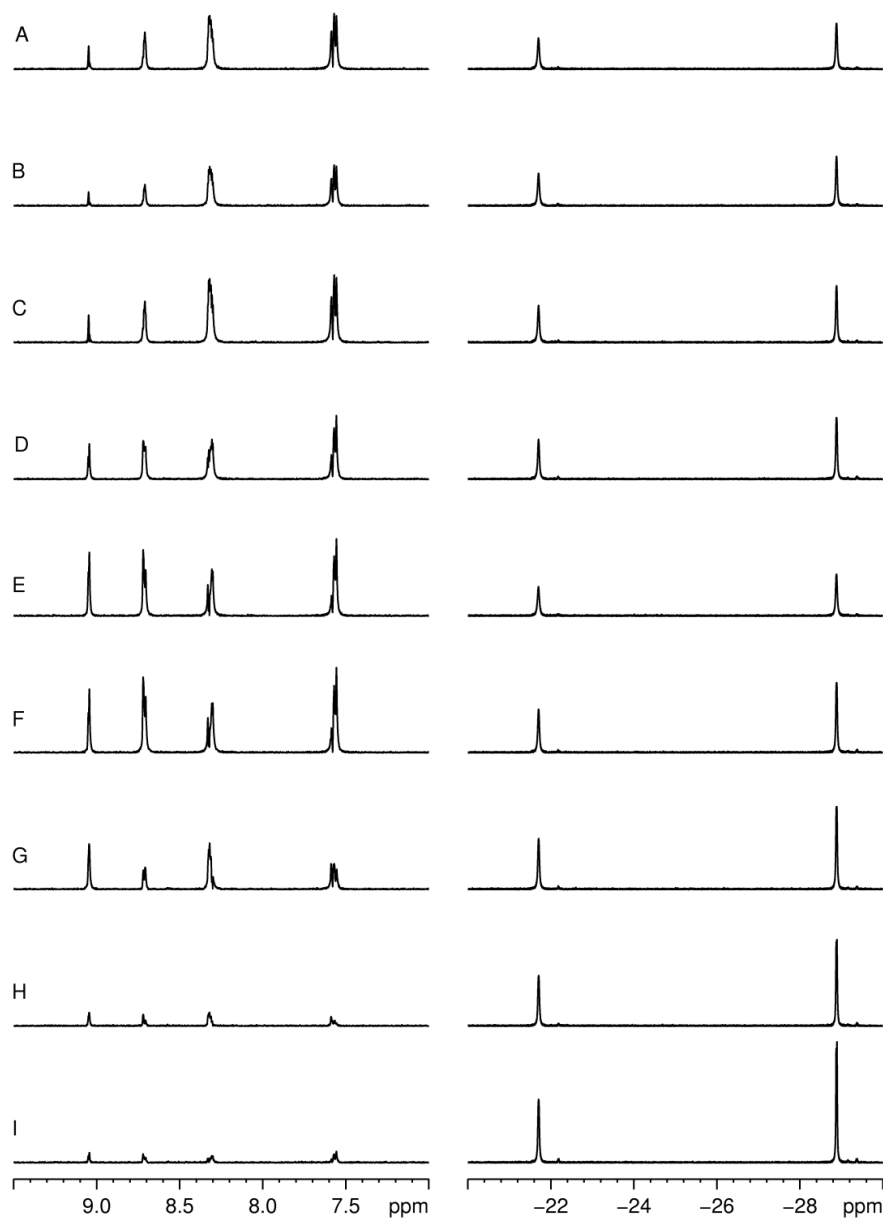


Figure 148: ^1H OPSY-dq NMR spectra of a sample containing 0.1 M nicotinamide and 5 mol% **1** in CD_3OD after polarisation transfer from $p\text{-H}_2$ at r.t. and; (A) 2.5×10^{-3} T; (B) 0×10^{-4} T; (C) -2.5×10^{-3} T; (D) -5×10^{-3} T; (E) -6.5×10^{-3} T; (F) -7.5×10^{-3} T; (G) -1×10^{-2} T; (H) -1.25×10^{-2} T; (I) -1.5×10^{-2} T

4.3.1.4. Proton signal enhancements as a function of temperature

Despite the signal enhancements being much less for nicotinamide when compared to pyridine using **1** (see Section 4.2.1.4), the same increasing trend in enhancements is observed as the temperature is increased. This is true for the PTFs of 2×10^{-4} T and 6.5×10^{-3} T (Figure 149). Again, when using [Ir(COD)(IMes)Cl], the signal enhancements at both magnetic fields reach a plateau at about room temperature (see Figure 150). As for **1** with pyridine, it is expected that the exchange rates would increase as the temperature increased and therefore at the higher temperatures the rates would be optimum for polarisation transfer. The maximum enhancement observed here for [Ir(COD)(IMes)Cl] corresponds to a temperature of ~ 30 °C, which is comparable to that seen for pyridine as the substrate (see Section 4.2.1.4). Therefore, it would be expected that the optimum exchange rates for polarisation transfer would be at this temperature. At higher temperatures, the rates become too fast so that the enhancements level off and as the temperature is increased further, the enhancements would eventually decrease.

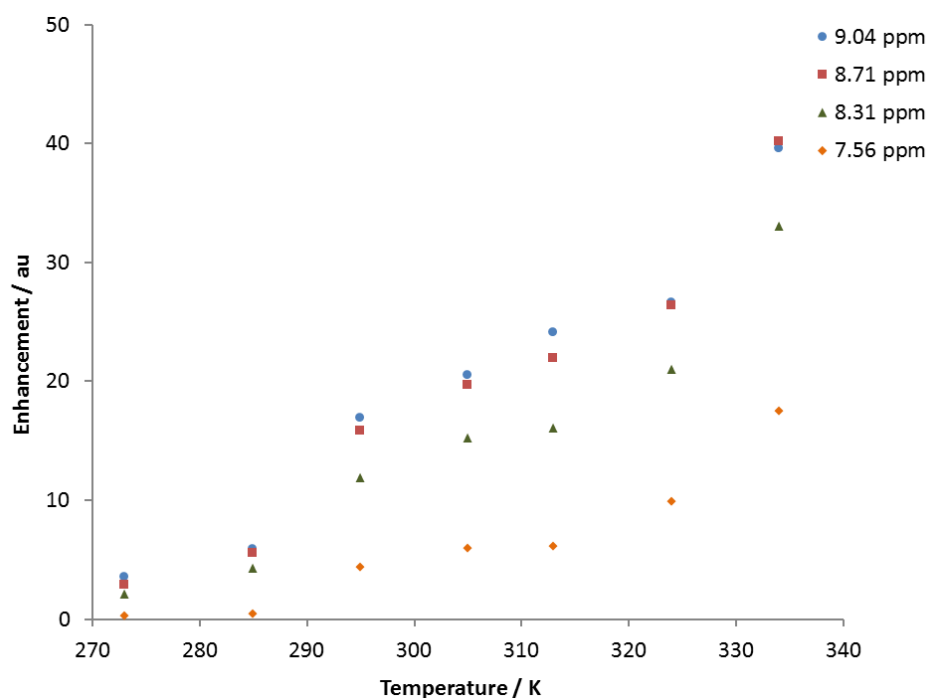


Figure 149: Nicotinamide proton enhancements as a function of temperature after polarisation transfer from $p\text{-H}_2$ using 5 mol% **1** and 0.1 M pyridine at 6.5×10^{-3} T

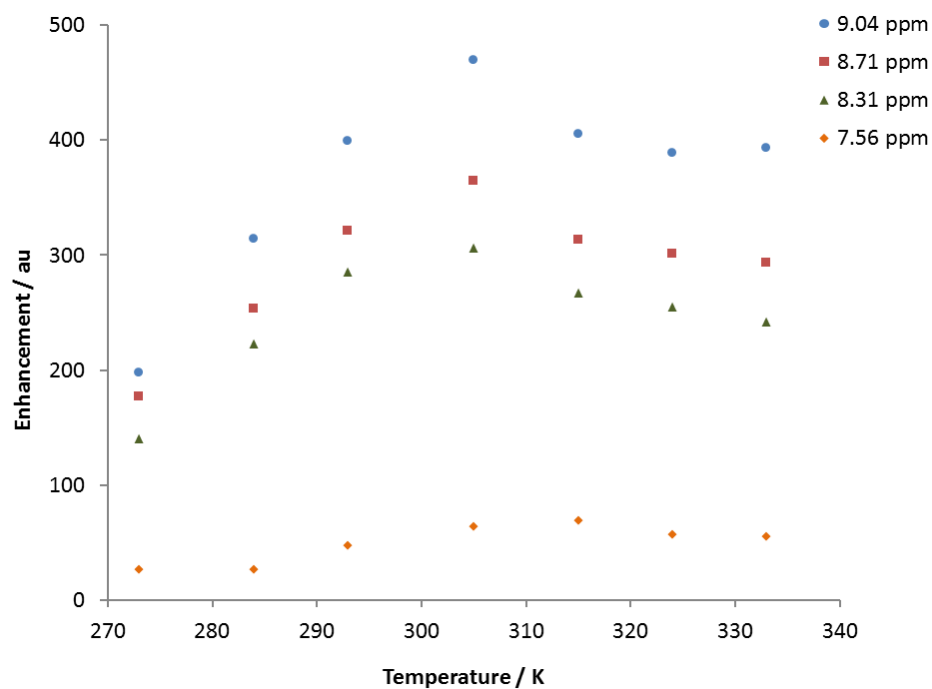


Figure 150: Nicotinamide proton enhancements as a function of temperature after polarisation transfer from $p\text{-H}_2$ using 5 mol% $\text{Ir}(\text{COD})(\text{IMes})\text{Cl}$ and 0.1 M pyridine at $6.5 \times 10^{-3} \text{ T}$

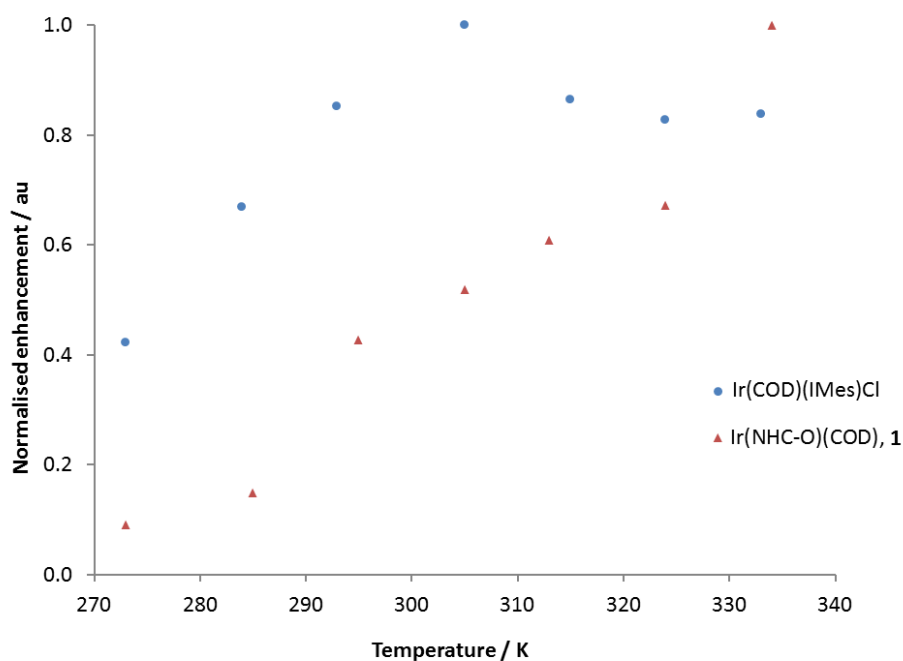


Figure 151: Temperature effects on normalised enhancements of the H_A ^1H NMR resonance of nicotinamide after polarisation transfer using $p\text{-H}_2$ at $6.5 \times 10^{-3} \text{ T}$; one containing nicotinamide (0.1 M) and $\text{Ir}(\text{COD})(\text{IMes})\text{Cl}$ (5 mol%) in CD_3OD (0.6 ml) and one containing nicotinamide (0.1 M) and **1** (5 mol%) in CD_3OD (0.6 ml).

4.3.2. Studies using complex 2 with nicotinaldehyde

Another pyridine derivative that was investigated was nicotinaldehyde, with the structure shown in Figure 152, due to it being a liquid and having high solubility in C_6D_6 , CD_2Cl_2 and CD_3OD . Other pyridine derivatives such as nicotinamide proved to be insoluble in CD_2Cl_2 and C_6D_6 and so could not be investigated further. The signal enhancements for the protons of nicotinaldehyde in C_6D_6 and CD_2Cl_2 after 48 hours are given in Table 35.

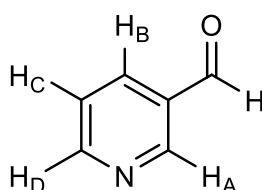


Figure 152: Nicotinaldehyde showing labelling of protons

Table 35: Nicotinaldehyde proton enhancement values using 0.05 M nicotinaldehyde with 14 mol% 2 in C_6D_6 and CD_2Cl_2 after activation for 48 hours and 5 days under 3 bars of H_2 at $6.5 \times 10^{-3} T$

Solvent	Starting material: Product ratio	Nicotinaldehyde 1H NMR SABRE enhancement (fold)				
		H	H _A	H _B	H _C	H _D
C_6D_6	~ 54: 46 (48 h)	74 ± 11	226 ± 10	183 ± 14	105 ± 15	209 ± 10
CD_2Cl_2	~ 30: 70 (48 h)	100 ± 11	486 ± 36	400 ± 32	148 ± 34	396 ± 65
C_6D_6	0: 100 (5 days)	75 ± 16	259 ± 17	209 ± 22	118 ± 22	244 ± 18
CD_2Cl_2	0: 100 (5 days)	81 ± 10	372 ± 25	318 ± 26	140 ± 22	314 ± 28

Retesting of these samples after 5 days showed that all the starting material had reacted. However, a slight decrease in the average enhancement factors was observed when using CD_2Cl_2 as the solvent, although there was a slight increase when using C_6D_6 , as detailed in Table 35. When analysing the spectra obtained from polarisation transfer studies, it was noted that in C_6D_6 and CD_2Cl_2 the major enhanced peaks are those corresponding to free nicotinaldehyde in solution as shown in Figure 153.

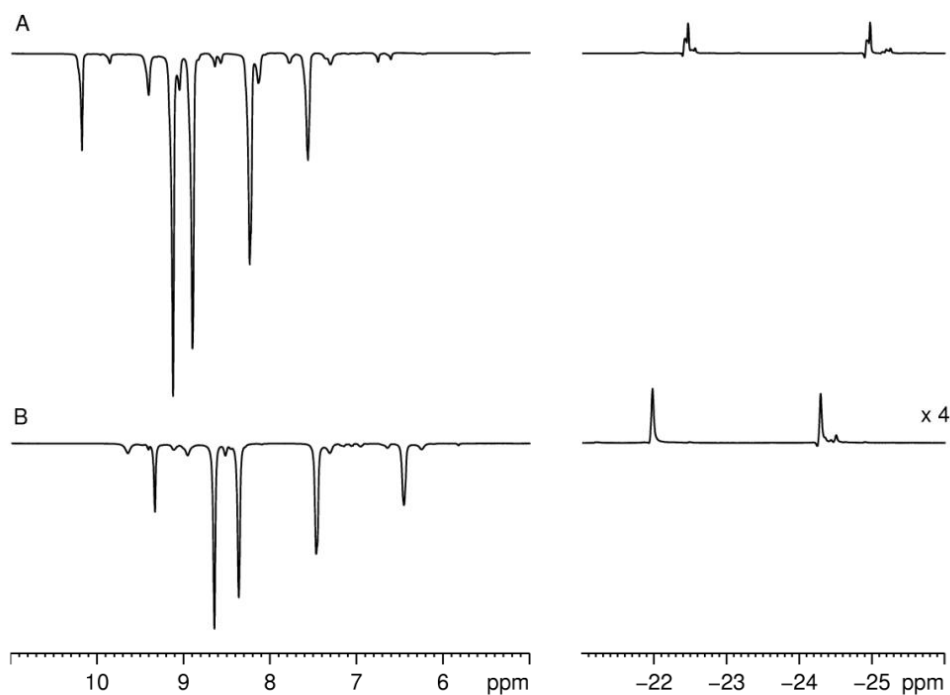


Figure 153: ^1H NMR spectra after shaking a 0.05 M nicotinaldehyde sample containing 14 mol% **2** in CD_2Cl_2 (A) and C_6D_6 (B) with $p\text{-H}_2$ at 6.5×10^{-3} T

The ^1H NMR chemical shifts of the hydride ligands present in the CD_2Cl_2 and C_6D_6 samples containing nicotinaldehyde enables the identification of their corresponding structures. The chemical shifts are very similar to the equivalent complexes formed when the substrate used is pyridine and thus the SABRE-active complexes formed here are the nicotinaldehyde derivatives of complex **8**.

In contrast, the CD_3OD sample shows enhanced signals for free nicotinaldehyde as well as another species containing aromatic protons. This is because nicotinaldehyde is not stable in methanol, but instead reacts in solution to form a hemiacetal.

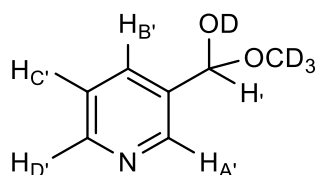


Figure 154: The structure and proton labels of the hemiacetal form of nicotinaldehyde

Figure 154 shows the structure of the hemiacetal species with the nicotinaldehyde: hemiacetal ratio being 1: 3, in a CD₃OD solution containing 0.05 M nicotinaldehyde. The enhanced ¹H NMR spectrum of this sample is shown in Figure 155, with the aromatic region of the spectrum expanded in Figure 156 along with labelled structures of nicotinaldehyde and its hemiacetal form.

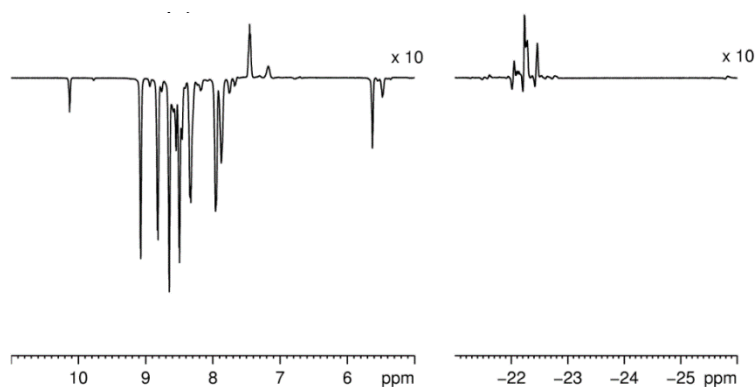


Figure 155: ¹H NMR spectrum after shaking a 0.05 M nicotinaldehyde sample containing 14 mol% **2** in CD₃OD with *p*-H₂ at 6.5×10^{-3} T at 298 K

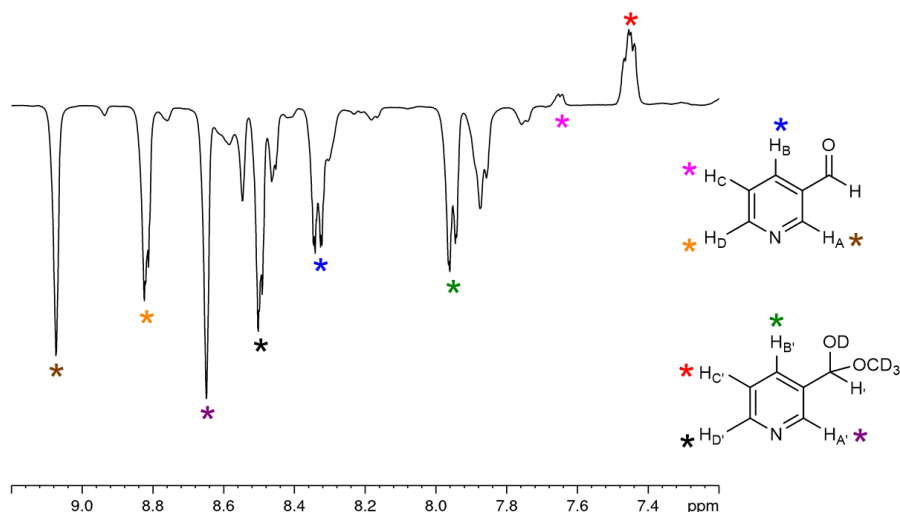


Figure 156: Aromatic region of the ¹H NMR spectra after shaking a 0.05 M nicotinaldehyde sample containing 14 mol% **2** in CD₃OD with *p*-H₂ at 6.5×10^{-3} T at 298 K, with the labelled structures and their corresponding ¹H NMR signals

Table 36: The proton enhancement values of nicotinaldehyde and its hemiacetal form, using a CD_3OD solution of 0.05 M nicotinaldehyde with 14 mol% **2** after 48 hours and 5 days at 6.5×10^{-3} T and 298 K

Substrate	1H label	Chemical shift / δ	1H NMR SABRE enhancement (fold)	
			After 48 h	After 5 days
Nicotin-aldehyde	H	10.13	7 ± 2	6 ± 1
	H _A	9.07	52 ± 8	41 ± 5
	H _B	8.33	67 ± 12	54 ± 6
	H _C	7.66	2 ± 2	2 ± 2
	H _D	8.82	57 ± 7	45 ± 5
Hemi-acetal form	H'	5.63	17 ± 4	12 ± 2
	H _A '	8.65	62 ± 7	49 ± 6
	H _B '	7.95	59 ± 10	41 ± 5
	H _C '	7.46	26 ± 7	22 ± 2
	H _D '	8.50	65 ± 6	63 ± 7

The signal enhancements of each proton of both nicotinaldehyde and its hemiacetal form are given in Table 36. They show that the aldehyde proton of nicotinaldehyde, and the same proton in the hemiacetal form after nucleophilic addition of methanol, are both enhanced. This polarisation arises from the 4J -coupling to the aromatic protons on the pyridyl ring and thus demonstrates that longer range coupling and transfer across other atoms is possible.

There are also multiple enhanced hydride signals observed in Figure 155, commensurate with several different SABRE-active catalysts present in solution. Since methanol can also act as a ligand in the SABRE process and receive polarisation (as observed in this study), many methanol-containing species are also present as depicted

in Figure 157. The wide variety of dihydride complexes present in solution explains the complicated hydride region of the ^1H NMR spectra.

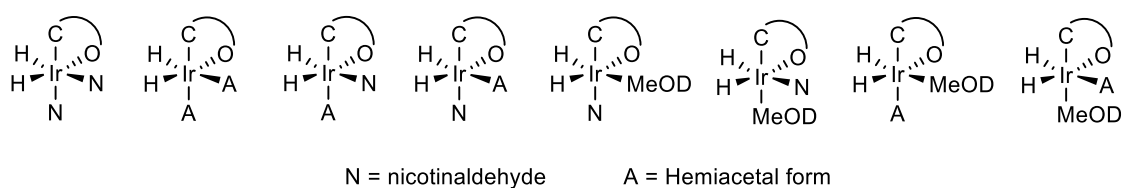


Figure 157: Different SABRE-active complexes formed in CD_3OD

4.3.3. Studies using complex 2 with nicotine

To look at a more biologically relevant molecule that still contains a pyridyl ring and exhibits good solubility in the desired solvents, (*S*)-nicotine was chosen. SABRE enhancements were analysed in C_6D_6 , CD_2Cl_2 and CD_3OD and were found to be more than ten times better in both C_6D_6 and CD_2Cl_2 when compared to CD_3OD .

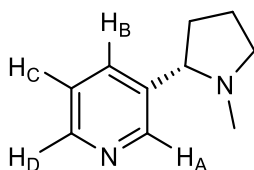


Figure 158: Nicotine showing labelling of protons

Table 37: ^1H NMR signal enhancements of the aromatic protons of nicotine using 0.05 M nicotine with 14 mol% **2** in the specified solvents under 3 bars of $p\text{-H}_2$ at 298 K and 6.5×10^{-3} T

Solvent	Nicotine ^1H NMR SABRE enhancement (fold)			
	H_A	H_B	H_C	H_D
C_6D_6	400 ± 54	315 ± 48	88 ± 30	338 ± 80
CD_2Cl_2	419 ± 51	381 ± 48	146 ± 44	386 ± 55
CD_3OD	29 ± 4	28 ± 3	3 ± 3	31 ± 3

As expected, both samples in CD_2Cl_2 and C_6D_6 at 298 K showed two major PHIP enhanced hydride signals at δ -22.60 and -25.44 in CD_2Cl_2 and at δ -21.85 and -24.33 in C_6D_6 . Several minor non-PHIP active hydrides were also visible. In CD_3OD , the Ir-O bond is again broken, consistent with the reactivity observed using pyridine and nicotinaldehyde. However, two enhanced hydride signals are visible at δ -22.21 and -22.27 as shown in Figure 159.

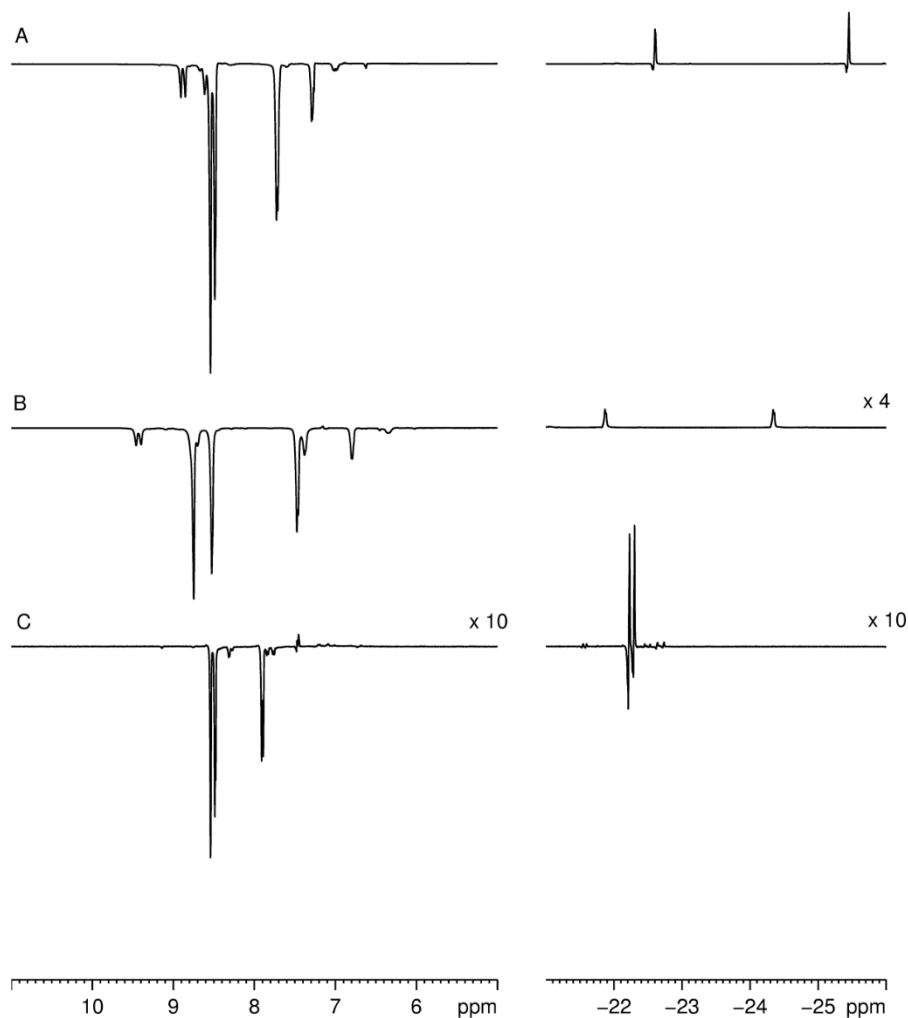


Figure 159: ^1H NMR spectra after shaking a 0.05 M nicotine sample containing 14 mol% **2** in CD_2Cl_2 (A), C_6D_6 (B) and CD_3OD (C) with $p\text{-H}_2$ at 6.5×10^{-3} T

On closer inspection, for the sample in CD_2Cl_2 , the thermal signal at δ -22.60 appears as two overlapping doublets after multiple scans, which both show a coupling constant of 7.5 Hz (see Figure 160). These are equal to the coupling corresponding to the doublet hydride signal at δ -25.44 . Upon cooling the sample to 240 K, both hydride signals now appear as two overlapping doublets with a common coupling constant of \sim

7.5 Hz (see Figure 160). For the C_6D_6 sample at 298 K, the two hydride signals also appear as overlapping doublets with common coupling constants of ~ 7.4 Hz. It is assumed that the same case exists here as for CD_2Cl_2 but the relatively high melting point of C_6D_6 prohibited lower temperature studies.

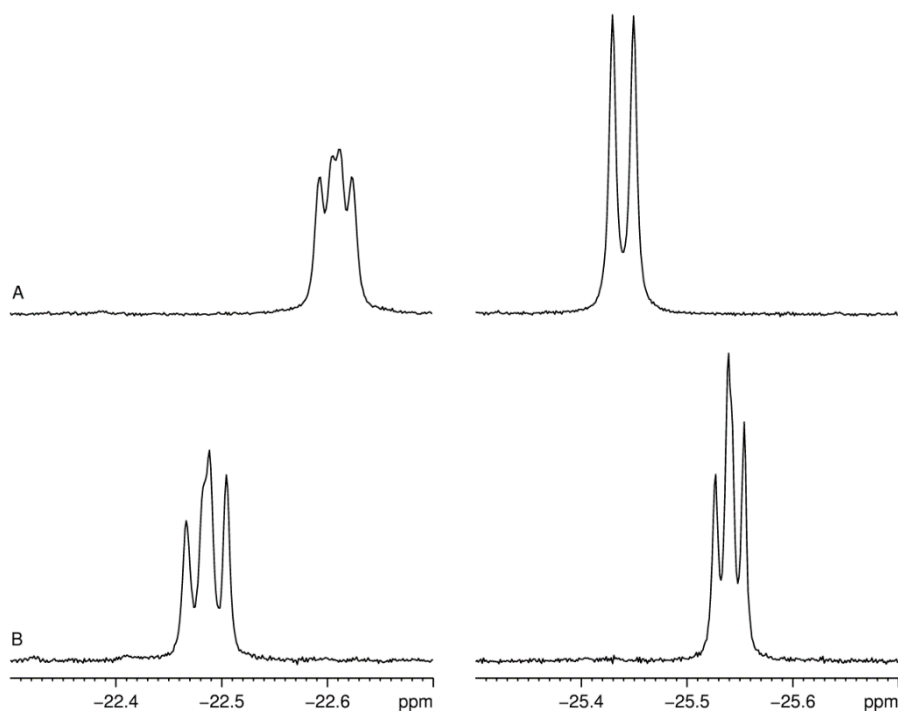


Figure 160: 1H NMR spectra of the major hydride signals present in a solution of δ_{nicotine} in CD_2Cl_2 at 298 K (A) and 240 K (B)

The fact that all three samples contain double sets of hydride signals is consistent with two isomers of δ_{nicotine} forming in solution. This is due to nicotine being chiral, which leads to the formation of two different species in each solution. This occurs when the nicotine ligand and oxygen ligand, that lie in the same plane as the hydride ligands, exchange positions due to nicotine exchange. This is discussed in detail in Section 3.2.1 for the substrate pyridine. The corresponding isomers are depicted in Figure 161. The aromatic regions of the 1H NMR spectra are also considerably complicated on cooling, as would be anticipated for solutions containing two very similar species in equilibrium.

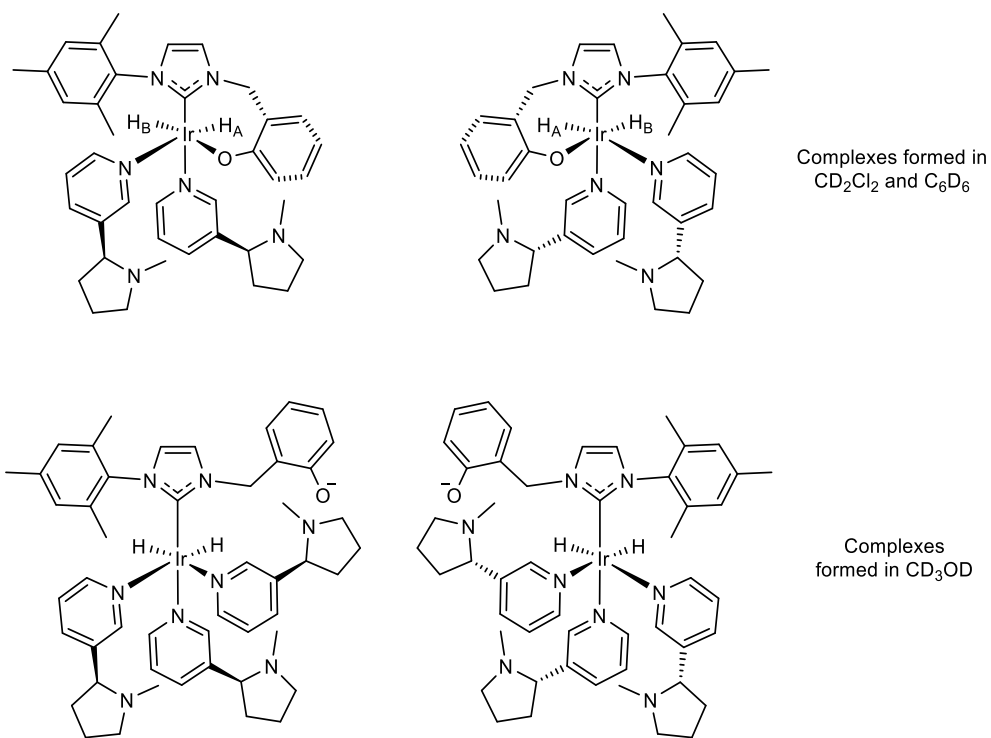


Figure 161: The isomers of δ_{nicotine} formed in CD₂Cl₂, C₆D₆ and CD₃OD, depending on the orientation of the chiral nicotine ligands

4.4. Conclusion

Due to the neutral nature of the bidentate iridium carbene complexes, and their ability to undergo both substrate and H₂ exchange, efficient polarisation transfer catalysis is observed in a wide range of solvents when the complexes are reacted with substrate under *p*-H₂. When using **6**, pyridine and nicotinamide demonstrate good levels of hyperpolarisation, achieved via the SABRE approach, with polarisation of both proton and carbon nuclei being possible. Complex **6** remains neutral in solution due to retention of its iridium-oxygen bond, in both polar protic, aprotic and non-polar solvents such as methanol, dichloromethane and benzene. The higher solubility of the pre-catalyst, **1**, in dichloromethane and benzene aids its reactivity, when compared to that in methanol and ethanol. For THF, the total associated ¹H NMR signal enhancements for the protons of pyridine show an increase of 1200-fold. Complexes **2**, **3** and **4**, once all activated with substrate and *p*-H₂, also all undergo substrate and hydrogen exchange and thus act as efficient SABRE catalysts, with the highest signal enhancements using each catalyst typically being observed in CD₂Cl₂. The best signal enhancements of the protons of pyridine are shown for each pre-catalyst in Table 38.

Table 38: Summary of the ¹H NMR signal enhancements for the protons of pyridine for samples of each pre-catalyst in CD₂Cl₂ at 298 K and 6.5 x 10⁻³ T

Pre-catalyst	R	Hammett parameter σ_p^-	Sample in CD ₂ Cl ₂	Pyridine ¹ H NMR SABRE enhancement (fold)		
				<i>ortho</i>	<i>meta</i>	<i>para</i>
1	NO ₂	1.27	0.05 M py 15 mol% 1	316 ± 68	237 ± 80	141 ± 33
2	H	0.00	0.07 M py 10 mol% 2	877 ± 32	337 ± 57	450 ± 22
3	COOMe	0.75	0.06 M py 10 mol% 3	778 ± 65	370 ± 78	416 ± 37
4	Cl	0.19	0.08 M py 9 mol% 4	1113 ± 137	586 ± 119	651 ± 78

The polarisation transfer process depends on several factors, which have been investigated to optimise the catalytic system. The ligand exchange rates during the SABRE process are very important to ensure the desired coupling network is established to enable polarisation transfer. In the polar aprotic and non-polar solvents, the ligand exchange rates are increased as described in Section 3.2.4 and here this is shown to correspond to larger signal enhancements. However, these ligand exchange processes adversely affect the T_1 relaxation of the protons of pyridine and therefore at low temperature, when exchange is inhibited, T_1 values of free pyridine increase whilst those of bound pyridine ligands decrease. This exemplifies the important role the catalyst plays in accelerating the relaxation of the substrate ligands.

Temperature also plays an important role in SABRE catalysis, with the level of signal enhancement being increased further through warming. The largest signal enhancements for both pyridine and nicotinamide were achieved at the highest temperature of ~ 330 K that could be safely studied. This is in stark contrast to the trend observed for $[\text{Ir}(\text{COD})(\text{IMes})\text{Cl}]$, where its optimum operating temperature has been reported as 274 K.⁹³ The magnetic field experienced by the sample at the point of catalytic magnetisation transfer is also particularly critical for SABRE. The most efficient Polarisation Transfer Field for both pyridine and nicotinamide, using the solvent methanol, was found to be $\sim 6.5 \times 10^{-3}$ T. The observations described here reflect a dramatic improvement in solvent tolerance of SABRE over that reported for the current best polarisation transfer catalysis precursor, $[\text{Ir}(\text{COD})(\text{IMes})\text{Cl}]$.

5. Optimisation of SABRE catalysis for a new ligand class

5.1. Introduction

Thus far, there are many examples in the literature demonstrating the hyperpolarisation of nitrogen-containing aromatic heterocycles, with pyridine being the model substrate as exemplified by the large number of publications detailing SABRE experiments.^{2, 79, 88, 93, 107-108, 225, 234-235} A significant amount of work has also been completed using pyridine derivatives such as nicotinamide.^{96, 236} One example uses nicotinic acid-modified oligopeptides²³⁷ with polarisation of the protons of the pyridyl unit acting as an NMR handle due to observation of enhanced signals. However, enhancements of the oligopeptides themselves are not observed. Some examples of heterocycles which demonstrate enhanced aromatic proton signals are shown in Figure 162.^{81, 84, 94, 97, 113, 238} Studies using pyridine and other derivatives are exemplified in this work, in Chapter 4.

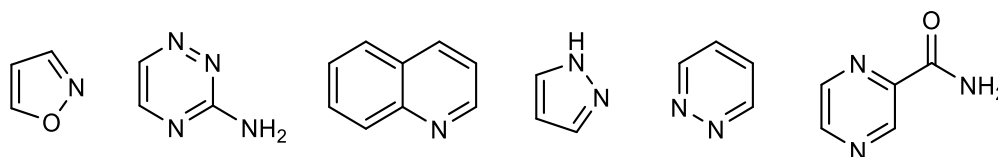


Figure 162: Nitrogen-containing heterocycles (from left to right); isoxazole,⁸¹ 3-amino-1,2,4-triazine,¹¹³ quinolone,²³⁸ pyrazole,⁸⁴ pyridazine,⁹⁴ and pyrazinamide⁹⁷

However, only a few examples of polarisation transfer to different ligand classes exist. One such example⁹⁹ demonstrates the feasibility of the SABRE process for polarising cyano-containing substrates such as acetonitrile, propionitrile and benzylnitrile, with an in-depth experimental and theoretical analysis completed using acetonitrile. Here, the atom which binds to the metal centre to aid polarisation transfer is still a nitrogen atom. This work shows the importance of establishing a coupling network between the *p*-H₂ derived hydride ligands and protons of the substrate ligands, as when the CH₃ group of acetonitrile was replaced with a CD₃ group, no polarisation transfer was observed.⁹⁹

In 2011, a study by Glögger et al.²³⁹ detailed signal enhancements of amino acids and oligopeptides in CD₃OD at very low magnetic field when Crabtree's catalyst was used. Binding of the amino acids was postulated to occur in two ways as shown in Figure 163, to facilitate polarisation transfer. The amino acids described are glycine, histidine and phenylalanine along with the oligopeptides Glycine-Glycine and Proline-Histidine-Leucine.

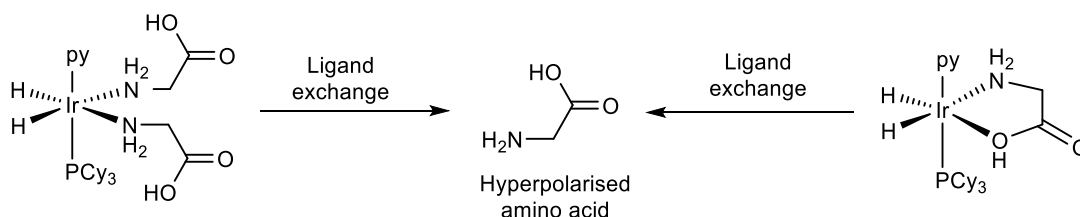


Figure 163: Two proposed binding modes between amino acids and activated Crabtree's catalyst that enable polarisation transfer when reacted with *p*-H₂²³⁹

Another example by Moreno et al.²⁴⁰ describes the observation of enhanced signals for the solvent, methanol, in which SABRE transfer is conducted. The enhanced proton signal that is observed is due to residual CD₃OH in the solution and they propose two mechanisms for its polarisation; either direct polarisation transfer via solvent binding (also noted previously⁸⁴ and as occurs for the heterocyclic substrates) or via proton exchange in acidic medium. The proton exchange route to polarisation transfer is shown in Figure 164.

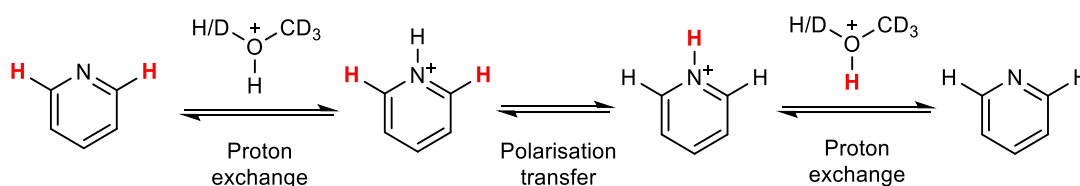


Figure 164: Route to observing enhanced signals for the solvent OH peak occurring via proton exchange in acidic medium²⁴⁰

Within the literature, the majority of hyperpolarisation experiments are conducted in deuterated protic solvents, with the most common being methanol. This therefore becomes a problem when any substrates that have exchangeable protons want to be exploited, as rapid H/D exchange with deuterated methanol occurs, inhibiting the SABRE process.⁸⁴ If systems containing exchangeable protons also contain an aromatic

nitrogen atom, then binding and SABRE activity in methanol is still possible, as demonstrated for the substrates pyrazole⁸⁴ and 4-aminopyridine.²⁴¹ However, the amino protons are not observed and thus cannot be analysed directly.

Amino groups are ubiquitous in nature. They are vital to life due to their presence in amino acids which make up peptides in all living things. Amino acids are also biochemical precursors to amine molecules and their degradation leads to the formation of amines. One example is the formation of serotonin from the amino acid tryptophan, via two enzymatic steps involving tryptophan hydroxylase and a carboxylase enzyme as shown in Figure 165.²⁴² This leads to formation of the important neurotransmitter serotonin, which is commonly associated with a feeling of happiness and well-being. Other important neurotransmitters incorporating amine functionalities include norepinephrine, dopamine and histamine and these are also shown in Figure 165.

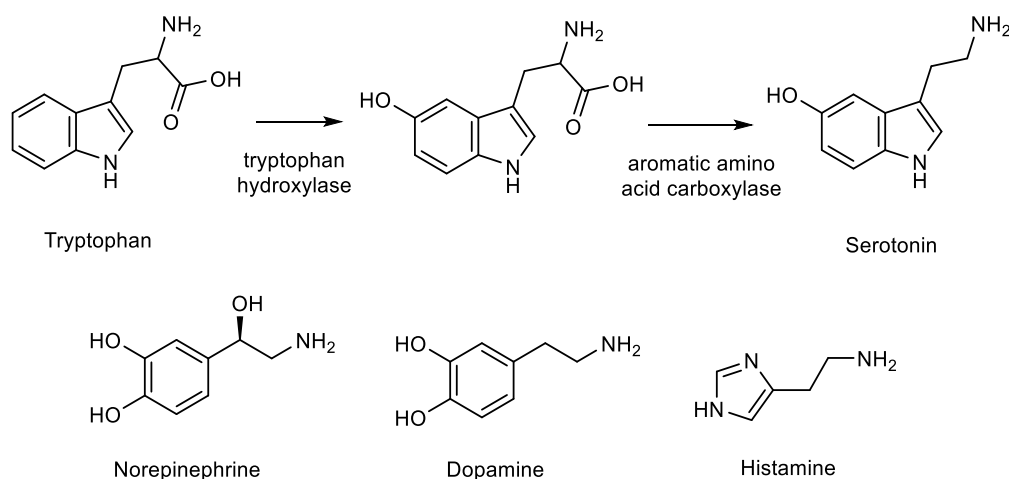


Figure 165: Biosynthesis of serotonin from tryptophan in the body²⁴² and structures of some other amine-containing neurotransmitters; norepinephrine, dopamine and histamine

Since amines are found throughout the body, particularly within the brain, amine-containing molecules are of huge pharmaceutical importance. This is because their biological activity can often be used to mimic or inhibit the action of the natural amines themselves or other species which can affect the natural amines. They can therefore serve as highly active and effective drugs to treat several illnesses. For example, drugs which act to increase the amount of serotonin are often targets for treatments for depression and anxiety, since serotonin is associated with positive moods.

One way to achieve this is to target the metabolic pathway that acts to decrease the availability of monoamine neurotransmitters. Many drug types have thus been developed as monoamine oxidase inhibitors (MAOI).²⁴³ These act to prevent the breakdown of monoamine neurotransmitters and thus increase their concentration within the body. They can therefore act as effective antidepressants. Some examples are shown in Figure 166.

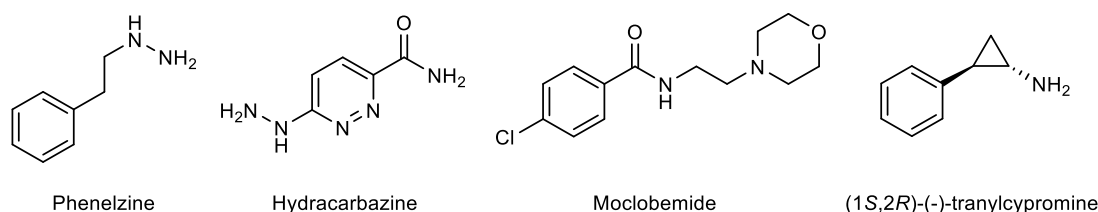


Figure 166: Examples of monoamine oxidase inhibitors containing amine groups; the amine is present as a hydrazine group in phenelzine and hydracarbazine, an amide group in moclobemide and a primary amine in (1S,2R)-(-)-tranylcypromine

Another important type of widely used drug is anaesthetics. There are two main classes of local anaesthetics; ester-containing compounds and amide-containing compounds. A number of these also contain amine functionalities as shown by the two structures in Figure 167. These local anaesthetics work by binding to sodium channels to prevent the propagation of impulses along a nerve.²⁴⁴⁻²⁴⁵

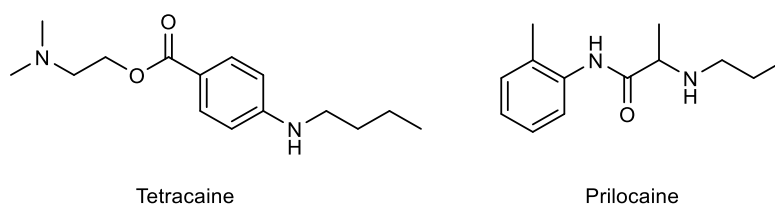


Figure 167: The structures of two local anaesthetics, tetracaine and prilocaine, both containing amine functionalities

Amines also have many industrial applications. One important industrial reaction is the Haber-Bosch process; the direct formation of ammonia from hydrogen and nitrogen. High temperatures of between 400 and 500 °C and high pressures of up to 250 bars are required, along with a heterogeneous metal catalyst.²⁴⁶ The catalyst is iron oxide-based, typically containing other metal oxides such as calcium, silicon and aluminium. The porosity of the material ensures a large surface area for the reaction to

occur and unreacted gases are recovered and reacted again to produce high yields of ammonia. The largest use of the ammonia produced in this process is as agricultural fertiliser to grow food crops, with other uses being as a household cleaner and as an important precursor for amine synthesis.

There are also several other industrial areas which rely on amine molecules. Many synthetic dyes are based on the aniline motif²⁴⁷⁻²⁴⁹ and are thus needed in order to form azo dyes, which have intense colours due to their highly active chromophore regions. The structure of aniline yellow is shown in Figure 168, with the azo region highlighted.

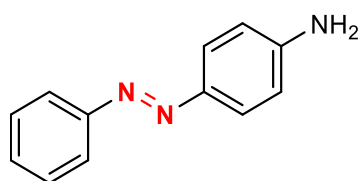


Figure 168: The structure of aniline yellow with the azo group highlighted in red

Fatty amine compounds are also important as they are widely used in formulations such as in the healthcare industry in personal care products and as additives in the lubricants industry. They are typically synthesised from naturally derived fatty acids via reaction with ammonia to form fatty nitrile compounds, followed by hydrogenation of the nitrile to form the fatty amine derivatives. These molecules act as surfactants due to their hydrophilic amine head groups and hydrophobic hydrocarbon chains and can thus reduce friction and corrosion in engines and emulsify cosmetic formulations.

This chapter focuses on a few amine molecules as substrates for the SABRE process. Some of the amine compounds employed are known neurotransmitters and are thus biologically compatible, which could prove important for MRI applications in the future. Complex **1** is used as the SABRE pre-catalyst due to its improved stability over the other bidentate carbene complex derivatives developed in this work.

5.2. Analysing polarisation transfer to amines

This section includes an analysis of several amino-containing substrates, from the simplest amine, ammonia, to the biologically relevant tryptamine molecule and investigates their reactivity with complex **1** in CD_2Cl_2 under an atmosphere of H_2 . The substrate molecules, ammonia, benzylamine, phenethylamine and tryptamine, are shown to react with complex **1** in the presence of H_2 to form several reactive complexes in solution, some of which undergo the relevant exchange processes that lead to observation of the SABRE effect in the proton resonances of the amine molecules. These tests reveal the formation of complex mixtures in solution, and a number of these species exhibit very broad signals due to the amine substrates being poor ligands and undergoing rapid ligand and proton exchange. These reasons thus precluded full characterisation of all the associated complexes and instead specific indicative ^1H NMR signals for particular complexes were used to aid individual assignments.

For a generic amine substrate, N, multiple different species exist as exemplified in Figure 169 and described for the specific amine substrates ammonia, benzylamine, phenethylamine and tryptamine respectively, in the following sections. The formation of these different species is substrate dependent and where possible, full characterisation of complexes containing specific substrates has been detailed in the following sections or given in the Experimental Sections 8.6.6 to 8.6.17. Otherwise, the complexes presented, are described based on similar species observed with different amine substrates and the hydride ligand signals are detailed.

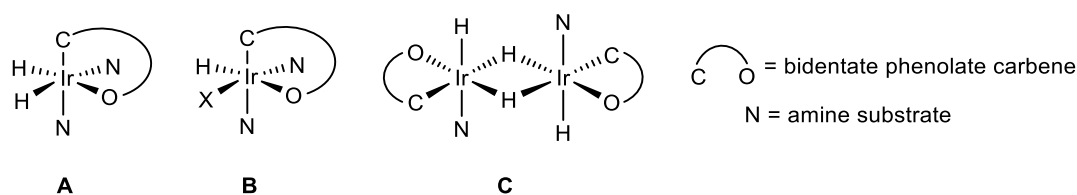


*Figure 169: Summary of the different complexes formed when **1** is reacted with an amine substrate in the presence of H_2 where **A** is the expected SABRE-active product as observed when pyridine is the substrate, **B** is a singlet hydride species which does not undergo PHIP and **C** is a dimer species seen at low concentrations of substrate*

5.2.1. Ammonia

In order to test the binding and polarisation transfer to the simplest amine, ammonia, enough gas to create a 0.1 M solution of ammonia was transferred, via a high vacuum line, into a CD_2Cl_2 solution containing 5 mol% **1**. After addition of H_2 and analysis with $p\text{-H}_2$ at 298 K after 48 hours of activation, the effect of polarisation transfer was evident in the ^1H NMR spectrum for free and bound NH_3 as well as for several hydride ligands. However, the signals were not enhanced and all signals were broad. Two broad hydride resonances corresponding to the SABRE-active iridium complex, **6**_{ammonia}, were seen at $\delta -23.15$ and -30.63 and the structure shown in Figure 170 is proposed based on that observed when pyridine is the substrate, as discussed in Section 2.4.1. A set of four sharper coupled hydride signals at $\delta -26.00$, -26.45 , -30.62 and -30.80 were also evident. These correspond to a dimeric species, **21**_{ammonia}, such as that depicted in Figure 170. However, their low concentration precluded full characterisation (see Section 5.2.3 for an in-depth discussion of the dimer present when the substrate is phenethylamine). To enable more accurate measurements and better control over the amount of amine used, liquid amines were then exploited.

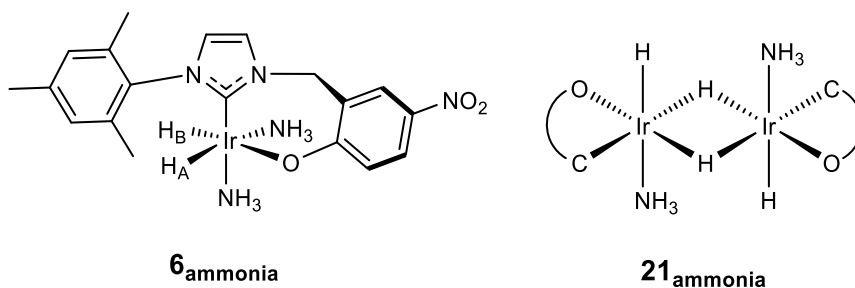


Figure 170: The SABRE-active monomer species, **6**_{ammonia}, and a postulated dimeric structure, **21**_{ammonia}

5.2.2. Benzylamine

Benzylamine was chosen as another simple amine. After activation of a CD_2Cl_2 sample containing 6.5 mol% **1** and enough benzylamine (18 equivalents) to form a 0.08 M solution, under 3 bars of H_2 at 298 K, two main species are evident, in an approximate ratio of 45: 55. The first species contains a pair of very broad hydride signals at approximately $\delta -23$ and -30 . Upon the addition of *p*- H_2 to this sample at 298 K, these two signals demonstrate slight PHIP along with enhanced signals for the protons of benzylamine as shown in Figure 171. These signals arise from the SABRE-active species, **6**_{benzylamine}, as shown in Figure 172 and as described for the substrate ammonia in Section 5.2.1.

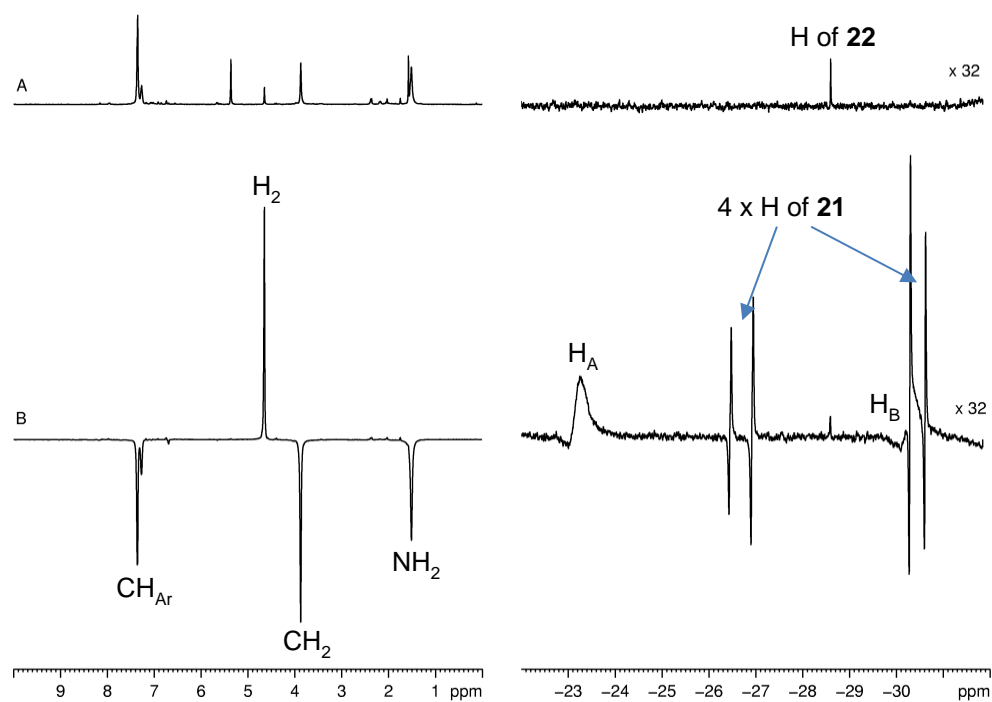


Figure 171: Single scan ^1H NMR spectra at thermal equilibrium (A) and on the addition of *p*- H_2 at 6.5×10^{-3} T (B) showing the polarised hydride ligands and the SABRE-enhanced benzylamine signals

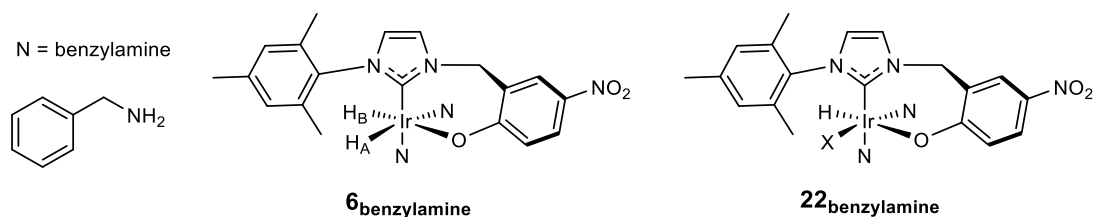


Figure 172: SABRE-active species **6**_{benzylamine} and complex **22**_{benzylamine} containing only one hydride ligand, formed on reaction of benzylamine with **1** in CD₂Cl₂ under 3 bars of H₂

The second species contains a sharp singlet hydride signal at $\delta -28.60$ which corresponds to a hydride ligand that lies *trans* to the phenolate arm. When examined with *p*-H₂, this singlet hydride signal shows no enhancement, indicating no ligand exchange. The structure for this species is shown as **22**_{benzylamine} in Figure 172, with the full structure shown in Figure 173. Full characterisation data are given in the Experimental Section 8.6.7. The ¹H NMR spectrum only shows four aromatic signals for the benzylamine ligand *trans* to the carbene ligand, consistent with C-H activation of the aromatic ring of benzylamine. Thus the coordination site labelled X in Figure 172 is a carbon atom. This is also commensurate with that observed for tryptamine as discussed in detail in Section 5.2.4. Upon cooling this sample to 258 K, the hydride ligands that correspond to **6**_{benzylamine} are considerably sharper and slightly shifted to $\delta -22.88$ and -30.50 . The hydride signal at $\delta -28.60$ for species **22**_{benzylamine} is not affected.

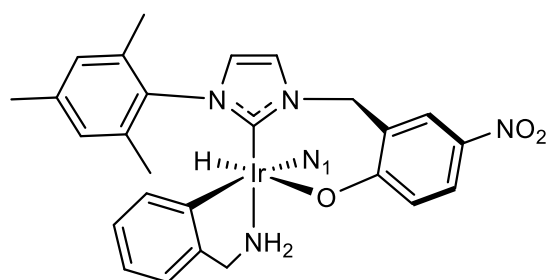


Figure 173: Full structure of complex **22**_{benzylamine} (*N*₁ signifies benzylamine)

Four much sharper PHIP enhanced hydride signals are also observed in the ¹H NMR spectrum at $\delta -26.45$, -26.94 , -30.30 and -30.63 when this sample is examined with *p*-H₂ at 298 K (see Figure 171). These are like those observed with ammonia as described in Section 5.2.1. This species is labelled **21**_{benzylamine} in Figure 174. Thermally these signals are only observed after a considerable number of scans and thus the

enhanced signals for the hydride ligands of **21**_{benzylamine} when using *p*-H₂ exemplify a major benefit of PHIP, in that previously unidentifiable minor species are seen.

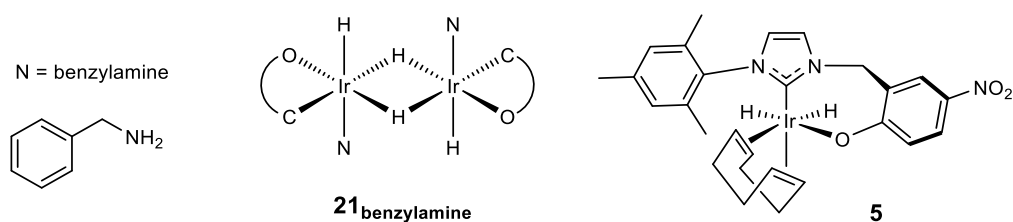


Figure 174: Iridium dimer **21**_{benzylamine} and the alkene-dihydride species **5**, formed on reaction of benzylamine with **1** in CD₂Cl₂ under 3 bars of H₂

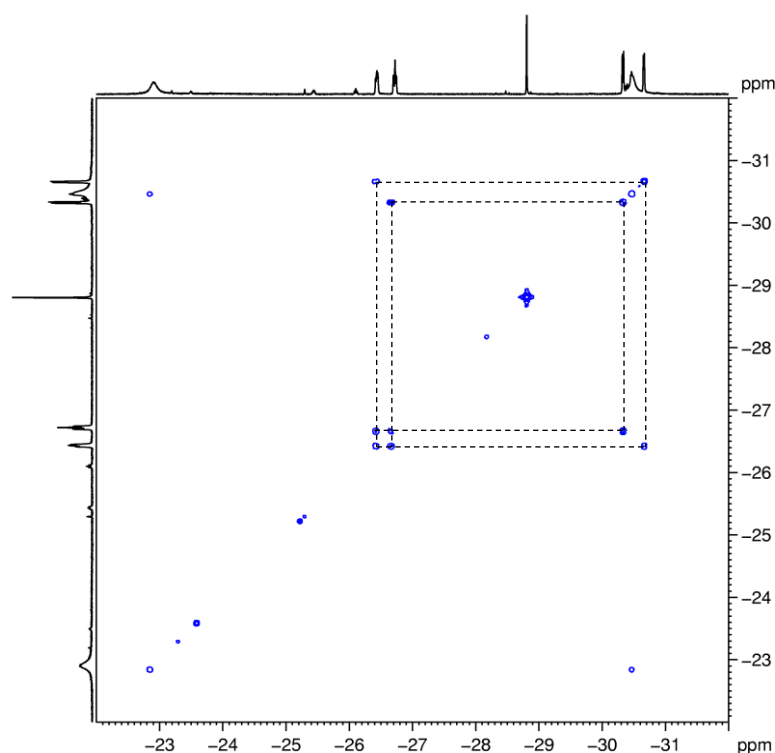


Figure 175: ¹H COSY NMR spectrum showing coupling between the four hydride signals of **21**_{benzylamine}

On cooling to 258 K, the four sharp hydride signals still exchange with *p*-H₂ and are shown to couple via a ¹H COSY NMR spectrum (see Figure 175). The two resonances, at about δ -27, are both doublets of doublets; at δ -26.45 with coupling constants of 5.6 and 9.0 Hz and at δ -26.72 with coupling constants of 8.1 and 9.0 Hz. The two at about δ -31 are doublets; at δ -30.33 with a coupling constant of 8.1 Hz and at δ -30.66 with a coupling constant of 5.6 Hz. Hence the formation of a tetrahydride-

containing species is confirmed, although further characterisation was again unachievable. A further species also becomes visible at 258 K, containing another pair of very broad hydride signals at δ -12.83 and -19.54 which corresponds to the alkene-dihydride intermediate **5** that still contains COD. This is common in these complexes, as previously detailed in Section 2.4.1, and proton resonances for the bound alkene protons exist at δ 2.69 and 2.44. The H₂ exchange at 298 K is too fast for this species to be observed, due to broadening of the signals into the baseline of the NMR spectrum as described previously in Section 2.4.2. However, after longer time periods it converts into the benzylamine-containing complexes with full hydrogenation of the COD.

Upon cooling to 258 K the ratio of **6**: **22**: **21**: **5** for this benzylamine-containing sample is approximately 51: 40: 3: 6 after 6 days of activation at room temperature under 3 bars of H₂. Upon decreasing the amount of benzylamine in solution, the amount of **21**_{benzylamine} increases such that a sample containing approximately two equivalents of benzylamine (0.03 M solution of benzylamine and 33 mol% **1**), at 263 K, contains a ratio of **6**: **22**: **21**: **5** of about 38: 24: 32: 5 after 5 days of activation under 3 bars of H₂. Characterisation of **21**_{benzylamine} is hindered by the overlapping of its corresponding ¹H NMR peaks.

Detailed in Table 39 are the corresponding SABRE ¹H NMR signal enhancements for the proton sites of benzylamine. It is obvious that polarisation is transferred a long distance through the molecule and that this is more effective when less benzylamine is used, even though the proportion of **6**_{benzylamine} drops.

*Table 39: SABRE ¹H NMR signal enhancements at 298 K and 6.5×10^{-3} T for the two samples containing 6.5 mol% **1** and 0.08 M benzylamine (~ 18 eq.) and 33 mol% **1** and 0.03 M benzylamine (~ 2 eq.)*

Proton signal of benzylamine	5 x CH _{Ar}	CH ₂	NH ₂
Thermal signal integral	5	2	2
Enhanced signal for ~ 18 eq. of benzylamine	8 ± 1	9 ± 1	7 ± 1
Enhanced signal for ~ 2 eq. of benzylamine	19 ± 1	4 ± 1	2 ± 1

5.2.3. Phenethylamine

To see if the polarisation could be transferred further within a molecule, phenethylamine was tested, as compared to benzylamine, it has one more CH₂ group between the amine and the aromatic ring. A CD₂Cl₂ sample containing approximately 33 mol% **1** and enough phenethylamine for a 0.03 M solution was prepared and both the SABRE-active species, **6**_{phenethylamine}, and the dimer, **21**_{phenethylamine}, were formed. Both complexes demonstrated PHIP, with the corresponding ¹H NMR signal intensity gains for the five aromatic protons and the two CH₂ groups of phenethylamine being 24 ± 3, 11 ± 1 and 13 ± 1-fold respectively, demonstrating therefore, a total signal increase for the protons of phenethylamine of approximately five times larger than the equivalent thermal signal. When the concentration of phenethylamine in solution was increased, such that the sample contained 5 mol% **1** and 0.1 M phenethylamine, the intensity gains decreased to approximately 3 ± 1 and 4 ± 1-fold for the two CH₂ groups of phenethylamine. The enhancement of the NH₂ group could not be quantified due to signal overlap, which led to the thermal signal corresponding to more than two protons. In this system, no singlet hydride signal was observed.

Complex **6**_{phenethylamine} showed very broad hydride signals at δ -23.20 and -30.60 which sharpened on cooling to 263 K. At 263 K, the four hydride signals for **21**_{phenethylamine} appear at δ -26.33, -26.71, -30.59 and -30.97. The two resonances at about δ -27 are again doublets of doublets; at δ -26.33 with coupling constants of 6.0 and 8.8 Hz and at δ -26.71 with coupling constants of 8.0 and 8.8 Hz. The two at about δ -31 are doublets; at δ -30.59 with a coupling constant of 8.0 Hz and at δ -30.97 with a coupling constant of 6.0 Hz. The ratio **6**: **21** was approximately 68: 32 at 263 K. Complex **21**_{phenethylamine} forms due to the low amount of amine present in solution and thus the complexes dimerise to stabilise the iridium metal centres. Therefore, when a sample containing only one equivalent of phenethylamine relative to pre-catalyst was prepared and activated under 3 bars of H₂ for 4 days, species **21**_{phenethylamine} was the only major species present in solution. When the sample was shaken with *p*-H₂ no enhancements were observed, showing that the route to PHIP enhancement of the hydride ligands of **21**_{phenethylamine} is via dimer cleavage, H₂ exchange and subsequent dimer reformation, which can only be possible when more than one equivalent of

substrate is present in solution. Hence, alone, this complex is not responsible for the SABRE activity.

Several tetrahydride iridium dimer species have been described in the literature that have similar structures to that proposed for **21**_{phenethylamine}. Three species are shown in Figure 176. Complexes A and B, described by Gruber et al. in 2013,²⁵⁰ form via addition of hydrogen and in the presence of acetonitrile or DCM respectively. Complex A has hydride ligand signals that appear at δ -17.77, -18.00, -20.04 and -20.24 in the ¹H NMR spectrum and on replacement of acetonitrile with DCM these shift to δ -16.15 and -26.46, and demonstrate more fluxional behaviour due to the weakly binding DCM molecules and their exchange with the bulk solvent. The hydride region of the ¹H NMR spectrum of complex A is shown in Figure 177, with the four terminal and bridging hydride ligands being inequivalent due to the orientation of the *iso*-propyl groups on the ligand. This is also commensurate with the complex being asymmetric.

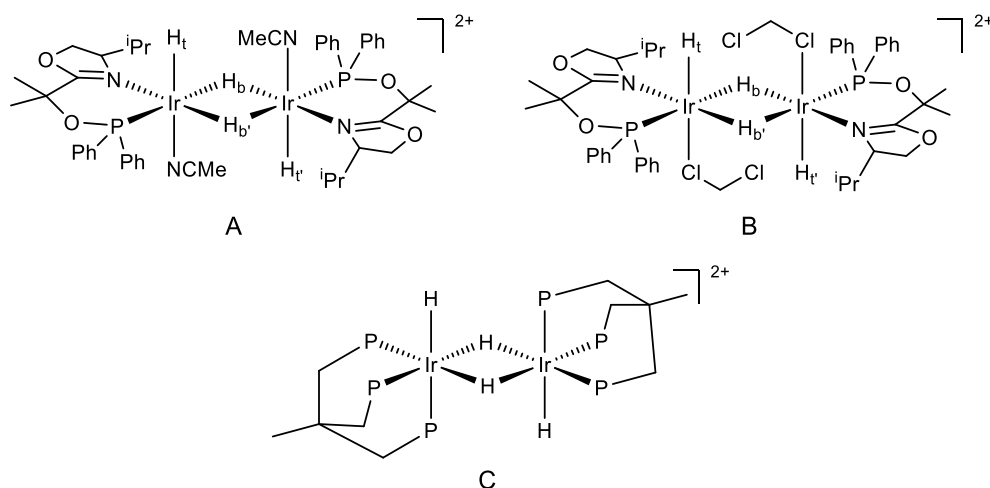


Figure 176: Three tetrahydride iridium dimer species described by Gruber et al.²⁵⁰ (A and B) and Bianchini et al.²⁵¹ (C)

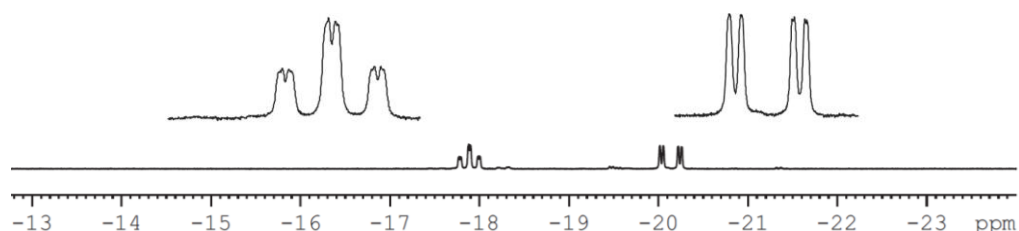


Figure 177: The hydride region of the ¹H NMR spectrum for complex A as detailed in Figure 176 (Reprinted with permission from Gruber, S.; Neuburger, M.; Pfaltz, A. *Organometallics* **2013**, *32*, 4702. Copyright © 2013 American Chemical Society)²⁵⁰

In the proposed structure of **21**_{phenethylamine} the inequivalent hydride signals arise due to the bent conformation and thus differing orientations of the seven-membered metallocyclic carbene ligand. This is equivalent to that observed for complex A shown in Figure 176 where the bidentate backbone and the fact that the two *iso*-propyl groups point downwards, lead to the hydride ligands becoming inequivalent as shown in the ¹H NMR spectrum of the hydride region of complex A in Figure 177.²⁵⁰

Complex C as shown in Figure 176, containing a tridentate phosphine ligand (triphos), was described by Bianchini et al.²⁵¹ in 1993 and was found to form in the solid state via dimerisation of an [Ir(H)₂(triphos)][BPh₄] fragment. This fragment formed from ethene loss from [Ir(H)₂(triphos)(C₂H₄)] [BPh₄]. The same ligand dissociation step from complex **6**, [Ir(H)₂(NHC-O)(amine)₂], to form [Ir(H)₂(NHC-O)(amine)] (which is a necessary mechanistic step in the SABRE process) can be followed by dimerisation rather than ligand binding when low concentrations of ligand are present. This leads to the formation of the dimer complex, **21**_{phenethylamine}. The structure of **21**_{phenethylamine} is given in Figure 178 and its characterisation data are given in the Experimental Section 8.6.6. Multiple overlapping signals due to the very similar chemical shifts of the two bidentate carbene ligands and the multiple amine ligands, means that in some cases full characterisation is not possible. At 243 K, a minor isomer is also present with hydride ligand signals at δ -25.33 (dd, ²J(HH) = 6.1, 7.8 Hz), -26.03 (dd, ²J(HH) = 7.8, 7.8 Hz), -30.46 (d, ²J(HH) = 6.1 Hz) and -30.53 (d, ²J(HH) = 7.8 Hz). Its very low concentration precluded full characterisation.

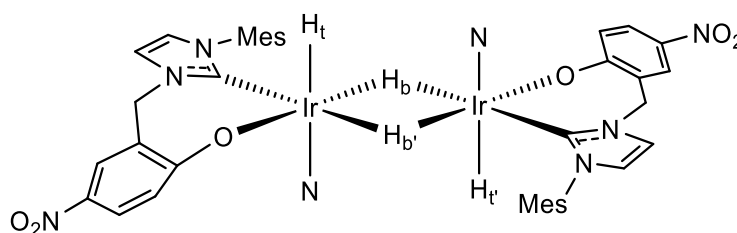


Figure 178: Line drawing of complex **21**_{phenethylamine} (*N* signifies phenethylamine)

5.2.4. Tryptamine

To expand the range of amines that could be polarised, the biologically relevant minor neurotransmitter tryptamine was chosen. Upon activation of a CD_2Cl_2 sample containing approximately 12 mol% **1** and enough tryptamine for a 0.04 M solution with H_2 at 298 K, one major species was formed in ~ 96 % yield with a minor species contributing the other ~ 4 %. The low solubility of tryptamine in CD_2Cl_2 meant higher concentrations of tryptamine could not be used. The minor species present in solution contained two inequivalent hydride ligands at δ -22.90 and -30.55 which were both broad at 298 K. Upon addition of *p*- H_2 , this species, **6**_{tryptamine} demonstrated SABRE and the two hydrides were evident as enhanced broad signals. Polarisation transfer was also seen to the NH_2 , two CH_2 groups and some aromatic protons of the tryptamine ligand although the signals were not enhanced. A dimer species, **21**_{tryptamine}, is also evident, and seen only under PHIP conditions, with enhanced ^1H NMR signals for the hydride ligands at δ -26.30, -26.85, -30.61 and -31.02. These structures are shown in Figure 179.

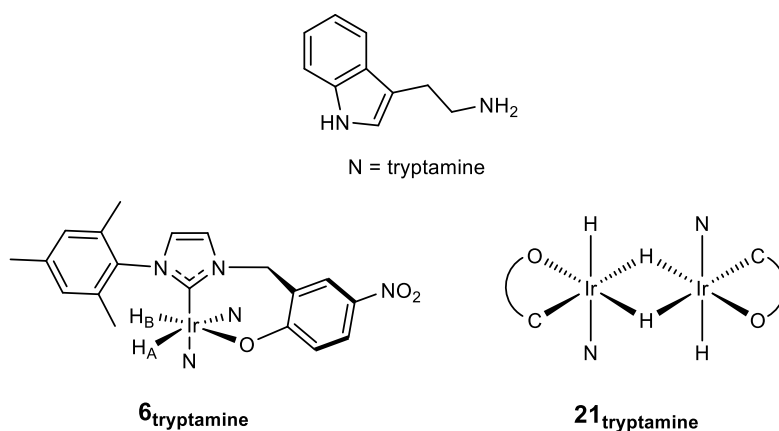
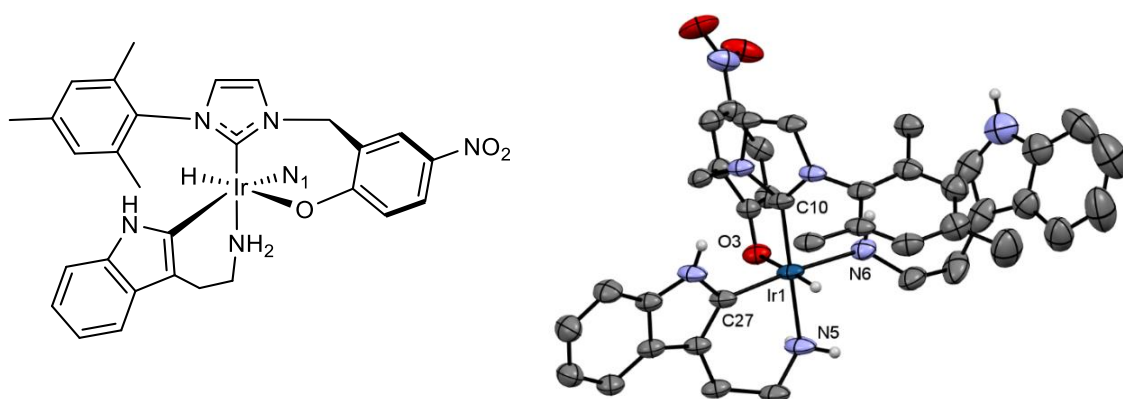


Figure 179: The structure of tryptamine, the SABRE-active monomer species, **6**_{tryptamine}, and the dimeric structure, **21**_{tryptamine} formed on reaction of tryptamine with **1** in CD_2Cl_2 under H_2

However, the major species, **22**_{tryptamine}, containing one singlet hydride signal in the ^1H NMR spectrum at δ -28.93, demonstrated no PHIP upon reaction with *p*- H_2 . The structure of **22**_{tryptamine} was confirmed by X-ray crystallography, in collaboration with Adrian Whitwood, Sam Hart and Rachel Bean in the XRD department at York. It is depicted in Figure 180 as an ORTEP plot, where the sixth ligand in the octahedral complex was identified as a carbon atom, due to C-H activation of the five-membered

ring of one of the tryptamine ligands (C27 in Figure 180) to form a six-membered metallocycle. The primary amine of each tryptamine ligand also binds to the iridium metal centre. A crystal suitable for X-ray diffraction was grown via the slow diffusion of toluene into a concentrated DCM solution of the complex. It crystallised in the R-3 space group, yielding unit cell parameters for a, b and c of 48.3824(6), 48.3824(6) and 10.78400(10) Å respectively and for α , β and γ of 90, 90 and 120 ° respectively. Key data for bond lengths and angles are shown in Table 40. The geometry around the iridium centre is distorted octahedral with the corresponding bond angles all being close to 90 °.



*Figure 180: ORTEP plot of **22**_{tryptamine}, showing the C-H activated metallocycle, with H atoms (apart from NH, NH₂ and hydride ligand) omitted for clarity and the thermal ellipsoids set at a 50 % probability level*

Table 40: Selected bond lengths and angles for the crystal structure of **22**_{tryptamine} as shown in Figure 180

Atoms	Length / Å	Atoms	Angle / °
Ir-O	2.235(2)	C(carbene)-Ir-O	97.69(10)
Ir-C(carbene)	1.985(3)	C(carbene)-Ir-C27	93.36(12)
Ir-C27	2.018(3)	C(carbene)-Ir-N5	177.15(11)
Ir-N5	2.136(3)	C(carbene)-Ir-N6	92.88(10)
Ir-N6	2.200(2)	O-Ir-C27	95.36(11)
		O-Ir-N5	79.74(10)
		O-Ir-N6	81.70(9)
		N5-Ir-N6	85.55(10)
		C27-Ir-N5	88.12(11)
		C27-Ir-N6	173.40(11)

5.2.5. Summary

Overall, these complexes, where weakly binding ligands have been used as substrates, demonstrate instability and degradation. This is potentially due to the very weak interactions not providing enough electron density to stabilise the iridium catalysts and intermediates. To aid stabilisation a neutral, strongly coordinating ligand could be added, such as triphenylphosphine. Previous work utilising Crabtree's catalyst has shown that incorporation of an NHC, as well as the existing phosphine ligand, has enabled the production of more stable, catalytically active complexes.²⁵²⁻²⁵⁴ Combining both a phosphine and an NHC has also been exploited previously for SABRE catalysts as reported by Fekete et al. in 2013.⁸⁶

5.3. Exploiting PPh₃ to aid complex stabilisation

5.3.1. Addition of PPh₃ to samples containing pyridine

To try and stabilise these amine-containing iridium carbene dihydride complexes, triphenylphosphine was chosen to be added as an extra ligand to samples using **1**. It was thought that the PPh₃ would bind *trans* to the carbene (as similar SABRE catalysts have been made previously)⁸⁶ thus creating only one site for substrate binding, therefore aiding stabilisation. Initially it was decided to add PPh₃ to complex **6**_{pyridine} in CD₂Cl₂ as the chemistry of this species has been well studied (see Section 2.4.1).²⁵⁵ On addition of PPh₃ a new species formed immediately and NMR spectroscopy confirmed that it contained the bidentate carbene, two hydride ligands, one pyridine ligand and one PPh₃ ligand. However, this was not the expected complex as the PPh₃ coordinated *trans* to a hydride ligand by replacing the labile pyridine ligand, thus blocking the pyridine exchange site required for SABRE, to form **23**_{pyridine} as shown in Figure 181. Therefore, due to this pyridine dissociation pathway no longer being available, no PHIP was observed thermally with *p*-H₂. This species is therefore the kinetic product as it is most easily and rapidly formed as the pyridine ligand is labile so can simply be replaced. At 298 K, the two hydride ligands, which share a common ²*J*(HH) coupling constant of 4.8 Hz, appear at δ -8.50, with a *trans* ²*J*(HP) coupling constant of 162.8 Hz, and at δ -27.32 with a *cis* ²*J*(HP) coupling constant of 10.8 Hz. This product formed due to the pyridine ligand *trans* to the hydride ligand being labile and the other pyridine ligand *trans* to the carbene being strongly bound.

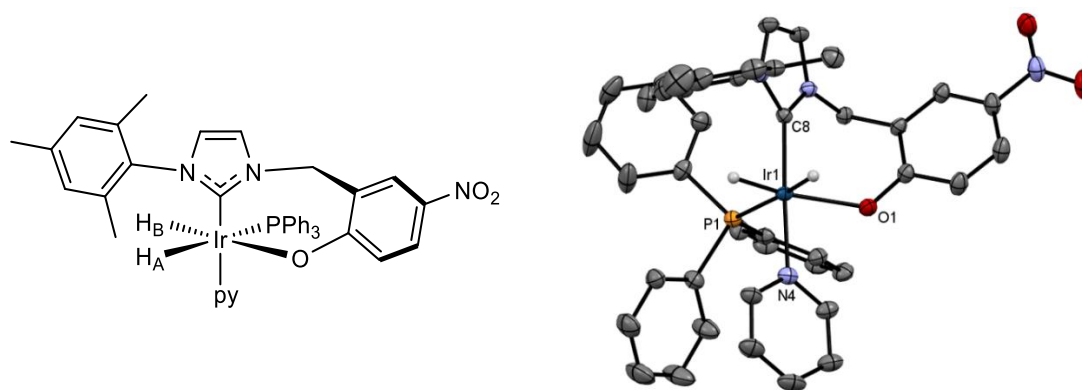


Figure 181: ORTEP plot of **23**_{pyridine} with solvent and H atoms omitted for clarity and the thermal ellipsoids set at a 50 % probability level

The crystal structure of **23**_{pyridine} is also shown in Figure 181 as an ORTEP plot and was determined in collaboration with Adrian Whitwood, Sam Hart and Rachel Bean in the XRD department at York. A single crystal, suitable for X-ray diffraction was grown via the slow diffusion of toluene into a concentrated solution of the complex in DCM. It crystallised into the $P2_12_12_1$ space group, yielding unit cell parameters for a, b and c of 13.63451(11), 16.69609(15) and 21.33132(16) Å respectively and for α , β and γ of 90, 90 and 90 ° respectively. Key data for bond lengths and angles are shown in Table 41. The geometry around the iridium centre is distorted octahedral with the corresponding bond angles all being close to 90 °. Full NMR characterisation data for **23**_{pyridine} are given in the Experimental Section 8.6.9.

Table 41: Selected bond lengths and angles for the crystal structure of **23**_{pyridine} as shown in Figure 181

Atoms	Length / Å	Atoms	Angle / °
Ir-O	2.218(3)	C(carbene)-Ir-O	95.22(12)
Ir-C(carbene)	1.978(3)	O-Ir-P	102.64(8)
Ir-P	2.3491(9)	O-Ir-N	84.92(11)
Ir-N	2.138(3)	C(carbene)-Ir-P	96.17(10)
		C(carbene)-Ir-N	173.39(13)
		P-Ir-N	90.24(8)

To determine whether the PPh₃ would always bind *trans* to a hydride, a CD₂Cl₂ sample of **1** with pyridine was remade, adding the PPh₃ to **1** and pyridine in CD₂Cl₂ and then activating under an atmosphere of H₂. This time, the reaction took several days to go to completion at room temperature and the species that formed was thus the more stable thermodynamic product, **24**_{pyridine}, as shown in Figure 182. The PPh₃ ligand is now *trans* to the carbene which reduces steric interactions, and the pyridine ligand is *trans* to a hydride ligand. The two hydride ligands now undergo exchange with H₂ thermally so demonstrate PHIP and SABRE when in the presence of *p*-H₂ and appear as very broad singlets at δ -21.73 and -28.93 at 298 K. On cooling to 273 K the hydride signals broaden into the baseline due to the exchange no longer being fast enough to be averaged and resolved in the ¹H NMR experiment. Upon heating to 303 K, they now appear as two broad doublets due to a common *cis* ²*J*(HP) coupling constant of 18.4 Hz with the ²*J*(HH) coupling not being visible due to the much more rapid H₂ exchange. The bis-phosphine complex, **25**, is also formed when excess phosphine is added. This complex does not demonstrate PHIP as the SABRE pyridine dissociation mechanism cannot occur. Upon the addition of further phosphine, all of **24**_{pyridine} converted into **25** (see Figure 182). The hydride signals for **25**, which share a common ²*J*(HH) coupling constant of 4.7 Hz, appear in the ¹H NMR spectrum at δ -9.6 and at δ -27.9 (which also has two ²*J*(PH_{*cis*}) coupling constants of 13.4 Hz). The signal at δ -9.6 also demonstrates a ²*J*(PH_{*cis*}) coupling constant of 22.9 Hz, and a much larger ²*J*(PH) coupling constant of 138.6 Hz, indicative of it also lying in a *trans* position to a PPh₃ ligand.

Photochemical PHIP of **25** was also investigated, however, no *p*-H₂ exchange was observed. The complex absorbs very weakly at 355 nm, the wavelength of the laser used, as the charge-transfer bands that can exist for these types of species and can be excited photochemically come at much higher energy.¹⁶⁶⁻¹⁶⁷ Characterisation data for **24**_{pyridine} and **25** are included in the Experimental Sections 8.6.10 and 8.6.11 respectively. Only partial characterisation data were obtained for **24**_{pyridine}, due to it undergoing rapid exchange and thus exhibiting some broad signals, for example for the CH₂ linker protons.

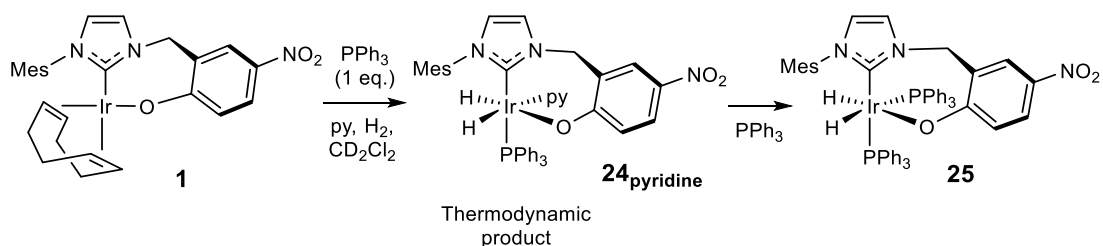


Figure 182: Formation of complex **24**_{pyridine} and **25**, with excess *PPh*₃ in solution

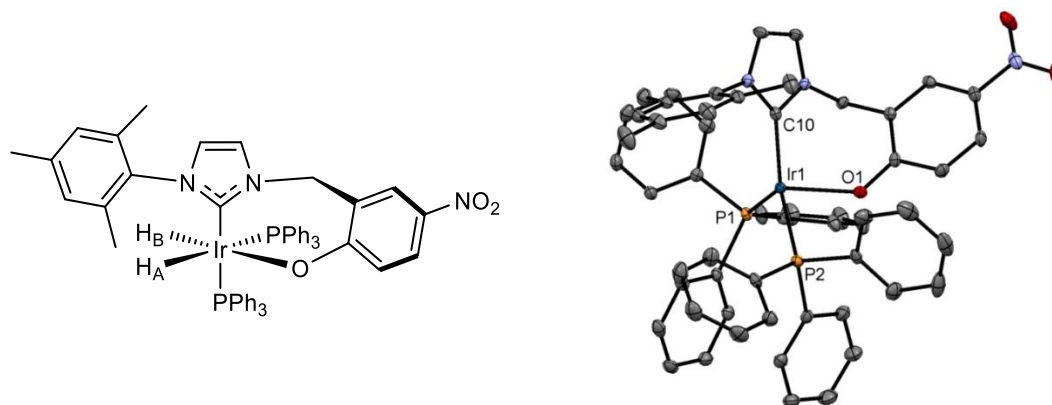


Figure 183: ORTEP plot of **25** with solvent and H atoms omitted for clarity and the thermal ellipsoids set at a 50 % probability level

The crystal structure of **25** is shown in Figure 183 as an ORTEP plot and was determined in collaboration with Adrian Whitwood, Sam Hart and Rachel Bean in the XRD department at York. A single crystal, suitable for X-ray diffraction, was grown from a concentrated solution of **25** in DCM. It crystallised into the $P2_1$ space group, yielding unit cell parameters for *a*, *b* and *c* of 13.01715(19), 15.90413(14) and 13.68980(17) Å respectively and for α , β and γ of 90, 113.2175(16) and 90 ° respectively. The residual electron density was 1 e Å⁻³ indicating a clean single crystal. Key data for bond lengths and angles are shown in Table 42. It is very like **23**_{pyridine}, with the geometry around the iridium centre again being distorted octahedral and the corresponding bond angles all being close to 90 °.

Table 42: Selected bond lengths and angles for the crystal structure of **25** as shown in Figure 183

Atoms	Length / Å	Atoms	Angle / °
Ir-O	2.226(2)	C(carbene)-Ir-O	94.95(9)
Ir-C(carbene)	2.033(3)	O-Ir-P1	99.95(5)
Ir-P1	2.3527(7)	O-Ir-P2	82.19(5)
Ir-P2	2.3076(7)	C(carbene)-Ir-P1	99.01(7)
		C(carbene)-Ir-P2	157.90(7)
		P1-Ir-P2	103.07(2)

As combining all the ligands with the pre-catalyst before adding H₂ led to the formation of a SABRE-active species, it was decided to explore this route. The addition of phosphine could potentially stabilise complexes where the substrate to be polarised is a very weakly binding ligand, as the five-coordinate intermediate where a substrate has dissociated would be more stable than a potential four-coordinate species (see Figure 184).

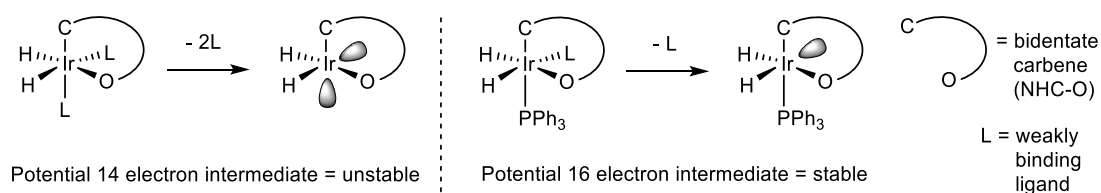
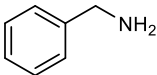


Figure 184: Potential intermediates formed when using weakly coordinating substrate ligands

5.3.2. Benzylamine

As benzylamine had been shown to polarise weakly when it was the only ligand present in solution (see Section 5.2.2) it was decided to test the hypothesis of involving PPh_3 to stabilise the complexes formed in solution to see if enhancements could be increased. The use of PPh_3 could help prevent formation of the inactive singlet hydride species $\mathbf{22}_{\text{benzylamine}}$ as discussed in Section 5.2.2. A CD_2Cl_2 sample containing **1**, PPh_3 and benzylamine was activated under an atmosphere of H_2 . At 298 K, three major hydride species were present in a ratio of 1: 2: 1 for the structures of $\mathbf{23}_{\text{benzylamine}}$: $\mathbf{24}_{\text{benzylamine}}$: $\mathbf{25}$ as shown in Figure 185, each containing two different hydride ligand environments. For two of these species, both hydride ligands gave very broad signals and subsequent cooling and warming enabled the signals to become more resolved. These three species are summarised in Figure 185.

N = benzylamine 

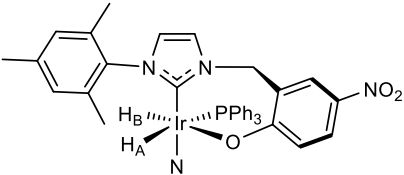
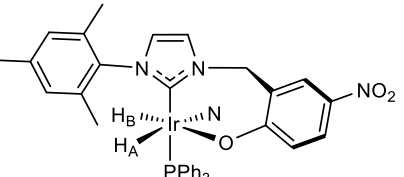
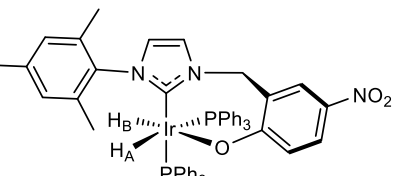
	T / K	H_A	H_B	PHIP or SABRE
 23_{benzylamine}	260	-8.66	-27.84	No
		dd, $^2J(\text{HH}) = 5.2 \text{ Hz}$ $^2J(\text{HP}) \text{ trans} = 161 \text{ Hz}$	dd, $^2J(\text{HH}) = 5.2 \text{ Hz}$ $^2J(\text{HP}) \text{ cis} = 10.8 \text{ Hz}$	
 24_{benzylamine}	303	-22.07	-29.72	Yes
		m, v. br	dd, v. br, $^2J(\text{HH}) \sim 7 \text{ Hz}$ $^2J(\text{HP}) \sim 16 \text{ Hz}$	
 25	303	-9.65	-27.89	No
		ddd, $^2J(\text{HH}) = 4.8 \text{ Hz}$ $^2J(\text{HP}) \text{ cis} = 22.5 \text{ Hz}$ $^2J(\text{HP}) \text{ trans} = 138 \text{ Hz}$	ddd, $^2J(\text{HH}) = 4.8 \text{ Hz}$ $^2J(\text{HP}) \text{ cis} = 13.2 \text{ Hz}$ $^2J(\text{HP}) \text{ cis} = 13.2 \text{ Hz}$	

Figure 185: The three major species identified in the hydride region present at 298 K for a sample containing **1**, PPh_3 and benzylamine under 3 bars of H_2 with hydride characterisation data detailed at the specified temperatures

The only species out of these three that undergoes exchange with hydrogen in solution is **24**benzylamine, where the benzylamine has bound *trans* to a hydride ligand. This enables the incorporation of *p*-H₂ into the complex and thus enables polarisation transfer to occur. This is exhibited in the enhanced spectra for the protons of the substrate benzylamine, where the NH₂, CH₂ and some aromatic protons are polarised due to SABRE (see Figure 186). Despite only half of the sample being a SABRE-active catalyst, the CH₂ group and five aromatic protons of benzylamine show signal enhancements of 88 ± 1 and 72 ± 2 -fold respectively. These are considerably larger than the enhancements observed for the sample without phosphine as detailed in Section 5.2.2. An enhanced signal for the NH₂ protons was observed, however, it was difficult to quantify due to the peak being very broad and overlapping with other signals within the ¹H NMR spectrum. The hydride ligand signals are also significantly enhanced.

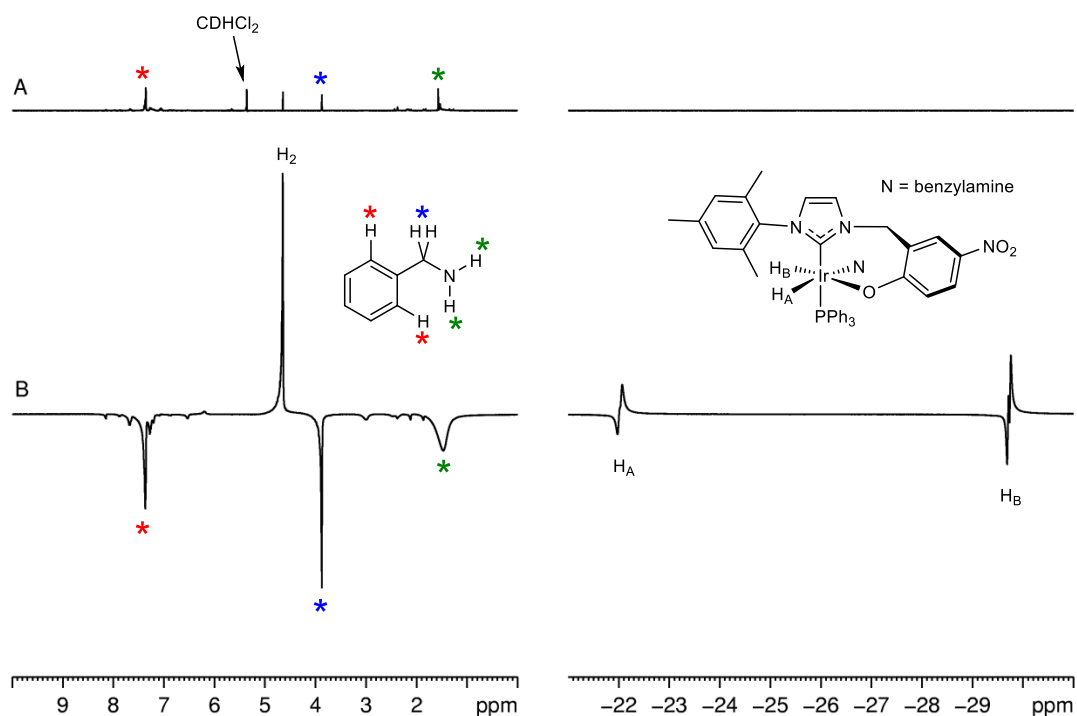


Figure 186: Thermal ¹H NMR spectrum for benzylamine (A) and hyperpolarised spectrum (B) at 6.5×10^{-3} T showing enhanced signals for the hydride ligands as well as for the amine, CH₂ and aromatic protons of benzylamine

5.3.3. Phenethylamine

To test with phenethylamine, a sample containing approximately 15 mol% **1**, phenethylamine (for a 0.025 M solution) and PPh₃ (for a 0.006 M solution) in CD₂Cl₂ was prepared. This reaction was not as clean as with benzylamine although similar major species were formed as well as some other minor impurities. Complex **23**_{phenethylamine} formed, with a ³¹P signal at δ 11.1, which proved to be SABRE-inactive and its active isomer, complex **24**_{phenethylamine} also formed, with a ³¹P signal at δ 22.4. Due to only approximately one equivalent of phosphine in the sample, no formation of **25** was observed. Instead, at 298 K, two very broad singlet hydride signals were visible at δ -23.13 and -30.49 which sharpened considerably on cooling to 250 K. These were shown to undergo PHIP and very broad enhanced signals were observed at 298 K due to the bis-phenethylamine complex, **6**_{phenethylamine}. This species is also expected to be SABRE-active as for the pyridine derivative studied in detail in Section 2.4.1.

At 298 K, the ratio of isomers **23**: **24**: **6** was observed to be 22: 41: 37 and the corresponding ¹H NMR signal enhancements for the five aromatic protons, the two CH₂ groups and the NH₂ group were 23 ± 1, 14 ± 1, 15 ± 1 and 16 ± 1-fold respectively. This represents a great improvement in the polarising capabilities of these catalysts when the solution contains a phosphine ligand capable of stabilising the complexes. On cooling to 250 K these three complexes now only constitute approximately 72 % of the total hydride-containing species in a 20: 20: 32 ratio respectively, with the other 28 % made up of minor species that are broadened into the baseline at 298 K. On increasing the concentration of PPh₃, the PHIP inactive complex **25** also forms as expected and as described in Section 5.3.1. A summary of these complexes is given in Figure 187, along with details of the hydride chemical shifts and couplings.

Over a longer time period, crystals formed which were found to correspond to 2-(phenyl)ethylammonium chloride via XRD, which is already a known structure.²⁵⁶ This shows that over time, deactivation and degradation of the sample occurs because the chloride salt is not able to be polarised. This also shows that the CD₂Cl₂ solvent is not innocent in these systems.

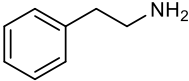
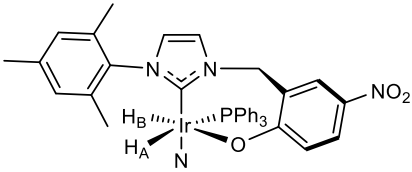
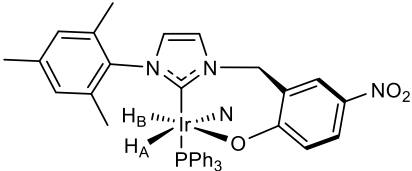
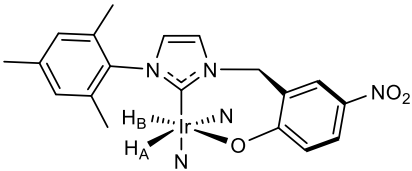
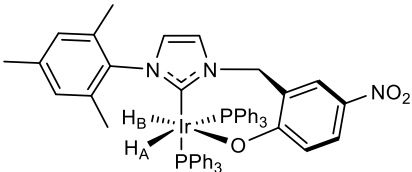
	T / K	H _A	H _B	PHIP or SABRE
<p>N = phenethylamine </p>  <p>23phenethylamine</p>	273	-8.85 dd, ² J(HH) = 4.8 Hz ² J (HP) <i>trans</i> = 162.5 Hz	-27.98 dd, ² J(HH) = 4.8 Hz ² J (HP) <i>cis</i> = 10.6 Hz	No
 <p>24phenethylamine</p>	303	-21.98 d, v. br ² J (HP) = 16.9 Hz	-29.86 dd, br ² J(HH) = 7.7 Hz ² J (HP) = 16.9 Hz	Yes
 <p>6phenethylamine</p>	298	-23.23 s, v. br	-30.49 s, v. br	Yes
 <p>25</p>	298	-9.64 ddd ² J(HH) = 4.4 Hz ² J (HP) <i>cis</i> = 22.7 Hz ² J (HP) <i>trans</i> = 138.7 Hz	-27.90 ddd ² J(HH) = 4.4 Hz ² J (HP) <i>cis</i> = 13.4 Hz ² J (HP) <i>cis</i> = 13.4 Hz	No

Figure 187: Major species present in an activated CD₂Cl₂ sample containing **1**, phenethylamine and PPh₃ under 3 bars of H₂ with hydride characterisation data detailed at the specified temperatures

5.3.4. Tryptamine

After one day of activation of **1** with tryptamine and PPh₃, under H₂ in CD₂Cl₂, four species were evident in the hydride region of the spectrum. These included the C-H activated singlet hydride species, **22**_{tryptamine}, and inactive SABRE species, **23**_{tryptamine}, as well as the SABRE-active species, **24**_{tryptamine}, now exhibiting enhanced hydride signals as doublets of doublets due to *cis*-phosphorus coupling as the substrate *trans* to the carbene is now a PPh₃ ligand. Complex **25** also forms as seen with other samples. The two hydride signals for **23**_{tryptamine} are very broad at 298 K which suggests fluxionality. The ratio of the four species **22**: **23**: **24**: **25** was 25: 24: 44: 7.

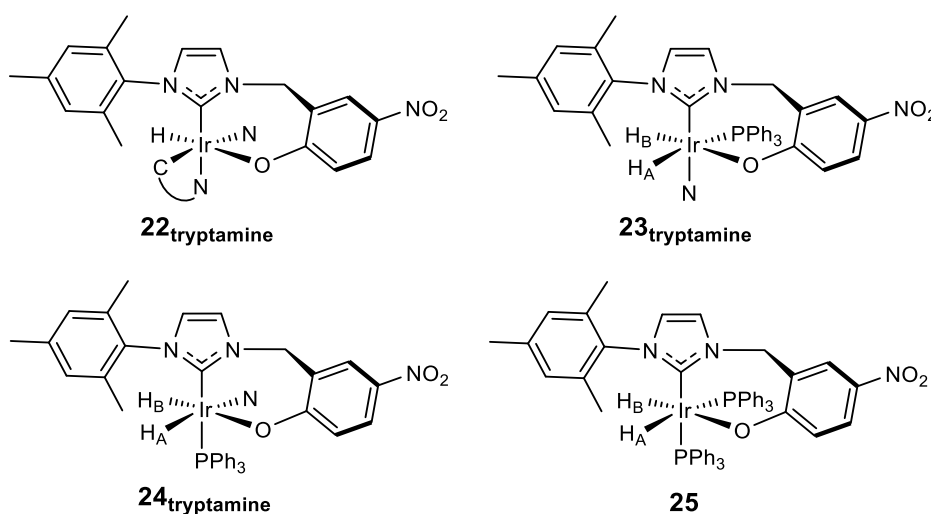


Figure 188: Major species present in an activated CD₂Cl₂ sample containing **1**, tryptamine and PPh₃ under 3 bars of H₂

After being left under an atmosphere of H₂ for a further 24 hours, only three species remained in the hydride region of the spectrum. The signals for **25** had disappeared and the ratios of the remaining three species had changed so that **22**: **23**: **24** was now 28: 24: 48. This suggests that the phosphine is not as strongly bound as anticipated but can be replaced by an amine ligand. Despite only 48 % of the sample being attributed to the SABRE-active species **24**_{tryptamine}, polarisation transfer was still evident throughout the tryptamine molecule as not only was the broad NH₂ peak enhanced, but the signals for the two CH₂ groups were increased by 9 ± 1 and 8 ± 1-fold respectively. The aromatic proton signals were also enhanced, with the total signal intensity approximately three times that of the thermal equilibrium signal. This shows that polarisation can be transferred through multiple bonds via *J*-coupling. These signals

were less enhanced compared to the benzylamine sample and the corresponding hydride signals were visibly larger. Also, the normal H₂ signal was large, suggesting rapid exchange and thus conversion of the *p*-H₂. This could explain why polarisation transfer was not so effective, if the *p*-H₂ was consumed without transferring its polarisation.

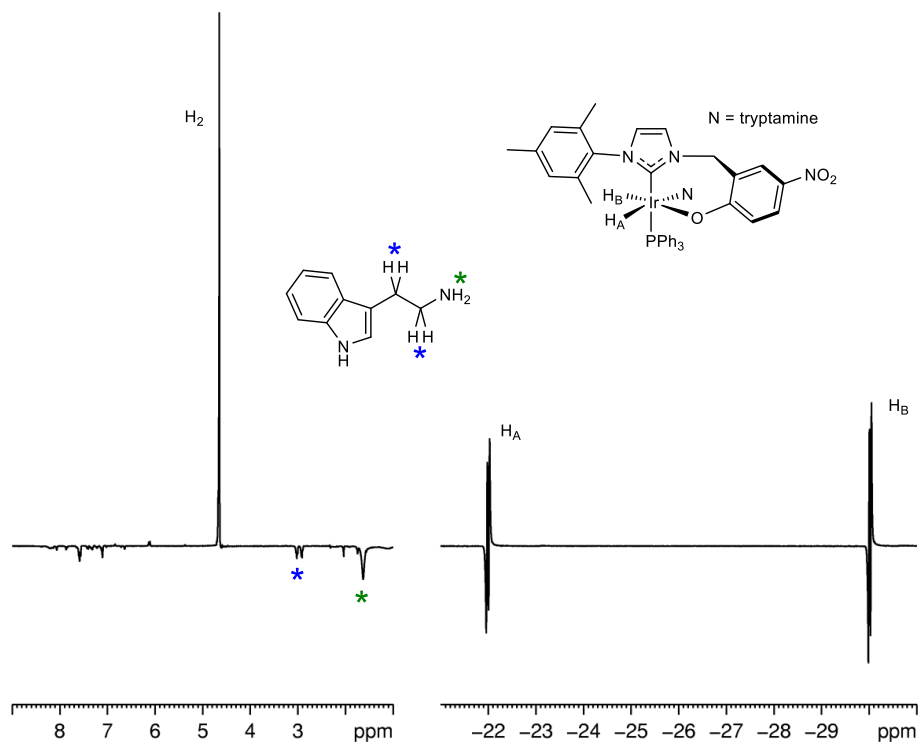


Figure 189: Enhanced ¹H NMR spectrum for tryptamine using **1** with PPh₃ and *p*-H₂ at 6.5×10^{-3} T showing significantly enhanced signals for the hydride ligands. A large H₂ signal is also observed, consistent with rapid consumption of *p*-H₂, and only minimal polarisation of the tryptamine substrate

5.4. Use of other phosphines

Due to the fact that multiple products form on addition of PPh_3 , it was decided to use different phosphine ligands to alter the steric and electronic properties of the complexes, related to the Tolman steric and electronic parameters as detailed in Section 1.2.^{30, 257} Initially PCy_3 was chosen, as the much bulkier ligand could inhibit binding of multiple phosphine ligands to the iridium metal centre. Phenethylamine was chosen as the amine to use due to it not forming the singlet hydride species, **22**, and therefore it providing the cleanest sample.

Table 43: Tolman Cone Angles and Electronic Parameters for five different phosphines

Phosphine	Steric effects: Cone Angle / °	Phosphine	Electronic effects: TEP / χ
PPh₃	145	PPh₃	12.9
PPh₂Cy	153	PBz₃	10.5
PⁱPr₃	160	PPh₂Cy	8.7
PBz₃	165	PⁱPr₃	3.0
PCy₃	170	PCy₃	0.3

5.4.1. PCy₃

First studies using PCy₃ as the phosphine ligand gave several different species in solution. When enough PCy₃ to make a 0.05 M solution was included in a sample containing 14 mol% **1** and phenethylamine (0.04 M solution) in CD₂Cl₂ activated under H₂, two isomers, like those observed previously, were present in solution, corresponding to **26**PCy₃ and **27**PCy₃ as shown in Figure 190. After 60 hours, complex **26**PCy₃ had rearranged to form **27**PCy₃ which presumably relieves the steric pressures that are present in **26**PCy₃, due to the large steric bulk of the PCy₃ ligand interacting unfavourably with the large steric bulk of the bidentate carbene ligand. This shows conversion from the kinetic product to the thermodynamic product. Characterisation data for **26**PCy₃ and **27**PCy₃ are given in the Experimental Sections 8.6.12 and 8.6.13 respectively. Multiple overlapping signals for the phenethylamine and PCy₃ ligands precluded their full characterisation. At 298 K, the hydride signals for the desired SABRE-active species, **27**PCy₃, appear at δ -23.90 for H_A and -30.97 for H_B, and are very broad, suggesting very rapid exchange. Therefore, the SABRE activity of this catalyst is very poor. The hydride signals for **26**PCy₃ are present at δ -10.59 (with a large *trans* HP coupling constant of 155.2 Hz) and -29.54. When analysing the ¹H NMR signal enhancements the effect of polarisation transfer is visible in the CH₂ groups and the aromatic protons show almost twice the signal when compared to the thermal spectrum. However, there is also a very broad signal for hydrogen in the enhanced spectra, again commensurate with very rapid *p*-H₂ exchange. On cooling to 263 K the hydride ligand signals for **27**PCy₃ sharpen and a ³¹P signal is observed at δ 17.2.

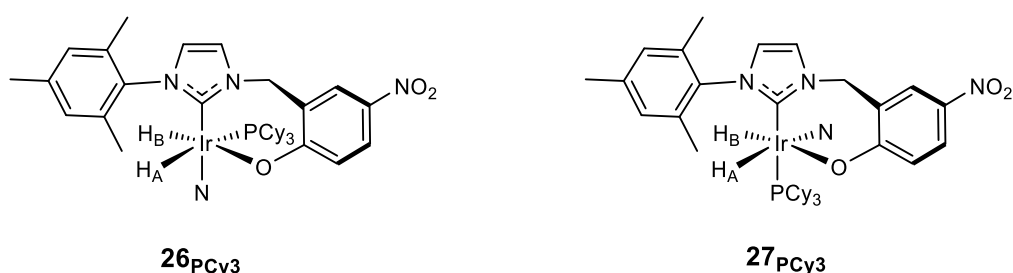


Figure 190: Labelled structures of complexes **26**PCy₃ and **27**PCy₃ where N is phenethylamine

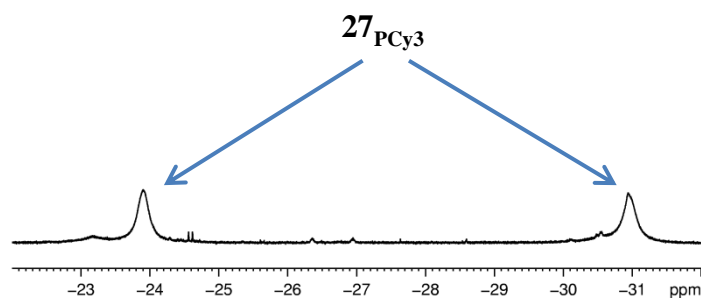


Figure 191: Broad hydride signals of **27**_{PCy₃} at 298 K in CD₂Cl₂

Another hydride signal was also present in the ¹H NMR spectrum of the solution as a triplet at δ -11.23 with a *cis*-phosphorus coupling constant of 12.1 Hz and a ³¹P signal at δ 31.7 at 263 K. This hydride species exhibits no signals for the carbene backbone, shows no coupling to any species other than PCy₃ and also forms in the absence of phenethylamine. Due to this hydride signal demonstrating *cis*-phosphorus coupling and being a triplet, two PCy₃ ligands must lie *trans* to one another to relieve steric crowding, which is also commensurate with their bulky size. This species is consistent with substitution of the carbene backbone that must occur due to the very bulky ligands not having enough space in the coordination sphere of the iridium metal centre. Similar observations have been described by Mann et al.²⁵⁸ for the iridium penta-hydride complex [Ir(H)₅(PEt₂Ph)₂] where a singlet hydride was observed at δ -11 with a *cis*-phosphorus coupling constant of 12 Hz. The corresponding ³¹P NMR spectrum with the ethyl groups decoupled, gave a sextet signal, consistent with coupling to five hydride ligands. These penta-hydride complexes have commonly been prepared from corresponding COD bis-phosphine complexes²⁵⁹ and have also been used to form multi-hydride-containing iridium complexes.²⁶⁰⁻²⁶⁴ The structure of complex **28**_{PCy₃} and its hydride and phosphorus signals at 263 K are shown in Figure 192 (see Experimental Section 8.6.14 for full characterisation data). The ratio of **27**: **28** was 95: 5 at 263 K for the sample containing 14 mol% **1**, phenethylamine (0.04 M solution) and PCy₃ (0.05 M solution).

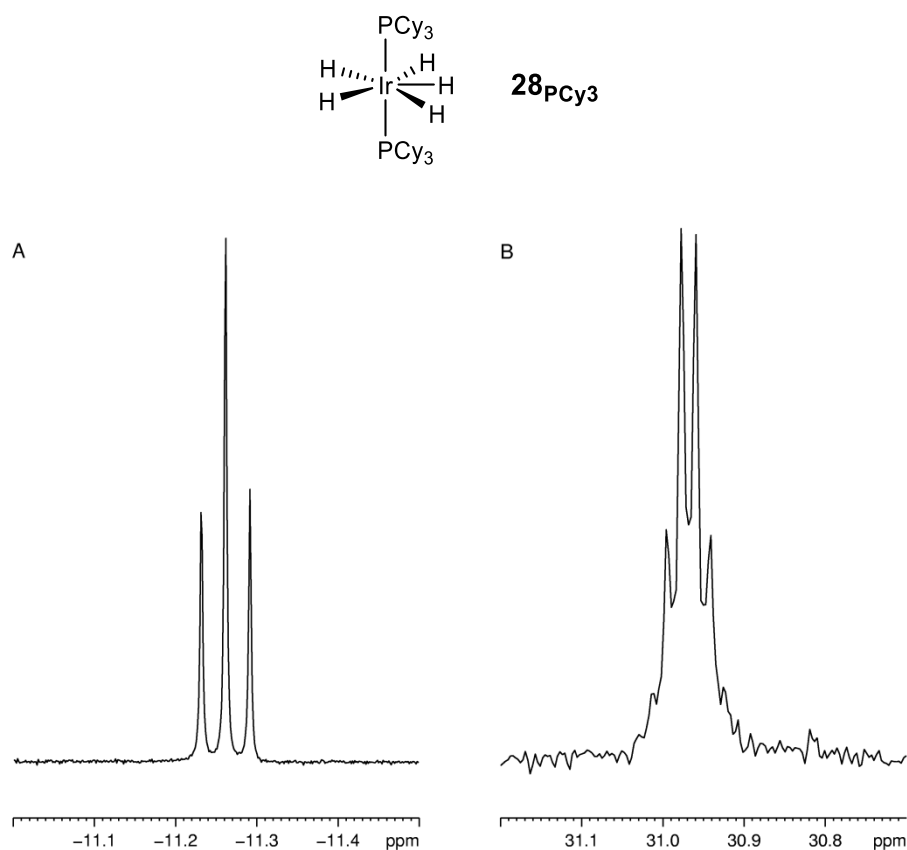


Figure 192: The structure of 28_{PCy_3} and its corresponding 1H and ^{31}P NMR spectra at 263 K, showing the hydride signal (A) and phosphorus signal (B) with the sextet splitting due to the five hydride ligands (cyclohexyl decoupled)

To confirm the identity and reactivity of 28_{PCy_3} , tetrafluoroboric acid diethyl ether complex was added to the CD_2Cl_2 NMR sample of 28_{PCy_3} along with acetonitrile. An immediate colour change was observed from dark orange to light yellow and subsequent NMR analysis confirmed the disappearance of the hydride signal at δ -11.23 . The reaction between $[Ir(H)_5(PCy_3)_2]$, tetrafluoroboric acid and acetonitrile is shown in Figure 193. An equivalent reaction using acetone was described by Xu et al. in 1996.²⁰⁴

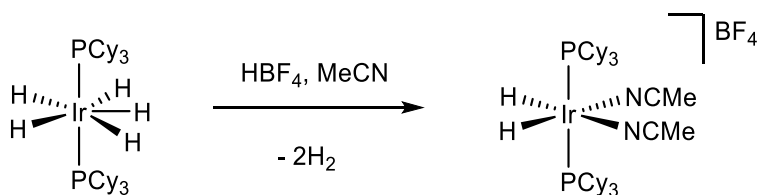


Figure 193: Reaction between $[Ir(H)_5(PCy_3)_2]$, 28_{PCy_3} , and HBF_4 in the presence of acetonitrile to form $[Ir(H)_2(MeCN)_2(PCy_3)_2][BF_4]$

A triplet hydride signal at $\delta -22.17$ with a *cis*-phosphorus coupling constant of 15.5 Hz is now observed with the corresponding ^{31}P signal at $\delta 22.6$ at 263 K as shown in Figure 194, with the structure of $[\text{Ir}(\text{H})_2(\text{MeCN})_2(\text{PCy}_3)_2][\text{BF}_4]$ shown above the spectra. Full characterisation data are included in Table 44 and Experimental Section 8.6.15.

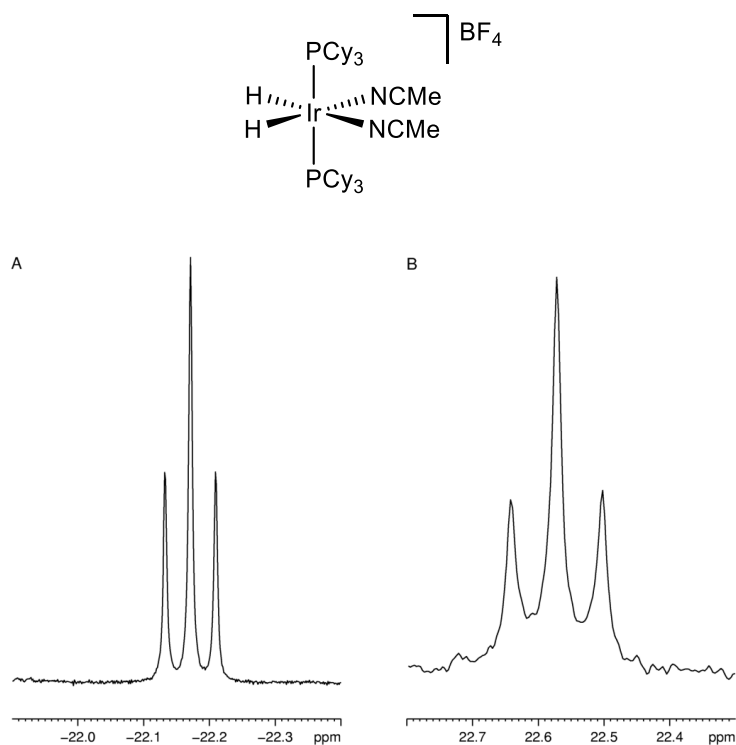


Figure 194: The structure of $[\text{Ir}(\text{H})_2(\text{MeCN})_2(\text{PCy}_3)_2][\text{BF}_4]$ and its corresponding ^1H and ^{31}P NMR spectra at 263 K, showing the hydride signal (A) and phosphorus signal (B) with the triplet splitting due to the two hydride ligands (cyclohexyl decoupled)

Table 44: NMR characterisation data at 263 K for $[\text{Ir}(\text{H})_2(\text{MeCN})_2(\text{PCy}_3)_2][\text{BF}_4]$

$[\text{Ir}(\text{H})_2(\text{MeCN})_2(\text{PCy}_3)_2][\text{BF}_4]$		
Ligand	$^1\text{H} / \delta$	$^{13}\text{C} / \delta$
MeCN	2.42 (s, 6H)	3.7, 120.2
PCy3	1.97-1.87 (m, 54H), 1.50-1.40 (m, 12H)	34.5, 29.5, 27.6, 26.6 (^{31}P 22.6)
H	-22.17 (t, $^2J(\text{HP}_{\text{cis}}) = 15.5$ Hz)	

Similar iridium solvent-containing complexes have previously been synthesised containing the solvent ligands acetonitrile, acetone, tetrahydrofuran, water as well as a number of small alcohol ligands.⁶⁹ The synthetic routes employed, commonly involve the direct formation of the solvent-containing complexes from the $[\text{Ir}(\text{COD})(\text{PR}_3)_2]$ precursors via reaction in the desired solvent under an atmosphere of hydrogen. However, one study by Gruet et al.²⁶⁰ in 2003 used the same synthetic route as shown in Figure 193 in order to produce the acetone-containing derivative, $[\text{Ir}(\text{H})_2(\text{OCMe}_2)_2(\text{PCy}_3)_2][\text{BF}_4]$ via protonation of $[\text{Ir}(\text{H})_5(\text{PCy}_3)_2]$.

The absence of the carbene ligand was further supported by the formation of crystals of the imidazolium tetrafluoroborate salt, as shown in Figure 195 and confirmed by X-ray crystallography in collaboration with Adrian Whitwood, Sam Hart and Rachel Bean in the XRD department at York. It crystallised into the R-3 space group, with unit cell parameters for a, b and c of 25.8153(3), 25.8153(3) and 15.33067(18) Å respectively and for α , β and γ of 90, 90 and 120 ° respectively. The bond angle, N1-C4-C5, is 113.27(11) °, which is larger than that of 109.8(5) ° observed for complex **1** (see Section 2.3). This is because of the absence of ring strain in the salt.

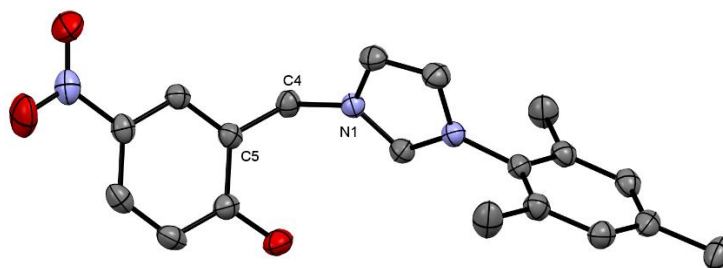


Figure 195: ORTEP plot of the imidazolium tetrafluoroborate salt with the BF_4 and H atoms omitted for clarity and the thermal ellipsoids set at a 50 % probability level

5.4.2. P^iPr_3

When changing the phosphine to P^iPr_3 , the reactivity observed is like that of PCy_3 . Here, at 298 K the SABRE-active catalyst, 27_{PiPr_3} , has broad signals at $\delta -23.56$ for H_A and -30.94 for H_B (see Figure 196). The triplet hydride species 28_{PiPr_3} has a signal at $\delta -11.32$ with a *cis*-phosphorus coupling constant of 12.3 Hz and a ^{31}P signal at $\delta 44.9$. P^iPr_3 is less bulky than PCy_3 and therefore a bis-phosphine dihydride complex 29_{PiPr_3} also forms which is observed to have a molecular cation signal at m/z 851.49 by LIFDI mass spectrometry. At 298 K, the hydride signals for 29_{PiPr_3} (see Figure 196) appear at $\delta -12.86$, with a *cis*-phosphorus coupling constant of 23.3 Hz, and at $\delta -31.49$ with a *cis*-phosphorus coupling constant of 15.4 Hz, with two ^{31}P signals at $\delta 23.6$ and 37.8 with a $^2J(PP_{trans})$ coupling constant of 337 Hz. On cooling to 263 K the hydride signals for the SABRE-active catalyst 27_{PiPr_3} sharpen and the ^{31}P signal appears at $\delta 27.0$. The ratio of 27 : 28 : 29 is approximately 14: 12: 74 at 243 K and thus due to its low concentration, full characterisation of 27_{PiPr_3} was not feasible. Characterisation data for the structures in Figure 197 are given in the Experimental Sections 8.6.13 and 8.6.16.

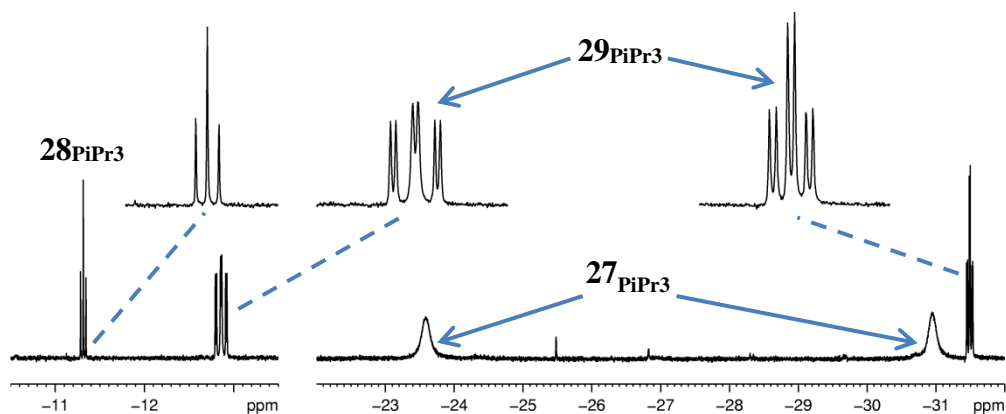


Figure 196: Hydride signals of 27_{PiPr_3} , 28_{PiPr_3} and 29_{PiPr_3} at 298 K in CD_2Cl_2

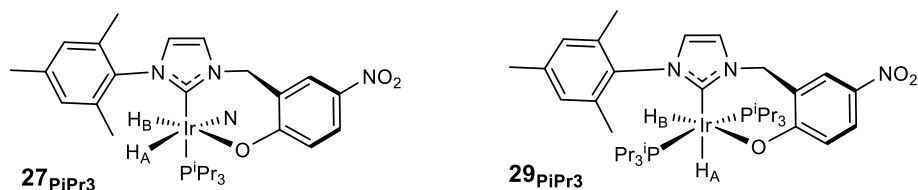


Figure 197: Labeled structures of 27_{PiPr_3} and 29_{PiPr_3} formed when P^iPr_3 is used

The SABRE analysis of this sample, containing 14 mol% **1**, phenethylamine (0.04 M solution) and enough PⁱPr₃ for a 0.05 M solution, showed that catalyst **27**PiPr₃ is much more effective at transferring polarisation when compared to the PCy₃ derivative. The signal enhancements for the five aromatic protons and the two CH₂ groups are 53 ± 1, 13 ± 2 and 17 ± 3-fold respectively, demonstrating significant improvement compared to a sample containing no phosphine. The ratio of **27**: **28**: **29** as shown in Figure 196, is 59: 3: 38 but after 8 days the ratio had changed to 91: 6: 3, due to dissociation of one phosphine ligand due to steric crowding, and the subsequent binding of an amine ligand.

5.4.3. PBz₃

Using PBz₃ the selectivity is reduced so that the speciation is more like that of PPh₃. Now, at 298 K the desired SABRE-active catalyst, **27**PBz₃ has hydride signals at δ -22.82 and -29.93, both with *cis*-phosphorus coupling constants of 19.3 Hz, and a ³¹P signal at δ 0.1. However, the inactive isomer, **26**PBz₃ also forms in low concentration, which precludes full characterisation, with hydride signals at δ -8.68, with a large *trans*-phosphorus coupling constant of 182.8 Hz, and at δ -28.16 with a ³¹P signal at δ -8.9. The bis-phosphine complex, **30**PBz₃ also forms, with hydride signals at δ -10.67, with *cis* and *trans*-phosphorus coupling constants of 25.9 and 153.0 Hz respectively, and δ -28.65, with two *cis*-phosphorus coupling constants of 12.0 Hz each. In complex **30**PBz₃, the phosphine ligands are *cis* to one another as PBz₃ is considerably less bulky than PCy₃ or PⁱPr₃. This also means that the degradation hydride product **28**, caused by too much steric bulk does not form. The structures of **26**PBz₃, **27**PBz₃ and **30**PBz₃ are shown in Figure 198 with the corresponding NMR characterisation data for **27**PBz₃ and **30**PBz₃ given in the Experimental Sections 8.6.13 and 8.6.17 respectively. The hydride region of the ¹H NMR spectrum at 298 K is shown in Figure 199, where the ratio of **26**: **27**: **30** is equal to 11: 75: 14.

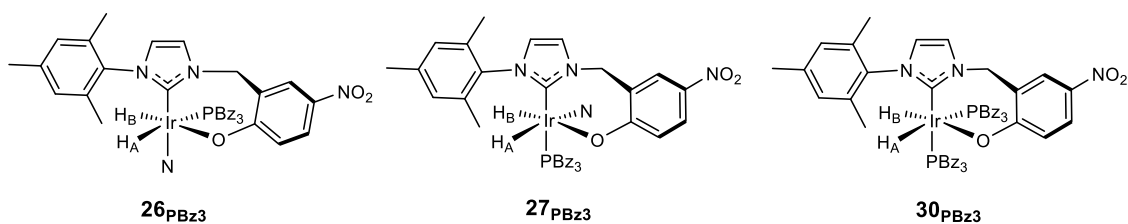


Figure 198: Labelled structures of **26_{PBz3}**, **27_{PBz3}** and **30_{PBz3}** formed when **1** is reacted with phenethylamine in the presence of PBz_3 and H_2

The SABRE analysis of this sample, containing 11 mol% **1**, phenethylamine (0.04 M solution) and enough PBz_3 for a 0.05 M solution, showed that catalyst **27_{PBz3}** is again effective at transferring polarisation when compared to both the PCy_3 and P^iPr_3 derivatives. The signal enhancements for the five aromatic protons could not be easily quantified due to overlap with the benzyl groups of the phosphine ligand but those corresponding to the CH_2 groups are 74 ± 11 and 70 ± 9 -fold enhanced respectively, again demonstrating significant improvement compared to a sample containing no phosphine.

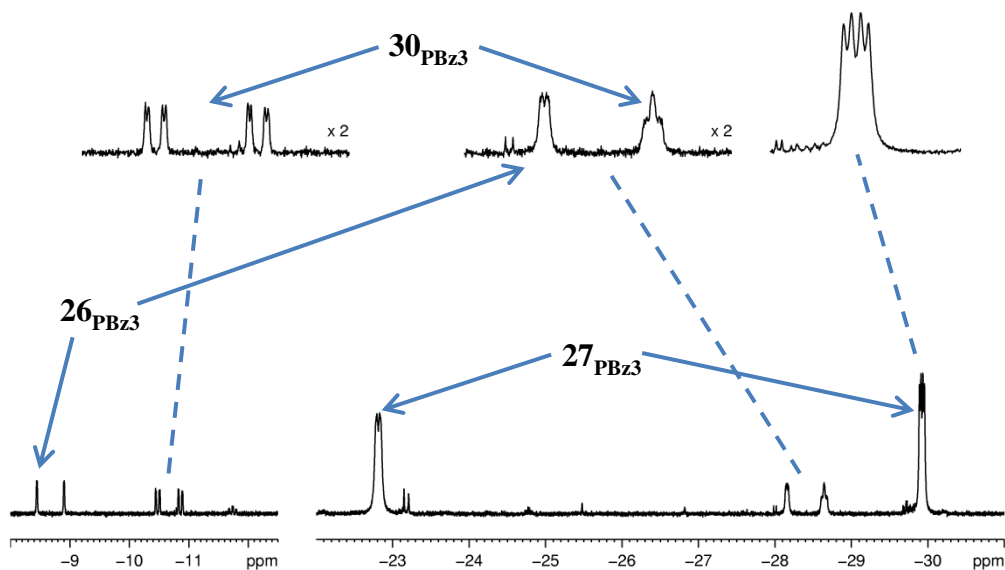


Figure 199: Hydride signals of **26_{PBz3}**, **27_{PBz3}** and **30_{PBz3}** at 298 K in CD_2Cl_2

5.4.4. PPh₂Cy

When the phosphine used is PPh₂Cy the speciation is like that of PBz₃. This is because at 298 K it forms the desired SABRE species, **27**_{PPh₂Cy}, with two broad hydride signals at δ -22.32 and -30.68 with the corresponding ³¹P signal at δ 23.5. The inactive isomer **26**_{PPh₂Cy} also forms in low concentration which precludes full characterisation, again with broad hydride signals appearing at δ -9.60, with a large *trans* phosphorus coupling constant of 162.8 Hz, and at δ -28.67. For this complex, the ³¹P signal is present at δ 14.7. The signals for the bis-phosphine complex, **30**_{PPh₂Cy} are the sharpest, consistent with it not undergoing exchange, and they are present at δ -10.20, with *cis* and *trans*-phosphorus coupling constants of 18.5 and 135.7 Hz respectively, and at δ -29.21, with two *cis*-phosphorus coupling constants of 13.0 Hz each. Again, NMR characterisation data for **27**_{PPh₂Cy} and **30**_{PPh₂Cy} are given in the Experimental Sections 8.6.13 and 8.6.17 respectively.

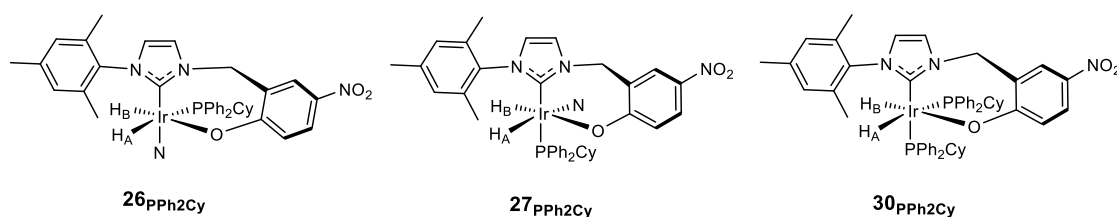


Figure 200: Labelled structures of **26**_{PPh₂Cy}, **27**_{PPh₂Cy} and **30**_{PPh₂Cy}

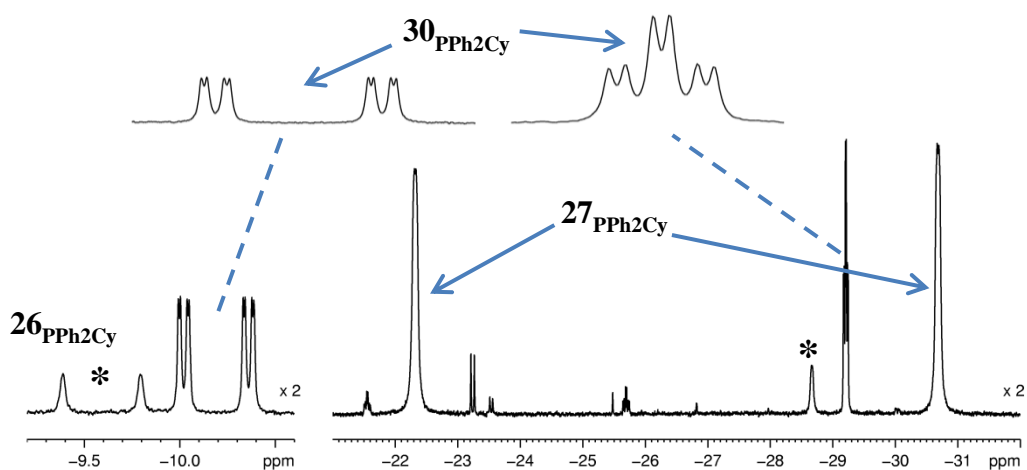


Figure 201: Hydride signals of **26**_{PPh₂Cy}, **27**_{PPh₂Cy} and **30**_{PPh₂Cy} at 298 K in CD₂Cl₂

The SABRE analysis of this sample, containing 11 mol% **1**, phenethylamine (0.04 M solution) and enough PPh₂Cy for a 0.05 M solution, showed that catalyst **27**_{PPh₂Cy} is effective at transferring polarisation when compared to the PCy₃ and PⁱPr₃ derivatives. The signal enhancements for the five aromatic protons could not be easily quantified due to overlap with the benzyl groups of the phosphine ligand but those corresponding to the CH₂ groups are 59 ± 3 and 48 ± 3 respectively, demonstrating improvement compared to a sample containing no phosphine. The ratio of **26**: **27**: **30** as shown in Figure 201 is 9: 62: 29 at 298 K.

5.4.5. Summary

Overall, the SABRE-active species, **27** is the most favourable complex when only the necessary amount of phosphine is present in solution. When excess phosphine is present, the formation of bis-phosphine species, **29** and **30**, which undergo no ligand exchange is favoured due to the stronger Ir-P bond in comparison to the Ir-N bond formed with the amine ligands. The *trans*-phosphine ligand arrangement in **29** is favoured for the bulkier phosphine ligands when compared to the *cis* arrangement in **30**, where the phosphine ligands have lower Tolman cone angles. Complexes **26** are the least stable amino-phosphine-containing isomers, due to the steric crowding caused by the bidentate carbene ligand being in a *cis* position to the phosphine ligand. To relieve the unfavourable steric effects, rearrangement to form **27** is possible, as seen for the PCy₃ containing complex. This is consistent with **26** being the minor isomer in solution.

5.5. Conclusion

In this chapter, the stable bidentate iridium carbene complex, **1**, has been exploited in the polar aprotic solvent dichloromethane to demonstrate SABRE of previously unexplored amine ligands as substrates. Using ammonia, benzylamine, phenethylamine and tryptamine, SABRE catalysts **6** form, equivalent to when pyridine is the substrate. However, several other complexes form which inhibit SABRE, as they do not undergo ligand exchange. The dimer species **21** shows that hydride ligands bridge iridium metal centres at low substrate concentrations and the formation of the singlet hydride complexes **22** indicate that the amine substrates easily undergo C-H activation.

To prevent formation of the SABRE-inactive complexes, the addition of phosphine was investigated to stabilise the species. The addition of PPh₃ to a pyridine sample of **1** in CD₂Cl₂ under H₂ leads to two isomers, the formation of which is dependent on the order of addition. The SABRE-inactive species **23** forms when PPh₃ is added to a pre-activated sample of **6**, thus to form the desired SABRE species, phosphine must be added before the addition of H₂. In this case, with pyridine, species **24** forms along with the bis-phosphine complex, which forms on addition of excess phosphine. However, when the same procedure was followed using the desired amine substrates, mixtures of **6**, **23**, **24** and **25** formed.

As both steric and electronic parameters of different phosphine ligands can greatly affect reactivity, the different phosphine co-ligands PCy₃, PⁱPr₃, PBz₃ and PPh₂Cy were tested. However, no selectivity was observed and the clean production of a sample containing only a SABRE-active complex was not achieved. The trend in speciation follows the electronic effects of the phosphines, rather than their steric effects; the complexes formed in the presence of PⁱPr₃ match those with PCy₃ and likewise PBz₃ and PPh₃ show similar reactivity. Both isomers **26** and **27** formed as well as bis-phosphine containing species. The unexpected formation of the penta-hydride complex **28** shows that very electron-donating phosphine ligands can stabilise the iridium metal centre in high oxidation state (Ir(V)).

6. Kinetic studies on the hydrogenation activity of a series of neutral iridium carbene catalysts

6.1. Introduction

NMR spectroscopy is a very versatile technique that is particularly useful for analysing mixtures due to its ability to distinguish different nuclei according to their chemical environment. This means that many different reactions can be analysed using NMR spectroscopy as long as signals for the starting material and product do not overlap. Thus, quantitative data can be extracted from sequential NMR spectra to gain information about reaction kinetics.

One such reaction pathway that can be followed using NMR spectroscopy involves the study of enzyme kinetics. For example, Eicher et al.²⁶⁵ used ³¹P NMR spectroscopy to analyse the change in concentration of a complex mixture containing two enzymes from *E. coli*, phosphoglucose isomerase and phosphofructokinase, in order to quantify the concentrations of the nucleotide phosphates, ATP and ADP. They chose to use ³¹P NMR to analyse the phosphates, due to its high natural abundance and gyromagnetic ratio.

A number of experiments aimed at students have also been developed using NMR to follow the progress of an enzyme reaction with an organic starting material.²⁶⁶⁻²⁶⁸ In 2015, Her et al.²⁶⁷ described a simple experiment, aimed at undergraduate students, for analysing the enzyme-catalysed hydrolysis of sucrose to glucose, using quantitative NMR, enabling the observation of a decrease in sucrose corresponding to an increase in the concentration of glucose.²⁶⁷ Knowing the initial concentration of substrate, the Michaelis-Menten equation could be used to determine the Michaelis constant, K_M and the maximum rate, V_{max} for the hydrolysis reaction. The NMR spectra acquired throughout the time course of the reaction are shown in Figure 202.

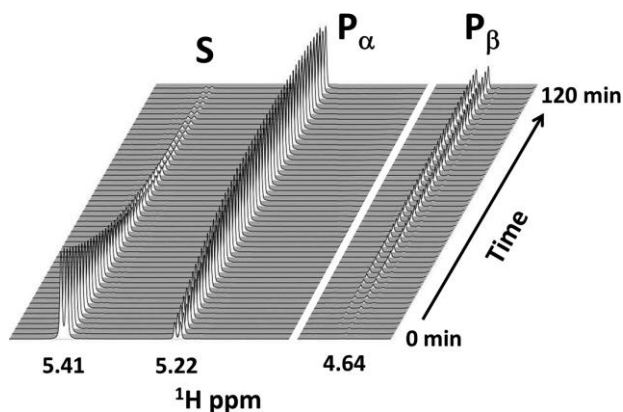


Figure 202: The NMR spectra acquired at different time intervals during the enzyme-catalysed hydrolysis of sucrose (S , δ 5.41) to form the product α -glucose (P_{α} , δ 5.22) and the slow conversion of α -glucose to β -glucose (P_{β} , δ 4.64) (Reprinted with permission from Her, C.; Alonzo, A. P.; Vang, J. Y.; Torres, E.; Krishnan, V. V. *J. Chem. Educ.* **2015**, *92*, 1943. Copyright © 2015 American Chemical Society)²⁶⁷

The importance of chemical shift differences between starting material and product when using NMR analysis has been demonstrated clearly by Butler et al.²⁶⁹ when they used ionic liquids as reaction media to study the reaction of benzonitrile oxide with ethyl *trans*-cinnamate as shown in Figure 203.

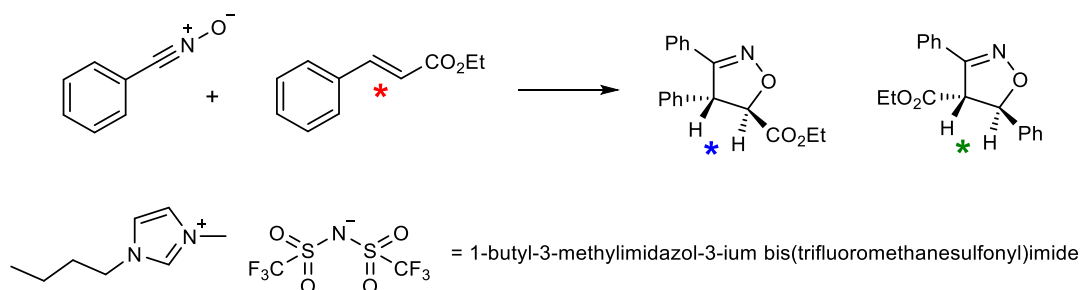


Figure 203: Reaction of benzonitrile oxide with ethyl *trans*-cinnamate completed in the ionic liquid 1-butyl-3-methylimidazol-3-ium bis(trifluoromethanesulfonyl)imide, with the starred protons indicating those used to monitor the progress of the reaction²⁶⁹

The ^1H NMR signals for the labelled protons of interest in the starting material and two products shown in Figure 203 fall in the chemical shift region between δ 4.40 and 6.60. The signals for the ionic liquid used, 1-butyl-3-methylimidazol-3-ium bis(trifluoromethanesulfonyl)imide, do not appear in the same region, hence the reaction could easily be monitored using ^1H NMR spectroscopy.²⁶⁹

Another useful reaction that can easily be followed using ^1H NMR is hydrogenation. Hydrogenation using a transition metal catalyst with hydrogen is a direct route used to reduce multiple bonds within organic substrates. This can be used to create saturated compounds or, with careful control, enables the production of partially hydrogenated species. This catalysis is commonly conducted using either homogeneous or heterogeneous catalysts. Kinetic studies of these reactions enable the determination of hydrogenation rates, which are calculated by fitting to a kinetic model which follows a set mechanism and therefore identification of intermediates in the reaction pathway is not possible. These studies traditionally monitor the rate of increase in the product concentration or consumption of starting material, using analytical methods such as NMR, IR etc.

One example is the heterogeneous hydrogenation of citral, the unsaturated aldehyde-containing substrate shown in Figure 204, which forms a number of reduced species as revealed in Figure 204.²⁷⁰⁻²⁷¹ The use of a Pt/SiO_2 catalyst under an atmosphere of hydrogen enables the hydrogenation of both the carbon-carbon double bonds and the aldehyde $\text{C}=\text{O}$ bond of citral. However, the selectivity can be tuned by changing the temperature of the reaction. At 298 K, limited selectivity is observed, although the most dominant species are the partially saturated aldehyde and alcohol species shown on the left side of Figure 204. In contrast, when the temperature is increased to 423 K, aldehyde hydrogenation is favoured over carbon-carbon double bond hydrogenation as shown on the right side of Figure 204.

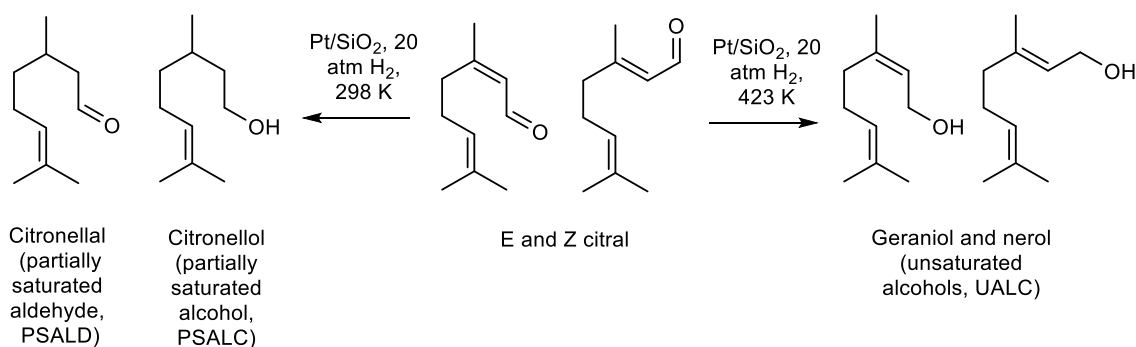


Figure 204: Selectivity observed on hydrogenation of citral in hexane using Pt/SiO_2 with 20 atm of H_2 , at 298 K to form the partially saturated aldehyde, citronellal, or the partially saturated alcohol, citronellol. At high temperature very little carbon-carbon double bond hydrogenation is observed which leads to the unsaturated alcohols geraniol and nerol²⁷⁰

For this reaction, the growth in product concentration over time, coupled with the decrease in the concentration of citral starting material at 423 K is shown in Figure 205. This speciation was followed using gas chromatography.

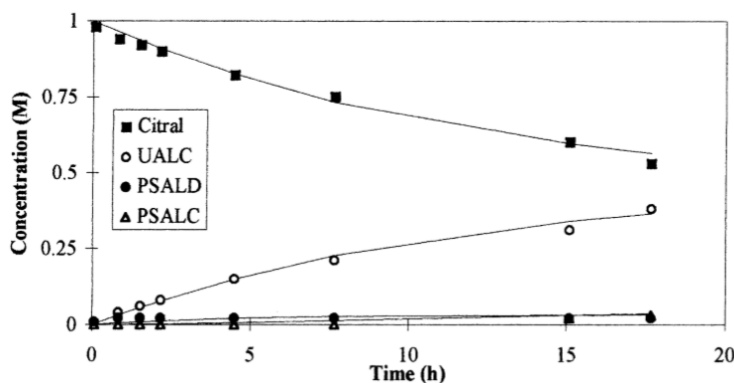


Figure 205: Reaction of citral in hexane with 20 atm of H_2 over a heterogeneous Pt/SiO_2 catalyst at 423 K showing the selectivity for the production of the alcohol (UALC) over the partially saturated species (PSALD and PSALC) as shown in Figure 204 (Reprinted from Singh, U. K.; Albert Vannice, M. *Journal of Catalysis* **2000**, 191, 165, Copyright © 2000, with permission from Elsevier)²⁷⁰

A number of transition metal complexes can be used to catalyze the homogeneous hydrogenation of multiple bonds. One iridium-based complex, $[Ir(COD)(PCy_3)(py)][PF_6]$, known as Crabtree's catalyst, has proven very active for the hydrogenation of a wide range of unsaturated species, both sterically unhindered and hindered. The importance of dihydride-dialkene complexes and their role in homogeneous hydrogenation reactions has also been investigated by Crabtree et al. Low temperature studies of the reaction of H_2 with $[Ir(COD)(PCy_3)(py)][PF_6]$ have demonstrated the formation of $[Ir(H)_2(COD)(PCy_3)(py)][PF_6]$ with hydride ligand signals at $\delta -12.7$ and -18.0 consistent with lying *trans* to COD and pyridine respectively.¹⁵⁷ On warming to room temperature, these signals disappear. This dihydride-dialkene complex was also shown not to form without excess COD in solution. This is consistent with its ability to easily hydrogenate COD to COA and thus without refreshing the supply of COD ligand, the dihydride-dialkene species cannot be observed.¹⁵⁷ Using this complex in hydrogenation reactions, the fastest kinetics were observed for the least hindered alkene substrates but hydrogenation rates of the most sterically hindered alkenes were shown to be considerably faster than for the least hindered alkenes when using Wilkinson's catalyst, $[RhCl(PPh_3)_3]$. These data are

summarised in Table 45, with the rates detailed as Turnover Frequencies (TOF) for the number of moles of substrate reduced per mole of catalyst per hour.

Table 45: Hydrogenation rates in moles of substrate reduced per mole of catalyst per hour for four different alkenes using Crabtree's iridium catalyst and Wilkinson's rhodium catalyst⁴⁴

Catalyst	Substrate and hydrogenation rates / mol substrate reduced (mol of catalyst) ⁻¹ h ⁻¹			
	Hexene	Cyclohexene	1-Methyl-cyclohexene	2,3-Dimethyl-but-2-ene
[Ir(COD)(PCy ₃)(py)][PF ₆]	6400	4500	3800	4000
[RhCl(PPh ₃) ₃]	60	70	-	0

Since the prediction of the PHIP phenomenon in 1986 by Bowers and Weitekamp²⁰ and its subsequent observation a year later,⁷⁷ there has been a large increase in its use to study reaction mechanisms and intermediates. A number of examples now exist, where the kinetics of a *parahydrogenation* reaction have been monitored.²⁷²⁻²⁷⁶ In 1992, Chinn and Eisenberg²⁷² described a quantitative method for analysing PHIP behaviour and using it to determine reaction rates. They termed this method Rates Of Catalytic Hydrogenation Estimated Spectroscopically Through Enhanced Resonances (ROCHESTER). When *p*-H₂ adds pairwise across a multiple bond, such as the double bond in ethyl (*Z*)- α -acetamidocinnamate using the catalyst [Rh(NBD)(chiraphos)][BF₄],²⁷² observation of the enhanced *p*-H₂ derived signals is possible using a small angle (30-45 °) detection pulse.^{272, 274} The enhanced signals can then be analysed over time, with a set of spectra being acquired every few seconds demonstrating a decaying signal, dependent on both the *p*-H₂ consumption and the effect of the system relaxing back to equilibrium. Calculation of reaction rates has been achieved using an excess of substrate meaning the hydrogenation follows *pseudo*-first order kinetics, with the decrease fitted to an exponential decay curve. This technique has also been examined further by Hübler et al.²⁷⁴ Another method is also described by Hübler et al. and named Dynamic PASADENA Spectroscopy (DYPAS). For this method, the reactions were studied using an NMR sequence involving *p*-H₂ addition

followed by a variable delay before acquisition. Varying the delay time enabled observation of the decreasing signal for both free and bound hydrogenated substrate as shown in Figure 206. Similar observations have been made by Wildschütz et al.²⁷⁵ during their study of the asymmetric hydrogenation of β -dehydroamino acids.

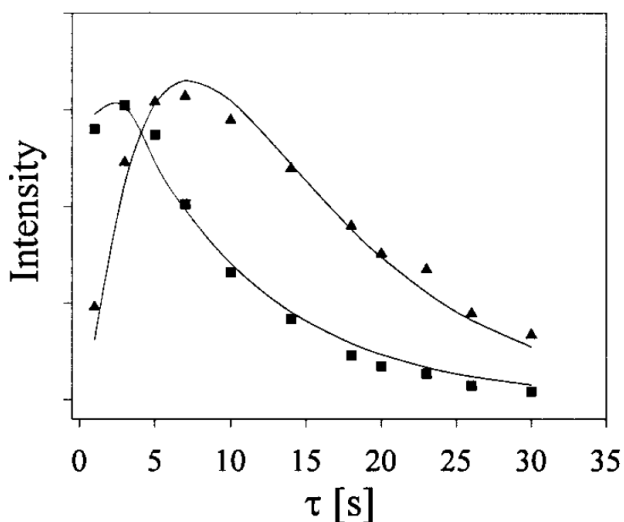


Figure 206: Intensities of enhanced signals for bound ethylbenzene (squares) and free ethylbenzene (triangles) formed from the hydrogenation of styrene using $[Rh(dppb)(COD)][BF_4]$ and the DYPAS NMR method (Reprinted with permission from Hubler, P.; Giernoth, R.; Kummerle, G.; Bargon, J. *J. Am. Chem. Soc.* **1999**, *121*, 5311. Copyright © 1999 American Chemical Society)²⁷⁴

More recently, 1H OPSY NMR experiments have been used to analyse a hydrogenation reaction²⁷⁶ without the need for re-addition of $p-H_2$ or a system having returned to thermal equilibrium. Consecutive 1H OPSY NMR experiments were used during this study, by Tang et al.²⁷⁶ due to the ability of OPSY NMR to destroy any magnetisation before recording each successive spectra. Thus, reactions can be followed until all the $p-H_2$ is consumed. Repeating the introduction of fresh $p-H_2$ into the solution enables repeat studies to be made, to see how the reaction changes over time. This is shown in Figure 207, where at the start of the reaction when fresh $p-H_2$ has been bubbled through or shaken into the solution, the enhanced signals show the largest intensity. As the reaction progresses and the $p-H_2$ is used up, the amount of hydrogenation occurring during each successive experiment decreases until no signal remains after 200 s. Upon reintroduction of $p-H_2$ into the solution, this trend is then repeated as shown in Figure 207.

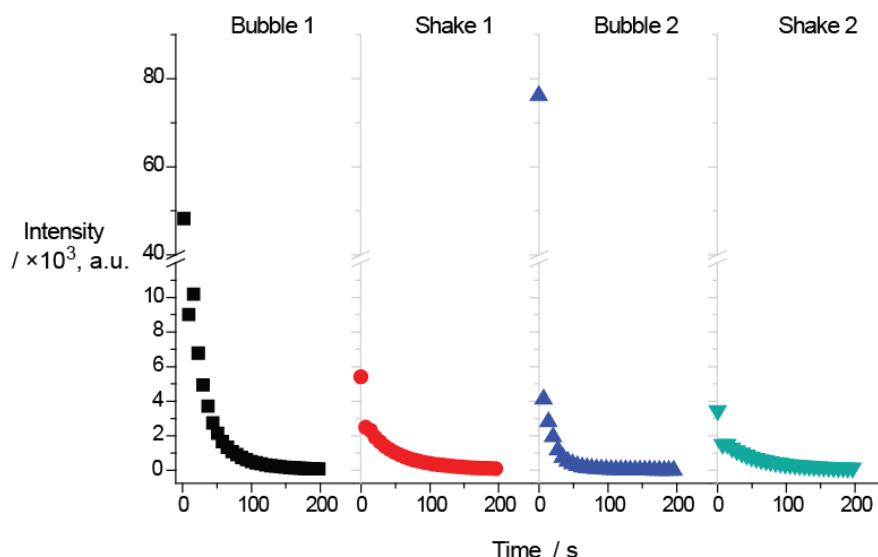


Figure 207: The decrease in ^1H OPSY NMR signal intensity observed during the hydrogenation of ethyl propiolate to ethyl acrylate using $[\text{Rh}(\text{COD})(\text{DIOP})][\text{BF}_4]$ as the catalyst. The hydrogenation was conducted in D_2O in the presence of SDS (sodium dodecyl sulfate) and consecutive ^1H OPSY NMR spectra were recorded until the enhanced signal intensity decreased to zero (Reproduced from Tang, J. A.; Gruppi, F.; Fleysher, R.; Sodickson, D. K.; Canary, J. W.; Jerschow, A. *Chem. Commun.* 2011, 47, 958 with permission of The Royal Society of Chemistry <http://dx.doi.org/10.1039/C0CC03421E>)²⁷⁶

The work in this chapter uses a similar approach to Tang et al.²⁷⁶ with analysis of the *parahydrogenation* of phenylacetylene completed using ^1H OPSY NMR experiments. Kinetic analysis is completed, following the decay of the enhanced signals and the rates of hydrogenation of phenylacetylene are analysed, comparing Crabtree's catalyst with the neutral bidentate iridium carbene complexes developed in this work. The observed rates of hydrogenation as a function of time can then be used, along with the corresponding hydrogen concentrations in solution, to determine the order of the reactions with respect to the hydrogen concentrations in solution. This provides an insight into the mechanism and any intermediates present during the hydrogenation reactions.

6.2. Monitoring the *parahydrogenation* of phenylacetylene

In this section, the hydrogenation activity of the iridium(I) carbene phenolate complexes developed in Chapter 2 is detailed. Their ability to act as hydrogenation catalysts is investigated using phenylacetylene as the substrate. This simple alkyne was chosen as the substrate to study as this eliminated the potential further complication that could arise from hydrogenation of a di-substituted starting material, which could form both *cis* and *trans* isomers. Phenylacetylene can first be hydrogenated to styrene and then further hydrogenated to form ethyl benzene as shown in Figure 208. When using *p*-H₂, *cis-trans* isomerisation of styrene is possible, however, after relaxation, both isomers are equivalent.

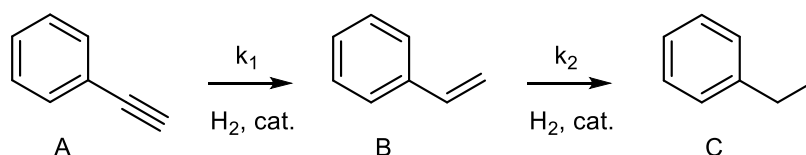


Figure 208: The hydrogenation of phenylacetylene to form styrene and then ethylbenzene

This section details the kinetic studies carried out by analysing ¹H OPSY NMR spectra and following the progress of each reaction. The neutral bidentate carbene complexes developed previously, **1**, **2**, **3** and **4** are compared to the reactivity of Crabtree's catalyst, under the same conditions, with the kinetic analysis following the consumption of *parahydrogen*. Combining the experimentally observed rate constants with the calculated hydrogen concentrations, the use of Letort's method of a double logarithmic plot of the hydrogen concentration vs the hydrogenation rate at each time has enabled the reaction order of hydrogen with respect to time, n_t to be estimated for each catalyst.

6.2.1. The use of ^1H OPSY NMR spectroscopy to study reaction kinetics

To compare the hydrogenation potential and efficiency of the newly-developed neutral bidentate carbene catalysts used for SABRE, CD_2Cl_2 samples were prepared containing 2.0 mol% catalyst and phenylacetylene as the compound to be hydrogenated (120 mM solutions of phenylacetylene). The catalysts tested were Crabtree's catalyst, $[\text{Ir}(\text{COD})(\text{PCy}_3)(\text{py})][\text{PF}_6]$, and the bidentate phenolate derivatives, **1**, **2**, **3** and **4**. The use of ^1H OPSY NMR spectra enables the analysis of protons that are specifically derived from *parahydrogen*. With OPSY NMR, upon incorporation of *parahydrogen* into a hydrogenated substrate, the observed signals are initially significantly enhanced. However, over time, the *p*- H_2 in solution is used up during the reaction. This means that the initially enhanced signal decreases in intensity so that upon repeated acquisition of spectra, less and less enhancement is seen, until no observable signal remains in the OPSY spectrum. The rate of proton signal decay can be used to determine the rate of hydrogen consumption and thus give an indication of the relative hydrogenation rates for the individual catalysts. The higher the value, the faster the hydrogenation reaction and the more active the catalyst. The OPSY sequence works by destroying the entire signal that is present before selecting only the magnetic states that are *p*- H_2 derived as described in Section 4.2.1. Therefore, each OPSY spectrum corresponds to the amount of hydrogenation that has occurred in the timeframe of the experiment.

After addition of *p*- H_2 to a sample of catalyst and phenylacetylene in CD_2Cl_2 , the sample was shaken in the Earth's field for ten seconds before being dropped into the NMR spectrometer for examination. One spectrum was recorded immediately after transfer to the magnet and a specific time delay was set between recording subsequent spectra. For faster reactions, the time delay chosen was shorter to allow collection of more data points before all the *p*- H_2 had been consumed. The decay was fitted to follow *pseudo*-first order kinetics as the phenylacetylene was in excess during the reaction, such that the change in concentration of phenylacetylene was essentially negligible. However, this assumption becomes less correct as the reaction progresses. Hydrogen is the limiting reagent, so using the isolation method for analysis, the calculated rate constant is k_{obs} . Once the signal had completely decayed the sample was removed from the spectrometer and reshaken for another ten seconds to redissolve fresh *parahydrogen*

from the headspace of the NMR tube. Due to the consumption of *p*-H₂, the concentration within the NMR tube is lower for the second shake in comparison to the first shake. However, in CD₂Cl₂, the solubility of 1.01 bars of H₂, at 298 K, is reported to be 1.51 ± 0.06 mM, and at the pressures used here, the pressure-concentration relationship is linear, so that at 3 bars, the concentration increases to 4.49 ± 0.18 mM.²⁷⁷ In comparison to the concentration of phenylacetylene, which is 120 mM, the concentration of H₂ is considerably lower and therefore this confirms that it is the limiting reagent. The amount of H₂ that this 3 bars of pressure supplies into the 1.8 mL headspace of a Young's NMR tube, is about 218 μmol, calculated using the ideal gas law, PV = nRT, where P is pressure (Pa), V is volume (m³), n is the number of moles, R is the ideal gas constant (8.314 J K⁻¹ mol⁻¹), and T is temperature (K). Thus, in 0.6 mL of sample, about 2.7 μmol of H₂ is soluble and used up during the first shake, meaning that for the second shake, the amount of H₂ remaining is 215.3 μmol and the amount of phenylacetylene remaining is 117.3 μmol. As these changes in concentration of both hydrogen and phenylacetylene are negligible, they cannot be the reason for the differing rates of hydrogen consumption and therefore any changes that are observed must be due to changes in reaction species and activity in solution.

After the second shake, the sample was again transferred into the magnet and more OPSY spectra were collected. The kinetic model used is shown below, where the concentration of alkene at time zero is at a maximum, which then decays according to the observed *pseudo*-rate constant, *k*_{obs}, as the *p*-H₂ is consumed.

$$[\textit{alkene}]_t = [\textit{alkene}]_0 e^{-k_{obs}t}$$

From these decay data, the amount of styrene produced over time can be calculated by cumulatively summing the enhanced signal intensities to gain a growth curve. These plots can also be used to calculate rate constants, as is the case for traditional kinetics measurements, when a growth in product concentration as a function of time is observed.

Using the *k*_{obs} values obtained from either method of kinetic analysis, the concentration of hydrogen in solution at each time point can also be calculated according to the model shown below, where the concentration of H₂ is at a maximum at

time zero. The rate of hydrogen consumption is the same as the rate of styrene production as hydrogen is the limiting reactant in solution.

$$[H_2] = [H_2]_0 e^{-k_{obs}t}$$

Using the calculated values for k_{obs} and their corresponding values for the concentration of hydrogen, the order of reaction can be calculated. This is achieved according to the formulae shown below, where v is the rate of reaction, k is the rate constant, c is the concentration of hydrogen and n is the corresponding reaction order.

$$v = kc^n$$

$$\log_{10}v = \log_{10}k + n\log_{10}c$$

A double-logarithmic plot of $\log_{10}v$ against $\log_{10}c$ gives a straight-line gradient which is equal to the order of the reaction. There are two methods of measuring and achieving this plot. The first involves measuring the reaction rates of a single reaction as the time progresses and the reactant concentration changes. This has been described as Letort's method of determining a reaction order with respect to time, n_t , and is possible here because the OPSY NMR method probes the rates of reaction as a function of time. A second method involves measuring initial reaction rates at different initial concentrations, which Letort referred to as the order with respect to concentration, n_c .

6.2.2. Hydrogenation of phenylacetylene using Crabtree's catalyst

For Crabtree's catalyst, the first shake gave an observed experimental rate constant for hydrogen decay of $(10.5 \pm 1.2) \times 10^{-2} \text{ s}^{-1}$ and $(10.4 \pm 1.0) \times 10^{-2} \text{ s}^{-1}$ for the two largest hydrogenated signals for styrene whilst the second shake proved slower, at $(3.24 \pm 0.09) \times 10^{-2} \text{ s}^{-1}$ and $(3.14 \pm 0.09) \times 10^{-2} \text{ s}^{-1}$ for the same two signals (Figure 209). This is consistent with deactivation of the catalyst during the hydrogenation reactions which therefore slows down the hydrogenation rates.⁴⁴ Furthermore, degradation visibly occurs over time as the solution darkens from yellow to brown and a precipitate forms. An enhanced signal for the proton of styrene at δ 5.81 is also

observed during these experiments, despite this proton not originating from *p*-H₂, due to cross polarisation.²²²

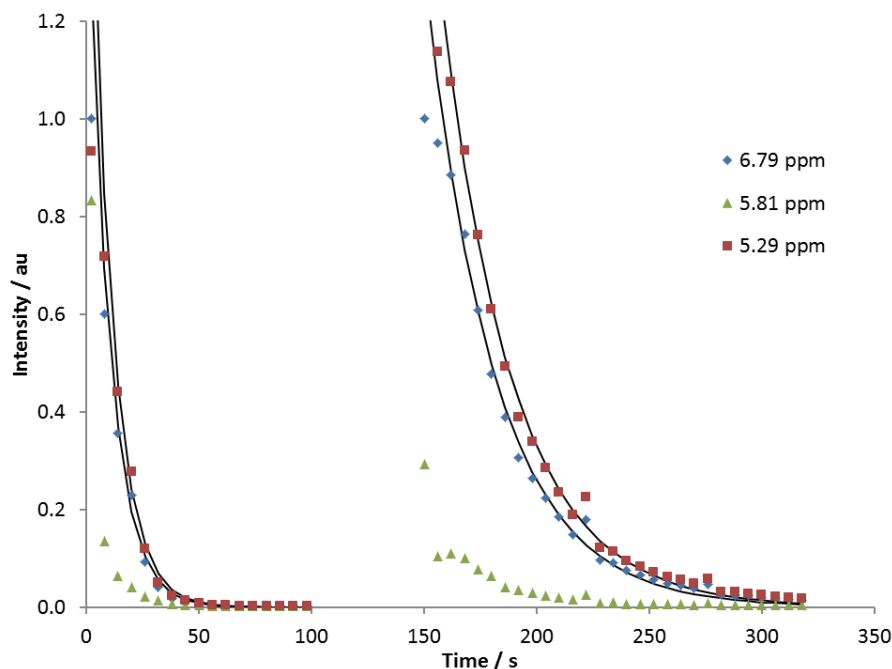


Figure 209: The decay of parahydrogen derived signals upon hydrogenation of phenylacetylene to styrene using Crabtree's catalyst, $[\text{Ir}(\text{COD})(\text{PCy}_3)(\text{py})][\text{PF}_6]$

During these measurements, a very small proton signal for H₂ is visible in the first few OPSY NMR spectra, which shows that the process is efficient as the *p*-H₂ that binds to the catalyst goes on to hydrogenate the substrate rather than dissociate without reacting. Hyperpolarised signals for COE were also visible in the OPSY NMR spectra, showing that activation of the catalyst requires the hydrogenation of the COD ligand and subsequent dissociation of the resulting COE. Thermal spectra recorded after each run show the absence of signals for H₂ or HD, indicating that all the H₂ in solution had been consumed to form the major product styrene (~ 90 %), along with a small amount of ethyl benzene, COE and some minor hydride-containing species (< 2 %). From these hydrogen decay data, the relative concentration of styrene has been calculated over time (Figure 210). For the first shake the rates were calculated as $(10.3 \pm 1.1) \times 10^{-2} \text{ s}^{-1}$ and $(10.2 \pm 1.1) \times 10^{-2} \text{ s}^{-1}$ for the two largest hydrogenated signals for styrene and for the second one they are $(3.03 \pm 0.03) \times 10^{-2} \text{ s}^{-1}$ and $(2.98 \pm 0.03) \times 10^{-2} \text{ s}^{-1}$ respectively. They therefore match those calculated from the *p*-H₂ decay graphs, as expected.

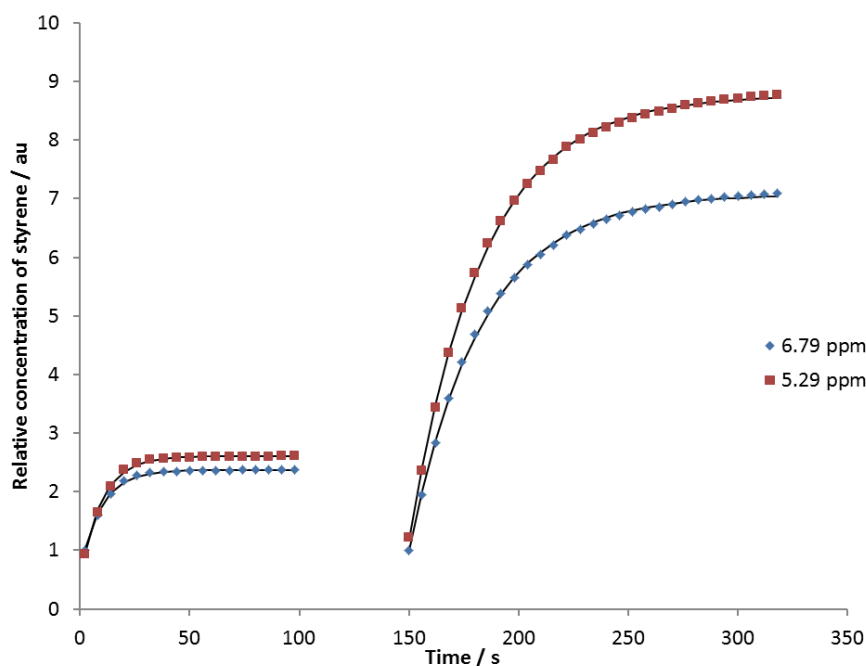


Figure 210: Relative concentration of styrene produced from summing the integrals of styrene after each OPSY spectrum using Crabtree's catalyst

Using Letort's method of a double logarithmic plot, the order of the reaction with respect to time, n_t , using Crabtree's catalyst was determined. Shake one gave an order of 1.10 ± 0.06 whereas for shake two the order decreased to 0.96 ± 0.02 , as shown in Figure 211. This suggests that initially about 10 % of the iridium centres have two molecules of hydrogen bound, but as the reaction progresses this decreases as there is a change in mechanism or speciation over time. This is consistent with deactivation of the catalyst due to the formation of iridium dimers as reported by Crabtree.⁴⁴ It could also be due to the fact that initial activation of Crabtree's catalyst requires two hydrogen molecules to fully hydrogenate the COD ligand and therefore the active species for hydrogenation, where COD is no longer present, is different to the starting complex.

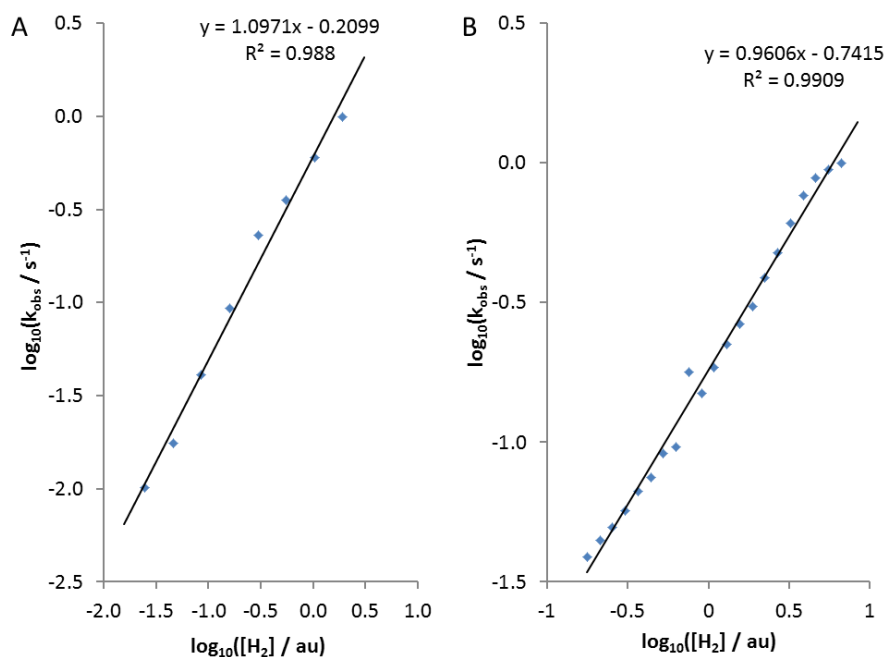


Figure 211: Letort's logarithmic graphs to determine reaction order with respect to time for shake one (A) and shake two (B) showing the decrease in order using Crabtree's catalyst

A repeat of this experiment using Crabtree's catalyst, with an identically made sample produced comparable results as shown in Table 46, showing that in the first shake, the reaction order with respect to time for the concentration of H₂ is more than 1.

Table 46: Rate and order values for two identically produced samples of Crabtree's catalyst used for the hydrogenation of phenylacetylene

Sample	Shake	¹ H NMR signal / δ	Initial rates / 10 ⁻² s ⁻¹	Cumulative rates / 10 ⁻² s ⁻¹	Order, n _t
A	1	6.79	(10.5 ± 1.2)	(10.3 ± 1.1)	1.10 ± 0.06
		5.29	(10.4 ± 1.0)	(10.2 ± 1.1)	1.06 ± 0.09
A	2	6.79	(3.24 ± 0.09)	(3.03 ± 0.03)	0.96 ± 0.02
		5.29	(3.14 ± 0.09)	(2.98 ± 0.03)	0.97 ± 0.02
B	1	6.79	(9.94 ± 0.61)	(9.11 ± 1.68)	1.14 ± 0.08
		5.29	(9.91 ± 0.62)	(8.65 ± 0.56)	1.22 ± 0.08
B	2	6.79	(2.76 ± 0.10)	(2.54 ± 0.05)	0.96 ± 0.02
		5.29	(2.77 ± 0.10)	(2.55 ± 0.05)	0.96 ± 0.02

6.2.3. Hydrogenation of phenylacetylene using the neutral bidentate carbene complexes

In contrast to observations using Crabtree's catalyst, for **1** there is no change in the rates between the first and second shake ($(2.93 \pm 0.61) \times 10^{-2} \text{ s}^{-1}$ and $(2.96 \pm 0.63) \times 10^{-2} \text{ s}^{-1}$ for the two largest hydrogenated signals for styrene for the first shake and $(2.95 \pm 0.73) \times 10^{-2} \text{ s}^{-1}$ and $(3.00 \pm 0.67) \times 10^{-2} \text{ s}^{-1}$ for the same signals for the second shake, see Figure 212). This suggests that degradation of the catalyst either does not occur or happens over a much longer time period than studied. This is consistent with no precipitation of degraded catalyst over longer time periods. Instead the catalyst may be resistant to forming the cluster type species that Crabtree's catalyst is reported to form.⁴⁴

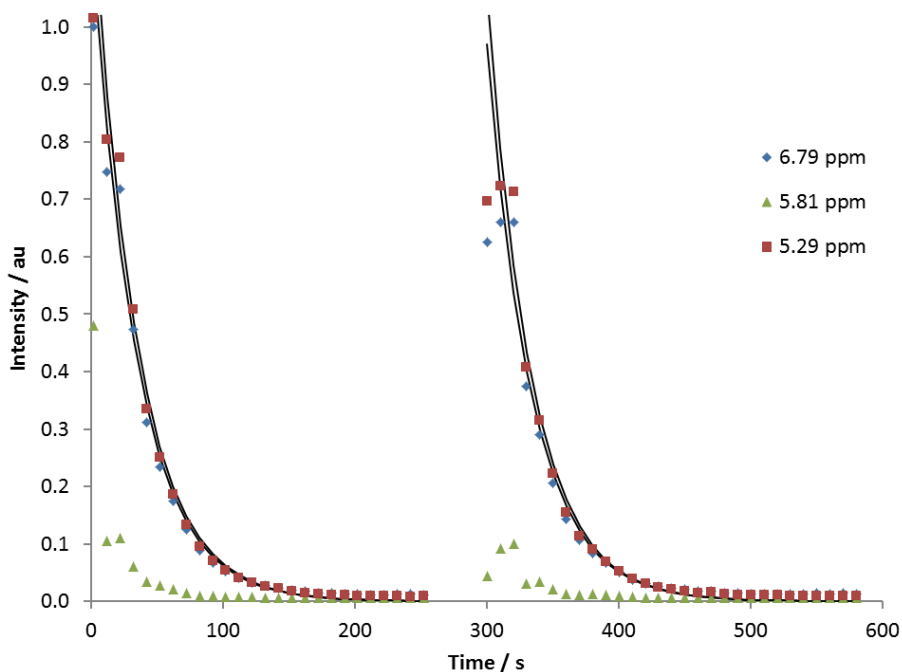


Figure 212: The decay of parahydrogen derived signals upon hydrogenation of phenylacetylene to styrene using **1**

This catalyst is, however, less efficient than Crabtree's catalyst as a larger signal for H_2 is observed at the start of the ^1H OPSY NMR experiments, albeit not enough to significantly hinder hydrogenation or affect kinetic modelling. Therefore, a small signal for hydrogen is observable in the thermal spectra recorded after each run, indicating that all the hydrogen in solution is not consumed during the reaction. During these reactions,

no enhanced signals for COE were observed and the proton spectrum recorded after the OPSY NMR runs indicates no hydrogenation of COD has occurred. An example system has been described previously, when, on the timescale of phenylacetylene hydrogenation, no hydrogenation of the diene of the catalyst occurs. Esteruelas et al. have studied phenylacetylene hydrogenation using $[\text{Rh}(\text{NBD})(\text{PPh}_3)_2][\text{BF}_4]$ where NBD is 2,5-norbornadiene²⁷⁸ or $[\text{Ir}(\text{COD})(\eta^2\text{-}i\text{-Pr}_2\text{PCH}_2\text{CH}_2\text{OMe})]$ where COD is 1,5-cyclooctadiene and have found the COD ligand to be stable.²⁷⁹ The stability of COD to hydrogenation in the complex $[\text{Ir}(\text{H})_2(\text{COD})(\text{dppm})][\text{BF}_4]$ at room temperature has also been studied²⁸⁰ and no decomposition has been observed, suggesting these diene complexes can form important stable intermediates in hydrogenation reactions.

On analysing the relative increase in styrene concentration over time (see Figure 213), the same values were again obtained for each shake; $(2.95 \pm 0.06) \times 10^{-2} \text{ s}^{-1}$ and $(3.05 \pm 0.07) \times 10^{-2} \text{ s}^{-1}$ for the two largest hydrogenated signals for styrene for the first shake and $(2.78 \pm 0.10) \times 10^{-2} \text{ s}^{-1}$ and $(2.93 \pm 0.06) \times 10^{-2} \text{ s}^{-1}$ for the second. The simulated data does not quite fit the experimental data due to the fact that the mechanism involves numerous steps and full hydrogenation does not occur. Furthermore, error is introduced in the analysis approach, as a minor amount of H_2 binds and falls off, without hydrogenation occurring.

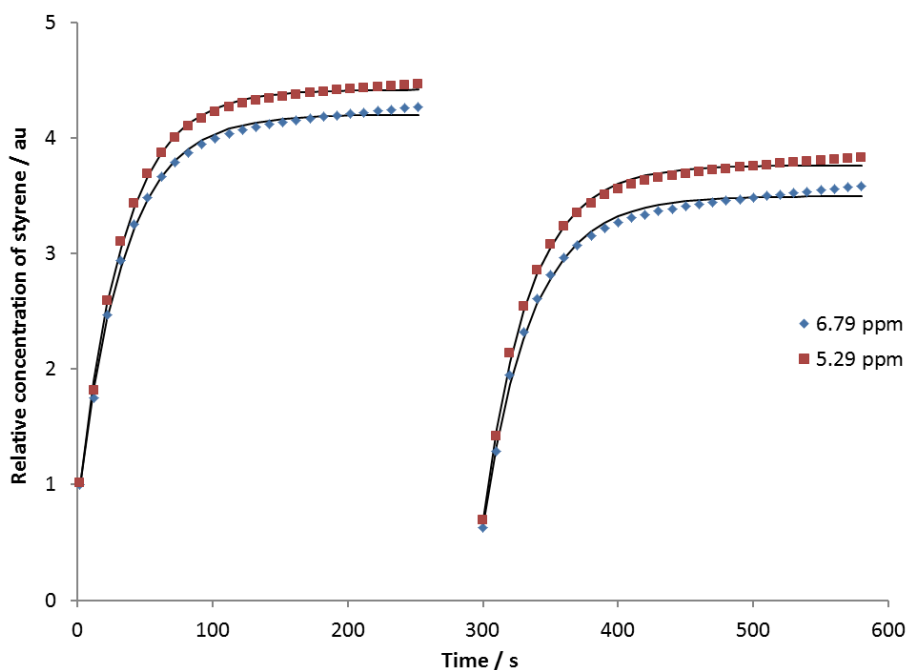


Figure 213: Relative concentration of styrene produced from summing the integrals of styrene after each OPSY spectrum using **1**

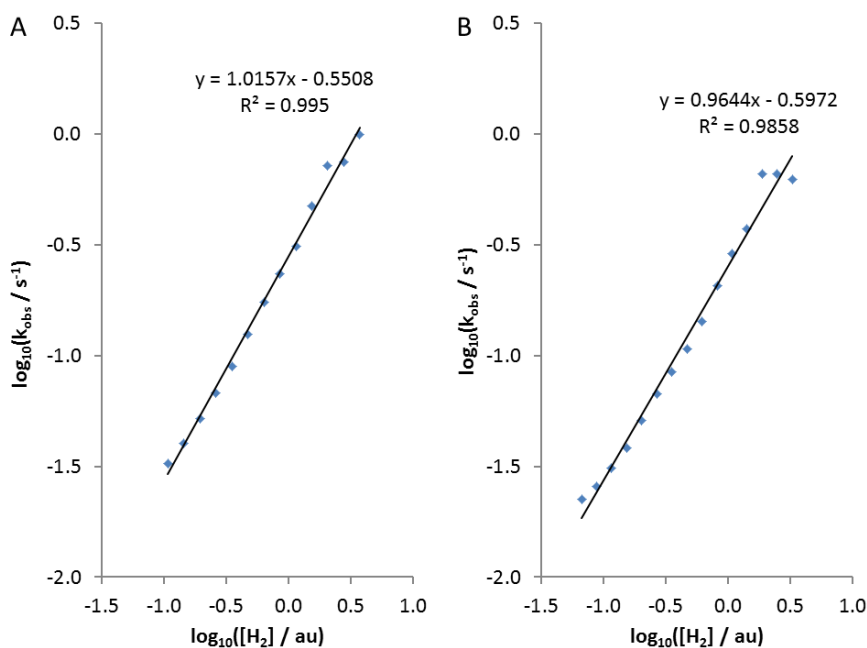


Figure 214: Letort's logarithmic graphs to determine reaction order with respect to time for shake one (A) and shake two (B) showing the constant order using **1**

When Letort's method was used to calculate the reaction order, the values for both shakes were close to 1 (1.02 ± 0.03 for shake one and 0.96 ± 0.05 for shake two, see Figure 214). The initial reaction order of 1 suggests that only one molecule of *p*-H₂ binds to the catalyst and that activation is very rapid, in contrast to when Crabtree's catalyst is used (see Section 6.4 for further discussion on the mechanism). The fact that the order of 1 is maintained for the second shake indicates again that only one molecule of *p*-H₂ binds to each catalyst centre during hydrogenation.

Upon moving to **3**, the rates recorded using the OPSY NMR analysis technique are slightly faster than for **1**, at $(3.98 \pm 0.41) \times 10^{-2} \text{ s}^{-1}$ and $(4.02 \pm 0.45) \times 10^{-2} \text{ s}^{-1}$ for the two largest hydrogenated signals for styrene for the first shake and $(4.23 \pm 0.34) \times 10^{-2} \text{ s}^{-1}$ and $(4.17 \pm 0.43) \times 10^{-2} \text{ s}^{-1}$ for the same signals for the second shake. They follow the same trend as for **1**, indicating that the reaction mechanism and speciation does not change over the time course of the reaction. On analysing the relative increase in styrene concentration over time, the same values were again obtained for each shake, however, they were lower values than those obtained from the original data and are less accurate due to the extra data manipulation; $(2.24 \pm 0.11) \times 10^{-2} \text{ s}^{-1}$ and $(2.26 \pm 0.11) \times 10^{-2} \text{ s}^{-1}$ for the two largest hydrogenated signals for styrene for the first shake and $(2.35 \pm 0.14) \times 10^{-2} \text{ s}^{-1}$ and $(2.36 \pm 0.13) \times 10^{-2} \text{ s}^{-1}$ for the second. The order of the reactions

again both correspond to approximately 1 (1.02 ± 0.05 for shake one and 1.01 ± 0.04 for shake two). There is a small signal for hydrogen in the first OPSY NMR spectra of each shake, once more indicating a small amount of ineffective hydrogen addition, although minimum effect on the simulated data is observed.

On changing to catalyst **4**, hydrogenation of phenylacetylene occurs with the observed rates corresponding to $(3.29 \pm 0.54) \times 10^{-2} \text{ s}^{-1}$ and $(3.10 \pm 0.19) \times 10^{-2} \text{ s}^{-1}$ for shake one and $(3.77 \pm 0.42) \times 10^{-2} \text{ s}^{-1}$ and $(4.01 \pm 0.33) \times 10^{-2} \text{ s}^{-1}$ for shake two. When using the cumulative summing approach, the model does not fit the data accurately, particularly towards the end of each measurement. The rate values are now much lower, at $(2.37 \pm 0.15) \times 10^{-2} \text{ s}^{-1}$ and $(2.59 \pm 0.15) \times 10^{-2} \text{ s}^{-1}$ for shake one and $(1.79 \pm 0.32) \times 10^{-2} \text{ s}^{-1}$ and $(2.20 \pm 0.33) \times 10^{-2} \text{ s}^{-1}$ for shake two. Hydrogen is now highly visible in the ^1H OPSY NMR spectra and the thermal spectra recorded after the *parahydrogenation* reaction has occurred. This is due to hydrogen exchanging with the complex but not being transferred to the phenylacetylene and therefore the hydrogen is not the limiting factor because it is not used up in solution during each shake. This allows hydrogenation using normal hydrogen to occur and therefore the rate measurements become less accurate. This is reflected in the numbers for the orders of reaction which are approximately equal at 1.29 ± 0.11 for shake one and 1.31 ± 0.13 for shake two. Because there is now excess hydrogen in solution, multiple hydrogen ligands have the potential to bind to the catalyst and change the reaction mechanism.

When the even less stable complex **2** is used, the reactivity is now very different to that observed for **1** and more like that of **4**. Here, a very substantial hydrogen peak is seen in the OPSY NMR spectra, which leads to a dramatic reduction in the hydrogenation capabilities of the catalyst. Thus, comparable hydrogen decay rates could not be calculated. This rapid consumption of *p*-H₂, without hydrogenation, is consistent with that observed on addition of hydrogen alone, to the catalyst and is also commensurate with the observation of a large thermal signal for hydrogen after the hydrogenation reaction. Here, the limiting step is no longer the hydrogenation process. Table 47 gives a summary of the observed hydrogenation rates and reaction orders calculated using Crabtree's catalyst, **1**, **3** and **4**. The initial OPSY spectra for phenylacetylene hydrogenation using Crabtree's catalyst, **1** and **2** are shown for comparison in Figure 215, with a significant H₂ signal being observable when using **2**.

Table 47: Average values for the hydrogenation rates of phenylacetylene to styrene using the enhanced signal decay data and the cumulatively summed data, along with the orders of reaction determined from the rate data based on the enhanced signal decay. The four catalysts detailed are Crabtree's catalyst and complexes 1, 3 and 4

Catalyst	Crabtree's	1	3	4
Shake one	10.5 ± 1.1	2.95 ± 0.62	4.00 ± 0.43	3.20 ± 0.37
Shake two	3.19 ± 0.09	2.98 ± 0.70	4.20 ± 0.39	3.89 ± 0.38
Cumulative one	10.3 ± 1.1	3.00 ± 0.07	2.25 ± 0.11	2.48 ± 0.15
Cumulative two	3.01 ± 0.03	2.86 ± 0.08	2.36 ± 0.14	2.00 ± 0.33
Order one	1.10 ± 0.06	1.02 ± 0.03	1.02 ± 0.05	1.29 ± 0.11
Order two	0.96 ± 0.02	0.96 ± 0.05	1.01 ± 0.04	1.31 ± 0.13

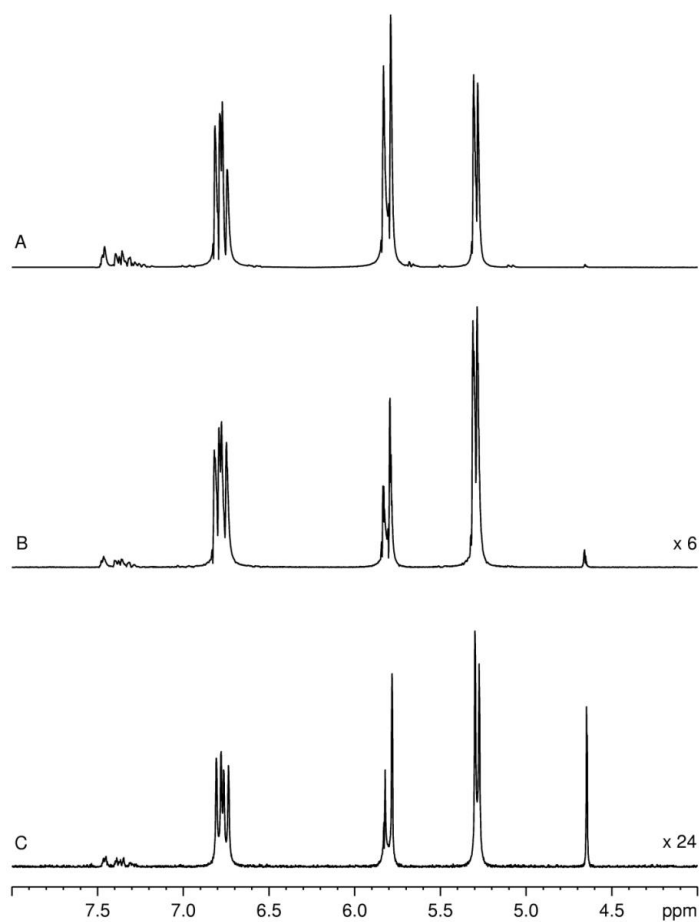


Figure 215: ^1H OPSY-dq spectra of the hydrogenation of phenylacetylene using Crabtree's catalyst (A), complex 1 (B) and complex 2 (C) showing the large signal for H_2 at $\sim \delta$ 4.6 in (C)

6.3. Monitoring the *parahydrogenation* of styrene

To gain an insight into the mechanism of hydrogenation, two CD₂Cl₂ samples both containing 2.0 mol% catalyst and enough styrene to produce 120 mM solutions were studied using the ¹H OPSY NMR method. Here, both catalysts, [Ir(COD)(PCy₃)(py)][PF₆] and **1**, were able to hydrogenate styrene to ethyl benzene; however, rates could not be determined for the two samples. This is because when using Crabtree's catalyst, the reaction occurred too rapidly, such that the majority of the *p*-H₂ had been consumed in the first ¹H OPSY NMR spectrum and this corresponded to an approximate conversion of 30 % from styrene to ethyl benzene, when comparing the resulting ¹H NMR spectrum with the spectrum prior to *p*-H₂ addition. No signals for excess H₂, HD or hydride species were present. Small enhanced signals were also visible in the ¹H OPSY NMR spectra for styrene itself, due to non-hydrogenative polarisation transfer to styrene. This may be from a SABRE-like effect due to coupling between the hydrides and styrene protons, although this only occurs at a low magnetic field and is therefore only visible in the first few scans. However, the observation of enhanced styrene may also be due to the alkyl-alkene equilibrium that is possible.²⁸¹ Partial hydrogenation of the styrene could occur to form the alkyl product which, without reductive elimination, could reform the η²-alkene. Coupling between the *p*-H₂ derived proton (highlighted in Figure 216) and the original styrene protons could then be the route to polarisation transfer and observation of enhanced styrene signals. Another route may be via reversible *p*-H₂ addition and moving of the *p*-H₂ atoms into the styrene molecule. For Crabtree's catalyst, only a minimal signal for COE is observed in the initial ¹H OPSY NMR spectrum, with the signal-to-noise being poorer than for the spectra of phenylacetylene hydrogenation.

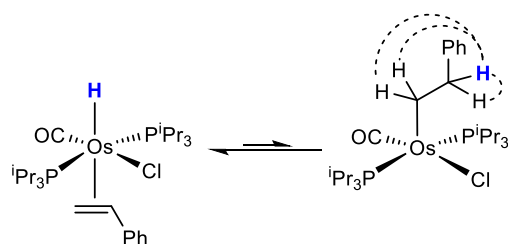


Figure 216: Reversible equilibration between the η^2 -alkene and alkyl form showing coupling that could lead to polarisation transfer described by Andriollo *et al.* for an osmium phosphine complex²⁸¹

For **1** the rates were much slower and after the first set of ^1H OPSY NMR measurements less than 5 % of the starting material had been hydrogenated to form ethyl benzene. In this sample, a large ^1H OPSY NMR signal was observed for H_2 as well as for styrene, meaning that oxidative addition and reductive elimination occurs without hydrogenation, but with polarisation transfer occurring to the alkene protons of styrene, such that they appear enhanced. This is demonstrated in Figure 217. Again for **1**, no hydrogenation of COD is observed. A comparison between the ^1H NMR spectrum recorded before *p*- H_2 addition and one recorded after *para*hydrogenation, shows a large signal for excess H_2 in solution.

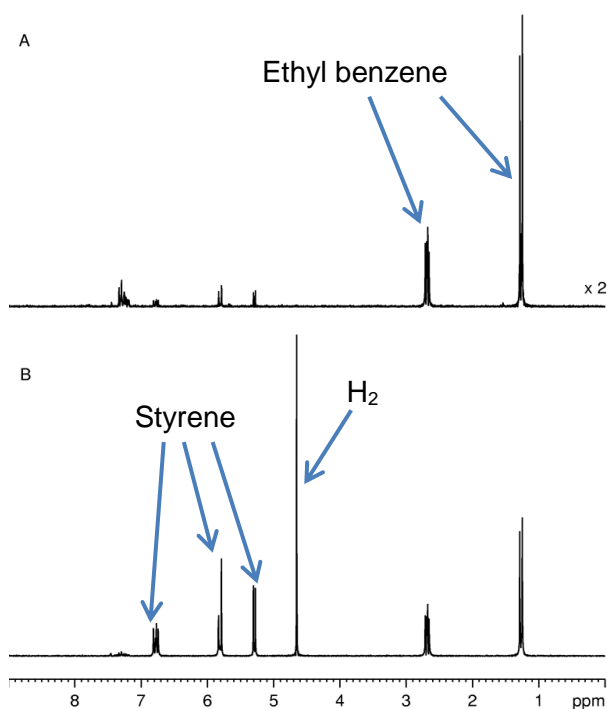


Figure 217: Hydrogenated signals for ethyl benzene using Crabtree's catalyst (A) and using **1** (B) also showing a large H_2 signal and enhanced styrene signals

6.4. Elucidating the hydrogenation mechanisms

Selectivity in hydrogenation reactions of triple bonds, to form either partially hydrogenated double bonds or fully hydrogenated saturated systems is a challenge. The over-hydrogenation of phenylacetylene to form ethylbenzene is commonly observed for the types of homogeneous catalysts used, with ethylbenzene being produced on a much slower timescale than styrene.^{278-279, 282} The ¹H OPSY NMR spectra shown in Figure 218 clearly show the differences between using Crabtree's catalyst, where hydrogenation of the COD ligand and subsequent catalyst decomposition and deactivation occurs, and using **1** where no COD hydrogenation is evident and the catalyst remains stable.

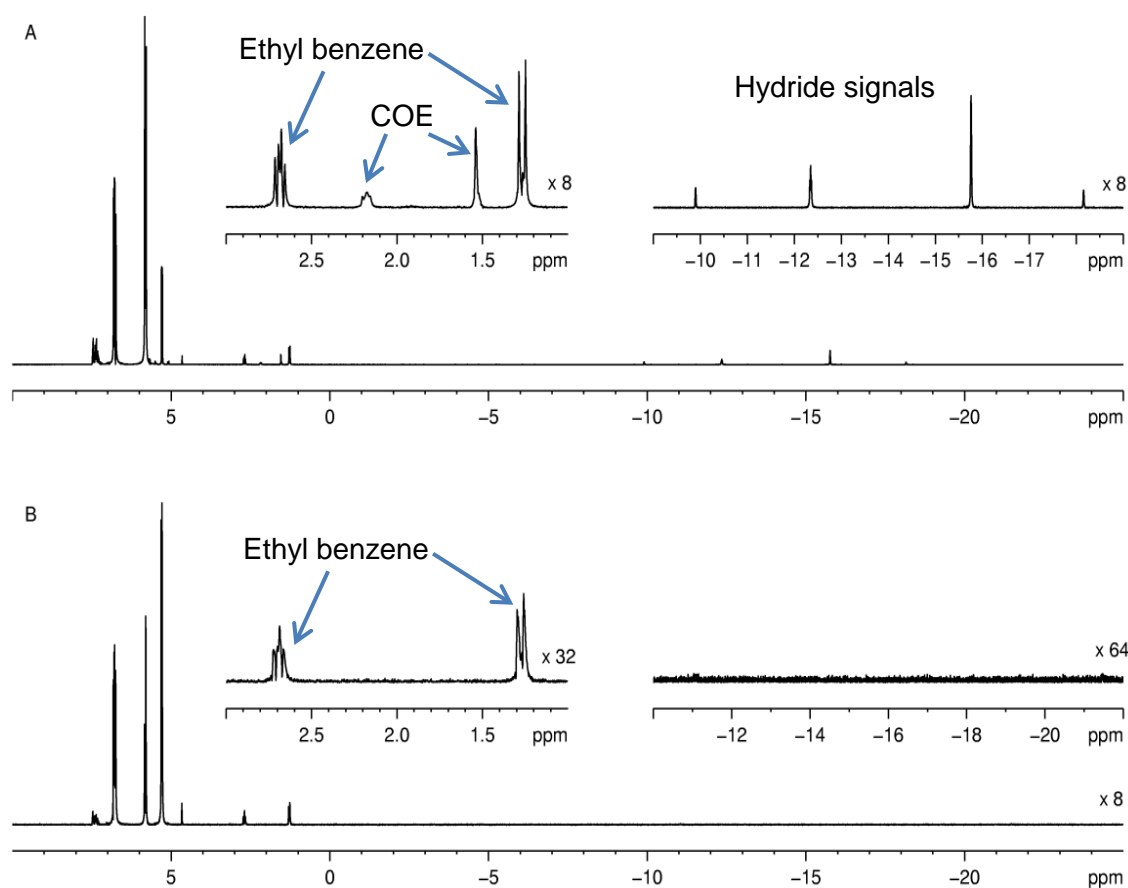


Figure 218: Initial ¹H OPSY-dq spectra for phenylacetylene hydrogenation using Crabtree's catalyst (A), showing signals for COE and hydride species (inset) and using complex **1** (B) with no signals corresponding to hydrogenation of COD or hydride species (inset)

When starting from styrene, hydrogenation to ethylbenzene has also been shown to occur. The fact that hydrogenation of styrene occurs, means that two possible mechanisms to produce ethyl benzene are possible when the starting material is phenylacetylene; either direct addition of two equivalents of H₂ to phenylacetylene without dissociation from the metal centre, or dissociation of styrene, followed by re-association and then a second hydrogenation step. However, because only very limited amounts of ethylbenzene are formed from phenylacetylene, particularly when using **1**, it suggests that most of the phenylacetylene must be hydrogenated to styrene, before the hydrogenation of styrene to ethylbenzene occurs.

When considering the mechanistic pathways of hydrogenation using Crabtree's catalyst and **1**, the relaxation of the *p*-H₂ derived hydride ligands is very important. If the relaxation rate of the *p*-H₂ derived nuclei is fast relative to the pairwise transfer of the hydrides to an unsaturated bond, then the spin states will have returned to equilibrium before an enhanced NMR spectrum can be acquired. This typically occurs if *p*-H₂ adds to a metal complex before an unsaturated substrate. However, if the relaxation is slow, as occurs when *p*-H₂ binds to a metal complex after another ligand, then enhanced spectra are observed, as the *p*-H₂ derived nuclei can rapidly add across a multiple bond.^{77, 222, 283}

When the catalyst is Crabtree's, the diene (COD) is easily hydrogenated and therefore the ligands that must bind to the metal centre must be alkyne or alkene substrates or solvent. As the substrates are hydrogenated, no ligands remain to stabilise the metal centre so decomposition occurs. A postulated mechanism, where the COD ligand is first hydrogenated, and the metal binds a substrate ligand and a solvent ligand, before the addition of fresh *p*-H₂ to enable *parahydrogenation*, is shown in Figure 219. In this case, phenylacetylene can be fully hydrogenated to ethylbenzene either directly or in multiple steps. During the reactions shown in Figure 219, using Crabtree's catalyst, relaxation effects should not cause a problem. This is because the mechanism proceeds via alkyne binding followed by oxidative addition of the hydrogen.⁶⁸ Rapid transfer to the alkyne follows, which limits the time available for relaxation of the hydrides when bound to the iridium metal centre and therefore this does not need to be factored in.

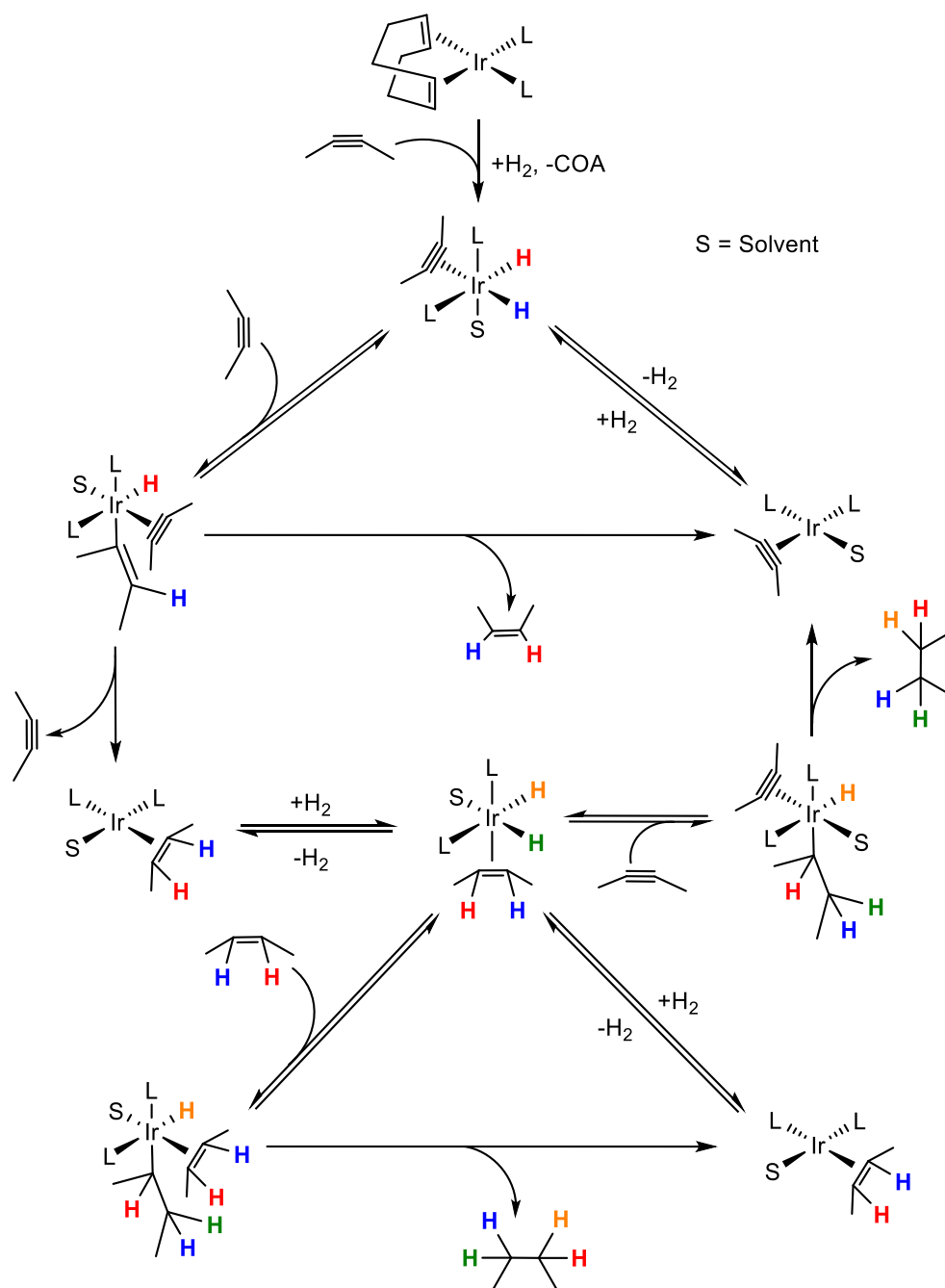


Figure 219: Possible mechanistic routes for hydrogenation to form ethyl benzene from phenylacetylene using Crabtree's catalyst

In comparison, a different route has been described in the literature for the hydrogenation catalyst, $[\text{Ir}(\text{COD})(^i\text{Pr}_2\text{PCH}_2\text{CH}_2\text{OMe})][\text{BF}_4]$, containing a diene and bidentate ligand, where the diene is hydrogenation resistant.²⁷⁹ Studies using $[\text{Ir}(\text{COD})(^i\text{Pr}_2\text{PCH}_2\text{CH}_2\text{OMe})][\text{BF}_4]$, as depicted in Figure 220, where the oxygen donor is a methoxy group, have shown the hydrido-alkynyl-dialkene complex **A** is the main species in solution. This is confirmed in the ¹H NMR spectrum by the presence of a

hydride ligand signal at $\delta -23.24$. The equivalent alkynyl complex is not observed when **1** is used and instead the dihydride-dialkene complex **5** is visible, with a structure like that shown for **B**. This complex is not seen when $[\text{Ir}(\text{COD})(^i\text{Pr}_2\text{PCH}_2\text{CH}_2\text{OMe})][\text{BF}_4]$ is used, but is proposed as an important intermediate. As no vacant site is available in complex **5** or in **B**, the mechanism suggested by Esteruelas et al.²⁷⁹ for hydrogenation using $[\text{Ir}(\text{COD})(^i\text{Pr}_2\text{PCH}_2\text{CH}_2\text{OMe})][\text{BF}_4]$, describes dissociation of the OMe group of the bidentate ligand in **B**, followed by coordination of the phenylacetylene to form **C**, and subsequent transfer of the hydride lying in a *cis* position to the alkyne. This produces the *trans*-hydrido-alkenyl complex shown in **D**. Hydrogen must then react with **D** to enable the reductive elimination of styrene.²⁷⁹ For this reaction, relaxation may have an important effect because when the dihydrogen addition occurs first, there is more time for relaxation of the hydride ligands when bound to the iridium metal centre before addition across the triple bond of the alkyne. In the case of complex **1**, dissociation of the phenolate oxygen has not been shown to occur under any previous reaction conditions. Instead, a vacant site for phenylacetylene binding may be created via dissociation and rebinding of one side of the COD ligand as the COD ligand has previously been shown to be labile.

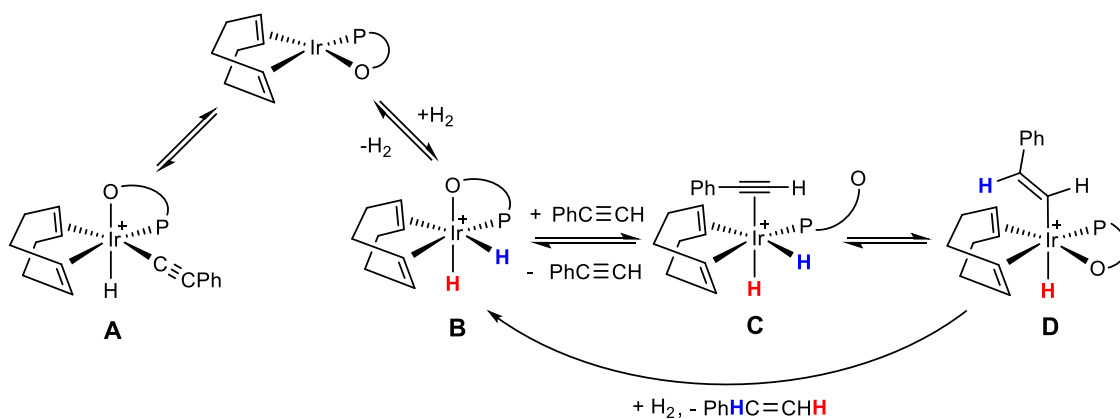


Figure 220: The proposed mechanistic pathway for the hydrogenation of phenylacetylene to form styrene using $[\text{Ir}(\text{COD})(^i\text{Pr}_2\text{PCH}_2\text{CH}_2\text{OMe})][\text{BF}_4]$ as described by Esteruelas et al.²⁷⁹

Although the dihydride-dialkene complex **5** is observed in small quantities during hydrogenation reactions when using **1**, the fact that significantly enhanced signals of the hydrogenation products are observed in the ^1H NMR spectra when complex **1** is used means that rapid relaxation effects are not in operation. Therefore, the pathway of hydrogen addition after ligand addition is most likely. However, as

hydrogenation of the COD ligand is not observed in the ^1H OPSY NMR spectra during the reactions, it is anticipated that only a very small proportion of the complex is rapidly converted to the active hydrogenation catalyst via intermediate **5**. The high amount of hydrogenation indicates that this small amount of complex is very active for hydrogenation of phenylacetylene. This is also commensurate with the slow reaction of complex **1** with pyridine and hydrogen when forming the SABRE active species as described in Section 2.4.1. This mechanism also suggests that double hydrogenation of phenylacetylene to ethylbenzene without elimination from the metal centre does not occur. The major points to consider are that;

1. no hydrogenation of the bound COD ligand is visible on the NMR timescale during the reaction
2. H_2 is observed in the ^1H OPSY NMR spectra due to rapid H_2 oxidative addition and reductive elimination without hydrogenation
3. the only observable hydride signals, at $\delta -11.0$ and -21.5 , are very small and correspond to the dihydride complex, **5**, as has previously been shown when only H_2 is added to complex **1** in CD_2Cl_2
4. the slow production of only small amounts of ethylbenzene is seen, due to formation of styrene having to occur first

Overall, for these iridium carbene complexes, H_2 binds reversibly and this can transfer reversibly into the alkyne, phenylacetylene, to form the alkene, styrene. Once a second hydrogenation step has occurred to form ethylbenzene, the alkane, the hydrogenation is no longer reversible. When looking at the mechanism using the neutral bidentate iridium carbene complexes, the electron density on the metal centre has a large effect on the stability and reactivity of the complexes. As the electron-donating ability of the complexes is increased, through the series from $\text{NO}_2 < \text{COOMe} < \text{Cl} < \text{H}$, the electron density on the metal increases. This leads to faster reversible binding of H_2 and subsequently a poorer ability to transfer H_2 into the alkyne to form the alkene. Therefore complex **1** is the most efficient hydrogenation catalyst out of the series, due to its greater ability to transfer the hydrogen.

6.5. Conclusion

In this chapter, a new method to analyse reaction kinetics and gain information about the order of reaction has been developed. The use of ^1H OPSY NMR experiments has facilitated the study of the *parahydrogenation* of phenylacetylene to styrene and ethyl benzene. The reactions followed the decrease in enhanced signal corresponding to the *p*- H_2 derived protons of styrene, commensurate with the consumption of *p*- H_2 . The reactivities of complexes **1**, **2**, **3** and **4** were investigated and compared to the reactivity of Crabtree's catalyst, $[\text{Ir}(\text{COD})(\text{PCy}_3)(\text{py})][\text{PF}_6]$. It was found that the neutral bidentate carbene derivatives act very differently to Crabtree's catalyst, with only hydrogenation of the phenylacetylene occurring and no hydrogenation of the COD ligand being observed as for hydrogenation using Crabtree's catalyst. When using the neutral bidentate carbene derivatives, the only minor hydride-containing products were those that are equivalent to complex **5** as discussed in Section 2.4.1, formed when hydrogen is added to **1**. No other stable hydride species were formed, in contrast to when Crabtree's catalyst was employed for hydrogenation. Furthermore, large signals for H_2 in solution were observed when complexes **2**, **3** and **4** were used, consistent with rapid oxidative addition and reductive elimination of *p*- H_2 without productive hydrogenation of the substrate occurring. This was not the case when Crabtree's catalyst was employed, thus demonstrating that it is far more efficient at hydrogenation compared to the neutral bidentate carbene derivatives.

The rates of *parahydrogen* consumption, equivalent to the rates of substrate formation, were used to gain information about the orders of reaction with respect to hydrogen. It was found that for Crabtree's catalyst the initial hydrogenation rates were approximately three times faster than the rates when using **1**, but over time the rates using Crabtree's catalyst decreased to be approximately equal to those of **1**. In addition, when using Crabtree's catalyst ~ 1.15 molecules of H_2 were needed for initial hydrogenation, but over time, due to changes in speciation, active catalyst form and degradation, this reduced to ~ 1 molecule. When using **1**, both the hydrogenation rates and reaction order stayed the same, with no catalyst degradation being observed and consistently only one molecule of hydrogen being bound to the catalyst at once.

7. Conclusions and future studies

The goal of this work was to synthesise neutral bidentate iridium carbene complexes and investigate their ability to transfer polarisation from *parahydrogen* to suitable substrates. The focus of this project was to use these complexes to improve the sensitivity of solution NMR. Several neutral pre-catalyst derivatives have been synthesised which contain a carbene ligand with a pendent phenolate group. The complexes incorporate a variety of electron-withdrawing substituents within the carbene backbone and they have proven to be efficient SABRE catalysts for a variety of different substrates in a range of different polarity solvents. Their potential to act as hydrogenation catalysts has also been investigated.

7.1. Development of neutral bidentate iridium carbene complexes

In Chapter 2, four new bidentate iridium carbene complexes have been developed with the structure shown in Figure 221. Overall, the four substituents H, Cl, COOMe and NO₂ have increasing Hammett σ_p^- values, of 0.00, 0.19, 0.75 and 1.27 respectively and thus their electron-withdrawing capabilities increase through the series.

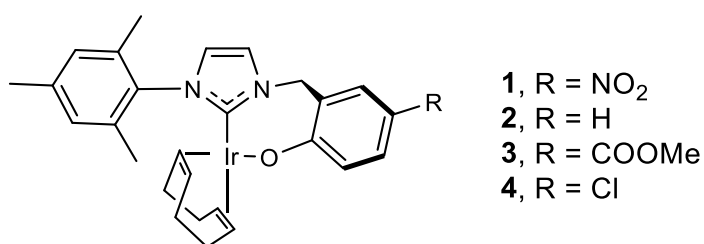


Figure 221: Structure of the neutral bidentate iridium carbene complexes with the described R group in the para position to the phenolate group

Multi-step synthetic procedures have been developed to synthesise these derivatives, with the simplest route being for **1**, due to the commercial availability of the benzyl bromide starting material. The other three complexes required multiple steps before the benzyl bromide could be reacted with mesityl imidazole to form the necessary imidazolium bromide salt precursor to the carbene ligand as shown in Figure

222. The iridium complexes were formed from the silver carbene complexes via transmetallation with $[\text{Ir}(\text{COD})\text{Cl}]_2$.

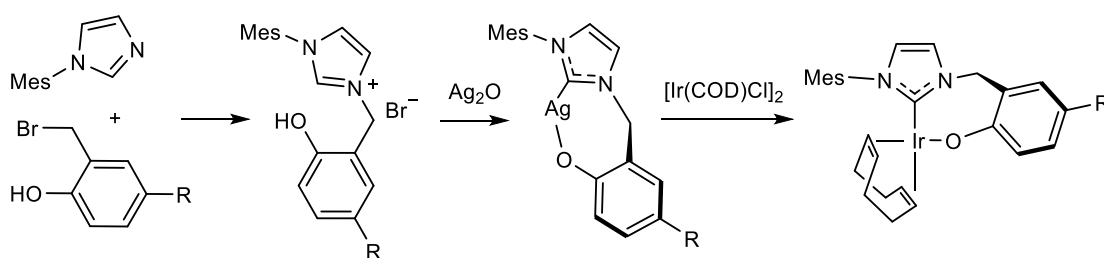


Figure 222: Main synthetic steps required to form the bidentate iridium carbene derivatives

Complexes **1**, **3**, and **4** exhibit fluxional behaviour in solution with their corresponding NMR spectra demonstrating temperature dependence. At 298 K, the ¹H NMR signals for the CH₂ linker protons and the COD CH protons are broadened into the baseline of the spectra. The signals for the CH₃ and CH aromatic protons of the mesityl ring are also broadened at 298 K, commensurate with rapid rotation around the C-N bond. On cooling, all the signals for **1**, **3** and **4** resolve. Complex **2**, however, does not exhibit this fluxional behaviour on the NMR timescale at 298 K and all its ¹H NMR signals are therefore resolved. Crystal structures of **1** and **3** have also been determined by XRD and show that the complexes adopt distorted square planar configurations, with their corresponding bond angles all being close to 90 °.

In CD₂Cl₂, in the presence of H₂, each complex undergoes the rapid and reversible addition of H₂ to form two very minor dialkene-dihydride isomers as shown in Figure 223. No reactivity with pyridine alone is observed for these complexes in CD₂Cl₂. However, in the presence of both pyridine and hydrogen, the COD ligand is slowly hydrogenated to COE and COA and bis-pyridyl dihydride complexes form as shown in Figure 223. Several singlet hydride species, as depicted in square brackets in Figure 223, thought to form during COD hydrogenation, are also present during these reactions, and they disappear over time.

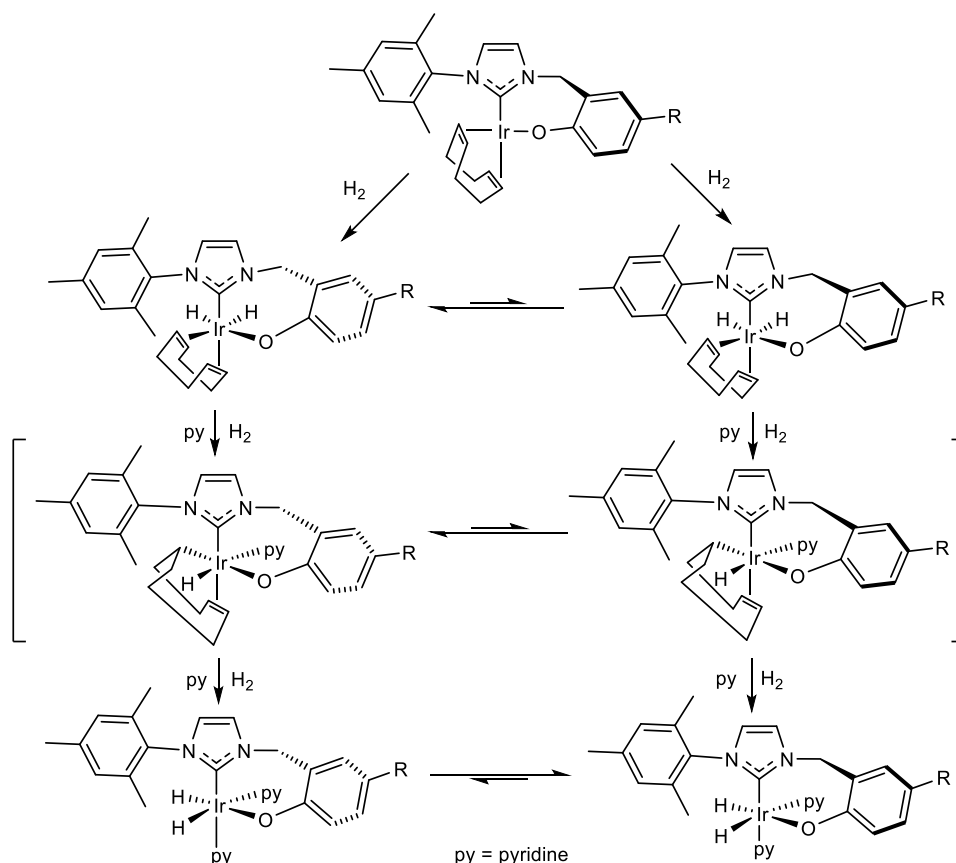


Figure 223: Formation of the dialkene-dihydride complexes, upon addition of H_2 and subsequent formation of the bis-pyridyl dihydride complexes in the presence of pyridine and H_2 , via singlet hydride intermediates. The isomer structures are also shown due to ring-flip of the seven-membered metallocycle

Due to ring-flip of the seven-membered metallocycle in the carbene backbone, and the potential for pyridine to bind to either side of the metallocycle, multiple isomers are present in solution as depicted in Figure 224. The relative equilibrium position is dependent on the electron-withdrawing capability of the substituent on the phenolate ring as detailed in Section 3.5. When the substrate is pyridine, **A** and **A'** are equivalent and **B** and **B'** are equivalent, as pyridine is not chiral. However, when chirality is introduced in the form of a chiral substrate, these are no longer equivalent and therefore 1H NMR signals for the isomers are visible as discussed in Section 4.3.3 for the substrate nicotine.

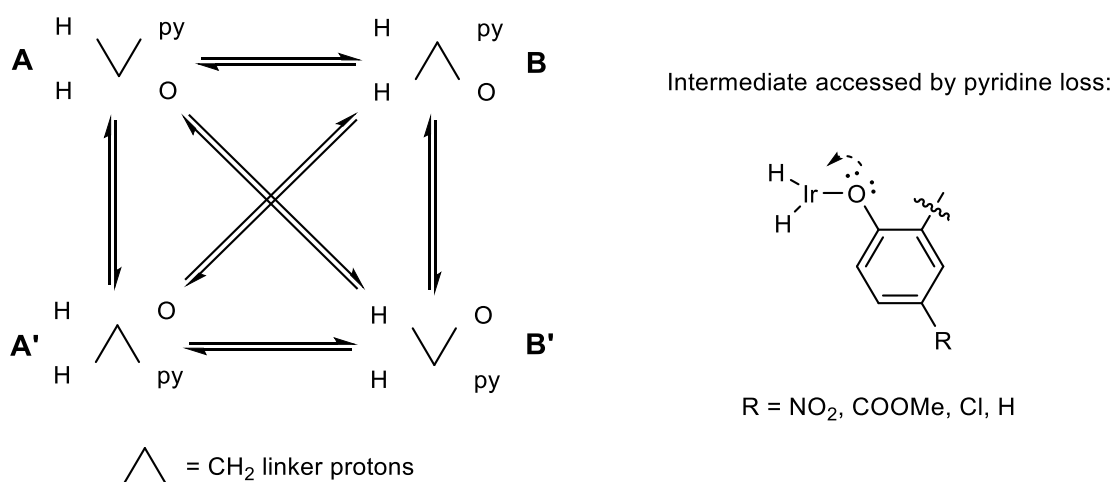


Figure 224: Summary of the isomer forms present for the bidentate iridium carbene dihydride complexes in solution and the intermediate that occurs on pyridine dissociation showing the electron-donating ability of the phenolate

In CD_3OD , the reactivity of **1** and **3** are very similar to when the solvent is CD_2Cl_2 . However, for complex **4**, the Ir-O bond becomes unstable in CD_3OD and a tris-pyridyl dihydride species forms alongside the bis-pyridyl dihydride species. When the substituent is H in **2**, which is even less electron-withdrawing, the activation pathway proceeded via initial iridium-oxygen bond cleavage to form a square planar iridium complex with the COD, carbene and pyridine ligands as depicted in Figure 225. Addition of hydrogen to this formed the alkene-dihydride complex with subsequent COD hydrogenation leading to the tris-pyridyl dihydride species (see Figure 225).

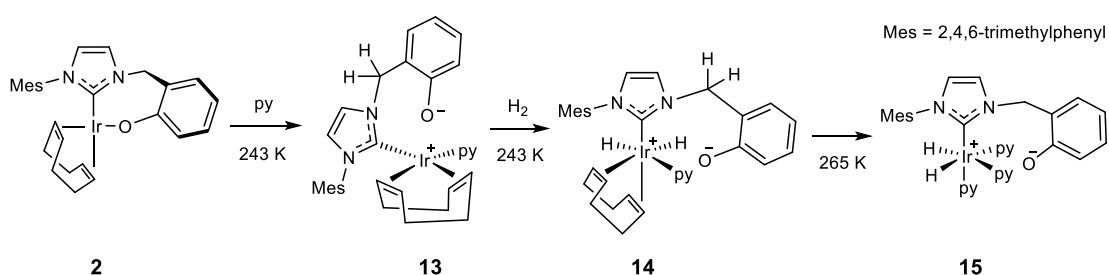
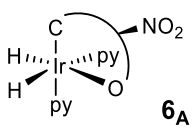
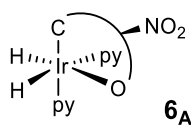
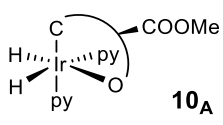
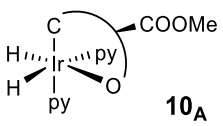
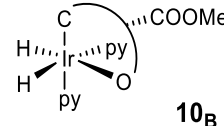
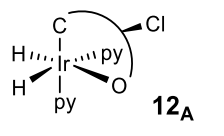
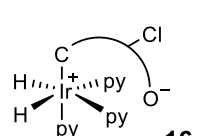
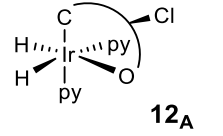
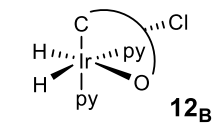
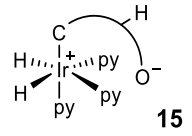
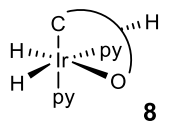


Figure 225: Reaction of **2** with pyridine, in CD_3OD , to form **13** and subsequent H_2 addition to form dihydride complex **14** before COD hydrogenation leads to complex **15**, with Ir-O bond dissociation

A summary of the different complexes formed in both CD_2Cl_2 and CD_3OD is given in Table 48, along with the ^1H NMR chemical shifts of the hydride ligands which are indicative of the isomer formed. The decreasing stability of the iridium-oxygen

bond, leading to its cleavage, indicates that the iridium centre cannot accommodate the extra electron density which arises from the phenolate bond. At higher electron densities, such as when the substituent on the phenolate is H, the oxygen ligand has a higher capability for σ - and π -donation as depicted in Figure 224. Therefore, it is preferential for the iridium-oxygen bond to break and a pyridine ligand to bind, so that the electron donation is lowered.

Table 48: Summary of the major SABRE-active products formed when the four pre-catalysts **1**, **2**, **3** and **4** are reacted with pyridine and hydrogen in methanol and dichloromethane

Pre-catalyst	Major product(s) formed with pyridine and H ₂ in CD ₃ OD	Major product(s) formed with pyridine and H ₂ in CD ₂ Cl ₂		
1	 6_A Hydrides δ -21 and -29	 6_A Hydrides δ -21 and -29		
3	 10_A Hydrides δ -21 and -29	 10_A Hydrides δ -21 and -29	 10_B Hydrides δ -22 and -25	
4	 12_A Hydrides δ -21 and -29	 16 Hydrides δ -22	 12_A Hydrides δ -21 and -29	 12_B Hydrides δ -22 and -25
2	 15 Hydrides δ -22	 8 Hydrides δ -22 and -25		

These complexes are yellow/orange in solution and all four of them exhibit charge-transfer bands in the visible region of the spectra, consistent with their respective colours. For **1**, an intraligand band at 406 nm with a molar absorption coefficient of $21060 \text{ dm}^3 \text{ mol}^{-1} \text{ cm}^{-1}$ masks the metal d-to-p-orbital transitions which are visible for the other complexes at approximately 380, 430 and 490 nm, with molar absorption coefficients of between approximately 300 and $3000 \text{ dm}^3 \text{ mol}^{-1} \text{ cm}^{-1}$. The IR spectra of the complexes show stretching frequencies at approximately 1970 cm^{-1} and 2060 cm^{-1} for the two CO ligands, one *trans* to the phenoxide and one *trans* to the carbene, indicating the σ -donating properties of the carbene and phenolate ligands.

In this work, the formation of the CO complexes was used to determine the significance of the π -donation to the iridium metal centre from the phenolate ligand. This gave an indication of the electron-donating capabilities of the differing substituents. However, these CO complexes could also be used as SABRE pre-catalysts, depending on the ease at which the CO ligands could be substituted for substrate and hydride ligands. They could also have the potential to be used as CO-releasing molecules (CORMs) for medicinal purposes.²⁸⁴

All the pyridine dihydride-containing complexes undergo both pyridine and H_2 exchange at 298 K, which enables the incorporation of fresh *para*hydrogen and new substrate into the complex. Therefore, they can act as SABRE catalysts. An analysis of the resultant exchange rates calculated using ^1H EXSY NMR experiments show that the rates increase as a function of temperature and are on the order of seconds. In CD_3OD , hydrogen-deuterium exchange also occurs between the complexes and deuterium from the solvent, thus affecting the hydrogenation potential of the catalysts. Furthermore, the pyridine exchange rates are independent of the concentration of pyridine whereas the hydrogen exchange rates depend on the pyridine concentration. Thus, the first step in the reaction pathway is the dissociation of pyridine, followed by the binding of fresh hydrogen, subsequent loss of the former hydrogen molecule and rebinding of pyridine. Thus, the analysis of the pyridine ligand exchange rates is more representative than the hydrogen ligand exchange rates, due to analysis of a single step in the pathway rather than multiple steps.

Due to the presence of the chelating ligand and ring-flipping of the seven-membered metallocycle, as previously described for the formation of different isomers, a hydride interconversion process also occurs, which depends on what side of the phenolate the pyridine ligand rebinds. Another hydride interconversion process is also possible due to the formation of a dihydrogen complex, which is low-lying in energy and allows rotation of the bound $\eta^2\text{-H}_2$ ligand. These processes are shown in Figure 226.

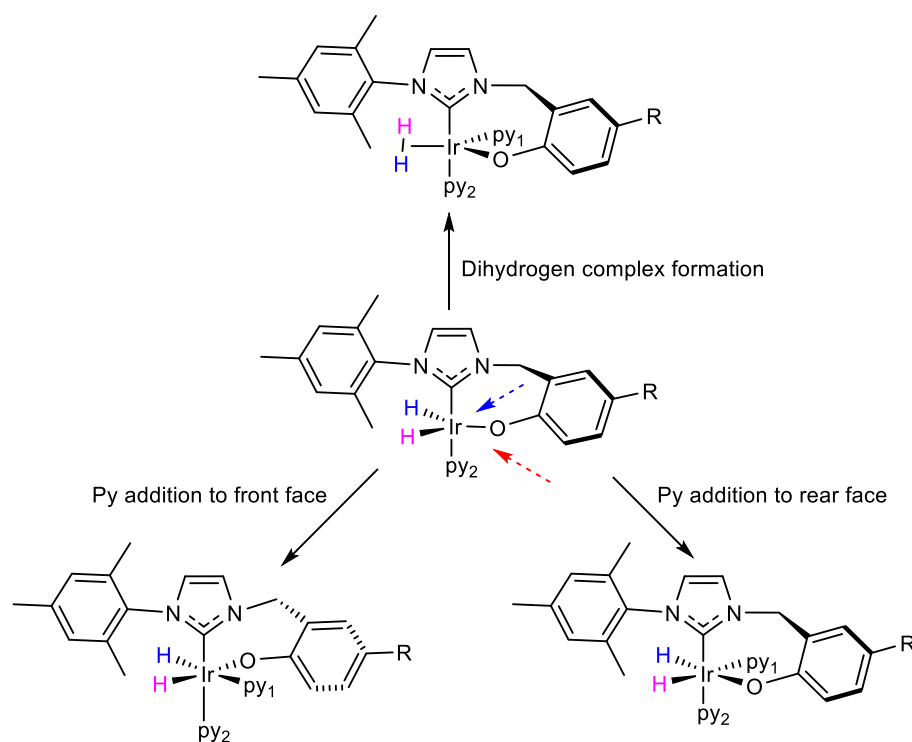


Figure 226: Hydride interconversion due to pyridine addition to differing faces of the bidentate ligand and the route to hydride interconversion via the formation of a dihydrogen intermediate

The solvent has also been shown to have a strong effect on the ligand exchange rates, as shown in a study when complex **6** was the active catalyst. The pyridine dissociation rates were shown to increase as the solvent polarity decreased, consistent with the inability of non-polar solvents to stabilise the 16-electron intermediate formed upon pyridine loss.

Further studies using **6** have been completed to determine the effect of ligand exchange on the T_1 relaxation of the protons of pyridine. At 298 K, when ligand exchange occurs, the T_1 values for the exchanging pyridine ligand are average values for the ligand free in solution and when bound to the metal centre. When the ligand is permanently bound to the metal centre, as for the pyridine ligand in the *trans* position to

the carbene ligand, its T_1 values are dramatically decreased due to assisted relaxation. This exchange effect has been exemplified using **6** in CD_2Cl_2 by cooling a sample from 298 K to 263 K to inhibit exchange, with the results detailed in Table 49. Any interaction between the substrate and catalyst promotes relaxation and thus during SABRE this decreases the lifetime of the hyperpolarised state.

*Table 49: T_1 values for the three proton sites of each of the three pyridine environments (free pyridine, pyridine trans to hydride and pyridine trans to carbene) within a CD_2Cl_2 solution of pyridine (0.05 M) once activated with **1** (15 mol%) under 3 bars of H_2 at 298 K and 263 K. The T_1 value for the para proton signal of the pyridine ligand bound trans to a hydride ligand could not be determined due to signal overlap*

	T_1 of free pyridine in solution / s			T_1 of pyridine bound trans to hydride / s			T_1 of pyridine bound trans to carbene / s		
	<i>o</i>	<i>m</i>	<i>p</i>	<i>o</i>	<i>m</i>	<i>p</i>	<i>o</i>	<i>m</i>	<i>p</i>
CD_2Cl_2									
At 298 K	10.4	12.9	13.8	8.5	11.4	12.8	2.8	3.4	4.9
At 263 K	16.3	15.5	15.5	2.3	1.8	-	1.8	2.1	2.7

To extend this study, derivatives of these complexes could be synthesised containing cyclooctene (COE) instead of COD.²⁸⁵⁻²⁸⁶ This may lead to decreased reaction times as the hydrogenation of COE should be faster than the hydrogenation of COD. Furthermore, the COE ligands will also be more labile due to the absence of the chelate effect. The SABRE activity of the iridium COE complex, $[IrCl(COE)_2]_2$, has recently been demonstrated by Iali et al., where it has been shown to undergo hydrogenation of one COE ligand, upon reaction with pyridine and hydrogen, to form the equivalent hydride species, $[IrCl(H)_2(COE)(py)_2]$.²⁸⁵ This negates the need for the incorporation of an NHC into the complex.

Further investigations into altering other parts of the bidentate carbene could also help to improve the reactivity of these species. Firstly, the substituents on the mesityl ring could be changed to see what effect the electronic properties of this ring have on the iridium metal centre. This study has been done to some extent, with the development of the series of symmetric NHC derivatives, I^tBu, ICy and IPr, although

these modifications mainly contribute to larger steric changes.^{87, 93} Their structures and corresponding Tolman Electronic Parameters, which are based on the average CO stretching frequencies of the complexes $[\text{Ir}(\text{NHC})(\text{CO})_2\text{Cl}]$, are shown in Figure 227.^{87,}
172

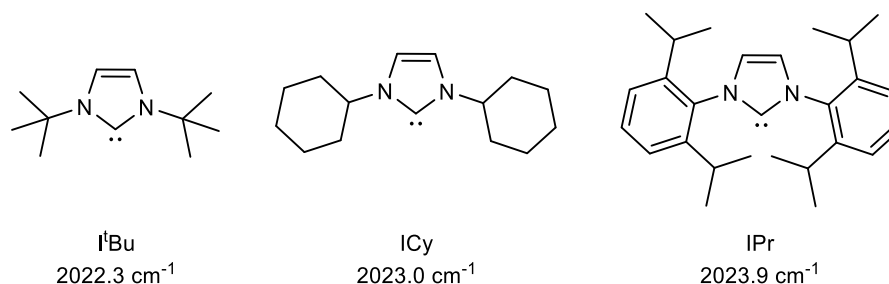


Figure 227: Structures and corresponding Tolman Electronic Parameters of three NHC derivatives

Secondly, changing the imidazole core may also prove to give enhanced activity for these complexes. In relation to the SABRE process, some studies have been done using SIMes and SIPr which involve modification of the rigidity of the imidazole ring, by making it a saturated system. In comparison to the unsaturated imidazole ring derivatives, IMes and IPr, these saturated systems are slightly less electron-donating and lead to faster ligand exchanges rates and consequently lower signal enhancements.⁹³ However, overall these electronic effects are very weak and again the major effects result from the steric properties of the NHC ligands.

Other examples involve adding extra substituents to the imidazole ring, for example chlorine substituents.¹⁷² Viciano et al.²⁸⁷ have created bis(dichloroimidazolylidene) ligands, as shown in Figure 228 and in comparison to the non-chlorinated versions, they donate less electron density via σ -donation which leads to higher activity for the hydrosilylation of terminal acetylenes (see Figure 228). More complex systems have also been developed with aromatic rings and extra heteroatoms included in the imidazole ring system, in order to tune the properties of different systems.²⁸⁸

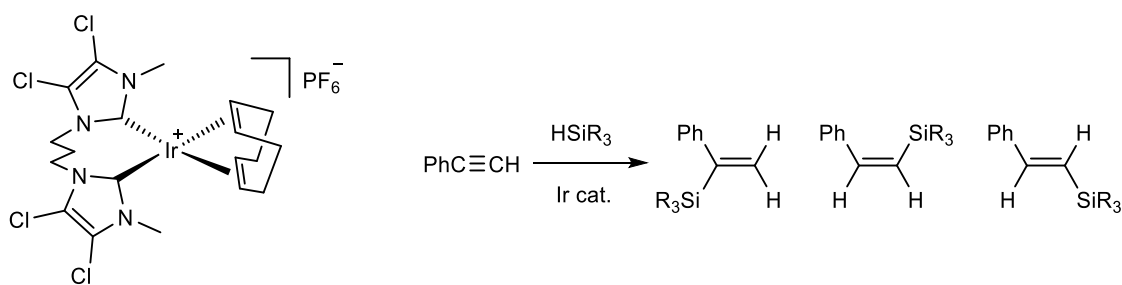


Figure 228: Bis(dichloroimidazolylidene) iridium complex developed by Viciano et al. for hydrosilylation of terminal acetylenes²⁸⁷

Thirdly, the oxygen linker could be changed to a softer nitrogen or sulfur donor atom. Several examples have been described in the literature.²⁸⁹⁻²⁹² One method of making complexes such as these, is via oxidative addition of an N-H bond, for example to an iridium pincer complex as shown in Figure 229 to form an anilide hydride species.²⁹⁰ However, they easily undergo reductive elimination to form stable iridium(I) complexes. In relation to sulfur donor atoms, Herberhold et al.²⁹² have described several thiol-containing species with half-sandwich iridium cores. However, these thiol ligands can react with multiple metal centres to form dimers, as they act as very good bridging ligands.²⁹¹ This would be undesirable for SABRE as detailed for a dimer complex in Section 5.2.3.

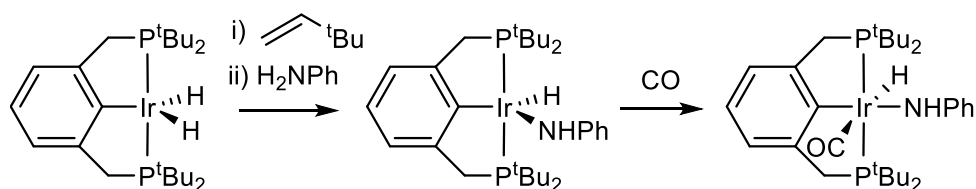


Figure 229: Formation of an anilide hydride iridium complex²⁹⁰

7.2. SABRE reactivity of neutral bidentate iridium carbene complexes

In order to determine how effective the catalysts are at polarisation transfer, SABRE studies using the neutral bidentate iridium carbene complexes have been completed in a range of different solvents. For the active catalysts which only contain two pyridine ligands, for example, all the complexes in CD_2Cl_2 , the hydride ligands are both magnetically and chemically inequivalent due to one lying *trans* to a nitrogen-donor substrate ligand and the other lying *trans* to the phenolate oxygen ligand. However, when the iridium-oxygen bond is cleaved, the hydride ligands are now chemically equivalent but magnetically inequivalent. When used with *para*hydrogen, significant signal enhancements of these hydride ligands are observed, alongside large signals for the protons of the substrate molecules. Most testing was completed using pyridine as the substrate as this is a model substrate for SABRE. Due to the neutral nature of the catalysts, good hyperpolarisation activity is observed in several solvents, with the most effective solvents being polar aprotic or non-polar. OPSY NMR experiments have been exploited as they enable the observation of only signals that are derived from the hyperpolarised state, thus eliminating any thermal signals.

When using **1**, polarisation transfer to the proton sites of pyridine is observed as well as to the carbon atoms, with the greatest signal enhancements being observed at a polarisation transfer field of -6.5×10^{-3} T and a temperature of 60 °C. The proton signal enhancements were found to increase as a function of temperature, commensurate with the increase in ligand exchange rates as detailed in Section 3.2.2. When comparing this SABRE activity to that seen when $[\text{Ir}(\text{COD})(\text{IMes})\text{Cl}]$ is used, the same polarisation transfer field produces the largest enhancements although the temperature dependence does not follow the same trend. For $[\text{Ir}(\text{COD})\text{IMes}\text{Cl}]$, the proton signal enhancements of pyridine decrease at higher temperatures, as the exchange rates become too fast for optimal transfer due to the amount of time for coupling to establish being too short. Polarisation transfer to nicotinamide follows similar trends to those seen for pyridine.

When analysing the effect of solvent on the enhancement values and ligand exchange rates, the highest enhancements were observed for pyridine in benzene, tetrahydrofuran and dichloromethane which equates to the most rapid pyridine

dissociation rates. Due to the neutral nature of the catalyst it also benefits from improved solubility in these solvents, which aids the SABRE process. When using the less stable complex **2**, the greatest enhancement values were obtained in dichloromethane with a total pyridine ^1H NMR enhancement of 1500-fold being possible, as described in Chapter 4. Polarisation transfer to nicotinaldehyde and nicotine (see Figure 230) were also investigated with dichloromethane again proving to be the most effective solvent for carrying out SABRE experiments. For nicotinaldehyde a total ^1H NMR enhancement of 1100-fold was achieved and for nicotine this proved to be 1300-fold for the four aromatic protons. When nicotinaldehyde was used in methanol, its hemiacetal form (see Figure 230) was also present in solution due to nucleophilic attack of the methanol solvent onto the carbonyl group of the aldehyde. This species also demonstrated enhanced signals. Complex **3** also gives the largest signal enhancements in dichloromethane where a total pyridine ^1H NMR enhancement of 1600-fold was observed. The chlorine-substituted complex **4** proved to be the most efficient polarisation transfer catalyst, with a total pyridine ^1H NMR signal enhancement of 2300-fold again being achieved in dichloromethane.

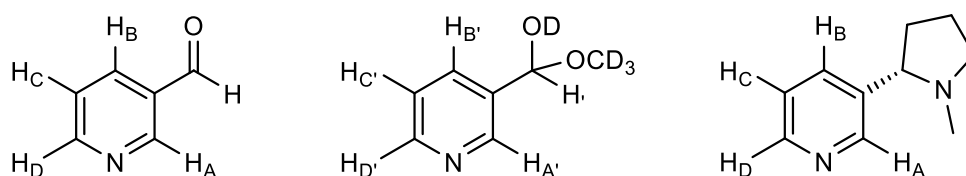


Figure 230: Structures of nicotinaldehyde, its hemiacetal form, and nicotine

Due to nicotine being a chiral substrate, it led to the production of both isomers **B** and **B'**, as shown in Figure 224, with the hydride ligands at about $\delta -22$ and -25 exhibiting only very small differences in chemical shift in the corresponding ^1H NMR spectra. This confirms that four isomers are possible and they are dependent on the orientation of the seven-membered metallocycle as well as the face of the carbene ligand at which the substrate rebinds and the chirality of the substrate.

The substrates typically used for SABRE studies are N-heterocycles. However, in Chapter 5, the SABRE approach has been expanded to use amine molecules as substrates. The use of a neutral pre-catalyst, **1**, in an aprotic solvent, dichloromethane, ensures no H/D exchange can occur and therefore this has enabled the polarisation

transfer from *parahydrogen* to several amine substrates including ammonia, benzylamine, tryptamine and phenethylamine as shown in Figure 231.

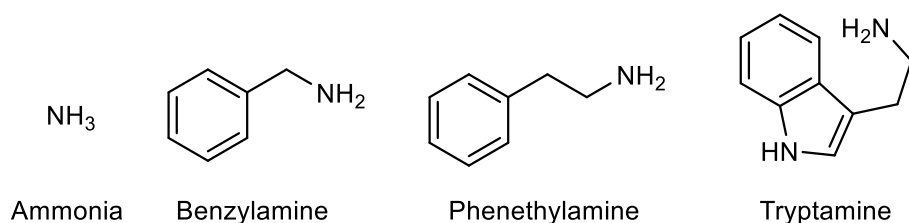


Figure 231: Structures of ammonia, benzylamine, phenethylamine and tryptamine

SABRE tests using the polarisation transfer pre-catalyst **1** in dichloromethane in the presence of the desired amine substrate and hydrogen have led to minimal polarisation transfer being observed. Several inactive complexes have also been observed to form, with an inactive dimer species, **21**, being common when low concentrations of substrate are used. The dimer complex forms to stabilise the iridium metal centres and its structure is shown in Figure 232. A singlet hydride species also forms (see Figure 232 for the structure of the complex formed with the substrate tryptamine), which is due to C-H activation of the aromatic ring of the amine substrates.

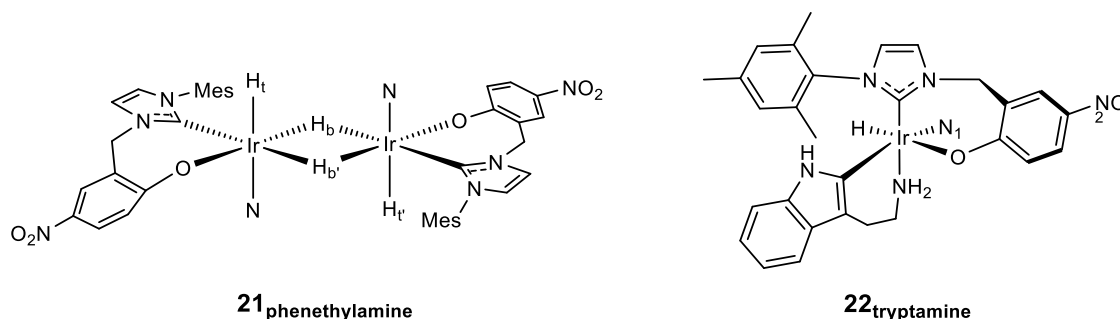


Figure 232: Inactive complexes formed using **1** under H₂ with amine substrates in CD₂Cl₂

To prevent formation of **21**, phosphine ligands have been added to samples used for SABRE in order to act as stabilising ligands and improve the SABRE activity. The order of ligand addition was shown to be important. This is because the ligand in the *trans* position to the carbene is not labile, and thus when phosphine is added to the pre-activated sample, the exchanging substrate ligand *trans* to the hydride ligand is replaced by a phosphine ligand, rendering the catalyst inactive. When the phosphine is added before activation with hydrogen, the active SABRE isomer with the phosphine lying *trans* to the carbene is favoured and subsequently proves to exhibit good SABRE

activity for the amine substrates tested. It is less favourable for the phosphine ligand to bind *trans* to the hydride ligand compared to the carbene, due to the stronger σ -donating capability of the hydride. The different complexes formed are shown in Figure 233, when PPh₃ is the phosphine that is used.

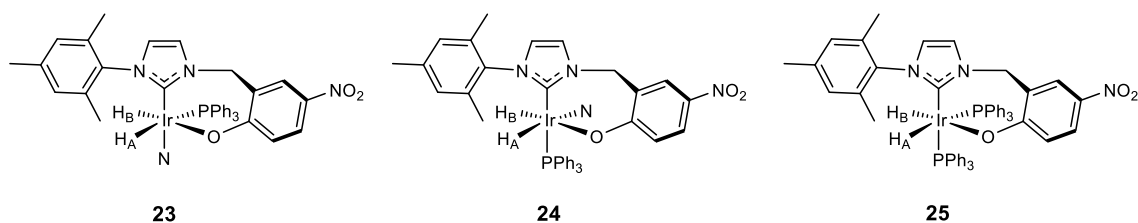


Figure 233: Isomers **23** and **24** and the bis-phosphine complex **25**

To investigate how the steric and electronic properties of the phosphine ligands affects the formation of the different complexes, several phosphine ligands have been investigated. As well as PPh₃, the phosphine ligands used were PCy₃, PBz₃, PⁱPr₃ and PPh₂Cy. Their cone angles vary from 145 ° for PPh₃ to 170 ° for PCy₃, with the electronic effects varying from 12.9 for PPh₃ to 0.3 for PCy₃ with PCy₃ being the most electron-donating. For all these phosphine ligands, the same set of complexes as shown in Figure 233 are formed. A different bis-phosphine isomer complex forms when the bulkiest phosphine ligands are used. This is because the ligands are too bulky to sit in a *cis* position and instead the *trans*-phosphine complex forms as shown in Figure 234. Furthermore, with the bulky phosphine ligands PCy₃ and PⁱPr₃, decomposition of the bidentate NHC ligand occurs due to the iridium metal centre not being able to accommodate the high steric bulk. Instead a penta-hydride complex, **28**, is formed as shown in Figure 234.

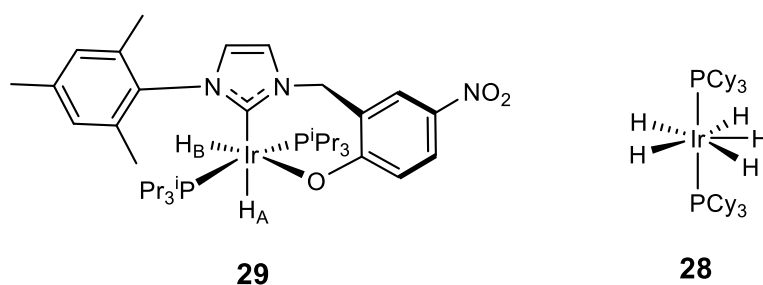


Figure 234: *Trans*-phosphine isomer, **29**, and [Ir(H)₅(PCy₃)₂], **28**

To improve the activity and selectivity of these amine polarisation studies, an extension of this work would involve tethering the phosphine ligand into the position *trans* to the carbene. This could prevent the formation of multiple isomers and may also prevent multi-addition of the phosphine ligand. A potential synthetic route is shown in Figure 235, with the $[\text{IrCl}(\text{COE})_2]_2$ dimer being used in the final step to form the desired SABRE pre-catalyst.

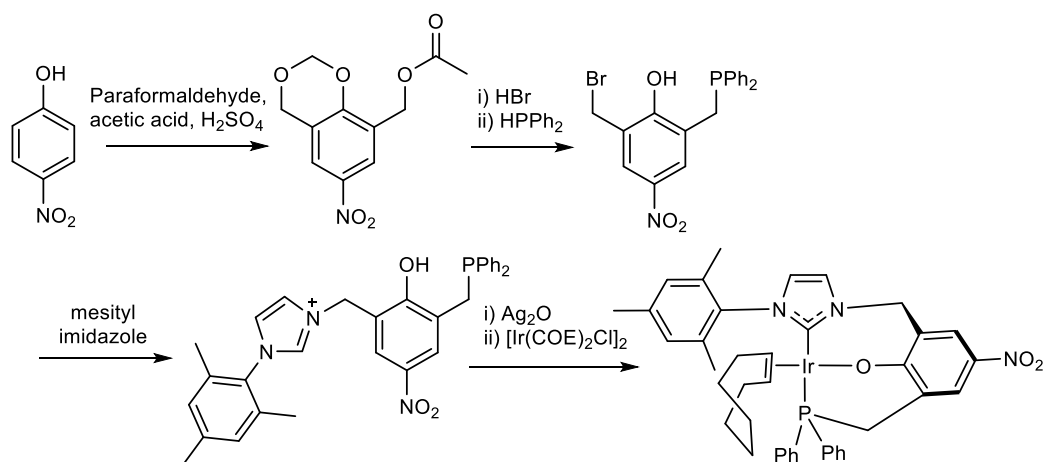


Figure 235: Potential synthetic route to form a tridentate iridium carbene complex containing a bound phenolate and phosphine ligand

The activation of this tridentate iridium complex with substrate and hydrogen would be predicted to form the desired SABRE-active catalyst as shown in Figure 236. The length of the alkyl linker to the phosphine complex can be modified to optimise the tridentate binding for the *trans*-phosphine-carbene arrangement.

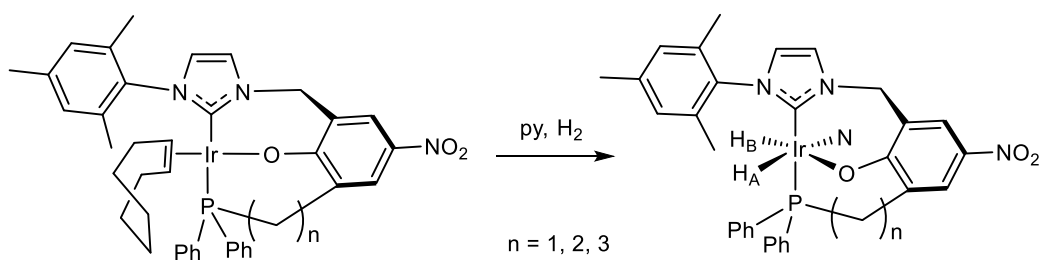


Figure 236: Formation of $[\text{Ir}(\text{H})_2(\text{P-NHC-O})(\text{py})]$ from $[\text{Ir}(\text{COE})(\text{P-NHC-O})]$

A further extension of this work would be to test the effect on reaction species formed, when using arsine ligands instead of phosphine ligands. However, with arsine ligands being more electron-donating than the corresponding phosphine derivatives, the

product formed with an arsine ligand in the *trans* position to the carbene may be considerably more unstable.

As discussed previously in Section 1.9, one area where the use of the SABRE technique is of particular interest, is in MRI diagnostics for medical applications. Since these complexes have very good solubility and activity in non-polar solvents, a phase extraction technique could be used. In this case, the polarisation transfer could occur in the organic phase before extraction of the hyperpolarised agent into the aqueous phase prior to injection into a patient. This would require the substrate molecule (contrast agent in MRI) to be soluble in both the aqueous and organic phases. This technique has been reported by Reineri et al.²⁹³ although the process involves hydrogenation of a suitable precursor with *p*-H₂ and subsequent hydrolysis with water in order for it to cross from the organic to the aqueous phase. This is shown in Figure 237, with an estimated 18.3 % polarisation of the ¹³C atom of 1-¹³C-2,3-*d*₂-succinic acid, based on the experiment being conducted with 98 % enriched *p*-H₂.

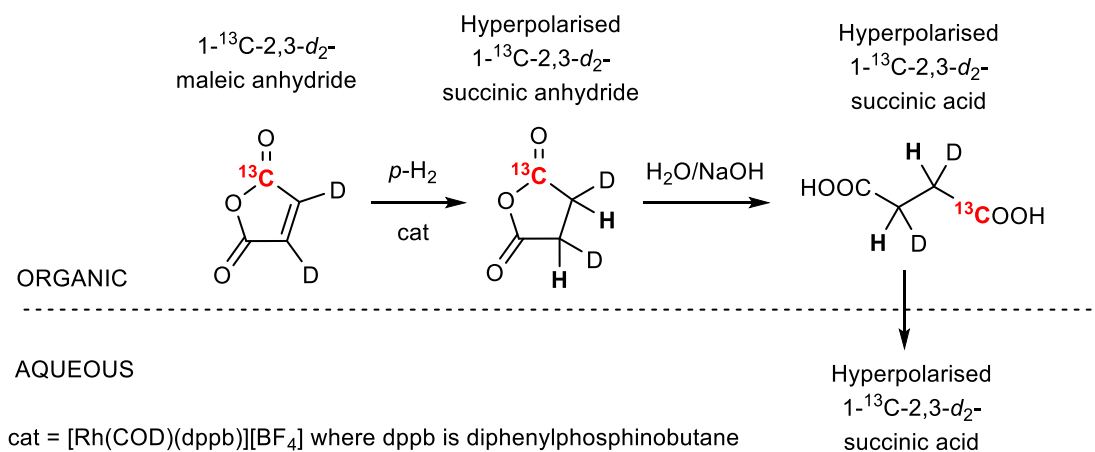


Figure 237: Demonstration of phase-extraction used to remove the polarisation transfer catalyst from hyperpolarised substrate, suitable for MRI studies²⁹³

7.3. Hydrogenation activity of neutral bidentate iridium carbene complexes

As iridium complexes have been described to act as efficient hydrogenation catalysts, Chapter 6 explores hydrogenation reactions and uses the developed neutral catalysts to study the hydrogenation of multiple bonds. The use of ^1H OPSY NMR experiments has facilitated the study of the *parahydrogenation* of the triple bond of phenylacetylene to form styrene and ethyl benzene as shown in Figure 238.

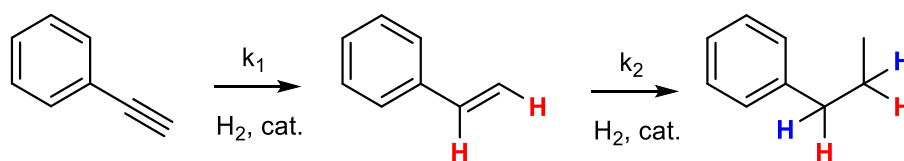


Figure 238: The hydrogenation of phenylacetylene to form styrene and ethyl benzene

The initial OPSY NMR spectrum recorded after addition of *p*- H_2 to a sample typically shows large enhanced signals for the protons of styrene (with minor enhanced signals present for ethyl benzene) that are *p*- H_2 -derived. A typical spectrum is shown in Figure 239 for the hydrogenation of phenylacetylene using Crabtree's catalyst.

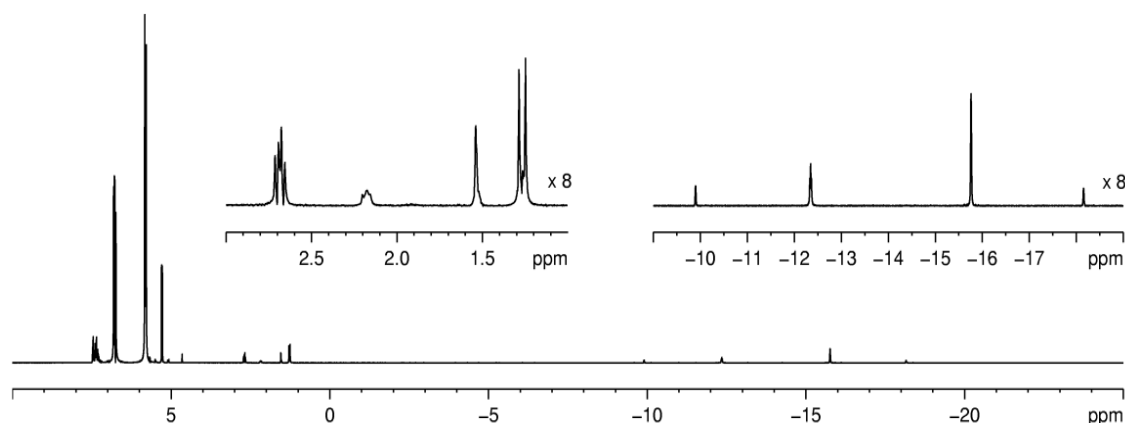


Figure 239: ^1H OPSY NMR spectrum after *p*- H_2 addition to a sample containing 2.0 mol% Crabtree's catalyst and 120 mM phenylacetylene in CD_2Cl_2 , showing the enhanced signals for styrene, ethyl benzene, COE and hydride species

As time passes, a decrease in the intensity of the signals occurs in subsequent spectra. This leads to an exponential decay being observed, corresponding to the consumption of *p*- H_2 . A cumulative summing approach can then be used to demonstrate

the growth in product concentration over time, as typically observed for kinetic studies. To continue this study, Letort's method of double logarithmic plots of the concentration of H_2 and the k_{obs} values has enabled the orders of reaction with respect to time to be calculated. Examples of these three plots are given in Figure 240 for the hydrogenation of phenylacetylene using **1**.

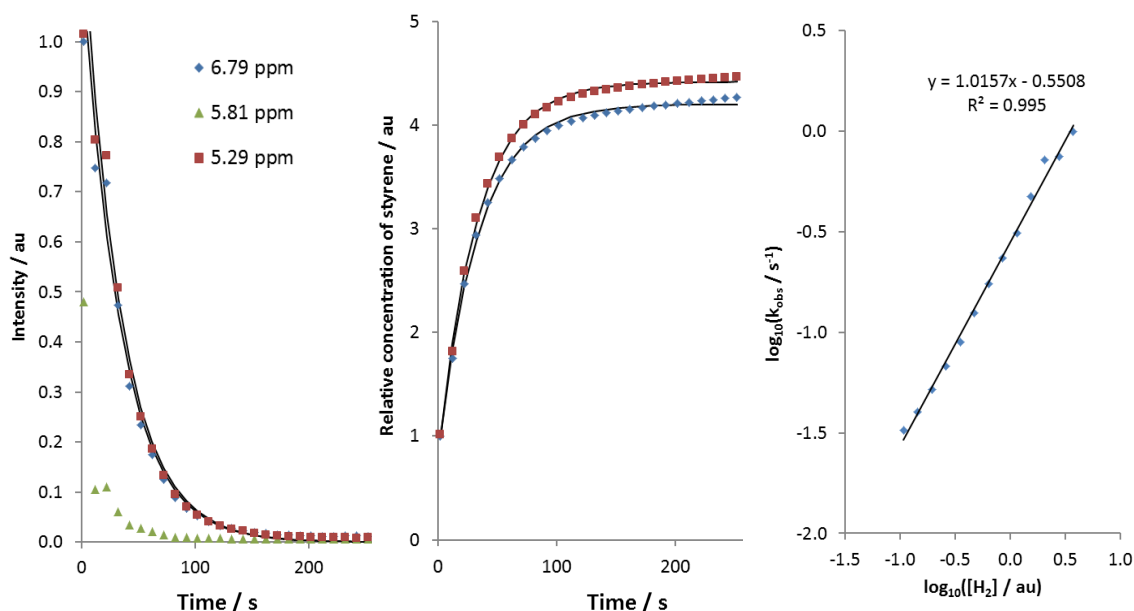


Figure 240: A decay curve corresponding to the observed rate of p - H_2 consumption for the hydrogenation of phenylacetylene using **1**, the growth curve corresponding to the production of styrene over time and the double logarithmic plot enabling the determination of the reaction order with respect to time

The reactivities of complexes **1**, **2**, **3** and **4** have been investigated and compared to the reactivity of Crabtree's catalyst, $[Ir(COD)(PCy_3)(py)][PF_6]$. During hydrogenation of phenylacetylene using Crabtree's catalyst, hydrogenation of the phenylacetylene to both styrene and ethyl benzene occurred. Several enhanced hydride signals were also seen along with enhanced signals corresponding to COE due to hydrogenation of the COD ligand of Crabtree's catalyst. Only a very small signal for H_2 was observed in the OPSY spectra, demonstrating that Crabtree's catalyst is very efficient at conducting hydrogenation of phenylacetylene.

In comparison, when **1**, **2**, **3** and **4** were used, no hydrogenation of the COD ligand occurred, suggesting a different hydrogenation mechanism. When using the neutral bidentate carbene derivatives, the only minor hydride-containing products were

those that are equivalent to complex **5** as discussed in Section 2.4.1, formed when hydrogen is added to **1**. Furthermore, large signals for H₂ in solution were observed when complexes **2**, **3** and **4** were used. This shows that these complexes rapidly add hydrogen but only carry out limited hydrogenation of the triple bond of phenylacetylene. Overall, the initial hydrogenation of phenylacetylene using Crabtree's catalyst was approximately three times faster than when using **1**, but over time the rates using Crabtree's catalyst decreased to be approximately equal to those of **1**, consistent with deactivation of Crabtree's catalyst. The order of reaction using Crabtree's catalyst also changed from ~ 1.15 when first reacted with *p*-H₂, to ~ 1 after the initial reaction had occurred. This is consistent with changes in speciation, active catalyst form and degradation. When using the neutral complexes, both the hydrogenation rates and reaction order stayed the same between successive shakes. No catalyst degradation was observed and consistently only one molecule of H₂ was calculated to be bound to the catalyst at once.

These studies have shown that the hydrogenation mechanisms between the different catalysts vary considerably. For Crabtree's catalyst, the COD ligand must be hydrogenated and replaced with alkyne or solvent ligands before H₂ binds to form the active dihydride species that can then hydrogenate phenylacetylene. However, for the neutral catalysts developed during this work, the COD ligand remains intact and a dihydride species forms first before rearrangement occurs to enable phenylacetylene to bind and be hydrogenated. Only a very minor amount of the catalyst may form the active hydrogenation species.

To extend this study, the hydrogenation of other species containing multiple bonds could be tested to determine the potential range of compounds that may be able to be hydrogenated. However, with the mechanism involving the addition of H₂ before the addition of substrate, and no COD hydrogenation, the hydrogenation of substrates that have a large steric bulk may be limited as the iridium metal centre may become inaccessible if the binding of larger ligands is required. Further studies to determine the route of phenylacetylene addition to the dihydrido-dialkene complex would prove useful in elucidating the full mechanistic pathway.

7.4. Summary

During this work, the aims originally set out in Section 1.10 have been met as several neutral bidentate iridium carbene complexes have been synthesised and developed as efficient polarisation transfer catalysts for the SABRE approach. The activity of these complexes has been optimised in several ways, for example by changing the solvent used for polarisation transfer, optimising the magnetic field at the point of magnetisation transfer and seeing the effect of temperature on the signal enhancement of substrates. These catalysts have also been used as hydrogenation catalysts and their reaction mechanisms for both SABRE and hydrogenation have been studied in-depth.

8. Experimental

8.1. Calculations

8.1.1. Method for calculating standard errors

Standard errors are calculated using the Jackknife method, eliminating each value from a set of values, in turn and then recalculating the parameters. The standard deviations are then calculated for each set of values and from this the standard error is calculated using the equations below.²³¹

Standard Deviation

$$s = \sqrt{\frac{\sum(x - \bar{x})^2}{(n - 1)}}$$

where: s = standard deviation

x = measured values

\bar{x} = sample mean

n = sample size

Standard Error

$$St\ error = \frac{s(n - 1)}{\sqrt{n}}$$

where: s = standard deviation

n = sample size

8.1.2. Arrhenius and Eyring-Polanyi equations used to calculate activation parameters

All the activation parameters are calculated from data that uses two times the value for the experimental rate constant because at the transition state the reaction has an equal probability of continuing forward to the products or going back to the reactants. The Arrhenius and Eyring-Polanyi equations used, are shown below.

Arrhenius equation:

$$k = Ae^{-E_a/RT}$$

$$\ln(k) = -\frac{E_a}{R} \left(\frac{1}{T}\right) + \ln(A)$$

where:

k = rate constant / s^{-1}

E_a = Activation energy / $J\ mol^{-1}$

T = temperature / K

R = Gas constant / $8.314\ J\ K^{-1}\ mol^{-1}$

A = Pre-exponential factor

Eyring-Polanyi equation:

$$k = \frac{k_B T}{h} e^{-\Delta G^\ddagger/RT}$$

$$\ln\left(\frac{k}{T}\right) = \frac{-\Delta H^\ddagger}{R} \left(\frac{1}{T}\right) + \ln\left(\frac{k_B}{h}\right) + \frac{\Delta S^\ddagger}{R}$$

where:

k = rate constant / s^{-1}

T = temperature / K

R = Gas constant / $8.314\ J\ K^{-1}\ mol^{-1}$

ΔH^\ddagger = enthalpy of activation / $J\ mol^{-1}$

ΔS^\ddagger = entropy of activation / $J\ K^{-1}$

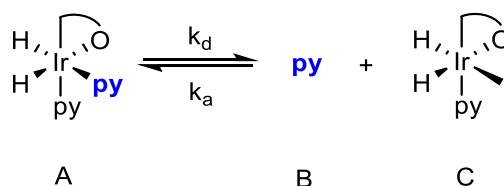
h = Planck's constant / $6.626 \times 10^{-34}\ kg\ m^2\ s^{-1}$

k_B = Boltzmann constant / $1.38 \times 10^{-23}\ J\ K^{-1}$

8.2. Modelling ligand exchange

8.2.1. Modelling pyridine ligand exchange in complexes of $[\text{Ir}(\text{H})_2(\text{R-NHC-O})(\text{py})_2]$

In these $[\text{Ir}(\text{H})_2(\text{R-NHC-O})(\text{py})_2]$ complexes, there is only one pyridine ligand that can exchange with free pyridine in the bulk solution and therefore a simple model can be used. This pyridine dissociation step is the first step that occurs within the mechanism of ligand exchange for SABRE and therefore can be easily modelled using the experimental data. The 16-electron intermediate C is very reactive so is likely to be trapped rapidly by other potential ligands in solution so itself will be in very low concentration. The concentration of pyridine is also much higher than the concentration of the iridium species so it is unlikely that the same pyridine ligand will rebind to the iridium centre, however, if this back reaction is not allowed within the model, then the quality of the data fit is reduced.



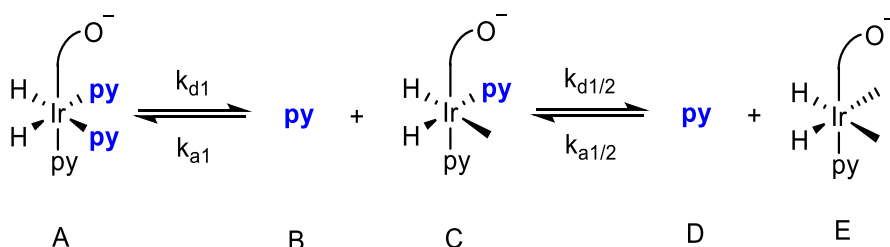
$$[A]_t = [A]_0 - k_d[A]t + k_a[B][C]t$$

$$[B]_t = [B]_0 + k_d[A]t - k_a[B][C]t$$

$$[C]_t = [C]_0 + k_d[A]t - k_a[B][C]t$$

8.2.2. Modelling pyridine ligand exchange in complexes of $[\text{Ir}(\text{H})_2(\text{R-NHC-O}^-)(\text{py})_3]^+$

In these $[\text{Ir}(\text{H})_2(\text{R-NHC-O}^-)(\text{py})_3]^+$ complexes, there are two pyridine ligands that are both *trans* to hydride ligands that have the potential to exchange with the same probability as each other. Here, the model is more complicated because there are now two steps that can lead to dissociation of the two starting pyridine ligands. The rate of pyridine loss for the second step will be half that of the first as there is now only one pyridine ligand that can dissociate, compared to two in the starting complex, where each has the same probability of dissociating.



$$[A]_t = [A]_0 - k_{d1}[A]t + k_{a1}[B][C]t$$

$$[B]_t = [B]_0 + k_{d1}[A]t - k_{a1}[B][C]t - \frac{k_{a1}}{2}[B]t$$

$$[C]_t = [C]_0 + k_{d1}[A]t - k_{a1}[B][C]t - \frac{k_{d1}}{2}[C]t + \frac{k_{a1}}{2}[D][E]t + \frac{k_{a1}}{2}[B][E]t$$

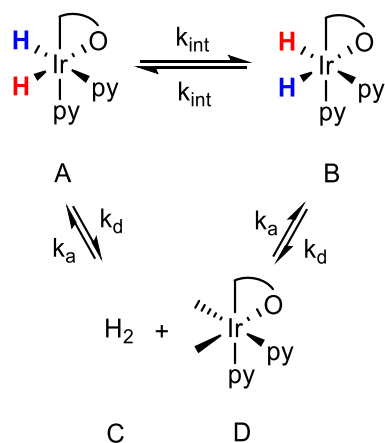
$$[D]_t = [D]_0 + \frac{k_{d1}}{2}[C]t - \frac{k_{a1}}{2}[D][E]t$$

$$[E]_t = [E]_0 + \frac{k_{d1}}{2}[C]t - \frac{k_{a1}}{2}[D][E]t$$

Species C can be reformed by the association of pyridine ligand D with very reactive species E and therefore, because D is essentially the same as B, species C can also be reformed from the association of pyridine ligand B with species E. The concentrations of the species containing bound pyridine ligands, A and C can be summed and those containing free pyridine, B and D can be summed and the pyridine dissociation rate can then be modelled using the intermediates. By allowing all the back reactions to occur in the model, the data can fit the model most effectively, despite any values for back reactions being insignificant.

8.2.3. Modelling H₂ ligand exchange in complexes of [Ir(H)₂(R-NHC-O)(py)₂]

For SABRE to be efficient, the hydride ligands must be lost and then re-added in a pairwise fashion to the iridium centre. In these [Ir(H)₂(R-NHC-O)(py)₂] complexes, the hydride ligands are inequivalent, so as well as undergoing H₂ loss, they also undergo a hydride interchange process which also has to be modelled. The interchange process between the hydride ligands of complexes A and B will occur at the same rate, k_{int} . The two hydride ligands can interchange and hydrogen loss can occur from both complexes with either arrangement of hydride ligands, at the same rate, k_d . Intermediate D is so reactive that it is likely to be immediately trapped by another ligand and so will have very low concentration in solution.



$$[A]_t = [A]_0 - k_{int}[A]t + k_{int}[B]t - k_d[A]t + k_a[C][D]t$$

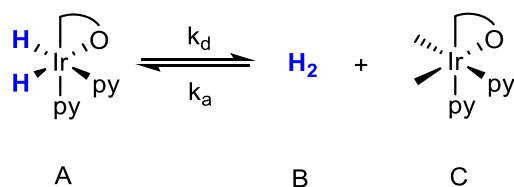
$$[B]_t = [B]_0 - k_{int}[B]t + k_{int}[A]t - k_d[B]t + k_a[C][D]t$$

$$[C]_t = [C]_0 + k_d[A]t + k_d[B]t - 2k_a[C][D]t$$

$$[D]_t = [D]_0 + k_d[A]t + k_d[B]t - 2k_a[C][D]t$$

8.2.4. Modelling H₂ ligand exchange in complexes of [Ir(H)₂(R-NHC-O⁻)(py)₃]⁺

Here, in these [Ir(H)₂(R-NHC-O⁻)(py)₃]⁺ complexes, the two hydride ligands are equivalent and so the model is like the model for a single pyridine loss process. The two hydride ligands are lost in a pairwise process to form dihydrogen. It is this that is analysed from the experimental data. The concentration of intermediate C, formed from H₂ loss would be very low as it is very unstable so would not be present in solution in the described form, thus its concentration is effectively negligible. Also, the probability of the same H₂ molecule that has dissociated, re-binding to the same iridium centre is very small, however, without allowing this back reaction to be modelled, the data fitting is not as concordant.



$$[A]_t = [A]_0 - k_d[A]t + k_a[B][C]t$$

$$[B]_t = [B]_0 + k_d[A]t - k_a[B][C]t$$

$$[C]_t = [C]_0 + k_d[A]t - k_a[B][C]t$$

For the step of dihydride loss to form dihydrogen, the actual mechanism involves many steps before dihydrogen loss occurs and therefore what is observed is a value that encompasses all these steps. However, they cannot all be modelled because there are a number of very short-lived intermediates that are not observed and one particular, very important intermediate for the SABRE process, which is the intermediate before the dihydrogen loss step, poses a number of problems. This is because the dihydrogen-dihydride intermediate, [Ir(H)₂(H₂)(R-NHC-O)(py)], which is how fresh *p*-H₂ is introduced into the complexes, can be viewed as a very short-lived species containing four fluxional hydride ligands, each with very short relaxation times. The concentration of this is thus expected to be very low at any one moment in time and modelling from this species, which is not observed, is problematic. Instead, the species that are observed are the initial dihydride complex which then undergoes several

reaction steps before it loses hydrogen, which is what is observed as the ‘product’ in the ^1H NMR spectrum. It is known that the rate of pyridine loss is the limiting factor affecting the process, as this is the first step in the SABRE mechanism. A way to increase the concentration of the important dihydrogen-dihydride intermediate in solution would be to increase the hydrogen pressure as this would increase the concentration of H_2 in solution. However, as this intermediate is not stable and is very fluxional the potential observed signals would be very broad and thus would not be useful for analysing via NMR.

8.3. Polarisation methods for NMR experiments

Polarisation transfer experiments were conducted in either a Young’s NMR tube² (Method A) or by using an automated polariser^{88,96} (Method B).

8.3.1. Method A²

For polarisation transfer experiments, using the shake-and-drop method, a Young’s NMR tube containing a solution of the relevant iridium catalyst, analyte and solvent (0.6 mL), formed the sample. This sample was degassed prior to the introduction of *parahydrogen* at a pressure of 3 bars. For the temperature studies in Sections 4.2.1 and 4.3.1, the sample was placed in a water bath of known temperature for 1 minute before shaking in the desired magnetic field (using the fringe field of the magnet) for 10 seconds before being rapidly transported to the magnet for interrogation by NMR spectroscopy.

8.3.2. Method B⁸⁸

Samples polarised using the polariser were achieved as follows. The polarisation chamber was charged with the relevant iridium catalyst, analyte to be polarised and CD_3OD (3 mL). *Parahydrogen* was introduced to the solution via six inlet tubes at a pressure of 3 bars for 10 seconds. This solution was then transferred into the Bruker Avance III series 400 MHz spectrometer equipped with a TXO flow probe head (flow

cell volume = 200 μ l) for interrogation by NMR using helium as a flow gas. A single transient was recorded for the nucleus of interest. Once interrogated, the solution was returned to the polarising chamber and this process repeated as required. A coil surrounded the reaction chamber such that a magnetic field could be generated in the z direction. This coil was designed to produce static DC fields in the range of -150 to 150×10^{-4} T. For field profiling five ^1H NMR spectra were collected at each point to ensure reproducibility.

8.3.3. Calculation of ^1H NMR enhancement factors

To calculate the enhancements observed for each of the ^1H NMR signals, the following formula was used:

$$E = \frac{S_{pol}}{S_{unpol}}$$

E = enhancement

S_{pol} = signal intensity of polarised sample

S_{unpol} = signal intensity of unpolarised (reference) sample

Experimentally, the reference NMR spectra were acquired with the same sample that was used for the hyperpolarised measurement after it had fully relaxed (typically 5-10 minutes at high magnetic field). Reference and polarised spectra were collected using identical acquisition parameters, particularly the receiver gain. The raw integrals of the relevant resonances in the polarised and unpolarised spectra were used to determine the enhancement levels. These ^1H NMR enhancement factors are field dependent, as detailed in Sections 4.2.1 and 4.3.1, and it is common practice to report these enhancement factors. However, a more unified measure is % polarisation.

8.4. General information

All experimental procedures were performed under an atmosphere of dinitrogen, using standard Schlenk line techniques or an MBraun Unilab glovebox, unless otherwise stated. General solvents for synthetic chemistry were dried using an Innovative Technology anhydrous solvent engineering system or were distilled from an appropriate drying agent under N₂ as necessary. *Parahydrogen* was prepared by cooling hydrogen gas over charcoal in a copper block at 30 K.

8.4.1. NMR

NMR measurements were made on a Bruker Avance III series 400 MHz NMR spectrometer (¹H at 400.13 MHz, ¹³C at 100.62 MHz, ³¹P at 162.0 MHz) and a 500 MHz NMR spectrometer (¹H at 500.13 MHz, ¹³C at 125.77 MHz, ¹⁵N at 50.7 MHz, ³¹P at 202.5 MHz). NMR samples were made up in Young's tap equipped 5 mm NMR tubes. The deuterated solvents (methanol-*d*₄, methanol-*d*₃, CDCl₃, C₆D₆, CD₂Cl₂, THF-*d*₈) were obtained from Sigma-Aldrich and Cambridge Isotope Laboratories (ethanol-*d*₆) and used as supplied. Multiplicities are given as s (singlet), d (doublet), t (triplet), m (multiplet), br (broad) and ps (*pseudo*).

8.4.2. X-ray Crystallography

Samples for single crystal X-ray analysis were typically grown by either slow diffusion of hexane or toluene into a DCM solution or by slow evaporation from a concentrated DCM solution of the sample. Suitable crystals were selected in collaboration with Adrian Whitwood, Sam Hart and Rachel Bean in the XRD department at York and crystallography data was collected on a SuperNova, single source at offset, Eos diffractometer. The crystals were kept at 110.05(10) K during data collection. Using Olex2,²⁹⁴ the structures were solved with the ShelXS²⁹⁵ structure solution program using Direct Methods and refined with the ShelXL²⁹⁵ refinement package using Least Squares minimisation. The structures were visualised using Mercury software.

8.4.3. UV-vis and IR

UV-visible absorption spectra were recorded on a Thermo Scientific Evolution Array UV-vis spectrophotometer (190-1100 nm) and processed using *VISIONcollect* software whereby background absorption spectra were subtracted from the sample spectra. IR spectra were recorded using a Bruker Tensor 37 FT-IR with a micro diamond ATR Probe (MIR).

8.4.4. Mass Spectrometry

Several mass spectrometers were used, with either the hard electrospray ionisation (ESI) technique or the softer liquid introduction field desorption ionisation (LIFDI) technique. For routine analysis, particularly during synthesis, a Bruker amaZon SL ESI LC/MSⁿ Ion Trap MS system coupled to a DIONEX HPLC system (with an APCI II source for LC coupling and a UV detector) was used. A Bruker micrOTOF (time-of-flight) instrument was also used. To prevent fragmentation, LIFDI was used with a Waters GCT Premier TOF spectrometer in order to gain information about larger, unstable metal complexes.

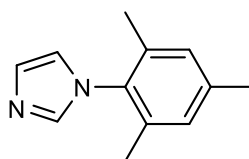
8.4.5. Elemental Analysis

A Sartorius SE2 analytical balance, able to accurately weigh 0.1 µg, was used to prepare samples for elemental analysis. Repeat data for each sample were collected on an Exeter Analytical CE-440 elemental analyser, which is calibrated against acetanilide standards. The amounts of carbon (C), hydrogen (H), and nitrogen (N) are reported as mean percentages.

8.5. Precursor synthesis

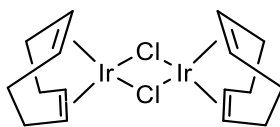
In this section, the synthetic procedures used to form 1-(2,4,6-trimethylphenyl)-1H-imidazole and $[\text{Ir}(\text{COD})\text{Cl}]_2$ are detailed. These two compounds are the starting materials that are needed to make all the different imidazolium salt derivatives and the subsequent iridium carbene complexes.

8.5.1. 1-(2,4,6-trimethylphenyl)-1H-imidazole¹²⁵



Glacial acetic acid (10 mL), aqueous formaldehyde (3 mL, 37 wt %, 40 mmol, 1 eq.) and aqueous glyoxal (4.6 mL, 40 wt %, 40 mmol, 1 eq.) were added to a round-bottom flask and heated at 70 °C. A solution of glacial acetic acid (10 mL), ammonium acetate (3.08 g, 40 mmol, 1 eq., in 2 mL water) and mesitylamine (5.6 mL, 40 mmol, 1 eq.) was added dropwise over a period of 30 min before the solution was left for 18 h. The reaction mixture was cooled to room temperature and was added dropwise to a stirred solution of sodium hydrogen carbonate (29.4 g in 300 mL water). The product formed a precipitate which was filtered off and washed with water before being allowed to air dry. The brown solid was recrystallised from ethyl acetate and was isolated via vacuum filtration (4.36 g, 59 %); ^1H NMR [CDCl_3 , 400 MHz, 298 K] δ 7.44 (s, 1H, $\text{CH}_{\text{imidazole}}$), 7.24 (s, 1H, $\text{CH}_{\text{imidazole}}$), 6.98 (s, 2H, 2 x $\text{CH}_{\text{mesityl}}$), 6.90 (s, 1H, $\text{CH}_{\text{imidazole}}$), 2.35 (s, 3H, CH_3), 2.00 (s, 6H, 2 x CH_3); $^{13}\text{C}\{^1\text{H}\}$ NMR [CDCl_3] δ 138.8, 137.5, 135.4, 133.4, 129.5, 129.0, 120.1, 21.0 (CH_3), 17.3 (2 x CH_3); MS [ESI] m/z 187.0 ($\text{M}+\text{H}$)⁺

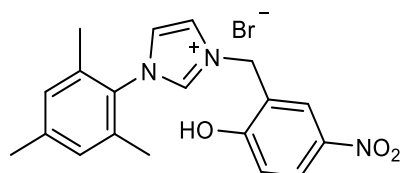
8.5.2. $[\text{Ir}(\text{COD})\text{Cl}]_2^{146}$



$\text{IrCl}_3 \cdot 3\text{H}_2\text{O}$ (1 g, 2.84 mmol), propan-2-ol (17 mL) and water (8.5 mL) were added to a round-bottom flask and nitrogen was bubbled through the solution for 2 h. COD (3.5 mL) was added and the solution was bubbled through with nitrogen for a further 15 min before the flask was fitted with a condenser and the solution was heated at 90 °C for 3 h under a nitrogen atmosphere. A red precipitate formed as the solution cooled and then the propan-2-ol was removed under reduced pressure. The resulting precipitate was filtered, washed with ice cold methanol and dried under vacuum (592 mg, 62 %); ^1H NMR [CDCl_3 , 400 MHz, 298 K] δ 4.26 (s br, 8H, 8 x CH), 2.28 (m br, 8H, 8 x CH), 1.55 (m br, 8H, 8 x CH); $^{13}\text{C}\{^1\text{H}\}$ NMR [CDCl_3] δ 62.1, 31.8

8.6. NO₂ carbene synthesis

8.6.1. 3-(2-hydroxy-5-nitrobenzyl)-1-(2,4,6-trimethylphenyl) imidazolium bromide¹²⁵



1-(2,4,6-trimethylphenyl)-1H-imidazole (0.61 g, 3.3 mmol, 1 eq.) and 2-hydroxy-5-nitrobenzyl bromide (0.76 g, 3.3 mmol, 1 eq.) were dissolved in toluene (8 mL). The resulting mixture was refluxed for 18 h and then the solution was cooled to room temperature. The precipitate was collected via vacuum filtration and was washed with diethyl ether (1.25 g, 91 %); ¹H NMR [DMSO, 400 MHz, 298 K] δ 11.81 (s, 1H, OH), 9.55 (s, 1H, CH_{imidazole}), 8.39 (d, 1H, ⁴J(HH) = 2.6 Hz, CH_{Ar}), 8.22 (dd, 1H, ⁴J(HH) = 2.6 Hz, ³J(HH) = 9.0 Hz, CH_{Ar}), 8.05 (s, 1H, CH_{imidazole}), 7.94 (s, 1H, CH_{imidazole}), 7.15 (s, 2H, 2 x CH_{mesityl}), 7.09 (d, 1H, ³J(HH) = 9.0 Hz, CH_{Ar}), 5.53 (s, 2H, CH₂), 2.33 (s, 3H, CH₃), 2.01 (s, 6H, 2 x CH₃); ¹³C{¹H} NMR [DMSO] δ 163.3 (C_{Ar}), 141.2 (C_{Ar}), 140.3 (C_{Ar}), 139.1 (CH_{imidazole}), 135.2 (C_{Ar}), 132.0 (C_{Ar}), 130.1 (2 x CH_{mesityl}), 128.1 (CH_{Ar}), 127.9 (CH_{Ar}), 125.0 (CH_{imidazole}), 124.1 (CH_{imidazole}), 122.2 (C_{Ar}), 116.7 (CH_{Ar}), 49.2 (CH₂), 21.5 (CH₃), 17.7 (2 x CH₃); MS [ESI] m/z 338.1 (M-Br)⁺; IR (cm⁻¹): ν_{OH} 1339, ν_{CO} 1279

A crystal suitable for X-ray diffraction was grown in the presence of HBF₄ as described in Section 5.4.1 with the ORTEP plot for the imidazolium tetrafluoroborate salt shown in Figure 241.

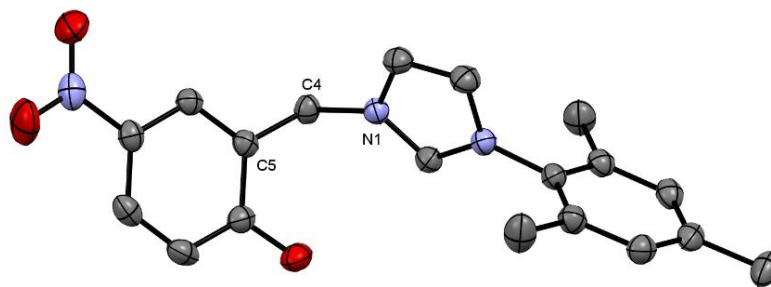
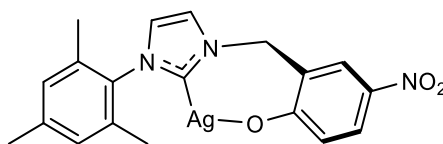


Figure 241: ORTEP plot of the imidazolium tetrafluoroborate salt with the BF₄ and H atoms omitted for clarity and the thermal ellipsoids set at a 50 % probability level

Table 50: Crystal data for the structural refinement of 3-(2-hydroxy-5-nitrobenzyl)-1-(2,4,6-trimethylphenyl) imidazolium tetrafluoroborate

Identification code	sbd1706	
Empirical formula and weight	C ₁₉ H ₂₀ BF ₄ N ₃ O ₃	425.19
Temperature / K	110.05(10)	
Crystal system and space group	trigonal	R-3
Unit cell dimensions	a / Å = 25.8153(3) b / Å = 25.8153(3) c / Å = 15.33067(18)	α / ° = 90 β / ° = 90 γ / ° = 120
Volume / Å³	8848.0(2)	
Z	18	
Density (calculated) / ρ_{calc} / g cm⁻³	1.436	
Absorption coefficient / μ / mm⁻¹	1.055	
F(000)	3960.0	
Crystal size / mm³	0.257 × 0.207 × 0.158	
Radiation	CuKα (λ = 1.54184)	
2θ range for data collection/°	6.992 to 142.124	
Index ranges	-31 ≤ h ≤ 31, -30 ≤ k ≤ 29, -18 ≤ l ≤ 17	
Reflections collected	14441	
Independent reflections	3775 [R _{int} = 0.0161, R _{sigma} = 0.0114]	
Data / restraints / parameters	3775 / 0 / 316	
Goodness-of-fit on F²	1.023	
Final R indexes [I ≥ 2σ (I)]	R ₁ = 0.0397, wR ₂ = 0.1046	
Final R indexes [all data]	R ₁ = 0.0421, wR ₂ = 0.1070	
Largest diff. peak / hole / e Å⁻³	0.33 / -0.22	

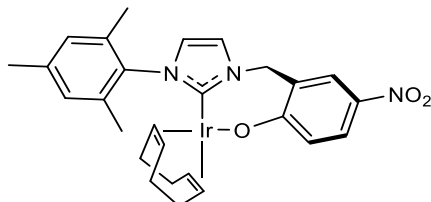
8.6.2. Silver(I) 3-(2-methylene-4-nitrophenolate)-1-(2,4,6-trimethylphenyl)imidazolylidene¹²⁵



3-(2-hydroxy-5-nitrobenzyl)-1-(2,4,6-trimethylphenyl) imidazolium bromide (500 mg, 1.2 mmol, 1 eq.), silver(I) oxide (569.4 mg, 2.5 mmol, 2 eq.) and 4 Å molecular sieves (1.12 g) were added to a round-bottom flask under a nitrogen atmosphere. Dried THF (8.5 mL) and toluene (8.5 mL) were added to the flask and the reaction mixture was stirred at reflux for 3 h. Once cooled to room temperature, the mixture was diluted with dichloromethane (80 mL), filtered through a pad of Celite and washed through with dichloromethane (2 x 5 mL). The solvent was removed under reduced pressure to produce a yellow solid (0.45 g, 85%); ¹H NMR [CDCl₃, 400 MHz, 298 K] δ 8.16 (s br, 1H, CH_{Ar}), 7.78 (s br, 1H, CH_{Ar}), 7.38 (s br, 1H, CH_{Ar}), 7.01 (s br, 2H, 2 x CH_{mesityl}), 6.99 (s br, 1H, CH_{Ar}), 5.84 (s br, 1H, CH_{Ar}), 5.27 (s br, 2H, CH₂), 2.42 (s, 3H, CH₃), 1.96 (s br, 6H, 2 x CH₃); ¹³C{¹H} NMR [CDCl₃] δ 174.7, 139.6, 137.2, 135.2, 134.5, 129.2 (2 x CH_{mesityl}), 127.2 (CH_{Ar}), 126.8 (CH_{Ar}), 124.4, 122.2, 121.9 (CH_{Ar}), 121.5 (CH_{Ar}), 50.3 (CH₂), 21.4 (CH₃), 17.9 (2 x CH₃); MS [ESI] m/z 783 (Ag dimer, protonated phenol groups)

Only partial ¹³C{¹H} NMR data could be obtained due to very broad and overlapping NMR signals.

8.6.3. Iridium(I) (3-(2-methylene-4-nitrophenolate)-1-(2,4,6-trimethylphenyl)imidazolylidene) (cyclooctadiene), 1¹⁴⁶



Silver(I) 3-(2-methylene-4-nitrophenolate)-1-(2,4,6-trimethylphenyl)imidazolylidene (170 mg, 0.38 mmol, 2 eq.) and [Ir(COD)Cl]₂ (129 mg, 0.19 mmol, 1 eq.) were added to a Schlenk flask under N₂. Dry THF (12 mL) was added and the reaction mixture was stirred overnight at room temperature. The mixture was diluted with DCM, filtered through Celite, purified by column chromatography (silica, DCM: acetone 80: 20) and evaporated to dryness to produce an orange/brown powder (0.23 g, 96 %); ¹H NMR [CD₂Cl₂, 500 MHz, 298 K] δ 8.17 (d, 1H, ⁴J(HH) = 3.0 Hz, CH_{Ar}), 7.96 (dd, 1H, ⁴J(HH) = 3.0 Hz, ³J(HH) = 9.3 Hz, CH_{Ar}), 7.14 (d, 1H, ³J(HH) = 1.9 Hz, CH_{imidazole}), 7.03 (s br, 2H, 2 x CH_{mesityl}), 6.72 (d, 1H, ³J(HH) = 1.9 Hz, CH_{imidazole}), 6.60 (s br, 1H, CH₂ linker), 6.57 (d, 1H, ³J(HH) = 9.3 Hz, CH_{Ar}), 4.79 (s br, 1H, CH₂ linker), 4.40 (s br, 2H, 2 x CH_{COD}), 3.30 (s br, 1H, CH_{COD}), 2.45 (s br, 1H, CH_{COD}), 2.39 (s, 3H, CH₃), 2.09 (s br, 4H, CH_{2(COD)}), 2.03 (s br, 6H, 2 x CH₃), 1.58 (s br, 4H, CH_{2(COD)}); ¹H NMR [CD₂Cl₂, 500 MHz, 253 K] δ 8.18 (d, 1H, ⁴J(HH) = 3.0 Hz, CH_{Ar}), 7.96 (dd, 1H, ⁴J(HH) = 3.0 Hz, ³J(HH) = 9.2 Hz), 7.14 (d, 1H, ³J(HH) = 1.9 Hz, CH_{imidazole}), 7.06 (s, 1H, CH_{mesityl}), 6.96 (s, 1H, CH_{mesityl}), 6.72 (d, 1H, ³J(HH) = 1.9 Hz, CH_{imidazole}), 6.60 (d, 1H, ²J(HH) = 14.0 Hz, CH₂ linker), 6.55 (d, 1H, ³J(HH) = 9.2 Hz, CH_{Ar}), 4.79 (d, 1H, ²J(HH) = 14.0 Hz, CH₂ linker), 4.42 (m, 1H, CH_{COD}), 4.26 (m, 1H, CH_{COD}), 3.27 (m, 1H, CH_{COD}), 2.41 (m, 1H, CH_{COD}), 2.36 (s, 3H, CH₃), 2.20-2.00 (m, 4H, 2 x CH_{2(COD)}), 2.07 (s, 3H, CH₃), 1.96 (s, 3H, CH₃), 1.68-1.53 (m, 4H, 2 x CH_{2(COD)}); ¹³C{¹H} NMR [CD₂Cl₂, 253 K] δ 175.7 (C-OIr), 175.1 (C-Ir), 139.0 (C_{Ar}), 136.1 (C_{Ar}), 135.5 (C_{Ar}), 134.4 (C_{Ar}), 134.0 (C_{Ar}), 129.1 (CH_{Ar}), 128.4 (CH_{Ar}), 127.0 (CH_{Ar}), 126.3 (CH_{Ar}), 123.4 (CH_{imidazole}), 123.2 (C_{Ar}), 121.5 (CH_{Ar}), 119.6 (CH_{imidazole}), 84.7 (CH), 84.6 (CH), 51.2 (CH₂), 49.7 (CH), 48.3 (CH), 34.5 (CH₂), 33.8 (CH₂), 28.9 (CH₂), 28.4 (CH₂), 21.0

(CH₃), 18.7 (CH₃), 17.6 (CH₃); MS [ESI] m/z 638.19 (M+H)⁺. Anal. Calcd for C₂₇H₃₀N₃O₃Ir (M_r = 636.77): C, 50.93; H, 4.75; N, 6.60. Found: C, 50.64; H, 4.52; N, 6.14.

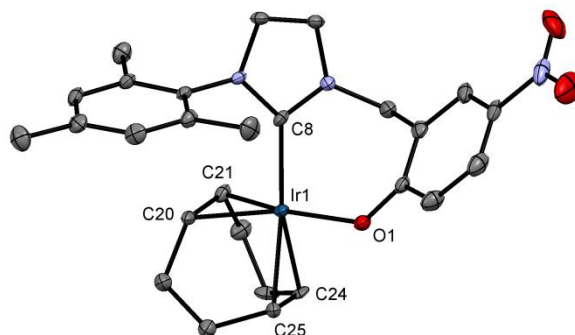


Figure 242: ORTEP plot of **1** with H atoms omitted for clarity and the thermal ellipsoids set at a 50 % probability level

Table S1: Crystal data for the structural refinement of **1**

Identification code	sbd1402	
Empirical formula and weight	C ₂₇ H ₃₀ IrN ₃ O ₃	644.77
Temperature / K	110.05(10)	
Crystal system and space group	monoclinic	P2 ₁ /n
Unit cell dimensions	a / Å = 8.7533(3) b / Å = 19.4098(11) c / Å = 13.9131(4)	α / ° = 90 β / ° = 90.472(3) γ / ° = 90
Volume / Å³	2363.77(17)	
Z	4	
Density (calculated) / ρ_{calc} / g cm⁻³	1.812	
Absorption coefficient / μ / mm⁻¹	5.918	
F(000)	1269.0	

Crystal size / mm³	0.1894 × 0.1261 × 0.0302
Radiation	MoK α ($\lambda = 0.71073$)
2Θ range for data collection/°	5.86 to 59.996
Index ranges	$-7 \leq h \leq 12, -23 \leq k \leq 27, -19 \leq l \leq 19$
Reflections collected	12799
Independent reflections	6892 [$R_{\text{int}} = 0.0326, R_{\text{sigma}} = 0.0509$]
Data / restraints / parameters	6892 / 0 / 321
Goodness-of-fit on F²	1.143
Final R indexes [$I \geq 2\sigma(I)$]	$R_1 = 0.0345, wR_2 = 0.0675$
Final R indexes [all data]	$R_1 = 0.0415, wR_2 = 0.0701$
Largest diff. peak / hole / e \AA^{-3}	1.81 / -1.39

UV-vis absorption data for complex **1** at six different concentrations are given in Table 52 with the corresponding absorption spectra shown in Figure 243.

*Table 52: Concentration and absorbance values for six samples of **1** in DCM at different concentrations*

Sample	Concentration / $\mu\text{mol dm}^{-3}$	Absorbance
A	60.4	1.05
B	48.3	0.84
C	29.0	0.52
D	23.2	0.42
E	16.2	0.30
F	6.5	0.13

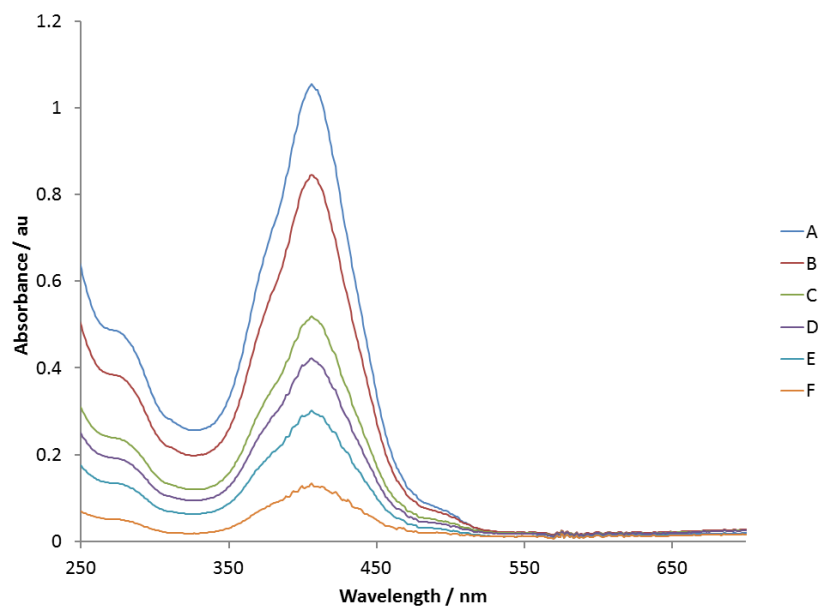


Figure 243: Visible region of the absorption spectra for **1** in DCM at different concentrations as listed in Table 52

The calibration graph in Figure 244 was used to gain the molar absorption coefficient for the absorption band of **1** as described in Section 2.6.1.

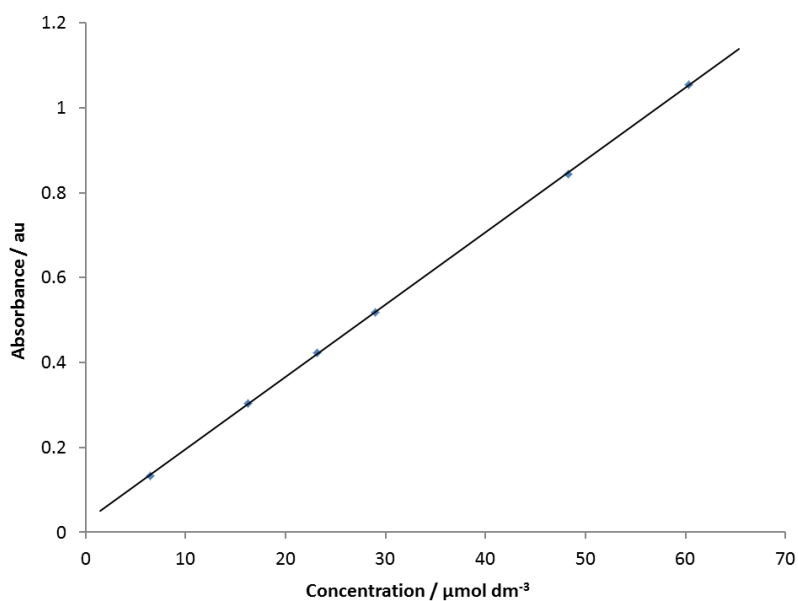
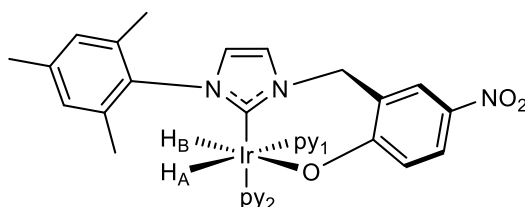


Figure 244: Calibration graph used to calculate the molar absorption coefficient for the absorption band of **1** at 406 nm using the data in Table 52

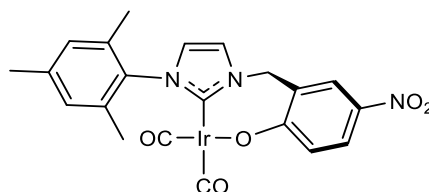
8.6.4. Iridium(III) (3-(2-methylene-4-nitrophenolate)-1-(2,4,6-trimethylphenyl)imidazolylidene)(dihydride)(pyridine)₂, 6A



To a Young's NMR tube was added **1** (10 mg, 16 μmol , 1 eq.), pyridine (3.8 μL , 47 μmol , 3 eq.) and CD_2Cl_2 (0.6 mL). The solution was then degassed three times on a high vacuum line using a freeze-thaw procedure with liquid N_2 , before the addition of 3 bars of H_2 . The mixture was then left to react at r.t. for 3 days; ^1H NMR [CD_2Cl_2 , 400 MHz, 233 K] δ 8.92 (m, 2H, 2 x $\text{CH}_{\text{py ortho}}$), 8.17 (d, 1H, $^4J(\text{HH}) = 2.8$ Hz, CH_{Ar}), 8.13 (m, 2H, 2 x $\text{CH}_{\text{py ortho}}$), 8.04 (dd, 1H, $^3J(\text{HH}) = 9.0$ Hz, $^4J(\text{HH}) = 2.8$ Hz, CH_{Ar}), 7.66 (m, 1H, $\text{CH}_{\text{py para}}$), 7.60 (m, 1H, $\text{CH}_{\text{py para}}$), 7.19 (d, 1H, $^3J(\text{HH}) = 1.5$ Hz, $\text{CH}_{\text{imidazole}}$), 7.11 (m, 2H, 2 x $\text{CH}_{\text{py meta}}$), 7.01 (s, 1H, $\text{CH}_{\text{mesityl}}$), 6.92 (m, 2H, 2 x $\text{CH}_{\text{py meta}}$), 6.69 (d, 1H, $^3J(\text{HH}) = 9.0$ Hz, CH_{Ar}), 6.61 (d, 1H, $^3J(\text{HH}) = 1.5$ Hz, $\text{CH}_{\text{imidazole}}$), 6.48 (d, 1H, $^2J(\text{HH}) = 13.6$ Hz, CH_2 linker), 6.46 (s, 1H, $\text{CH}_{\text{mesityl}}$), 4.46 (d, 1H, $^2J(\text{HH}) = 13.6$ Hz, CH_2 linker), 2.31 (s, 3H, CH_3), 2.16 (s, 3H, CH_3), 0.93 (s, 3H, CH_3), -21.36 (d, 1H, $^2J(\text{HH}) = 8.9$ Hz), -28.88 (d, 1H, $^2J(\text{HH}) = 8.9$ Hz); $^{13}\text{C}\{^1\text{H}\}$ NMR [CD_2Cl_2] δ 177.7 (C-O), 175.5 (C-Ir), 154.6 (2 x $\text{CH}_{\text{py ortho}}$), 152.8 (2 x $\text{CH}_{\text{py ortho}}$), 137.9 (C_{Ar}), 137.0 (C_{Ar}), 136.5 (C_{Ar}), 136.0 (C_{Ar}), 135.8 ($\text{CH}_{\text{py para}}$), 135.5 ($\text{CH}_{\text{py para}}$), 132.2 (C_{Ar}), 128.7 ($\text{CH}_{\text{mesityl}}$), 128.1 ($\text{CH}_{\text{mesityl}}$), 127.2 (CH_{Ar}), 126.9 (CH_{Ar}), 124.8 (C_{Ar}), 124.7 (2 x $\text{CH}_{\text{py meta}}$), 124.5 (2 x $\text{CH}_{\text{py meta}}$), 122.2 (CH_{Ar}), 120.5 ($\text{CH}_{\text{imidazole}}$), 120.0 ($\text{CH}_{\text{imidazole}}$), 51.7 (CH_2), 25.3 (CH_3), 21.0 (CH_3), 16.6 (CH_3); ^{15}N NMR [CD_2Cl_2] δ 192.5, 190.9

The $^{13}\text{C}\{^1\text{H}\}$ spectrum showed large peaks for COD, COE and COA but the active catalyst signals were not visible, even after multiple scans, due to sample dilution. The carbene carbon and other quaternary carbon signals were identified using an HMBC pulse sequence exploiting the long-range coupling, with the coupling constant optimised at 6 Hz.

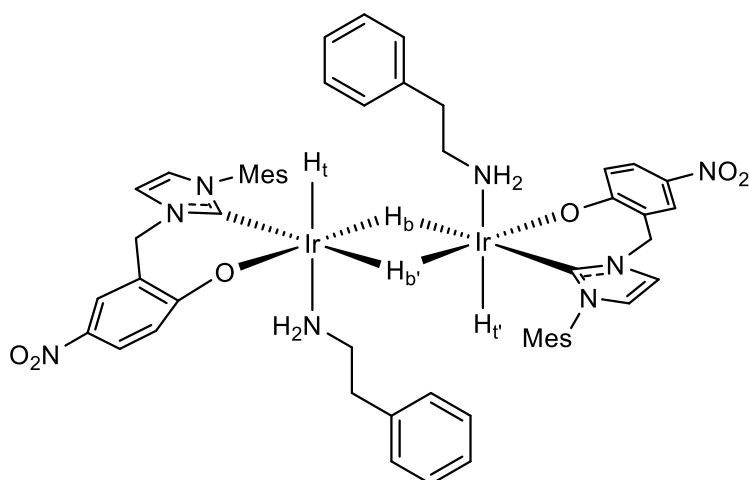
8.6.5. Iridium(I) (3-(2-methylene-4-nitrophenolate)-1-(2,4,6-trimethylphenyl)imidazolylidene) (dicarbonyl), 17



Iridium(I) (3-(2-methylene-4-nitrophenolate)-1-(2,4,6-trimethylphenyl)imidazolylidene) (cyclooctadiene) (20 mg, 0.0314 mmol, 1 eq.) was dissolved in DCM (2 mL) and the mixture was stirred at r.t. whilst CO was bubbled through for 2 min. Stirring under an atmosphere of CO was continued for 10 min before the solution was purged with N₂ and the solvent was removed. The residue was triturated with hexane to afford a yellow solid (12 mg, 67 %); ¹H NMR [CD₂Cl₂, 400 MHz, 298 K] δ 8.20 (d, 1H, ⁴J(HH) = 3.0 Hz, CH_{Ar}), 8.04 (dd, 1H, ⁴J(HH) = 3.0 Hz, ³J(HH) = 9.2 Hz, CH_{Ar}), 7.28 (d, 1H, ³J(HH) = 1.9 Hz, CH_{imidazole}), 7.06 (s, 2H, 2 x CH_{mesityl}), 6.93 (d, 1H, ³J(HH) = 1.9 Hz, CH_{imidazole}), 6.74 (d, 1H, ³J(HH) = 9.2 Hz, CH_{Ar}), 5.43 (s br, 2H, CH₂), 2.40 (s, 3H, CH₃), 2.01 (s, 6H, 2 x CH₃); ¹³C{¹H} NMR [CD₂Cl₂] δ 181.9 (C=O), 173.3 (C=O), 173.0 (C-Ir), 151.3 (C-O), 139.9 (C_{Ar}), 136.2 (C_{Ar}), 135.2 (2 x C_{Ar}), 134.7 (C_{Ar}), 129.1 (2 x CH_{mesityl}), 126.3 (CH_{Ar}), 126.2 (CH_{Ar}), 123.5 (C_{Ar}), 123.4 (CH_{imidazole}), 121.9 (CH_{Ar}), 121.0 (CH_{imidazole}), 50.6 (CH₂), 20.9 (CH₃), 17.8 (2 x CH₃); MS [ESI] m/z 586.1 (M+H)⁺; IR ν_{CO} (cm⁻¹): 2065.5, 1971.9

8.6.6. Iridium carbene phenethylamine dimer,

21phenethylamine

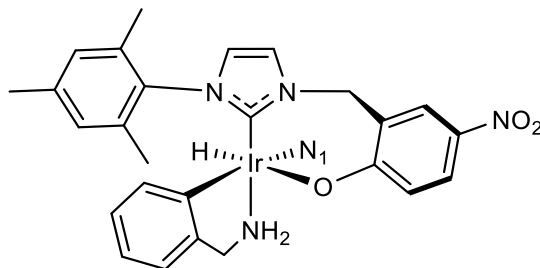


To a Young's NMR tube was added **1** (5 mg, 8 μmol , 1 eq.), phenethylamine (1 μL , 8 μmol , 1 eq.) and CD_2Cl_2 (0.6 mL). The solution was then degassed three times on a high vacuum line using a freeze-thaw procedure with liquid N_2 , before the addition of 3 bars of H_2 . The mixture was then left to react at r.t. for 3 days; ^1H NMR [CD_2Cl_2 , 400 MHz, 243 K] δ 8.16 (d, 1H, $^4J(\text{HH}) = 2.6$ Hz, CH_{Ar}), 8.15 (d, 1H, $^4J(\text{HH}) = 2.6$ Hz, CH_{Ar}), 8.05 (dd, 1H, $^4J(\text{HH}) = 2.6$ Hz, $^3J(\text{HH}) = 9.2$ Hz, CH_{Ar}), 8.00 (dd, 1H, $^4J(\text{HH}) = 2.6$ Hz, $^3J(\text{HH}) = 9.2$ Hz, CH_{Ar}), 7.36-7.2 (m, 5H, 5 x CH_{Ar}), 7.20 (d, 1H, $^3J(\text{HH}) = 2.2$ Hz, $\text{CH}_{\text{imidazole}}$), 7.05-6.94 (m, 5H, 5 x CH_{Ar}), 7.04 (d, 1H, $^3J(\text{HH}) = 1.7$ Hz, $\text{CH}_{\text{imidazole}}$), 7.00 (s, 1H, $\text{CH}_{\text{mesityl}}$), 6.96 (s, 1H, $\text{CH}_{\text{mesityl}}$), 6.86 (d, 1H, $^2J(\text{HH}) = 14.2$ Hz, CH_2), 6.86 (s, 1H, $\text{CH}_{\text{mesityl}}$), 6.70 (d, 1H, $^3J(\text{HH}) = 2.2$ Hz, $\text{CH}_{\text{imidazole}}$), 6.60 (d, 1H, $^3J(\text{HH}) = 9.2$ Hz, CH_{Ar}), 6.53 (d, 1H, $^3J(\text{HH}) = 1.7$ Hz, $\text{CH}_{\text{imidazole}}$), 6.34 (d, 1H, $^3J(\text{HH}) = 9.2$ Hz, CH_{Ar}), 6.25 (d, 1H, $^2J(\text{HH}) = 13.7$ Hz, CH_2), 4.19 (d, 1H, $^2J(\text{HH}) = 14.2$ Hz, CH_2), 4.16 (d, 1H, $^2J(\text{HH}) = 13.7$ Hz, CH_2), 2.35-2.28 (m br, 4H, CH_{alkyl}), 2.31 (s, 3H, CH_3), 2.27 (s, 3H, CH_3), 2.16-2.08 (m br, 4H, CH_{alkyl}), 1.83 (s, 3H, CH_3), 1.76 (s, 3H, CH_3), 1.68 (s, 3H, CH_3), 1.53 (s, 3H, CH_3), -26.30 (dd, 1H, $^2J(\text{HH}) = 6.1$ Hz, $^2J(\text{HH}) = 8.1$ Hz, H_t), -26.54 (dd, 1H, $^2J(\text{HH}) = 8.1$ Hz, $^2J(\text{HH}) = 8.1$ Hz, H_t'), -30.59 (d, 1H, $^2J(\text{HH}) = 8.1$ Hz, H_b), -30.97 (d, 1H, $^2J(\text{HH}) = 6.1$ Hz, H_b'); $^{13}\text{C}\{^1\text{H}\}$ NMR [CD_2Cl_2] δ 177.6 (C_{Ar}), 176.9 (C_{Ar}), 156.3 (C-Ir), 150.8 (C-Ir), 139.0 ($\text{C}_{\text{mesityl}}$), 138.5 ($\text{C}_{\text{mesityl}}$), 138.5 ($\text{C}_{\text{mesityl}}$), 137.4 ($\text{C}_{\text{mesityl}}$), 136.5 ($\text{C}_{\text{mesityl}}$), 135.9 ($\text{C}_{\text{mesityl}}$), 135.3 ($\text{C}_{\text{mesityl}}$), 134.1 (C_{Ar}), 133.0 ($\text{C}_{\text{mesityl}}$), 132.5 (C_{Ar}), 129.8 ($\text{CH}_{\text{mesityl}}$), 129.2 (CH_{Ar}), 129.0 ($\text{CH}_{\text{mesityl}}$), 128.8 (CH_{Ar}), 128.4 ($\text{CH}_{\text{mesityl}}$), 128.4 (CH_{Ar}), 128.3 (CH_{Ar}), 128.2 ($\text{CH}_{\text{mesityl}}$), 128.0 (CH_{Ar}), 126.8

(CH_{Ar}), 126.7 (CH_{Ar}), 121.4 (CH_{Ar}), 121.4 (CH_{imidazole}), 121.3 (CH_{Ar}), 121.0 (CH_{imidazole}), 119.7 (CH_{imidazole}), 119.3 (CH_{imidazole}), 51.6 (CH₂), 50.9 (CH₂), 19.3 (CH₃), 18.3 (CH₃), 18.0 (CH₃), 17.6 (CH₃)

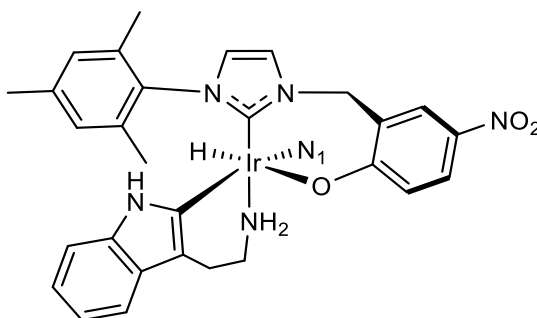
In some places this characterisation data is incomplete due to multiple overlapping signals for the very similar chemical shifts of the two bidentate carbene ligands and the multiple amine ligands.

8.6.7. Iridium(III) (3-(2-methylene-4-nitrophenolate)-1-(2,4,6-trimethylphenyl)imidazolylidene)(hydride)(benzylamine)(C-H activated benzylamine), 22_{benzylamine}



To a Young's NMR tube was added **1** (5 mg, 8 μ mol, 1 eq.), benzylamine (1.7 μ L, 16 μ mol, 2 eq.) and CD₂Cl₂ (0.6 mL). The solution was then degassed three times on a high vacuum line using a freeze-thaw procedure with liquid N₂, before the addition of 3 bars of H₂. The mixture was then left to react at r.t. for 3 days; ¹H NMR [CD₂Cl₂, 400 MHz, 298 K] δ 8.15 (d, 1H, ⁴*J*(HH) = 2.9 Hz, CH_{Ar}), 7.95 (dd, 1H, ⁴*J*(HH) = 2.9 Hz, ³*J*(HH) = 8.8 Hz, CH_{Ar}), 7.40-7.34 (m, 4H, 4 x CH_{Ar}), 7.33 (d, 1H, ³*J*(HH) = 2.1 Hz, CH_{imidazole}), 7.06 (m, 1H, CH_{Ar}), 7.02 (s, 1H, CH_{mesityl}), 6.90 (s, 1H, CH_{mesityl}), 6.90 (m, 1H, CH_{Ar}), 6.85 (d, 1H, ³*J*(HH) = 2.1 Hz, CH_{imidazole}), 6.80-6.70 (m, 3H, CH_{Ar}), 6.54 (d, 1H, ³*J*(HH) = 8.8 Hz, CH_{Ar}), 5.63 (d, 1H, ²*J*(HH) = 13.8 Hz, CH₂ linker), 4.41 (d, 1H, ²*J*(HH) = 13.8 Hz, CH₂ linker), 4.34 (ddd, 1H, ²*J*(HH) = 13.9 Hz, ³*J*(HH) = 5.5 Hz, ³*J*(HH) = 5.5 Hz, CH₂), 3.96 (ddd, 1H, ²*J*(HH) = 13.9 Hz, ³*J*(HH) = 6.5 Hz, ³*J*(HH) = 6.5 Hz, CH₂), 3.89 (s br, 1H, NH₂), 3.64 (ddd, 1H, ²*J*(HH) = 13.3 Hz, ³*J*(HH) = 9.8 Hz, ³*J*(HH) = 4.1 Hz, CH₂), 3.46 (ddd, 1H, ²*J*(HH) = 13.3 Hz, ²*J*(HH) = 9.5 Hz, ³*J*(HH) = 6.2 Hz, CH₂), 3.39 (s br, 1H, NH₂), 2.70 (t br, 1H, ³*J*(HH) = 9.8 Hz, NH₂), 2.35 (s, 3H, CH₃), 2.33 (s br, 1H, NH₂), 2.02 (s, 3H, CH₃), 1.74 (s, 3H, CH₃), -28.50 (s, 1H); ¹³C{¹H} NMR [CD₂Cl₂] δ 177.6 (C-Ir), 157.7 (C-O), 138.6 (C_{Ar}), 137.3 (C_{Ar}), 136.6 (CH_{Ar}), 136.3 (C_{Ar}), 133.5 (C_{Ar}), 133.4 (C_{Ar}), 129.4 (CH_{Ar}), 129.3 (CH_{mesityl}), 129.0 (CH_{Ar}), 128.9 (CH_{Ar}), 128.4 (CH_{mesityl}), 127.9 (CH_{Ar}), 127.6 (CH_{Ar}), 127.4 (CH_{Ar}), 126.4 (CH_{Ar}), 125.5 (C_{Ar}), 124.8 (CH_{Ar}), 122.0 (CH_{Ar}), 121.5 (CH_{imidazole}), 121.0 (CH_{Ar}), 120.7 (CH_{imidazole}), 120.0 (CH_{Ar}), 119.6 (C_{Ar}), 53.2 (CH₂), 50.8 (CH₂), 50.4 (CH₂), 20.7 (CH₃), 18.7 (CH₃), 17.4 (CH₃)

8.6.8. Iridium(III) (3-(2-methylene-4-nitrophenolate)-1-(2,4,6-trimethylphenyl)imidazolyli-dene)(hydride)(tryptamine)(C-H activated tryptamine), **22_{tryptamine}**



To a Young's NMR tube was added **1** (5 mg, 8 μmol , 1 eq.), tryptamine (2.5 mg, 16 μmol , 2 eq.) and CD_2Cl_2 (0.6 mL). The solution was then degassed three times on a high vacuum line using a freeze-thaw procedure with liquid N_2 , before the addition of 3 bars of H_2 . The mixture was then left to react at r.t. for 3 days; ^1H NMR [CD_2Cl_2 , 400 MHz, 298 K] δ 8.02 (d, 1H, $^4J(\text{HH}) = 3.1$ Hz, CH_{Ar}), 7.86 (dd, 1H, $^4J(\text{HH}) = 3.1$ Hz, $^3J(\text{HH}) = 9.0$ Hz, CH_{Ar}), 7.47 (d, 1H, $^3J(\text{HH}) = 7.6$ Hz, CH_{Ar}), 7.38 (d, 1H, $^3J(\text{HH}) = 7.6$ Hz, CH_{Ar}), 7.31 (d, 1H, $^3J(\text{HH}) = 1.6$ Hz, $\text{CH}_{\text{imidazole}}$), 7.27 (t, 1H, $^3J(\text{HH}) = 7.6$ Hz, CH_{Ar}), 7.17 (t, 1H, $^3J(\text{HH}) = 7.6$ Hz, CH_{Ar}), 7.15 (d, 1H, $^3J(\text{HH}) = 7.6$ Hz, CH_{Ar}), 7.03 (d, 1H, $^3J(\text{HH}) = 7.6$ Hz, CH_{Ar}), 7.00 (s, 1H, CH_{Ar}), 6.98 (s, 1H, $\text{CH}_{\text{mesityl}}$), 6.94 (s, 1H, CH_{Ar}), 6.87 (d, 1H, $^3J(\text{HH}) = 1.6$ Hz, $\text{CH}_{\text{imidazole}}$), 6.83 (t, 1H, $^3J(\text{HH}) = 7.6$ Hz, CH_{Ar}), 6.78 (s, 1H, $\text{CH}_{\text{mesityl}}$), 6.70 (t, 1H, $^3J(\text{HH}) = 7.6$ Hz, CH_{Ar}), 6.22 (d, 1H, $^3J(\text{HH}) = 9.0$ Hz, CH_{Ar}), 5.27 (d, 1H, $^2J(\text{HH}) = 13.8$ Hz, CH_2 linker), 4.19 (d, 1H, $^2J(\text{HH}) = 13.8$ Hz, CH_2 linker), 3.42 (s, 2H, NH_2), 3.24 (m, 1H, CH_2), 3.01 (m, 1H, CH_2), 2.93 (m, 1H, CH_2), 2.83 (m, 1H, CH_2), 2.71 (m, 1H, CH_2), 2.67 (m, 1H, CH_2), 2.56 (m, 1H, CH_2), 2.41 (m, 1H, CH_2), 2.30 (s, 3H, CH_3), 2.15 (s, 3H, CH_3), 1.67 (s, 3H, CH_3), -28.94 (s, 1H); $^{13}\text{C}\{^1\text{H}\}$ NMR [CD_2Cl_2] δ 177.1 (C-O), 155.5 (C-Ir), 138.8 (C_{Ar}), 138.3 (C_{Ar}), 136.6 (C_{Ar}), 136.5 (C_{Ar}), 136.5 (C_{Ar}), 133.5 (C_{Ar}), 133.3 (C- NO_2), 129.7 (CH_{Ar}), 129.7 (C_{Ar}), 129.5 (CH_{Ar}), 128.5 (CH_{Ar}), 127.7 (CH_{Ar}), 127.4 (CH_{Ar}), 126.5 (CH_{Ar}), 126.5 (C_{Ar}), 124.6 (C_{Ar}), 122.6 (CH_{Ar}), 122.5 (CH_{Ar}), 121.7 (CH_{Ar}), 121.5 (CH_{Ar}), 120.9 (CH_{Ar}), 119.7 (C_{Ar}), 117.0 (CH_{Ar}), 115.9 (CH_{Ar}), 113.3 (CH_{Ar}), 111.6 (CH_{Ar}), 110.9 (CH_{Ar}),

108.7 (C_{Ar}), 107.6 (CH_{Ar}), 50.5 (CH₂), 45.5 (CH₂), 43.4 (CH₂), 28.7 (CH₂), 25.8 (CH₂), 20.8 (CH₃), 19.0 (CH₃), 17.3 (CH₃)

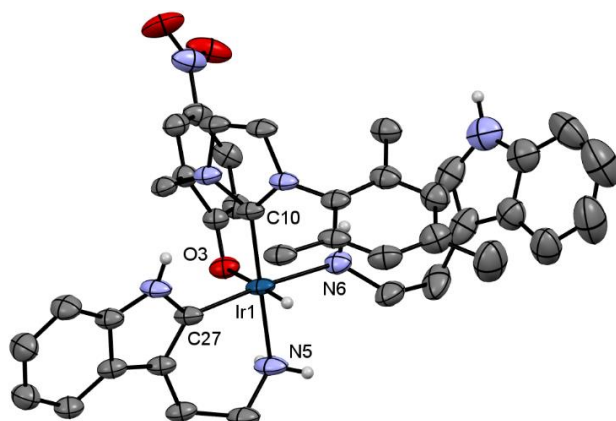


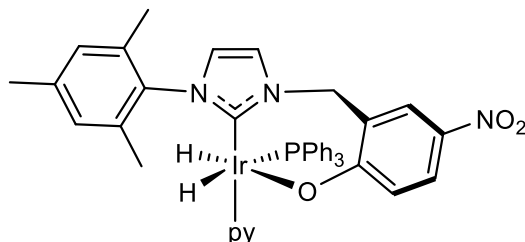
Figure 245: ORTEP plot of **22**_{tryptamine}, with H atoms (apart from the NH, NH₂ and hydride ligand) omitted for clarity and the thermal ellipsoids set at a 50 % probability level

Table 53: Crystal data for the structural refinement of **22**_{tryptamine}

Identification code	sbd1630	
Empirical formula and weight	C ₃₉ H ₄₂ IrN ₇ O ₃	848.99
Temperature / K	110.05(10)	
Crystal system and space group	trigonal	R-3
Unit cell dimensions	a / Å = 48.3824(6) b / Å = 48.3824(6) c / Å = 10.78400(10)	α / ° = 90 β / ° = 90 γ / ° = 120
Volume / Å³	21861.8(6)	
Z	18	
Density (calculated) / ρ_{calc} / g cm⁻³	1.161	
Absorption coefficient / μ / mm⁻¹	5.603	
F(000)	7668.0	

Crystal size / mm³	0.348 × 0.061 × 0.044
Radiation	CuKα (λ = 1.54184)
2θ range for data collection/°	7.308 to 134.142
Index ranges	-57 ≤ h ≤ 43, -47 ≤ k ≤ 57, -12 ≤ l ≤ 12
Reflections collected	43702
Independent reflections	8684 [R _{int} = 0.0419, R _{sigma} = 0.0247]
Data / restraints / parameters	8684 / 1 / 460
Goodness-of-fit on F²	1.022
Final R indexes [I ≥ 2σ (I)]	R ₁ = 0.0285, wR ₂ = 0.0729
Final R indexes [all data]	R ₁ = 0.0309, wR ₂ = 0.0743
Largest diff. peak / hole / e Å⁻³	0.90 / -0.66

8.6.9. Iridium(III) (3-(2-methylene-4-nitrophenolate)-1-(2,4,6-trimethylphenyl)imidazolyldiene)(dihydride)(pyridine) (triphenylphosphine), 23_{pyridine}



To a Young's NMR tube was added **1** (2 mg, 3.2 μmol , 1 eq.), pyridine (0.8 μL , 9.4 μmol , 3 eq.) and CD_2Cl_2 (0.6 mL). The solution was then degassed three times on a high vacuum line using a freeze-thaw procedure with liquid N_2 , before the addition of 3 bars of H_2 . The mixture was then left to react at r.t. for 3 days. Once reacted to form **6**, PPh_3 (0.8 mg, 3.2 μmol , 1 eq.) was added to the NMR tube and the mixture was degassed three times again before 3 bars of H_2 were added; ^1H NMR [CD_2Cl_2 , 400 MHz, 263 K] δ 8.74 (m, 2H, 2 x $\text{CH}_{\text{py ortho}}$), 8.00 (s br, 1H, CH_{Ar}), 7.38 (m, 1H, $\text{CH}_{\text{py para}}$), 7.36 (m br, 1H, CH_{Ar}), 7.31-7.06 (m, 15H, 15 x CH_{Ar}), 7.02 (d, 1H, $^3J(\text{HH}) = 1.6$ Hz, $\text{CH}_{\text{imidazole}}$), 6.92 (s, 1H, $\text{CH}_{\text{mesityl}}$), 6.89 (s, 1H, $\text{CH}_{\text{mesityl}}$), 6.78 (m, 2H, 2 x $\text{CH}_{\text{py meta}}$), 6.75 (d, 1H, $^3J(\text{HH}) = 1.6$ Hz, $\text{CH}_{\text{imidazole}}$), 6.68 (d, 1H, $^3J(\text{HH}) = 9.7$ Hz, CH_{Ar}), 4.72 (d, 1H, $^2J(\text{HH}) = 14.0$ Hz, CH_2 linker), 3.68 (d, 1H, $^2J(\text{HH}) = 14.0$ Hz, CH_2 linker), 2.38 (s, 3H, CH_3), 1.82 (s, 3H, CH_3), 1.39 (s, 3H, CH_3), -8.47 (dd, 1H, $^2J(\text{HH}) = 5.0$ Hz, $^2J(\text{HP}_{\text{trans}}) = 163.2$ Hz), -27.31 (dd, 1H, $^2J(\text{HH}) = 5.0$ Hz, $^2J(\text{HP}_{\text{cis}}) = 10.6$ Hz); $^{13}\text{C}\{^1\text{H}\}$ NMR [CD_2Cl_2] δ 181.7 (C-OIr), 155.8 (2 x $\text{CH}_{\text{py ortho}}$), 150.2 (C-Ir), 138.1 (C_{Ar}), 138.0 (C_{Ar}), 136.9 (C_{Ar}), 135.3 ($\text{CH}_{\text{py para}}$), 134.9 (C_{Ar}), 134.4 (3 x C_{Ar}), 134.0 (3 x CH_{Ar}), 133.8 (6 x CH_{Ar}), 133.0 (C_{Ar}), 128.8 ($\text{CH}_{\text{mesityl}}$), 128.7 ($\text{CH}_{\text{mesityl}}$), 128.1 (6 x CH_{Ar}), 127.0 (CH_{Ar}), 125.6 (C_{Ar}), 124.0 (2 x $\text{CH}_{\text{py meta}}$), 123.8 (CH_{Ar}), 121.0 ($\text{CH}_{\text{imidazole}}$), 120.9 ($\text{CH}_{\text{imidazole}}$), 119.7 (CH_{Ar}), 48.9 (CH_2), 21.0 (CH_3), 19.0 (CH_3), 18.2 (CH_3); $^{31}\text{P}\{^1\text{H}\}$ NMR [CD_2Cl_2] 13.6 (s)

For this complex, the $^{13}\text{C}\{^1\text{H}\}$ data were collected via indirect HMQC methods and as such the ^{31}P - ^{13}C couplings were not observed.

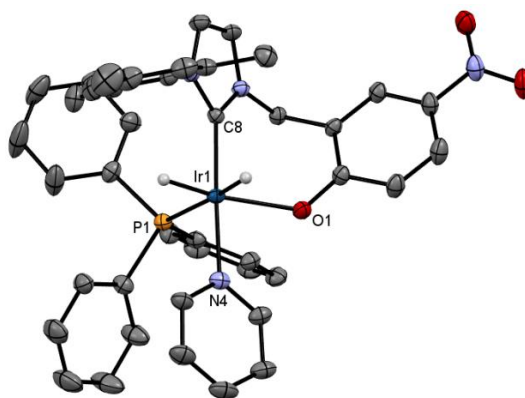


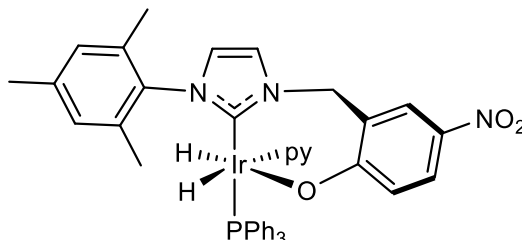
Figure 246: ORTEP plot of **23**_{pyridine}, with solvent and H atoms omitted for clarity and the thermal ellipsoids set at a 50 % probability level

Table 54: Crystal data for the structural refinement of **23**_{pyridine}

Identification code	sbd1631	
Empirical formula and weight	C ₅₆ H ₅₆ IrN ₄ O ₃ P	1056.21
Temperature / K	110.05(10)	
Crystal system and space group	orthorhombic	P2 ₁ 2 ₁ 2 ₁
Unit cell dimensions	a / Å = 13.63451(11) b / Å = 16.69609(15) c / Å = 21.33132(16)	α / ° = 90 β / ° = 90 γ / ° = 90
Volume / Å³	4855.93(7)	
Z	4	
Density (calculated) / ρ_{calc} / g cm⁻³	1.445	
Absorption coefficient / μ / mm⁻¹	2.831	
F(000)	2144.0	
Crystal size / mm³	0.146 × 0.131 × 0.102	
Radiation	MoKα (λ = 0.71073)	
2θ range for data collection/°	6.732 to 60.16	

Index ranges	$-19 \leq h \leq 19, -23 \leq k \leq 22, -11 \leq l \leq 30$
Reflections collected	39802
Independent reflections	14222 [$R_{\text{int}} = 0.0262, R_{\text{sigma}} = 0.0302$]
Data / restraints / parameters	14222 / 180 / 625
Goodness-of-fit on F^2	1.065
Final R indexes [$I \geq 2\sigma(I)$]	$R_1 = 0.0236, wR_2 = 0.0517$
Final R indexes [all data]	$R_1 = 0.0272, wR_2 = 0.0536$
Largest diff. peak / hole / $e \text{ \AA}^{-3}$	0.88 / -0.70

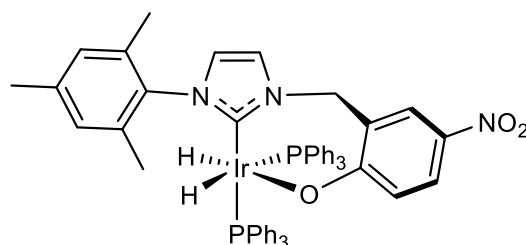
8.6.10. Iridium(III) (3-(2-methylene-4-nitrophenolate)-1-(2,4,6-trimethylphenyl)imidazolylidene)(dihydride)(pyridine)(triphenylphosphine), 24_{pyridine}



To a Young's NMR tube was added **1** (2 mg, 3.2 μmol , 1 eq.), pyridine (0.8 μL , 9.4 μmol , 3 eq.), PPh_3 (0.8 mg, 3.2 μmol , 1 eq.) and CD_2Cl_2 (0.6 mL). The solution was then degassed three times on a high vacuum line using a freeze-thaw procedure with liquid N_2 , before the addition of 3 bars of H_2 . The mixture was then left to react at r.t. for 3 days; ^1H NMR [CD_2Cl_2 , 400 MHz, 298 K] δ 8.16 (d, 1H, $^4J(\text{HH}) = 3.2$ Hz, CH_{Ar}), 7.93 (dd, 1H, $^4J(\text{HH}) = 3.2$ Hz, $^3J(\text{HH}) = 9.3$ Hz, CH_{Ar}), 7.88 (m, 2H, 2 x CH_{py} *ortho*), 7.64 (m, 3H, 3 x CH_{Ar}), 7.46 (m, 6H, 6 x CH_{Ar}), 7.36 (m, 1H, CH_{py} *para*), 7.29 (s br, $\text{CH}_{\text{imidazole}}$), 7.27-7.18 (m, 6H, 6 x CH_{Ar}), 7.04 (s, 1H, $\text{CH}_{\text{mesityl}}$), 6.77 (s br, $\text{CH}_{\text{imidazole}}$), 6.57 (m, 2H, 2 x CH_{py} *meta*), 6.52 (s, 1H, $\text{CH}_{\text{mesityl}}$), 6.33 (d, 1H, $^3J(\text{HH}) = 9.3$ Hz, CH_{Ar}), 2.33 (s br, 3H, CH_3), 2.19 (s br, 3H, CH_3), 1.19 (s v. br, 3H, CH_3), -21.73 (s br), -28.93 (s br); $^{13}\text{C}\{^1\text{H}\}$ NMR [CD_2Cl_2] δ 177.9 (C-OIr), 138.0 (C_{Ar}), 137.3 (C_{Ar}), 136.3 (C_{Ar}), 134.2 (6 x CH_{Ar}), 133.9 (6 x CH_{Ar}), 132.3 (C_{Ar}), 128.9 ($\text{CH}_{\text{mesityl}}$), 128.3 ($\text{CH}_{\text{mesityl}}$), 127.8 (4 x CH_{Ar}), 126.7 (CH_{Ar}), 124.5 (C_{Ar}), 124.0 (2 x CH_{py}), 123.7 (CH_{py}), 121.7 (CH_{Ar}), 120.9 ($\text{CH}_{\text{imidazole}}$), 120.6 ($\text{CH}_{\text{imidazole}}$), 20.7 (CH_3), 18.6 (CH_3); $^{31}\text{P}\{^1\text{H}\}$ NMR [CD_2Cl_2] 22.4 (s)

For this complex, the $^{13}\text{C}\{^1\text{H}\}$ data were collected via indirect HMQC methods and as such the ^{31}P - ^{13}C couplings were not observed. Full characterisation data are not available due to the complex undergoing rapid exchange and therefore exhibiting signal broadening.

8.6.11. Iridium(III) (3-(2-methylene-4-nitrophenolate)-1-(2,4,6-trimethylphenyl)imidazolyldiene)(dihydride)(PPh₃)₂, **25**



To a CD₂Cl₂ sample of **24** (3.2 μmol, 1 eq.) in a Young's NMR tube was added PPh₃ (1.6 mg, 6.4 μmol, 2 eq.). The solution was then degassed three times on a high vacuum line using a freeze-thaw procedure with liquid N₂, before the addition of 3 bars of H₂; ¹H NMR [CD₂Cl₂, 400 MHz, 298 K] δ 7.96 (d, 1H, ⁴J(HH) = 3.2 Hz, CH_{Ar}), 7.79 (dd, 1H, ⁴J(HH) = 3.2 Hz, ³J(HH) = 9.0 Hz, CH_{Ar}), 7.28-7.18 (m, 12H, 12 x CH_{Ar}), 7.17 (d, 1H, ³J(HH) = 1.6 Hz, CH_{imidazole}), 7.10-7.02 (m, 18H, 18 x CH_{Ar}), 6.99 (s, 1H, CH_{mesityl}), 6.96 (s, 1H, CH_{mesityl}), 6.86 (d, 1H, ³J(HH) = 1.6 Hz, CH_{imidazole}), 5.72 (d, 1H, ³J(HH) = 9.0 Hz, CH_{Ar}), 5.38 (d, 1H, ²J(HH) = 13.5 Hz, CH₂ linker), 3.92 (d, 1H, ²J(HH) = 13.5 Hz, CH₂ linker), 2.43 (s, 3H, CH₃), 1.82 (s, 3H, CH₃), 1.34 (s, 3H, CH₃), -9.6 (ddd, 1H, ²J(HH) = 4.7 Hz, ²J(HP_{cis}) = 22.9 Hz, ²J(HP_{trans}) = 138.6 Hz), -27.9 (ddd, 1H, ²J(HH) = 4.7 Hz, ²J(HP_{cis}) = 13.4 Hz, ²J(HP_{cis}) = 13.4 Hz); ¹³C{¹H} NMR [CD₂Cl₂] δ 180.0 (C-OIr), 165.6 (C-Ir), 138.5 (C_{Ar}), 137.9 (C_{Ar}), 136.1 (C_{Ar}), 135.0 (C_{Ar}), 134.3 (C_{Ar}), 133.8 (C_{Ar}), 132.6 (C_{Ar}), 129.1 (CH_{Ar} and CH_{mesityl}), 128.7 (2 x CH_{Ar}), 128.6 (2 x CH_{Ar}), 128.2 (CH_{mesityl}), 127.6 (2 x CH_{Ar}), 127.2 (2 x CH_{Ar}), 126.8 (2 x CH_{Ar}), 126.3 (CH_{Ar}), 125.5 (C_{Ar}), 121.8 (CH_{imidazole}), 121.3 (CH_{Ar}), 120.8 (CH_{imidazole}), 50.1 (CH₂), 20.9 (CH₃), 18.6 (CH₃), 17.3 (CH₃); ³¹P{¹H} NMR [CD₂Cl₂, 400 MHz, 298 K] 15.2 (s), 4.5 (s); MS [LIFDI] m/z 1055.36 (M⁺)

For this complex, the ¹³C{¹H} data were collected via indirect HMQC methods and as such the ³¹P-¹³C couplings were not observed. The ³¹P{¹H} data were also collected using indirect methods, hence the ³¹P-³¹P coupling data are not presented.

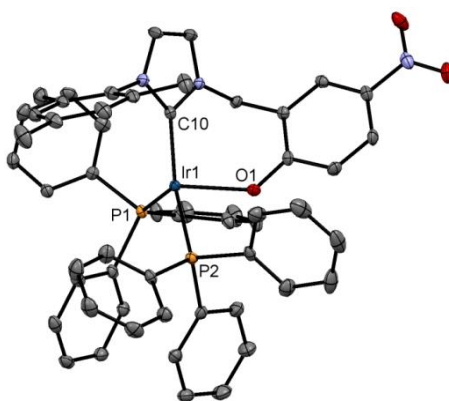


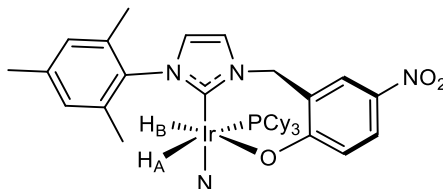
Figure 247: ORTEP plot of **25**, with solvent and H atoms omitted for clarity and the thermal ellipsoids set at a 50 % probability level

Table 55: Crystal data for the structural refinement of **25**

Identification code	sbd1514	
Empirical formula and weight	$C_{57}H_{52}Cl_4IrN_3O_3P_2$	1222.96
Temperature / K	110.05(10)	
Crystal system and space group	monoclinic	$P2_1$
Unit cell dimensions	$a / \text{\AA} = 13.01715(19)$ $b / \text{\AA} = 15.90413(14)$ $c / \text{\AA} = 13.68980(17)$	$\alpha / ^\circ = 90$ $\beta / ^\circ = 113.2175(16)$ $\gamma / ^\circ = 90$
Volume / \AA^3	2604.63(6)	
Z	2	
Density (calculated) / $\rho_{\text{calc}} / \text{g cm}^{-3}$	1.559	
Absorption coefficient / μ / mm^{-1}	2.878	
F(000)	1228.0	
Crystal size / mm^3	$0.2972 \times 0.1132 \times 0.0988$	
Radiation	MoK α ($\lambda = 0.71070$)	
2θ range for data collection/$^\circ$	6.78 to 63.86	

Index ranges	$-19 \leq h \leq 18, -23 \leq k \leq 23, -19 \leq l \leq 19$
Reflections collected	32785
Independent reflections	15727 [$R_{\text{int}} = 0.0272, R_{\text{sigma}} = 0.0405$]
Data / restraints / parameters	15727 / 1 / 644
Goodness-of-fit on F^2	1.053
Final R indexes [$I \geq 2\sigma(I)$]	$R_1 = 0.0245, wR_2 = 0.0528$
Final R indexes [all data]	$R_1 = 0.0291, wR_2 = 0.0551$
Largest diff. peak / hole / $e \text{ \AA}^{-3}$	1.06 / -0.75

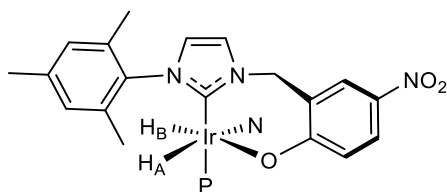
8.6.12. Iridium(III) (3-(2-methylene-4-nitrophenolate)-1-(2,4,6-trimethylphenyl)imidazolylidene)(PCy₃)(phenethylamine) (dihydride), 26_{PCy₃}



To a Young's NMR tube was added **1** (7 mg, 11 μ mol, 1 eq.), phenethylamine (1.4 μ L, 11 μ mol, 1 eq.), PCy₃ (3.1 mg, 11 μ mol, 1 eq.) and CD₂Cl₂ (0.6 mL). The solution was then degassed three times on a high vacuum line using a freeze-thaw procedure with liquid N₂, before the addition of 3 bars of H₂. The mixture was then left to react at r.t. for 3 days; ¹H NMR [CD₂Cl₂, 400 MHz, 243 K] δ 8.12 (d, 1H, ⁴J(HH) = 2.7 Hz, CH_{Ar}), 7.97 (dd, 1H, ⁴J(HH) = 3.0 Hz, ³J(HH) = 9.1 Hz, CH_{Ar}), 7.29-7.22 (m, 3H, 3 x CH_{Ar}), 7.19 (m, 2H, 2 x CH_{Ar}), 7.07 (d, 1H, ³J(HH) = 1.9 Hz, CH_{imidazole}), 6.94 (s, 1H, CH_{mesityl}), 6.91 (s, 1H, CH_{mesityl}), 6.67 (d, 1H, ³J(HH) = 1.9 Hz, CH_{imidazole}), 6.45 (d, 1H, ³J(HH) = 9.1 Hz, CH_{Ar}), 5.79 (d, 1H, ²J(HH) = 13.2 Hz, CH₂ linker), 4.32 (d, 1H, ²J(HH) = 13.2 Hz, CH₂ linker), 3.30 (m, 1H, CH₂), 2.98 (m, 1H, CH₂), 2.74 (m, 1H, CH₂), 2.33 (s, 3H, CH₃), 2.27 (m, 1H, CH₂), 2.03 (s, 3H, CH₃), 2.00 (m, 12H, CH₂), 1.74 (m, 12H, CH₂), 1.73 (s, 3H, CH₃), 1.51 (m, 6H, CH₂), -10.59 (dd, 1H, ²J(HH) = 4.7 Hz, ²J(HP_{trans}) = 155.2 Hz), -29.54 (dd, 1H, ²J(HH) = 4.7 Hz, ²J(HP_{cis}) = 10.8 Hz); ¹³C{¹H} NMR [CD₂Cl₂] δ 180.8 (C-O), 154.5 (C-Ir), 138.6 (C_{Ar}), 137.5 (C_{Ar}), 136.7 (C_{Ar}), 134.8 (C_{Ar}), 132.3 (C_{Ar}), 129.2 (CH_{Ar}), 129.0 (CH_{mesityl}), 128.4 (CH_{Ar}), 128.4 (CH_{mesityl}), 128.2 (CH_{Ar}), 127.7 (CH_{Ar}), 126.8 (CH_{Ar}), 126.7 (CH_{Ar}), 124.9 (C_{Ar}), 120.8 (CH_{imidazole}), 120.0 (CH_{Ar}), 119.8 (CH_{imidazole}), 56.1 (CH₂), 50.0 (CH₂), 39.4 (CH₂), 29.1 (CH₂), 21.0 (CH₃), 19.4 (CH₃), 18.9 (CH₃)

For this complex, the ¹³C{¹H} data were collected via indirect HMQC methods and as such the ³¹P-¹³C couplings were not observed. Multiple overlapping signals for the phenethylamine and PCy₃ ligands precluded their full characterisation. Since **26**_{PCy₃} is formed in low concentration and it converts into **27**_{PCy₃} over the course of hours, no ³¹P signal could be identified.

8.6.13. Iridium(III) (3-(2-methylene-4-nitrophenolate)-1-(2,4,6-trimethylphenyl)imidazolyldiene)(PR₃)(phenethylamine) (dihydride), 27



To a Young's NMR tube was added **1** (7 mg, 11 μ mol, 1 eq.), phenethylamine (1.4 μ L, 11 μ mol, 1 eq.), PR₃ (PCy₃, PⁱPr₃, PBz₃ or PPh₂Cy, 11 μ mol, 1 eq.) and CD₂Cl₂ (0.6 mL). The solution was then degassed three times on a high vacuum line using a freeze-thaw procedure with liquid N₂, before the addition of 3 bars of H₂. The mixture was then left to react at r.t. for 3 days.

For these species, the ¹³C{¹H} data were collected via indirect HMQC methods and as such the ³¹P-¹³C couplings were not observed. Furthermore, partial NMR data are given in some cases, where multiple overlapping signals for a mixture of complexes in solution precluded full spectroscopic data determination.

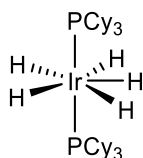
27_{PCy₃}: ¹H NMR [CD₂Cl₂, 400 MHz, 243 K] δ 8.12 (s br, 1H, CH_{Ar}), 7.92 (dd, 1H, ⁴J(HH) = 3.1 Hz, ³J(HH) = 9.3 Hz, CH_{Ar}), 7.36 (s, 1H, CH_{mesityl}), 7.29 (s br, 1H, CH_{imidazole}), 7.06-6.97 (m, 5H, 5 x CH_{Ar}), 7.05 (s, 1H, CH_{mesityl}), 6.89 (s br, 1H, CH_{imidazole}), 6.29 (d, 1H, ²J(HH) = 13.2 Hz, CH₂ linker), 6.24 (d, 1H, ³J(HH) = 9.3 Hz, CH_{Ar}), 4.38 (d, 1H, ²J(HH) = 13.2 Hz, CH₂ linker), 2.39 (s, 3H, CH₃), 2.34 (m, 2H, CH₂), 2.15 (s, 3H, CH₃), 2.12 (m, 12H, CH₂), 2.09 (m, 2H, CH₂), 2.00 (s, 3H, CH₃), 1.85 (m, 12H, CH₂), 1.61 (m, 6H, CH₂), 1.09 (m, 3H, CH), -23.51 (dd, 1H, ²J(HH) = 7.5 Hz, ²J(HP_{cis}) = 18.0 Hz), -30.66 (dd, 1H, ²J(HH) = 7.5 Hz, ²J(HP_{cis}) = 18.0 Hz); ¹³C{¹H} NMR [CD₂Cl₂] δ 178.7 (C-O), 174.9 (C-Ir), 138.9 (C_{Ar}), 137.7 (C_{Ar}), 136.8 (C_{Ar}), 134.3 (C_{Ar}), 131.1 (C_{Ar}), 129.4 (CH_{mesityl}), 129.4 (CH_{Ar}), 128.8 (CH_{Ar}), 128.3 (CH_{Ar}), 128.0 (CH_{mesityl}), 127.8 (CH_{Ar}), 126.7 (CH_{Ar}), 126.7 (CH_{Ar}), 124.8 (C_{Ar}), 121.7 (CH_{Ar}), 120.6 (CH_{imidazole}), 120.3 (CH_{imidazole}), 51.4 (CH₂), 34.5 (CH₂), 27.7 (CH₂), 21.0 (CH₃), 19.4 (CH₃), 18.7 (CH₂), 17.7 (CH₃); ³¹P{¹H} NMR [CD₂Cl₂, 263 K] 17.2 (s)

27PPr3: ^1H NMR [CD_2Cl_2 , 400 MHz, 243 K] δ 8.11 (d, 1H, $^4J(\text{HH}) = 3.1$ Hz, CH_{Ar}), 7.91 (dd, 1H, $^4J(\text{HH}) = 3.1$ Hz, $^3J(\text{HH}) = 9.3$ Hz, CH_{Ar}), 7.37-7.22 (m, 5H, 5 x CH_{Ar}), 7.04 (s br, 1H, $\text{CH}_{\text{imidazole}}$), 7.03 (s, 1H, $\text{CH}_{\text{mesityl}}$), 6.91 (s, 1H, $\text{CH}_{\text{mesityl}}$), 6.85 (s br, 1H, $\text{CH}_{\text{imidazole}}$), 6.48 (d, 1H, $^2J(\text{HH}) = 13.8$ Hz, CH_2 linker), 6.25 (d, 1H $^3J(\text{HH}) = 9.3$ Hz, CH_{Ar}), 4.36 (d, 1H, $^2J(\text{HH}) = 13.8$ Hz, CH_2 linker), 2.39 (s, 3H, CH_3), 2.17 (m, 2H, CH_2), 2.16 (s, 3H, CH_3), 2.15 (m, 3H, 3 x CH), 2.00 (s, 3H, CH_3), 1.50 (m, 2H, CH_2), 0.94 (dd, 18H, $^3J(\text{HH}) = 7.1$ Hz, $^2J(\text{HP}_{\text{cis}}) = 12.0$ Hz, 6 x CH_3), -23.25 (dd, 1H, $^2J(\text{HH}) = 8.1$ Hz, $^2J(\text{HP}_{\text{cis}}) = 19.0$ Hz), -30.78 (dd, 1H, $^2J(\text{HH}) = 8.1$ Hz, $^2J(\text{HP}_{\text{cis}}) = 17.5$ Hz); $^{31}\text{P}\{^1\text{H}\}$ NMR [CD_2Cl_2 , 243 K] 26.1 (s)

27PBz3: ^1H NMR [CD_2Cl_2 , 400 MHz, 243 K] δ 8.11 (d, 1H, $^4J(\text{HH}) = 2.8$ Hz, CH_{Ar}), 7.93 (dd, 1H, $^4J(\text{HH}) = 2.8$ Hz, $^3J = 9.2$ Hz, CH_{Ar}), 7.29 (m, 3H, 3 x CH_{Ar}), 7.24 (m, 6H, 6 x CH_{Ar}), 7.14 (m, 6H, 6 x CH_{Ar}), 7.10 (m, 1H, CH_{Ar}), 7.07 (m, 2H, 2 x CH_{Ar}), 7.01 (s, 1H, $\text{CH}_{\text{mesityl}}$), 6.90 (s, 1H, $\text{CH}_{\text{mesityl}}$), 6.75 (m, 2H, 2 x CH_{Ar}), 6.43 (d, 1H, $^3J(\text{HH}) = 9.2$ Hz, CH_{Ar}), 5.18 (d, 1H, $^2J(\text{HH}) = 13.5$ Hz, CH_2 linker), 3.94 (d, 1H, $^2J(\text{HH}) = 13.5$ Hz, CH_2 linker), 3.24 (dd, 3H, $^2J(\text{PH}) = 8.7$ Hz, $^2J(\text{HH}) = 13.0$ Hz, CH_2), 3.04 (m, 1H, CH_2), 2.92 (m, 1H, CH_2), 2.89 (dd, 3H, $^2J(\text{PH}) = 7.0$ Hz, $^2J(\text{HH}) = 13.0$ Hz, CH_2), 2.83 (m, 1H, CH_2), 2.73 (m, 1H, CH_2), 2.30 (s, 3H, CH_3), 2.01 (s, 3H, CH_3), 1.83 (s, 3H, CH_3), -22.64 (s br, 1H), -29.85 (s br, 1H); $^{13}\text{C}\{^1\text{H}\}$ NMR [CD_2Cl_2] δ 179.2 (C-O), 138.6 (C_{Ar}), 138.4 (C_{Ar}), 133.7 (C_{Ar}), 133.4 (C_{Ar}), 131.6 (C_{Ar}), 130.5 (CH_{Ar}), 130.4 (CH_{Ar}), 129.5 ($\text{CH}_{\text{mesityl}}$), 128.7 (CH_{Ar}), 128.3 ($\text{CH}_{\text{mesityl}}$), 128.3 (CH_{Ar}), 128.0 (CH_{Ar}), 127.8 (CH_{Ar}), 126.5 (CH_{Ar}), 125.9 (CH_{Ar}), 124.0 (C_{Ar}), 121.6 (CH_{Ar}), 120.9 (CH_{Ar}), 120.9 (C_{Ar}), 50.7 (CH_2), 43.9 (CH_2), 40.2 (CH_2), 35.7 (CH_2), 20.7 (CH_3), 18.6 (CH_3), 17.5 (CH_3); $^{31}\text{P}\{^1\text{H}\}$ NMR [CD_2Cl_2 , 298 K] 0.1 (s)

27PPh2Cy: ^1H NMR [CD_2Cl_2 , 400 MHz, 303 K] δ 8.15 (d, 1H, $^4J(\text{HH}) = 3.0$ Hz, CH_{Ar}), 7.90 (dd, 1H, $^4J(\text{HH}) = 3.0$ Hz, $^3J(\text{HH}) = 9.3$ Hz, CH_{Ar}), 7.90 (m, 1H, CH_{Ar}), 7.80 (m, 2H, CH_{Ar}), 7.20 (m, 2H, 2 x CH_{Ar}), 6.98 (s, 1H, $\text{CH}_{\text{mesityl}}$), 6.96 (m, 2H, 2 x CH_{Ar}), 6.86 (s, 1H, $\text{CH}_{\text{mesityl}}$), 6.31 (d, 1H, $^3J(\text{HH}) = 9.3$ Hz, CH_{Ar}), 6.05 (s br, 1H, CH_2 linker), 4.64 (s br, 1H, CH_2 linker), 2.11 (s, 3H, CH_3), 2.27 (s, 3H, CH_3), 1.86 (s, 3H, CH_3), -22.32 (s br, 1H), -30.68 (s br, 1H); $^{13}\text{C}\{^1\text{H}\}$ NMR [CD_2Cl_2] δ 178.8 (C-O), 138.3 (C_{Ar}), 137.3 (C_{Ar}), 136.8 (C_{Ar}), 133.8 (C_{Ar}), 132.4 (C_{Ar}), 129.1 ($\text{CH}_{\text{mesityl}}$), 128.1 ($\text{CH}_{\text{mesityl}}$), 127.4 (CH_{Ar}), 126.5 (CH_{Ar}), 124.8 (C_{Ar}), 121.3 (CH_{Ar}), 20.2 (CH_3), 18.7 (CH_3), 17.5 (CH_3); $^{31}\text{P}\{^1\text{H}\}$ NMR [CD_2Cl_2 , 298 K] 23.5 (s)

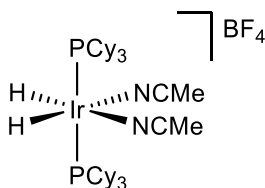
8.6.14. $[\text{Ir}(\text{H})_5(\text{PCy}_3)_2]$, **28**_{PCy₃}



To a Young's NMR tube was added **1** (7 mg, 11 μmol , 1 eq.), PCy₃ (6.2 mg, 22 μmol , 2 eq.) and CD₂Cl₂ (0.6 mL). The solution was then degassed three times on a high vacuum line using a freeze-thaw procedure with liquid N₂, before the addition of 3 bars of H₂. The mixture was then left to react at r.t. for 3 days; ¹H NMR [CD₂Cl₂, 400 MHz, 263 K] δ 2.00-1.00 (br m, 66H, PCy₃ ligands), -11.23 (t, 5H, ²J(HP_{cis}) = 12.1 Hz); ³¹P{¹H} NMR [CD₂Cl₂] 31.7 (s)

Due to the presence of the degraded carbene ligand and excess unreacted phosphine in solution, the NMR spectra did not show the clean formation of **28**_{PCy₃. Multiple overlapping signals in the alkyl region of the ¹H and ¹³C NMR spectra precluded full determination of the specific proton and carbon resonances assigned to the cyclohexyl groups.}

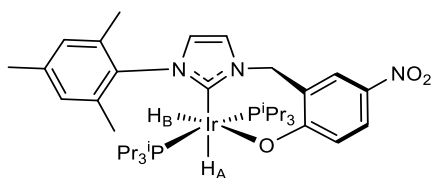
8.6.15. $[\text{Ir}(\text{H})_2(\text{MeCN})_2(\text{PCy}_3)_2][\text{BF}_4]$



To a CD_2Cl_2 solution of **28**_{PCy₃} (11 μmol , 1 eq.) in a Young's NMR tube was added tetrafluoroboric acid diethyl ether complex (1.8 μL , 11 μmol , 1 eq.) and acetonitrile (1 μL , 22 μmol , 2 eq.). The solution was then degassed three times on a high vacuum line using a freeze-thaw procedure with liquid N_2 , before the addition of 3 bars of H_2 ; ^1H NMR [CD_2Cl_2 , 400 MHz, 263 K] δ 2.42 (s, 6H, 2 x MeCN), 1.97-1.87 (m, 54H, PCy₃), 1.50-1.40 (m, 12H, PCy₃), -22.17 (t, 2H, $^2J(\text{HP}_{\text{cis}}) = 15.5$ Hz); $^{13}\text{C}\{^1\text{H}\}$ NMR [CD_2Cl_2] 120.2 (2 x CN), 34.5 (CH_{alkyl}), 29.5 (CH_{alkyl}), 27.6 (CH_{alkyl}), 26.6 (CH_{alkyl}), 3.7 (2 x CH_3); $^{31}\text{P}\{^1\text{H}\}$ NMR 22.6 (s)

For this complex, the $^{13}\text{C}\{^1\text{H}\}$ data were collected via indirect HMQC methods and as such the ^{31}P - ^{13}C couplings were not observed.

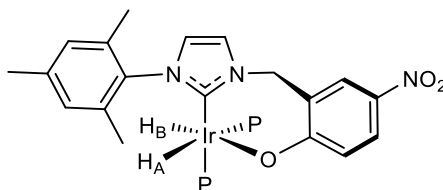
8.6.16. Iridium(III) (3-(2-methylene-4-nitrophenolate)-1-(2,4,6-trimethylphenyl)imidazolyldiene)(PⁱPr₃)₂(dihydride), 29



To a Young's NMR tube was added **1** (7 mg, 11 μmol , 1 eq.), phenethylamine (1.4 μL , 11 μmol , 1 eq.), PⁱPr₃ (4.2 μL , 22 μmol , 2 eq.) and CD₂Cl₂ (0.6 mL). The solution was then degassed three times on a high vacuum line using a freeze-thaw procedure with liquid N₂, before the addition of 3 bars of H₂. The mixture was then left to react at r.t. for 3 days; ¹H NMR [CD₂Cl₂, 400 MHz, 243 K] δ 8.15 (d, 1H, ⁴J(HH) = 3.2 Hz, CH_{Ar}), 7.89 (dd, 1H, ⁴J(HH) = 3.2 Hz, ³J(HH) = 9.5 Hz, CH_{Ar}), 7.28 (d, 1H, ³J(HH) = 1.9 Hz, CH_{imidazole}), 6.90 (s, 1H, CH_{mesityl}), 6.87 (s, 1H, CH_{mesityl}), 6.86 (d, 1H, ³J(HH) = 1.9 Hz, CH_{imidazole}), 6.24 (d, 1H, ³J(HH) = 9.5 Hz, CH_{Ar}), 5.96 (d, 1H, ²J(HH) = 13.3 Hz, CH₂ linker), 4.35 (d, 1H, ²J(HH) = 13.3 Hz, CH₂ linker), 2.27 (s, 3H, CH₃), 2.20 (s, 3H, CH₃), 2.17 (m, 3H, 3 x CH), 1.89 (s, 3H, CH₃), 1.51 (m, 3H, 3 x CH), 1.24 (m, 18H, 6 x CH₃), 1.16 (m, 18H, 6 x CH₃), -12.73 (ddd, 1H, ²J(HH) = 5.6 Hz, ²J(HP_{cis}) = 20.5 Hz, ²J(HP_{cis}) = 25.9 Hz), -31.40 (ddd, 1H, ²J(HH) = 5.6 Hz, ²J(HP_{cis}) = 15.1 Hz, ²J(HP_{cis}) = 15.1 Hz); ¹³C{¹H} NMR [CD₂Cl₂] δ 180.5 (C-O), 177.1 (C-Ir), 138.3 (C_{Ar}), 137.3 (C_{Ar}), 136.6 (C_{Ar}), 134.9 (C_{Ar}), 131.3 (C_{Ar}), 129.0 (CH_{mesityl}), 128.4 (CH_{mesityl}), 128.0 (CH_{Ar}), 126.8 (CH_{Ar}), 124.4 (C_{Ar}), 124.0 (CH_{imidazole}), 121.0 (CH_{imidazole}), 120.3 (CH_{Ar}), 51.4 (CH₂), 25.9 (3 x CH), 25.3 (3 x CH), 21.8 (CH₃), 20.6 (CH₃), 19.7 (6 x CH₃), 18.4 (CH₃), 16.2 (6 x CH₃); ³¹P NMR [CD₂Cl₂] 37.6 (ddd, ²J(PP_{trans}) = 329 Hz, ²J(PH_{cis}) = 18.0 Hz, ²J(PH_{cis}) = 11.5 Hz), 22.0 (ddd, ²J(PP_{trans}) = 329 Hz, ²J(PH_{cis}) = 23.1 Hz, ²J(PH_{cis}) = 12.3 Hz); MS [LIFDI] m/z 851.49 (M⁺)

For this complex, the ¹³C{¹H} data were collected via indirect HMQC methods and as such the ³¹P-¹³C couplings were not observed. Due to excess PⁱPr₃ in solution, as well as the presence of phenethylamine, multiple overlapping signals in the alkyl region of the ¹H NMR spectrum precluded determination of the ¹H-³¹P couplings.

8.6.17. Iridium(III) (3-(2-methylene-4-nitrophenolate)-1-(2,4,6-trimethylphenyl)imidazolylidene)(PR₃)₂(dihydride), 30



To a Young's NMR tube was added **1** (7 mg, 11 μ mol, 1 eq.), phenethylamine (1.4 μ L, 11 μ mol, 1 eq.), PR₃ (PBz₃ or PPh₂Cy, 22 μ mol, 2 eq.) and CD₂Cl₂ (0.6 mL). The solution was then degassed three times on a high vacuum line using a freeze-thaw procedure with liquid N₂, before the addition of 3 bars of H₂. The mixture was then left to react at r.t. for 3 days.

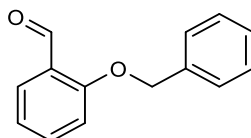
30PBz₃: ¹H NMR [CD₂Cl₂, 400 MHz, 263 K] δ 8.14 (d, 1H, ⁴*J*(HH) = 2.8 Hz, CH_{Ar}), 7.97 (dd, 1H, ⁴*J*(HH) = 2.8 Hz, ³*J*(HH) = 9.3 Hz, CH_{Ar}), 7.32 (s br, 1H, CH_{imidazole}), 7.32 (m, 3H, 3 x CH_{Ar}), 7.24 (s, 1H, CH_{mesityl}), 7.24 (m, 3H, 3 x CH_{Ar}), 7.19 (m, 6H, 6 x CH_{Ar}), 7.18 (m, 6H, 6 x CH_{Ar}), 6.91 (m, 6H, 6 x CH_{Ar}), 6.89 (s br, 1H, CH_{imidazole}), 6.78 (s, 1H, CH_{mesityl}), 6.78 (m, 6H, 6 x CH_{Ar}), 6.60 (d, 1H, ³*J*(HH) = 9.3 Hz, CH_{Ar}), 5.61 (d, 1H, ²*J*(HH) = 13.3 Hz, CH₂ linker), 4.26 (d, 1H, ²*J*(HH) = 13.3 Hz, CH₂ linker), 3.02 (dd, 3H, ²*J*(PH) = 6.8 Hz, ²*J*(HH) = 13.0 Hz, CH₂), 2.88 (dd, 3H, ²*J*(PH) = 8.5 Hz, ²*J*(HH) = 14.3 Hz, CH₂), 2.81 (dd, 3H, ²*J*(PH) = 6.6 Hz, ²*J*(HH) = 13.0 Hz, CH₂), 2.66 (d br, 3H, ²*J*(HH) = 14.3 Hz, CH₂), 2.28 (s, 3H, CH₃), 2.07 (s, 3H, CH₃), 1.73 (s, 3H, CH₃), -10.61 (ddd, 1H, ²*J*(HH) = 4.9 Hz, ²*J*(HP_{cis}) = 25.6 Hz, ²*J*(HP_{trans}) = 153.4 Hz), -28.63 (ddd, 1H, ²*J*(HH) = 4.9 Hz, ²*J*(HP_{cis}) = 13.6 Hz, ²*J*(HP_{cis}) = 13.6 Hz); ¹³C {¹H} NMR [CD₂Cl₂] δ 178.3 (C-O), 167.8 (C-Ir), 138.3 (C_{Ar}), 138.2 (C_{Ar}), 136.3 (C_{Ar}), 134.3 (C_{Ar}), 132.0 (C_{Ar}), 131.0 (CH_{Ar}), 130.4 (CH_{Ar}), 129.5 (CH_{Ar}), 129.0 (CH_{Ar}), 128.9 (CH_{mesityl}), 128.2 (CH_{mesityl}), 127.6 (CH_{Ar}), 126.9 (CH_{Ar}), 126.3 (C_{Ar}), 125.9 (CH_{Ar}), 124.2 (C_{Ar}), 122.0 (CH_{imidazole}), 122.0 (CH_{Ar}), 121.9 (CH_{Ar}), 120.9 (C_{Ar}), 120.9 (CH_{imidazole}), 50.8 (CH₂), 36.9 (CH₂), 32.6 (CH₂), 20.8 (CH₃), 19.4 (CH₃), 19.0 (CH₃); ³¹P NMR [CD₂Cl₂] δ 4.0 (ddd, ²*J*(PH_{cis}) = 13.6 Hz, ²*J*(PH_{cis}) = 13.6 Hz, ²*J*(PP_{cis}) = 15.1 Hz), -15.8 (ddd, ²*J*(PH_{cis}) = 25.6 Hz, ²*J*(PP_{cis}) = 15.1 Hz, ²*J*(PH_{trans}) = 153.4 Hz)

30PPh₂Cy: ¹H NMR [CD₂Cl₂, 400 MHz, 303 K] δ 8.09 (d, 1H, ⁴J(HH) = 2.8 Hz, CH_{Ar}), 7.68 (dd, 1H, ⁴J(HH) = 3.2 Hz, ³J(HH) = 9.3 Hz, CH_{Ar}), 7.49 (m, 4H, 4 x CH_{Ar}), 7.32 (m, 2H, 2 x CH_{Ar}), 7.32 (m, 2H, 2 x CH_{Ar}), 7.31 (m, 2H, 2 x CH_{Ar}), 7.28 (s br, 1H, CH_{imidazole}), 7.24 (m, 4H, 4 x CH_{Ar}), 7.15 (m, 2H, 2 x CH_{Ar}), 7.05 (m, 2H, 2 x CH_{Ar}), 6.98 (m, 2H, 2 x CH_{Ar}), 6.95 (s, 1H, CH_{mesityl}), 6.91 (s, 1H, CH_{mesityl}), 6.89 (s br, 1H, CH_{imidazole}), 5.86 (d, 1H, ²J(HH) = 13.5 Hz, CH₂ linker), 5.37 (d, 1H, ³J(HH) = 9.3 Hz, CH_{Ar}), 4.37 (d, 1H, ²J(HH) = 13.5 Hz, CH₂ linker), 2.39 (m, 2H, CH₂), 2.37 (s, 3H, CH₃), 2.27 (m, 2H, CH₂), 2.11 (m, 4H, CH₂), 2.03 (m, 4H, CH₂), 1.98 (s, 3H, CH₃), 1.86 (m, 4H, CH₂), 1.80 (m, 4H, CH₂), 1.32 (s, 3H, CH₃), -10.23 (ddd, 1H, ²J(HH) = 4.2 Hz, ²J(HP_{cis}) = 18.4 Hz, ²J(HP_{trans}) = 135.7 Hz), -29.20 (ddd, 1H, ²J(HH) = 4.2 Hz, ²J(HP_{cis}) = 12.9 Hz, ²J(HP_{cis}) = 12.9 Hz); ¹³C{¹H} NMR [CD₂Cl₂] δ 181.4 (C-O), 166.0 (C-Ir), 138.3 (C_{Ar}), 137.9 (C_{Ar}), 136.7 (C_{Ar}), 134.8 (CH_{Ar}), 134.7 (C_{Ar}), 133.9 (CH_{Ar}), 133.6 (CH_{Ar}), 133.4 (CH_{Ar}), 132.5 (C_{Ar}), 129.2 (CH_{mesityl}), 128.7 (CH_{Ar}), 128.3 (CH_{mesityl}), 128.1 (C_{Ar}), 127.4 (CH_{Ar}), 127.2 (C_{Ar}), 126.7 (CH_{Ar}), 126.2 (CH_{Ar}), 125.8 (C_{Ar}), 121.9 (CH_{imidazole}), 121.0 (CH_{imidazole}), 120.8 (CH_{Ar}), 50.6 (CH₂), 20.8 (CH₃), 19.4 (CH₃), 16.5 (CH₃); ³¹P{¹H} NMR [CD₂Cl₂] δ 19.6 (s br), 8.6 (s br)

For these species, the ¹³C{¹H} data were collected via indirect HMQC methods and as such the ³¹P-¹³C couplings were not observed. Furthermore, partial NMR data are given in some cases, where multiple overlapping signals for a mixture of complexes in solution precluded full spectroscopic data determination.

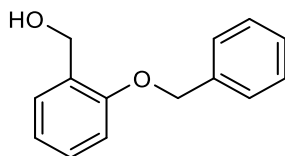
8.7. H carbene synthesis

8.7.1. 2-benzyloxybenzaldehyde



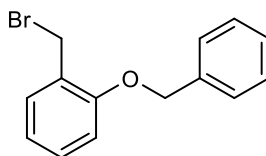
To a solution of 2-hydroxybenzaldehyde (4.36 mL, 41 mmol, 1 eq.) in dry acetone (50 mL) under nitrogen, was added K₂CO₃ (7.36 g, 53 mmol, 1.3 eq.) followed by benzyl bromide (6.32 mL, 53 mmol, 1.3 eq.) and the mixture was stirred at reflux for 2 h. The acetone was removed, water and ethyl acetate were added and the mixture was extracted with ethyl acetate, dried over MgSO₄, filtered and concentrated. The product was purified by column chromatography (silica, hexane: ethyl acetate, 9: 1) to afford a pale yellow oil (7.78 g, 90 %); ¹H NMR [CDCl₃, 500 MHz, 298 K] δ 10.60 (s, 1H, CHO), 7.89 (dd, 1H, ³J(HH) = 7.6 Hz, ⁴J(HH) = 1.7 Hz, CH_{Ar}), 7.56 (dt, 1H, ³J(HH) = 7.6 Hz, ⁴J(HH) = 1.7 Hz, CH_{Ar}), 7.49-7.36 (m, 5H, 5 x CH_{Ar}), 7.09 (s, 1H, CH_{Ar}), 7.08 (s, 1H, CH_{Ar}), 5.23 (s, 2H, CH₂); ¹³C{¹H} NMR [CDCl₃] 190.2 (C=O), 161.5 (C_{Ar}O), 136.5 (C_{Ar}), 136.3 (CH_{Ar}), 129.2 (2 x CH_{Ar}), 128.9 (CH_{Ar}), 128.7 (CH_{Ar}), 127.7 (2 x CH_{Ar}), 125.7 (C_{Ar}), 121.5 (CH_{Ar}), 113.5 (CH_{Ar}), 70.9 (CH₂); MS [ESI] m/z 235.07 (M+Na)⁺

8.7.2. 2-benzyloxybenzyl alcohol¹⁴⁸



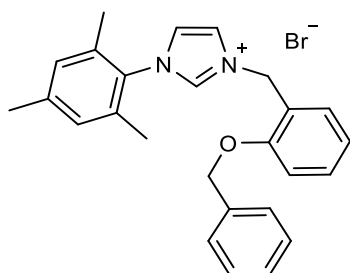
To a solution of 2-benzyloxybenzaldehyde (2 g, 9.42 mmol, 1 eq.) in MeOH (30 mL) at 0 °C was added NaBH₄ (713 mg, 18.8 mmol, 2 eq.) portionwise over 10 min. After the evolution of gas was complete, the mixture was warmed to room temperature and stirred for 30 min. The solvent was removed and water and ethyl acetate were added. The mixture was extracted with ethyl acetate, dried over MgSO₄, filtered and concentrated to afford a pale yellow oil (2.00 g, 99 %); ¹H NMR [CDCl₃, 500 MHz, 298 K] δ 7.48-7.39 (m, 4H, 4 x CH_{Ar}), 7.39-7.30 (m, 2H, 2 x CH_{Ar}), 7.30-7.26 (m, 1H, CH_{Ar}), 7.02-6.95 (m, 2H, 2 x CH_{Ar}), 5.15 (s, 2H, CH₂), 4.77 (d, 2H, ³J(HH) = 6.4 Hz, CH₂OH), 2.30 (t, 1H, ³J(HH) = 6.4 Hz, OH); ¹³C{¹H} NMR [CDCl₃] 157.1 (C_{Ar}O), 137.2 (C_{Ar}), 129.9 (C_{Ar}), 129.4 (CH_{Ar}), 129.3 (CH_{Ar}), 129.2 (2 x CH_{Ar}), 128.6 (CH_{Ar}), 127.8 (2 x CH_{Ar}), 121.5 (CH_{Ar}), 112.1 (CH_{Ar}), 70.5 (CH₂O), 62.7 (CH₂OH); MS [ESI] m/z 237.09 (M+Na)⁺

8.7.3. 2-benzyloxybenzyl bromide



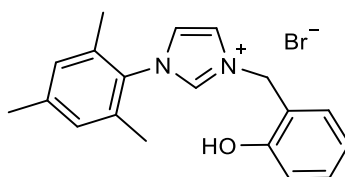
To a solution of 2-benzyloxy benzyl alcohol (1.4 g, 6.53 mmol, 1 eq.) in DCM (20 mL) under N₂ at ~ 5 °C was added PBr₃ (1.24 mL, 13.1 mmol, 2 eq.) and the mixture was stirred at room temperature for 2 h. Cold water was added whilst stirring before the mixture was extracted with ethyl acetate. The organic layers were washed with water, then brine then dried over MgSO₄, filtered and concentrated to afford the product (1.3 g, 72 %); ¹H NMR [CDCl₃, 400 MHz, 298 K] δ 7.53 (ps d, 2H, ³J(HH) = 7.3 Hz, 2 x CH_{Ar}), 7.43 (ps t, 2H, ³J(HH) = 7.3 Hz, 2 x CH_{Ar}), 7.40-7.35 (m, 2H, 2 x CH_{Ar}), 7.32-7.27 (m, 1H, CH_{Ar}), 6.99-6.94 (m, 2H, 2 x CH_{Ar}), 5.19 (s, 2H, CH₂), 4.65 (s, 2H, CH₂Br); ¹³C{¹H} NMR [CDCl₃] 156.6 (C_{Ar}O), 136.9 (C_{Ar}), 131.0 (CH_{Ar}), 130.2 (CH_{Ar}), 128.6 (2 x CH_{Ar}), 128.0 (CH_{Ar}), 127.2 (2 x CH_{Ar}), 126.5 (C_{Ar}), 121.0 (CH_{Ar}), 112.4 (CH_{Ar}), 70.1 (CH₂O), 29.2 (CH₂Br)

8.7.4. 3-(2-benzyloxy benzyl)-1-(2,4,6-trimethylphenyl) imidazolium bromide



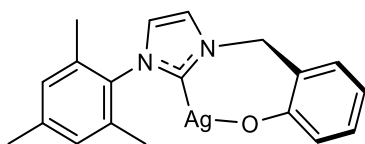
2-benzyloxy benzyl bromide (1.3 g, 4.69 mmol, 1 eq.) and 1-(2,4,6-trimethylphenyl)-1H-imidazole (0.87 g, 4.69 mmol, 1 eq.) were dissolved in toluene (20 mL) and heated at reflux for 2 h. The solution was cooled to room temperature and the resulting precipitate was filtered, washed with diethyl ether and air dried to afford a cream solid (1.5 g, 70 %); $^1\text{H NMR}$ [DMSO, 400 MHz, 298 K] δ 9.37 (t, 1H, $^4J(\text{HH}) = 1.7$ Hz, $\text{CH}_{\text{imidazole}}$), 7.92 (t, 1H, $^4J(\text{HH}) = 1.7$ Hz, $\text{CH}_{\text{imidazole}}$), 7.89 (t, 1H, $^4J(\text{HH}) = 1.7$ Hz, $\text{CH}_{\text{imidazole}}$), 7.44-7.39 (m, 3H, 3 x CH_{Ar}), 7.39-7.36 (m, 1H, CH_{Ar}), 7.36-7.32 (m, 2H, 2 x CH_{Ar}), 7.32-7.30 (m, 1H, CH_{Ar}), 7.17 (d, 1H, $^3J(\text{HH}) = 8.2$ Hz, CH_{Ar}), 7.05 (t, 1H, $^3J(\text{HH}) = 7.4$ Hz, CH_{Ar}), 5.52 (s, 2H, CH_2), 5.20 (s, 2H, CH_2), 2.32 (s, 3H, CH_3), 1.92 (s, 6H, 2 x CH_3); $^{13}\text{C}\{^1\text{H}\}$ NMR [DMSO] 156.7 (C_{ArO}), 140.8 (C_{Ar}), 138.1 (C_{Ar}), 137.1 ($\text{CH}_{\text{imidazole}}$), 134.7 (2 x C_{Ar}), 131.5 (C_{Ar}), 131.4 (CH_{Ar}), 130.9 (CH_{Ar}), 129.7 (2 x $\text{CH}_{\text{mesityl}}$), 128.9 (2 x CH_{Ar}), 128.4 (CH_{Ar}), 127.7 (2 x CH_{Ar}), 124.5 ($\text{CH}_{\text{imidazole}}$), 123.7 ($\text{CH}_{\text{imidazole}}$), 122.6 (C_{Ar}), 121.5 (CH_{Ar}), 113.1 (CH_{Ar}), 69.8 (CH_2O), 49.3 (CH_2), 21.1 (CH_3), 17.2 (2 x CH_3); MS [ESI] m/z 383.2 ($\text{M}-\text{Br}$) $^+$

8.7.5. 3-(2-hydroxy benzyl)-1-(2,4,6-trimethylphenyl) imidazolium bromide



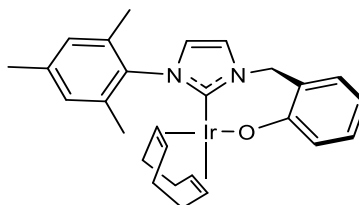
To a Parr reactor was added 3-(2-benzyloxy benzyl)-1-(2,4,6-trimethylphenyl) imidazolium bromide (800 mg, 1.73 mmol, 1 eq.), palladium hydroxide on carbon (80 mg, 10 % by weight) and methanol (15 mL) and the mixture was stirred at 35 °C under 5 bars of H₂ for 20 h. Starting material was still present by LCMS so the solution was stirred again under 5 bars of H₂ at 45 °C for 6 h. Upon completion of the reaction by LCMS, the mixture was filtered through Celite, washed with DCM and concentrated to afford a yellow solid (644 mg, 100 %); ¹H NMR [DMSO, 400 MHz, 298 K] δ 9.48 (s, 1H, CH_{imidazole}), 7.91 (s, 1H, CH_{imidazole}), 7.87 (s, 1H, CH_{imidazole}), 7.35 (dd, 1H, ⁴J(HH) = 1.2 Hz, ³J(HH) = 7.6 Hz, CH_{Ar}), 7.25 (dt, 1H, ⁴J(HH) = 1.2 Hz, ³J(HH) = 7.6 Hz, CH_{Ar}), 7.14 (s, 2H, CH_{mesityl}), 6.93-6.85 (m, 2H, 2 x CH_{Ar}), 5.42 (s, 2H, CH₂), 2.33 (s, 3H, CH₃), 2.00 (s, 6H, 2 x CH₃); ¹³C{¹H} NMR [DMSO] 156.5 (C_{Ar}O), 140.7 (C_{Ar}), 138.4 (C_{Ar}), 138.2 (CH_{imidazole}), 134.8 (2 x C_{Ar}), 131.0 (CH_{Ar}), 130.8 (CH_{Ar}), 129.6 (2 x CH_{mesityl}), 124.3 (CH_{imidazole}), 123.5 (CH_{imidazole}), 120.9 (C_{Ar}), 119.6 (CH_{Ar}), 115.9 (CH_{Ar}), 49.4 (CH₂), 21.0 (CH₃), 17.3 (2 x CH₃); MS [ESI] m/z 293.1 (M-Br)⁺

8.7.6. Silver(I) 3-(2-methylenephenoate)-1-(2,4,6-trimethylphenyl)imidazolylidene



To a flask containing 3-(2-hydroxy benzyl)-1-(2,4,6-trimethylphenyl) imidazolium bromide (177 mg, 0.474 mmol, 1 eq.), silver(I) oxide (61 mg, 0.261 mmol, 0.55 eq.) and molecular sieves 4 Å (400 mg), under a nitrogen atmosphere in the dark, was added DCM (10 mL) and the solution was stirred at room temperature for 16 h. The mixture was filtered through Celite, washed with DCM and the solvent was removed under reduced pressure to afford a pale pink oil (120 mg, 63 %); ^1H NMR [CDCl_3 , 500 MHz, 298 K] all signals broad, δ 7.16 (s, 1H, CH_{Ar}), 7.10 (s, 1H, CH_{Ar}), 7.03 (s, 1H, CH_{Ar}), 7.00 (s, 1H, CH_{Ar}), 6.82 (s, 2H, 2 x CH_{Ar}), 6.75 (s, 1H, CH_{Ar}), 6.56 (s, 1H, CH_{Ar}), 5.41 (s, 2H, CH_2), 2.38 (s, 3H, CH_3), 1.68 (s, 6H, 2 x CH_3); Partial $^{13}\text{C}\{^1\text{H}\}$ NMR [CDCl_3] δ 130.0 (CH_{Ar}), 128.9 (2 x CH_{Ar}), 121.4 (CH_{Ar}), 121.3 (CH_{Ar}), 121.2 (CH_{Ar}), 119.6 (CH_{Ar}), 114.9 (CH_{Ar}), 52.0 (CH_2), 21.1 (CH_3), 17.5 (2 x CH_3); MS [ESI] m/z 693 (Ag dimer, protonated phenol groups)

8.7.7. Iridium(I) (3-(2-methylenephenoate)-1-(2,4,6-trimethylphenyl)imidazolylidene) (cyclooctadiene), 2



To a Schlenk flask was added $[\text{Ir}(\text{COD})\text{Cl}]_2$ (67 mg, 0.10 mmol, 0.5 eq.) and $\text{Ag}(\text{H-NHC-O})$ (80 mg, 0.20 mmol, 1 eq.) and once under an atmosphere of N_2 , dry DCM (5 mL) and dry THF (1 mL) were added. The reaction was stirred in the dark at r.t. for 4 h. The mixture was filtered over Celite, washed with DCM and the solvent was removed under reduced pressure. The product was washed through a silica plug with DCM: acetone 9: 1 and the solvent was removed under reduced pressure (repeated three times) to afford an orange solid (50 mg, 42 %). The product was stored in a glovebox. ^1H NMR $[\text{CD}_2\text{Cl}_2, 500 \text{ MHz}, 294 \text{ K}]$ δ 7.34 (dd, 1H, $^3J(\text{HH}) = 7.5 \text{ Hz}$, $^4J(\text{HH}) = 1.6 \text{ Hz}$, CH_{Ar}), 7.30 (ddd, 1H, $^3J(\text{HH}) = 7.7 \text{ Hz}$, $^3J(\text{HH}) = 7.6 \text{ Hz}$, $^4J(\text{HH}) = 1.6 \text{ Hz}$, CH_{Ar}), 7.04 (s, 1H, $\text{CH}_{\text{mesityl}}$), 6.96 (ddd, 1H, $^3J(\text{HH}) = 7.5 \text{ Hz}$, $^3J(\text{HH}) = 7.6 \text{ Hz}$, $^4J(\text{HH}) = 1.2 \text{ Hz}$, CH_{Ar}), 6.94 (s, 1H, $\text{CH}_{\text{mesityl}}$), 6.93 (dd, 1H, $^3J(\text{HH}) = 7.7 \text{ Hz}$, $^4J(\text{HH}) = 1.2 \text{ Hz}$, CH_{Ar}), 6.84 (d, 1H, $^3J(\text{HH}) = 2.0 \text{ Hz}$, $\text{CH}_{\text{imidazole}}$), 6.76 (d, 1H, $^3J(\text{HH}) = 2.0 \text{ Hz}$, $\text{CH}_{\text{imidazole}}$), 6.55 (d, 1H, $^2J(\text{HH}) = 14.9 \text{ Hz}$, CH_2), 5.15 (d, 1H, $^2J(\text{HH}) = 14.9 \text{ Hz}$, CH_2), 4.39 (m, 2H, 2 x CH_{COD}), 3.22 (m, 1H, CH_{COD}), 2.78 (m, 1H, CH_{COD}), 2.36 (s, 3H, CH_3), 2.27 (s, 3H, CH_3), 2.17 (m, 1H, $\text{CH}_2(\text{COD})$), 2.06 (m, 1H, $\text{CH}_2(\text{COD})$), 1.94 (s, 3H, CH_3), 1.81 (m, 1H, $\text{CH}_2(\text{COD})$), 1.59 (m, 2H, $\text{CH}_2(\text{COD})$), 1.48 (m, 1H, $\text{CH}_2(\text{COD})$), 1.39 (m, 1H, $\text{CH}_2(\text{COD})$), 1.19 (m, 1H), 1.48 (m, 1H, $\text{CH}_2(\text{COD})$); $^{13}\text{C}\{^1\text{H}\}$ NMR $[\text{CD}_2\text{Cl}_2]$ δ 179.4 (C-Ir), 155.8 (C-O), 138.6 (C_{Ar}), 136.5 (C_{Ar}), 135.6 (C_{Ar}), 134.3 (C_{Ar}), 131.5 (CH_{Ar}), 130.3 (CH_{Ar}), 129.2 ($\text{CH}_{\text{mesityl}}$), 128.1 ($\text{CH}_{\text{mesityl}}$), 123.2 ($\text{CH}_{\text{imidazole}}$), 121.1 (C_{Ar}), 120.1 (CH_{Ar}), 119.7 ($\text{CH}_{\text{imidazole}}$), 117.6 (CH_{Ar}), 83.6 (CH_{COD}), 83.4 (CH_{COD}), 53.1 (CH_{COD}), 51.6 (CH_{COD}), 51.3 (CH_2), 34.8 ($\text{CH}_2(\text{COD})$), 29.8 ($\text{CH}_2(\text{COD})$), 28.6 ($\text{CH}_2(\text{COD})$), 28.4 ($\text{CH}_2(\text{COD})$), 20.6 (CH_3), 19.1 (CH_3), 17.5 (CH_3); MS [ESI] m/z 591.2 ($\text{M}+\text{H}^+$)

^1H NMR [CD_3OD , 500 MHz, 243 K] δ 7.38 (d, 1H, $^3J(\text{HH}) = 2.0$ Hz, $\text{CH}_{\text{imidazole}}$), 7.37 (dd, 1H, $^3J(\text{HH}) = 8.0$ Hz, $^4J(\text{HH}) = 1.4$ Hz, CH_{Ar}), 7.30 (ddd, 1H, $^3J(\text{HH}) = 8.0$ Hz, $^3J(\text{HH}) = 8.0$ Hz, $^4J(\text{HH}) = 1.7$ Hz, CH_{Ar}), 7.13 (s, 1H, $\text{CH}_{\text{mesityl}}$), 7.08 (d, 1H, $^3J(\text{HH}) = 2.0$ Hz, $\text{CH}_{\text{imidazole}}$), 7.06 (s, 1H, $\text{CH}_{\text{mesityl}}$), 6.92 (d br, $^3J(\text{HH}) = 8.0$ Hz, 1H, CH_{Ar}), 6.91 (d br, $^3J(\text{HH}) = 8.0$ Hz, 1H, CH_{Ar}), 6.26 (d, 1H, $^2J(\text{HH}) = 15.0$ Hz, CH_2), 5.30 (d, 1H, $^2J(\text{HH}) = 15.0$ Hz, CH_2), 4.39 (m, 1H, CH_{COD}), 4.28 (m, 1H, CH_{COD}), 3.20 (m, 1H, CH_{COD}), 2.86 (m, 1H, CH_{COD}), 2.43 (s, 3H, CH_3), 2.35 (s, 3H, CH_3), 2.11 (m, 1H, $\text{CH}_2(\text{COD})$), 2.03 (m, 1H, $\text{CH}_2(\text{COD})$), 1.98 (s, 3H, CH_3), 1.78 (m, 1H, $\text{CH}_2(\text{COD})$), 1.55 (m, 2H, 2 x $\text{CH}_2(\text{COD})$), 1.46 (m, 1H, $\text{CH}_2(\text{COD})$), 1.37 (m, 1H, $\text{CH}_2(\text{COD})$), 1.24 (m, 1H, $\text{CH}_2(\text{COD})$); $^{13}\text{C}\{^1\text{H}\}$ NMR [CD_3OD] δ 178.4 (C-Ir), 155.6 (C-O), 138.6 (C_{Ar}), 136.1 (C_{Ar}), 129.9 (CH_{Ar}), 129.8 (C_{Ar}), 129.1 (CH_{Ar}), 128.9 (C_{Ar}), 128.0 (C_{Ar}), 127.9 ($\text{CH}_{\text{mesityl}}$), 128.9 ($\text{CH}_{\text{mesityl}}$), 123.1 ($\text{CH}_{\text{imidazole}}$), 119.0 (CH_{Ar}), 121.6 ($\text{CH}_{\text{imidazole}}$), 114.6 (CH_{Ar}), 81.9 (CH_{COD}), 81.3 (CH_{COD}), 52.6 (CH_{COD}), 51.3 (CH_{COD}), 49.7 (CH_2), 33.8 ($\text{CH}_2(\text{COD})$), 32.3 ($\text{CH}_2(\text{COD})$), 28.9 ($\text{CH}_2(\text{COD})$), 28.4 ($\text{CH}_2(\text{COD})$), 19.9 (CH_3), 18.6 (CH_3), 16.9 (CH_3)

UV-vis absorption data for complex **2** at six different concentrations are given in Table 56 with the corresponding absorption spectra shown in Figure 248.

Table 56: Concentration and absorbance values for six samples of 2 in DCM at different concentrations

Sample	Concentration / $\mu\text{mol dm}^{-3}$	Absorbance		
		At 373 nm	At 425 nm	At 490 nm
A	676	0.70	0.91	0.18
B	338	0.35	0.45	0.09
C	270	0.29	0.37	0.08
D	216	0.24	0.30	0.07
E	173	0.19	0.24	0.05
F	138	0.15	0.20	0.04

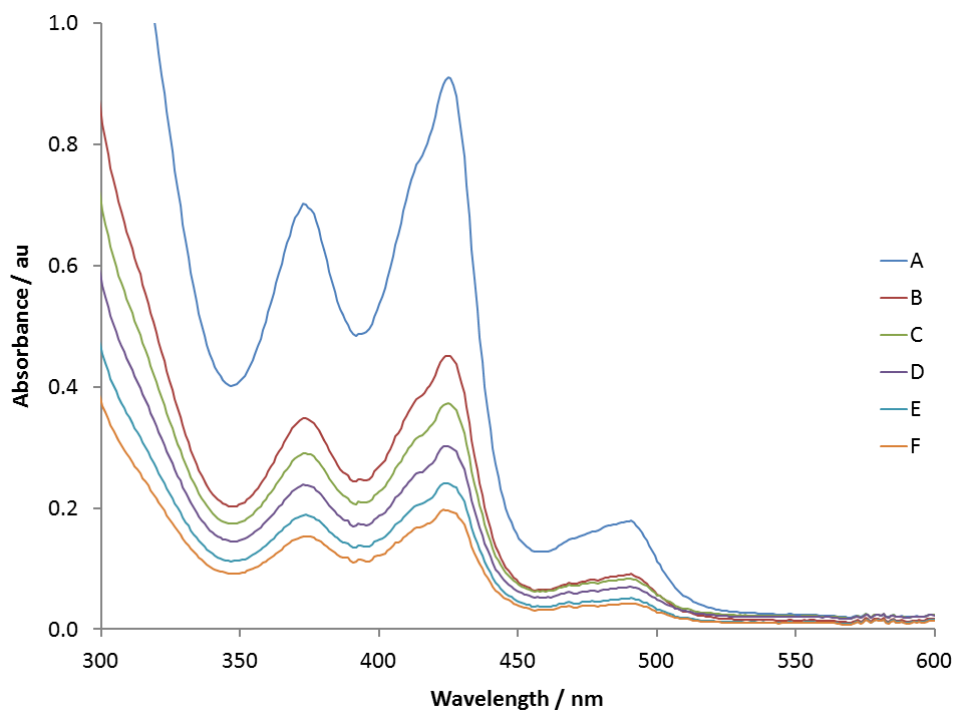


Figure 248: Visible region of the absorption spectra for **2** in DCM at different concentrations as listed in Table 56

The calibration graph in Figure 249 was used to gain the molar absorption coefficients for the absorption bands of **2** as described in Section 2.6.1.

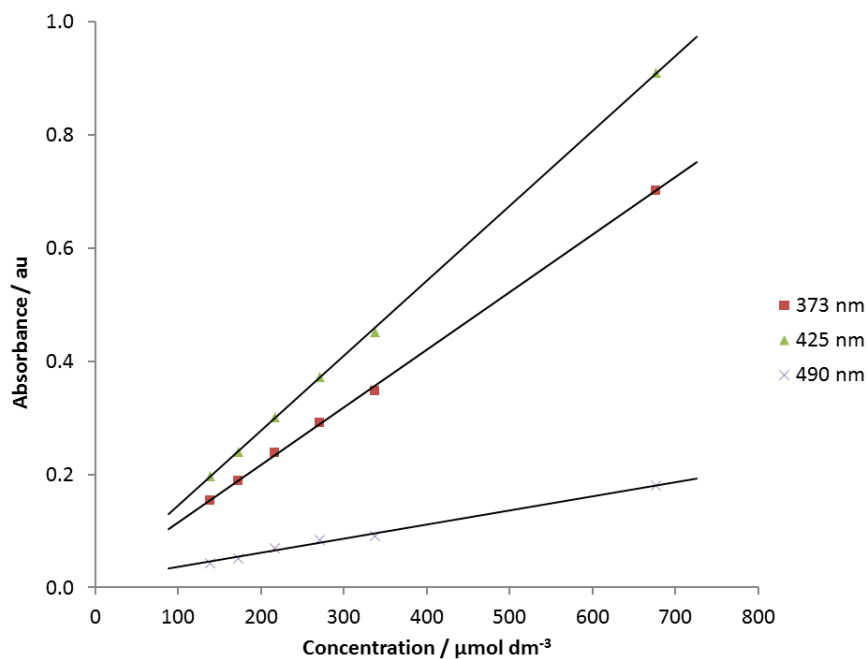
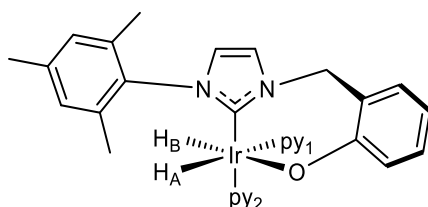


Figure 249: Calibration graph used to calculate the molar absorption coefficients for the three absorption bands of **2** in DCM at 373, 425 and 490 nm using the data in Table 56

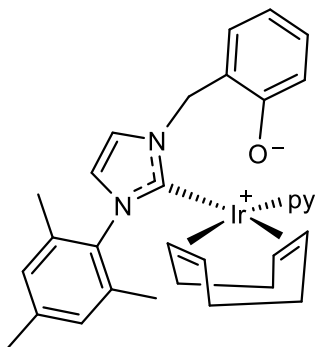
8.7.8. Iridium(III) (3-(2-methylenephenolate)-1-(2,4,6-trimethylphenyl)imidazolylidene) (dihydride)(pyridine)₂, 8



To a Young's NMR tube was added **2** (10 mg, 17 μmol , 1 eq.), pyridine (3.8 μL , 47 μmol , 2.8 eq.) and CD_2Cl_2 or C_6D_6 (0.6 mL). The solution was then degassed three times on a high vacuum line using a freeze-thaw procedure with liquid N_2 , before the addition of 3 bars of H_2 . The mixture was then left to react at r.t. for 1 day; ^1H NMR [CD_2Cl_2 , 400 MHz, 298 K] δ 8.81 (m, 2H, 2 x $\text{CH}_{\text{py ortho}}$), 8.75 (m, 2H, 2 x $\text{CH}_{\text{py ortho}}$), 7.65 (m, 1H, $\text{CH}_{\text{py para}}$), 7.58 (m, 1H, $\text{CH}_{\text{py para}}$), 7.24 (ddd, 1H, $^3J(\text{HH}) = 7.8$ Hz, $^3J(\text{HH}) = 7.8$ Hz, $^4J(\text{HH}) = 1.8$ Hz, CH_{Ar}), 7.18 (dd, 1H, $^3J(\text{HH}) = 7.8$ Hz, $^4J(\text{HH}) = 1.8$ Hz, CH_{Ar}), 7.02 (m, 2H, 2 x $\text{CH}_{\text{py meta}}$), 6.99 (m, 2H, 2 x $\text{CH}_{\text{py meta}}$), 6.93 (s, 1H, $\text{CH}_{\text{mesityl}}$), 6.89 (dd br, 1H, $^3J(\text{HH}) = 7.8$ Hz, $^3J(\text{HH}) = 7.8$ Hz, CH_{Ar}), 6.87 (dd, 1H, $^3J(\text{HH}) = 7.8$ Hz, $^4J(\text{HH}) = 1.2$ Hz, CH_{Ar}), 6.62 (d, 1H, $^3J(\text{HH}) = 2.2$ Hz, $\text{CH}_{\text{imidazole}}$), 6.58 (d, 1H, $^3J(\text{HH}) = 2.2$ Hz, $\text{CH}_{\text{imidazole}}$), 6.49 (s, 1H, $\text{CH}_{\text{mesityl}}$), 5.76 (d, 1H, $^2J(\text{HH}) = 14.5$ Hz, CH_2 linker), 5.29 (d, 1H, $^2J(\text{HH}) = 14.5$ Hz, CH_2 linker), 2.23 (s, 3H, CH_3), 2.17 (s, 3H, CH_3), 1.80 (s, 3H, CH_3), -22.55 (d, 1H, $^2J(\text{HH}) = 8.2$ Hz), -25.49 (d, 1H, $^2J(\text{HH}) = 8.2$ Hz); $^{13}\text{C}\{^1\text{H}\}$ NMR [CD_2Cl_2] δ 156.5 (C-O), 155.7 (2 x $\text{CH}_{\text{py ortho}}$), 138.1 (C_{Ar}), 137.6 (C_{Ar}), 135.9 (C_{Ar}), 135.0 ($\text{CH}_{\text{py para}}$), 135.0 (C_{Ar}), 131.4 (CH_{Ar}), 129.7 (CH_{Ar}), 128.6 ($\text{CH}_{\text{mesityl}}$), 128.0 ($\text{CH}_{\text{mesityl}}$), 124.5 (2 x $\text{CH}_{\text{py meta}}$), 124.3 (2 x $\text{CH}_{\text{py meta}}$), 123.3 (C_{Ar}), 120.8 ($\text{CH}_{\text{imidazole}}$), 119.4 (CH_{Ar}), 119.1 ($\text{CH}_{\text{imidazole}}$), 118.0 (CH_{Ar}), 52.5 (CH_2), 20.6 (CH_3), 18.2 (CH_3), 17.8 (CH_3)

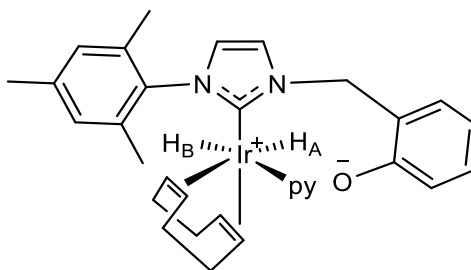
^1H NMR [C_6D_6 , 400 MHz, 298 K] δ 9.04 (m, 2H, 2 x $\text{CH}_{\text{py ortho}}$), 9.04 (m, 2H, 2 x $\text{CH}_{\text{py ortho}}$), 7.21 (dd, 1H, $^3J(\text{HH}) = 7.2$ Hz, $^4J(\text{HH}) = 1.1$ Hz, CH_{Ar}), 7.12 (dt, 1H, $^3J(\text{HH}) = 7.2$ Hz, $^4J(\text{HH}) = 1.6$ Hz, CH_{Ar}), 6.90 (dd, 1H, $^3J(\text{HH}) = 7.2$ Hz, $^4J(\text{HH}) = 1.6$ Hz, CH_{Ar}), 6.75 (dt, 1H, $^3J(\text{HH}) = 7.2$ Hz, $^4J(\text{HH}) = 1.1$ Hz, CH_{Ar}), 6.73 (s, 1H, $\text{CH}_{\text{mesityl}}$), 6.68 (m, 1H, $\text{CH}_{\text{py para}}$), 6.57 (m, 1H, $\text{CH}_{\text{py para}}$), 6.48 (d, 1H, $^3J(\text{HH}) = 2.2$ Hz, $\text{CH}_{\text{imidazole}}$), 6.33 (d, 1H, $^2J(\text{HH}) = 14.6$ Hz, CH_2 linker), 6.26 (m, 2H, 2 x $\text{CH}_{\text{py meta}}$), 6.18 (s, 1H, $\text{CH}_{\text{mesityl}}$), 6.14 (m, 2H, 2 x $\text{CH}_{\text{py meta}}$), 6.01 (d, 1H, $^3J(\text{HH}) = 2.2$ Hz, $\text{CH}_{\text{imidazole}}$), 5.70 (d, 1H, $^2J(\text{HH}) = 14.6$ Hz, CH_2 linker), 2.44 (s, 3H, CH_3), 1.98 (s, 3H, CH_3), 1.78 (s, 3H, CH_3), -21.91 (d, 1H, $^2J(\text{HH}) = 7.7$ Hz), -24.50 (d, 1H, $^2J(\text{HH}) = 7.7$ Hz); $^{13}\text{C}\{^1\text{H}\}$ NMR [C_6D_6] δ 157.7 (C-O), 155.9 (2 x $\text{CH}_{\text{py ortho}}$), 155.3 (C-Ir), 154.5 (2 x $\text{CH}_{\text{py ortho}}$), 138.5 (C_{Ar}), 136.9 (C_{Ar}), 136.2 (C_{Ar}), 135.4 (C_{Ar}), 133.9 ($\text{CH}_{\text{py para}}$), 131.3 (CH_{Ar}), 129.7 (CH_{Ar}), 128.6 ($\text{CH}_{\text{mesityl}}$), 127.9 ($\text{CH}_{\text{mesityl}}$), 123.7 (C_{Ar}), 123.6 (2 x $\text{CH}_{\text{py meta}}$), 123.6 (2 x $\text{CH}_{\text{py meta}}$), 119.9 ($\text{CH}_{\text{imidazole}}$), 119.3 ($\text{CH}_{\text{imidazole}}$), 119.1 (CH_{Ar}), 118.9 (CH_{Ar}), 53.4 (CH_2), 20.4 (CH_3), 18.6 (CH_3), 18.0 (CH_3)

8.7.9. Iridium(I) (3-(2-methylenephenoxy)-(2,4,6-trimethylphenyl)imidazolylidene) (cyclooctadiene)(pyridine), 13



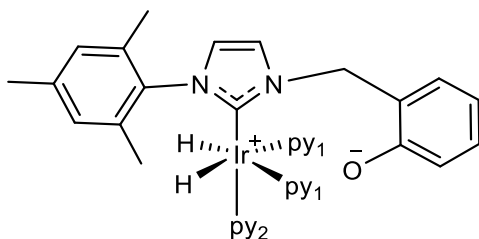
To a Young's NMR tube was added **2** (10 mg, 17 μmol , 1 eq.), pyridine (3.8 μL , 47 μmol , 2.8 eq.) and CD_3OD (0.6 mL). The solution was then degassed three times on a high vacuum line using a freeze-thaw procedure with a dry ice/acetone bath; ^1H NMR [CD_3OD , 400 MHz, 243 K] δ 7.97 (m, 2H, 2 x $\text{CH}_{\text{py ortho}}$), 7.83 (m, 1H, $\text{CH}_{\text{py para}}$), 7.34 (m, 2H, 2 x $\text{CH}_{\text{py meta}}$), 7.32 (s br, 1H, $\text{CH}_{\text{imidazole}}$), 7.31 (dd br, $^3J(\text{HH}) = 7.0$ Hz, $^3J(\text{HH}) = 7.0$ Hz, 1H, CH_{Ar}), 7.16 (d br, $^3J(\text{HH}) = 7.0$ Hz, 1H, CH_{Ar}), 7.22 (s br, 1H, $\text{CH}_{\text{mesityl}}$), 7.12 (s br, 1H, $\text{CH}_{\text{imidazole}}$), 6.83 (s br, 1H, $\text{CH}_{\text{mesityl}}$), 6.93 (d br, $^3J(\text{HH}) = 7.0$ Hz, 1H, CH_{Ar}), 6.89 (dd br, $^3J(\text{HH}) = 7.0$ Hz, $^3J(\text{HH}) = 7.0$ Hz, 1H, CH_{Ar}), 6.40 (d, 1H, $^2J(\text{HH}) = 14.6$ Hz, CH_2), 5.64 (d, 1H, $^2J(\text{HH}) = 14.6$ Hz, CH_2), 4.02 (m, 1H, CH_{COD}), 3.86 (m, 1H, CH_{COD}), 3.78 (m, 1H, CH_{COD}), 3.27 (m, 1H, CH_{COD}), 2.48 (m, 1H, $\text{CH}_2(\text{COD})$), 2.41 (s, 3H, CH_3), 2.31 (s, 3H, CH_3), 2.36 (m, 1H, $\text{CH}_2(\text{COD})$), 2.20 (m, 1H, $\text{CH}_2(\text{COD})$), 2.09 (m, 1H, $\text{CH}_2(\text{COD})$), 1.98 (m, 2H, 2 x $\text{CH}_2(\text{COD})$), 1.67 (m, 1H, $\text{CH}_2(\text{COD})$), 1.57 (m, 1H, $\text{CH}_2(\text{COD})$), 0.88 (s, 3H, CH_3); $^{13}\text{C}\{^1\text{H}\}$ NMR [CD_3OD] δ 177.0 (C-Ir), 155.8 (C-O), 151.1 (2 x $\text{CH}_{\text{py ortho}}$), 139.4 (C_{Ar}), 137.8 ($\text{CH}_{\text{py para}}$), 136.6 (C_{Ar}), 134.9 (C_{Ar}), 134.8 (C_{Ar}), 129.7 (CH_{Ar}), 129.5 (CH_{Ar}), 129.0 ($\text{CH}_{\text{mesityl}}$), 128.7 ($\text{CH}_{\text{mesityl}}$), 125.9 (2 x $\text{CH}_{\text{py meta}}$), 123.9 ($\text{CH}_{\text{imidazole}}$), 123.0 (C_{Ar}), 122.6 ($\text{CH}_{\text{imidazole}}$), 119.3 (CH_{Ar}), 114.7 (CH_{Ar}), 83.5 (CH_{COD}), 80.3 (CH_{COD}), 65.4 (CH_{COD}), 62.9 (CH_{COD}), 50.7 (CH_2), 33.8 ($\text{CH}_2(\text{COD})$), 31.2 ($\text{CH}_2(\text{COD})$), 30.3 ($\text{CH}_2(\text{COD})$), 27.3 ($\text{CH}_2(\text{COD})$), 19.9 (CH_3), 17.0 (CH_3), 15.2 (CH_3); ^{15}N NMR [CD_3OD] 248

8.7.10. Iridium(III) (3-(2-methylenephenoxy)-1-(2,4,6-trimethylphenyl)imidazolylidene) (cyclooctadiene)(dihydride)(pyridine), 14



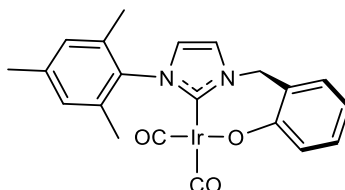
To a degassed CD₃OD solution of **13** (17 μmol, 1 eq.) in a dry ice/acetone bath at -78 °C was added 3 bars of H₂ and the mixture was analysed immediately at low temperature; ¹H NMR [CD₃OD, 400 MHz, 243 K] δ 8.99 (m, 2H, 2 x CH_{py ortho}), 7.89 (m, 1H, CH_{py para}), 7.37 (m, 2H, 2 x CH_{py meta}), 7.22 (s br, 1H, CH_{imidazole}), 7.17 (s br, 1H, CH_{imidazole}), 7.13 (s br, 2H, 2 x CH_{mesityl}), 7.11 (dd br, ³J(HH) = 7.5 Hz, ³J(HH) = 8.0 Hz, 1H, CH_{Ar}), 6.73 (d br, ³J(HH) = 8.0 Hz, 1H, CH_{Ar}), 6.70 (dd br, ³J(HH) = 7.5 Hz, ³J(HH) = 7.5 Hz, 1H, CH_{Ar}), 6.50 (d br, ³J(HH) = 7.5 Hz, 1H, CH_{Ar}), 5.00 (d, 1H, ²J(HH) = 15.2 Hz, CH₂), 4.89 (m, 1H, CH_{COD}), 4.77 (m, 1H, CH_{COD}), 4.71 (m, 1H, CH_{COD}), 4.70 (d, 1H, ²J(HH) = 15.2 Hz, CH₂), 4.00 (m, 1H, CH_{COD}), 2.60 (m, 2H, 2 x CH_{2(COD)}), 2.50 (m, 1H, CH_{2(COD)}), 2.38 (s, 3H, CH₃), 2.37 (m, 1H, CH_{2(COD)}), 2.08 (s, 3H, CH₃), 2.07 (s, 3H, CH₃), 1.97 (m, 1H, CH_{2(COD)}), 1.94 (m, 2H, 2 x CH_{2(COD)}), 1.80 (m, 1H, CH_{2(COD)}), -12.34 (s, 1H), -17.50 (d, 1H, ²J(NH) = 16.8 Hz); ¹³C{¹H} NMR [CD₃OD] δ 177.1 (C-Ir), 157.7 (2 x CH_{py ortho}), 154.7 (C-O), 139.1 (C_{Ar}), 138.1 (C_{Ar}), 137.6 (CH_{py para}), 135.1 (C_{Ar}), 134.6 (C_{Ar}), 129.0 (CH_{mesityl}), 128.9 (CH_{mesityl}), 128.8 (C_{Ar}), 127.2 (CH_{Ar}), 125.7 (2 x CH_{py meta}), 123.8 (CH_{Ar}), 123.7 (CH_{imidazole}), 122.9 (CH_{imidazole}), 118.9 (CH_{Ar}), 114.2 (CH_{Ar}), 91.5 (CH_{COD}), 90.5 (CH_{COD}), 80.1 (CH_{COD}), 79.0 (CH_{COD}), 49.6 (CH₂), 36.0 (CH_{2(COD)}), 31.0 (CH_{2(COD)}), 30.1 (CH_{2(COD)}), 25.3 (CH_{2(COD)}), 19.8 (CH₃), 16.8 (CH₃), 16.7 (CH₃); ¹⁵N NMR [CD₃OD] 227

8.7.11. Iridium(III) (3-(2-methylenephenoxy)-1-(2,4,6-trimethylphenyl)imidazolylidene) (dihydride)(pyridine)₃, 15



Upon warming a solution of **14** in CD₃OD under 3 bars of H₂ at r.t., the formation of **15** was observed; ¹H NMR [CD₃OD, 400 MHz, 298 K] δ 8.41 (m, 4H, 4 x CH_{py ortho}), 8.23 (m, 2H, 2 x CH_{py ortho}), 7.87 (m, 1H, CH_{py para}), 7.82 (m, 2H, 2 x CH_{py para}), 7.22 (m, 4H, 4 x CH_{py meta}), 7.15 (s, 1H, CH_{imidazole}), 7.11 (m, 2H, 2 x CH_{py meta}), 7.07 (dd br, ³J(HH) = 7.3 Hz, ³J(HH) = 7.3 Hz, 1H, CH_{Ar}), 6.96 (s, 1H, CH_{imidazole}), 6.80 (d br, ³J(HH) = 7.3 Hz, 1H, CH_{Ar}), 6.75 (dd br, ³J(HH) = 7.3 Hz, ³J(HH) = 7.3 Hz, 1H, CH_{Ar}), 6.71 (s, 2H, 2 x CH_{mesityl}), 6.70 (d br, ³J(HH) = 7.3 Hz, 1H, CH_{Ar}), 4.83 (s, 2H, CH₂), 2.07 (s, 6H, 2 x CH₃), 2.24 (s, 3H, CH₃), -22.33 (s, 2H); ¹³C{¹H} NMR [CD₃OD] δ 179.0 (C-Ir), 155.5 (2 x CH_{py ortho}), 154.4 (C-O), 153.8 (4 x CH_{py ortho}), 138.4 (C_{Ar}), 137.7 (C_{Ar}), 136.5 (2 x CH_{py para}), 136.4 (CH_{py para}), 135.2 (2 x C_{Ar}), 128.6 (2 x CH_{mesityl}), 128.2 (CH_{Ar}), 127.7 (CH_{Ar}), 125.8 (4 x CH_{py meta}), 125.5 (2 x CH_{py meta}), 123.4 (C_{Ar}), 122.3 (CH_{imidazole}), 121.4 (CH_{imidazole}), 118.9 (CH_{Ar}), 114.3 (CH_{Ar}), 48.3 (CH₂), 19.6 (CH₃), 17.4 (2 x CH₃); ¹⁵N NMR [CD₃OD] 258 (py₁), 240 (py₂)

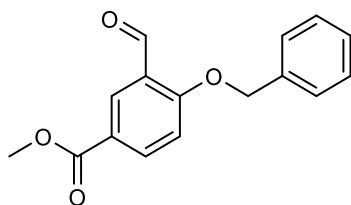
8.7.12. Iridium(I) (3-(2-methylenephenoate)-1-(2,4,6-trimethylphenyl)imidazolylidene) (dicarbonyl), 18



Iridium(I) (3-(2-methylenephenoate)-1-(2,4,6-trimethylphenyl)imidazolylidene) (cyclooctadiene) (20 mg, 0.0338 mmol, 1eq.) was dissolved in DCM (2 mL) and the mixture was stirred at r.t. whilst CO was bubbled through for 2 min. Stirring under an atmosphere of CO was continued for 10 min before the solution was purged with N₂ and the solvent was removed. The residue was triturated with hexane to afford a beige solid (14 mg, 78 %); ¹H NMR [CD₂Cl₂, 500 MHz, 298 K] δ 7.45 (ps dd, 1H, ³J(HH) = 7.5 Hz, ⁴J(HH) = 1.7 Hz, CH_{Ar}), 7.35 (ps dt, 1H, ³J(HH) = 7.9 Hz, ³J(HH) = 1.7 Hz, CH_{Ar}), 7.16 (d, 1H, ³J(HH) = 1.9 Hz, CH_{imidazole}), 7.06 (s, 2H, 2 x CH_{mesityl}), 7.03 (ps dt, 1H, ³J(HH) = 7.6 Hz, ⁴J(HH) = 1.3 Hz, CH_{Ar}), 6.98 (d, 1H, ³J(HH) = 1.9 Hz, CH_{imidazole}), 6.96 (ps dd, 1H, ³J(HH) = 8.1 Hz, ⁴J(HH) = 0.8 Hz, CH_{Ar}), 5.69 (s br, 2H, CH₂), 2.41 (s, 3H, CH₃), 2.11 (s, 6H, 2 x CH₃); ¹³C{¹H} NMR [CD₂Cl₂] δ 181.0 (C=O), 174.4 (C-Ir), 167.7 (C=O), 154.8 (C-O), 139.7 (C_{Ar}), 135.1 (2 x C_{Ar}), 131.4 (CH_{Ar}), 130.6 (CH_{Ar}), 129.1 (2 x CH_{mesityl}), 123.5 (CH_{imidazole}), 121.7 (CH_{imidazole}), 121.3 (C_{Ar}), 120.9 (CH_{Ar}), 116.8 (CH_{Ar}), 50.7 (CH₂), 20.9 (CH₃), 17.9 (2 x CH₃); MS [ESI] m/z 541.1 (M+H)⁺; IR ν_{CO} (cm⁻¹): 2058.3, 1974.3

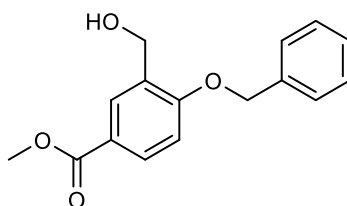
8.8. COOMe carbene synthesis

8.8.1. Methyl 4-benzyloxy-3-formyl benzoate



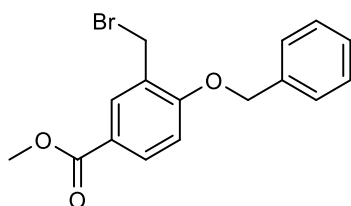
To a solution of methyl 3-formyl-4-hydroxy benzoate (400 mg, 2.22 mmol, 1 eq.) in MeCN (10 mL) under N₂ was added K₂CO₃ (399 mg, 2.89 mmol, 1.3 eq.) followed by benzyl bromide (0.34 mL, 2.89 mmol, 1.3 eq.) and the mixture was heated at 82 °C for 2 h. Water and ethyl acetate were added and the mixture was extracted with ethyl acetate. The organic layers were dried over MgSO₄, filtered and concentrated. The product was purified by column chromatography (silica, hexane: ethyl acetate, 8: 2) to afford a white solid (512 mg, 85 %); ¹H NMR [CDCl₃, 400 MHz, 298 K] δ 10.57 (s, 1H, CHO), 8.56 (d, 1H, ⁴J(HH) = 2.0 Hz, CH_{Ar}), 8.25 (dd, 1H, ⁴J(HH) = 2.0 Hz, ³J(HH) = 8.6 Hz, CH_{Ar}), 7.52-7.38 (m, 5H, 5 x CH_{Ar}), 7.14 (d, 1H, ³J(HH) = 8.6 Hz, CH_{Ar}), 5.30 (s, 2H, CH₂), 3.94 (s, 3H, CH₃); ¹³C{¹H} NMR [CDCl₃] 188.9 (HC=O), 166.0 (C=O), 163.9 (C_{Ar}O), 137.1 (CH_{Ar}), 135.3 (C_{Ar}), 130.6 (CH_{Ar}), 128.9 (2 x CH_{Ar}), 128.6 (CH_{Ar}), 127.4 (2 x CH_{Ar}), 124.8 (C_{Ar}), 123.2 (C_{Ar}), 112.9 (CH_{Ar}), 70.9 (CH₂), 52.2 (CH₃); MS [ESI] m/z 293.08 (M+Na)⁺

8.8.2. Methyl 4-benzyloxy-3-hydroxymethyl benzoate



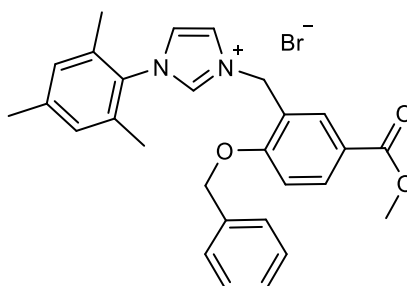
To a solution of methyl 4-benzyloxy-3-formyl benzoate (500 mg, 1.85 mmol, 1 eq.) in MeOH (20 mL) was added NaBH₄ (210 mg, 5.55 mmol, 3 eq.) and the mixture was stirred at r.t. for 1.5 h. Water was added and the mixture was extracted with DCM. Organic layers were dried over MgSO₄, filtered and concentrated to afford a colourless oil (466 mg, 92 %); ¹H NMR [CDCl₃, 400 MHz, 298 K] δ 8.06 (d, 1H, ⁴J(HH) = 2.0 Hz, CH_{Ar}), 8.02 (dd, 1H, ⁴J(HH) = 2.0 Hz, ³J(HH) = 8.7 Hz, CH_{Ar}), 7.47-7.36 (m, 5H, 5 x CH_{Ar}), 7.01 (d, 1H, ³J(HH) = 8.7 Hz, CH_{Ar}), 5.21 (s, 2H, CH₂), 4.80 (d, 2H, ³J(HH) = 6.5 Hz, CH₂OH), 3.93 (s, 3H, CH₃), 2.23 (t, 1H, ³J(HH) = 6.5 Hz, OH); ¹³C{¹H} NMR [CDCl₃] 166.8 (C=O), 160.1 (C_{Ar}O), 136.0 (C_{Ar}), 131.2 (CH_{Ar}), 130.2 (CH_{Ar}), 129.5 (C_{Ar}), 128.8 (2 x CH_{Ar}), 128.4 (CH_{Ar}), 127.4 (2 x CH_{Ar}), 122.8 (C_{Ar}), 111.1 (CH_{Ar}), 70.3 (CH₂), 61.6 (CH₂OH), 52.0 (CH₃); MS [ESI] m/z 295.09 (M+Na)⁺

8.8.3. Methyl 4-benzyloxy-3-bromomethyl benzoate benzoate



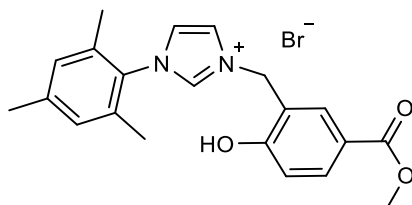
To a solution of methyl 4-benzyloxy-3-hydroxymethyl benzoate (2 g, 7.34 mmol, 1 eq.) in DCM under N₂ was added PBr₃ (0.91 mL, 11 mmol, 1.3 eq.) and the mixture was stirred at r.t. for 1.5 h. Water was added slowly whilst stirring and the mixture was extracted with ethyl acetate. The organic layers were washed with brine, dried over MgSO₄, filtered and concentrated. The product was purified by column chromatography (silica, hexane: ethyl acetate, 7: 3) to afford a white solid (1.57 g, 64 %); ¹H NMR [CDCl₃, 400 MHz, 298 K] δ 8.09 (d, 1H, ⁴J(HH) = 2.1 Hz, CH_{Ar}), 8.01 (dd, 1H, ⁴J(HH) = 2.1 Hz, ³J(HH) = 8.7 Hz, CH_{Ar}), 7.54-7.50 (m, 2H, 2 x CH_{Ar}), 7.47-7.36 (m, 3H, 3 x CH_{Ar}), 6.99 (d, 1H, ³J(HH) = 8.7 Hz, CH_{Ar}), 5.26 (s, 2H, CH₂), 4.63 (s, 2H, CH₂), 3.92 (s, 3H, CH₃); ¹³C{¹H} NMR [CDCl₃] 166.4 (C=O), 160.1 (C_{Ar}O), 136.0 (C_{Ar}), 132.5 (CH_{Ar}), 132.2 (CH_{Ar}), 128.7 (2 x CH_{Ar}), 128.2 (CH_{Ar}), 127.2 (2 x CH_{Ar}), 126.5 (C_{Ar}), 122.8 (C_{Ar}), 111.7 (CH_{Ar}), 70.4 (CH₂), 52.1 (CH₃), 28.2 (CH₂); MS [ESI] m/z 357.01 (M+Na)⁺

8.8.4. 3-(methyl 4-benzyloxy-3-benzyl benzoate)-1-(2,4,6-trimethylphenyl) imidazolium bromide



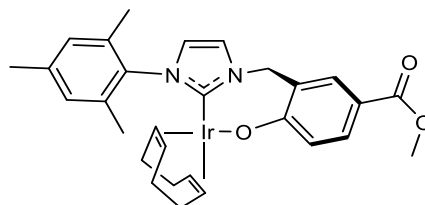
Methyl 4-benzyloxy-3-bromomethyl benzoate (260 mg, 0.776 mmol, 1 eq.) and 1-(2,4,6-trimethylphenyl)-1H-imidazole (144 mg, 0.776 mmol, 1 eq.) were dissolved in toluene (10 mL) and heated at 70 °C for 20 h. The solution was cooled to r.t. and diethyl ether was added. The white precipitate was filtered and the filtrate was concentrated, triturated with diethyl ether and refiltered to afford more white solid (336 mg, 94 %); ^1H NMR [DMSO, 400 MHz, 298 K] δ 9.40 (s br, 1H, $\text{CH}_{\text{imidazole}}$), 8.05 (dd, 1H, $^4J(\text{HH}) = 2.1$ Hz, $^3J(\text{HH}) = 8.6$ Hz, CH_{Ar}), 8.02 (t, 1H, $^4J(\text{HH}) = 1.7$ Hz, $\text{CH}_{\text{imidazole}}$), 7.95 (d, 1H, $^4J(\text{HH}) = 2.1$ Hz, CH_{Ar}), 7.93 (t, 1H, $^4J(\text{HH}) = 1.7$ Hz, $\text{CH}_{\text{imidazole}}$), 7.44-7.42 (m, 2H, 2 x CH_{Ar}), 7.40-7.33 (m, 3H, 3 x CH_{Ar}), 7.33 (d, 1H, $^3J(\text{HH}) = 8.6$ Hz, CH_{Ar}), 7.14 (s, 2H, 2 x $\text{CH}_{\text{mesityl}}$), 5.61 (s, 2H, CH_2), 5.31 (s, 2H, CH_2), 3.84 (s, 3H, OCH_3), 2.33 (s, 3H, CH_3), 1.95 (s, 6H, 2 x CH_3); $^{13}\text{C}\{^1\text{H}\}$ NMR [DMSO] 166.1 (C=O), 160.5 ($\text{C}_{\text{Ar}}\text{O}$), 140.8 (C_{Ar}), 138.3 ($\text{CH}_{\text{imidazole}}$), 136.4 (C_{Ar}), 134.7 (2 x C_{Ar}), 132.9 (CH_{Ar}), 131.7 (C_{Ar}), 131.6 (CH_{Ar}), 129.7 (2 x $\text{CH}_{\text{mesityl}}$), 129.0 (2 x CH_{Ar}), 128.7 (CH_{Ar}), 127.9 (2 x CH_{Ar}), 124.5 ($\text{CH}_{\text{imidazole}}$), 124.0 ($\text{CH}_{\text{imidazole}}$), 123.2 (C_{Ar}), 122.6 (C_{Ar}), 113.1 (CH_{Ar}), 70.4 (CH_2), 52.5 (OCH_3), 49.0 (CH_2), 21.1 (CH_3), 17.2 (2 x CH_3); MS [ESI] m/z 441.3 ($\text{M}-\text{Br}$) $^+$

8.8.5. 3-(methyl 3-benzyl-4-hydroxy benzoate)-1-(2,4,6-trimethylphenyl) imidazolium bromide



To a Parr reactor was added 3-(methyl 4-benzyloxy-3-benzyl benzoate)-1-(2,4,6-trimethylphenyl) imidazolium bromide (200 mg, 0.384 mmol, 1 eq.), palladium hydroxide on carbon (24 mg, 12 % by weight) and methanol (10 mL) and the mixture was heated at 45 °C under 5 bars of H₂ for 18 h. The mixture was filtered over Celite, washed with methanol and concentrated to afford a pale brown solid (165 mg, 100 %); ¹H NMR [DMSO, 400 MHz, 298 K] δ 9.51 (t br, 1H, ⁴J(HH) = 1.7 Hz, CH_{imidazole}), 7.99 (t, 1H, ⁴J(HH) = 1.7 Hz, CH_{imidazole}), 7.94 (d, 1H, ⁴J(HH) = 2.2 Hz, CH_{Ar}), 7.90 (t, 1H, ⁴J(HH) = 1.7 Hz, CH_{imidazole}), 7.86 (dd, 1H, ⁴J(HH) = 2.2 Hz, ³J(HH) = 8.6 Hz, CH_{Ar}), 7.14 (s, 2H, 2 x CH_{mesityl}), 6.94 (d, 1H, ³J(HH) = 8.6 Hz, CH_{Ar}), 5.46 (s, 2H, CH₂), 3.80 (s, 3H, OCH₃), 2.33 (s, 3H, CH₃), 2.00 (s, 6H, 2 x CH₃); ¹³C{¹H} NMR [DMSO] 166.3 (C=O), 161.6 (C_{Ar}O), 140.8 (C_{Ar}), 138.6 (CH_{imidazole}), 134.8 (2 x C_{Ar}), 132.3 (CH_{Ar}), 132.3 (CH_{Ar}), 131.7 (C_{Ar}), 129.7 (2 x CH_{mesityl}), 124.4 (CH_{imidazole}), 123.8 (CH_{imidazole}), 121.4 (C_{Ar}), 115.9 (CH_{Ar}), 52.5 (OCH₃), 49.2 (CH₂), 21.1 (CH₃), 17.3 (2 x CH₃); MS [ESI] m/z 351.3 (M-Br)⁺

8.8.6. Iridium(I) (3-(methyl 3-benzyl-4-hydroxy benzoate)-1-(2,4,6-trimethylphenyl) imidazolylidene)(cyclooctadiene), 3



To a Schlenk flask containing 3-(methyl 3-benzyl-4-hydroxy benzoate)-1-(2,4,6-trimethylphenyl) imidazolium bromide (150 mg, 0.348 mmol, 1 eq), silver(I) oxide (161 mg, 0.696 mmol, 2 eq) and molecular sieves 4 Å (600 mg) under an atmosphere of N₂ in the dark, was added DCM (10 mL) and the mixture was stirred at r.t. for 3 h. To this was then added [Ir(COD)Cl]₂ (117 mg, 0.174 mmol, 0.5 eq) and the mixture was stirred at r.t. for a further 1 h. The mixture was then filtered over Celite and silica, washed with DCM: acetone, 4: 1 and concentrated under reduced pressure to afford an orange solid (178 mg, 79 %); ¹H NMR [CD₂Cl₂, 400 MHz, 243 K] δ 7.87 (d, 1H, ⁴J(HH) = 2.2 Hz, CH_{Ar}), 7.68 (dd, 1H, ³J(HH) = 8.8 Hz, ⁴J(HH) = 2.2 Hz, CH_{Ar}), 7.12 (d, 1H, ³J(HH) = 1.8 Hz, CH_{imidazole}), 7.04 (s br, 1H, CH_{mesityl}), 6.95 (s br, 1H, CH_{mesityl}), 6.69 (s br, 1H, ³J(HH) = 1.8 Hz, CH_{imidazole}), 6.55 (d, 1H, ³J(HH) = 8.8 Hz, CH_{Ar}), 6.53 (d br, 1H, ²J(HH) = 13.6 Hz, CH₂ linker), 4.75 (d br, 1H, ²J(HH) = 13.6 Hz, CH₂ linker), 4.34 (br m, 1H, CH_{COD}), 4.28 (br m, 1H, CH_{COD}), 3.80 (s, 3H, OCH₃), 3.17 (br m, 1H, CH_{COD}), 2.36 (s br, 4H, CH₃, CH_{COD}), 2.18-2.10 (m, 3H, CH₂(COD)), 2.05 (s, 3H, CH₃), 1.96 (s br, 4H, CH₃, CH₂(COD)), 1.59-1.35 (s br, 4H, 2 x CH₂(COD)); ¹³C{¹H} NMR [CD₂Cl₂] δ 174.8 (C-Ir), 173.3 (C-OIr), 167.4 (OC=O), 139.0 (C_{Ar}), 136.2 (C_{Ar}), 135.7 (C_{Ar}), 134.4 (C_{Ar}), 131.9 (CH_{Ar}), 131.4 (CH_{Ar}), 129.1 (CH_{mesityl}), 128.3 (CH_{mesityl}), 123.9 (C_{Ar}), 123.3 (CH_{imidazole}), 121.2 (CH_{Ar}), 119.6 (CH_{imidazole}), 114.2 (C_{Ar}), 84.5 (CH), 84.0 (CH), 51.6 (OCH₃), 51.4 (CH₂), 48.5 (CH), 47.4 (CH), 34.4 (CH₂), 33.4 (CH₂), 29.0 (CH₂), 28.3 (CH₂), 21.0 (CH₃), 18.7 (CH₃), 17.7 (CH₃); MS [ESI] m/z 649.2 (M⁺)

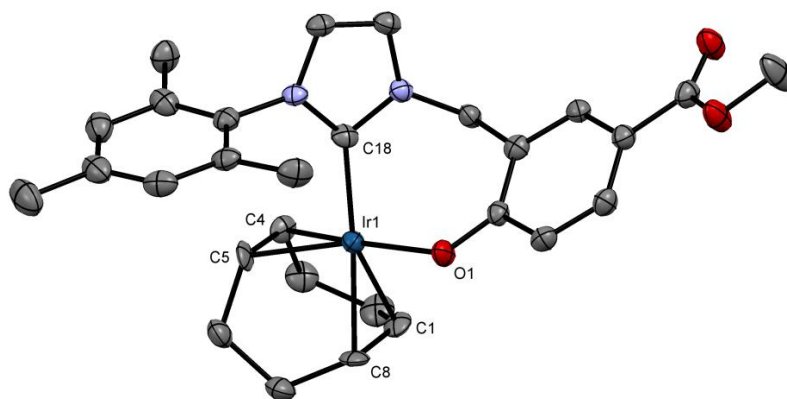


Figure 250: ORTEP plot of **3** with H atoms omitted for clarity and the thermal ellipsoids set at a 50 % probability level

Table 57: Crystal data for the structural refinement of **3**

Identification code	sbd1626	
Empirical formula and weight	C ₂₉ H ₃₃ IrN ₂ O ₃	649.77
Temperature / K	110.05(10)	
Crystal system and space group	triclinic	P-1
Unit cell dimensions	a / Å = 13.7657(5) b / Å = 14.4796(6) c / Å = 14.5701(6)	α / ° = 61.959(4) β / ° = 87.209(3) γ / ° = 80.925(3)
Volume / Å³	2530.06(19)	
Z	4	
Density (calculated) / ρ_{calc} / g cm⁻³	1.706	
Absorption coefficient / μ / mm⁻¹	10.480	
F(000)	1288.0	
Crystal size / mm³	0.106 × 0.078 × 0.059	
Radiation	CuKα (λ = 1.54184)	
2θ range for data collection/°	6.876 to 142.366	

Index ranges	$-16 \leq h \leq 13, -17 \leq k \leq 17, -17 \leq l \leq 17$
Reflections collected	36840
Independent reflections	9696 [$R_{\text{int}} = 0.0424, R_{\text{sigma}} = 0.0322$]
Data / restraints / parameters	9696 / 0 / 639
Goodness-of-fit on F^2	1.046
Final R indexes [$I \geq 2\sigma(I)$]	$R_1 = 0.0310, wR_2 = 0.0790$
Final R indexes [all data]	$R_1 = 0.0349, wR_2 = 0.0822$
Largest diff. peak / hole / $e \text{ \AA}^{-3}$	1.13 / -1.18

UV-vis absorption data for complex **3** at eight different concentrations are given in Table 58 with the corresponding absorption spectra shown in Figure 251.

Table 58: Concentration and absorbance values for eight samples of 3 in DCM at different concentrations

	Concentration / $\mu\text{mol dm}^{-3}$	Absorbance		
Sample		At 380 nm	At 432 nm	At 491 nm
A	385	1.31	0.62	0.21
B	308	1.06	0.50	0.17
C	215	0.75	0.36	0.13
D	172	0.62	0.31	0.12
E	154	0.55	0.27	0.11
F	103	0.40	0.20	0.09
G	77	0.30	0.16	0.08
H	41	0.19	0.11	0.06

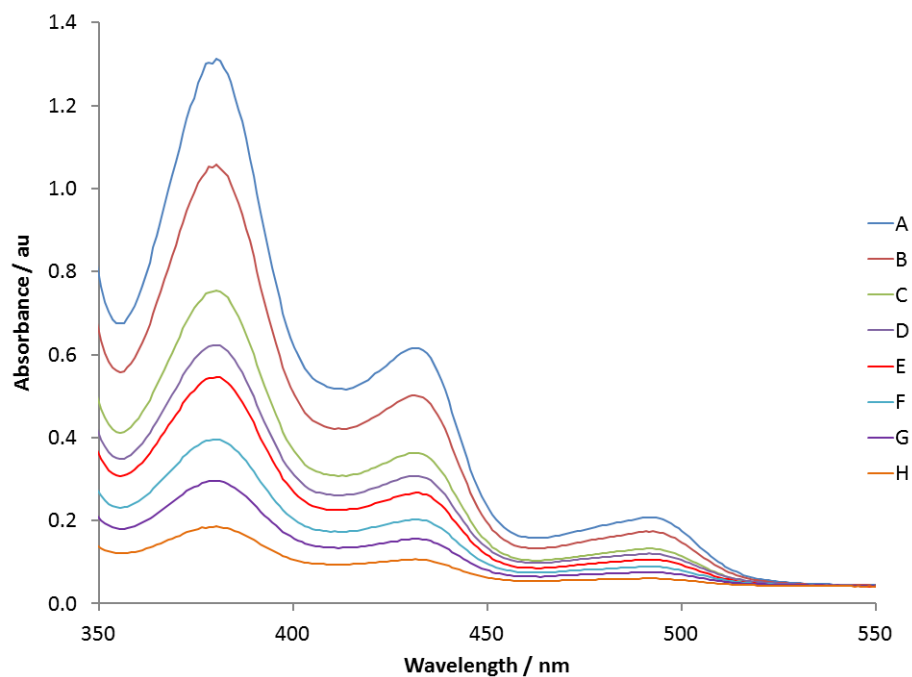


Figure 251: Visible region of the absorption spectra for **3** in DCM at different concentrations as listed in Table 58

The calibration graph in Figure 252 was used to gain the molar absorption coefficients for the absorption bands of **3** as described in Section 2.6.1.

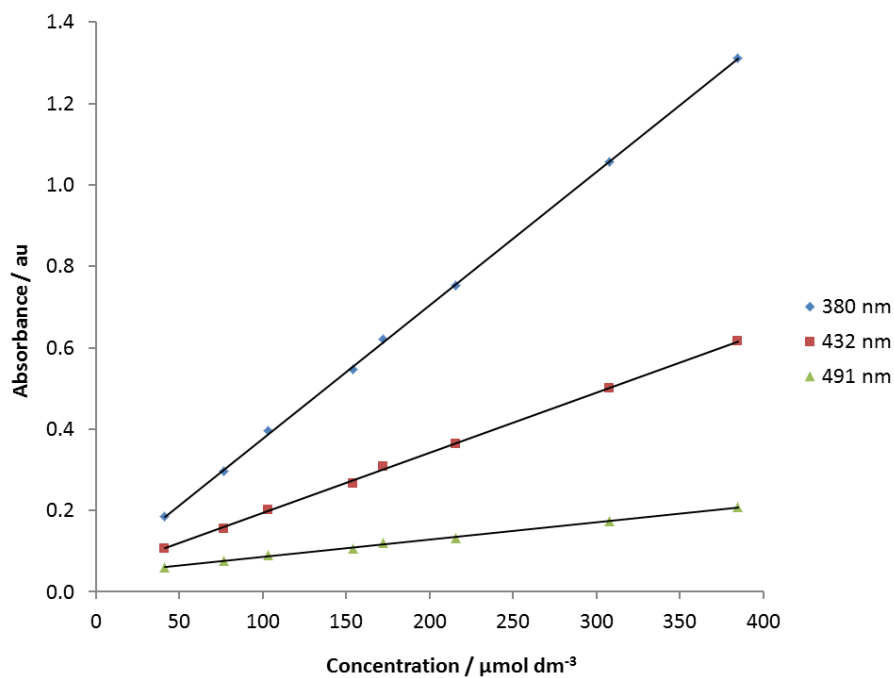
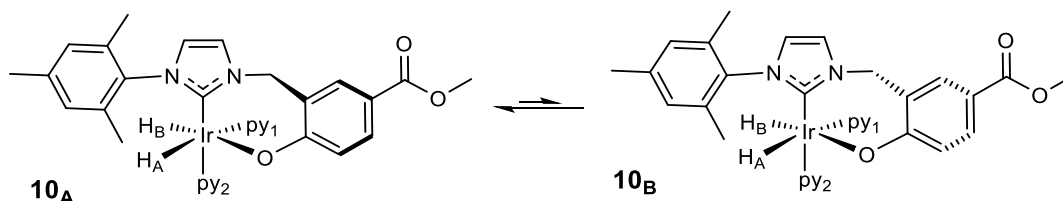


Figure 252: Calibration graph used to calculate the molar absorption coefficients for the three absorption bands of **3** at 380, 432 and 491 nm using the data in Table 58

8.8.7. Iridium(III) (3-(methyl 3-benzyl-4-hydroxy benzoate)-1-(2,4,6-trimethylphenyl) imidazolylidene)(dihydride)(pyridine)₂, 10_A and 10_B



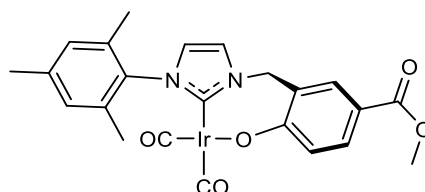
To a Young's NMR tube was added **3** (10 mg, 15 μmol , 1 eq.), pyridine (3.8 μL , 47 μmol , 3 eq.) and CD_2Cl_2 or CD_3OD (0.6 mL). The solution was then degassed three times on a high vacuum line using a freeze-thaw procedure with either liquid N_2 (for CD_2Cl_2) or a dry ice/acetone bath (for CD_3OD), before the addition of 3 bars of H_2 . The mixture was then left to react at r.t. for 2 days.

10_A: ^1H NMR [CD_2Cl_2 , 400 MHz, 303 K] δ 9.02 (m, 2H, 2 x $\text{CH}_{\text{py ortho}}$), 8.41 (m, 2H, 2 x $\text{CH}_{\text{py ortho}}$), 7.85 (d, 1H, $^4J(\text{HH}) = 2.7$ Hz, CH_{Ar}), 7.77 (dd, 1H, $^4J(\text{HH}) = 2.7$ Hz, $^3J(\text{HH}) = 8.6$ Hz, CH_{Ar}), 7.64 (m, 1H, $\text{CH}_{\text{py para}}$), 7.31 (m, 1H, $\text{CH}_{\text{py para}}$), 7.15 (d, 1H, $^3J(\text{HH}) = 2.1$ Hz, $\text{CH}_{\text{imidazole}}$), 7.09 (m, 2H, 2 x $\text{CH}_{\text{py meta}}$), 7.00 (s br, 1H, $\text{CH}_{\text{mesityl}}$), 6.96 (m, 2H, 2 x $\text{CH}_{\text{py meta}}$), 6.73 (d, 1H, $^3J(\text{HH}) = 8.6$ Hz, CH_{Ar}), 6.60 (d, 1H, $^3J(\text{HH}) = 2.1$ Hz, $\text{CH}_{\text{imidazole}}$), 6.59 (s br, 1H, $\text{CH}_{\text{mesityl}}$), 6.15 (d br, 1H, $^2J(\text{HH}) = 13.1$ Hz, CH_2 linker), 4.56 (d br, 1H, $^2J(\text{HH}) = 13.1$ Hz, CH_2 linker), 3.83 (s, 3H, CH_3), 2.34 (s br, 3H, CH_3), 2.12 (s br, 3H, CH_3), 2.02 (s br, 3H, CH_3), -21.95 (d, 1H, $^2J(\text{HH}) = 8.3$ Hz), -28.48 (d, 1H, $^2J(\text{HH}) = 8.3$ Hz); $^{13}\text{C}\{^1\text{H}\}$ NMR [CD_2Cl_2] δ 175.2 (C-O), 167.6 (C=O), 156.2 (C-Ir), 154.7 (2 x $\text{CH}_{\text{py ortho}}$), 153.9 (2 x $\text{CH}_{\text{py ortho}}$), 138.7 (C_{Ar}), 137.5 (C_{Ar}), 136.7 (C_{Ar}), 135.2 ($\text{CH}_{\text{py para}}$), 134.4 ($\text{CH}_{\text{py para}}$), 132.4 (CH_{Ar}), 131.5 (CH_{Ar}), 128.8 (C_{Ar}), 128.5 ($\text{CH}_{\text{mesityl}}$), 127.8 ($\text{CH}_{\text{mesityl}}$), 125.0 (C_{Ar}), 124.2 (2 x $\text{CH}_{\text{py meta}}$), 122.9 (2 x $\text{CH}_{\text{py meta}}$), 121.7 (CH_{Ar}), 120.0 ($\text{CH}_{\text{imidazole}}$), 119.8 ($\text{CH}_{\text{imidazole}}$), 111.9 (C_{Ar}), 51.9 (CH_2), 50.7 (CH_3), 20.7 (CH_3), 18.9 (CH_3), 17.9 (CH_3)

10A: ^1H NMR [CD_3OD , 400 MHz, 298 K] δ 8.90 (m, 2H, 2 x $\text{CH}_{\text{py ortho}}$), 8.23 (m, 2H, 2 x $\text{CH}_{\text{py ortho}}$), 7.94 (d, 1H, $^4J(\text{HH}) = 2.3$ Hz, CH_{Ar}), 7.77 (dd, 1H, $^4J(\text{HH}) = 2.3$ Hz, $^3J(\text{HH}) = 8.6$ Hz, CH_{Ar}), 7.75 (m, 1H, $\text{CH}_{\text{py para}}$), 7.69 (m, 1H, $\text{CH}_{\text{py para}}$), 7.39 (d, 1H, $^3J(\text{HH}) = 2.0$ Hz, $\text{CH}_{\text{imidazole}}$), 7.15 (m, 2H, 2 x $\text{CH}_{\text{py meta}}$), 7.01 (m, 2H, 2 x $\text{CH}_{\text{py meta}}$), 6.98 (s br, 1H, $\text{CH}_{\text{mesityl}}$), 6.80 (d, 1H, $^3J(\text{HH}) = 8.6$ Hz, CH_{Ar}), 6.72 (d, 1H, $^3J(\text{HH}) = 2.0$ Hz, $\text{CH}_{\text{imidazole}}$), 6.51 (s br, 1H, $\text{CH}_{\text{mesityl}}$), 6.17 (d br, 1H, $^2J(\text{HH}) = 12.6$ Hz, CH_2 linker), 4.63 (d br, 1H, $^2J(\text{HH}) = 12.6$ Hz, CH_2 linker), 3.85 (s, 3H, CH_3), 2.29 (s br, 3H, CH_3), 2.11 (s br, 3H, CH_3), 1.09 (s br, 3H, CH_3), -21.66 (s br, 1H), -29.04 (s br, 1H); $^{13}\text{C}\{^1\text{H}\}$ NMR [CD_3OD] δ 174.7 (C-O), 168.5 (C=O), 154.7 (C-Ir), 154.5 (2 x $\text{CH}_{\text{py ortho}}$), 153.7 (2 x $\text{CH}_{\text{py ortho}}$), 137.5 (C_{Ar}), 137.5 (C_{Ar}), 136.2 (C_{Ar}), 135.6 ($\text{CH}_{\text{py para}}$), 135.5 ($\text{CH}_{\text{py para}}$), 135.4 (C_{Ar}), 132.2 (CH_{Ar}), 131.2 (CH_{Ar}), 128.4 ($\text{CH}_{\text{mesityl}}$), 127.8 ($\text{CH}_{\text{mesityl}}$), 126.5 (C_{Ar}), 124.4 (2 x $\text{CH}_{\text{py meta}}$), 124.2 (2 x $\text{CH}_{\text{py meta}}$), 122.1 (CH_{Ar}), 120.3 ($\text{CH}_{\text{imidazole}}$), 120.0 ($\text{CH}_{\text{imidazole}}$), 113.4 (C_{Ar}), 50.5 (CH_2), 50.3 (CH_3), 19.6 (CH_3), 17.9 (CH_3), 15.7 (CH_3)

10B: ^1H NMR [CD_2Cl_2 , 400 MHz, 303 K] δ 8.84 (m, 2H, 2 x $\text{CH}_{\text{py ortho}}$), 8.77 (m, 2H, 2 x $\text{CH}_{\text{py ortho}}$), 7.94 (dd, 1H, $^4J(\text{HH}) = 2.2$ Hz, $^3J(\text{HH}) = 8.2$ Hz, CH_{Ar}), 7.91 (d, 1H, $^4J(\text{HH}) = 2.2$ Hz, CH_{Ar}), 7.69 (m, 1H, $\text{CH}_{\text{py para}}$), 7.60 (m, 1H, $\text{CH}_{\text{py para}}$), 7.06 (m, 2H, 2 x $\text{CH}_{\text{py meta}}$), 7.01 (m, 2H, 2 x $\text{CH}_{\text{py meta}}$), 6.96 (s, 1H, $\text{CH}_{\text{mesityl}}$), 6.94 (d, 1H, $^3J(\text{HH}) = 8.2$ Hz, CH_{Ar}), 6.64 (d, 1H, $^3J(\text{HH}) = 2.2$ Hz, $\text{CH}_{\text{imidazole}}$), 6.61 (d, 1H, $^3J(\text{HH}) = 2.2$ Hz, $\text{CH}_{\text{imidazole}}$), 6.54 (s, 1H, $\text{CH}_{\text{mesityl}}$), 5.87 (d, 1H, $^2J(\text{HH}) = 14.5$ Hz, CH_2 linker), 5.32 (d, 1H, $^2J(\text{HH}) = 14.5$ Hz, CH_2 linker), 3.90 (s, 3H, CH_3), 2.26 (s, 3H, CH_3), 2.19 (s, 3H, CH_3), 1.83 (s, 3H, CH_3), -22.56 (d, 1H, $^2J(\text{HH}) = 8.0$ Hz), -25.47 (d, 1H, $^2J(\text{HH}) = 8.0$ Hz); $^{13}\text{C}\{^1\text{H}\}$ NMR [CD_2Cl_2] δ 166.4 (C=O), 160.9 (C-O), 155.7 (2 x $\text{CH}_{\text{py ortho}}$), 155.2 (C-Ir), 154.2 (2 x $\text{CH}_{\text{py ortho}}$), 138.2 (C_{Ar}), 137.7 (C_{Ar}), 136.1 (C_{Ar}), 135.3 ($\text{CH}_{\text{py para}}$), 135.1 (C_{Ar}), 135.1 ($\text{CH}_{\text{py para}}$), 133.4 (CH_{Ar}), 132.7 (C_{Ar}), 131.7 (CH_{Ar}), 128.6 ($\text{CH}_{\text{mesityl}}$), 128.3 ($\text{CH}_{\text{mesityl}}$), 124.7 (2 x $\text{CH}_{\text{py meta}}$), 124.4 (2 x $\text{CH}_{\text{py meta}}$), 123.4 (C_{Ar}), 123.0 ($\text{CH}_{\text{imidazole}}$), 119.4 ($\text{CH}_{\text{imidazole}}$), 118.0 (CH_{Ar}), 52.2 (CH_2), 51.6 (CH_3), 20.4 (CH_3), 18.3 (CH_3), 17.7 (CH_3)

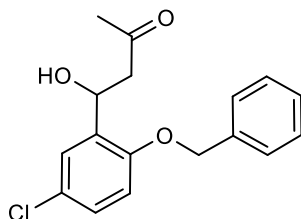
8.8.8. Iridium(I) (3-(methyl 3-benzyl-4-hydroxy benzoate)-1-(2,4,6-trimethylphenyl) imidazolylidene)(dicarbonyl), 20



Iridium(I) (3-(methyl 3-benzyl-4-hydroxy benzoate)-1-(2,4,6-trimethylphenyl) imidazolylidene)(cyclooctadiene) (20 mg, 0.0308 mmol, 1eq.) was dissolved in DCM (2 mL) and the mixture was stirred at r.t. whilst CO was bubbled through for 2 min. Stirring under an atmosphere of CO was continued for 10 min before the solution was purged with N₂ and the solvent was removed. The residue was triturated with hexane to afford a yellow solid (12 mg, 67 %); ¹H NMR [CD₂Cl₂, 400 MHz, 298 K] δ 7.92 (d, 1H, ⁴J(HH) = 2.2 Hz, CH_{Ar}), 7.79 (dd, 1H, ⁴J(HH) = 2.2 Hz, ³J(HH) = 8.7 Hz, CH_{Ar}), 7.25 (d, 1H, ³J(HH) = 1.7 Hz, CH_{imidazole}), 7.04 (s, 2H, 2 x CH_{mesityl}), 6.89 (d, 1H, ³J(HH) = 1.7 Hz, CH_{imidazole}), 6.72 (d, 1H, ³J(HH) = 8.7 Hz, CH_{Ar}), 5.39 (s br, 2H, CH₂), 3.84 (s, 3H, OCH₃), 2.39 (s, 3H, CH₃), 2.00 (s, 6H, 2 x CH₃); ¹³C{¹H} NMR [CD₂Cl₂] δ 182.1 (C=O), 173.1 (C-Ir), 170.7 (OC_{Ar}), 168.9 (C=O), 167.0 (OC=O), 139.7 (C_{Ar}), 135.3 (2 x C_{Ar}), 135.0 (C_{Ar}), 131.7 (CH_{Ar}), 131.5 (CH_{Ar}), 129.1 (2 x CH_{mesityl}), 123.9 (C_{Ar}), 123.3 (CH_{imidazole}), 121.6 (CH_{Ar}), 120.9 (CH_{imidazole}), 116.7 (C_{Ar}), 51.3 (OCH₃), 50.9 (CH₂), 20.9 (CH₃), 17.9 (2 x CH₃); MS [ESI] m/z 599.1 (M+H)⁺; IR ν_{CO} (cm⁻¹): 2050.2, 1964.0

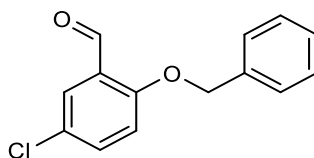
8.9. Cl carbene synthesis

8.9.1. 4-hydroxy-4-(2-benzyloxy-5-chlorophenyl)-2-butanone



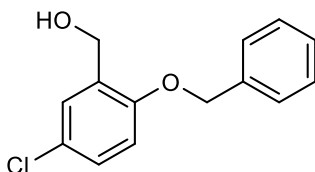
To a solution of 5-chlorosalicylaldehyde (1 g, 6.39 mmol, 1 eq.) in dry acetone (20 mL) under N₂ was added K₂CO₃ (1.15 g, 8.30 mmol, 1.3 eq.) followed by benzyl bromide (0.99 mL, 8.30 mmol, 1.3 eq.) and the mixture was heated at 40 °C for 64 h. The solution was cooled to r.t. and the solvent was evaporated. Saturated aqueous NaHCO₃ was added and the mixture was extracted with ethyl acetate. The organic layers were dried over MgSO₄, filtered and concentrated. The product was purified by column chromatography (silica, hexane: ethyl acetate, 9: 1 to 4: 6) to afford a white solid (1.60 g, 82 %); ¹H NMR [CDCl₃, 400 MHz, 298 K] δ 7.51 (d, 1H, ⁴J(HH) = 2.7 Hz, CH_{Ar}), 7.44-7.33 (m, 5H, 5 x CH_{Ar}), 7.20 (dd, 1H, ⁴J(HH) = 2.7 Hz, ³J(HH) = 8.7 Hz, CH_{Ar}), 6.86 (d, 1H, ³J(HH) = 8.7 Hz, CH_{Ar}), 5.45 (ddd, 1H, ³J(HH) = 2.6 Hz, ³J(HH) = 3.9 Hz, ³J(HH) = 9.5 Hz, CHOH), 5.10 (s, 2H, CH₂), 3.48 (d, 1H, ³J(HH) = 3.9 Hz, OH), 2.98 (dd, 1H, ³J(HH) = 2.6 Hz, ²J(HH) = 17.6 Hz, CH₂), 2.71 (dd, 1H, ³J(HH) = 9.5 Hz, ²J(HH) = 17.6 Hz, CH₂), 2.16 (s, 3H, CH₃); ¹³C{¹H} NMR [CDCl₃] 209.4 (C=O), 153.2 (C_{Ar}), 136.4 (C_{Ar}), 133.2 (C_{Ar}), 128.8 (2 x CH_{Ar}), 128.2 (CH_{Ar}), 127.9 (CH_{Ar}), 127.2 (2 x CH_{Ar}), 126.7 (CH_{Ar}), 126.5 (C_{Ar}), 112.9 (CH_{Ar}), 70.5 (OCH₂), 65.0 (CHOH), 50.0 (CH₂C=O), 30.7 (CH₃); MS [ESI] m/z 327.1 (M+Na)⁺; IR ν_{CO} (cm⁻¹): 1699.0

8.9.2. 2-benzyloxy-5-chloro benzaldehyde



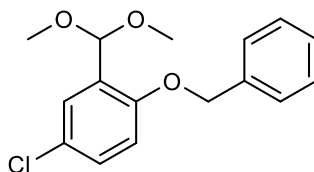
To a dry DMF (5 mL) solution of 5-chloro-2-hydroxybenzaldehyde (200 mg, 1.28 mmol, 1 eq.) under N₂, was added K₂CO₃ (230 mg, 1.66 mmol, 1.3 eq.) and benzyl bromide (0.2 mL, 1.66 mmol, 1.3 eq.). The solution was stirred at 60 °C for 18 h, before being cooled to r.t. Then water and diethyl ether were added. The ether layers were dried over MgSO₄, filtered and concentrated to afford a white solid (293 mg, 93 %); ¹H NMR [CDCl₃, 400 MHz, 298 K] δ 10.50 (s, 1H, CHO), 7.83 (d, 1H, ⁴J(HH) = 2.7 Hz, CH_{Ar}), 7.49 (dd, 1H, ⁴J(HH) = 2.7 Hz, ³J(HH) = 8.8 Hz, CH_{Ar}), 7.46-7.37 (m, 5H, 5 x CH_{Ar}), 7.03 (d, 1H, ³J(HH) = 8.8 Hz, CH_{Ar}), 5.21 (s, 2H, CH₂); ¹³C{¹H} NMR [CDCl₃] 188.4 (C=O), 159.5 (C_{Ar}O), 135.6 (C_{Ar}), 135.4 (CH_{Ar}), 128.8 (2 x CH_{Ar}), 128.5 (CH_{Ar}), 128.1 (CH_{Ar}), 127.4 (2 x CH_{Ar}), 126.8 (C_{Ar}), 126.1 (C_{Ar}), 114.8 (CH_{Ar}), 71.0 (CH₂); MS [ESI] m/z 269.03 (M+Na)⁺

8.9.3. 2-benzyloxy-5-chloro benzyl alcohol



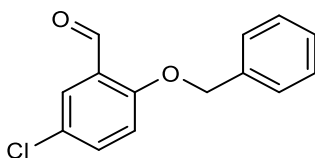
To a stirred solution of 2-benzyloxy-5-chloro benzaldehyde (293 mg, 1.19 mmol, 1 eq.) in MeOH (25 mL) was added NaBH₄ (90 mg, 2.38 mmol, 2 eq.) slowly. The mixture was stirred at r.t. for 3 h before the solvent was removed and water was added. The residue was extracted with ethyl acetate and the organic layers were dried over MgSO₄, filtered and concentrated to afford a colourless oil (262 mg, 89 %); ¹H NMR [CDCl₃, 400 MHz, 298 K] δ 7.44-7.36 (m, 5H, 5 x CH_{Ar}), 7.35 (d, 1H, ⁴J(HH) = 2.7 Hz, CH_{Ar}), 7.23 (dd, 1H, ⁴J(HH) = 2.7 Hz, ³J(HH) = 8.6 Hz, CH_{Ar}), 6.89 (d, 1H, ³J(HH) = 8.6 Hz, CH_{Ar}), 5.12 (s, 2H, CH₂), 4.73 (d br, 2H, ³J(HH) = 4.7 Hz, CH₂OH), 2.21 (t br, 1H, ³J(HH) = 4.7 Hz, OH); ¹³C{¹H} NMR [CDCl₃] 154.9 (C_{Ar}O), 136.3 (C_{Ar}), 131.3 (C_{Ar}), 128.8 (2 x CH_{Ar}), 128.5 (CH_{Ar}), 128.3 (2 x CH_{Ar}), 127.4 (2 x CH_{Ar}), 126.0 (C_{Ar}), 112.8 (CH_{Ar}), 70.4 (CH₂), 61.4 (CH₂OH); MS [ESI] m/z 271.05 (M+Na)⁺

8.9.4. 2-benzyloxy-5-chloro benzaldehyde dimethyl acetal



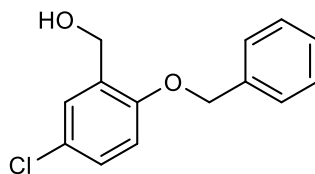
To a solution of 2-benzyloxy-5-chloro benzaldehyde (1.40 g, 5.68 mmol, 1 eq.) in MeOH (50 mL) was added NaBH₄ (430 mg, 11.4 mmol, 2 eq.) slowly. The mixture was stirred at r.t. for 2 h. The solvent was removed and water was added. The mixture was extracted with ethyl acetate and the organic layers were dried over MgSO₄, filtered and concentrated to afford a white solid (1.43 g, 86 %); ¹H NMR [CDCl₃, 400 MHz, 298 K] δ 7.55 (d, 1H, ⁴J(HH) = 2.7 Hz, CH_{Ar}), 7.46-7.34 (m, 5H, 5 x CH_{Ar}), 7.24 (dd, 1H, ⁴J(HH) = 2.7 Hz, ³J(HH) = 8.8 Hz, CH_{Ar}), 6.88 (d, 1H, ³J(HH) = 8.8 Hz, CH_{Ar}), 5.69 (s, 1H, CH), 5.13 (s, 2H, CH₂O), 3.39 (s, 6H, 2 x CH₃); ¹³C{¹H} NMR [CDCl₃] 154.7 (C_{Ar}O), 136.7 (C_{Ar}), 129.3 (CH_{Ar}), 128.6 (2 x CH_{Ar}), 128.5 (C_{Ar}), 128.0 (CH_{Ar}), 127.6 (CH_{Ar}), 127.1 (2 x CH_{Ar}), 125.9 (C_{Ar}), 113.6 (CH_{Ar}), 98.7 (CH), 70.5 (CH₂), 53.9 (2 x CH₃)

8.9.5. 2-benzyloxy-5-chloro benzaldehyde



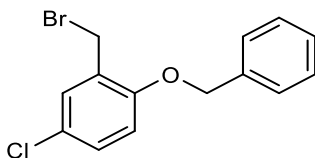
To a solution of 2-benzyloxy-5-chloro benzaldehyde dimethyl acetal (1.43 g, 4.88 mmol, 1 eq.) in toluene (50 mL) was added *paratoluenesulfonic acid* (90 mg, 10 mol%) and the mixture was stirred at r.t. for 18 h. Saturated aqueous NaHCO_3 was added and the mixture was extracted with ethyl acetate. The organic layers were dried over MgSO_4 , filtered and concentrated. The resulting residue was triturated with hexane and filtered to afford a white solid (675 mg, 56 %): $^1\text{H NMR}$ [CDCl_3 , 400 MHz, 298 K] δ 10.50 (s, 1H, CHO), 7.83 (d, 1H, $^4J(\text{HH}) = 2.7$ Hz, CH_{Ar}), 7.49 (dd, 1H, $^4J(\text{HH}) = 2.7$ Hz, $^3J(\text{HH}) = 8.8$ Hz, CH_{Ar}), 7.46-7.37 (m, 5H, 5 x CH_{Ar}), 7.03 (d, 1H, $^3J(\text{HH}) = 8.8$ Hz, CH_{Ar}), 5.21 (s, 2H, CH_2); $^{13}\text{C}\{^1\text{H}\}$ NMR [CDCl_3] 188.4 (C=O), 159.5 ($\text{C}_{\text{Ar}}\text{O}$), 135.6 (C_{Ar}), 135.4 (CH_{Ar}), 128.8 (2 x CH_{Ar}), 128.5 (CH_{Ar}), 128.1 (CH_{Ar}), 127.4 (2 x CH_{Ar}), 126.8 (C_{Ar}), 126.1 (C_{Ar}), 114.8 (CH_{Ar}), 71.0 (CH_2); MS [ESI] m/z 269.03 ($\text{M}+\text{Na}$)⁺

8.9.6. 2-benzyloxy-5-chloro benzyl alcohol



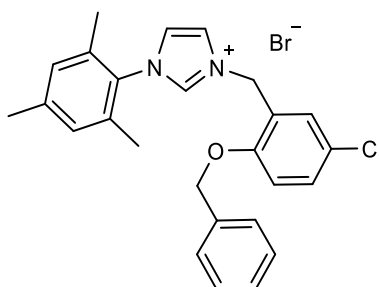
To a solution of 2-benzyloxy-5-chloro benzaldehyde (600 mg, 2.43 mmol, 1 eq.) in THF (10 mL) was added NaBH₄ (184 mg, 4.86 mmol, 2 eq.) and the solution was stirred at room temperature for 1 h. Water and ethyl acetate were added and the organic layers were washed with brine, dried over MgSO₄, filtered and concentrated to afford a colourless oil (600 mg, 99 %); ¹H NMR [CDCl₃, 400 MHz, 298 K] δ 7.44-7.36 (m, 5H, 5 x CH_{Ar}), 7.35 (d, 1H, ⁴J(HH) = 2.7 Hz, CH_{Ar}), 7.23 (dd, 1H, ⁴J(HH) = 2.7 Hz, ³J(HH) = 8.6 Hz, CH_{Ar}), 6.89 (d, 1H, ³J(HH) = 8.6 Hz, CH_{Ar}), 5.12 (s, 2H, CH₂), 4.73 (d br, 2H, ³J(HH) = 4.7 Hz, CH₂OH), 2.21 (t br, 1H, ³J(HH) = 4.7 Hz, OH); ¹³C{¹H} NMR [CDCl₃] 154.9 (C_{Ar}O), 136.3 (C_{Ar}), 131.3 (C_{Ar}), 128.8 (2 x CH_{Ar}), 128.5 (CH_{Ar}), 128.3 (2 x CH_{Ar}), 127.4 (2 x CH_{Ar}), 126.0 (C_{Ar}), 112.8 (CH_{Ar}), 70.4 (CH₂), 61.4 (CH₂OH); MS [ESI] m/z 271.05 (M+Na)⁺

8.9.7. 2-benzyloxy-5-chloro benzyl bromide



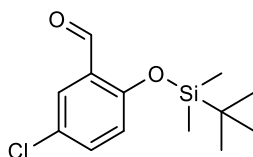
To a solution of 2-benzyloxy-5-chloro benzyl alcohol (262 mg, 1.05 mmol, 1 eq.) in DCM (5 mL) under N₂ at ~ 5 °C was added PBr₃ (0.2 mL, 2.11 mmol, 2 eq.). The mixture was stirred at r.t. for 2 h. Cold water was added and the mixture was extracted with ethyl acetate. The organic layers were dried over MgSO₄, filtered, concentrated and purified by column chromatography (silica, hexane: ethyl acetate, 8: 2) to afford a white solid (214 mg, 65 %); ¹H NMR [CDCl₃, 500 MHz, 298 K] δ 7.49-7.45 (m, 2H, 2 x CH_{Ar}), 7.43-7.38 (m, 2H, 2 x CH_{Ar}), 7.37-7.32 (m, 1H, CH_{Ar}), 7.34 (d, 1H, ⁴J(HH) = 2.9 Hz, CH_{Ar}), 7.21 (dd, 1H, ⁴J(HH) = 2.9 Hz, ³J(HH) = 8.6 Hz, CH_{Ar}), 6.85 (d, 1H, ³J(HH) = 8.6 Hz, CH_{Ar}), 5.14 (s, 2H, CH₂), 4.53 (s, 2H, CH₂Br); ¹³C{¹H} NMR [CDCl₃] 155.1 (C_{Ar}O), 136.4 (C_{Ar}), 130.7 (CH_{Ar}), 129.7 (CH_{Ar}), 128.7 (2 x CH_{Ar}), 128.2 (C_{Ar}), 128.1 (CH_{Ar}), 127.2 (2 x CH_{Ar}), 125.7 (C_{Ar}), 113.6 (CH_{Ar}), 70.5 (CH₂O), 27.8 (CH₂Br)

8.9.8. 3-(2-benzyloxy-5-chloro benzyl)-1-(2,4,6-trimethylphenyl) imidazolium bromide



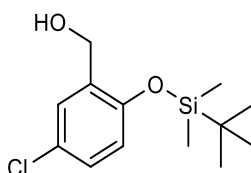
2-benzyloxy-5-chloro benzyl bromide (214 mg, 0.69 mmol, 1 eq.) and 1-(2,4,6-trimethylphenyl)-1H-imidazole (128 mg, 0.69 mmol, 1 eq.) were dissolved in toluene (5 mL) and heated at 70 °C for 16 h. The solution was cooled to room temperature and the white precipitate was filtered. The filtrate was concentrated and the resulting residue was triturated with diethyl ether. The white precipitate that formed was filtered, washed with diethyl ether and air dried to afford a white solid (288 mg, 84 %); ^1H NMR [DMSO, 400 MHz, 298 K] δ 9.38 (ps t, 1H, $^4J(\text{HH}) = 1.5$ Hz, $\text{CH}_{\text{imidazole}}$), 8.00 (ps t, 1H, $^4J(\text{HH}) = 1.8$ Hz, $\text{CH}_{\text{imidazole}}$), 7.91 (ps t, 1H, $^4J(\text{HH}) = 1.8$ Hz, $\text{CH}_{\text{imidazole}}$), 7.52-7.46 (m, 2H, 2 x CH_{Ar}), 7.42-7.30 (m, 5H, 5 x CH_{Ar}), 7.20 (d, 1H, $^3J(\text{HH}) = 8.8$ Hz, CH_{Ar}), 7.12 (s, 2H, 2 x $\text{CH}_{\text{mesityl}}$), 5.51 (s, 2H, CH_2), 5.21 (s, 2H, CH_2), 2.32 (s, 3H, CH_3), 1.92 (s, 6H, 2 x CH_3); $^{13}\text{C}\{^1\text{H}\}$ NMR [DMSO] 155.6 (C_{Ar}), 140.7 (C_{Ar}), 138.2 ($\text{CH}_{\text{imidazole}}$), 136.8 (C_{Ar}), 134.7 (2 x C_{Ar}), 131.6 (C_{Ar}), 130.7 (CH_{Ar}), 130.8 (CH_{Ar}), 129.7 (2 x $\text{CH}_{\text{mesityl}}$), 129.0 (2 x CH_{Ar}), 128.3 (CH_{Ar}), 127.8 (2 x CH_{Ar}), 124.4 ($\text{CH}_{\text{imidazole}}$), 123.7 ($\text{CH}_{\text{imidazole}}$), 123.6 (C_{Ar}), 114.7 (CH_{Ar}), 70.1 (CH_2), 48.7 (CH_2), 21.1 (CH_3), 17.3 (2 x CH_3); MS [ESI] m/z 417.3 ($\text{M}-\text{Br}$) $^+$

8.9.9. 2-(*tert*-butyldimethylsilyloxy)-5-chloro benzaldehyde



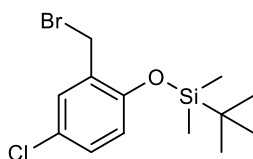
To a solution of 5-chloro-2-hydroxybenzaldehyde (1.5 g, 9.58 mmol, 1 eq.) in DCM (20 mL) was added triethylamine (2.0 mL, 14.4 mmol, 1.5 eq.) followed by TBDMSCl (2.17 g, 14.4 mmol, 1.5 eq.) and the mixture was stirred at r.t. for 20 h. Water was added and the mixture was extracted with DCM. The organic layers were washed with brine, dried over MgSO₄, filtered and concentrated. The resulting residue was purified by column chromatography (silica, hexane: ethyl acetate, 9: 1) to afford an off white solid (2.36 g, 91 %); ¹H NMR [CDCl₃, 400 MHz, 298 K] δ 10.40 (s, 1H, CHO), 7.79 (d, 1H, ⁴J(HH) = 2.8 Hz, CH_{Ar}), 7.43 (dd, 1H, ⁴J(HH) = 2.8 Hz, ³J(HH) = 8.8 Hz, CH_{Ar}), 6.86 (d, 1H, ³J(HH) = 8.8 Hz, CH_{Ar}), 1.04 (s, 9H, 3 x CH₃), 0.30 (s, 6H, 2 x CH₃); ¹³C{¹H} NMR [CDCl₃] 188.9 (C=O), 157.4 (C_{Ar}O), 135.4 (CH_{Ar}), 128.1 (C_{Ar}), 127.9 (CH_{Ar}), 127.1 (C_{Ar}), 121.7 (CH_{Ar}), 25.6 (3 x CH₃), 18.4 (C(CH₃)₃), -4.3 (2 x CH₃); MS [ESI] m/z 293.07 (M+Na)⁺

8.9.10. 2-(*tert*-butyldimethylsilyloxy)-5-chloro benzyl alcohol



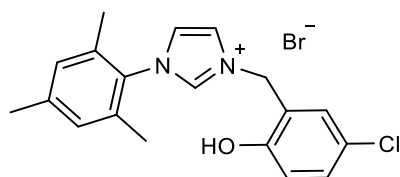
To a solution of 2-(*tert*-butyldimethylsilyloxy)-5-chloro benzaldehyde (2.26 g, 8.34 mmol, 1 eq.) in MeOH (30 mL) at ~ 15 °C was added NaBH₄ (474 mg, 12.5 mmol, 1.5 eq.) portionwise and the mixture was stirred at r.t. for 30 mins. MeOH was removed under reduced pressure and water was added. The mixture was extracted with DCM and the organic layers were dried over MgSO₄, filtered and concentrated to afford a pale yellow oil (1.97 g, 86 %); ¹H NMR [CDCl₃, 500 MHz, 298 K] δ 7.32 (d, 1H, ⁴J(HH) = 2.8 Hz, CH_{Ar}), 7.12 (dd, 1H, ⁴J(HH) = 2.8 Hz, ³J(HH) = 8.6 Hz, CH_{Ar}), 6.73 (d, 1H, ³J(HH) = 8.6 Hz, CH_{Ar}), 4.64 (d, 2H, ³J(HH) = 6.1 Hz, CH₂), 1.97 (t, 1H, ³J(HH) = 6.1 Hz, OH), 1.01 (s, 9H, 3 x CH₃), 0.24 (s, 6H, 2 x CH₃); ¹³C{¹H} NMR [CDCl₃] 151.9 (C_{Ar}O), 133.2 (C_{Ar}), 128.4 (CH_{Ar}), 128.2 (CH_{Ar}), 126.2 (C_{Ar}), 119.5 (CH_{Ar}), 61.3 (CH₂OH), 25.7 (3 x CH₃), 18.2 (C(CH₃)₃), -4.2 (2 x CH₃); MS [ESI] m/z 295.09 (M+Na)⁺

8.9.11. 2-(*tert*-butyldimethylsilyloxy)-5-chloro benzyl bromide



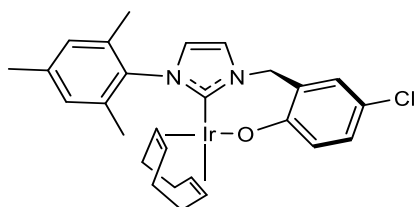
To a solution of 2-(*tert*-butyldimethylsilyloxy)-5-chloro benzyl alcohol (1.85 g, 6.78 mmol, 1 eq.) in DCM (30 mL) under N₂ in an ice-water bath, was added PBr₃ (1.16 mL, 12.2 mmol, 1.8 eq.) dropwise and the mixture was stirred for 1 h. The mixture was poured into ice and ethyl acetate was added. The mixture was extracted with ethyl acetate and the organic layers were dried over MgSO₄, filtered and concentrated. The product was purified by column chromatography (silica, hexane: ethyl acetate, 9: 1) to afford a pale yellow oil (700 mg, 31 %); ¹H NMR [CDCl₃, 400 MHz, 298 K] δ 7.33 (d, 1H, ⁴J(HH) = 2.7 Hz, CH_{Ar}), 7.15 (dd, 1H, ⁴J(HH) = 2.7 Hz, ³J(HH) = 8.7 Hz, CH_{Ar}), 6.76 (d, 1H, ³J(HH) = 8.7 Hz, CH_{Ar}), 4.47 (s, 2H, CH₂), 1.07 (s, 9H, 3 x CH₃), 0.30 (s, 6H, 2 x CH₃); ¹³C{¹H} NMR [CDCl₃] 152.5 (C_{Ar}O), 130.9 (CH_{Ar}), 130.1 (C_{Ar}), 129.7 (CH_{Ar}), 125.9 (C_{Ar}), 119.8 (CH_{Ar}), 28.0 (CH₂), 25.8 (3 x CH₃), 18.3 (C(CH₃)₃), -4.2 (2 x CH₃)

8.9.12. 3-(5-chloro-2-hydroxybenzyl)-1-(2,4,6-trimethylphenyl) imidazolium bromide



2-(*tert*-butyldimethylsilyloxy)-5-chloro benzyl bromide (400 mg, 1.19 mmol, 1 eq.) and mesityl imidazole (222 mg, 1.19 mmol, 1 eq.) were dissolved in toluene (10 mL) and the solution was heated at 110 °C for 48 h. the solution was cooled to r.t. and diethyl ether was added. The precipitate was filtered and washed with diethyl ether to afford a brown solid (360 mg, 74 %); ^1H NMR [DMSO, 400 MHz, 298 K] δ 10.43 (s, 1H, OH), 9.51 (s br, 1H, CH_{imidazole}), 7.99 (ps t, 1H, $^4J(\text{HH}) = 1.5$ Hz, CH_{imidazole}), 7.91 (ps t, 1H, $^4J(\text{HH}) = 1.5$ Hz, CH_{imidazole}), 7.48 (d, 1H, $^4J(\text{HH}) = 2.6$ Hz, CH_{Ar}), 7.32 (dd, 1H, $^4J(\text{HH}) = 2.6$ Hz, $^3J(\text{HH}) = 8.6$ Hz, CH_{Ar}), 7.16 (s, 2H, 2 x CH_{mesityl}), 6.92 (d, 1H, $^3J(\text{HH}) = 8.6$ Hz, CH_{Ar}), 5.40 (s, 2H, CH₂), 2.34 (s, 3H, CH₃), 2.01 (s, 6H, 2 x CH₃); $^{13}\text{C}\{^1\text{H}\}$ NMR [DMSO] δ 155.5 (C_{Ar}), 140.7 (C_{Ar}), 138.4 (CH_{imidazole}), 134.7 (2 x C_{Ar}), 131.5 (C_{Ar}), 130.6 (CH_{Ar}), 130.5 (CH_{Ar}), 129.5 (2 x CH_{mesityl}), 124.4 (CH_{imidazole}), 123.5 (CH_{imidazole}), 123.0 (C_{Ar}), 122.7 (C_{Ar}), 117.5 (CH_{Ar}), 48.9 (CH₂), 21.0 (CH₃), 17.3 (2 x CH₃); MS [ESI] m/z 327.3 (M-Br)⁺

8.9.13. Iridium(I) (3-(5-chloro-2-methylene phenolate)-1-(2,4,6-trimethylphenyl) imidazolylidene)(cyclooctadiene), 4



To a Schlenk flask containing 3-(5-chloro-2-hydroxybenzyl)-1-(2,4,6-trimethylphenyl) imidazolium bromide (150 mg, 0.368 mmol, 1 eq), silver(I) oxide (171 mg, 0.736 mmol, 2 eq.) and molecular sieves 4 Å (600 mg) under an atmosphere of N₂ in the dark, was added DCM (10 mL) and the mixture was stirred at r.t. for 3 h. To this was then added [Ir(COD)Cl]₂ (124 mg, 0.184 mmol, 0.5 eq) and the mixture was stirred at r.t. for a further 1 h. The mixture was then filtered over Celite and silica, washed with DCM: acetone, 4: 1 and concentrated under reduced pressure to afford an orange solid (190 mg, 83 %); ¹H NMR [CD₂Cl₂, 400 MHz, 243 K] δ 7.09 (d, 1H, ⁴J(HH) = 2.8 Hz, CH_{Ar}), 7.07 (d, 1H, ³J(HH) = 1.9 Hz, CH_{imidazole}), 7.03 (s br, 1H, CH_{mesityl}), 6.97 (dd, 1H, ⁴J(HH) = 2.8 Hz, ³J(HH) = 8.9 Hz), 6.94 (s br, 1H, CH_{mesityl}), 6.69 (d, 1H, ³J(HH) = 1.9 Hz, CH_{imidazole}), 6.51 (d, 1H, ³J(HH) = 8.9 Hz, CH_{Ar}), 6.44 (d, 1H, ²J(HH) = 13.7 Hz, CH₂ linker), 4.60 (d, 1H, ²J(HH) = 13.7 Hz, CH₂ linker), 4.32 (m, 1H, CH_{COD}), 4.27 (m, 1H, CH_{COD}), 3.09 (m, 1H, CH_{COD}), 2.35 (s, 3H, CH₃), 2.26 (m, 1H, CH_{COD}), 2.16 – 2.09 (m, 2H, CH_{2(COD)}), 2.01 (s br, 3H, CH₃), 1.98 (m, 1H, CH_{2(COD)}), 1.96 (s br, 3H, CH₃), 1.69 – 1.45 (m, 4H, 2 x CH_{2(COD)}), 1.36 (m, 1H, CH_{2(COD)}); ¹³C{¹H} NMR [CD₂Cl₂, 248 K] δ 175.0 (C-Ir), 166.9 (C-OIr), 138.8 (C_{Ar}), 136.2 (C_{Ar}), 135.8 (C_{Ar}), 134.2 (C_{Ar}), 129.3 (CH_{Ar}), 129.1 (CH_{mesityl}), 128.6 (CH_{Ar}), 128.3 (CH_{mesityl}), 125.6 (C_{Ar}), 123.3 (CH_{imidazole}), 122.4 (CH_{Ar}), 119.5 (CH_{imidazole}), 116.7 (C_{Ar}), 84.4 (CH), 84.1 (CH), 50.9 (CH₂), 47.5 (CH), 46.4 (CH), 34.5 (CH₂), 33.9 (CH₂), 28.9 (CH₂), 28.3 (CH₂), 21.0 (CH₃), 18.6 (CH₃), 17.7 (CH₃); MS [ESI] m/z 627.2 (M⁺)

UV-vis absorption data for complex **4** at seven different concentrations are given in Table 59 with the corresponding absorption spectra shown in Figure 253.

*Table 59: Concentration and absorbance values for seven samples of **4** in DCM at different concentrations*

Sample	Concentration / $\mu\text{mol dm}^{-3}$	Absorbance		
		At 381 nm	At 430 nm	At 491 nm
A	319	0.79	0.51	0.16
B	256	0.64	0.42	0.13
C	204	0.52	0.34	0.11
D	164	0.42	0.28	0.10
E	131	0.34	0.23	0.08
F	105	0.28	0.19	0.07
G	63	0.17	0.12	0.05

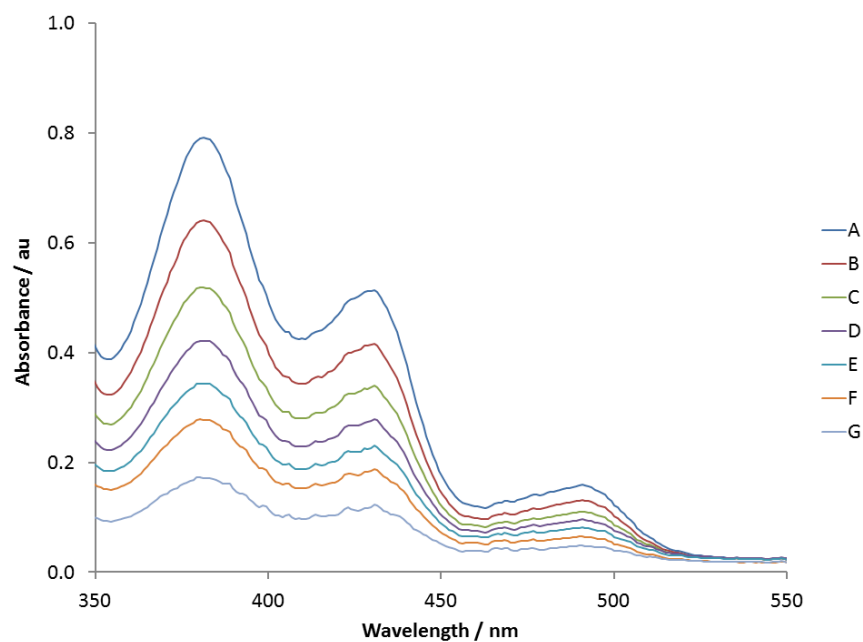


*Figure 253: Visible region of the absorption spectra for **4** in DCM at different concentrations as listed in Table 59*

The calibration graph in Figure 254 was used to gain the molar absorption coefficients for the absorption bands of **4** as described in Section 2.6.1.

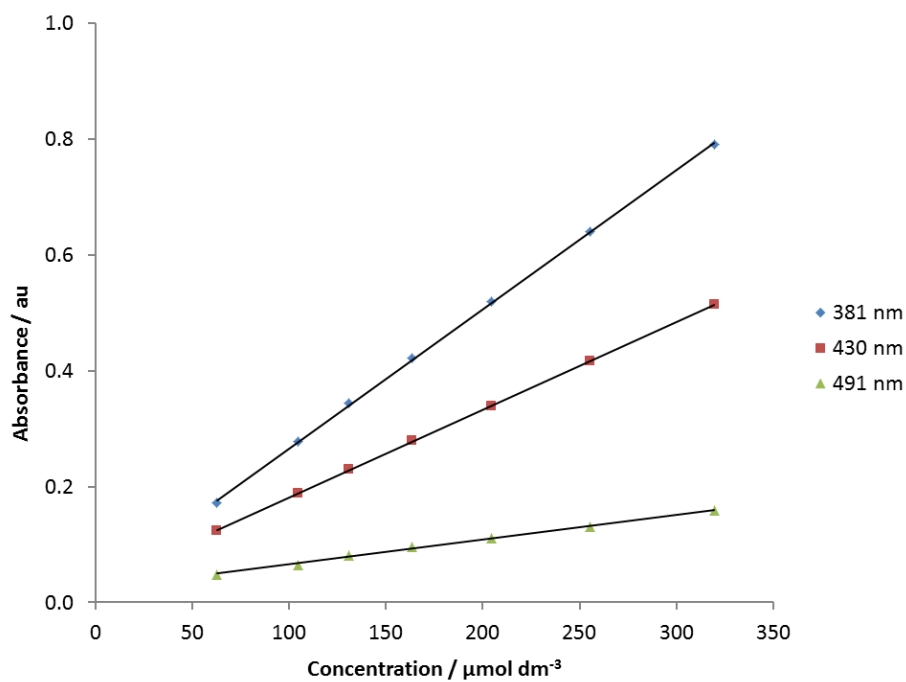
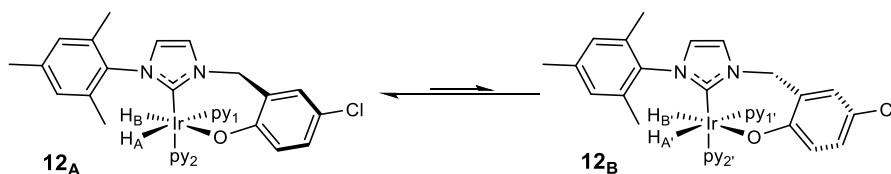


Figure 254: Calibration graph used to calculate the molar absorption coefficients for the three absorption bands of **4** at 381, 430 and 491 nm using the data in Table 59

8.9.14. Iridium(III) (3-(5-chloro-2-methylene phenolate)-1-(2,4,6-trimethylphenyl) imidazolylidene)(dihydride)(pyridine)₂, 12_A and 12_B



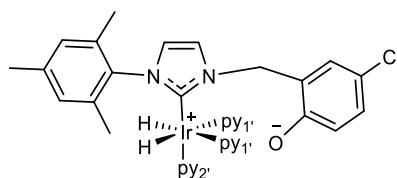
To a Young's NMR tube was added **4** (10 mg, 16 μmol , 1 eq.), pyridine (3.8 μL , 47 μmol , 3 eq.) and CD_2Cl_2 or CD_3OD (0.6 mL). The solution was then degassed three times on a high vacuum line using a freeze-thaw procedure with either liquid N_2 (for CD_2Cl_2) or a dry ice/acetone bath (for CD_3OD), before the addition of 3 bars of H_2 . The mixture was then left to react at r.t. for 2 days.

12_A: ^1H NMR [CD_2Cl_2 , 400 MHz, 298 K] δ 9.02 (m, 2H, 2 x $\text{CH}_{\text{py ortho}}$), 8.46 (m, 2H, 2 x $\text{CH}_{\text{py ortho}}$), 7.63 (m, 2H, 2 x $\text{CH}_{\text{py para}}$), 7.09 (d, 1H, $^3J(\text{HH}) = 2.1$ Hz, $\text{CH}_{\text{imidazole}}$), 7.07 (m, 2H, 2 x $\text{CH}_{\text{py meta}}$), 7.06 (d, 1H, $^4J(\text{HH}) = 3.2$ Hz, CH_{Ar}), 7.00 (dd, 1H, $^4J(\text{HH}) = 3.2$ Hz, $^3J(\text{HH}) = 8.7$ Hz, CH_{Ar}), 6.99 (s, 1H, $\text{CH}_{\text{mesityl}}$), 6.70 (d, 1H, $^3J(\text{HH}) = 8.7$ Hz, CH_{Ar}), 6.62 (s, 1H, $\text{CH}_{\text{mesityl}}$), 6.61 (d, 1H, $^3J(\text{HH}) = 2.1$ Hz, $\text{CH}_{\text{imidazole}}$), 5.95 (d br, 1H, $^2J(\text{HH}) = 12.0$ Hz, CH_2 linker), 4.48 (d br, 1H, $^2J(\text{HH}) = 12.0$ Hz, CH_2 linker), 2.33 (s, 3H, CH_3), 2.10 (s, 3H, CH_3), -22.08 (s br, 1H), -28.12 (d br, 1H, $^2J(\text{HH}) = 7.0$ Hz); $^{13}\text{C}\{^1\text{H}\}$ NMR [CD_2Cl_2] δ 168.8 (C-O), 154.9 ($\text{CH}_{\text{py ortho}}$), 154.0 ($\text{CH}_{\text{py ortho}}$), 137.5 (C_{Ar}), 135.1 ($\text{CH}_{\text{py para}}$), 128.7 (CH_{Ar}), 128.6 ($\text{CH}_{\text{mesityl}}$), 128.0 ($\text{CH}_{\text{mesityl}}$), 126.7 (C- NO_2), 124.2 (CH_{Ar}), 124.2 ($\text{CH}_{\text{py meta}}$), 122.8 (CH_{Ar}), 120.0 ($\text{CH}_{\text{imidazole}}$), 119.8 ($\text{CH}_{\text{imidazole}}$), 114.2 (C_{Ar}), 51.6 (CH_2), 20.7 (CH_3), 18.8 (CH_3)

12A: ^1H NMR [CD_3OD , 400 MHz, 298 K] δ 8.92 (m, 2H, 2 x $\text{CH}_{\text{py ortho}}$), 8.29 (m, 2H, 2 x $\text{CH}_{\text{py ortho}}$), 7.76 (m, 2H, 2 x $\text{CH}_{\text{py para}}$), 7.73 (m, 2H, 2 x $\text{CH}_{\text{py para}}$), 7.22 (d, 1H, $^4J(\text{HH}) = 2.3$ Hz, CH_{Ar}), 7.40 (d, 1H, $^3J(\text{HH}) = 2.0$ Hz, $\text{CH}_{\text{imidazole}}$), 7.18 (m, 2H, 2 x $\text{CH}_{\text{py meta}}$), 7.04 (dd, 1H, $^4J(\text{HH}) = 2.3$ Hz, $^3J(\text{HH}) = 8.6$ Hz, CH_{Ar}), 7.04 (m, 2H, 2 x $\text{CH}_{\text{py meta}}$), 7.00 (s br, 1H, ($\text{CH}_{\text{mesityl}}$)), 6.81 (d, 1H, $^3J(\text{HH}) = 8.6$ Hz, CH_{Ar}), 6.75 (d, 1H, $^3J(\text{HH}) = 2.0$ Hz, $\text{CH}_{\text{imidazole}}$), 6.56 (s br, 1H, $\text{CH}_{\text{mesityl}}$), 6.11 (d br, 1H, $^2J(\text{HH}) = 13.1$ Hz, CH_2 linker), 4.60 (d br, 1H, $^2J(\text{HH}) = 13.1$ Hz, CH_2 linker), 2.32 (s, 3H, CH_3), 2.13 (s, 3H, CH_3), 1.16 (s, 3H, CH_3), -21.72 (s br, 1H), -28.72 (s br, 1H); $^{13}\text{C}\{^1\text{H}\}$ NMR [CD_3OD] δ 166.9 (C-O), 154.8 ($\text{CH}_{\text{py ortho}}$), 154.1 ($\text{CH}_{\text{py ortho}}$), 137.4 (C_{Ar}), 136.3 (C_{Ar}), 135.7 ($\text{CH}_{\text{py para}}$), 135.5 (C_{Ar}), 135.1 ($\text{CH}_{\text{py para}}$), 128.9 (CH_{Ar}), 128.5 (C_{Ar}), 128.4 (CH_{Ar}), 128.2 ($\text{CH}_{\text{mesityl}}$), 127.7 ($\text{CH}_{\text{mesityl}}$), 124.4 ($\text{CH}_{\text{py meta}}$), 124.2 ($\text{CH}_{\text{py meta}}$), 123.4 (CH_{Ar}), 120.2 ($\text{CH}_{\text{imidazole}}$), 119.9 ($\text{CH}_{\text{imidazole}}$), 117.3 (C_{Ar}), 50.2 (CH_2), 19.6 (CH_3), 17.8 (CH_3), 15.9 (CH_3)

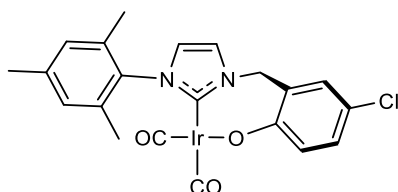
12B: ^1H NMR [CD_2Cl_2 , 400 MHz, 298 K] δ 8.81 (m, 2H, 2 x $\text{CH}_{\text{py ortho}}$), 8.75 (m, 2H, 2 x $\text{CH}_{\text{py ortho}}$), 7.65 (m, 1H, $\text{CH}_{\text{py para}}$), 7.60 (m, 2H, 2 x $\text{CH}_{\text{py para}}$), 7.22 (dd, 1H, $^4J(\text{HH}) = 2.7$ Hz, $^3J(\text{HH}) = 8.6$ Hz, CH_{Ar}), 7.19 (d, 1H, $^4J(\text{HH}) = 2.7$ Hz, CH_{Ar}), 7.03 (m, 2H, 2 x $\text{CH}_{\text{py meta}}$), 7.01 (m, 2H, 2 x $\text{CH}_{\text{py meta}}$), 6.96 (s, 1H, $\text{CH}_{\text{mesityl}}$), 6.86 (d, 1H, $^3J(\text{HH}) = 8.6$ Hz, CH_{Ar}), 6.50 (s, 1H, $\text{CH}_{\text{mesityl}}$), 5.76 (d, 1H, $^2J(\text{HH}) = 14.6$ Hz, CH_2 linker), 5.34 (d, 1H, $^2J(\text{HH}) = 14.6$ Hz, CH_2 linker), 2.26 (s, 3H, CH_3), 2.19 (s, 3H, CH_3), 1.81 (s, 3H, CH_3), -22.55 (d, 1H, $^2J(\text{HH}) = 8.0$ Hz), -25.50 (d, 1H, $^2J(\text{HH}) = 8.0$ Hz); $^{13}\text{C}\{^1\text{H}\}$ NMR [CD_2Cl_2] δ 155.7 ($\text{CH}_{\text{py ortho}}$), 154.2 ($\text{CH}_{\text{py ortho}}$), 135.4 ($\text{CH}_{\text{py para}}$), 135.2 ($\text{CH}_{\text{py para}}$), 130.7 (CH_{Ar}), 128.2 ($\text{CH}_{\text{mesityl}}$), 129.5 (CH_{Ar}), 124.4 ($\text{CH}_{\text{py meta}}$), 123.9 (CH_{Ar}), 119.6 (C_{Ar}), 52.2 (CH_2), 20.5 (CH_3), 18.2 (CH_3), 17.9 (CH_3)

8.9.15. Iridium(III) (3-(5-chloro-2-methylene phenoxy)-1-(2,4,6-trimethylphenyl) imidazolylidene)(dihydride)(pyridine)₃, 16



To a Young's NMR tube was added **4** (10 mg, 16 μmol , 1 eq.), pyridine (3.8 μL , 47 μmol , 3 eq.) and CD_3OD (0.6 mL). The solution was then degassed three times on a high vacuum line using a freeze-thaw procedure with a dry ice/acetone bath, before the addition of 3 bars of H_2 . The mixture was then left to react at r.t. for 2 days; ^1H NMR [CD_3OD , 400 MHz, 298 K] δ 8.44 (m, 2H, 2 x $\text{CH}_{\text{py ortho}}$), 8.23 (m, 2H, 2 x $\text{CH}_{\text{py ortho}}$), 7.85 (m, 2H, 2 x $\text{CH}_{\text{py para}}$), 7.81 (m, 2H, 2 x $\text{CH}_{\text{py para}}$), 7.26 (m, 2H, 2 x $\text{CH}_{\text{py meta}}$), 7.25 (d, 1H, $^4J(\text{HH}) = 2.3$ Hz, CH_{Ar}), 7.13 (m, 2H, 2 x $\text{CH}_{\text{py meta}}$), 7.06 (s br, 1H, $\text{CH}_{\text{imidazole}}$), 7.05 (dd, 1H, $^4J(\text{HH}) = 2.3$ Hz, $^3J(\text{HH}) = 8.6$ Hz, CH_{Ar}), 6.77 (s br, 2H, 2 x $\text{CH}_{\text{mesityl}}$), 6.68 (d, 1H, $^3J(\text{HH}) = 8.6$ Hz, CH_{Ar}), 6.63 (s br, 1H, $\text{CH}_{\text{imidazole}}$), 4.88 (s, 2H, CH_2 linker), 2.27 (s, 3H, CH_3), 2.13 (s, 6H, 2 x CH_3), -22.29 (s, 2H); $^{13}\text{C}\{^1\text{H}\}$ NMR [CD_3OD] δ 154.2 ($\text{CH}_{\text{py ortho}}$), 153.9 (C-O), 153.7 ($\text{CH}_{\text{py ortho}}$), 138.4 (C_{Ar}), 137.6 (C_{Ar}), 136.5 ($\text{CH}_{\text{py para}}$), 136.5 ($\text{CH}_{\text{py para}}$), 136.3 (2 x C_{Ar}), 128.5 (2 x $\text{CH}_{\text{mesityl}}$), 127.0 ($\text{CH}_{\text{imidazole}}$), 125.8 (C_{Ar}), 125.7 ($\text{CH}_{\text{py meta}}$), 125.4 ($\text{CH}_{\text{py meta}}$), 123.2 (C_{Ar}), 122.6 (CH_{Ar}), 121.5 (CH_{Ar}), 115.7 (CH_{Ar}), 48.0 (CH_2), 19.7 (CH_3), 17.4 (2 x CH_3)

8.9.16. Iridium(I) (3-(5-chloro-2-methylene phenolate)-1-(2,4,6-trimethylphenyl) imidazolylidene)(dicarbonyl), 19



Iridium(I) (3-(5-chloro-2-methylene phenolate)-1-(2,4,6-trimethylphenyl) imidazolylidene)(cyclooctadiene) (20 mg, 0.0348 mmol, 1eq.) was dissolved in DCM (2 mL) and the mixture was stirred at r.t. whilst CO was bubbled through for 2 min. Stirring under an atmosphere of CO was continued for 10 min before the solution was purged with N₂ and the solvent was removed. The residue was triturated with hexane to afford a beige solid (15 mg, 83 %); ¹H NMR [CD₂Cl₂, 500 MHz, 298 K] δ 7.21 (d, 1H, ³J(HH) = 1.9 Hz, CH_{imidazole}), 7.15 (d, 1H, ⁴J(HH) = 2.8 Hz, CH_{Ar}), 7.08 (dd, 1H, ⁴J(HH) = 2.8 Hz, ³J(HH) = 8.8 Hz, CH_{Ar}), 7.04 (s, 2H, 2 x CH_{mesityl}), 6.90 (d, 1H, ³J(HH) = 1.9 Hz, CH_{imidazole}), 6.68 (d, 1H, ³J(HH) = 8.8 Hz, CH_{Ar}), 5.28 (s br, 2H, CH₂), 2.39 (s, 3H, CH₃), 2.00 (s, 6H, 2 x CH₃); ¹³C{¹H} NMR [CD₂Cl₂] δ 182.2 (C=O), 173.3 (C-Ir), 169.2 (C=O), 164.4 (OC_{Ar}), 139.7 (C_{Ar}), 135.4 (2 x C_{Ar}), 129.8 (CH_{Ar}), 129.1 (2 x CH_{mesityl}), 128.6 (C_{Ar}), 128.4 (CH_{Ar}), 125.6 (C_{Ar}), 123.4 (CH_{imidazole}), 122.9 (CH_{Ar}), 120.9 (CH_{imidazole}), 119.1 (C_{Ar}), 50.7 (CH₂), 20.8 (CH₃), 17.9 (2 x CH₃); MS [ESI] m/z 575.0 (M+H)⁺; IR ν_{CO} (cm⁻¹): 2058.9, 1974.8

Abbreviations

ALTADENA	Adiabatic Longitudinal Transport After Dissociation Engenders Net Alignment
BINAP	2,2'-bis(diphenylphosphino)-1,1'-binaphthyl
^t Bu	<i>Tert</i> -butyl
Bz	Benzyl
COA	Cyclooctane
COD	Cyclooctadiene
COE	Cyclooctene
CORM	CO-Releasing Molecule
COSY	Correlation Spectroscopy
Cy	Cyclohexyl
DCM	Dichloromethane
DFT	Density Functional Theory
DMF	Dimethylformamide
DNP	Dynamic Nuclear Polarisation
EPR	Electron Paramagnetic Resonance
EtOH	Ethanol
ESI	Electrospray Ionisation
EXSY	Exchange Spectroscopy
HMBC	Heteronuclear Multiple Bond Correlation
HMQC	Heteronuclear Multiple Quantum Correlation
IMes	1,3-bis(2,4,6-trimethylphenyl)imidazole-2-ylidene
INEPT	Insensitive Nuclei Enhanced by Polarisation Transfer

LCMS	Liquid Chromatography Mass Spectrometry
LIFDI	Liquid Injection Field Desorption Ionisation
MeOH	Methanol
MRI	Magnetic Resonance Imaging
MS	Mass Spectrometry
NHC	N-Heterocyclic Carbene
NMR	Nuclear Magnetic Resonance
nOe	Nuclear Overhauser Effect
NOESY	Nuclear Overhauser Effect Spectroscopy
OPSY	Only <i>Parahydrogen</i> Spectroscopy
ORTEP	Oak Ridge Thermal Ellipsoid Plot Program
PASADENA	<i>Parahydrogen</i> And Synthesis Allow Dramatically Enhanced Nuclear Alignment
Ph	Phenyl
<i>p</i> -H ₂	<i>Parahydrogen</i>
PHIP	<i>Para</i> Hydrogen Induced Polarisation
PHOX	Phosphinooxazoline-type ligand
ⁱ Pr	Isopropyl
PTF	Polarisation Transfer Field
py	Pyridine
SABRE	Signal Amplification By Reversible Exchange
THF	Tetrahydrofuran
UV-vis	Ultraviolet-visible light
XRD	X-ray Diffraction

References

1. Green, R. A.; Adams, R. W.; Duckett, S. B.; Mewis, R. E.; Williamson, D. C.; Green, G. G. R., *Prog. Nucl. Magn. Reson. Spectrosc.* **2012**, *67*, 1-48.
2. Adams, R. W.; Aguilar, J. A.; Atkinson, K. D.; Cowley, M. J.; Elliott, P. I. P.; Duckett, S. B.; Green, G. G. R.; Khazal, I. G.; Lopez-Serrano, J.; Williamson, D. C., *Science* **2009**, *323*, 1708-1711.
3. Lisitza, N.; Muradian, I.; Frederick, E.; Patz, S.; Hatabu, H.; Chekmenev, E. Y., *J. Chem. Phys.* **2009**, *131*, 044508 1-5.
4. Walker, T. G.; Happer, W., *Rev. Mod. Phys.* **1997**, *69*, 629-642.
5. Suter, D., *J. Magn. Reson.* **1992**, *99*, 495-506.
6. Happer, W., *Rev. Mod. Phys.* **1972**, *44*, 169-249.
7. Nikolaou, P.; Coffey, A. M.; Walkup, L. L.; Gust, B. M.; Whiting, N.; Newton, H.; Barcus, S.; Muradyan, I.; Dabaghyan, M.; Moroz, G. D.; Rosen, M. S.; Patz, S.; Barlow, M. J.; Chekmenev, E. Y.; Goodson, B. M., *Proc. Natl. Acad. Sci. U.S.A.* **2013**, *110*, 14150-14155.
8. Nikolaou, P.; Goodson, B. M.; Chekmenev, E. Y., *Chem. Eur. J.* **2015**, *21*, 3156-3166.
9. Overhauser, A. W., *Phys. Rev.* **1953**, *92*, 411-415.
10. Maly, T.; Debelouchina, G. T.; Bajaj, V. S.; Hu, K. N.; Joo, C. G.; Mak-Jurkauskas, M. L.; Sirigiri, J. R.; van der Wel, P. C. A.; Herzfeld, J.; Temkin, R. J.; Griffin, R. G., *J. Chem. Phys.* **2008**, *128*, 052211 1-19.
11. Wolber, J.; Ellner, F.; Fridlund, B.; Gram, A.; Johannesson, H.; Hansson, G.; Hansson, L. H.; Lerche, M. H.; Mansson, S.; Servin, R.; Thaning, M.; Golman, K.; Ardenkjaer-Larsen, J. H., *Nucl. Instr. Meth. Phys. Res.* **2004**, *526*, 173-181.
12. Abragam, A.; Goldman, M., *Rep. Prog. Phys.* **1978**, *41*, 395-467.

13. Wollan, D. S., *Phys. Rev. B* **1976**, *13*, 3671-3685.
14. Wollan, D. S., *Phys. Rev. B* **1976**, *13*, 3686-3696.
15. Roe, D. C.; Kating, P. M.; Krusic, P. J.; Smart, B. E., *Top. Catal.* **1998**, *5*, 133-147.
16. Duckett, S. B.; Wood, N. J., *Coord. Chem. Rev.* **2008**, *252*, 2278-2291.
17. Bargon, J.; Kandels, J.; Woelk, K., *Angew. Chem. Int. Ed. Engl.* **1990**, *29*, 58-59.
18. Berlinsky, A. J.; Hardy, W. N., *Phys. Rev. B* **1973**, *8*, 5013-5017.
19. Motizuki, K.; Nagamiya, T., *J. Phys. Soc. Jpn.* **1956**, *11*, 93-104.
20. Bowers, C. R.; Weitekamp, D. P., *Phys. Rev. Lett.* **1986**, *57*, 2645-2648.
21. Jang, M.; Duckett, S. B.; Eisenberg, R., *Organometallics* **1996**, *15*, 2863-2865.
22. Koch, A.; Ulrich, C.; Bargon, J., *Tetrahedron* **2000**, *56*, 3177-3179.
23. de Frémont, P.; Marion, N.; Nolan, S. P., *Coord. Chem. Rev.* **2009**, *253*, 862-892.
24. Fischer, E. O.; Maasböl, A., *Angew. Chem. Int. Ed. Engl.* **1964**, *3*, 580-581.
25. Dötz, K. H.; Stendel, J., *Chem. Rev.* **2009**, *109*, 3227-3274.
26. Bourissou, D.; Guerret, O.; Gabbaï, F. P.; Bertrand, G., *Chem. Rev.* **2000**, *100*, 39-92.
27. Montgomery, C. D., *J. Chem. Educ.* **2015**, *92*, 1653-1660.
28. Arduengo, A. J.; Harlow, R. L.; Kline, M., *J. Am. Chem. Soc.* **1991**, *113*, 361-363.
29. Huang, J.; Jafarpour, L.; Hillier, A. C.; Stevens, E. D.; Nolan, S. P., *Organometallics* **2001**, *20*, 2878-2882.
30. Tolman, C. A., *Chem. Rev.* **1977**, *77*, 313-348.
31. Crabtree, R. H., *J. Organomet. Chem.* **2005**, *690*, 5451-5457.
32. Schrock, R. R., *J. Am. Chem. Soc.* **1974**, *96*, 6796-6797.

33. Schwab, P.; France, M. B.; Ziller, J. W.; Grubbs, R. H., *Angew. Chem. Int. Ed. Engl.* **1995**, *34*, 2039-2041.
34. Scholl, M.; Ding, S.; Lee, C. W.; Grubbs, R. H., *Org. Lett.* **1999**, *1*, 953-956.
35. Vougioukalakis, G. C.; Grubbs, R. H., *Chem. Rev.* **2009**, *110*, 1746-1787.
36. Chakraborty, S.; Bhattacharya, P.; Dai, H.; Guan, H., *Acc. Chem. Res.* **2015**, *48*, 1995-2003.
37. Prakasham, A. P.; Ghosh, P., *Inorg. Chim. Acta* **2015**, *431*, 61-100.
38. Nelson, D. J., *Eur. J. Inorg. Chem.* **2015**, *2015*, 2012-2027.
39. Bagal, D. B.; Bhanage, B. M., *Adv. Synth. Catal.* **2015**, *357*, 883-900.
40. Younus, H. A.; Su, W.; Ahmad, N.; Chen, S.; Verpoort, F., *Adv. Synth. Catal.* **2015**, *357*, 283-330.
41. Xie, J.-H.; Bao, D.-H.; Zhou, Q.-L., *Synthesis-Stuttgart* **2015**, *47*, 460-471.
42. Pritchard, J.; Filonenko, G. A.; van Putten, R.; Hensen, E. J. M.; Pidko, E. A., *Chem. Soc. Rev.* **2015**, *44*, 3808-3833.
43. O, W. W. N.; Lough, A. J.; Morris, R. H., *Organometallics* **2013**, *32*, 3808-3818.
44. Crabtree, R., *Acc. Chem. Res.* **1979**, *12*, 331-337.
45. Bayne, J. M.; Stephan, D. W., *Chem. Soc. Rev.* **2016**, *45*, 765-774.
46. Stephan, D. W., *Science* **2016**, *354*, aaf7229 1-8.
47. Courtemanche, M. A.; Pulis, A. P.; Rochette, E.; Legare, M. A.; Stephan, D. W.; Fontaine, F. G., *Chem. Commun.* **2015**, *51*, 9797-9800.
48. Longobardi, L. E.; Russell, C. A.; Green, M.; Townsend, N. S.; Wang, K.; Holmes, A. J.; Duckett, S. B.; McGrady, J. E.; Stephan, D. W., *J. Am. Chem. Soc.* **2014**, *136*, 13453-13457.
49. Sabatier, P.; Senderens, J. B., *Comptes Rendus Acad. Sci.* **1900**, *131*, 187-190.

50. Sabatier, P.; Senderens, J. B., *Comptes Rendus Acad. Sci.* **1901**, 132, 210-212.
51. Sabatier, P.; Mailhe, A., *Comptes Rendus Acad. Sci.* **1904**, 138, 245-249.
52. Sabatier, P.; Mailhe, A., *Comptes Rendus Acad. Sci.* **1907**, 144, 784-786.
53. Sabatier, P.; Senderens, J. B., *Comptes Rendus Acad. Sci.* **1902**, 134, 514-516.
54. Lindlar, H., *Helv. Chim. Acta* **1952**, 35, 446-456.
55. Raney, M., *Ind. Eng. Chem. Res.* **1940**, 32, 1199-1203.
56. Covert, L. W.; Adkins, H., *J. Am. Chem. Soc.* **1932**, 54, 4116-4117.
57. Raney, M. Method of producing finely-divided nickel. 1927.
58. Mattson, B.; Foster, W.; Greimann, J.; Hoette, T.; Le, N.; Mirich, A.; Wankum, S.; Cabri, A.; Reichenbacher, C.; Schwanke, E., *J. Chem. Educ.* **2013**, 90, 613-619.
59. Horiuti, I.; Polanyi, M., *J. Chem. Soc. Faraday Trans.* **1934**, 30, 1164-1172.
60. Young, J. F.; Osborn, J. A.; Jardine, F. H.; Wilkinson, G., *Chem. Commun.* **1965**, 0, 131-132.
61. Jardine, F. H.; Osborn, J. A.; Wilkinson, G.; Young, J. F., *Chem. Ind.* **1965**, 0, 560-561.
62. Coffey, R. S. and Imperial Chemical Industries, British Patent no. 1, 121, 642, 1965.
63. Evans, D.; Osborn, J. A.; Jardine, F. H.; Wilkinson, G., *Nature* **1965**, 208, 1203-1204.
64. Schrock, R. R.; Osborn, J. A., *J. Am. Chem. Soc.* **1976**, 98, 2134-2143.
65. Schrock, R. R.; Osborn, J. A., *J. Am. Chem. Soc.* **1976**, 98, 2143-2147.
66. Schrock, R. R.; Osborn, J. A., *J. Am. Chem. Soc.* **1976**, 98, 4450-4455.
67. Schrock, R. R.; Osborn, J. A., *J. Chem. Soc., Chem. Commun.* **1970**, 0, 567-568.

68. Halpern, J., *Inorg. Chim. Acta* **1981**, *50*, 11-19.
69. Crabtree, R. H.; Demou, P. C.; Eden, D.; Mihelcic, J. M.; Parnell, C. A.; Quirk, J. M.; Morris, G. E., *J. Am. Chem. Soc.* **1982**, *104*, 6994-7001.
70. Wysocki, J.; Ortega, N.; Glorius, F., *Angew. Chem. Int. Ed.* **2014**, *53*, 8751-8755.
71. Wysocki, J.; Schleppehorst, C.; Glorius, F., *Synlett* **2015**, *26*, 1557-1562.
72. Chen, Z. P.; Zhou, Y. G., *Synthesis-Stuttgart* **2016**, *48*, 1769-1781.
73. Motevalli, S.; Sokeirik, Y.; Ghanem, A., *Eur. J. Org. Chem.* **2016**, *2016*, 1459-1475.
74. Giernoth, R.; Heinrich, H.; Adams, N. J.; Deeth, R. J.; Bargon, J.; Brown, J. M., *J. Am. Chem. Soc.* **2000**, *122*, 12381-12382.
75. Duckett, S. B.; Newell, C. L.; Eisenberg, R., *J. Am. Chem. Soc.* **1994**, *116*, 10548-10556.
76. Giernoth, R.; Huebler, P.; Bargon, J., *Angew. Chem. Int. Ed.* **1998**, *37*, 2473-2475.
77. Bowers, C. R.; Weitekamp, D. P., *J. Am. Chem. Soc.* **1987**, *109*, 5541-5542.
78. Pravica, M. G.; Weitekamp, D. P., *Chem. Phys. Lett.* **1988**, *145*, 255-258.
79. Eshuis, N.; Hermkens, N.; van Weerdenburg, B. J. A.; Feiters, M. C.; Rutjes, F. P. J. T.; Wijmenga, S. S.; Tessari, M., *J. Am. Chem. Soc.* **2014**, *136*, 2695-2698.
80. Eshuis, N.; Aspers, R. L. E. G.; van Weerdenburg, B. J. A.; Feiters, M. C.; Rutjes, F. P. J. T.; Wijmenga, S. S.; Tessari, M., *Angew. Chem. Int. Ed.* **2015**, *54*, 14527-14530.
81. Eshuis, N.; van Weerdenburg, B. J. A.; Feiters, M. C.; Rutjes, F. P. J. T.; Wijmenga, S. S.; Tessari, M., *Angew. Chem. Int. Ed.* **2015**, *54*, 1481-1484.
82. Lopez-Serrano, J.; Duckett, S. B.; Lledos, A., *J. Am. Chem. Soc.* **2006**, *128*, 9596-9597.

83. Atkinson, K. D.; Cowley, M. J.; Elliott, P. I. P.; Duckett, S. B.; Green, G. G. R.; Lopez-Serrano, J.; Whitwood, A. C., *J. Am. Chem. Soc.* **2009**, *131*, 13362-13368.
84. Dücker, E. B.; Kuhn, L. T.; Münnemann, K.; Griesinger, C., *J. Magn. Reson.* **2012**, *214*, 159-165.
85. Atkinson, K. D.; Cowley, M. J.; Duckett, S. B.; Elliott, P. I. P.; Green, G. G. R.; Lopez-Serrano, J.; Khazal, I. G.; Whitwood, A. C., *Inorg. Chem.* **2009**, *48*, 663-670.
86. Fekete, M.; Bayfield, O.; Duckett, S. B.; Hart, S.; Mewis, R. E.; Pridmore, N.; Rayner, P. J.; Whitwood, A., *Inorg. Chem.* **2013**, *52*, 13453-13461.
87. van Weerdenburg, B. J. A.; Glögler, S.; Eshuis, N.; Engwerda, A. H. J.; Smits, J. M. M.; de Gelder, R.; Appelt, S.; Wymenga, S. S.; Tessari, M.; Feiters, M. C.; Blumich, B.; Rutjes, F. P. J. T., *Chem. Commun.* **2013**, *49*, 7388-7390.
88. Cowley, M. J.; Adams, R. W.; Atkinson, K. D.; Cockett, M. C. R.; Duckett, S. B.; Green, G. G. R.; Lohman, J. A. B.; Kerssebaum, R.; Kilgour, D.; Mewis, R. E., *J. Am. Chem. Soc.* **2011**, *133*, 6134-6137.
89. Adams, R. W.; Duckett, S. B.; Green, R. A.; Williamson, D. C.; Green, G. G. R., *J. Chem. Phys.* **2009**, *131*, 194505 1-15.
90. Ivanov, K. L.; Pravdivtsev, A. N.; Yurkovskaya, A. V.; Vieth, H.-M.; Kaptein, R., *Prog. Nucl. Magn. Reson. Spectrosc.* **2014**, *81*, 1-36.
91. Barskiy, D. A.; Pravdivtsev, A. N.; Ivanov, K. L.; Kovtunov, K. V.; Koptyug, I. V., *Phys. Chem. Chem. Phys.* **2016**, *18*, 89-93.
92. Crabtree, R. H.; Davis, M. W., *J. Org. Chem.* **1986**, *51*, 2655-2661.
93. Lloyd, L. S.; Asghar, A.; Burns, M. J.; Charlton, A.; Coombes, S.; Cowley, M. J.; Dear, G. J.; Duckett, S. B.; Genov, G. R.; Green, G. G. R.; Highton, L. A. R.; Hooper, A. J. J.; Khan, M.; Khazal, I. G.; Lewis, R. J.; Mewis, R. E.; Roberts, A. D.; Ruddlesden, A. J., *Catal. Sci. Technol.* **2014**, *4*, 3544-3554.

94. Appleby, K. M.; Mewis, R. E.; Oлару, A. M.; Green, G. G. R.; Fairlamb, I. J. S.; Duckett, S. B., *Chem. Sci.* **2015**, *6*, 3981-3993.
95. Hoevener, J.-B.; Schwaderlapp, N.; Borowiak, R.; Lickert, T.; Duckett, S. B.; Mewis, R. E.; Adams, R. W.; Burns, M. J.; Highton, L. A. R.; Green, G. G. R.; Oлару, A.; Hennig, J.; von Elverfeldt, D., *Anal. Chem.* **2014**, *86*, 1767-1774.
96. Mewis, R. E.; Atkinson, K. D.; Cowley, M. J.; Duckett, S. B.; Green, G. G. R.; Green, R. A.; Highton, L. A. R.; Kilgour, D.; Lloyd, L. S.; Lohman, J. A. B.; Williamson, D. C., *Magn. Reson. Chem.* **2014**, *52*, 358-69.
97. Zeng, H.; Xu, J.; Gillen, J.; McMahon, M. T.; Artemov, D.; Tyburn, J.-M.; Lohman, J. A. B.; Mewis, R. E.; Atkinson, K. D.; Green, G. G. R.; Duckett, S. B.; van Zijl, P. C. M., *J. Magn. Reson.* **2013**, *237*, 73-78.
98. Holmes, A. J.; Rayner, P. J.; Cowley, M. J.; Green, G. G. R.; Whitwood, A. C.; Duckett, S. B., *Dalton Trans.* **2015**, *44*, 1077-1083.
99. Mewis, R. E.; Green, R. A.; Cockett, M. C. R.; Cowley, M. J.; Duckett, S. B.; Green, G. G. R.; John, R. O.; Rayner, P. J.; Williamson, D. C., *J. Phys. Chem. B* **2015**, *119*, 1416-1424.
100. Pravdivtsev, A. N.; Yurkovskaya, A. V.; Zimmermann, H.; Vieth, H.-M.; Ivanov, K. L., *RSC Adv.* **2015**, *5*, 63615-63623.
101. Morris, G. A.; Freeman, R., *J. Am. Chem. Soc.* **1979**, *101*, 760-762.
102. Natterer, J.; Bargon, J., *Prog. Nucl. Magn. Reson. Spectrosc.* **1997**, *31*, 293-315.
103. Barkemeyer, J.; Bargon, J.; Sengstschmid, H.; Freeman, R., *J. Magn. Reson. Ser. A* **1996**, *120*, 129-132.
104. Haake, M.; Natterer, J.; Bargon, J., *J. Am. Chem. Soc.* **1996**, *118*, 8688-8691.
105. Eisenschmid, T. C.; McDonald, J.; Eisenberg, R.; Lawler, R. G., *J. Am. Chem. Soc.* **1989**, *111*, 7267-7269.
106. Barkemeyer, J.; Haake, M.; Bargon, J., *J. Am. Chem. Soc.* **1995**, *117*, 2927-2928.

107. Theis, T.; Truong, M. L.; Coffey, A. M.; Shchepin, R. V.; Waddell, K. W.; Shi, F.; Goodson, B. M.; Warren, W. S.; Chekmenev, E. Y., *J. Am. Chem. Soc.* **2015**, *137*, 1404-1407.
108. Truong, M. L.; Theis, T.; Coffey, A. M.; Shchepin, R. V.; Waddell, K. W.; Shi, F.; Goodson, B. M.; Warren, W. S.; Chekmenev, E. Y., *J. Phys. Chem. C* **2015**, *119*, 8786-8797.
109. Burns, M. J.; Rayner, P. J.; Green, G. G. R.; Highton, L. A. R.; Mewis, R. E.; Duckett, S. B., *J. Phys. Chem. B* **2015**, *119*, 5020-5027.
110. Zhivonitko, V. V.; Skovpin, I. V.; Koptuyug, I. V., *Chem. Commun.* **2015**, *51*, 2506-2509.
111. Rayner, P. J.; Burns, M. J.; Olaru, A. M.; Norcott, P.; Fekete, M.; Green, G. G. R.; Highton, L. A. R.; Mewis, R. E.; Duckett, S. B., *Proc. Natl. Acad. Sci. U.S.A.* **2017**, *114*, E3188-E3194.
112. Duckett, S. B.; Mewis, R. E., *Acc. Chem. Res.* **2012**, *45*, 1247-1257.
113. Zeng, H.; Xu, J.; McMahon, M. T.; Lohman, J. A. B.; van Zijl, P. C. M., *J. Magn. Reson.* **2014**, *246*, 119-121.
114. Fekete, M.; Gibard, C.; Dear, G. J.; Green, G. G. R.; Hooper, A. J. J.; Roberts, A. D.; Cisnetti, F.; Duckett, S. B., *Dalton Trans.* **2015**, *44*, 7870-7880.
115. Spannring, P.; Reile, I.; Emondts, M.; Schleker, P. P. M.; Hermkens, N. K. J.; van der Zwaluw, N. G. J.; van Weerdenburg, B. J. A.; Tinnemans, P.; Tessari, M.; Blumich, B.; Rutjes, F. P. J. T.; Feiters, M. C., *Chemistry* **2016**, *22*, 9277-82.
116. Colell, J. F. P.; Emondts, M.; Logan, A. W. J.; Shen, K.; Bae, J.; Shchepin, R. V.; Ortiz, G. X.; Spannring, P.; Wang, Q.; Malcolmson, S. J.; Chekmenev, E. Y.; Feiters, M. C.; Rutjes, F.; Blumich, B.; Theis, T.; Warren, W. S., *J. Am. Chem. Soc.* **2017**, *139*, 7761-7767.
117. Mewis, R. E.; Fekete, M.; Green, G. G. R.; Whitwood, A. C.; Duckett, S. B., *Chem. Commun.* **2015**, *51*, 9857-9859.

118. Shi, F.; Coffey, A. M.; Waddell, K. W.; Chekmenev, E. Y.; Goodson, B. M., *Angew. Chem. Int. Ed.* **2014**, *53*, 7495-7498.
119. Shi, F.; Coffey, A. M.; Waddell, K. W.; Chekmenev, E. Y.; Goodson, B. M., *J. Phys. Chem. C* **2015**, *119*, 7525-7533.
120. Pileio, G.; Bowen, S.; Laustsen, C.; Tayler, M. C. D.; Hill-Cousins, J. T.; Brown, L. J.; Brown, R. C. D.; Ardenkjaer-Larsen, J. H.; Levitt, M. H., *J. Am. Chem. Soc.* **2013**, *135*, 5084-5088.
121. Stevanato, G.; Hill-Cousins, J. T.; Hakansson, P.; Roy, S. S.; Brown, L. J.; Brown, R. C. D.; Pileio, G.; Levitt, M. H., *Angew. Chem. Int. Ed.* **2015**, *54*, 3740-3743.
122. Feng, Y.; Theis, T.; Wu, T.-L.; Claytor, K.; Warren, W. S., *J. Chem. Phys.* **2014**, *141*, 134307 1-13.
123. Feng, Y.; Theis, T.; Liang, X.; Wang, Q.; Zhou, P.; Warren, W. S., *J. Am. Chem. Soc.* **2013**, *135*, 9632-9635.
124. Roy, S. S.; Rayner, P. J.; Norcott, P.; Green, G. G. R.; Duckett, S. B., *Phys. Chem. Chem. Phys.* **2016**, *18*, 24905-24911.
125. Occhipinti, G.; Jensen, V. R.; Tornroos, K. W.; Froystein, N. A.; Bjorsvik, H. R., *Tetrahedron* **2009**, *65*, 7186-7194.
126. Arduengo, A. J.; Gentry, F. P. J.; Taverkere, P. K.; Simmons, H. E. (E.I. Du Pont de Nemours & Co., USA). 2001.
127. Hintermann, L., *Beilstein J. Org. Chem.* **2007**, *3*, 1-5.
128. Ibrahim, H.; Bala, M. D., *Tetrahedron Lett.* **2014**, *55*, 6351-6353.
129. He, W.-P.; Zhou, B.-H.; Zhou, Y.-L.; Li, X.-R.; Fan, L.-M.; Shou, H.-W.; Li, J., *Tetrahedron Lett.* **2016**, *57*, 3152-3155.
130. Furstner, A.; Alcarazo, M.; Cesar, V.; Lehmann, C. W., *Chem. Commun.* **2006**, *0*, 2176-2178.

131. Zhang, X.; Wang, D. Y.; Emge, T. J.; Goldman, A. S., *Inorg. Chim. Acta* **2011**, *369*, 253-259.
132. Zhang, W.-H.; Chien, S. W.; Hor, T. S. A., *Coord. Chem. Rev.* **2011**, *255*, 1991-2024.
133. Chikkali, S. H.; van der Vlugt, J. I.; Reek, J. N. H., *Coord. Chem. Rev.* **2014**, *262*, 1-15.
134. Rees, W. M.; Atwood, J. D., *Organometallics* **1985**, *4*, 402-404.
135. Rees, W. M.; Churchill, M. R.; Fettinger, J. C.; Atwood, J. D., *Organometallics* **1985**, *4*, 2179-2185.
136. Bernard, K. A.; Atwood, J. D., *Organometallics* **1989**, *8*, 795-800.
137. Janik, T. S.; Bernard, K. A.; Churchill, M. R.; Atwood, J. D., *J. Organomet. Chem.* **1987**, *323*, 247-259.
138. Romain, C.; Fliedel, C.; Bellemin-Lapponnaz, S.; Dagorne, S., *Organometallics* **2014**, *33*, 5730-5739.
139. Zhang, M.; Ni, X.; Shen, Z., *Organometallics* **2014**, *33*, 6861-6867.
140. Giles, R.; O'Neill, J.; Lee, J. H.; Chiu, M. K.; Jung, K. W., *Tetrahedron Lett.* **2013**, *54*, 4083-4085.
141. Napoli, M.; Saturnino, C.; Cianciulli, E. I.; Varcamonti, M.; Zanfardino, A.; Tommonaro, G.; Longo, P., *J. Organomet. Chem.* **2013**, *725*, 46-53.
142. Horeglad, P.; Ablialimov, O.; Szczepaniak, G.; Dąbrowska, A. M.; Dranka, M.; Zachara, J., *Organometallics* **2014**, *33*, 100-111.
143. Arnold, P. L.; Scarisbrick, A. C.; Blake, A. J.; Wilson, C., *Chem. Commun.* **2001**, *0*, 2340-2341.
144. Weinberg, D. R.; Hazari, N.; Labinger, J. A.; Bercaw, J. E., *Organometallics* **2010**, *29*, 89-100.

145. Hansch, C.; Leo, A.; Taft, R. W., *Chem. Rev.* **1991**, *91*, 165-195.
146. Herde, J. L.; Lambert, J. C.; Senoff, C. V.; Cushing, M. A., In *Inorg. Syn.*, John Wiley & Sons, Inc.: 2007; pp 18-20.
147. Schuster, V. L.; Chi, Y.; Wasmuth, A. S.; Pottorf, R. S.; Olson, G. L. Prostaglandin Transporter Inhibitors and Uses Thereof. WO2011/37610 A1, 2011.
148. Somu, R. V.; Boshoff, H.; Qiao, C.; Bennett, E. M.; Barry, C. E.; Aldrich, C. C., *J. Med. Chem.* **2005**, *49*, 31-34.
149. Sagrera, G.; Seoane, G., *Synthesis-Stuttgart* **2009**, *0*, 4190-4202.
150. Peng, H. M.; Webster, R. D.; Li, X., *Organometallics* **2008**, *27*, 4484-4493.
151. Hore, P. J., *Nuclear Magnetic Resonance*. Oxford Science Publications: 2011.
152. Coluccini, C.; Grilli, S.; Lunazzi, L.; Mazzanti, A., *J. Org. Chem.* **2003**, *68*, 7266-7273.
153. Kappert, W.; Sander, W.; Landgrafe, C., *Liebigs Ann.-Recl.* **1997**, *1997*, 2519-2524.
154. Kownacki, I.; Kubicki, M.; Szubert, K.; Marciniak, B., *J. Organomet. Chem.* **2008**, *693*, 321-328.
155. Hillier, A. C.; Lee, H. M.; Stevens, E. D.; Nolan, S. P., *Organometallics* **2001**, *20*, 4246-4252.
156. Crabtree, R. H.; Felkin, H.; Khan, T.; Morris, G. E., *J. Organomet. Chem.* **1978**, *144*, C15-C17.
157. Crabtree, R. H.; Felkin, H.; Fillebeen-Khan, T.; Morris, G. E., *J. Organomet. Chem.* **1979**, *168*, 183-195.
158. Martin, M.; Sola, E.; Torres, O.; Plou, P.; Oro, L. A., *Organometallics* **2003**, *22*, 5406-5417.

159. Searles, K.; Pink, M.; Caulton, K. G.; Mindiola, D. J., *Dalton Trans.* **2012**, *41*, 9619-9622.
160. Deutsch, P. P.; Eisenberg, R., *Chem. Rev.* **1988**, *88*, 1147-1161.
161. Alvarez, P.; Gimeno, J.; Lastra, E.; García-Granda, S.; Van der Maelen, J. F.; Bassetti, M., *Organometallics* **2001**, *20*, 3762-3771.
162. Campora, J.; Lopez, J. A.; Palma, P.; del Rio, D.; Carmona, E.; Valerga, P.; Graiff, C.; Tiripicchio, A., *Inorg. Chem.* **2001**, *40*, 4116-4126.
163. Stott, K.; Keeler, J.; Van, Q. N.; Shaka, A. J., *J. Magn. Reson.* **1997**, *125*, 302-324.
164. Luo, Y.-R.; Kerr, J. A., *CRC Handbook of Chemistry and Physics* **2012**, *89*.
165. Cronin, L.; Nicasio, M. C.; Perutz, R. N.; Peters, R. G.; Roddick, D. M.; Whittlesey, M. K., *J. Am. Chem. Soc.* **1995**, *117*, 10047-10054.
166. Geoffroy, G. L.; Isci, H.; Litrenti, J.; Mason, W. R., *Inorg. Chem.* **1977**, *16*, 1950-1955.
167. Brady, R.; Flynn, B. R.; Geoffroy, G. L.; Gray, H. B.; Peone, J.; Vaska, L., *Inorg. Chem.* **1976**, *15*, 1485-1488.
168. Geoffroy, G. L.; Hammond, G. S.; Gray, H. B., *J. Am. Chem. Soc.* **1975**, *97*, 3933-3936.
169. Nicasio, M. C.; Perutz, R. N.; Tekkaya, A., *Organometallics* **1998**, *17*, 5557-5564.
170. Hall, C.; Jones, W. D.; Mawby, R. J.; Osman, R.; Perutz, R. N.; Whittlesey, M. K., *J. Am. Chem. Soc.* **1992**, *114*, 7425-7435.
171. Campian, M. V.; Perutz, R. N.; Procacci, B.; Thatcher, R. J.; Torres, O.; Whitwood, A. C., *J. Am. Chem. Soc.* **2012**, *134*, 3480-3497.

172. Kelly, R. A.; Clavier, H.; Giudice, S.; Scott, N. M.; Stevens, E. D.; Bordner, J.; Samardjiev, I.; Hoff, C. D.; Cavallo, L.; Nolan, S. P., *Organometallics* **2008**, *27*, 202-210.
173. Wang, D.; Astruc, D., *Chem. Rev.* **2015**, *115*, 6621-6686.
174. Gildner, P. G.; Colacot, T. J., *Organometallics* **2015**, *34*, 5497-5508.
175. Cavinato, G.; Toniolo, L., *Molecules* **2014**, *19*, 15116-15161.
176. Fang, W. W.; Zhu, H. B.; Deng, Q. Y.; Liu, S. L.; Liu, X. Y.; Shen, Y. J.; Tu, T., *Synthesis-Stuttgart* **2014**, *46*, 1689-1708.
177. Mikhailine, A. A.; Morris, R. H., *Inorg. Chem.* **2010**, *49*, 11039-11044.
178. Colacot, T. J., *Platinum Met. Rev.* **2011**, *55*, 84-90.
179. Astruc, D., *Anal. Bioanal. Chem.* **2011**, *399*, 1811-1814.
180. Hu, A.; Ngo, H. L.; Lin, W., *Angew. Chem. Int. Ed.* **2004**, *43*, 2501-2504.
181. Zhao, J.; Hesslink, H.; Hartwig, J. F., *J. Am. Chem. Soc.* **2001**, *123*, 7220-7227.
182. Hammett, L. P., *Chem. Rev.* **1935**, *17*, 125-136.
183. Hammett, L. P., *J. Am. Chem. Soc.* **1937**, *59*, 96-103.
184. Rimoldi, M.; Fodor, D.; van Bokhoven, J. A.; Mezzetti, A., *Chem. Commun.* **2013**, *49*, 11314-11316.
185. Gottker-Schnetmann, I.; Brookhart, M., *J. Am. Chem. Soc.* **2004**, *126*, 9330-9338.
186. Gottker-Schnetmann, I.; White, P. S.; Brookhart, M., *Organometallics* **2004**, *23*, 1766-1776.
187. Choualeb, A.; Lough, A. J.; Gusev, D. G., *Organometallics* **2007**, *26*, 5224-5229.
188. Wisniewski, L. L.; Mediati, M.; Jensen, C. M.; Zilm, K. W., *J. Am. Chem. Soc.* **1993**, *115*, 7533-7534.
189. Mediati, M.; Tachibana, G. N.; Jensen, C. M., *Inorg. Chem.* **1992**, *31*, 1827-1832.

190. Mediati, M.; Tachibana, G. N.; Jensen, C. M., *Inorg. Chem.* **1990**, *29*, 3-5.
191. Li, S. H.; Hall, M. B.; Eckert, J.; Jensen, C. M.; Albinati, A., *J. Am. Chem. Soc.* **2000**, *122*, 2903-2910.
192. Eckert, J.; Jensen, C. M.; Koetzle, T. F.; Lehusebo, T.; Nicol, J.; Wu, P., *J. Am. Chem. Soc.* **1995**, *117*, 7271-7272.
193. Hebden, T. J.; Goldberg, K. I.; Heinekey, D. M.; Zhang, X. W.; Emge, T. J.; Goldman, A. S.; Krogh-Jespersen, K., *Inorg. Chem.* **2010**, *49*, 1733-1742.
194. Polukeev, A. V.; Marcos, R.; Ahlquist, M. S. G.; Wendt, O. F., *Organometallics* **2016**, *35*, 2600-2608.
195. Hauger, B. E.; Gusev, D.; Caulton, K. G., *J. Am. Chem. Soc.* **1994**, *116*, 208-214.
196. Russegger, P.; Brickmann, J., *Chem. Phys. Lett.* **1975**, *30*, 276-278.
197. Ugi, I.; Marquarding, D.; Klusacek, H.; Gillespie, P.; Ramirez, F., *Acc. Chem. Res.* **1971**, *4*, 288-296.
198. Couzijn, E. P. A.; Slootweg, J. C.; Ehlers, A. W.; Lammertsma, K., *J. Am. Chem. Soc.* **2010**, *132*, 18127-18140.
199. Bailar, J. C., *J. Inorg. Nucl. Chem.* **1958**, *8*, 165-175.
200. Rodger, A.; Johnson, B. F. G., *Inorg. Chem.* **1988**, *27*, 3061-3062.
201. Zampella, G.; Fantucci, P.; De Gioia, L., *Chem. Commun.* **2010**, *46*, 8824-8826.
202. Ray, P.; Dutt, N. K., *J. Indian Chem. Soc.* **1943**, *20*, 81.
203. Amati, M.; Lelj, F., *Theor. Chem. Acc.* **2008**, *120*, 447-457.
204. Xu, W.; Lough, A. J.; Morris, R. H., *Inorg. Chem.* **1996**, *35*, 1549-1555.
205. Park, S. H.; Lough, A. J.; Yap, G. P. A.; Morris, R. H., *J. Organomet. Chem.* **2000**, *609*, 110-122.

206. Stevens, R. C.; Bau, R.; Milstein, D.; Blum, O.; Koetzle, T. F., *J. Chem. Soc., Dalton Trans.* **1990**, 0, 1429-1432.
207. Lau, C. P.; Ng, S. M.; Jia, G. C.; Lin, Z. Y., *Coord. Chem. Rev.* **2007**, 251, 2223-2237.
208. Belkova, N. V.; Epstein, L. M.; Filippov, O. A.; Shubina, E. S., *Chem. Rev.* **2016**, 116, 8545-8587.
209. Crabtree, R. H.; Siegbahn, P. E. M.; Eisenstein, O.; Rheingold, A. L., *Acc. Chem. Res.* **1996**, 29, 348-354.
210. Lee, J. C.; Rheingold, A. L.; Muller, B.; Pregosin, P. S.; Crabtree, R. H., *J. Chem. Soc., Chem. Commun.* **1994**, 0, 1021-1022.
211. Gottker-Schnetmann, I.; Heinekey, D. M.; Brookhart, M., *J. Am. Chem. Soc.* **2006**, 128, 17114-17119.
212. Gelabert, R.; Moreno, M.; Lluch, J. M.; Lledos, A.; Pons, V.; Heinekey, D. M., *J. Am. Chem. Soc.* **2004**, 126, 8813-8822.
213. Li, J.; Dickson, R. M.; Ziegler, T., *J. Am. Chem. Soc.* **1995**, 117, 11482-11487.
214. Morris, R. H., *Coord. Chem. Rev.* **2008**, 252, 2381-2394.
215. Sato, T.; Hamada, Y.; Sumikawa, M.; Araki, S.; Yamamoto, H., *Ind. Eng. Chem. Res.* **2014**, 53, 19331-19337.
216. Smith, Q. A.; Gordon, M. S.; Slipchenko, L. V., *J. Phys. Chem. A* **2011**, 115, 4598-4609.
217. Hohenstein, E. G.; Sherrill, C. D., *J. Phys. Chem. A* **2009**, 113, 878-886.
218. Mishra, B. K.; Sathyamurthy, N., *J. Phys. Chem. A* **2005**, 109, 6-8.
219. Adam, W.; Grimison, A.; Hoffmann, R.; Deortiz, C. Z., *J. Am. Chem. Soc.* **1968**, 90, 1509-1516.

220. Fan, H. Y.; Moliva, C. D.; Eliason, J. K.; Olson, J. L.; Green, D. D.; Gealy, M. W.; Ulness, D. J., *Chem. Phys. Lett.* **2009**, *479*, 43-46.
221. Findlay, T. J. V.; Kidman, A. D., *Aust. J. Chem.* **1965**, *18*, 521.
222. Eisenschmid, T. C.; Kirss, R. U.; Deutsch, P. P.; Hommeltoft, S. I.; Eisenberg, R.; Bargon, J.; Lawler, R. G.; Balch, A. L., *J. Am. Chem. Soc.* **1987**, *109*, 8089-8091.
223. Duckett, S. B.; Mawby, R. J.; Partridge, M. G., *Chem. Commun.* **1996**, *0*, 383-384.
224. Torres, O.; Procacci, B.; Halse, M. E.; Adams, R. W.; Blazina, D.; Duckett, S. B.; Eguillor, B.; Green, R. A.; Perutz, R. N.; Williamson, D. C., *J. Am. Chem. Soc.* **2014**, *136*, 10124-10131.
225. Shi, F.; He, P.; Best, Q. A.; Groome, K.; Truong, M. L.; Coffey, A. M.; Zimay, G.; Shchepin, R. V.; Waddell, K. W.; Chekmenev, E. Y.; Goodson, B. M., *J. Phys. Chem. C* **2016**, *120*, 12149-12156.
226. Zhou, Z. J.; Yu, J.; Colell, J. F. P.; Laasner, R.; Logan, A.; Barskiy, D. A.; Shchepin, R. V.; Chekmenev, E. Y.; Bum, V.; Warren, W. S.; Theis, T., *J. Phys. Chem. Lett.* **2017**, *8*, 3008-3014.
227. Barskiy, D. A.; Shchepin, R. V.; Tanner, C. P. N.; Colell, J. F. P.; Goodson, B. M.; Theis, T.; Warren, W. S.; Chekmenev, E. Y., *ChemPhysChem* **2017**, *18*, 1493-1498.
228. Colell, J. F. P.; Logan, A. W. J.; Zhou, Z. J.; Shchepin, R. V.; Barskiy, D. A.; Ortiz, G. X.; Wang, Q.; Malcolmson, S. J.; Chekmenev, E. Y.; Warren, W. S.; Theis, T., *J. Phys. Chem. C* **2017**, *121*, 6626-6634.
229. Aguilar, J. A.; Adams, R. W.; Duckett, S. B.; Green, G. G. R.; Kandiah, R., *J. Magn. Reson.* **2011**, *208*, 49-57.
230. Aguilar, J. A.; Elliott, P. I. P.; Lopez-Serrano, J.; Adams, R. W.; Duckett, S. B., *Chem. Commun.* **2007**, *0*, 1183-1185.
231. Harris, D. C., *J. Chem. Educ.* **1998**, *75*, 119-121.

232. Belenky, P.; Bogan, K. L.; Brenner, C., *Trends Biochem. Sci.* **2007**, *32*, 12-19.
233. Knip, M.; Douek, F. I.; Moore, T. W. P.; Gillmor, A. H.; McLean, M. A. E.; Bingley, J. P.; Gale, M. E. A., *Diabetologia* **2000**, *43*, 1337-1345.
234. Hövener, J.-B.; Knecht, S.; Schwaderlapp, N.; Hennig, J.; von Elverfeldt, D., *ChemPhysChem* **2014**, *15*, 2451-2457.
235. Theis, T.; Truong, M.; Coffey, A. M.; Chekmenev, E. Y.; Warren, W. S., *J. Magn. Reson.* **2014**, *248*, 23-26.
236. Daniele, V.; Legrand, F.-X.; Berthault, P.; Dumez, J.-N.; Huber, G., *ChemPhysChem* **2015**, *16*, 3413-3417.
237. Ratajczyk, T.; Gutmann, T.; Bernatowicz, P.; Buntkowsky, G.; Frydel, J.; Fedorczyk, B., *Chem. Eur. J.* **2015**, *21*, 12616-12619.
238. Lloyd, L. S.; Adams, R. W.; Bernstein, M.; Coombes, S.; Duckett, S. B.; Green, G. G. R.; Lewis, R. J.; Mewis, R. E.; Sleigh, C. J., *J. Am. Chem. Soc.* **2012**, *134*, 12904-12907.
239. Glöggl, S.; Mueller, R.; Colell, J.; Emondts, M.; Dabrowski, M.; Bluemich, B.; Appelt, S., *Phys. Chem. Chem. Phys.* **2011**, *13*, 13759-13764.
240. Moreno, K. X.; Nasr, K.; Milne, M.; Sherry, A. D.; Goux, W. J., *J. Magn. Reson.* **2015**, *257*, 15-23.
241. Halse, M. E., *TrAC, Trends Anal. Chem.* **2016**, *83*, Part A, 76-83.
242. Morgan, L. D.; Baker, H.; Yeoman, M. S.; Patel, B. A., *Analyst* **2012**, *137*, 1409-1415.
243. Fisar, Z., *Prog. Neuropsychopharmacol. Biol. Psychiatry* **2016**, *69*, 112-124.
244. Aburawi, E. H.; Souid, A. K., *Eur. J. Drug Metab. Ph.* **2014**, *39*, 293-299.
245. Ickert, I.; Herten, M.; Vogl, M.; Ziskoven, C.; Zilkens, C.; Krauspe, R.; Kircher, J., *Knee Surg. Sports Traumatol. Arthrosc.* **2015**, *23*, 2674-2681.

246. Kandemir, T.; Schuster, M. E.; Senyshyn, A.; Behrens, M.; Schlogl, R., *Angew. Chem. Int. Ed.* **2013**, *52*, 12723-12726.
247. Shah, T. B.; Shiny, R. S.; Dixit, R. B.; Dixit, B. C., *J. Saudi Chem. Soc.* **2014**, *18*, 985-992.
248. Monir, K.; Ghosh, M.; Mishra, S.; Majee, A.; Hajra, A., *Eur. J. Org. Chem.* **2014**, *2014*, 1096-1102.
249. Chakraborty, A.; Jana, S.; Kibriya, G.; Dey, A.; Hajra, A., *RSC Adv.* **2016**, *6*, 34146-34152.
250. Gruber, S.; Neuburger, M.; Pfaltz, A., *Organometallics* **2013**, *32*, 4702-4711.
251. Bianchini, C.; Farnetti, E.; Graziani, M.; Kaspar, J.; Vizza, F., *J. Am. Chem. Soc.* **1993**, *115*, 1753-1759.
252. Vazquez-Serrano, L. D.; Owens, B. T.; Buriak, J. M., *Inorg. Chim. Acta* **2006**, *359*, 2786-2797.
253. Brown, J. A.; Irvine, S.; Kennedy, A. R.; Kerr, W. J.; Andersson, S.; Nilsson, G. N., *Chem. Commun.* **2008**, *0*, 1115-1117.
254. Lee, H. M.; Jiang, T.; Stevens, E. D.; Nolan, S. P., *Organometallics* **2001**, *20*, 1255-1258.
255. Ruddlesden, A. J.; Mewis, R. E.; Green, G. G. R.; Whitwood, A. C.; Duckett, S. B., *Organometallics* **2015**, *34*, 2997-3006.
256. Horn, E.; Tiekink, E. R. T.; Jones, G. P.; Naiola, B. P.; Paleg, L. G., *Acta Crystallogr. C* **1990**, *46*, 1575-1576.
257. White, D.; Taverner, B. C.; Coville, N. J.; Wade, P. W., *J. Organomet. Chem.* **1995**, *495*, 41-51.
258. Mann, B. E.; Masters, C.; Shaw, B. L., *J. Inorg. Nucl. Chem.* **1971**, *33*, 2195-2204.
259. Esteruelas, M. A.; Lopez, A. M.; Olivan, M., *Chem. Rev.* **2016**, *116*, 8770-8847.

260. Gruet, K.; Clot, E.; Eisenstein, O.; Lee, D. H.; Patel, B.; Macchioni, A.; Crabtree, R. H., *New J. Chem.* **2003**, *27*, 80-87.
261. Kovacevic, A.; Grundemann, S.; Miecznikowski, J. R.; Clot, E.; Eisenstein, O.; Crabtree, R. H., *Chem. Commun.* **2002**, *0*, 2580-2581.
262. Landau, S. E.; Groh, K. E.; Lough, A. J.; Morris, R. H., *Inorg. Chem.* **2002**, *41*, 2995-3007.
263. Loza, M.; Faller, J. W.; Crabtree, R. H., *Inorg. Chem.* **1995**, *34*, 2937-2941.
264. Dobereiner, G. E.; Wu, J. G.; Manas, M. G.; Schley, N. D.; Takase, M. K.; Crabtree, R. H.; Hazari, N.; Maseras, F.; Nova, A., *Inorg. Chem.* **2012**, *51*, 9683-9693.
265. Eicher, J. J.; Snoep, L. J.; Rohwer, M. J., *Metabolites* **2012**, *2*, 818-843.
266. Olsen, R. J.; Olsen, J. A.; Giles, G. A., *J. Chem. Educ.* **2010**, *87*, 956-957.
267. Her, C.; Alonzo, A. P.; Vang, J. Y.; Torres, E.; Krishnan, V. V., *J. Chem. Educ.* **2015**, *92*, 1943-1948.
268. Kehlbeck, J. D.; Slack, C. C.; Turnbull, M. T.; Kohler, S. J., *J. Chem. Educ.* **2014**, *91*, 734-738.
269. Butler, B. J.; Thomas, D. S.; Hook, J. M.; Harper, J. B., *Magn. Reson. Chem.* **2016**, *54*, 423-428.
270. Singh, U. K.; Albert Vannice, M., *J. Catal.* **2000**, *191*, 165-180.
271. Singh, U. K.; Vannice, M. A., *Appl. Catal. A* **2001**, *213*, 1-24.
272. Chinn, M. S.; Eisenberg, R., *J. Am. Chem. Soc.* **1992**, *114*, 1908-1909.
273. Kating, P.; Wandelt, A.; Selke, R.; Bargon, J., *J. Phys. Chem.* **1993**, *97*, 13313-13317.
274. Hubler, P.; Giernoth, R.; Kummerle, G.; Bargon, J., *J. Am. Chem. Soc.* **1999**, *121*, 5311-5318.

275. Wildschutz, S.; Hubler, P.; Bargon, J., *ChemPhysChem* **2001**, *2*, 328-331.
276. Tang, J. A.; Gruppi, F.; Fleysher, R.; Sodickson, D. K.; Canary, J. W.; Jerschow, A., *Chem. Commun.* **2011**, *47*, 958-960.
277. Kruger, M. B.; Selle, C.; Heller, D.; Baumann, W., *J. Chem. Eng. Data* **2012**, *57*, 1737-1744.
278. Esteruelas, M. A.; Gonzalez, I.; Herrero, J.; Oro, L. A., *J. Organomet. Chem.* **1998**, *551*, 49-53.
279. Esteruelas, M. A.; Lopez, A. M.; Oro, L. A.; Perez, A.; Schulz, M.; Werner, H., *Organometallics* **1993**, *12*, 1823-1830.
280. Esteruelas, M. A.; Oliván, M.; Oro, L. A.; Schulz, M.; Sola, E.; Werner, H., *Organometallics* **1992**, *11*, 3659-3664.
281. Andriollo, A.; Esteruelas, M. A.; Meyer, U.; Oro, L. A.; Sanchezdelgado, R. A.; Sola, E.; Valero, C.; Werner, H., *J. Am. Chem. Soc.* **1989**, *111*, 7431-7437.
282. Bacchi, A.; Carcelli, M.; Costa, M.; Leporati, A.; Leporati, E.; Pelagatti, P.; Pelizzi, C.; Pelizzi, G., *J. Organomet. Chem.* **1997**, *535*, 107-120.
283. Kirss, R. U.; Eisenschmid, T. C.; Eisenberg, R., *J. Am. Chem. Soc.* **1988**, *110*, 8564-8566.
284. Simpson, P. V.; Radacki, K.; Braunschweig, H.; Schatzschneider, U., *J. Organomet. Chem.* **2015**, *782*, 116-123.
285. Iali, W.; Green, G. G. R.; Hart, S. J.; Whitwood, A. C.; Duckett, S. B., *Inorg. Chem.* **2016**, *55*, 11639-11643.
286. Nelson, D. J.; Truscott, B. J.; Slawin, A. M. Z.; Nolan, S. P., *Inorg. Chem.* **2013**, *52*, 12674-12681.
287. Viciano, M.; Mas-Marza, E.; Sanau, M.; Peris, E., *Organometallics* **2006**, *25*, 3063-3069.

288. Zhang, Y. Z.; Clavadetscher, J.; Bachmann, M.; Blacque, O.; Venkatesan, K., *Inorg. Chem.* **2014**, *53*, 756-771.
289. Ibarra-Vazquez, M. F.; Cortes-Llamas, S. A.; Peregrina-Lucano, A. A.; Alvarado-Rodriguez, J. G.; Manriquez-Gonzalez, R.; Lopez-Dellamary, F. A.; Moreno-Brambila, M. I.; Rangel-Salas, I. I., *Inorg. Chim. Acta* **2016**, *451*, 209-215.
290. Kanzelberger, M.; Zhang, X. W.; Emge, T. J.; Goldman, A. S.; Zhao, J.; Incarvito, C.; Hartwig, J. F., *J. Am. Chem. Soc.* **2003**, *125*, 13644-13645.
291. Gupta, G.; Murray, B. S.; Dyson, P. J.; Therrien, B., *J. Organomet. Chem.* **2014**, *767*, 78-82.
292. Herberhold, M.; Guo-Xin, J.; Rheingold, A. L., *J. Organomet. Chem.* **1998**, *570*, 241-246.
293. Reineri, F.; Viale, A.; Ellena, S.; Boi, T.; Daniele, V.; Gobetto, R.; Aime, S., *Angew. Chem. Int. Ed.* **2011**, *50*, 7350-7353.
294. Dolomanov, O. V.; Bourhis, L. J.; Gildea, R. J.; Howard, J. A. K.; Puschmann, H., *J. Appl. Crystallogr.* **2009**, *42*, 339-341.
295. Sheldrick, G. M., *Acta Crystallogr. A* **2008**, *64*, 112-122.